

# **PROGRESS IN RESEARCH**

**April 1, 2010 - March 31, 2011**

## **CYCLOTRON INSTITUTE**

**Texas A&M University**

**College Station, Texas**

**PROGRESS IN RESEARCH**

**APRIL 1, 2010- MARCH 31, 2011**

**Prepared By**

**The Cyclotron Institute Staff**

**Texas A&M University**

**College Station, TX 77843-3366**

**Phone: (979) 845-1411**

**Fax: (979) 845-1899**

**Web: <http://cyclotron.tamu.edu>**

**August 2011**

## TABLE OF CONTENTS

**Introduction** ..... X  
R.E. Tribble, Director

### SECTION I: NUCLEAR STRUCTURE, FUNDAMENTAL INTERACTIONS AND ASTROPHYSICS

**Splitting of the giant monopole resonance in  $^{92}\text{Mo}$**  ..... I-1  
D. H. Youngblood, Y. -W. Lui, Krishichayan, J. Button, S. Shlomo, and M. Urin

**Giant monopole resonances in nuclei around A ~ 90 region**..... I-3  
Krishichayan, Y. -W. Lui, J. Button, and D. H. Youngblood

**Measurement of the  $^{14}\text{C}(\text{d},\text{p})^{15}\text{C}$  reaction at  $E_d=60$  MeV** ..... I-5  
M. McCleskey, A. M. Mukhamedzhanov, L. Trache, R. E. Tribble, V. Goldberg, Y.-W. Lui,  
B. Roeder, E. Simmons, and A. Spiridon

**The beta delayed proton and gamma decay of  $^{27}\text{P}$  for nuclear astrophysics**..... I-9  
E. Simmons, L. Trache, A. Banu, M. McCleskey, A. Saastamoinen, B. Roeder, A. Spiridon,  
R.E. Tribble, T. Davinson, P. J. Woods, G. J. Lotay, J. Wallace, and D. Doherty

**SAMURAI-Si – a status report**..... I-13  
L. Trache and R. E. Tribble

**Superallowed beta decay** ..... I-15  
J. C. Hardy, I. S. Towner, V. E. Jacob, N. Nica, L. Chen, V. Horvat, H. I. Park, J. Goodwin,  
L. Trache, and R. E. Tribble

**Half-life of the superallowed  $\beta$ -emitter  $^{46}\text{V}$**  ..... I-19  
H. I. Park, J. C. Hardy, V. E. Jacob, L. Chen, J. Goodwin, V. Horvat, N. Nica,  
E. Simmons, L. Trache, and R. E. Tribble

**High precision half-life measurement of the superallowed  $\beta$ -emitter  $^{38}\text{Ca}$** ..... I-23  
H. I. Park, J. C. Hardy, V. E. Jacob, A. Banu, L. Chen, V. V. Golovko, J. Goodwin,  
V. Horvat, N. Nica, E. Simmons, L. Trache, and R. E. Tribble

**Measurement of branching-ratios in the  $\beta$  decay of  $^{38}\text{Ca}$** ..... I-27  
H. I. Park, J. C. Hardy, V. E. Jacob, L. Chen, J. R. Goodwin, V. Horvat, N. Nica,  
L. Trache, and R. E. Tribble

<b>JYFLTRAP : <math>Q_{EC}</math>-values of the superallowed decays of <math>^{10}\text{C}</math>, <math>^{34}\text{Ar}</math>, <math>^{38}\text{Ca}</math> and <math>^{46}\text{V}</math> .....</b>	<b>I-29</b>
J. C. Hardy	
<b>Tests of internal-conversion theory with precise <math>\gamma</math>- and x-ray spectroscopy: the case of <math>^{119}\text{Sn}^m</math>.....</b>	<b>I-32</b>
N. Nica, J. C. Hardy, V. Horvath, V. E. Iacob, V. Siller, and M. B. Trzhaskovskaya	
<b>Test of claims that radioactive half-lives depend on the Earth-Sun distance.....</b>	<b>I-34</b>
J. R. Goodwin, V. E. Iacob, and J. C. Hardy	
<b>United States nuclear data program evaluated nuclear structure data file (ENSDF): Five years of data evaluation at Texas A&amp;M .....</b>	<b>I-38</b>
N. Nica, J. C. Hardy, and B. Singh	
<b>TRIUMF : Precise half-life measurement of the superallowed <math>\beta^+</math> emitter <math>^{38}\text{K}^m</math> .....</b>	<b>I-39</b>
J. C. Hardy and V. E. Iacob	
<b>Isospin symmetry breaking in the <math>\beta</math> decay of <math>^{32}\text{Cl}</math>.....</b>	<b>I-41</b>
C. Bordeanu, A. García, J. C. Hardy, V. E. Iacob, D. Melconian, N. Nica, H. I. Park, G. Tabacaru, L. Trache, I. S. Towner, S. Triambak, R. E. Tribble, and Y. Zhai	
<b>Penning trap facility – Program for the study of fundamental weak interaction .....</b>	<b>I-44</b>
R. S. Behling, B. Fenker, M. Mehlman, D. Melconian, and P. D. Shidling	
<b>Precise life-time measurements of <math>T = 1/2</math> mirror transition .....</b>	<b>I-46</b>
R. S. Behling, B. Fenker, J. C. Hardy, V. E. Iacob, M. Mehlman, D. Melconian, B. T. Roeder, P. D. Shidling, and H. Stephens	
<b>Upgrade of the <math>^{37}\text{K}</math> asymmetry measurement experiment .....</b>	<b>I-48</b>
S. Behling, B. Fenker, M. Mehlman, D. Melconian, and P. Shidling	
<b>Production and separation of new secondary beams <math>^{30}\text{P}</math> and <math>^{27}\text{P}</math> .....</b>	<b>I-49</b>
E. Simmons, L. Trache, B. Roeder, M. McCleskey, A. Spiridon, and R.E. Tribble	
<b>Using the K-150 cyclotron to measure proton reaction cross sections on separated isotopes.....</b>	<b>I-52</b>
M. H. Mohzoon, R. J. Charity, J. Elson, R. Shane, L. G. Sobotka, M. McCleskey, E. Simmons, and L. Trache	
<b>The commissioning run for the Texas-Edinburgh-Catania silicon array (TECSA): Measurement of the <math>d(^{14}\text{C},p)^{15}\text{C}</math> at 11.7 MeV/u .....</b>	<b>I-54</b>
B. T. Roeder, M. McCleskey, L. Trache, A. A. Alharbi, A. Banu, S. Cherubini, T. Davinson, V. Z. Goldberg, M. Gulino, R. G. Pizzone, E. Simmons, R. Spartà, A. Spiridon, C. Spitaleri, J. P. Wallace, R. E. Tribble, and P. J. Woods	

<b>Toward understanding relativistic heavy-ion collisions with the STAR detector at RHIC .....</b>	<b>I-57</b>
M. Cervantes, M. Codrington, A. Hamed, S. Mioduszewski, Y. Mohammed, and the STAR Collaboration	
<b>New trigger logic for the STAR forward meson spectrometer .....</b>	<b>I-61</b>
J. C. Martinez, P. Djawotho, C. A. Gagliardi, and the STAR Collaboration	
<b>Spin physics with STAR at RHIC .....</b>	<b>I-63</b>
Z. Chang, P. Djawotho, J. L. Drachenberg, C. A. Gagliardi, L. Huo, R. E. Tribble, and the STAR Collaboration	
<b>TWIST: Measuring the space-time structure of muon decay .....</b>	<b>I-67</b>
C. A. Gagliardi, R. E. Tribble, and the TWIST Collaboration	

## SECTION II: HEAVY ION REACTIONS

<b>The nuclear matter free symmetry energy at <math>0.03 \leq \rho/\rho_0 \leq 0</math> .....</b>	<b>II-1</b>
L. Qin, K. Hagel, R. Wada, J. B. Natowitz, S. Shlomo, A. Bonasera, G. Roepke, Z. Chen, M. Huang, J. Wang, H. Zheng, S. Kowalski, M. Barbui, M. Rodrigues, K. Schmidt, D. Fabris, M. Lunardon, S. Moretto, G. Nebbia, S. Pesente, V. Rizzi, G. Viesti, M. Cinausero, G. Prete, T. Keutgen, Y. El Masri, and Z. Majka	
<b>Laboratory tests of astrophysical equations of state at low densities .....</b>	<b>II-3</b>
L. Qin, K. Hagel, R. Wada, J. B. Natowitz, S. Shlomo, A. Bonasera, G. Roepke, Z. Chen, M. Huang, J. Wang, H. Zheng, S. Kowalski, M. Barbui, M. Rodrigues, K. Schmidt, D. Fabris, M. Lunardon, S. Moretto, G. Nebbia, S. Pesente, V. Rizzi, G. Viesti, M. Cinausero, G. Prete, T. Keutgen, Y. El Masri, and Z. Majka	
<b>Search for heavy and superheavy systems in <math>^{197}\text{Au} + ^{232}\text{Th}</math> collisions near the Coulomb barrier ....</b>	<b>II-5</b>
M. Barbui, K. Hagel, J. B. Natowitz, M. R. D. Rodrigues, K. Schmidt, R. Wada, Z. Majka, H. Zheng, M. Barbarino and A. Bonasera	
<b>Energy calibration of the <math>^{40}\text{Ca} + ^{40}\text{Ca}</math> data taken on the NIMROD-ISiS array .....</b>	<b>II-8</b>
K. Schmidt, C. Bottosso, J. B. Natowitz, K. Hagel, R. Wada, M. Huang, A. Bonasera, M. Barbui, M. Rodrigues, G. Liu, G. Viesti, S. Moretto, G. Prete, S. Pesente, D. Fabris, Y. El Masri, T. Keutgen, S. Kowalski, and A. Kumar	
<b>Neutron yield from d-d reaction in laser induced gas cluster explosions. ....</b>	<b>II-11</b>
M. Barbui, A. Bonasera, K. Hagel, J. B. Natowitz, M. R. D. Rodrigues, K. Schmidt, R. Wada, H. Zheng, M. Barbarino, W. Bang, T. Ditmire, G. Dyer, H. Quevedo, and A. Bernstein	

<b>New gas stopper for heavy element chemistry research.....</b>	<b>II-14</b>
M. C. Alfonso and C. M. Folden III	
<b>Projectile influence on EVR production in <math>^{48}\text{Ca}</math>, <math>^{54}\text{Cr}</math> + <math>^{162}\text{Dy}</math> fusion-evaporation reactions and its relation to synthesis of element 120.....</b>	<b>II-19</b>
D. A. Mayorov, M. C. Alfonso, T. A. Werke, and C. M. Folden III	
<b>Investigation of the de-excitation mechanism in Fermi energy heavy ion collisions.....</b>	<b>II-23</b>
R. Tripathi, A. Bonasera, S. Wuenschel, L. W. May, Z. Kohley, P. Marini, A. McIntosh, G. A. Souliotis, S. Galanopoulos, K. Hagel, D. V. Shetty, K. Huseman, S. N. Soisson, B. C. Stein, and S. J. Yennello	
<b>Investigation of the role of quasiprojectile isospin in nuclear fragmentation .....</b>	<b>II-26</b>
R. Tripathi, A. Bonasera, S. Wuenschel, L. W. May, Z. Kohley, P. Marini, A. McIntosh, G. A. Souliotis, S. Galanopoulos, K. Hagel, D. V. Shetty, K. Huseman, S. N. Soisson, B. C. Stein, and S. J. Yennello	
<b>Isoscaling studies in <math>^{86}\text{Kr}+^{112,124}\text{Sn}</math>, <math>^{197}\text{Au}</math> reactions at <math>E_{lab}=30</math> MeV/nucleon.....</b>	<b>II-30</b>
R. Tripathi, B. C. Stein, Z. Kohley, L. W. May, P. Marini, A. Bonasera, G. A. Souliotis, S. Wuenschel, S. Galanopoulos, D. V. Shetty, K. Huseman, S. N. Soisson, and S. J. Yennello	
<b>Source reconstruction and caloric curves in <math>^{70}\text{Zn} + ^{70}\text{Zn}</math> at <math>E/A = 35\text{MeV}</math> .....</b>	<b>II-34</b>
A. B. McIntosh, A. Bonasera, S. Galanopoulos, K. Hagel, L. Heilborn, Z. Kohley, P. Marini, L. W. May, A. Raphelt, D. V. Shetty, W. B. Smith, S. N. Soisson, G. A. Souliotis, B. C. Stein, R. Tripathi, S. Wuenschel, and S. J. Yennello	
<b>Isoscaling, isobaric yield ratio and the symmetry energy: interpretation of the results with SMM .....</b>	<b>II-36</b>
P. Marini, A. Botvina, A. Bonasera, Z. Kohley, L. W. May, R. Tripathi, S. Wuenschel, and S. J. Yennello	
<b>Constraining the symmetry energy at supra-saturation densities with measurements of neutron and proton elliptic flow - the Microball at GSI.....</b>	<b>II-41</b>
P. Marini, P. Cammarata, L. Heilborn, L. May and S. J. Yennello for the ASY-EOS Collaboration	
<b>Constraining the symmetry energy with isotopic yield distributions.....</b>	<b>II-44</b>
P. Marini, G. Souliotis, A. Bonasera, S. N. Soisson, R. Tripathi, L. W. May, A. McIntosh, and S. J. Yennello	
<b>Observed suppression of fermionic fluctuations in heavy-ion reactions.....</b>	<b>II-48</b>
B. C. Stein, Hua Zheng, Aldo Bonasera, and S. J. Yennello	

<b>Isospin diffusion and equilibration in heavy-ion reactions .....</b>	<b>II-51</b>
L. W. May, Z. Kohley, S. Behling, G. Bonasera, J. Erchinger, L. Heilborn, P. Marini, A. McIntosh, A. Raphelt, G. Souliotis, B. Stein, R. Tripathi, T. Werke, and S. J. Yennello	
<b>Investigation of the affect of a Coulomb force on velocity distributions in multifragmentation...</b>	<b>II-53</b>
L. Heilborn, G. Souliotis, S. Soisson, P. Cammarata, P. Marini, L. W. May, A. McIntosh, A. Raphelt, B. Stein, and S. Yennello	
<b>Studies on antisymmetrized molecular dynamics (AMD) and isoscaling .....</b>	<b>II-56</b>
A. Raphelt, Z. Kohley, P. Cammarata, P. Marini, L. W. May, A. McIntosh, and S. J. Yennello	
<b>Production of neutron-rich nuclides in peripheral collisions of <math>^{86}\text{Kr}</math> (15 MeV/nucleon) projectiles with <math>^{64}\text{Ni}</math>, <math>^{58}\text{Ni}</math> and <math>^{124}\text{Sn}</math>, <math>^{112}\text{Sn}</math> targets.....</b>	<b>II-59</b>
G. A. Souliotis, M. Veselsky, S. Galanopoulos, Z. Kohley, L. May, D. V. Shetty, B. C. Stein, and S. J. Yennello	

### SECTION III: NUCLEAR THEORY

<b>Astrophysical <math>S</math> factor for the <math>^{15}\text{N}(p,\gamma)^{16}\text{O}</math> reaction .....</b>	<b>III-1</b>
A. M. Mukhamedzhanov, M. La Cognata, and V. Kroha	
<b>High accuracy <math>^{18}\text{O}(p,\alpha)^{15}\text{N}</math> reaction rate at AGB nucleosynthesis relevant temperatures.....</b>	<b>III-2</b>
M. La Cognata, C. Spitaleri, and A. M. Mukhamedzhanov	
<b>Low-energy d+d fusion reactions via the Trojan horse method .....</b>	<b>III-3</b>
A. Tumino, C. Spitaleri, A. M. Mukhamedzhanov, S. Typel, M. Aliotta, V. Burjan, M. Gimenez del Santo, G. G. Kiss, V. Kroha, Z. Hons, M. La Cognata, L. Lamia, J. Mrazek, R. G. Pizzone, S. Piskor, G. G. Rapisarda, S. Romano, M. L. Sergi, and R. Sparta	
<b>New theory of deuteron stripping to bound states and resonances .....</b>	<b>III-4</b>
A. M. Mukhamedzhanov	
<b>Reexamination of the astrophysical <math>S</math> factor for the <math>\alpha+d\rightarrow ^6\text{Li}+\gamma</math> reaction .....</b>	<b>III-5</b>
A. M. Mukhamedzhanov, L. D. Blokhintsev, and B. F. Irgaziev	
<b>Unitary correlation in nuclear reaction theory: Separation of nuclear reactions and spectroscopic factors .....</b>	<b>III-6</b>
A. M. Mukhamedzhanov and A. S. Kadyrov	
<b>Density and temperature of fermions and bosons from quantum fluctuations.....</b>	<b>III-7</b>
Hua Zheng and Aldo Bonasera	

<b>Charmonium production and elliptic flow in relativistic heavy ion collisions .....</b>	<b>III-14</b>
T. Song, C. M. Ko, S. H. Lee, and J. Xu	
<b>Density matrix expansion for the isospin- and momentum-dependent MDI interaction.....</b>	<b>III-16</b>
J. Xu and C. M. Ko	
<b>Dilepton production in schematic causal viscous hydrodynamics.....</b>	<b>III-18</b>
T. Song, K. C. Han, and C. M. Ko	
<b>Effects of triangular flow on di-hadron azimuthal correlations in relativistic heavy ion collisions.....</b>	<b>III-20</b>
J. Xu and C. M. Ko	
<b>Identifying multi-quark hadrons from heavy ion collisions .....</b>	<b>III-21</b>
S. Cho, T. Furumoto, T. Hyodo, D. Jido, C. M. Ko, S. H. Lee, M. Nielsen, A. Ohnishi, T. Sekihara, S. Yasui, and K. Yazaki	
<b>Pb-Pb collisions at <math>\sqrt{s_{NN}} = 2.76</math> TeV in a multiphase transport model.....</b>	<b>III-23</b>
J. Xu and C. M. Ko	
<b>Determining the proton and neutron transition matrix elements from Coulomb-nuclear interference in hadron inelastic scattering .....</b>	<b>III-25</b>
S. Shlomo, M. R. Anders, and M. R. D. Rodrigues	
<b>Isoscalar and isovector giant resonances in <math>^{40}\text{Ca}</math> and <math>^{48}\text{Ca}</math>.....</b>	<b>III-26</b>
M. R. Anders, S. Shlomo, T. Sil, D. H. Youngblood, Y.-W. Lui, and Krishichayan	
<b>Isoscalar giant monopole resonance in <math>^{48}\text{Ca}</math> .....</b>	<b>III-28</b>
Y. -W. Lui, D. H. Youngblood, S. Shlomo, X. Chen, Y. Tokimoto, Krishichayan, M. Anders, and J. Button	
<b>Event-by-event jet quenching .....</b>	<b>III-31</b>
R. J. Fries, R. Rodriguez, and E. Ramirez	
<b>The initial state of high energy nuclear collisions .....</b>	<b>III-33</b>
R. J. Fries and G. Chen	
<b>Charmonium production in heavy-ion collisions at the large hadron collider.....</b>	<b>III-34</b>
X. Zhao and R. Rapp	
<b>Scaling of elliptic flow, recombination and sequential freeze-out of hadrons in heavy-ion collisions .....</b>	<b>III-37</b>
Min He, Rainer J. Fries, and Ralf Rapp	

<b>Self-consistent evaluation of charm and charmonium properties in the quark-gluon plasma .....</b>	<b>III-40</b>
F. Riek and R. Rapp	

<b>Thermal relaxation of charm in hadronic matter .....</b>	<b>III-42</b>
Min He, Rainer J. Fries, and Ralf Rapp	

<b>Hartree-Fock-Bogoliubov calculations of the isospin-symmetry-breaking correction in superallowed Fermi beta decay .....</b>	<b>III-44</b>
I. S. Towner and J. C. Hardy	

**SECTION IV: ATOMIC, MOLECULAR AND MATERIALS SCIENCE**

<b>Kinetic energy release in the dissociations of doubly and triply charged molecular ions .....</b>	<b>IV-1</b>
V. Horvat and R. L. Watson	

**SECTION V: SUPERCONDUCTING CYCLOTRON, INSTRUMENTATION AND RIB UPGRADE**

<b>K500 operations and development .....</b>	<b>V-1</b>
D. P. May, G. J. Kim, H. L. Clark, and F. P. Abegglen	

<b>Texas A&amp;M cyclotron radiation effects facility April 1, 2010 – March 31, 2011 .....</b>	<b>V-3</b>
H. L. Clark, J. Brinkley, G. Chubarian, V. Horvat, B. Hyman, B. Roeder, and G. Tabacaru	

<b>Cyclotron computing .....</b>	<b>V-5</b>
R. Burch and K. Hagel	

<b>Cyclotron Institute upgrade project .....</b>	<b>V-7</b>
H. L. Clark, F. Abegglen, G. Chubarian, G. Derrig, G. Kim, D. May, and G. Tabacaru	

<b>Shielding evaluation for the light ion guide and heavy ion guide .....</b>	<b>V-12</b>
G. Tabacaru, H. L. Clark, G. Chubaryan, G. Derrig, F. P. Abegglen, and L. Rodriguez	

<b>Active bases in NIMROD .....</b>	<b>V-15</b>
K. Hagel, A. J. Henryson and T. Cowden	

<b>Experimental and theoretical cross section study for production of medically</b>	
---	--

<b>important radioisotopes <math>^{52}\text{Mn}</math>, <math>^{51}\text{Cr}</math> and <math>^{46,47}\text{Sc}</math>.....</b>	<b>V-17</b>
A. Alharbi, M. McCleskey, B. Roeder, A. Spiridon, E. Simmons, L. Trache, and R. E. Tribble	
<b>Production cross-sections of medical radioisotopes from proton bombardment of <math>^{\text{nat}}\text{Mo}</math> .....</b>	<b>V-20</b>
A. Spiridon, A. A. Alharbi, M. McCleskey, A. Banu, G. Tabacaru, B. Roeder, E. Simmons, L. Trache, and R. E. Tribble	
<b>First in-beam commissioning test of AIDA.....</b>	<b>V-24</b>
T. Davinson, Z. Liu, J. P. Wallace, P. J. Woods, R. D. Page, P. J. Coleman-Smith, I. Lazarus, S. Letts, V. F. E. Pucknell, J. Simpson, D. Braga, S. L. Thomas, L. Trache, A. Alharbi, A. Banu, M. McCleskey, B. Roeder, E. Simmons, A. Spiridon, and R. E. Tribble	
<b>Design and use of a new implantation station for beta-delayed decay experiments .....</b>	<b>V-26</b>
E. Simmons, M. McCleskey, and L. Trache	
<b>TABS – an ASIC-based electronics system at Texas A&amp;M .....</b>	<b>V-28</b>
M. McCleskey, J. Elson, L. G. Sobotka, L. Trache, J. Blackmon, M. Matos, B. Roeder, E. Simmons, A. Spiridon, and R. E. Tribble	
<b>AstroBox – a new type of low energy proton detector .....</b>	<b>V-31</b>
E. Simmons, M. McCleskey, A. Spiridon, L. Trache, B. Roeder, R. E. Tribble E. Pollacco, M. Kebbiri, and G. Pascovici	
<b>SAMURAI TPC: Conceptual design of a time projection chamber .....</b>	<b>V-33</b>
A. B. McIntosh, J. Barney, J. Dunn, J. Gilbert, T. Isobe, K. Klein, M. Famiano, F. Lu, W. G. Lynch, N. W. Maass, T. Murakami, R. Olsen, A. Taketani, M. B. Tsang, and S. J. Yennello	
<b>Delta-ray simulations for the SAMURAI-Si project at RIKEN .....</b>	<b>V-35</b>
Brian Roeder	
<b>The Wiener VME-USB controller for data acquisition: A status report.....</b>	<b>V-39</b>
Kris Hagel and Brian Roeder	
<b>Diffusion of <math>^{18,19}\text{Ne}</math> out of mylar tape.....</b>	<b>V-42</b>
V. E. Iacob and J. C. Hardy	
<b>Digital beta counting for high-precision nuclear beta-decay experiments .....</b>	<b>V-46</b>
L. Chen and J. C. Hardy	
<b>Preparation of an <math>^{115}\text{In}</math> source.....</b>	<b>V-50</b>
J. Goodwin, N. Nica, and J. C. Hardy	

<b>Spectra of time differences between consecutive pulses measured with a new TDC-based data-acquisition system.....</b>	<b>V-51</b>
V. Horvat and J. C. Hardy	

<b>Assembly and test runs of decay detector for ISGMR study .....</b>	<b>V-55</b>
J. Button, R. Polis, C. Canahui, Krishichayan, Y. -W. Lui, and D. H. Youngblood	

**SECTION VI: PUBLICATIONS**

<b>Papers published .....</b>	<b>VI-1</b>
-------------------------------	-------------

**SECTION VII: APPENDIX**

<b>Talks presented .....</b>	<b>VII-1</b>
<b>Research personnel and engineering staff .....</b>	<b>VII-9</b>
<b>Students.....</b>	<b>VII-10</b>
<b>Organizational chart.....</b>	<b>VII-11</b>
<b>Graduate degree students.....</b>	<b>VII-12</b>
<b>Institute colloquia and seminars.....</b>	<b>VII-13</b>

**Introduction**  
**April 1, 2010 – March 31, 2011**

Progress in research and operations at the Texas A&M Cyclotron Institute is summarized in this report for the period April, 1, 2010 through March 31, 2011. The format follows that of previous years. Sections I through IV contain reports from individual research projects. Operation and technical developments are given in Section V. Section VI lists the publications with Cyclotron Institute authors and the Appendix gives additional information including talks presented by members of the Institute during the past year. Once again, the full volume of this year's Progress in Research is available only on our web site (<http://cyclotron.tamu.edu>). *Since most of the contributions presented here are truly reports on progress in research, results and conclusions should not be quoted from the report without the consent of the authors.*

We have now completed 6 1/2 years of the Upgrade Project, which ultimately will give us accelerated radioactive beams at intermediate energies. The progress on the project continues to be good. The K150 cyclotron is operational for both positive-ion and negative-ion beams. In the fall of 2010, we completed the installation and testing of new radiation monitoring equipment and during our January, 2011 shutdown we integrated the two accelerators and all of the beam lines into a single interlock system. We have used the K150 cyclotron for several test experiments in the spring. The ion-guide cave shielding was installed starting in late November, 2010. The shielding was tested for radiation leaks with a high intensity proton beam in the spring of 2011. Work is now underway to mount all of the power supplies needed for the ions guides and the Charge Breeding ECR ion source on top of the shielding blocks. We are anticipating beam into the light-ion guide during the fall of 2011.

The Nuclear Solutions Institute was approved by the TAMU Board of Regents in September, 2010. With the approval, we have begun searches for two senior level radiochemistry faculty members and a senior level experimental nuclear physics faculty member. We hope to fill those positions during this next year. Starting in summer, 2010, an architect firm began developing plans for adding a second floor to the office wing of our building. As is typical, it has taken longer than anticipated to move from the plans to the start of construction. The most likely time now for a construction start is October, 2011.

As in previous reports, I have pulled out some highlights of work over the past year. Those that are noteworthy are given below.

Research highlights:

- (1) New measurements of half-lives for  $^{38}\text{Ca}$ ,  $^{38}\text{K}^m$  and  $^{46}\text{V}$  have been completed along with improvements in QEC values for  $^{10}\text{C}$ ,  $^{34}\text{Ar}$ ,  $^{38}\text{Ca}$  and  $^{46}\text{V}$ . These measurements provide substantial improvement in the precision of known super-allowed transitions.

- (2) A new value for the ANC of  $^{14}\text{C}+n\rightarrow^{15}\text{C}$  has been determined from several different neutron transfer reactions. The ANC is used to obtain the  $^{14}\text{C}(n,\gamma)^{15}\text{C}$  capture cross section. The new result is in good agreement with the most recent direct measurement.
- (3) A thermal-rate equation approach with in-medium charmonium spectral properties has been used to predict  $J/\psi$  observables at the Large Hadron Collider; first ALICE data presented at Quark Matter 2011 confirm these predictions.
- (4) Experimental investigations of cluster formation in low-density nuclear matter have been employed to derive equilibrium constraints for cluster formation. The data have been used to test predictions of several theoretical astrophysical EOS models and provide important new constraints on these model calculations. Measurements of the density dependence of the free symmetry-energy coefficients in this low-density clustered matter have been found to be in very good agreement with values calculated using a quantum statistical model which incorporates in-medium effects on the binding energies.
- (5) New measurements of the  $\gamma$  decay of  $^{32}\text{Cl}$  have revealed the largest ever observed isospin-symmetry breaking in a super-allowed Fermi transition of 5.4(8)%. The result is in good agreement with shell-model calculations and it validates the calculations for other *sd*-shell nuclei.
- (6) The  $^{162}\text{Dy}(^{54}\text{Cr},4n)^{212}\text{Th}$  reaction has been studied as an analog for the production of element 120 in the  $^{248}\text{Cm}(^{54}\text{Cr},4n)^{298}120$  reaction. The results suggest that the cross section for this new element will be extremely sensitive to the size of its fission barrier.
- (7) The role of isospin asymmetry of the fragmenting source in multi-fragmentation was studied using the Landau free energy approach, which is applicable to systems in the vicinity of a critical point. The mirror-nuclei yield ratios show an exponential dependence on the isospin asymmetry of the fragmenting source, as expected from the model, suggesting that it is an order parameter.
- (8) Using a multiphase transport model, we have shown that the triangular flow is appreciable in relativistic heavy-ion collisions as a result of fluctuations in collision geometry and has a significant effect on the away-side structure in the dihadron azimuthal correlations triggered by emitted jets.
- (9) A new, high-precision measurement of the longitudinal double-spin asymmetry for inclusive jet production has been completed with STAR that significantly reduces the uncertainty of the gluon polarization in the proton.

- (10) A new theory of (d,p) stripping to bound states and resonances has been developed that provides a universal R-matrix approach to treat both binary reactions and stripping in terms of the same observables – reduced widths (ANCs) and R-matrix boundary conditions.
- (11) The influence of fluctuations and inhomogeneity on measurements of jet quenching in high energy nuclear collisions has been studied for the first time.

As in the past, Institute scientists remain active in a number of collaborative research efforts around the world. Major programs include: mass measurements using the Penning Traps at Argonne National Laboratory and the University of Jyväskylä; continued work with the STAR collaboration at RHIC; and the measurement of neutron beta decay with the UCNA collaboration.

Once again, I am indebted to Dr. Y.-W. Lui for assembling this report.

R.E. Tribble  
August 8, 2011

## **SECTION I**

# **NUCLEAR STRUCTURE, FUNDAMENTAL INTERACTIONS, AND ASTROPHYSICS**

## Splitting of the giant monopole resonance in $^{92}\text{Mo}$

D. H. Youngblood, Y. -W. Lui, Krishichayan, J. Button, S. Shlomo, and M. Urin<sup>1</sup>

The mass 90 region is a transitional region for the giant monopole resonance(GMR). In  $^{90}\text{Zr}$  about 78% of the strength lies in a symmetric peak[1], with the rest in a shoulder about 7 MeV higher in energy. In heavier (spherical) nuclei the monopole strength is concentrated in a mostly symmetrical peak, and in lighter nuclei the strength is located either in a peak with significant tailing to the high energy side or with obvious broad components above the main peak. We investigated[2]  $^{90,92}\text{Zr}$ ,  $^{92,96,100}\text{Mo}$  and the results are shown in Fig. 1.  $^{92}\text{Mo}$  stood out with about 65% of the E0 EWSR strength located in a broad high energy peak ( $\sim 24$  MeV) and the remainder in a narrower peak at  $\sim 16.9$  MeV[2]. Another contribution to this report describes a second  $^{92}\text{Mo}$  experiment which verified the earlier result, and also shows results for  $^{94}\text{Zr}$  and  $^{98}\text{Mo}$ .

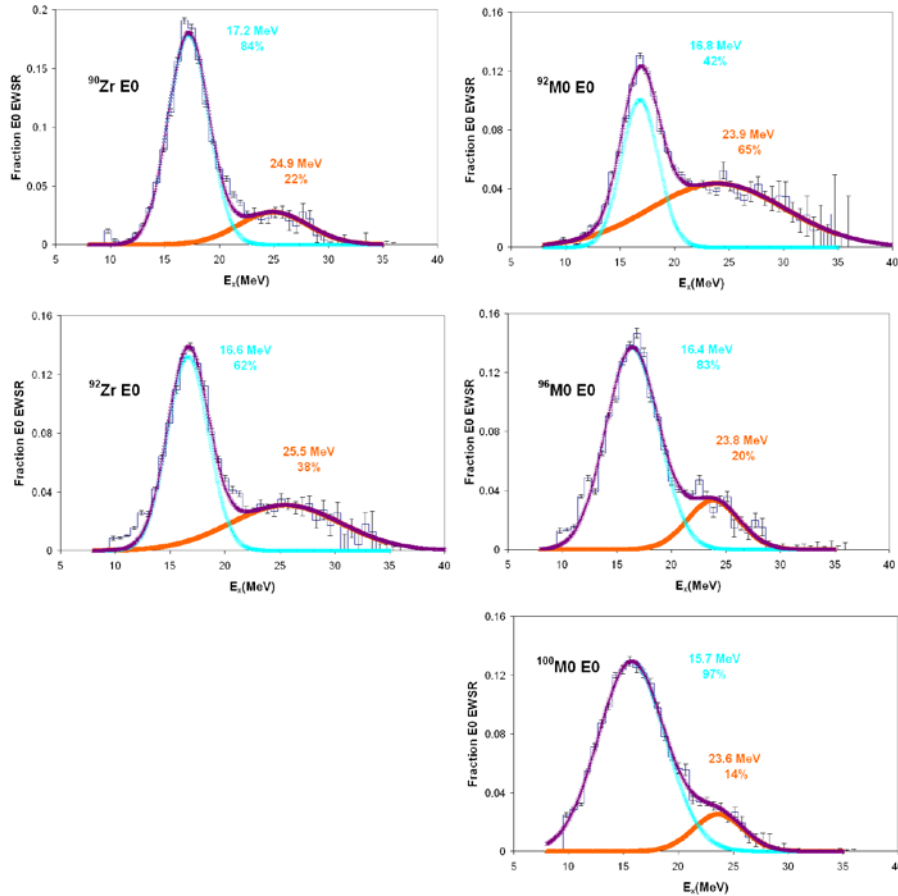


**FIG. 1.** GMR strength in Zr and Mo nuclei. The centroids and E0 EWSR strengths of the two components obtained with collective model transition densities are shown.

To attempt to understand the behavior in  $^{92}\text{Mo}$ , in a collaboration with Dr. Shlomo(TAMU) and Dr. Michael Urin (Moscow), Dr. Urin's group calculated microscopic transition densities for  $^{92}\text{Mo}$  using

Woods-Saxon based RPA and we used them to calculate cross sections for E0 excitation at  $E_x=17.5$  MeV and 27.5 MeV. Using the collective transition density, the cross section for excitation of the ISGMR at  $E_x=27.5$  MeV is  $\sim 1/5$  that at  $E_x=17.5$  MeV, whereas with the microscopic transition density this ratio is  $\sim 1/12$ . Thus, using the microscopic transition density will enhance the upper peak by more than a factor of 2 in  $^{92}\text{Mo}$  and result in the upper peak alone exhausting more than 100% of the EWSR.

We also investigated the possibility that this second peak could be the ‘‘overtone’’ ISGMR (operator  $r^4Y_{00}$ ) [3]. Dr. Shlomo provided the collective transition density and sum rule for the overtone and we did 2 calculations. The first assumed that the second peak was entirely due to the overtone. That would require 228% of the sum rule for the overtone and leave only the 42% of the EWSR for  $r^2Y_{00}$  in the lower peak (lower panel in Fig. 2). We then placed the overtone at twice the energy of the ISGMR with twice the width, with 100% of the  $r^4Y_{00}$  sum rule and subtracted that from the  $^{92}\text{Mo}$  E0 strength shown in Fig. 1. This is shown in the upper panel of Fig. 2 and leaves E0 strength corresponding to 91% of the  $r^2Y_{00}$  sum rule, which is quite plausible. Unfortunately this interpretation does not work for  $^{90}\text{Zr}$  or  $^{96,100}\text{Mo}$ , because the  $r^4Y_{00}$  strength would considerably exceed the strength seen experimentally in the higher energy region.

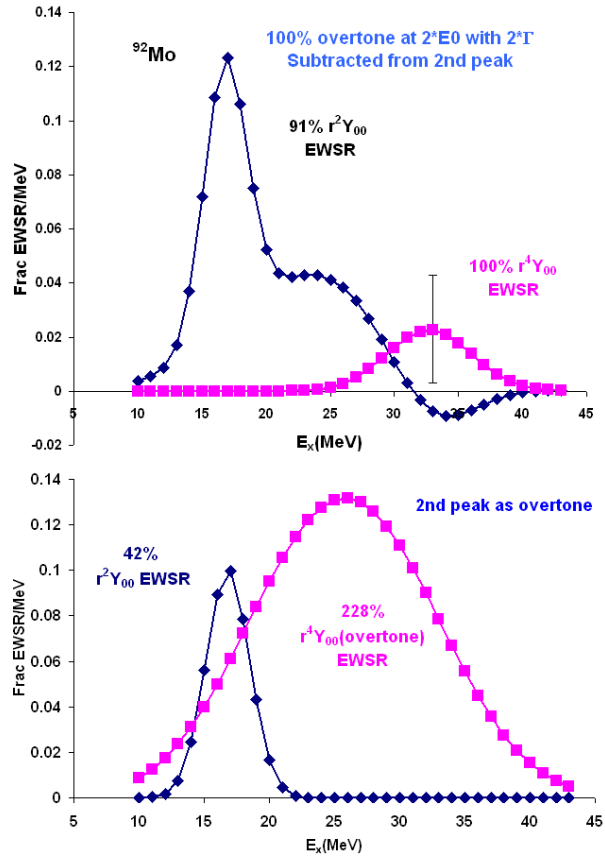


FIG. 2. Two assumptions about overtone in  $^{92}\text{Mo}$ .

- [1] D.H. Youngblood, H.L. Clark and Y.-W. Lui, Phys. Rev. Lett. **82**, 691(1999); D.H. Youngblood, Y.-W. Lui, B. John, Y. Tokimoto, , H.L. Clark, and X. Chen, Phys. Rev. C **69**, 054312 (2004).
- [2] D.H. Youngblood, Y.-W. Lui, Krishichayan, J. Button, and R. Polis, *Progress in Research*, Cyclotron Institute, Texas A&M University (2008-2009), p. I-1.
- [3] M.L. Gorelik, I.V. Safonov, and M.H. Urin, Phys. Rev. C **69**, 054322 (2004);

## Giant monopole resonances in nuclei around A ~ 90 region

Krishichayan, Y. -W. Lui, J. Button, and D. H. Youngblood

The giant resonances are small amplitude collective modes of excitations of nuclei and have been extensively studied for several decades over a wide mass region. The study of the isoscalar giant monopole resonance (ISGMR), in which protons and neutrons in a nucleus move in-phase and oscillate with spherical symmetry, is important because its energy ( $E_{\text{GMR}}$ ) is related to the incompressibility of nuclear matter ( $K_{\text{nm}}$ ). In the scaling model, the energy of GMR is given by  $E_{\text{GMR}} = (m_3/m_1)^{1/2}$ , where  $m_k = \Sigma(E_n - E_0)^k |<0|r^2|n>|^2$ . Using alpha inelastic scattering we have studied giant resonances in nuclei over a wide range of A ( $12 \leq A \leq 208$ ) using the Texas A&M K500 cyclotron facility.

In a previous report [1], we discussed the results of measurements of the ISGMR in Zr and Mo isotopes ( $^{90,92}\text{Zr}$ ,  $^{92,96,100}\text{Mo}$ ), emphasizing the occurrence of the broad peaks in the higher side of excitation energy. Whereas in  $^{90}\text{Zr}$ , higher component contains ~ 22% of the E0 EWSR, in  $^{92}\text{Zr}$ , the higher component at  $E_x = 25.5$  MeV contains 38% of the E0 strength and in  $^{92}\text{Mo}$ , the higher broad peak contains 65% of the E0 EWSR. Due to the strength of this higher energy component, the centroid energy for the ISGMR in  $^{92}\text{Mo}$  is 2 MeV higher than in  $^{90}\text{Zr}$ . High energy components of ISGMR in  $^{96,100}\text{Mo}$  isotopes were also apparent, but with strengths comparable to  $^{90}\text{Zr}$ .

In order to confirm those results we re-measured the E0 strength in  $^{92}\text{Mo}$  and in the same experimental run studied  $^{94}\text{Zr}$ , and  $^{98}\text{Mo}$  to provide additional ISGMR information on ZR and Mo isotopes. The GR data for these nuclei were collected with inelastic scattering of 240 MeV alpha particles using the MDM spectrometer at small angles including  $0^\circ$ . The horizontal acceptance of the spectrometer was  $4^\circ$  and ray tracing was used to reconstruct the scattering angle. The vertical acceptance was set at  $2^\circ$ . The focal plane detector measured position and angle in the scattering plane and covered from  $E_x \sim 8$  MeV to  $E_x > 55$  MeV, depending on the scattering angle. Position resolution of approximately 0.9 mm and scattering angle resolution of about  $0.09^\circ$  were obtained. The multipole components of the giant resonance peak were obtained by dividing the peak into multiple regions (bins) by excitation energy [2] and then comparing the angular distributions obtained for each of these bins to distorted wave Born approximation (DWBA) calculations. There are some subjective elements to this analysis, particularly the choice of shapes and amplitudes for the continuum, which we try to mitigate somewhat by doing a number of analyses with different background choices, then averaging the final results. The analysis of the previous data was done by one of us (Youngblood), so in an attempt to remove any personal bias, the analysis of this data was done by Krishichayan. As an additional check, Krishichayan also did the DWBA calculations used in his multipole fits.

Fig. 1 shows the E0 strengths Krishichayan obtained for  $^{94}\text{Zr}$  and  $^{92,98}\text{Mo}$ . The results for  $^{92}\text{Mo}$  are in good agreement with those reported in Ref. [1], with ~ 57% of the E0 EWSR contained in a high energy component of ISGMR centered at 24.1 MeV, while the lower peak at 16.7 MeV contains only ~ 43 % of total E0 strength. In  $^{98}\text{Mo}$  the upper component at 23.9 MeV contains 17% of the E0 EWSR, right between the 20% in  $^{96}\text{Mo}$  and the 14% in  $^{100}\text{Mo}$ . The distribution of E0 strength in  $^{94}\text{Zr}$  is similar to  $^{90}\text{Zr}$  with the higher component containing 22% of E0 strength whereas lower narrow peak contains 84%

of E0 EWSR. The lower peak in  $^{94}\text{Zr}$  is somewhat broader than in  $^{90}\text{Zr}$ , consistent with the trend in the Mo isotopes where the lower peak broadens considerably as the neutron number increases.

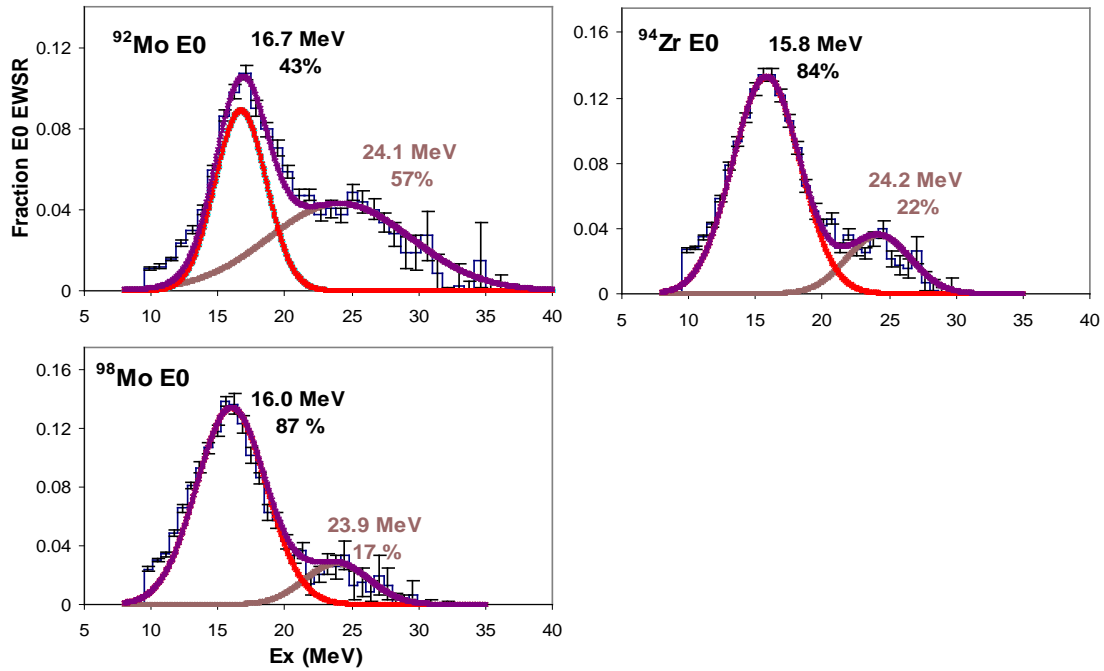


**FIG. 1.** ISGMR strength in  $^{92}\text{Mo}$ ,  $^{98}\text{Mo}$ , and  $^{94}\text{Zr}$  nuclei. The centroids and E0 EWSR strengths of the two components obtained with collective model transition densities are shown.

- [1] D.H. Youngblood, Y.-W. Lui, Krishichayan, J. Button, and R. Polis, *Progress in Research*, Cyclotron Institute, Texas A&M University (2008-2009), p. I-1.
- [2] D.H. Youngblood *et al.*, *Phys. Rev. C* **69**, 054312 (2004).

## Measurement of the $^{14}\text{C}(\text{d},\text{p})^{15}\text{C}$ reaction at $E_d=60$ MeV

M. McCleskey, A. M. Mukhamedzhanov, L. Trache, R. E. Tribble, V. Goldberg, Y.-W. Lui,  
B. Roeder, E. Simmons, and A. Spiridon

This reaction has recently been measured at Texas A&M University Cyclotron Institute using a 60 MeV total energy deuteron beam from the K500 super-conducting cyclotron. The deuteron beam impinged on a thin ( $\sim 335$   $\mu\text{g}/\text{cm}^2$ ), high-purity, self-supporting  $^{14}\text{C}$  target and reaction products were measured using the MDM spectrometer and the Oxford ionization chamber detector. This measurement was previously attempted in February 2008, however the available solid angle defining slit proved to be too big ( $4^\circ \times 2^\circ$ ) for the acceptance of the Oxford detector. Typically a  $4^\circ \times 1^\circ$  slit is used with this detector, however no slit of adequate thickness for deuterons of this energy was available, and while a raytrace calculation indicated that the larger slit would be acceptable, this proved not to be the case. A good particle identification was obtained from the 2008 experiment, however, the measurement had to be repeated to obtain the angular distribution needed.

This measurement is part of an ongoing project [1] to investigate the use of the asymptotic normalization coefficient (ANC) to fix the external contribution to the DWBA transition matrix element and thereby experimentally determine the single particle ANC (SPANC) in order to remove this otherwise arbitrary and potentially significant parameter dependence in the determination of the spectroscopic factor [2]. The relatively high energy deuteron beam was selected to maximize the interior contribution to the reaction while at the same time being a decent compromise for both cross section and description within the DWBA.

The beam accelerated by the K500 was 30 MeV/nucleon HD+, which was then stripped after the machine to give the 60 MeV deuterons. This beam was taken through the beam analysis system (BAS) [3] in order to improve the momentum and position resolution of the beam at the target. After the  $^{14}\text{C}$  target a new, thicker  $4^\circ \times 1^\circ$  acceptance slit defined that acceptance of the spectrometer. Elastic scattering and (d,p) were both measured. These were also measured on a  $^{12}\text{C}$  target with the same spectrometer settings in order to subtract contributions from  $^{12}\text{C}$  impurity in the  $^{14}\text{C}$  target. The  $^{14}\text{C}$  target was found to have approximately  $1.6 \times 10^{18}$  atoms/ $\text{cm}^2$   $^{12}\text{C}$ , or about 11% by number. Elastic scattering on the  $^{12}\text{C}$  target was also measured and this was used to correct the elastic angular distribution for scattering on  $^{14}\text{C}$ . Thickness of the  $^{14}\text{C}$  target was measured in beam using a  $^{20}\text{Ne}$  beam at 15 MeV/nucleon. A gold foil was placed behind the  $^{14}\text{C}$  target and elastic scattering was measured at small angles using a single, narrow acceptance slit. After the position in the focal plane was measured for the combined  $^{14}\text{C} + \text{Au}$  target, the  $^{14}\text{C}$  target was removed and the difference in position in the focal plane was measured. Using the programs RAYTRACE [4] and LISE [5] the thickness of the  $^{14}\text{C}$  target was then determined.

Particle identification for this run was also improved over the measurement made in 2008 by using a thicker scintillator. Because of the high energy and low Z of the reaction products very little energy was deposited in the Oxford detector ionization chamber (used to measure  $\Delta E$  for the  $\Delta E$ - $E_{\text{res}}$  particle ID) and the products were not stopped in the  $1/4''$  scintillator. For this new measurement a new 1.5'' thick scintillator and associated light guides were fabricated and installed. Both deuterons and

protons stop in the new scintillator, and the light output is roughly proportional to their distance traveled (much longer for the highly penetrating protons). The resulting improvement in particle identification is shown in Fig. 1. In addition to this, an updated electronics scheme using all in-cave electronics was utilized.

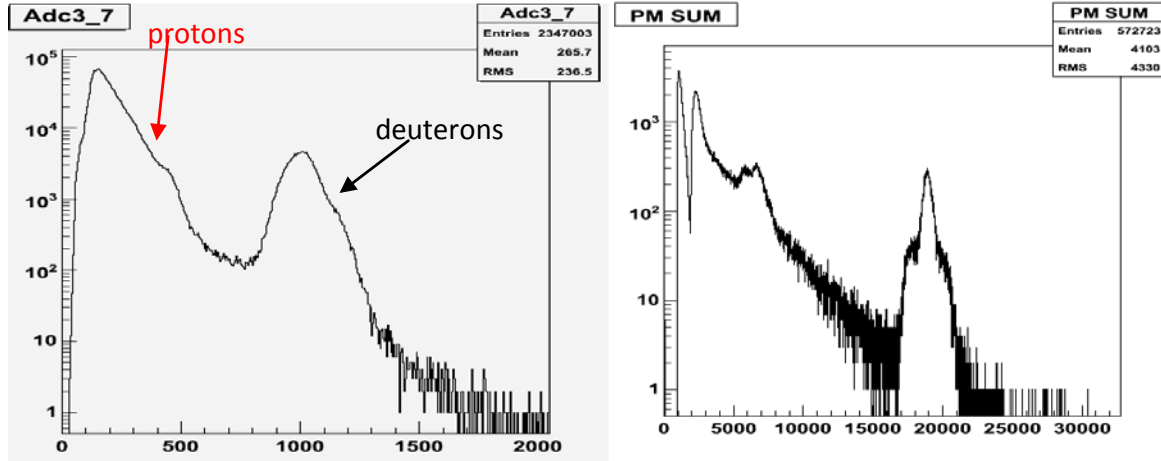


**FIG. 1.** On the left, particle identification in 2008 using a 0.25” thick scintillator and on the right particle identification from the most recent experiment using a new, 1.5” thick scintillator.

The elastic scattering was fit using an OMP of the WS form. The global potential parameterization of Ref. [6] was used as a seed. To improve the fit, spin orbit coupling and the surface imaginary terms were neglected. A grid search for values of the real volume potential was performed to find local  $\chi^2$  minima (Fig. 2). The local minima were then used for a further fit over all six optical model parameters. The three fits are shown in Fig. 3. The potential parameters are given in Table I.

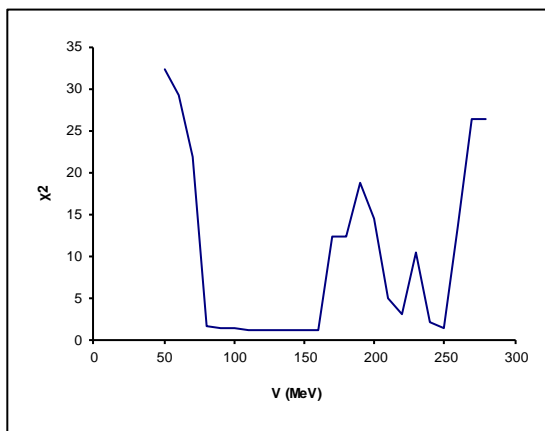


**FIG. 2.** Grid search in V.

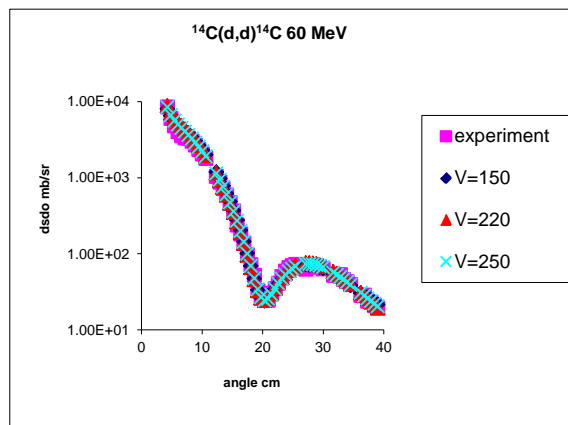


**FIG. 3.** Elastic scattering of 60 MeV deuterons on  $^{14}\text{C}$  shown with optical model fits.

**Table I.** Summary of optical potentials for elastic scattering of 60 MeV deuterons on  $^{14}\text{C}$ .

	V (MeV)	W (MeV)	$r_v$ (fm)	$r_w$ (fm)	$a_v$ (fm)	$a_w$ (fm)	$\chi^2$
WS1	274	17.3	1.79	2.54	0.729	1.30	1.43 7
WS2	151	8.05	1.36	4.59	0.920	0.913	1.19
WS3	376	3.88	1.24	5.56	0.739	0.861	0.87 1

An adiabatic distorted wave approximation calculation (ADWA) was made using potentials taken from the CH89 [7] parameterization. In the ADWA the breakup of the deuteron in the entrance channel is handled explicitly and the transition matrix for a (d,p) reaction

$$\tilde{T} = \langle \chi^{(-)} \phi_{nA} | V_{np} | \Psi^{(+)} \rangle \quad (1)$$

reduces to [8]

$$\tilde{T}_{ADW} = \langle \chi^{(-)} \phi_{pA} | V_{pn} | \tilde{\chi} \phi_{pn} \rangle \quad (2)$$

where the n-p effective interaction,  $V_{pn}$ , is taken to be zero range and

$$[E + \dot{q}_0 - T_R - \bar{V}] \tilde{\chi} = 0. \quad (3)$$

Here  $\dot{q}_0$  is the deuteron binding energy and

$$\bar{V} = V_n + V_p + V_C \quad (4)$$

where  $V_n$  and  $V_p$  are, respectively, the neutron and proton optical potentials evaluated at half of the deuteron energy.  $V_C$  is the Coulomb potential. Finite range effects on the deuteron potential can be approximated by [9]

$$U_{FR} \approx \frac{\langle \phi_d | V_{np} (V_n + V_p) | \phi_d \rangle}{\langle \phi_d | V_{pn} | \phi_d \rangle}. \quad (5)$$

This potential still contains the proton- and neutron-target optical potentials evaluated at half the deuteron energy, but the evaluation is significantly more complex, requiring integration over the deuteron wave function along with the n-p interaction. A simple approximation of the finite range effect was given

by Ref. [10] and this, along with the formulation of ref. [9], were examined for several cases in Ref. [11]. For both approximations an increase in real and imaginary diffuseness and real and imaginary depths was observed, though the two approximations differed in amount. For all ADWA calculations performed here the Wales-Johnson approximation of Ref. [10] was used for simplicity of calculation.

The ADWA has the advantage that only nucleon optical potentials are required, for which CH89 was utilized. The Reid soft core potential [12] was used for the n-p interaction. The calculations were made using the code FRESKO [13]. The experimental angular distribution and calculation for the transfer to the ground state and first excited state is shown in Fig. 4. Both show a good match to the data at forward angles, while the calculation deviates from the experiment at larger angles.

Analysis of this experiment is ongoing.

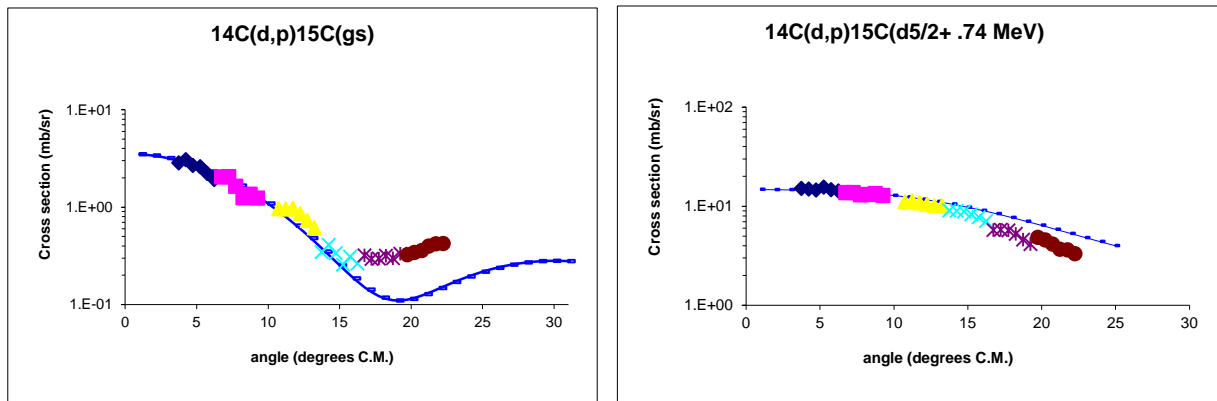


**FIG. 4.** On the left is (d,p) going to the ground state of  $^{15}\text{C}$  and on the right is transfer to the 1<sup>st</sup> excited state. In both the blue line is the ADWA calculation, in the case of the transfer to the excited state there is a renormalization factor of 0.8 and for the ground state the calculation was not renormalized.

- [1] M. McCleskey *et al.* *Progress in Research*, Cyclotron Institute, Texas A&M University (2009-2010) p. I-42.
- [2] A.M. Mukhamedzhanov and F.M. Nunes. *Phys. Rev. C* **72**, 017602 (2005).
- [3] D.H. Youngblood and J.D. Bronson, *Nucl. Instrum. Methods Phys. Res.* **A361**, 37 (1995).
- [4] S. Kowalski and E.A. Enge, computer code RAYTRACE (unpublished), University of Oxford, England, UK, 1986
- [5] O.B. Tarasov and D. Bazin, *Nucl. Instrum. Methods Phys. Res.* **B266**, 4657 (2008).
- [6] S.M. El-Kadi *et al.* *Nucl. Phys.* **A390**, 509-540 (1982).
- [7] R.L. Varner, *Phys. Rep.* **201**, 57 (1991).
- [8] R.C. Johnson and P.J.R. Soper, *Phys. Rev. C* **1**, 976 (1970).
- [9] R.C. Johnson P.C. Tandy, *Nucl. Phys.* **A235**, 56 (1974).
- [10] G.L. Wales and R.C. Johnson, *Nucl. Phys.* **A274**, 168 (1976).
- [11] N.B. Nguyen, F.M. Nunes and R.C. Johnson, *Phys. Rev. C* **82**, 014611 (2010).
- [12] I.J. Thompson, *Comput. Phys. Rep.* **7**, 167 (1988)

## The beta delayed proton and gamma decay of $^{27}\text{P}$ for nuclear astrophysics

E. Simmons, L. Trache, A. Banu, M. McCleskey, A. Saastamoinen,<sup>1</sup> B. Roeder, A. Spiridon, R.E. Tribble, T. Davinson,<sup>2</sup> P. J. Woods,<sup>2</sup> G. J. Lotay,<sup>2</sup> J. Wallace,<sup>2</sup> and D. Doherty<sup>2</sup>

<sup>1</sup>*Department of Physics, University of Jyväskylä, Jyväskylä, Finland*

<sup>2</sup>*School of Physics, University of Edinburgh, Edinburgh, United Kingdom*

In 1982 a high-resolution gamma-ray detector was placed on a NASA spacecraft and it recorded, for the first time, a gamma ray peak at 1.809 MeV. These gamma rays result from the de-excitation of an excited state in  $^{26}\text{Mg}$ , which itself is created by the  $\beta^+$  decay of  $^{26}\text{Al}$  ( $T_{1/2}=0.7$  My). The discovery of this gamma line was a clear indication of ongoing nucleosynthesis. The creation site of  $^{26}\text{Al}$  is still under debate. It is thought to be produced in hydrogen burning and in explosive helium burning in novae and supernovae, and possibly also in the H-burning in outer shells of red giant stars [1]. When  $^{26}\text{Al}$  is created in novae, the reaction chain is:  $^{24}\text{Mg}(p, \gamma)^{25}\text{Al}(\beta^+ \nu)^{25}\text{Mg}(p, \gamma)^{26}\text{Al}$ , but this chain can be by-passed by another chain:  $^{25}\text{Al}(p, \gamma)^{26}\text{Si}(p, \gamma)^{27}\text{P}$  and it can also be destroyed. Having a better understanding of the reactions involved in the creation and destruction of  $^{26}\text{Al}$  will lead us to a better understanding of how much and where  $^{26}\text{Al}$  is created, and thus, to a greater understanding of the evolution of stars. The study of  $^{27}\text{P}$  adds to other proton-rich nuclei in the sd-shell ( $^{23}\text{Al}$ ,  $^{31}\text{Cl}$  and  $^{20}\text{Mg}$ ), which have already been studied by our group. The study of  $^{27}\text{P}$  decay (also a  $T_z=-3/2$  nucleus) could add significant knowledge to our understanding of creation and destruction of  $^{26}\text{Al}$ .

The reaction  $^{26m}\text{Al}(p, \gamma)^{27}\text{Si}^*$  is dominated by two-step resonant captures. Due to the low cross sections in the lab at astrophysical energies we can study this process only by an indirect method,

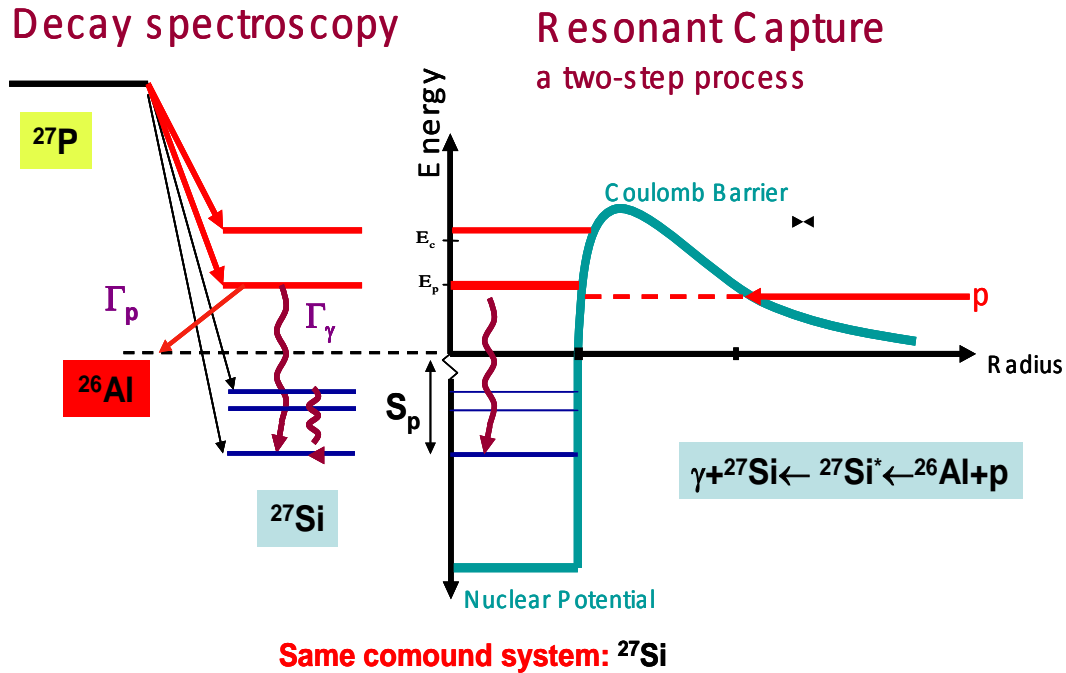


**FIG. 1.** Indirect method used to study resonances in the  $^{26m}\text{Al}(p, \gamma)$  reaction. Note that they populate states in the same compound system  $^{27}\text{Si}$ .

through the  $\beta$ -delayed proton emission of  $^{27}\text{P}$ , which has a half-life of 260(80) ms. This indirect method involves  $^{27}\text{P}$   $\beta^+$  decaying to  $^{27}\text{Si}^*$ , which was originally cited as having a 0.07% beta-delayed proton-decay branching. States that are populated above the proton threshold in  $^{27}\text{Si}$  ( $S_p = 7.463$  MeV) can then decay by proton emission to  $^{26}\text{Al}$ ; see Fig. 1. The difficulty in these types of experiments is that the low energy protons of greatest interest must compete with the beta-background, which is usually the dominant feature in the Si detectors at this energy range (0 - 400 keV).

## The Experiment

The primary beam from the K500 superconducting cyclotron,  $^{28}\text{Si}$  at 40 MeV/u, struck a hydrogen gas target (kept at a pressure of 2 atm and liquid nitrogen temperatures), and several residual nuclei were thus created. The nuclei of interest in this experiment are created by a (p,2n) fusion-evaporation reaction. The exotic secondary beam was then taken through the rest of MARS in order to separate out our desired  $^{27}\text{P}$  nuclei with as few impurities as possible. By the time it reached the target detector used to fine tune the beam, it had an energy of about 34 MeV/u. With the coffin slits closed to  $\pm 0.4$  cm we ended up with a production rate of about 2.9 events/nC and total impurities of about 10.4%, most of which were  $^{25}\text{Si}$  and  $^{24}\text{Al}$ , but since they have different ranges in Si than  $^{27}\text{P}$ , we could implant them in different locations.

A technique that we have had great success with in past experiments involves implanting the desired parent nucleus ( $^{27}\text{P}$ ) in the center of a thin Si detector where the resulting  $\beta^+$  decay will then occur at rest. Two HpGe gamma-ray detectors were also utilized for this experiment, one on either side of a newly designed implantation station that would allow us to move them in even closer to the Si detectors than what was previously achievable; see Fig 2. We used a telescope design for the Si detector arrangement; a thin (45  $\mu\text{m}$  and later a 104  $\mu\text{m}$ ) double sided strip detector (DSSD), the p-detector, which was sandwiched between two thick (300  $\mu\text{m}$  and 1 mm) Si detectors (referred to here as the  $\beta$ -detectors).

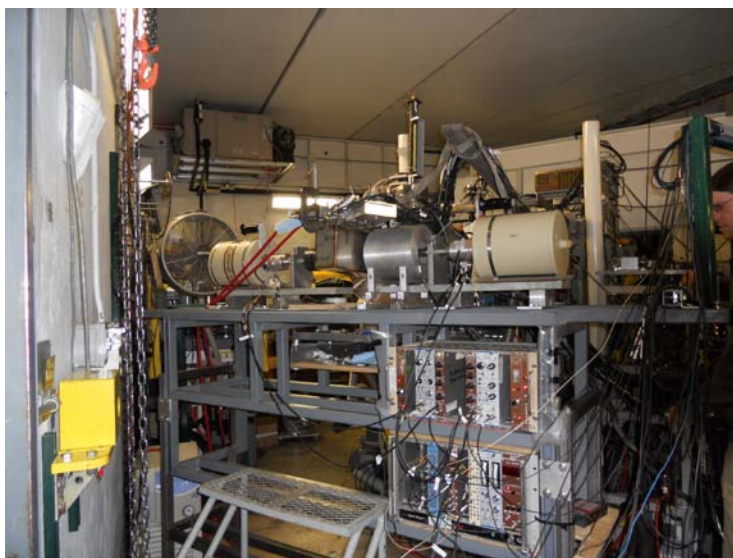


**FIG. 2.** The experimental Setup: two HpGe Detectors were used, one on either side of the Si detectors located inside the chamber.

These beta-detectors were used to reduce the background. The precise implantation in the middle of a very thin detector is obtainable because of the combination of good momentum control in MARS, and by the ability to change the angle of a rotating Al degrader foil that was placed in the implantation station, right in front of the Si detectors. Using the  $\beta$ -detectors, p-detector and HpGe detectors, and pulsing of the beam from the cyclotron, we were able to measure, simultaneously, the  $\beta$ -p and  $\beta$ - $\gamma$  coincidences.

### Preliminary Results

The gamma ray spectra turned out very well. The design of the new implantation station with improved efficiency, the good beam and low noise conditions gave very clean spectra. Extended energy calibrations were done using the well known gamma lines from  $^{24}\text{Al}$  as well as a couple lines from the other beams impurities ( $^{26}\text{Si}$  and  $^{22}\text{Mg}$ ). Natural background peaks are not present due to the coincidences included in the electronics trigger. The spectra were further improved by gating on the beta-gamma TAC signal; see Fig 3(b). The measured gamma-ray decay spectrum allows us the build for the first time the decay scheme of  $^{27}\text{P}$ . So far, analysis has also shown several  $^{27}\text{Si}$  gamma lines not previously reported. For the proton side of the experiment, the major problems we encountered were the large background from the betas below 400 keV and the lower than expected branching ratios of the protons. We now determine that this branching is more like 0.03 - 0.04% instead of the 0.07% previously reported. For once, noise was not our main problem. With both sides of the silicon BB2 detector (proton detector) calibrated, gain matched and summed we could clearly see the 731(2) keV and 612(2) keV protons

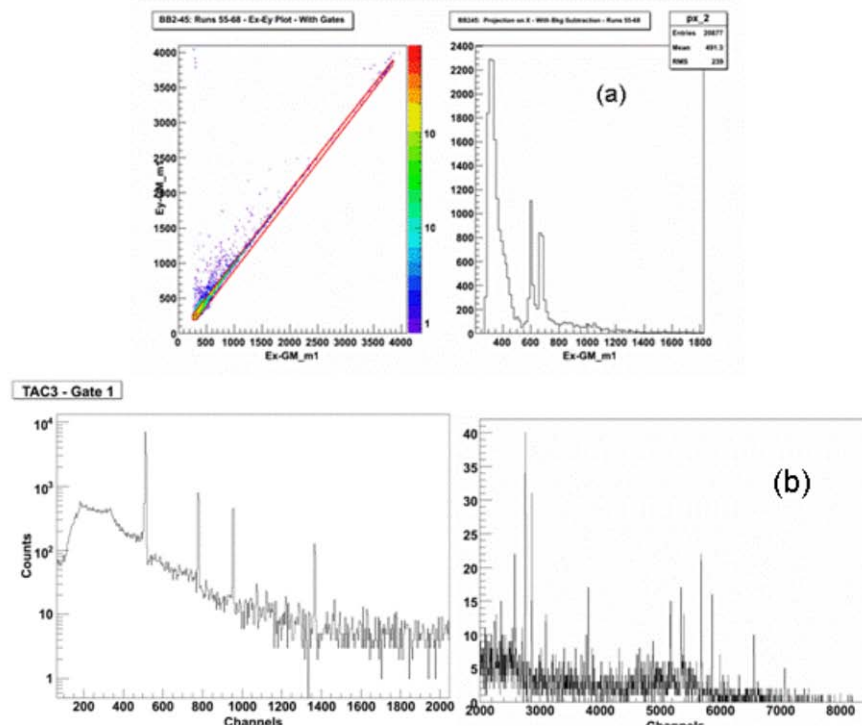


**FIG. 3.** Preliminary Spectra Results from the experiment, the top shows the BB2-45 p-detector preliminary results and the bottom (b) shows the results of  $^{27}\text{Si}$  gamma spectrum.

peaks, and even what looks to be the 466 (3) keV peak [2] when some of the background was removed. Below about 400 keV, all we see so far are betas. Analysis is ongoing; see Fig 3(a).

In April-May 2011 a lifetime measurement was undertaken with the tape transport system, with expectations of greatly improving upon the uncertainty (to under 1%) – analysis of that data is now underway.

[1] N. Prantzos and R. Diehl, Phys. Rep. **267**, 1 (1996).

[2] T.J. Ognibene *et al.*, Phys. Rev C **54**, 1098 (1996).

## SAMURAI-Si – a status report

L. Trache and R. E. Tribble

Last year a TWL (Texas-Washington-Louisiana) collaboration was established with groups from Washington University in St. Louis, MO (prof. LG Sobotka), Louisiana State University in Baton Rouge, LA (prof. J. Blackmon) and TAMU-Commerce in Commerce, TX (prof. C. Bertulani) to study the **“breakup of loosely bound nuclei at intermediate energies for nuclear astrophysics and the development of a position sensitive microstrip detector system and its readout electronics using ASICs technologies”**. The activities are planned also in collaboration with a group (prof. Motobayashi) from the RIKEN Nishina Center for Accelerator-Based Science in Wako, Japan. The microstrip detector is envisaged to be placed between the target and the entry into the SAMURAI spectrometer [1], a complex device under construction at the Radioactive Ion Beam Facility (RIBF) of RIKEN. The US side of the collaboration is financed by DOE and we name the construction part of it the SAMURAI-Si collaboration. This is a brief status report of the latter.

The goal is to build a detector system that can give simultaneously the angles of motion of the proton and the heavy core resulting from the dissociation of a projectile moving at up to 350 MeV/u. The solution accepted now is to use Si multi-strip detectors to determine the x, y positions at two locations, separated by a distance. The main problems that occur are:

- the size of detectors and the position resolution required. These set the number of channels to be handled. The current accepted design parameters are: detectors to cover a diameter of about 10 cm and a 0.75 mm resolution in both x and y directions.
- a very large dynamic range (energy losses from 2-300 keV for protons to 600 MeV for HI). This sets the design parameters of the electronics used.

Discussions at four meetings (in St. Louis, College Station and Wako) between the members of the collaboration determined initially the main lines of the work and then considered the results and problems of the various solutions proposed.

We are considering testing different silicon strip detectors, both double-sided and single-sided, made by Micron Semiconductors Ltd or by Hamamatsu Co.

Due to the large number of channels involved it was decided that we will use an ASIC solution for the handling of the detector signals. The electronics is based on the HINP16 chip, the electronics environment and the software developed at WU with their S. Illinois University collaborators [2]. Before the final product, to be installed at RIBF, a 512 channels system (named TABS) will be developed and tested at TAMU. A number of steps were taken here at TAMU, at WU and LSU, to have compatible equipment and installed software that would enable and facilitate tests of various parts of the equipment. It was determined that in order to meet the requirement of the very large dynamic range a new revision (rev 4) of the HINP16 chip must be designed and made and/or external CSA must be made. The WU group is working on the former, while our Japanese colleagues are working on two different solutions of the latter.

In order to streamline the choice and design process, a number of simulations of the detector system were made.

In the next three reports, progresses on these above topics are presented in more detail.

[1] Large-Acceptance Multi-Particle Spectrometer SAMURAI Construction Proposal, version 2010.

[2] G.L. Engel *et al*, Nucl. Instrum. Methods Phys. Res. **A573**, 418 (2007).

## Superallowed beta decay

J. C. Hardy, I. S. Towner, V. E. Jacob, N. Nica, L. Chen, V. Horvat, H. I. Park, J. Goodwin,  
L. Trache, and R. E. Tribble

Superallowed  $0^+ \rightarrow 0^+$  beta decay between T=1 analogue states has been a subject of continuous and often intense study for five decades. The  $ft$  values of such transitions are nearly independent of nuclear-structure ambiguities and depend uniquely on the vector part of the weak interaction. Their measurement gives us access to clean tests of some of the fundamental precepts of weak-interaction theory, and, over the years, this strong motivation has led to very high precision being achieved in both the experiments and the theory used to interpret them. We have a major program at the Cyclotron Institute to study superallowed beta decay.

To obtain the  $ft$  value for any transition, three quantities must be measured: the half life of the parent, the  $Q_{EC}$  value for the transition of interest and the branching ratio for that transition. Our most recent complete survey of existing data on these superallowed decays, published in 2009 [1] provided a critical evaluation of all the experimental data and obtained final  $ft$  values from the averaged results, to which improved radiative and isospin-symmetry-breaking corrections [2] were applied in order to derive a final set of “corrected  $ft$  values”, denoted  $Ft$ . One of the new features added at that time was that we calculated the radial-overlap correction,  $\delta_{C2}$ , with Hartree-Fock radial wave functions as well as the Saxon-Woods wave functions we have used before. The differences in the results from these two methods are used as a measure of the systematic uncertainty to be applied to the theoretical corrections. These differences also offer the possibility that measured  $ft$  values with the highest precision could actually distinguish between the two methods and thereby reduce the systematic uncertainty.

With the updated world data and improved corrections the  $Ft$  values were seen to be completely consistent with one another, thus demonstrating the constancy of  $G_V$  to 1.3 parts in  $10^4$ . Not only is this an important confirmation of the Conserved Vector Current (CVC) hypothesis but it sets the stage for using the average value of  $G_V$  to test a fundamental principle of the electroweak standard model: the unitarity of the Cabibbo-Kobayashi-Maskawa (CKM) matrix. The up-down quark mixing element of that matrix,  $V_{ud}$ , is given by  $V_{ud} = G_V / G_F$ , where  $G_F$  is the weak interaction constant for the purely leptonic muon decay. The value of  $V_{ud}$  is a key component of the most demanding test available for the unitarity of the CKM matrix, the sum of squares of its top-row elements [1]. As elaborated in our recent review article on the evaluation of  $V_{ud}$  [3], superallowed nuclear beta decays provide by far the most precise and reliable value for  $V_{ud}$  and, in fact, that element is also the most precisely known one in the CKM matrix – by an order of magnitude! Its current value [1,3] is 0.97425(22), a result that yields a CKM unitarity sum of 0.99990(60) [3], in full agreement with the standard-model expectation, and carrying the smallest uncertainty yet obtained.

This result is not only a significant verification of the standard model but the uncertainty quoted on the sum provides a tight limit on any possible new physics beyond the standard model, such as right-hand currents, extra Z bosons or supersymmetric models. In short, superallowed  $0^+ \rightarrow 0^+$  beta decay

provides a high-profile application of nuclear-physics measurements to the study of fundamental symmetries, a subject of vital interest to both nuclear and particle physicists. Although much has already been achieved in this field by nuclear physicists, improvements are still possible. Reducing the uncertainty on the unitarity sum – and, with it, the scope for new physics – remains the primary goal of our research program.

Our approach follows from the observation [1,3] that the second largest contributor to the uncertainty in  $V_{ud}$  is the theoretical uncertainty in the nuclear-structure-dependent corrections,  $\delta_{NS}$  and  $\delta_C$ , used in the derivation of the  $Ft$  values. Though these corrections are only of order 1%, their effect is very significant: Fig. 1, which is taken from our 2009 survey [1], shows the result of applying  $\delta_{NS}$  and  $\delta_C$  (together with  $\delta'_R$ , which is nearly independent of  $Z$ ). Obviously they act very well to remove the considerable “scatter” in  $Ft$  values apparent in the left panel, replacing it with the consistent set of corrected  $Ft$  values appearing in the right panel. Since these corrections were determined [2] completely independently of the superallowed decay data, this consistency in  $Ft$  values is already a powerful validation of these calculated corrections, but obviously the remaining uncertainty still influences the

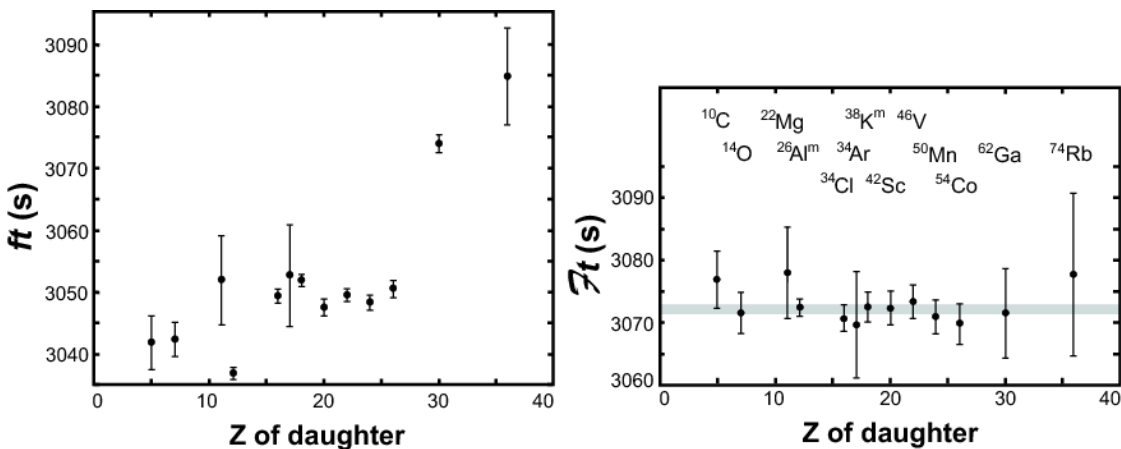


**FIG. 1.** Results from the 2009 survey [1]. The uncorrected  $Ft$  values for the thirteen best known superallowed decays (left) are compared with the same results after corrections have been applied (right). The grey band in the right-hand panel is the average  $Ft$  value, including its uncertainty.

final result for  $V_{ud}$ .

Our approach follows from the observation [1,3] that the second largest contributor to the uncertainty in  $V_{ud}$  is the theoretical uncertainty in the nuclear-structure-dependent corrections,  $\delta_{NS}$  and  $\delta_C$ , used in the derivation of the  $Ft$  values. Though these corrections are only of order 1%, their effect is very significant: Fig. 1, which is taken from our 2009 survey [1], shows the result of applying  $\delta_{NS}$  and  $\delta_C$  (together with  $\delta'_R$ , which is nearly independent of  $Z$ ). Obviously they act very well to remove the considerable “scatter” in  $Ft$  values apparent in the left panel, replacing it with the consistent set of corrected  $Ft$  values appearing in the right panel. Since these corrections were determined [2] completely independently of the superallowed decay data, this consistency in  $Ft$  values is already a powerful

validation of these calculated corrections, but obviously the remaining uncertainty still influences the final result for  $V_{ud}$ .

Even though the 2009 survey [1] included more than 145 individual measurements relating to 13 precisely known  $ft$  values, it is still possible for well selected experiments to make real improvements in the validation tests of the nuclear-structure-dependent correction terms. At TAMU we are currently focusing on adding to the  $ft$ -value list new superallowed transitions, selected from amongst those with *large* calculated corrections. If the  $ft$  values measured for cases with large calculated corrections also turn into corrected  $Ft$  values that are consistent with the others, then this must verify the calculations' reliability for the existing cases, which have smaller corrections. We are studying decays from  $T_z = -1$  parent nuclei, which consistently have higher predicted structure-dependent correction terms than the well known  $T_z = 0$  cases. In that context, during this past year we have published our half-life measurement for the decay of  $^{26}\text{Si}$  [4] and submitted a manuscript on the half-life of  $^{38}\text{Ca}$  [5] to Physical Review C. Unfortunately, we have found that  $^{18}\text{Ne}$  cannot be studied with our system since it defuses out of Mylar in a time comparable to its half-life [6]. We are also well advanced on a measurement of the branching ratios in the decay of  $^{38}\text{Ca}$  [7] and, in collaboration with the JYFLTRAP group at Jyvaskyla, Finland, we have measured the  $Q_{EC}$  values for the decays of  $^{10}\text{C}$ ,  $^{34}\text{Ar}$  and  $^{38}\text{Ca}$  [8]. At the same time, we have been exploring from a theoretical perspective [9] what else can be learned from a more exact experimental characterization of the nuclear-structure-dependent correction terms.

There are also compelling reasons to confirm and improve the  $ft$  values for the  $T_z = 0$  cases as well. After all, these are the transitions that principally determine the value of  $V_{ud}$ . Since  $^{46}\text{V}$  was a key transition that led to important improvements in the structure-dependent corrections when its  $Q_{EC}$  value was found to have been incorrectly measured by reaction studies in the past, we have completed a re-measurement of both its  $Q_{EC}$  value [8] and its half-life [10] and confirmed that no errors are lurking in either place.

We are also endeavoring to improve our data acquisition techniques for half-life measurements by a variety of means, including a new TDC-based data-acquisition system [11] and a digital-pulse-analysis system for the signals from our  $4\pi$  proportional gas counter [12]. We are working to eliminate spurious pulses and to reduce our system dead time. Since we limit our count rate to avoid too large a dead-time correction, any reduction in the dead time itself will translate directly into improved statistical uncertainties on our measurements.

- [1] J.C. Hardy and I.S. Towner, *Phys. Rev. C* **79**, 055502 (2009).
- [2] I.S. Towner and J.C. Hardy, *Phys. Rev. C* **77**, 025501 (2008).
- [3] I.S. Towner and J.C. Hardy, *Rep. Prog. Phys.* **73**, 046301 (2010).
- [4] V.E. Iacob, J.C. Hardy, A. Banu, L. Chen, V.V. Golovko, J. Goodwin, V. Horvat, N. Nica, H.I. Park, L. Trache and R.E. Tribble, *Phys. Rev. C* **82**, 035502 (2010).
- [5] H.I. Park, J.C. Hardy, V.E. Iacob, A. Banu, L. Chen, V.V. Golovko, J. Goodwin, V. Horvat, N. Nica, E. Simmons, L. Trache and R.E. Tribble, *Progress in Research*, Cyclotron Institute, Texas A&M University (2010-2011), p. I-23.

- [6] V.E. Iacob and J.C. Hardy, *Progress in Research*, Cyclotron Institute, Texas A&M University (2010-2011), p. V-50.
- [7] H.I. Park, J.C. Hardy, V.E. Iacob, A. Banu, L. Chen, V.V. Golovko, J. Goodwin, V. Horvat, N. Nica, E. Simmons, L. Trache and R.E. Tribble, *Progress in Research*, Cyclotron Institute, Texas A&M University (2010-2011), p. I-27.
- [8] T. Eronen, D. Gorelov, J. Hakala, J.C. Hardy, A. Jokinen, A. Kankainen, V.S. Kolhinen, I.D. Moore, H. Penttila, M. Reponen, J. Rissanen, A. Saastamoinen and J. Aysto, *Phys. Rev. C* **83**, 055501 (2011).
- [9] I.S. Towner and J.C. Hardy, *Progress in Research*, Cyclotron Institute, Texas A&M University (2010-2011), p. III-44.
- [10] H.I. Park, J.C. Hardy, V.E. Iacob, L. Chen, J. Goodwin, V. Horvat, N. Nica, E. Simmons, L. Trache and R.E. Tribble, *Progress in Research*, Cyclotron Institute, Texas A&M University (2010-2011), p. I-19.
- [11] V. Horvat and J.C. Hardy, *Progress in Research*, Cyclotron Institute, Texas A&M University (2010-2011), p. V-59.
- [12] L. Chen and J.C. Hardy, , *Progress in Research*, Cyclotron Institute, Texas A&M University (2010-2011), p. V-54.

## Half-life of the superallowed $\beta$ -emitter $^{46}\text{V}$

H. I. Park, J. C. Hardy, V. E. Jacob, L. Chen, J. Goodwin, V. Horvat, N. Nica, E. Simmons,  
L. Trache, and R. E. Tribble

The decay of  $^{46}\text{V}$  was the first of the nine best-known superallowed transitions to have its  $Q_{EC}$  value measured (in 2005) with an on-line Penning trap [1]. The result differed significantly from the previously accepted result -- a longstanding reaction-based  $Q_{EC}$  value -- and shifted the  $^{46}\text{V}$   $ft$  value two standard deviations out of agreement with other well-known superallowed transitions. This apparent deviation from the conserved vector current (CVC) expectation raised several concerns, among them the possibility of systematic differences between reaction and Penning-trap measurements of  $Q$  values. As a result, several other measurements were performed, two with Penning-traps and one reaction based. All confirmed the new result.

In parallel with these experimental studies, the theory used in the analysis of the  $^{46}\text{V}$  results was carefully reexamined as well and, as a result, the isospin-symmetry-breaking corrections were improved [2] by the inclusion of core orbitals in the model space used in the calculation. This improvement had the largest effect on the  $^{46}\text{V}$  transition, but also had smaller effects on other superallowed transitions, especially on those in the  $f_{7/2}$  shell. These new corrections, which were incorporated into the most recent survey of world data [3], eliminated the  $^{46}\text{V}$  anomaly, restored the consistency with CVC and retained agreement with CKM matrix unitarity.

All these experimental and theoretical studies proceeded under the tacit assumption that the previously accepted half-life of  $^{46}\text{V}$  was completely correct. Although there was no reason to suspect that this half-life result was in error, there had not been any reason to suspect that there was anything wrong with the now-discredited  $Q_{EC}$  value either. We have addressed this potential weakness and have made a new measurement of the  $^{46}\text{V}$  half-life, which confirms the average of previous measurements but is a factor of two more precise than the best of them.

In that measurement, we produced  $^{46}\text{V}$  via the  $^1\text{H}(^{47}\text{Ti}, 2n)$  reaction at a primary beam energy of 32A MeV. A  $^{46}\text{V}$  beam was obtained at the focal plane of the MARS spectrometer, from which it exited the vacuum system through a 50- $\mu\text{m}$  thick Kapton window, passed through a 0.3-mm-thick BC404 scintillator and a stack of aluminum degraders, and finally stopped in the 76- $\mu\text{m}$  thick aluminized Mylar tape of our fast tape-transport system. In addition to  $^{46}\text{V}$ , there were four reaction products,  $^{42}\text{Sc}$  ( $t_{1/2} = 680.72$  ms),  $^{43}\text{Sc}$  ( $t_{1/2} = 3.891$  h),  $^{44}\text{Ti}$  ( $t_{1/2} = 60.0$  y) and  $^{45}\text{Ti}$  ( $t_{1/2} = 3.083$  h), that appeared between the extraction slits and were thus weak contaminants in the extracted  $^{46}\text{V}$  beam. The presence of  $^{44,45}\text{Ti}$  and  $^{43}\text{Sc}$  was not problematic since their half-lives are more than four orders of magnitude longer than 423-ms  $^{46}\text{V}$ . Our only concern was  $^{42}\text{Sc}$ , another superallowed  $\beta$ -emitter with a rather similar half-life to that of  $^{46}\text{V}$ . With the focal-plane acceptance slits of MARS set to a width of 7 mm, the total extracted beam contained 0.12% of  $^{42}\text{Sc}$  nuclei. To minimize the effect of this small contaminant on our measurement, we carefully adjusted the distribution of implanted  $^{46}\text{V}$  in the Mylar tape by setting the thickness of Al degraders to minimize the number of  $^{42}\text{Sc}$  ions stopping in the tape. Finally, the composition of the beam

exiting MARS was checked on a daily basis during our half-life measurement. There were no appreciable changes observed in the extracted beam composition at any time.

After  $^{46}\text{V}$  was collected on the tape for 0.3 or 0.5 s, the cyclotron beam was interrupted and the collected sample was moved in 180 ms to the center of a  $4\pi$  proportional gas counter. Multiscaled signals from the counter were recorded for 10 s into two separate 500-channel time spectra, each corresponding to a different pre-set dominant dead-time. This “collect-move-count” cycle was repeated until high statistics were obtained. In its shielded location, the gas counter had a background rate of about 0.5 counts/s, which was 4 orders of magnitude lower than the initial count rate for each collected sample. In all, we recorded over 65 million  $\beta$  events from 14,422 cycles divided into 16 runs, which had various combinations of different bias voltages for the  $4\pi$  proportional gas counter, discriminator thresholds, and dominant dead times.

The implantation profiles of  $^{46}\text{V}$  and  $^{42}\text{Sc}$  as determined by a combination of measurement (for  $^{46}\text{V}$ ) and calculation (for  $^{42}\text{Sc}$ ) are shown in Fig. 1. Although it is too small to be visible in the figure, our detailed scan of  $^{46}\text{V}$  activity versus degrader thickness showed evidence of a very weak tail, amounting to  $\sim 1\%$  of the total, extending to the left of the depth distribution. We take this result to be a good gauge of the upper limit for how many  $^{42}\text{Sc}$  nuclei could have been retained in the collection tape. With this approach we can then conclude that the  $^{42}\text{Sc}/^{46}\text{V}$  ratio in the collected samples was less than 0.0015 %.

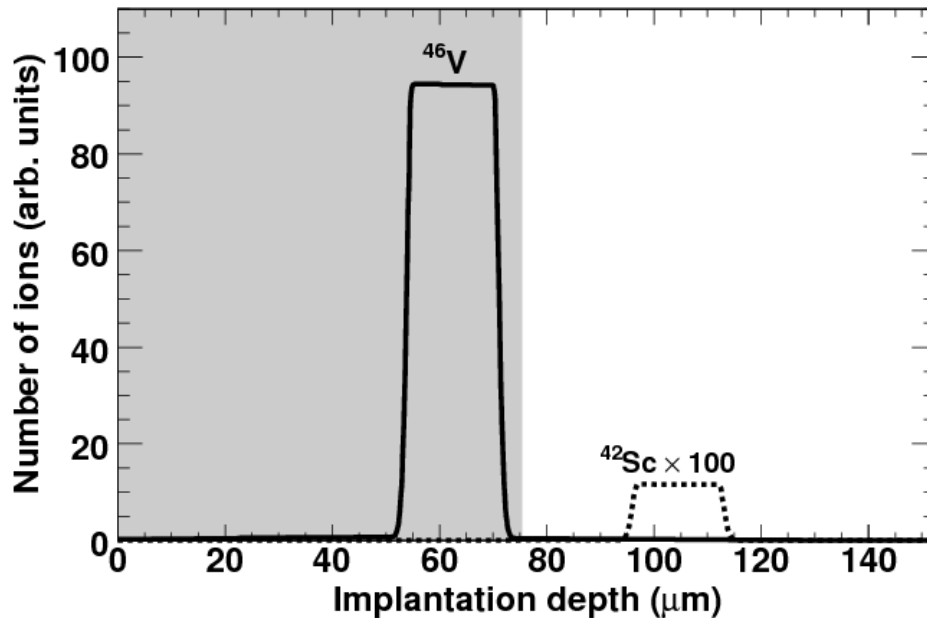
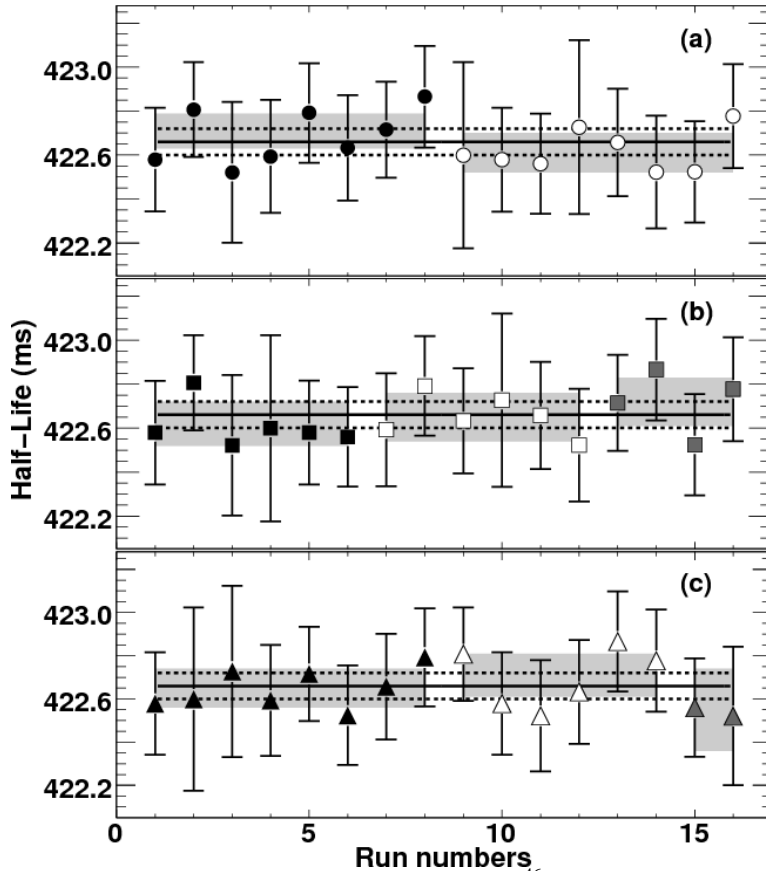


FIG. 1. The implantation profiles of  $^{46}\text{V}$  (solid line) and  $^{42}\text{Sc}$  (dashed line) in and beyond the Mylar tape, under the conditions applying to our half-life measurements. The beams enter from the left. The shaded region corresponds to the actual thickness of our collection tape: all ions within the shaded region are collected in our sample; all others are not.

We also used a second independent method to search for any evidence of  $^{42}\text{Sc}$  activity by examining the recorded time-decay spectra. We fitted each spectrum from the 16 individual runs with a

function including two exponentials, one each for the decays of  $^{46}\text{V}$  and  $^{42}\text{Sc}$ , together with a constant background. In the first fit, we set the initial  $^{42}\text{Sc}/^{46}\text{V}$  ratio of intensities to the 0.0015% value just obtained; set the half-life of  $^{42}\text{Sc}$  to its world-average value, 680.72 ms [3]; and extracted a half-life for  $^{46}\text{V}$ . Then we refitted the same 16 spectra with the initial  $^{42}\text{Sc}/^{46}\text{V}$  ratio as the adjustable parameter. In this case, the half-life of  $^{42}\text{Sc}$  was again set to its world-average value but the  $^{46}\text{V}$  half-life was fixed at a range of values around the average value obtained from the first fit. We found that the  $^{42}\text{Sc}/^{46}\text{V}$  ratio obtained from the fits was very insensitive to the half-life used for  $^{46}\text{V}$ , and that, in all cases, the ratio was less than 0.01%. In arriving at the final half-life for  $^{46}\text{V}$  and its uncertainty, we have adopted a very conservative range for the  $^{42}\text{Sc}/^{46}\text{V}$  ratio, taking the value to be 0.006(6)%.

We fitted the data from each of the 16 runs separately, incorporating three components:  $^{46}\text{V}$ ,  $^{42}\text{Sc}$  and a constant background. The half-life of  $^{42}\text{Sc}$  was fixed at its known value of 680.72 ms [3] and the initial activity of  $^{42}\text{Sc}$  relative to  $^{46}\text{V}$  was set at 0.006%. Since each run was obtained with a different combination of detection settings, we could use the individually fitted half-lives of  $^{46}\text{V}$  to test for any systematic dependence on those settings. As displayed in Fig. 2, the half-life results showed no



**FIG. 2.** Test for possible systematic bias in the  $^{46}\text{V}$  half-life measurement due to three different detection parameters: (a) two detector biases, 2650V/2750V, represented by black/open circles; (b) three discriminator settings, 150 mV/200 mV/250 mV, represented by black/open/grey squares; (c) three imposed dead times, 4  $\mu\text{s}$ /6 $\mu\text{s}$  /8 $\mu\text{s}$ , represented by black/open/grey triangles. Note that the runs have been grouped differently in each part of the figure. In all cases, the grey bands represent the  $\pm\sigma$  limits of the average for a given condition. The average value for the half-life is 422.66(6) ms (statistical uncertainty only) with  $\chi^2/\text{ndf} = 3.3/15$ . The average value for all the runs appears as the solid line, with dashed lines as uncertainty limits.

systematic dependence on detector bias voltage, discriminator threshold setting, or the dominant dead time we imposed in the electronics, the average half-life yielding a remarkably low value for the normalized  $\chi^2$  of 0.2. With this degree of consistency in the data, we can be confident that any systematic dependence on detection parameters must be negligible with respect to our quoted statistical uncertainty.

Our final result for the half-life of  $^{46}\text{V}$  is 422.66(6) ms. The quoted uncertainty includes provision for uncertainty in the  $^{42}\text{Sc}/^{46}\text{V}$  ratio. This result is a factor of two more precise than the best previous result [4], with which it is completely consistent. If our half-life value is combined with previous measurements of the same quantity, it yields a new world average of 422.62(05) ms. This is statistically consistent with the previous world average [3] but is more than a factor of two more precise. Evidently, the important experimental components of the  $^{46}\text{V}$  superallowed transition -- its half-life and  $Q_{\text{EC}}$  value -- have now been satisfactorily confirmed and improved. The  $Ft$  value for this transition is certainly not anomalous at the 0.08% level of precision currently quoted on that quantity.

- [1] G. Savard, F. Buchinger, J.A. Clark, J.E. Crawford, S. Gulick, J.C. Hardy, A.A. Hecht, J.K.P. Lee, A.F. Levand, N.D. Scielzo, H. Sharma, K.S. Sharma, I. Tanihata, A.C.C. Villari, and Y. Wang, *Phys. Rev. Lett.* **95**, 102501 (2005).
- [2] I.S. Towner and J.C. Hardy, *Phys. Rev. C* **77**, 025501 (2008).
- [3] J.C. Hardy and I.S. Towner, *Phys. Rev. C* **79**, 055502 (2009).
- [4] V.T. Koslowsky, E. Hagberg, J.C. Hardy, G. Savard, H. Schmeing, K.S. Sharma and X.J. Sun, *Nucl. Instrum. Methods Phys. Res.* **A401**, 289 (1997).

## High precision half-life measurement of the superallowed $\beta$ -emitter $^{38}\text{Ca}$

H. I. Park, J. C. Hardy, V. E. Jacob, A. Banu, L. Chen, V. V. Golovko, J. Goodwin, V. Horvat,  
N. Nica, E. Simmons, L. Trache, and R. E. Tribble

We have now analyzed the results obtained from our half-life measurement of  $^{38}\text{Ca}$ . In that measurement, we produced  $^{38}\text{Ca}$  via the  $^1\text{H}(^{39}\text{K}, 2n)$  reaction at a primary beam energy of 30A MeV. A 99%-pure  $^{38}\text{Ca}$  beam was obtained at the focal plane of the MARS spectrometer, from which it exited the vacuum system through a 50- $\mu\text{m}$  thick Kapton window, passed through a 0.3-mm-thick BC404 scintillator and a stack of aluminum degraders, and finally stopped in the 76- $\mu\text{m}$  thick aluminized Mylar tape of our fast tape-transport system. The combination of  $q/m$  selectivity in MARS and range separation in the degraders provided implanted samples that we determined to be better than 99.6% pure. After  $^{38}\text{Ca}$  was collected on the tape for 1 s, the cyclotron beam was interrupted and the collected sample was moved in 198 ms to the center of a  $4\pi$  proportional gas counter. Multiscaled signals from the counter were recorded for 15 s into two separate 500-channel time spectra, each corresponding to a different pre-set dominant dead-time. This “collect-move-count” cycle was repeated until high statistics were obtained. In its shielded location, the gas counter had a background rate of about 0.5 counts/s, which was 3-4 orders of magnitude lower than the initial count rate for each collected sample.

In all, we recorded over 125 million  $\beta$  events from 11,271 cycles divided into 32 separate runs. The total time-decay spectrum obtained from the combined runs is presented in Fig. 1, where we also show

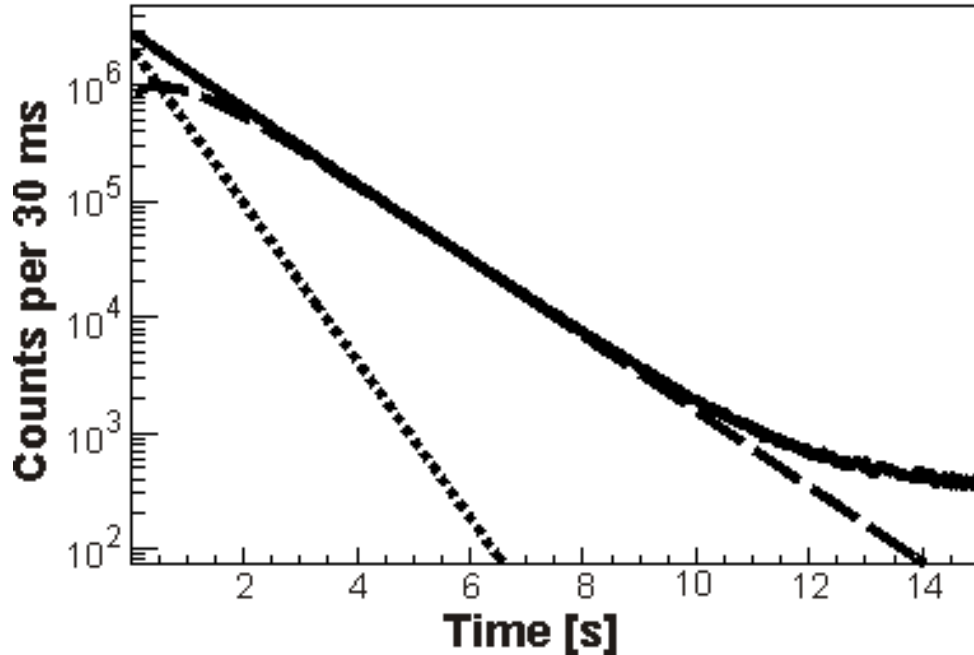


**FIG. 1.** Measured time-decay spectrum (solid line) obtained for the total of all data obtained from the  $\beta^+$  decay of  $^{38}\text{Ca}$  and its daughter  $^{38}\text{K}^m$ . The dotted/dashed lines represent the derived  $^{38}\text{Ca}/^{38}\text{K}^m$  contributions.

the separate contributions from the decays of the  $^{38}\text{Ca}$  parent and the  $^{38}\text{K}^m$  daughter.

As our detection system does not disentangle the two components, the only information that can be processed is the combined parent-daughter decay. A detailed analysis of the coupled  $^{38}\text{Ca}$  and  $^{38}\text{K}^{\text{m}}$  decay equations gives for the total detected rate as

$$\Delta_{\text{tot}} = C_1 e^{-\lambda_1 t} + C_2 e^{-\lambda_2 t}, \quad (1)$$

with

$$C_1 = N_1 \varepsilon_2 \lambda_1 \left( \frac{\varepsilon_1}{\varepsilon_2} - \frac{\lambda_2}{\lambda_1 - \lambda_2} \right) \quad (2)$$

$$C_2 = N_1 \varepsilon_2 \lambda_2 \left( \frac{N_2}{N_1} + \frac{\lambda_1}{\lambda_1 - \lambda_2} \right), \quad (3)$$

where  $t$  is the time elapsed after the end of the collect period;  $N_{1,2}$  are the numbers of  $^{38}\text{Ca}$  and  $^{38}\text{K}^{\text{m}}$  nuclei present in the sample at  $t = 0$ ;  $\varepsilon_{1,2}$  are the experimental efficiencies for detecting the positrons from the respective decays; and  $\lambda_{1,2}$  are the corresponding decay constants. Note that if  $\varepsilon_1 = \varepsilon_2$  and  $\lambda_1 = 2\lambda_2$ , the coefficient  $C_1$  vanishes and the total decay rate is fully determined by  $C_2 e^{-\lambda_2 t}$ . This is very nearly the case for  $^{38}\text{Ca}$  and  $^{38}\text{K}^{\text{m}}$ , which have decay constants that are related by a factor of 2.1. Consequently for our measurements, the coefficient  $C_1$  is more than a factor of 10 smaller than  $C_2$ . The impact is clearly evident in Fig. 1, where the total spectrum deviates very little from a one-component decay curve with the daughter's decay-constant. This is similar to the situation we encountered for our  $^{34}\text{Ar}$  [1] and  $^{26}\text{Si}$  [2] experiments.

As we did in those previous measurements, we calculated the ratio  $N_1/N_2$  from the production of  $^{38}\text{K}^{\text{m}}$  (via  $^{38}\text{Ca}$  decay) over each collection period, based on the rate of deposit of  $^{38}\text{Ca}$  as measured with the scintillator located just before the degraders at the exit to MARS. For these coupled decays it might easily be assumed that the efficiency ratio,  $\varepsilon_1/\varepsilon_2$ , equals unity since both activities were observed with identical geometry, a very low electronic threshold and nearly 100% overall efficiency. However, there is also a threshold energy arising from the fact that low-energy positrons are stopped in the aluminized Mylar transport-tape (half-thickness, 38  $\mu\text{m}$ ) and in the Havar windows of the gas counter (1.5  $\mu\text{m}$  thick), never reaching the active volume of the detector. The impact of this effective threshold on the efficiency ratio becomes significant when the end-points and/or shapes of the parent and daughter  $\beta$  spectra are significantly different from one another. By Monte Carlo simulations we determined this ratio to be  $\varepsilon_1/\varepsilon_2 = 1.00042(5)$  for this mass-38 measurement.

To test the robustness of our results, each run was obtained with a different combination of critical detection settings: detector bias, discriminator threshold and major dead-time combination. As seen in Fig. 2, the half-life results show no systematic dependence on detector bias or discriminator threshold. Although not illustrated, the results were also found to be independent of both the imposed circuit dead time and the length of time for which the sample was collected.

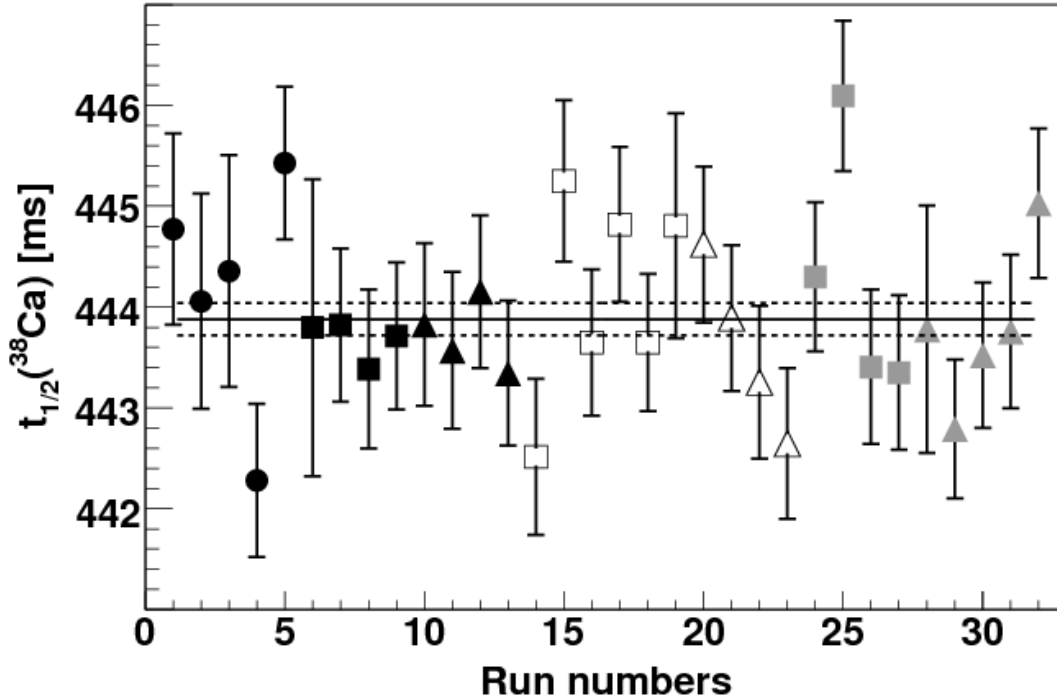


**FIG. 2.** Test for possible systematic bias in the  $^{38}\text{Ca}$  half-life measurement due to discriminator threshold or detector voltage. The three detector biases, 2600 V, 2700 V and 2800 V are represented by the symbol shapes  $\square$  and  $\Delta$ , respectively; b lack/open/grey symbols represent the three discriminator settings, 150 mV/200 mV/250 mV. The average value for the half-life is 443.88(16) ms (statistical uncertainty only) with  $\chi^2/ndf = 39/31$ . The average value appears as the solid line, with dashed lines as uncertainty limits

Further tests of the half-life stability versus undetected short-lived impurities or rate-dependent counting losses were performed by the standard “front-channel-chopping” technique, which involves separate fits to subsets of the data with successively longer time periods removed from the beginning of the counting cycle. Here too the derived half-life proved to be stable: no statistically significant change was observed as the starting time for the fit was systematically changed.

The error budget and final result for the  $^{38}\text{Ca}$  half-life is given in Table I. Four out of the five previous measurements of the  $^{38}\text{Ca}$  half-life were made before 1980 and with quoted uncertainties more than thirty times

**Table I.** Error budget for the  $^{38}\text{Ca}$  half-life measurement.

Source	Uncertainty (ms)
statistics	0.16
sample impurity ( $^{35}\text{Ar}$ )	0.23
$t_{1/2}(^{38}\text{K}^m)$	0.22
Efficiency ratio, $\varepsilon_1/\varepsilon_2$	0.01
Total	0.36
$^{38}\text{Ca}$ half-life result (ms)	443.88(36)

larger than ours: 470(20) ms [3], 439(12) ms [4], 450(70) ms [5] and 430(12) ms [6]. These were each obtained by observation and analysis of the decay of  $\beta$ -delayed  $\gamma$ -rays from the daughter,  $^{38}\text{K}$ . The first result lies about one-and-a-half of its error bar away from our quoted half-life; the other three agree well within their error bars. There is a much more recent measured value, 443.8(19) ms [7], which was obtained in a similar manner to ours, from a measurement of the decay positrons in a gas counter; in their case, though, sample purity was achieved by collecting the  $^{38}\text{Ca}$  first in a Penning trap. Our half-life result agrees well with theirs but with an uncertainty five times smaller.

- [1] V.E. Jacob, J.C. Hardy, J.F. Brinkley, C.A. Gagliardi, V.E. Mayes, N. Nica, M. Sanchez-Vega, G. Tabacaru, L. Trache and R.E. Tribble, *Phys. Rev. C* **74**, 055502 (2006).
- [2] V.E. Jacob, J.C. Hardy, A. Banu, L. Chen, V.V. Golovko, J. Goodwin, V. Horvat, N. Nica, H.I. Park, L. Trache and R.E. Tribble, *Phys. Rev. C* **82**, 035502 (2010).
- [3] R.W. Kavanagh, A. Gallmann, E. Aslanides, F. Jundt and E. Jacobs, *Phys. Rev.* **175**, 1426 (1968).
- [4] A. Gallmann, E. Aslanides, F. Jundt and E. Jacobs, *Phys. Rev.* **186**, 1160 (1969).
- [5] J. Zioni, A.A. Jaffe, E. Friedman, N. Haik, R. Schectman and D. Nir, *Nucl. Phys. A* **181**, 465 (1972).
- [6] H.S. Wilson, R.W. Kavanagh and F.M. Mann, *Phys. Rev. C* **22**, 1696 (1980).
- [7] B. Blank, A. Bey, I. Matea, J. Souin, L. Audirac, M.J.G. Borge, G. Canchel, P. Delahaye, F. Delalee, C.-E. Demonchy, R. Domnguez-Reyes, L.M. Fraile, J. Giovinazzo, Tran Trong Hui, J. Huikari, D. Lunney, F. Munoz, J.-L. Pedroza, C. Plaisir, P. Delahaye, F.L. Serani, S. Sturm, O. Tengblad and F. Wenander, *Eur. Phys. J. A* **44**, 363 (2010).

## Measurement of branching-ratios in the $\beta$ decay of $^{38}\text{Ca}$

H. I. Park, J. C. Hardy, V. E. Jacob, L. Chen, J. R. Goodwin, V. Horvat, N. Nica,  
L. Trache, and R. E. Tribble

We have been making steady progress towards our goal of being able to measure the branching ratios for superallowed transitions with a precision of  $\sim 0.1\%$ . This report documents our progress on such measurements for the decay of  $^{38}\text{Ca}$ . In these measurements,  $^{38}\text{Ca}$  was produced with the same reaction and primary beam energy used in the half-life measurement for  $^{38}\text{Ca}$  [1], and the activity was collected on, and transported by, our fast tape-transport system. In our first test measurement, we used a *collect-move-count* cycle of 1.5-0.180-1.5 s, and measured time-tagged  $\beta$ - $\gamma$  coincidence events with a 1-mm-thick plastic scintillator for  $\beta$  particles and our well-calibrated 70% HPGe detector for  $\gamma$  rays. In a five-day run, approximately 2.5-million  $\beta$ - $\gamma$  coincidence events were recorded, which corresponded to about 100-million  $\beta$  singles. Although the overall statistics were insufficient to achieve our targeted precision, the analysis of these data showed that the measured relative  $\gamma$ -ray intensities were consistent with the values previously measured in Ref. [2].

After this measurement, improvements were made in the experimental equipment, which allowed us to measure the electronic dead times and the source-to-detector distance cycle by cycle. The former was achieved by pulser signals from a constant frequency pulse generator measured in coincidence with gating signals from  $\beta$ -singles events,  $\gamma$ -singles events, and  $\beta$ - $\gamma$  coincidence events. The addition of a laser triangulation device into our system also allowed us to determine the source-to-detector distance accurate to  $\pm 0.1$  mm in the range from 9 to 19 cm [3]. With this upgraded system, every detection cycle is now tagged with its own source-to-detector distance. This increases the precision we can achieve in a branching-ratio measurement to the limit defined by the precision of the absolute efficiency of the  $\gamma$ -ray detector. These improvements were implemented into a second measurement of the branching-ratio of  $^{38}\text{Ca}$ .

The second measurement involved a seven-day run, in which we collected approximately 7 million  $\beta$ - $\gamma$  coincidence events from over 300 million  $\beta$  singles in 50 separate runs, including 3 runs used as room-background measurements. However, our analysis revealed that, of the total number of events that triggered  $\beta$ - $\gamma$  coincidences, approximately 20% were not recorded as complete events in our data-acquisition system because either the  $\beta$  or  $\gamma$  energy (or both) was below the threshold of the corresponding ADC. To resolve this problem, we are currently implementing various improvements to our data-acquisition electronics. One of our major focuses is to ensure that all events causing a  $\beta$ - $\gamma$  trigger have  $\beta$  and  $\gamma$  energies that are in the range of our ADC's; and to independently measure dead-times by recording the number of  $\beta$ - $\gamma$  coincidence triggers in the data stream on a cycle-by-cycle basis. We are also planning to employ the pulser method for measuring pile-up losses in the coincident  $\gamma$  rays. Once these improvements have been made, we will be one step closer to the 0.1% precision we seek for the branching-ratio measurement of  $^{38}\text{Ca}$ .

- [1] H.I. Park, J.C. Hardy, V.E. Jacob, A. Banu, L. Chen, V.V. Golovko, J. Goodwin, V. Horvat, N. Nica, E. Simmons, L.Trache, and R.E. Tribble, *Progress in Research*, Cyclotron Institute, Texas A&M University (2010-2011), p. XXX.
- [2] B.D. Anderson, A.R. Baldwin, P. Baumann, B.A. Brown, F. Didierjean, C.C. Foster, L.A.C. Garcia, A. Huck, R. Madey, D.M. Manley, G. Marguier, M. Ramdhane, H. Ravn, C. Richard-Serre, G. Walter and J.W. Watson, *Phys. Rev. C* **54**, 602 (1996).
- [3] L. Chen and J.C. Hardy, *Progress in Research*, Cyclotron Institute, Texas A&M University (2009-2010), p. V-29.

## JYFLTRAP : $Q_{EC}$ -values of the superallowed decays of $^{10}\text{C}$ , $^{34}\text{Ar}$ , $^{38}\text{Ca}$ and $^{46}\text{V}$

J. C. Hardy

This We have now completed and published four successful measurements of the  $Q_{EC}$  values for superallowed  $0^+ \rightarrow 0^+$  transitions from  $T_z = 0$  and  $T_z = -1$  nuclei using the JYFLTRAP Penning-trap mass spectrometer at the University of Jyvaskyla cyclotron facility in Finland. The first contained the results for  $^{26}\text{Al}^m$ ,  $^{42}\text{Sc}$  and  $^{46}\text{V}$  [1]; the second,  $^{50}\text{Mn}$  and  $^{54}\text{Co}$  [2] and the third,  $^{34}\text{Cl}$  and  $^{38}\text{K}^m$  [3]. In the most recent [4], our collaboration determined the  $Q_{EC}$  values for the superallowed decays of  $^{10}\text{C}$ ,  $^{34}\text{Ar}$ ,  $^{38}\text{Ca}$  and  $^{46}\text{V}$ . Our original intention was to measure the  $Q_{EC}$  values for  $^{10}\text{C}$  and  $^{14}\text{O}$  but the latter proved to be impossible because of the presence of relatively high levels of residual  $^{14}\text{N}$  in the system. We decided to defer the  $^{14}\text{O}$  measurement and measure three other superallowed  $Q_{EC}$  values instead. All three had been measured previously with a Penning trap, but with JYFLTRAP we could reduce the experimental uncertainties by a substantial amount.

As we did in our previous experiments, we produced  $^{10}\text{C}$  and  $^{46}\text{V}$  via  $(p,n)$  reactions. A powerful advantage of this approach is that, not only were the superallowed emitters of interest produced in the primary reactions but ions from the target material itself – the beta-decay daughters of these emitters – were also released by elastic scattering of the cyclotron beam. To produce  $^{34}\text{Ar}$  and  $^{38}\text{Ca}$  we used  $(p,2n)$  reactions, with their daughters and granddaughters produced by  $(p,pn)$  and  $(p,2p)$  reactions. As explained in Ref. [1], with the JYFLTRAP system we can isolate a specific nuclide from the reaction products and measure the cyclotron frequency of its ions in the Penning trap. For each determination of a  $Q_{EC}$  value, the cyclotron frequency measurements were interleaved: first we recorded a frequency scan for the daughter, then for the mother, then for the daughter and so on. This way, most potential systematic effects could be reduced to a minimum or eliminated. For each measurement, data were collected in several sets, each comprising  $\sim 10$  pairs of parent-daughter frequency scans taken under the same conditions.

Our four new  $Q_{EC}$ -value results for superallowed transitions are shown in Figure 1, where they are compared with previous measurements of the same quantities. The agreement is generally good although our uncertainties are much smaller than the others. Only for  $^{34}\text{Ar}$  is there a significant disagreement with an earlier measurement. In this case, that earlier measurement also used a Penning trap – ISOLTRAP [6] – but, while our measurement obtained the  $^{34}\text{Ar}$   $Q_{EC}$  value directly by a measurement of the frequency ratio of the daughter to parent ions, theirs used  $^{39}\text{K}$  as a reference ion. Thus, to get the  $^{34}\text{Ar}$   $Q_{EC}$  value, the mass of the daughter  $^{34}\text{Cl}$  also had to be linked to  $^{39}\text{K}$ . This link via  $^{39}\text{K} - 5$  mass units away – may well have been the source of their error.

Our results also appear in Table I, where they are compared with the equivalent values that appeared in the most recent survey of superallowed  $0^+ \rightarrow 0^+$  nuclear  $\beta$  decay [5]. In all cases, our new results have reduced the uncertainties considerably, although for  $^{34}\text{Ar}$  the reduction is constrained by the inconsistency already noted between our result and one of the previous measurements [6]. That inconsistency leads to a normalized  $\chi^2$  of 7 for the average and, following the procedures used in [5], we increase the uncertainty on the average by a scale factor equal to the square root of the normalized  $\chi^2$ .

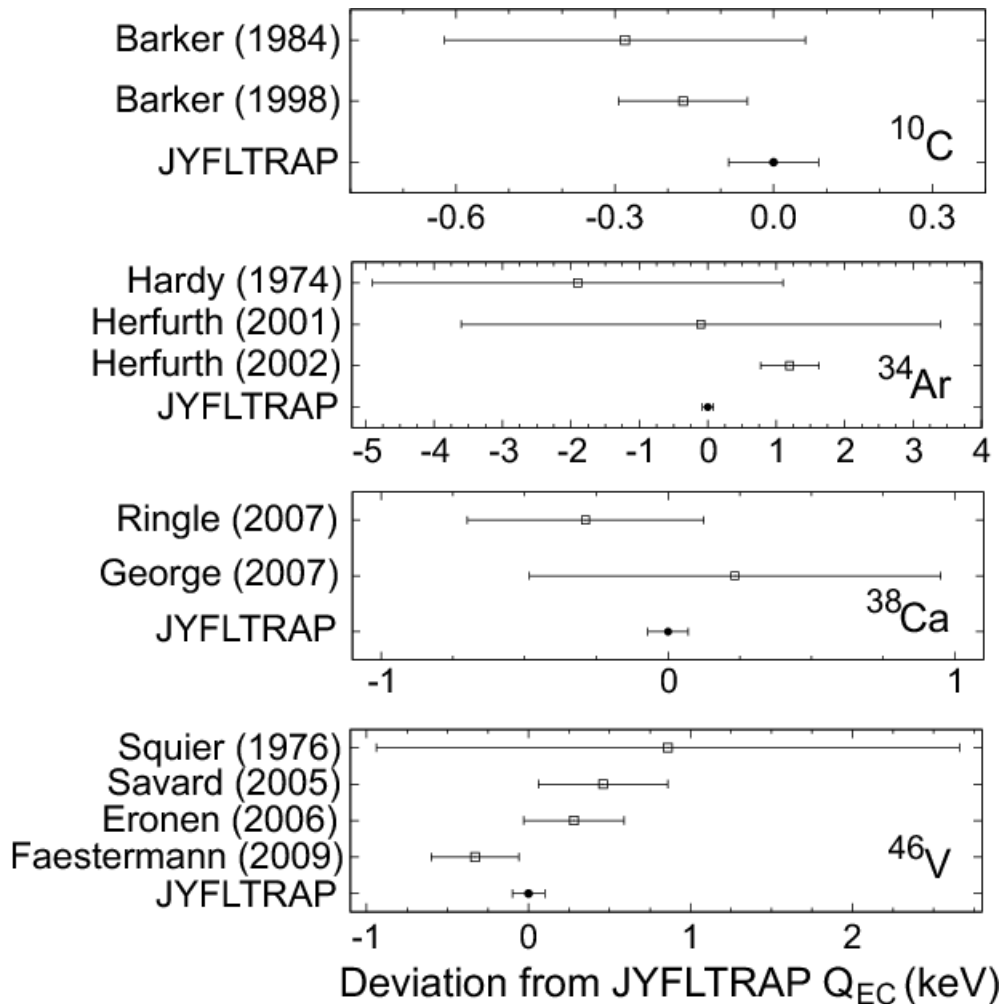


**FIG. 1.** Comparison of our  $Q_{EC}$ -value measurements, labeled JYFLTRAP, with previous measurements. For each transition, our result is plotted at 0 on the abscissa, and the other results are plotted as differences ( $Q_{EC}^{\text{LIT}} - Q_{EC}^{\text{JYFLTRAP}}$ ). The details of the previous references are given in our published paper [4].

**Table I.** The four  $Q_{EC}$  values for superallowed transitions that were obtained in this work. Also shown are the equivalent values quoted in the most recent survey of data [5] and the new weighted averages including our measurements.

Parent	Daughter	$Q_{EC}$ values (keV)		
		This work	Survey [5]	Average
$^{10}\text{C}$	$^{10}\text{B}$	1908.05(8)	1907.87(11)	1907.99(7)
$^{34}\text{Ar}$	$^{34}\text{Cl}$	6061.83(8)	6062.98(48)	6061.86(21)
$^{38}\text{Ca}$	$^{38}\text{K}^m$	6612.12(7)	6611.75(41)	6612.11(7)
$^{46}\text{V}$	$^{46}\text{Ti}$	7052.44(10)	7052.40(16)	7052.45(9)

We plan to complete our measurements on the “traditional nine” superallowed transitions by measuring the  $Q_{EC}$  value for  $^{14}\text{O}$  in an improved experimental set-up in the future.

- [1] T. Eronen, V. Elomaa, U. Hager, J. Hakala, A. Jokinen, A. Kankainen, I. Moore, H. Penttilä, S. Rahaman, A. Saastamoinen, T. Sonoda, J. Äystö, J.C. Hardy and V. Kolhinen, Phys. Rev. Lett. **97**, 232501 (2006).
- [2] T. Eronen, V.-V. Elomaa, U. Hager, J. Hakala, J.C. Hardy, A. Jokinen, A. Kankainen, I.D. Moore, H. Penttilä, S. Rahaman, S. Rinta-Antila, J. Rissanen, A. Saastamoinen, T. Sonoda, C. Weber and J. Aysto, Phys. Rev. Lett. **100**, 132502 (2008).
- [3] T. Eronen, V.-V. Elomaa, J. Hakala, J.C. Hardy, A. Jokinen, I.D. Moore, M. Reponen, J. Rissanen, A. Saastamoinen, C. Weber and J. Aysto, Phys. Rev. Lett. **103**, 252501 (2009).
- [4] T. Eronen, D. Gorelov, J. Hakala, J.C. Hardy, A. Jokinen, A. Kankainen, V.S. Kolhinen, I.D. Moore, H. Penttilä, M. Reponen, J. Rissanen, A. Saastamoinen and J. Aysto, Phys. Rev. C **83**, 055501 (2011).
- [5] J.C. Hardy and I.S. Towner, Phys. Rev. C **79**, 055502 (2009).
- [6] F. Herfurth *et al.*, Eur. Phys. J. A **15**, 17 (2002).

## Tests of internal-conversion theory with precise $\gamma$ - and x-ray spectroscopy: the case of $^{119}\text{Sn}^m$

N. Nica, J. C. Hardy, V. Horvath, V. E. Iacob, V. Siller, and M. B. Trzhaskovskaya<sup>1</sup>

<sup>1</sup>*Petersburg Nuclear Physics Institute, Gatchina RU-188300, Russia*

We have been making precision measurements of the Internal Conversion Coefficients (ICCs) of high-multipolarity transitions to establish the accuracy of calculated ICCs and, in particular, to discriminate between the theoretical prescriptions used to deal with the atomic vacancy left by the emitted electron. We are now extending our series of measurements to the 65.7-keV  $M4$  transition in  $^{119}\text{Sn}^m$ , which has a lower  $Z$  than any case we have examined so far. This transition originates from the 293.1-day isomeric state at 89.5 keV in  $^{119}\text{Sn}^m$ , which decays 100% by cascade via a 65.7-keV  $M4$  and a 24-keV  $M1/E2$  transition. Since the latter cannot convert in the  $K$  shell, the  $K$  x rays in the measured photon spectrum from this decay scheme are exclusively from the  $M4$  transition. Consequently, the  $K$  conversion coefficient for the  $M4$  transition can be determined from the equation

$$\alpha_K \omega_K = \frac{N_K}{N_\gamma} \cdot \frac{\varepsilon_\gamma}{\varepsilon_K},$$

where  $\omega_K$  is the fluorescence yield;  $N_K$  and  $N_\gamma$  are the total numbers of observed  $K$  x rays and 65.7-keV  $\gamma$  rays, respectively; and  $\varepsilon_K$  and  $\varepsilon_\gamma$  are the corresponding detector efficiencies. This is our standard method for making such measurements and, although our detector efficiency in the 25-29 keV region of the  $K$  x-rays is not as well established as it is at higher energies, we still anticipate being able to measure the ICC to a precision of  $\sim 2\%$ . This is sufficient precision to distinguish between the theory that ignores the atomic vacancy and the one that includes it, since the calculated ICC values differ from one another by 4.9%.

The main difficulty of this measurement comes from the large value of the ICC,  $\sim 5000$ , which means that the  $\gamma$ -ray component of the 65.7-keV transition is extremely weak and difficult to detect. This difficulty is further increased by the small cross section for thermal-neutron capture on  $^{118}\text{Sn}$ ,  $\sim 10$  mb, which we use to produce  $^{119}\text{Sn}^m$ . Finally, our provider, Trace Science International, had difficulty with rolling thin tin metallic foils for us, so the best sample we received of 99%-enriched  $^{118}\text{Sn}$  was a foil 1  $\text{cm}^2$  in area and about 8  $\mu\text{m}$  thick. Such a thick source led to the attenuation of  $K$  x rays being about 1.5% greater than the attenuation of 65.7-keV  $\gamma$  rays, a rather high value for precision work.

At a thermal neutron flux of  $7.5 \times 10^{12}$  n/( $\text{cm}^2$  s) in the Texas A&M Triga reactor, 120 hours of activation time were needed to yield a subsequent rate of 160,000 events the 65.7 $\gamma$ -ray peak per month of counting with our HPGe detector at 15.1 cm from cap to foil. Such a long activation time led to some unwanted effects: the thin tin foil adhered to its aluminum container, so we found it “stuck” at the bottom of the can; in addition, a corrosion process of some kind affected the surface of the foil. However, despite these impediments we were able to free the foil and use it for data acquisition with our HPGe detector.

Because of the weakness of the 65.7-keV  $\gamma$ -ray, we designed and produced a Cu-Pb detector shield to reduce the counting rate in our detector from room background by a factor of about 50 compared to the normal unshielded background. Under these conditions we acquired a spectrum for 45 days.

Our impurity analysis of the acquired spectrum revealed the presence of  $^{113}\text{Sn}$ ,  $^{117}\text{Sn}^m$ , and  $^{125}\text{Sb}$ , all of which contribute at the level of a few percent to the 25-29 keV energy region where the tin K x rays appear. Two other impurities,  $^{75}\text{Se}$  and  $^{182}\text{Ta}$ , were seen to contribute much more strongly (20% for  $^{75}\text{Se}$  and 30% for  $^{182}\text{Ta}$ ) to the region of the 65.7-keV  $\gamma$  ray. In the case of  $^{182}\text{Ta}$ , the subtraction of the impurity presented problems because the main  $^{182}\text{Ta}$  peak at 67.7 keV is a mixture of a strong  $\gamma$  ray plus three  $\text{K}_\beta$  x-rays components. For this reason we did an auxiliary experiment in which we activated a thin foil of pure  $^{181}\text{Ta}$  to produce a pure spectrum of  $^{182}\text{Ta}$  decay. We will use this result to provide a template for the contribution of the  $^{182}\text{Ta}$  impurity in our  $^{119}\text{Sn}^m$  data.

We also plan to activate an  $^{115}\text{In}$  target to produce  $^{116}\text{In}$ , which  $\beta$  decays to  $^{116}\text{Sn}$  and produces  $\gamma$  rays and tin x rays of known relative intensity. We will use a measurement of the resulting spectrum to get an efficiency-calibration point exactly at the Sn Kx-ray energy. Also we plan to address the problem of Compton scattering affecting the Sn Kx-ray energy region by Monte Carlo simulations and by measurements with a thin silicon x-ray detector.

## Test of claims that radioactive half-lives depend on the Earth-Sun distance

J. R. Goodwin, V. E. Jacob, and J. C. Hardy

Several recent publications by J.H. Jenkins and E. Fischbach [1-4] have claimed to find evidence that radioactive half-lives vary as a function of the Earth-to-Sun distance at the time of measurement. When the first of these claims appeared as an arXiv preprint, we had already made three sequential measurements of the half-life of the  $\beta$ -decay of  $^{198}\text{Au}$  for experiments involving other claims of changes in radioactive half-lives [5, 6]; we then decided to append four additional measurements of the  $^{198}\text{Au}$  half-life, with the measurements to be conducted at times such that the seven measurements as a whole would cover, fairly evenly, a typical perihelion-aphelion interval

The major claims by Jenkins and Fischbach [2] are based upon their interpretation of published data taken by others – one set of measurements having been performed at the Brookhaven National Laboratory (BNL) [7] and the other at the Physikalisch Technische Bundesanstalt (PTB) in Germany [8]. The BNL measurements compared the decay rate of  $^{32}\text{Si}$  ( $t_{1/2} = 172$  yr) to that of  $^{36}\text{Cl}$  ( $t_{1/2} = 300,000$  yr) on a regular basis, over four years; they used an end-window gas-flow proportional counter to detect decay  $\beta$  particles. The PTB measurements, which were made for calibration purposes, periodically obtained the decay rate of  $^{226}\text{Ra}$  ( $t_{1/2} = 1600$  yr) over 11 years, using a high-pressure  $4\pi\gamma$  ionization chamber. The data from both groups show a weak, but statistically significant oscillatory behavior of the decay rate, with a period of one year. Both the groups acknowledged the oscillations in their data, the group from BNL noting that the oscillations corresponded with seasonal variations in temperature and humidity, which could have affected the relative absorption of the  $\beta$  particles from  $^{32}\text{Si}$  and  $^{36}\text{Cl}$ ; the PTB group attributed them to background radioactivity, such as radon and daughter products, which show seasonal concentration changes.

In their reanalysis of the data, Jenkins and Fischbach superimposed a plot of the Earth-Sun distance over the sequence of half-life values measured by each group. A copy of their plot [2] for the BNL  $^{32}\text{Si}$  data appears in Fig. 1. The solid (cyclic) line is a plot of  $1/R^2$ , where  $R$  is the Earth-Sun distance in astronomical units; each individual data point represents the average of 4 runs, each lasting 10 hr. They conclude [2] that there is a strong correlation between the oscillations in the data and the Earth-Sun distance, and they speculate that this correlation could arise from a terrestrial modulation in the fine-structure constant, caused by a scalar field from the sun, or could arise because the terrestrial radioactive nuclei are interacting in some way with the neutrino flux from the sun. They even present an argument for how this latter might cause the “phase shift” between the  $1/R^2$  curve and the BNL (and PTB) data.

Since both the BNL and PTB measurements were of totally non-discriminated decay rates for long-lived radioactivities, any observed cyclic variations cannot definitely be attributed to variations in the half-lives involved. A variety of other factors, such as the seasonal effects already mentioned, could plausibly be involved, and their elimination requires elaborate argumentation [4] – and is certainly open to debate [9].

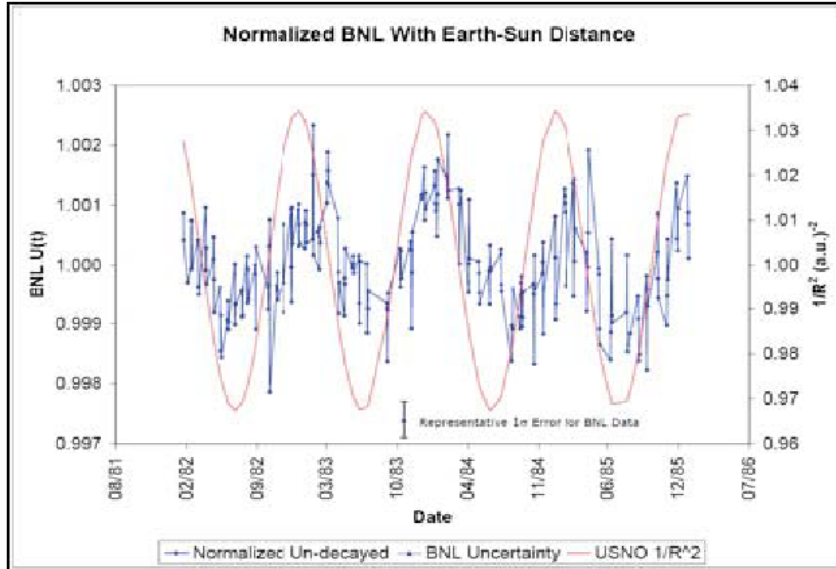


**FIG. 1.** Plot of  $U(t)$  for the raw BNL  $^{32}\text{Si}/^{36}\text{Cl}$  ratio (points) together with  $1/R^2$ , where  $R$  is the Earth-Sun distance. The values of  $U(t)$  are obtained by multiplying each data point by  $\exp(+\lambda t)$ , where  $\lambda = (\ln 2)/t_{1/2}$  with  $t_{1/2} = 172$  yr for  $^{32}\text{Si}$ . The left axis gives the scale for the normalized  $U(t)$ , and the right axis denotes the values of  $1/R^2$  in  $1/(\text{a.u.})^2$ .

Plot of  $U(t)$  for the raw BNL  $^{32}\text{Si}/^{36}\text{Cl}$  ratio (points) together with  $1/R^2$ , where  $R$  is the Earth-Sun distance. The values of  $U(t)$  are obtained by multiplying each data point by  $\exp(+\lambda t)$ , where  $\lambda = (\ln 2)/t_{1/2}$  with  $t_{1/2} = 172$  yr for  $^{32}\text{Si}$ . The left axis gives the scale for the normalized  $U(t)$ , and the right axis denotes the values of  $1/R^2$  in  $1/(\text{a.u.})^2$ .

We used the procedures we have described previously [5]. For each measurement, a circular disc of 99.99+% pure gold, 10 mm in diameter and 0.1 mm thick, was activated by being placed in a flux of  $\sim 10^{10}$  neutrons/cm<sup>2</sup>·s, for 10 s, at the Texas A&M Triga reactor. It was then placed in a fixed geometry with respect to a 70% HPGe detector, and not moved for the approximately one-month duration of the measurement. Over 100 consecutive  $\gamma$ -ray spectra were acquired for a pre-set live time, and then saved. We extracted the number of counts in the 411-keV  $\gamma$ -ray peak in each spectrum using the least-square peak-fitting program GF3 (in the RADware series, [10]), and corrected the results for small residual, rate-dependent effects, which we had determined from an independent measurement [5, 6]. We then fitted the decay curve obtained from this analysis using the method of maximum-likelihood with a single-exponential, in a code based on ROOT [11].

How does our result compare with the BNL-observed activity oscillations, upon which Jenkins, Fischbach *et al.* base their claims? In Figure 2 we present the BNL activity results plotted against the dates of their measurement over a period of four years from early 1982 to early 1986. The dotted curve shows the  $1/R^2$  behavior of the Earth-Sun distance over the same period, which is very nearly a pure sine

wave. We have therefore fitted the BNL data with a sine wave, which has a fixed one-year period but variable amplitude and phase shift. A least squares fit to the data, shown as the dashed curve in the figure, yielded an amplitude of  $7.9(3) \times 10^{-4}$  and a phase shift of  $35(2)$  d relative to the  $1/R^2$  plot. This phase shift was also noted by Jenkins [2].

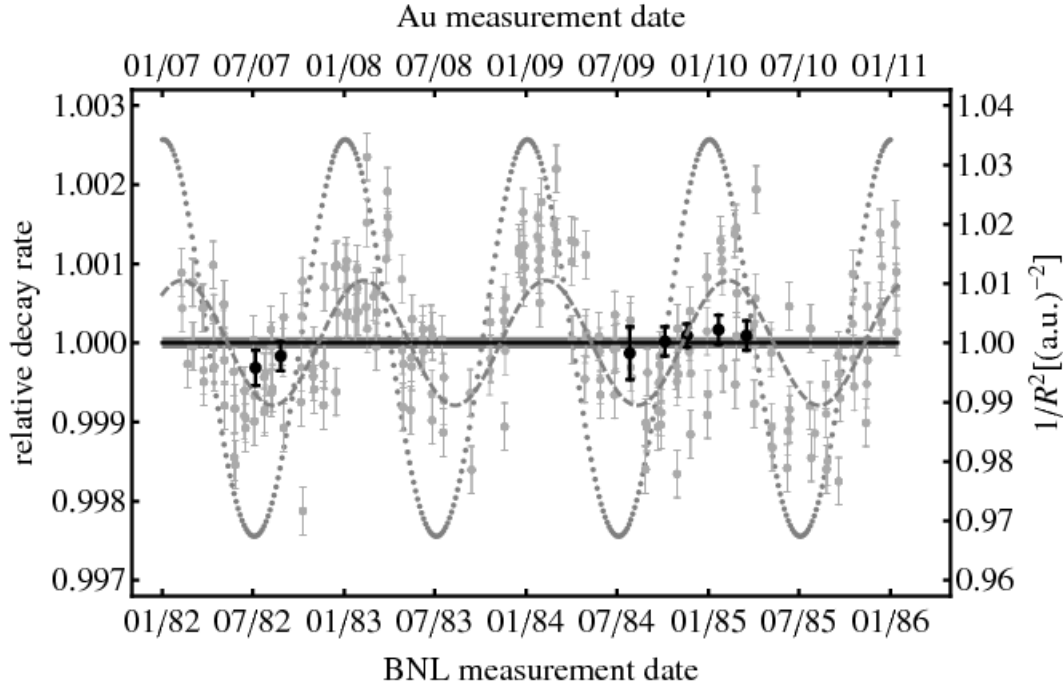


**FIG. 2.** The BNL data for the activity ratio,  $^{32}\text{Si}/^{36}\text{Cl}$  [7], as published in [2], are plotted as grey circles with error bars (referred to the vertical axis at the left) against the dates of their measurement between 1982 and 1985 (horizontal axis at the bottom). The dotted curve shows the  $1/R^2$  behavior of the Earth-Sun distance, where  $R$  is measured in astronomical units, a.u. (vertical scale at the right), over the same period; and the dashed curve gives our fit to the BNL data (see text). Our seven results for the decay rate of  $^{198}\text{Au}$  normalized to their average value (with the same vertical scale as the BNL data) are plotted as black circles with error bars against their dates (shown on the horizontal axis at the top, which is shifted exactly 25 years compared to the bottom scale).

Since the BNL measurements were of activity not half-life we plot our results in Fig. 2 as decay rates,  $\lambda (= \ln 2 / t_{1/2})$ , normalized to their average; they appear as black circles with error bars. The time scale for our measurements has been displaced by exactly 25 years from the BNL scale, so our data appear with the same perihelion synchronization. The horizontal shaded band shows the one-standard-deviation uncertainty limits on the average value from our results. Our data are statistically consistent with a constant half-life value to within a relative precision of  $\pm 7 \times 10^{-5}$ , an order of magnitude smaller than the amplitude of the oscillations attributed to the BNL data.

[1] J.H. Jenkins and E. Fischbach, *Astropart. Phys.* **31**, 407 (2009).

- [2] J.H. Jenkins, E. Fischbach, J.B. Buncher, J.T. Gruenwald, D.E. Krause and J.J. Mattes, *Astropart. Phys.* **32**, 42 (2010).
- [3] E. Fischbach, J.B. Buncher, J.T. Gruenwald, J.H. Jenkins D.E. Krause, J.J. Mattes and J.R. Newport, *Space Sci. Rev.* **145**, 285 (2009).
- [4] J.H. Jenkins, D.W. Mundy and E. Fischbach, *Nucl. Instrum.. Methods Phys. Res.* **A620**, 332 (2010).
- [5] J.R. Goodwin, V.V. Golovko, V.E. Iacob and J.C. Hardy, *Eur. Phys. J. A* **34**, 271 (2007).
- [6] J.R. Goodwin, V.E. Iacob, N. Nica, A. Dibidad and J.C. Hardy, *Phys. Rev. C* **82**, 044320 (2010).
- [7] D. Alburger, G. Harbottle and E.F. Norton, *Earth and Planet. Sci. Lett.* **78**, 168 (1986).
- [8] H. Siegert, H. Schrader and U. Schotzig, *Appl. Radiat. Isot.* **49**, 1397 (1998).
- [9] H. Schrader, *Appl. Radiat. And Isot.*, **68**, 1583 (2010)..
- [10] D. Radford, <http://radware.phy.ornl.gov/main.html> (private communication).
- [11] R. Brun, F. Rademakers, *Nucl. Instrum. Methods Phys. Res.* **A389**, 81 (1997).

**United States nuclear data program evaluated nuclear structure data file (ENSDF):  
Five years of data evaluation at Texas A&M**

N. Nica,<sup>1</sup> J. C. Hardy, and B. Singh<sup>2</sup>

<sup>1</sup>under contract with Brookhaven National Laboratory

<sup>2</sup>McMaster University, Hamilton, Ontario, Canada

This was the sixth consecutive year that we have been an important participant in the nationwide United States Nuclear Data Program (USNDP). This is a national interest activity financed by DOE, through which the relevant nuclear-science results in virtually all world publications are retrieved and put together in a large Evaluated Nuclear Structure Data File (ENSDF) database according to *general policies* [1], a set of rules that make possible a standard approach through which the data are uniformly evaluated. This activity is supported by a relatively small group of professionals organized as a national data network located mostly in national institutes but also hosted by few universities. The nuclear data network is the nodal point for the wide dissemination of nuclear knowledge to many customers, from those in basic science to those engaged in commercial applications in American and international businesses.

The US network is the most consistent part of an international network similarly organized worldwide. The output is published in the Nuclear Data Sheets, an Elsevier publication, and also is disseminated by different on-line databases which can be retrieved at the NNDC site (<http://www.nndc.bnl.gov>), IAEA Vienna's site (<http://www-nds.iaea.org>) and several other locations.

During these years we covered essentially all the regions of the periodic table. The superheavy A=252 mass chain, the very data-rich mid-mass chains, A=147 and A=140, and the relatively lighter chains, A=97 and A=84, have all been published previously in Nuclear Data Sheets; the A=77 and A=34 chains will soon appear in the same journal. Since nuclear-data evaluation depends critically on the experience of the evaluator, with a veteran evaluator typically completing only a couple of mass chains per year, coverage of such a wide range of A chains in such a short time is a considerable accomplishment. This once more testifies to Texas A&M's qualifications to be considered a national evaluation center.

This past year was the second one in which evaluations were done in collaboration with B. Singh from McMaster University, Canada. We completed the A=36 and A=37 mass chains [2]. Both incorporate several hundred data-significant publications and were unusually demanding since all previous evaluations had been done by P. Endt and co-authors, who used their own methods and format, and published in the journal Nuclear Physics A. Thus, we had to cover the whole history of these nuclei from the very beginning, requiring us to review and reorganize everything ever published on these mass chains. As an innovation we also included unbound resonant states in our evaluation, something that has generally not been done in ENSDF. We did so to accommodate the astrophysics community, which has become interested in such information in recent years.

[1] Nucl. Data Sheets **111**, v (2010).

[2] N. Nica, J.C. Hardy, and B. Singh, Nuclear Data Sheets (accepted).

## TRIUMF : Precise half-life measurement of the superallowed $\beta^+$ emitter $^{38}\text{K}^m$

J. C. Hardy and V. E. Iacob

Some years ago we participated in a collaborative experiment to measure the half-life of the superallowed  $\beta^+$  emitter  $^{38}\text{K}^m$  at the Isotope Separator and Accelerator (ISAC) facility at TRIUMF in Vancouver, Canada. The result has now been published [1].

A radioactive beam of  $\sim 5 \times 10^5$  ions/s of mixed  $^{38}\text{K}$  and  $^{38}\text{K}^m$  was obtained from a production target combined with a surface-ionization ion source. By pulsing the TRIUMF proton beam and collecting samples for only 0.3 s we could favor  $^{38}\text{K}^m$  ( $t_{1/2} = 924$  ms) over  $^{38}\text{K}$  ( $t_{1/2} = 7.6$  min) by a factor of 60-80. We performed the experiment by implanting this 29-keV radioactive beam into the aluminized Mylar tape of a fast tape-transport system. After the 0.3-s collection time, the beam was interrupted and the sample was moved out of the vacuum chamber through two stages of differential pumping, finally being positioned at the center of a  $4\pi$  continuous-gas-flow proportional  $\beta$  counter. This counter and the subsequent electronics were very similar to the system we routinely use at the Texas A&M cyclotron (for example, see Ref. [2]). The data were analyzed in parallel at both TRIUMF and Texas A&M. The two results were in good agreement.

There have been five previous measurements of the half-life of  $^{38}\text{K}^m$  that have been quoted with uncertainties within a factor of ten of the present measurement [3-7]. As can be seen in Figure 1, our result is a factor of two more precise than any of the previous ones. The weighted average of all six measurements is  $924.33 \pm 0.12$  ms but with an unsatisfactory reduced  $\chi^2$  of 4.83. As is the usual practice

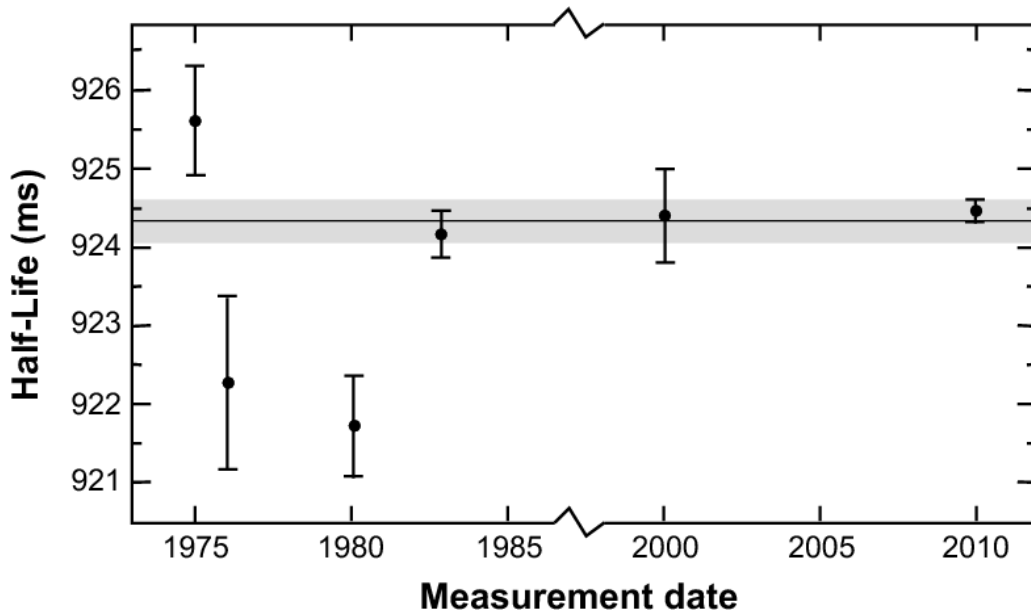


**FIG. 1.** The data points represent all published measurements of the  $^{38}\text{K}^m$  half-life with quoted uncertainties that are within a factor of 10 of the present measurement. The results are plotted in chronological order from left to right, with measurement 6 being the present result. The weighted average, 924.33 ms, is given by the horizontal line, with its scaled uncertainty,  $\pm 0.27$  ms, represented by the grey band. Note that the uncertainty on the average has been increased by a scale factor equal to the square root of the reduced  $\chi^2$  for all six results, which is 4.83.

in the periodic surveys of superallowed  $\beta$  decay (for example, Ref. [8]), we follow the method of the Particle Data Group and inflate the uncertainty quoted on the average by a “scale factor,” which is essentially equal to the square root of the reduced  $\chi^2$ . This result for the average,  $924.33 \pm 0.27$  ms, is the one shown as a horizontal band in the figure.

From the figure it can also be seen that the three most recent measurements are in excellent agreement with one another, while the two Wilkinson measurements [5,6] are significantly below the average, the most recent of the two being four of its standard deviations from the average. Although there is no obvious reason from the original papers to disregard these two measurements, it can be noted that if they are removed from the averaging process, the weighted average becomes  $924.44 \pm 0.14$  ms with a scale factor of 1.1. This observation may perhaps provide some motivation for attempting in the future and even more precise measurement of the  $^{38}\text{K}^m$  half-life with the goal of making the suspect Wilkinson measurements statistically irrelevant.

- [1] G.C. Ball, G. Boisvert, P. Bricault, R. Churchman, M. Dombisky, T. Lindner, J.A. Macdonald, E. Vandervoort, S. Bishop, J.M. D’Auria, J.C. Hardy, V.E. Jacob, J.R. Leslie and H.-B. Mak, Phys. Rev. C **82**, 045501 (2010).
- [2] V.E. Jacob, J.C. Hardy, A. Banu, L. Chen, V.V. Golovko, J. Goodwin, V. Horvat, N. Nica, H.I. Park, L. Trache and R.E. Tribble, Phys. Rev. C **82**, 035502 (2010).
- [3] G.T.A. Squier, W.E. Burcham, J.M. Freeman, R.J. Petty, S.D. Hoath, and J.S. Ryder, Nucl. Phys. **A242**, 62 (1975).
- [4] D.H. Wilkinson, D.E. Alburger, Phys. Rev. C **13**, 2517 (1976).
- [5] D.H. Wilkinson, A. Gallmann, and D.E. Alburger, Phys. Rev. C **18**, 401 (1978).
- [6] V.T. Koslowsky, E. Hagberg, J.C. Hardy, R.E. Azuma, E.T.H. Clifford, H.C. Evans, H. Schmeing, U.J. Schrewe, and K.S. Sharma, Nucl. Phys. **A405**, 29 (1983).
- [7] P. H. Barker and M. S. Wu, Phys. Rev. C **62**, 054302 (2000).
- [8] J.C. Hardy and I.S. Towner, Phys. Rev. C **79**, 055502 (2009).

## Isospin symmetry breaking in the $\beta$ decay of $^{32}\text{Cl}$

C. Bordeanu,<sup>1,2</sup> A. García,<sup>1</sup> J. C. Hardy, V. E. Jacob, D. Melconian, N. Nica, H. I. Park, G. Tabacaru, L. Trache, I. S. Towner, S. Triambak,<sup>1,3</sup> R. E. Tribble, and Y. Zhai

<sup>1</sup>*CENPA, University of Washington, Seattle, Washington*

<sup>2</sup>*Institute of Nuclear Research, Debrecen, Hungary*

<sup>3</sup>*University of Delhi, Delhi, India*

The  $\beta^+$  decay of  $^{32}\text{Cl}$  has been investigated using the fast tape-transport system at the Cyclotron Institute to improve measurements of the  $\gamma$  branches. This work is motivated by the impact it can have on improving the theoretical isospin-symmetry breaking (ISB) corrections to the  $ft$  values of pure Fermi  $\beta$  decays: first, our shell-model prediction for the ISB correction of this decay's  $T=1$  to  $T=1$  isobaric analogue transition is  $\delta_C=4.6(5)\%$ , significantly larger than the cases used to test CVC, measure  $V_{ud}$  and test CKM unitarity. Secondly, a recent experiment measuring  $\delta_C$  in the  $T=2$  decay of  $^{32}\text{Ar}$  requires precise knowledge of the  $\gamma$  branches from its decay; this can be improved with the present work because decays of  $^{32}\text{Ar}$  are partially followed by decays of  $^{32}\text{Cl}$  and thus provide an *in situ* efficiency calibration for  $\gamma$ s.

The experiment was carried out at the Cyclotron Institute using a primary beam of  $^{32}\text{S}$  which was produced by the ECR ion source and injected into the K500 superconducting cyclotron to accelerate it to 24.8 MeV/nucleon. The 400 nA  $^{32}\text{S}$  beam exited the cyclotron and was directed towards the target chamber of the Momentum Achromatic Recoil Separator (MARS). A secondary beam of  $^{32}\text{Cl}$  was produced via the inverse kinematic transfer reaction,  $^1\text{H}(^{32}\text{S},n)^{32}\text{Cl}$  on a LN<sub>2</sub> cooled, hydrogen gas target at approximately 1.4 atm. MARS was used to spatially separate the reaction products, resulting in a  $^{32}\text{Cl}$  beam with an intensity of  $\approx 2 \times 10^5$  ions/s. The activity was implanted mid-way in a 76  $\mu\text{m}$  Aluminized-mylar tape which, as part of a fast tape-transport system, transferred the activity 180 cm away where  $\beta$ - $\gamma$  coincidences were measured using a thin plastic scintillator and precisely-calibrated HPGe detector. Figure 1 shows the  $\gamma$  spectrum where almost every statistically significant peak is associated with the decay of  $^{32}\text{Cl}$ ; the only prominent contaminant is from  $^{30}\text{S}$ , which is well separated from any of the  $^{32}\text{Cl}$   $\gamma$  energies.

Critical to the success of this experiment was the very precise efficiency calibration of the HPGe detector [1-3]. This previous work determined the efficiency to  $\pm 0.2\%$  from 50-1400 keV, and from 1.4-3.5 MeV it is known to  $\pm 0.4\%$ . We extended this efficiency out to 7.2 MeV, the energy range of the HPGe detector in this experiment, using Monte Carlo simulations. Since it is nevertheless an extrapolation, we assign a conservative 1% uncertainty from 3.5-5 MeV and even more conservative 5% uncertainty from 5-7 MeV. Similar simulations of the plastic scintillator's efficiency showed that it was independent of the  $\beta$  end-point energy. After fitting the areas of the  $\gamma$  peaks, we converted the observed yields into  $\beta$  branches to state  $i$ ,  $\beta_i$ , and  $\gamma$  branches from state  $i$  to state  $j$ ,  $\gamma_{i,j}$ , using an equation similar to:

$$N_{i,j}^{\gamma} = N_{\text{tot}} \left[ \beta_i \eta_i + \sum_{k>i} \beta_k \eta_k \gamma_{k,i} \right] \epsilon_{i,j} \quad (1)$$

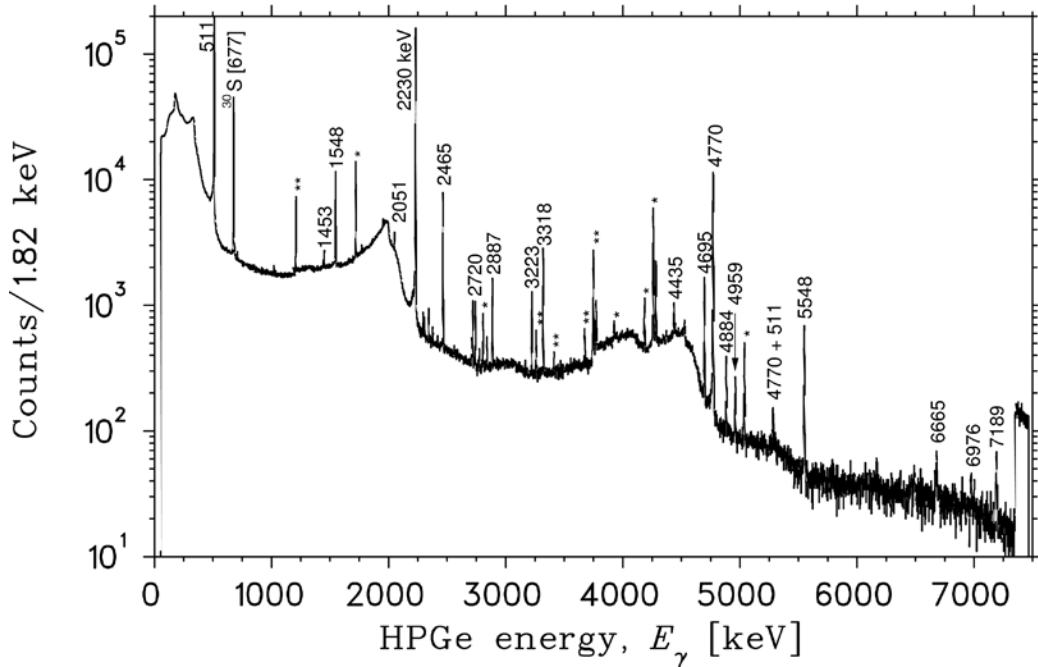


**FIG. 1.** The  $\gamma$  spectrum observed by the HPGe detector, with prominent peaks from the decay of  $^{32}\text{Cl}$  labeled (a \* indicates a single-escape peak and a \*\* indicates a double-escape). The only significant background peak is at 677 keV from the  $^{30}\text{S}$  contamination.

where  $N_{i,j}^{\gamma}$  is the observed number of counts at energy  $E_{i,j}$  is the total number of decays, and the  $\beta$  and  $\gamma$  efficiencies are  $\eta$  and  $\epsilon$  respectively. Small corrections to Eq. (1) that are included in the analysis but omitted here for clarity are required to account for (a) summing with cascade  $\gamma$ s from above and below, and (b) summing with 511 annihilation radiation since this is a  $\beta^+$  decay. From the 34 photopeaks we observed associated with the decay of  $^{32}\text{Cl}$ , we improved the precision of known branches by about an order of magnitude, and found 22 new  $\gamma$  transitions, placing limits on 10 others. The result is shown graphically in decay scheme of Fig. 2. As indicated, the unseen ground state branch was taken from the work of Armini *et al.* [4] and the ENSDF Data Tables [5] were used to provide excitation energies and  $\gamma$  branches when necessary. Branches to higher levels that could not be observed in our experiment were estimated using shell-model calculations using the USD, USDA and USDB potentials, indicating 0.60(10)% of the  $\beta$  strength would also be missed. The range of energies spanned by the shell-model prediction includes  $\beta$ -delayed proton- and  $\alpha$ -emitting states seen by Honkanen *et al.* [6].

Our integrated  $\beta$  strength over the range of end-point energies observed compares well with the prediction of the shell-model calculations, indicating that the quality of the USD wave functions is good. For the decay to the 7002-keV  $1^+_2$ ,  $T=1$  isobaric analogue state, the shell model predicts a very weak Gamow-Teller strength; this gives us the opportunity to study this transition as if it were a pure Fermi decay, compare it the precisely measured pure Fermi transitions [7], and deduce the amount of isospin-symmetry breaking in this transition. A large ISB effect is anticipated because a  $1+$ ,  $T=0$  state is only 188 keV away, leading to mixing between these states of differing isospin. With our isobaric analogue branch measured to better than 1%, we find an ISB effect of  $(\delta_C - \delta_{NS}) = 5.4(8)\%$ , the largest yet

determined and about 5% larger than typical values found in superallowed pure Fermi transitions in the s,d-shell. This result agrees well with the shell-model prediction of 4.8(5)% and represents an important validation of the shell-model used to extract  $V_{ud}$  from precisely measured  $ft$  values.

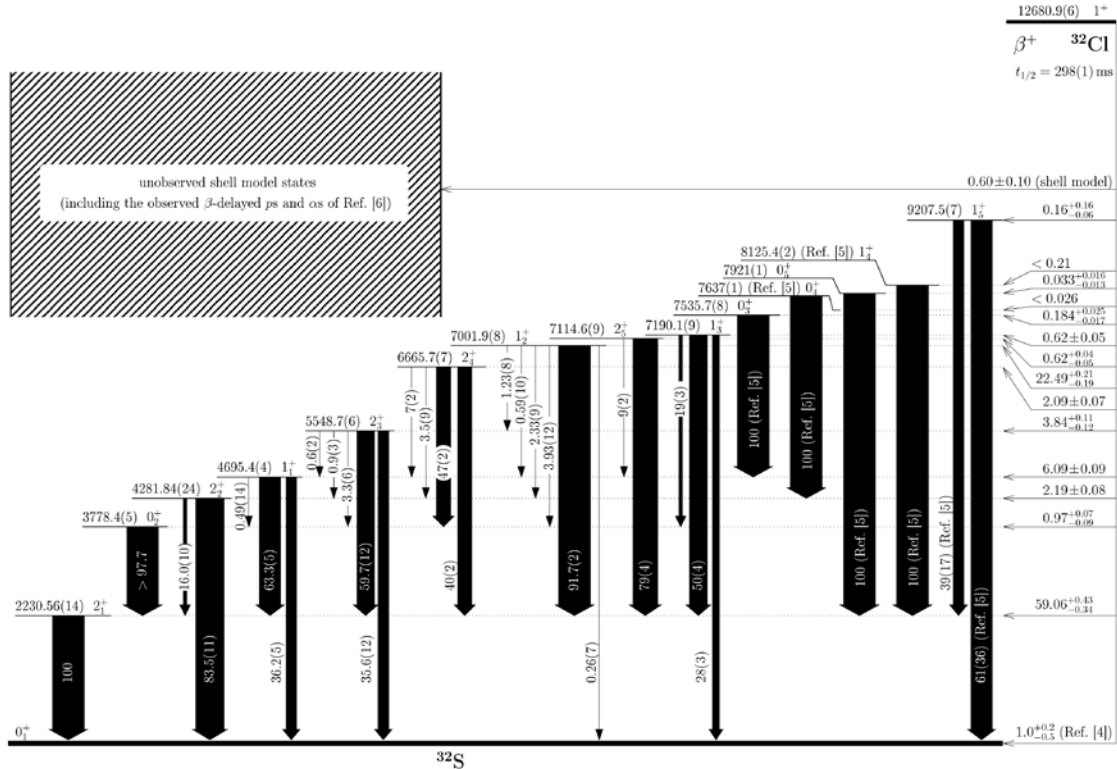


**FIG. 2.** Decay scheme for <sup>32</sup>Cl, summarizing the b and g branches deduced from this work (unless otherwise noted). All branches are expressed in percent.

- [1] J.C. Hardy *et al.*, Appl. Radiat. Isot. **56**, 65 (2002).
- [2] R.G. Helmer *et al.*, Nucl. Instrum. Methods Phys. Res. A **511**, 360 (2003).
- [3] R.G. Helmer *et al.*, Appl. Radiat. Isot. **60**, 173 (2004).
- [4] A.J. Armini, J.W. Sunier and J.R. Richardson, Phys. Rev. **165**, 1194 (1968).
- [5] Evaluated Nuclear Structure Data File (ENSDF), <http://www.nndc.bnl.gov/ensdf/>.
- [6] J. Honkanen *et al.*, Nucl. Phys. A **330**, 429 (1979).
- [7] J.C. Hardy and I.S. Towner, Phys. Rev. C **79**, 055502 (2009).

## Penning trap facility – Program for the study of fundamental weak interaction

R. S. Behling, B. Fenker, M. Mehlman, D. Melconian, and P. D. Shidling

The initial program of the Penning trap facility at the Institute involves measuring the  $ft$  values and correlation parameters of  $T=2$  superallowed  $\beta$ -delayed proton emitters. Such measurements will: improve our understanding of isospin-mixing corrections [1]; provide new nuclei with which we may extract additional measurements of  $V_{ud}$  (used to test unitarity of the CKM matrix); and search for possible scalar currents in the weak interaction via the b-n correlation parameter. The facility will also allow us to carry out mass measurements of stable and radioactive nuclei with life-times as short as  $\approx 400$  ms.

The radioactive beams for the present program will be produced by the upgrade project. The high intensity primary beam from the re-commissioned K150 Cyclotron will be bombarded on a  $^3\text{He}$  gas target. Reaction products of interest will be separated from other reaction products using BigSol, a large bore 7-Tesla superconducting solenoid. Following BigSol, the beam will be stopped in a gas catcher. The low-energy secondary beam will be extracted from the gas catcher and transported through a multi-RFQ to the Penning trap facility.

The beam line optics from the multi-RFQ to the setup has been designed using SIMION [2]. Secondary beams will be accelerated to 15 keV for efficient transport. Two einzel lens and two pairs of steering plates will be used to focus and direct the beam upward through the roof planks. Ions will be deflected twice by  $90^\circ$  using deflecting mirrors and will be directed further using an einzel lens into the injection optics. Before injection into the RFQ, the beam must first be electrostatically decelerated down to energy in the range of 10 to 20 eV. This is accomplished by placing the RFQ and the injection optics on a potential slightly below the corresponding ion beam energy.

Ions will be cooled and bunched using a segmented gas-filled RFQ. The ions will enter the RFQ with an energy around 15 eV. The RFQ is 700 mm long with  $r_0 = 6$  mm. In order to apply the longitudinal potential, the structure is divided axially into 24 segments. The radius of each segment is  $r = 7$  mm and the segments are all separated by a 1.0 mm gap. The gas-filled RFQ will be operated at room temperature at a pressure of  $1 \times 10^{-2}$  mbar. A longitudinal electric field equal to 0.75 V/cm will be applied over the segments of the system. The ions will be accumulated by forming a shallow potential well on the final three electrodes. Simulations show that the ions will reach equilibrium in less than 700  $\mu\text{s}$ . In the present simulation, the ions are further cooled and accumulated into the trap potential minimum for an additional period of 2 ms. Bunched ions will be extracted from the RFQ and pass through the extraction optics, which consists of an extraction plate and einzel lens, and then will be accelerated to 2.7 keV in the first pulsing cavity. Once the ions are inside the pulsing cavity, its potential will be switched down to ground potential and the ions will leave the cavity without any further change in their kinetic energy. The ions will be refocused with the help another einzel lens and will be deflected  $90^\circ$  with a third electrostatic mirror. A pair of einzel lens will be used to further focus and direct the beam into the second pulsing cavity, located inside the superconducting magnet. Ions will be decelerated to a few tens of electron volts by pulsing the second pulsing cavity with a potential slightly below the incoming ion energy. Ions will

enter the first purification trap at ground potential with an energy of  $\approx 80$  eV, time spread of  $1.7 \mu\text{s}$ , and an energy spread of 6 eV.

We have designed the Penning trap to have the flexibility of carrying out  $\beta$ -delayed proton decay studies and precision mass measurement of isotopes. The Penning trap system, consisting of a two cylindrical traps in a superconducting magnet with field strength of 7 Tesla has a very open geometry and will be especially useful for decay studies.

The first trap is used as a purification trap. The trap is a seven electrode cylindrical trap with inner diameter of 32 mm and total length about 212 mm. The trap has been designed to efficiently capture and cool the bunched ions using a pressure of  $1 \times 10^{-5}$  mbar.

The second Penning trap, the measurement trap, is also cylindrical with an inner diameter around 90 mm. It utilizes a tunable, orthogonalized 5 electrode geometry. The measurement trap will have a larger diameter than any other existing Penning trap facility, uniquely allowing for full radial containment of up to 4 MeV protons produced in the T=2 superallowed  $\beta$ -decays.

The large-bore magnet from Magnex Scientific will arrive on September 20<sup>th</sup>, 2011. The design of beamlines leading up to the Penning trap magnet is shown in Fig.1. The mechanical design of different components of the facility is in progress and we expect to begin building components later this year.

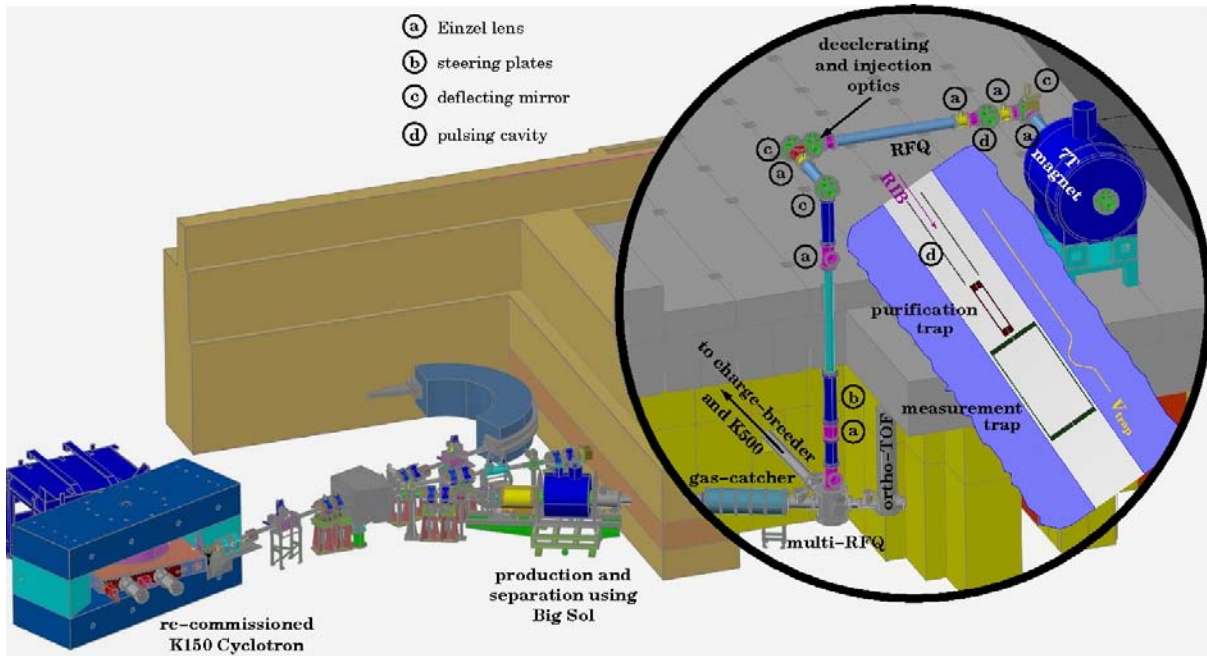


**FIG. 1.** Layout of the Penning trap facility. Primary beams from the recommissioned K150 cyclotron will produce radioactive ions in front of BigSol which will separate contaminants before the beam is stopped in the gas-catcher. Ions will be transported to the Penning trap magnet as shown.

[1] M. Bhattacharya *et al.*, Phys. rev. C **77**, 065503 (2008).

[2] SIMION Version 9.0.

## Precise life-time measurements of $T = 1/2$ mirror transition

R. S. Behling, B. Fenker, J. C. Hardy, V. E. Jacob, M. Mehlman, D. Melconian, B. T. Roeder, P. D. Shidling, and H. Stephens

To determine the correlation parameters of the  $\beta$  decay in  $T=1/2$  mirror transition, the  $ft$  value is needed to determine  $\rho$ , the ratio of Gamow-Teller to Fermi matrix elements. A recent review of all  $T=1/2$   $\beta$  mirror decays [1] indicates that  $^{37}\text{K}$  and  $^{21}\text{Na}$  are of great interest and possibly the best candidates for testing the Standard Model. In order to make the Standard Model predictions of the correlation parameters negligible compared to planned experiments [2,3], we have measured the life-times of  $^{37}\text{K}$  and  $^{21}\text{Na}$ . The half-lives in these cases are the largest contributors to the total uncertainty of their  $ft$  values.

$^{37}\text{K}$  was produced via the  $p(^{38}\text{Ar}, 2n)^{37}\text{K}$  reaction in inverse kinematic at a primary beam energy of 29 MeV/u. The Momentum Achromatic Recoil Spectrometer (MARS) was used to produce a secondary beam of  $^{37}\text{K}$  with a purity of 98.5%. The secondary beam exited the vacuum system through a Kapton foil and then passed through a thick plastic scintillator, a series of Al degraders and eventually implanted in the centre of an Al-Mylar tape. The fast-tape transport system quickly transported the sample to a well shielded location, placing it in the centre of a  $4\pi$  proportional gas counter [4]. The total data set was divided into 13 runs with different settings of the experimental parameters: bias voltage, discriminator threshold, dominant dead-times and thickness of the Al degrader. Each run consisted of 100-300 cycles, which yielded a total of  $4 \times 10^6$   $\beta$  events. Data was analyzed in two different ways. In the first method (summed fit), each cycle was dead-time corrected and the cycles from a given run were summed and fit using the Levenberg-Marquardt  $\chi^2$  minimization algorithm. In the second method (global fit) all the cycles were simultaneously fit in a given run with a single half-life parameter but with different background levels. The fit function consists of four exponentials ( $^{37}\text{K}$ ,  $^{35}\text{Ar}$ ,  $^{34}\text{Cl}$  and  $^{33}\text{Cl}$ ) plus a constant background. The decay curve observed with the global fit overlaid is shown in the left plot of Fig. 1. The results of all the sets is shown on the right of Fig. 1 as well as the average of the global fits.

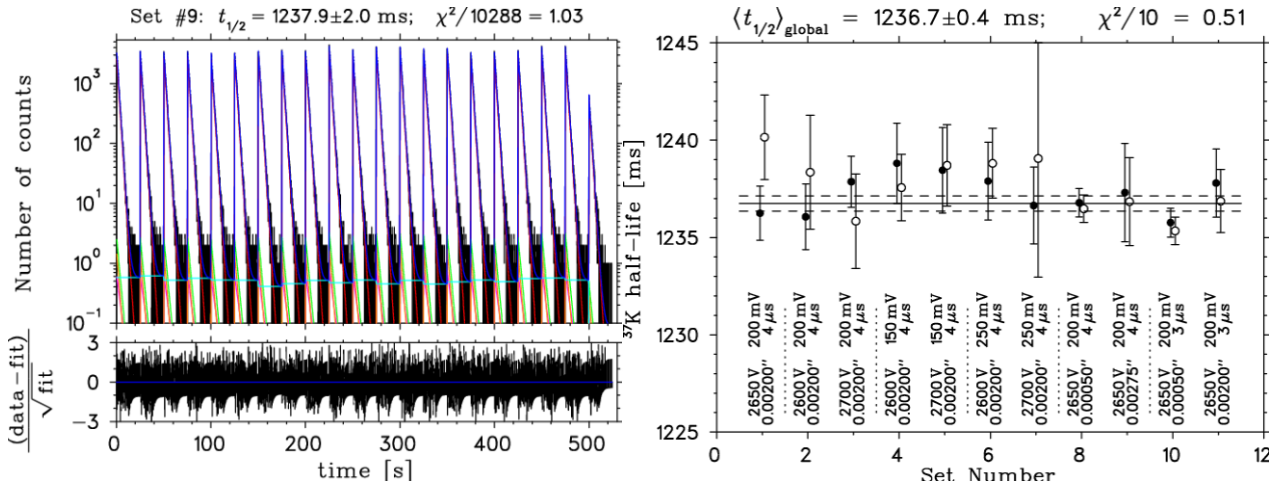


**FIG. 1.** Left panel: typical decay curve containing 14 cycles in a single run and fit using the global analysis. Right panel: life-times of all sets and average using the global analysis (filled circles), with each set's experimental conditions indicated. Results of the summed analysis are also shown (open circles) and can be seen to agree with the global analysis.

The two analyses yield the same result in the half-life to within  $\pm 0.30$  ms. Our final result for the  $^{37}\text{K}$  half-life is  $t_{1/2} = 1236.5 \pm 0.5 \pm 0.8$  ms [5], where the first uncertainty is statistical and the second is from systematics. The dominant systematic arises from the  $^{35}\text{Ar}$  and  $^{33,34}\text{Cl}$  contaminants. The present measurement improves over the previous measurement [6] by almost an order of magnitude.

$^{21}\text{Na}$  was produced via the  $p(^{22}\text{Ne}, 2n)^{21}\text{Na}$  reaction in inverse kinematic at a primary beam energy of 25 MeV/u. MARS was again used to produce a secondary beam of  $^{21}\text{Na}$ , this time with a purity of 99.9%. We followed the same procedure as described above for measuring the half-life of  $^{21}\text{Na}$  and to check for possible systematic effects. The analysis is in progress to extract the precise half-life with an associated error budget.

- [1] O. Naviliat-Cuncic and N. Severijns, *Phys. Rev. Lett* **102**, 142302 (2009).
- [2] D. Ashery *et al.*, *Progress in Research*, Cyclotron Institute, Texas A&M University (2009-2010) p. I-58.
- [3] P.A. Vetter *et al.*, *Phys. Rev. C* **77**, 035502 (2008).
- [4] V.E. Iacob *et al.*, *Phys. Rev. C* **82**, 035502 (2010).
- [5] To be submitted to *Phys. Rev. C*.
- [6] G. Azuelos *et al.*, *Phys. Rev. C* **15**, 1847 (1977).

## Upgrade of the $^{37}\text{K}$ asymmetry measurement experiment

S. Behling, B. Fenker, M. Mehlman, D. Melconian, and P. Shidling

It was reported last year that our efforts to upgrade the TRINAT apparatus had moved into the construction stage. Many of the critical components needed for the experiment have now been designed and fabricated and are currently being assembled in preparation for a short trial run of the experiment scheduled at TRIUMF in the fall of 2011. The purpose of this test run is to ensure that the new detector systems and acquisition software are all working as expected and to give us an idea of any unforeseen sources of systematic uncertainty that could be corrected or at least accounted for in the production run that will be scheduled early next year after the TRIUMF shutdown if all of the systems behave reasonably well in fall test run.

The main vacuum chamber is in the final stages of construction at the TRIUMF machine shop and will be completed and installed by the end of August. The completion and installation is a prerequisite for any changes required to the complicated optical setup. The reorganization of the optics should be very minimal and is not expected to take more than one week. These two tasks will be carried out by our collaborators in Vancouver. The main contribution from Texas A&M to the experimental upgrade is the construction and commissioning of two (identical) new beta telescopes that consist of a 40x40mm Micron BB1 silicon strip detector backed by large plastic BC408 scintillator; the telescopes will be encased within a re-entrant flange with a thin beryllium window on the front to allow the betas into the detectors while preserving the large pressure differential.

We have received the silicon strip detectors from Micron as well as the specially-designed preamps built at TRIUMF. We are currently in the process of building and testing an electronics setup to power the detectors and preamps and record the output using a CAEN V1740 digitizer. In order to facilitate testing we have built a test vacuum chamber here at the Cyclotron Institute with a precision source mount and collimator that will allow us to characterize the strip detector behavior with respect to the orientation of the incoming betas.

The plastic scintillators were built at the TRIUMF scintillator shop and have been tested in conjunction with their PMTs and lightguides. We performed tests to find the best wrappings for the light guides to maximize light collection and performed tests to find the ideal length of light guide to use in our experimental setup that would allow us room to include magnetic shielding around our PMTs. These tests allowed us to settle on the final design that will be used for the fall test run.

In the next few months we will be putting the strip detectors and scintillators together into the telescope assembly and write the software necessary to handle the pulses coming from the different detectors and devise a triggering scheme that will veto background events giving us the best results for the asymmetry experiment.

## Production and separation of new secondary beams $^{30}\text{P}$ and $^{27}\text{P}$

E. Simmons, L. Trache, B. Roeder, M. McCleskey, A. Spiridon, and R. E. Tribble

The Momentum Achromat Recoil Spectrometer (MARS) at TAMU was used for the production and separation of both  $^{30}\text{P}$  and  $^{27}\text{P}$ . The nuclear astrophysical motivation for studying  $^{30}\text{P}$  is its importance in explosive hydrogen burning in novae. The reaction rate for its radiative proton capture is known only with large uncertainty. This reaction, like others our group has previously studied in the sd-shell is dominated by capture through low-energy resonances, and is thus, very difficult to study directly. An indirect method to study this reaction was done previously through the beta-delayed proton and gamma decay of  $^{31}\text{Cl}$ . Another reaction of interest is  $^{30}\text{P}(d,p)^{31}\text{S}$ , which we intend to measure in inverse kinematics with TECSA.

Similarly, there is a nuclear astrophysical motivation for the production of  $^{27}\text{P}$ . It was, shortly after this production test, used in another beta-delayed proton and gamma decay experiment. The experiment was done in order to study the destruction reaction of  $^{26\text{m}}\text{Al}(p,\gamma)^{27}\text{Si}^*$ . The discovery in 1982 of the 1.809 MeV gamma-ray line for the decay of  $^{26}\text{Al}$  was the first key proof of ongoing nucleosynthesis in the Galaxy. However, many things are still not clearly understood, for example, such as the provenience and abundance of  $^{26}\text{Al}$  in our Galaxy.

### The Production and Separation of $^{30}\text{P}$

For the production and separation of  $^{30}\text{P}$ , the primary beam from the K500 superconducting cyclotron was  $^{30}\text{Si}$  at 18 MeV/u. The fragment of interest,  $^{30}\text{P}$ , is created when the primary beam struck the hydrogen gas cell target (kept at 2 atm and liquid nitrogen temperature) and a (p,n) charge-exchange reaction occurs.

The separation of exotic  $^{30}\text{P}$  from the other fragments was performed in MARS. By the time  $^{30}\text{P}$  reached our target detector it was at an energy of 14.2 MeV/u. After optimizing magnet settings we found that the best rate was between 10,500 and 11,000 events/nC with the coffin slits at  $\pm 1.0$  cm. The total impurities were about 4%, most of which was  $^{28}\text{Si}$  (having the same magnetic rigidity as  $^{30}\text{P}$  meant that we could not get rid of all of it, but only minimize it as much as possible with different slits. See Figure 1). With primary beam from an enriched silane gas, we expect to be able to obtain a secondary  $^{30}\text{P}$  beam of about  $10^6$  pps, which will make a TECSA experiment possible.

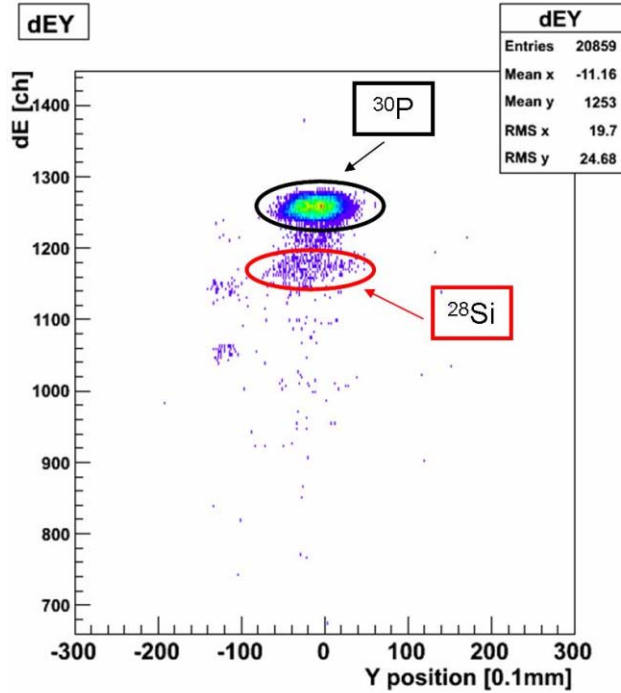


FIG. 1. Results from the  $^{30}\text{P}$  Production and Separation.

### The Production and Separation of $^{27}\text{P}$

The second production test performed using MARS during this same experiment, was the production and separation of  $^{27}\text{P}$ , using a 40 MeV/u  $^{28}\text{Si}$  beam from the K500 superconducting cyclotron. This  $^{28}\text{Si}$  beam hit our hydrogen gas cell target, kept at  $p = 2$  atm and liquid nitrogen temperature, and a fusion evaporation ( $p,2n$ ) reaction produced the  $^{27}\text{P}$  fragments of interest. The exotic secondary beam was then taken through MARS and  $^{27}\text{P}$  was separated out of the mix. By the time it reached the target detector  $^{27}\text{P}$  had an energy of about 34 MeV/u. The final rate on our detector was about 6 events per enC measured in the coffin or about 85 per pnC for a momentum spread of  $\pm 0.6\%$  obtained with the coffin slits open at  $\pm 1.0$  cm. The total rate at the target detector was around 3000 pps, in line with other rates we obtained for  $T_z = -3/2$  nuclei in this region.

The test also showed that we had about 28% total impurities, most of which was  $^{24}\text{Al}$ , slipping in from the neighboring  $N=Z-2$  line of nuclei. This  $^{24}\text{Al}$  impurity could later be diminished to below 10% by closing acceptance slits, sometimes at the expense of the production of  $^{27}\text{P}$ . However, as at the same rigidity,  $^{24}\text{Al}$  has a longer range in Si, with about 60  $\mu\text{m}$ , which will put it out of our implantation detector and will not contribute in the proton spectra, but will be stopped in the back beta-detector and will give impurity peaks (identifiable though!) in the gamma-ray spectra. However, this  $^{24}\text{Al}$  impurity was actually to our advantage in experiment. We were able to use it for extended energy and efficiency calibrations (up to 8 MeV) for the high purity germanium detectors.

dEY

29-Oct-2010 15:14:18

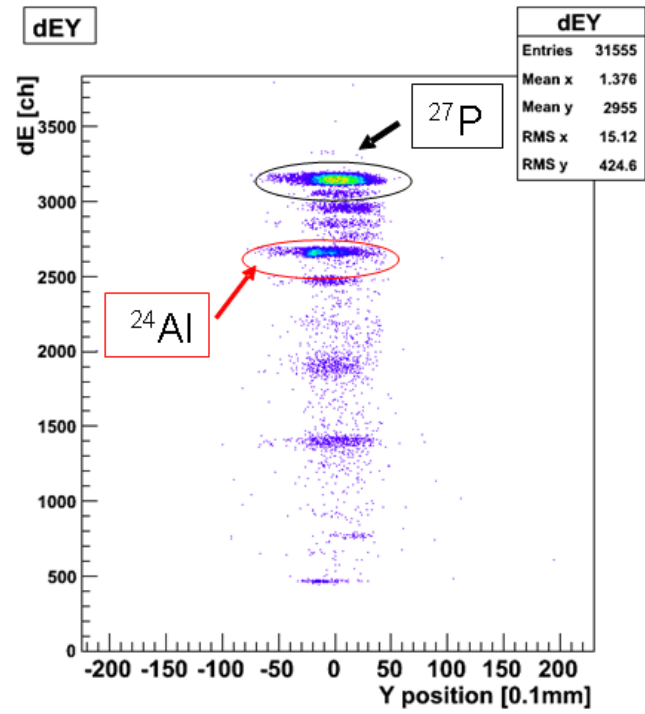


FIG. 2. Final tuning results for  $^{27}\text{P}$  production test.

## Using the K-150 cyclotron to measure proton reaction cross sections on separated isotopes

M. H. Mohzoon,<sup>1</sup> R. J. Charity,<sup>1</sup> J. Elson,<sup>1</sup> R. Shane,<sup>1</sup> L. G. Sobotka,<sup>1</sup>

M. McCleskey, E. Simmons, and L. Trache

<sup>1</sup>*Dept. of Physics and Dept of Chemistry, Washington University, St. Louis, Mo*

This Using the rejuvenated K-150 cyclotron, a new program was started measuring  $\sigma_{rxn}(p)$  for stable but rare isotopes. These cross sections are accurate reporters of the integrated strength of the imaginary component of the optical model ( $J_W$ ) and the isotopically resolved data is far from complete, see the Table I and [1].

An apparatus was constructed at WU modeled after the one used by Carlson [2], see Fig. 1. It consists of two very thin "passing detectors", several annular ring beam "veto" detectors, a central "plug" detector at zero degrees, and an energy analyzing detector at forward angles. The beam is defined by scoring on the "passing" and missing the "veto" detectors. To first order, the unreacted beam (this includes most of the elastic) hits the center "plug" (detector 5 in Fig. 1). The reacted beam events are defined as those which score on the passing detector (detectors 1 and 2 in Fig. 1), miss the veto detectors (detectors 3 and 4), do not hit the center plug (detector 5) or score with less than the elastic energy in the final energy analyzing detector (detector 6, in Fig. 1). These experiments require very little, but a low divergence, beam and thick ( $\sim 45$  mg/cm<sup>2</sup>) and uniform separated isotope targets.

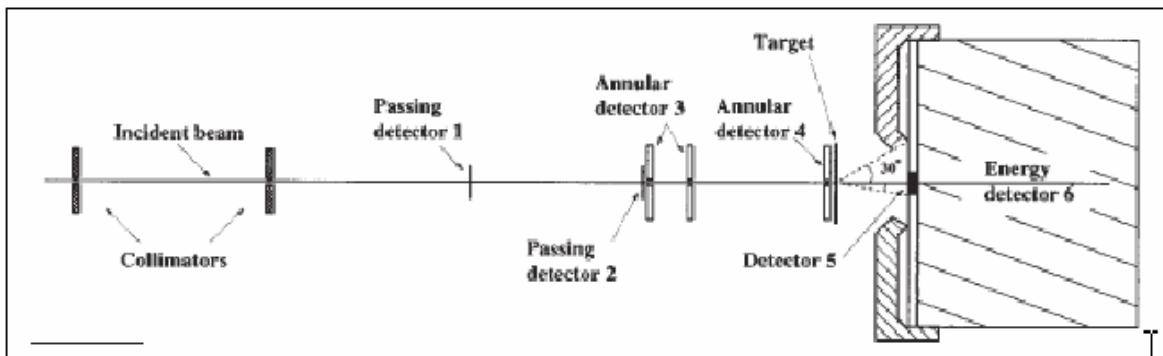


**FIG. 1.** The logical elements of  $\sigma_{rxn}(p)$  apparatus.

In March of 2011 there was a test run, the first run using the revitalized 88" cyclotron, using a natural Ni target. In this test, the K-150 supplied a 30 MeV proton beam, all of the detectors functioned but a cross section was extracted that was 35% above the literature value. A second test run, with improved collimation (beam definition) and detector alignment capabilities is required before physics generating experiments can be undertaken. Ultimately we intend to supply data from 20-60 MeV, in 10 MeV steps (with uncertainties of less than 5%) for the cases listed in Table I without high precision entries.

**Table I.** Status of  $\sigma_{\text{rxn}}(p)$  for isotope isotone chains.

<b>Z=28 (%)</b>	<b>E<sub>p</sub>(MeV)</b>	<b>N=28 (%)</b>	<b>E<sub>p</sub>(MeV)</b>
<sup>58</sup> Ni (68.3)	Good data set	<sup>48</sup> Ca (0.187)	23.,25.3,30.3,35.1, 39.9,45.3,48.,700
<sup>60</sup> Ni (26.1)	Good data set	<sup>50</sup> Ti (5.4)	60.8*
<sup>62</sup> Ni (3.59)	14.5, 40.0*, 60.8*	<sup>52</sup> Cr (83.8)	60.8*
<sup>64</sup> Ni (0.91)	40.0*, 60.8*	<sup>54</sup> Fe (5.9)	Complete data set
<b>Z=40 (%)</b>	<b>E<sub>p</sub>(MeV)</b>	<b>N=40 (%)</b>	<b>E<sub>p</sub>(MeV)</b>
<sup>90</sup> Zr (51.45)	14.5, 30.0, 40.0 49.5, 60.8	<sup>70</sup> Zn (0.6)	nothing
<sup>92</sup> Zr (17.15)	14.5	<sup>72</sup> Ge (27.4)	nothing
<sup>94</sup> Zr (17.38)	14.5	<sup>74</sup> Se (0.9)	nothing
<sup>96</sup> Zr (2.80)	60.8*		
<b>Z=50 (%)</b>	<b>E<sub>p</sub>(MeV)</b>	<b>N=50</b>	<b>E<sub>p</sub>(MeV)</b>
<sup>xxx</sup> Sn	Excellent data	<sup>88</sup> Sr (82.58)	nothing
		<sup>90</sup> Zr (51.45)	14.5, 30.0, 40.0 49.5, 60.8
		<sup>92</sup> Mo (14.84)	nothing

\* Large statistical errors (~&gt; 10%)

[1] R.F. Carlson, At. Data and Nucl. Data Tables **63**, 93 (1996).[2] R.F. Carlson, et al. Phys. Rev. C **53**, 2919 (1996).

**The commissioning run for the Texas-Edinburgh-Catania silicon array (TECSA):  
Measurement of the  $d(^{14}\text{C},p)^{15}\text{C}$  at 11.7 MeV/u**

B. T. Roeder, M. McCleskey, L. Trache, A. A. Alharbi, A. Banu, S. Cherubini,<sup>1</sup> T. Davinson,<sup>2</sup>  
V. Z. Goldberg, M. Gulino,<sup>1</sup> R. G. Pizzone,<sup>1</sup> E. Simmons, R. Spartà,<sup>1</sup> A. Spiridon,  
C. Spitaleri,<sup>1</sup> J. P. Wallace,<sup>2</sup> R. E. Tribble, and P. J. Woods<sup>2</sup>

<sup>1</sup>*INFN Laboratori Nazionali del Sud & DMFCI Università di Catania, 95123 Catania, Italy*

<sup>2</sup>*School of Physics and Astronomy, University of Edinburgh, Edinburgh, EH9 3JZ, United Kingdom*

The Texas A&M-Edinburgh-Catania Silicon detector Array (TECSA) is a collaborative effort to construct a silicon detector array with high efficiency and high granularity for use in experiments at the Texas A&M Cyclotron Institute (TAMU-CI). The array consists of up to 16 Micron Semiconductor Ltd. YY1-300 silicon detectors (MSL-YY1) [1] and up to 256 channels (16 Si detectors sectors  $\times$  16 strips per detector) of associated electronics [2]. TECSA will be used to study reactions to obtain information relevant for nuclear astrophysics by indirect methods such as the asymptotic normalization coefficient (ANC) and Trojan Horse Method THM). Details on the TECSA detector setup at TAMU-CI can be found in last-year's annual report [3] and in a recently published article [4].

In an experiment conducted in May 2010, TECSA was commissioned at TAMU-CI by measuring the  $d(^{14}\text{C},p)^{15}\text{C}$  reaction in inverse kinematics as a precursor to future measurements with rare isotope beams. The  $^{14}\text{C}$  beam for the experiment was obtained as a primary beam from the K500 cyclotron at 11.7 MeV/u and delivered to the MARS spectrometer. The beam was tuned through MARS with no primary production target in place. Then, the beam spot was tuned at the TECSA reaction target position on a position sensitive silicon detector. This target detector was a MSL type-MSPSD TL 20 position sensitive detector with four-corner readout [5]. A beam spot size of 3mm  $\times$  1mm (FWHM) was obtained.

Following the beam tuning, the  $^{14}\text{C}$  impinged on a target of deuterated-polyethylene ( $\text{CD}_2$ ) with areal density of  $251 \pm 5 \mu\text{g}/\text{cm}^2$  and D:H ratio enriched to 98%. For this reaction, it was expected that the protons from the forward center-of-mass angles would be detected at the backward lab angles. Thus, TECSA was mounted upstream of the  $\text{CD}_2$  target in the flat configuration. The detector thickness of  $\approx 300 \mu\text{m}$  was sufficient to stop the protons from the reaction at all angles measured. Also, the detector ring has a hole in middle to allow the  $^{14}\text{C}$  beam to pass through it on its way to the target.

A typical spectrum for the  $d(^{14}\text{C},p)^{15}\text{C}$  reaction for the TECSA ring centered at  $\theta_{\text{lab}} = 156.4^\circ$  is shown in Fig. 1. In the figure, protons resulting from the population of the ground and first excited states of  $^{15}\text{C}$  are observed. A peak

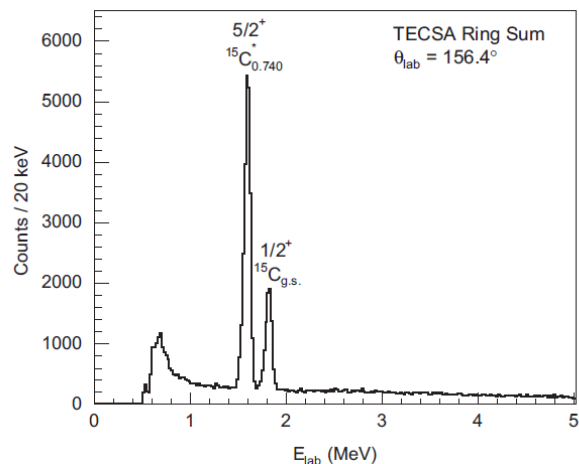


**FIG. 1.** Typical energy-matched spectrum from the  $d(^{14}\text{C},p)^{15}\text{C}$  measurement.

resolution of  $\approx 100$  keV (FWHM) was obtained, which arose mainly from the thickness of the target and the kinematic resolution ( $\Delta E/\Delta\theta$ ). The background under the peaks was due to reactions of the beam with the carbon in the  $\text{CD}_2$  target (as observed from background measurements on a natural carbon target), and events uncorrelated with the  $^{14}\text{C}$  beam such as cosmic rays and residue from the  $\alpha$ -source used to calibrate the detectors.

The proton yields were measured for the  $^{15}\text{C}$  ground and 0.740 MeV states over the angular range  $102^\circ < \theta_{\text{lab}} < 165^\circ$ . To cover this angular range, the  $\text{CD}_2$  target was positioned at 20, 12, 5, and 2.8 cm from the center of TECSA along the beam axis. With this angular range, the differential cross sections for  $^{15}\text{C}$  states were measured from  $4^\circ < \theta_{\text{CM}} < 34^\circ$  in the center of mass system. These data were then compared with distorted-wave Born approximation (DWBA) calculations carried out with the program TWFNR [6]. The calculations were performed assuming the orbital angular momentum and spin values found for the  $^{15}\text{C}$  states in previous work. The results of these calculations are shown in Figure 2. The details of these calculations, including the optical potentials used, are given in Ref. [4]. While better descriptions of these data are likely possible, the general features of the angular distributions are reproduced, and the difference in the angular momenta of the two states is clearly seen.

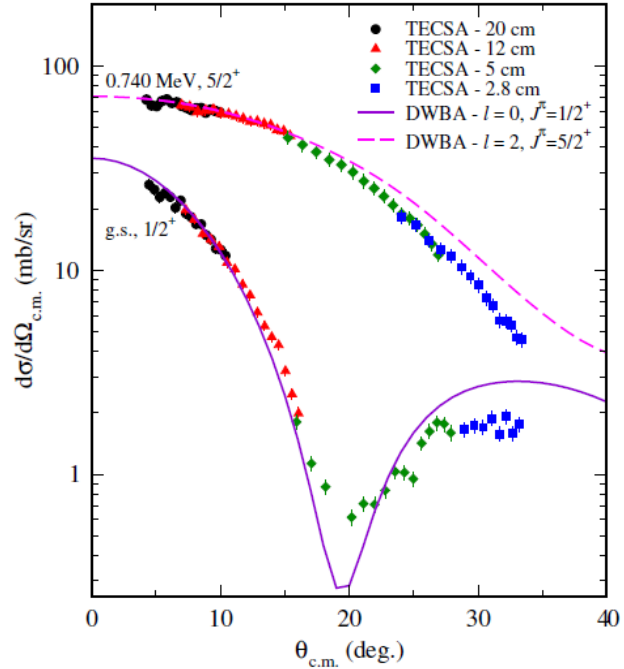


**FIG. 2.** Angular distributions obtained from the  $d(^{14}\text{C},p)^{15}\text{C}$  experiment.

Following this successful measurement, we tried to investigate the utility of the TECSA detector for measuring reactions with genuine rare isotope beams produced as secondary beams with MARS. Using the available  $^{14}\text{C}$  primary beam at 11.7 MeV/u and deuterium gas in the MARS production target, secondary beams of  $^{12,13}\text{B}$  were produced using the reactions  $d(^{14}\text{C}, ^{13}\text{B})^3\text{He}$  and  $d(^{14}\text{C}, ^{12}\text{B})^4\text{He}$ . The goal of these measurements was to investigate the  $d(^{12}\text{B},p)^{13}\text{B}$  and  $d(^{13}\text{B},p)^{14}\text{B}$  reactions with TECSA. These reactions were expected to have cross sections similar in magnitude to those observed in the  $d(^{14}\text{C},p)^{15}\text{C}$  experiment. A production rate of 130 eV/nC was obtained for the  $^{13}\text{B}$ , but the low primary beam current of 16 enA limited the total secondary beam rate to  $\sim 2 \times 10^3$  pps. Similarly, the production rate for the  $^{12}\text{B}$  beam was 154 eV/nC, but even with the higher beam current available at this point in the experiment of 120 enA, the maximum secondary beam rate available was around  $2 \times 10^4$  pps. Thus, the reaction signals from  $d(^{12}\text{B},p)^{13}\text{B}$  and  $d(^{13}\text{B},p)^{14}\text{B}$  were not observable due to the combination of  $\sim 10^4$  less beam current (than was used in the  $^{14}\text{C}$  experiment) and background that arose from the presence of the  $^{14}\text{C}$  primary beam in the experimental hall (likely from secondary neutrons produced when the  $^{14}\text{C}$  primary

beam impinged on the D<sub>2</sub> gas production target). Some of this background was able to be removed by adding a plastic scintillator/PMT system to the setup such that events not in coincidence with the beam could be excluded. However, the rate of available secondary beam was still too low to observe a signal from the reactions. At the end of the experiment, a signal was obtained with this system from the d(<sup>14</sup>C,p)<sup>15</sup>C reaction from the <sup>15</sup>C<sub>0.740 MeV</sub> state in the situation that the <sup>14</sup>C primary beam rate was reduced to ~ 1 × 10<sup>5</sup> pps. Improvements to the chamber mechanics and better treatment of the timing signals are expected to make future measurements with secondary rare isotope beams more feasible.

In conclusion, we have successfully constructed and commissioned TECSA in an experiment that measured d(<sup>14</sup>C,p)<sup>15</sup>C in inverse kinematics at 11.7 MeV/u. TECSA will be available for experiments at TAMU-CI for the next few years. In the near future, TECSA will be used for further experiments with rare isotope beams prepared with MARS. However, as was shown in the attempt to measure with <sup>12,13</sup>B secondary beams from MARS, beam production rates of > 10<sup>5</sup> pps are necessary for good measurements. After the TAMU-CI T-Rex upgrade, it will be possible to use TECSA, (or similar Si detector arrays) to conduct experiments similar to the d(<sup>14</sup>C,p)<sup>15</sup>C measurement with rare isotope beams reaccelerated by the K500 cyclotron.

- [1] T. Davinson *et al.*, Nucl. Instrum. Methods Phys. Res. **A454**, 350 (2000).
- [2] S.L. Thomas *et al.*, Nucl. Instrum. Methods Phys. Res. **A288**, 245 (1990).
- [3] M. McCleskey *et al.*, *Progress in Research*, Cyclotron Institute, Texas A&M University (2009-2010), V-34, [http://cyclotron.tamu.edu/2010 Progress Report/index.html](http://cyclotron.tamu.edu/2010%20Progress%20Report/index.html).
- [4] B.T. Roeder *et al.*, Nucl. Instrum. Methods Phys. Res. **A634**, 71 (2011).
- [5] A. Banu *et al.*, Nucl. Instrum. Methods Phys. Res. **A593**, 399 (2008).
- [6] M. Igarashi *et al.*, Computer program TWOFNR, Surrey University Version.

# Toward understanding relativistic heavy-ion collisions with the STAR detector at RHIC

M. Cervantes, M. Codrington, A. Hamed, S. Mioduszewski, Y. Mohammed,  
and the STAR Collaboration

We have pursued the following physics analyses: I) bottomonium (Upsilon) production via Upsilon+hadron correlations, II) long-range pseudorapidity correlations in heavy-ion collisions via high- $p_T$   $\pi^0$  and direct  $\gamma$  triggers, and III) the energy loss mechanism in heavy-ion collisions via the azimuthal anisotropy of high- $p_T$   $\pi^0$  and direct photons. Finally, we have been involved in simulations for a STAR upgrade project, the Muon Telescope Detector.

## I. Upsilon + Hadron Correlations:

We have performed the Upsilon+hadron correlation analysis on the Run-9 p+p data set, as well as the Run-8 d+Au data set. Figure 1 (left) shows the reconstructed mass from  $e^+e^-$  pairs (black) and like-sign pairs (red) from our Run-9 analysis. Figure 1 (right) shows the background-subtracted mass distribution.

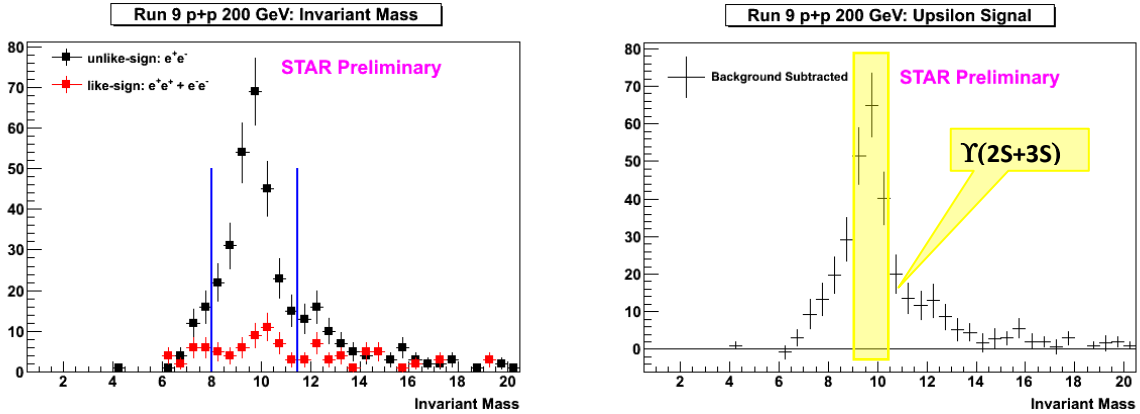


**FIG. 1.** (Left) Invariant mass distribution of  $e^+e^-$  pairs (black) and like-sign pairs (red) calculated in p+p events. (Right) Background-subtracted mass distribution.

The high signal to background ratio enables us to perform an analysis of Upsilon + Hadron correlations. Possible insight into the prompt production mechanism of heavy quarkonium can be obtained from hadronic activity measured near the Upsilon. Figure 2 shows our results for the azimuthal correlation between hadrons and the Upsilon in (left) d+Au events and (right) p+p events.

These plots are not yet corrected for the efficiencies of the associated hadrons. We have spent quite some time developing the cuts on associated hadrons to best reject pile-up tracks. We have calculated the efficiencies for our track cuts using pions embedded in d+Au events, and recently have also done the same for pions embedded in p+p events. This allows us to apply the final efficiency corrections.

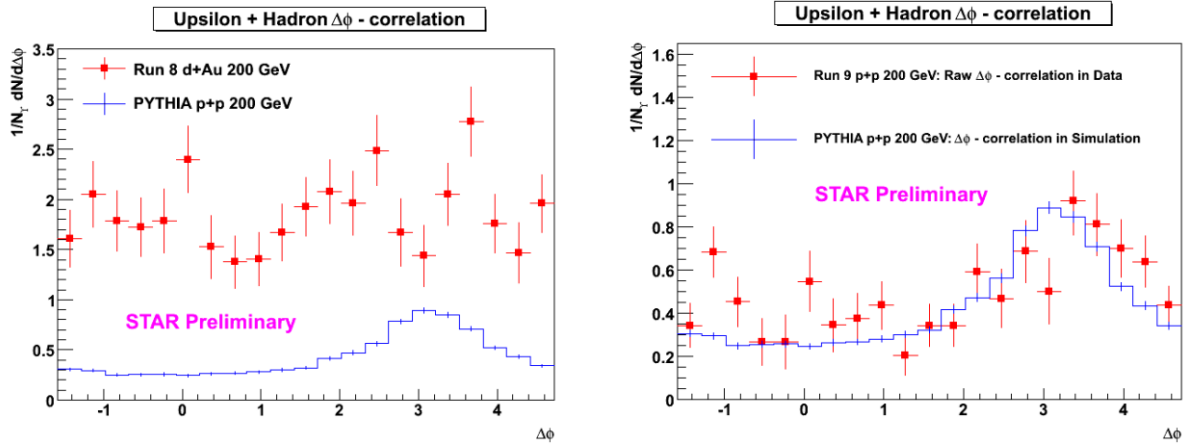


FIG. 2. Raw  $\Delta\phi$ -correlation of hadrons with respect to the Upsilon in (left) d+Au events and (right) p+p events.

## II. The “ridge” via high- $p_T$ $\gamma/\pi^0$ triggers:

The “ridge” has been observed as a long-range correlation in  $\Delta\eta$  with respect to a high  $p_T$  trigger. It has previously only been measured in correlations with charged hadron triggers. This previous measurement has large uncertainties (including large statistical errors for  $p_T > 5$  GeV/c) making it difficult to conclude whether the ridge persists up to trigger  $p_T$  exceeding 5 GeV/c. We are extending the measurement of the ridge to higher  $p_T$  using photon triggers. Figure 3 shows the ridge yield in central Au+Au events, extracted by two different methods shown in the left and right plots, as a function of trigger  $p_T$ . The results are shown for inclusive photon triggers,  $\pi^0$  triggers, and triggers rich in direct photons. The direct  $\gamma/\pi^0$  discrimination is performed using the transverse shower profile measured with

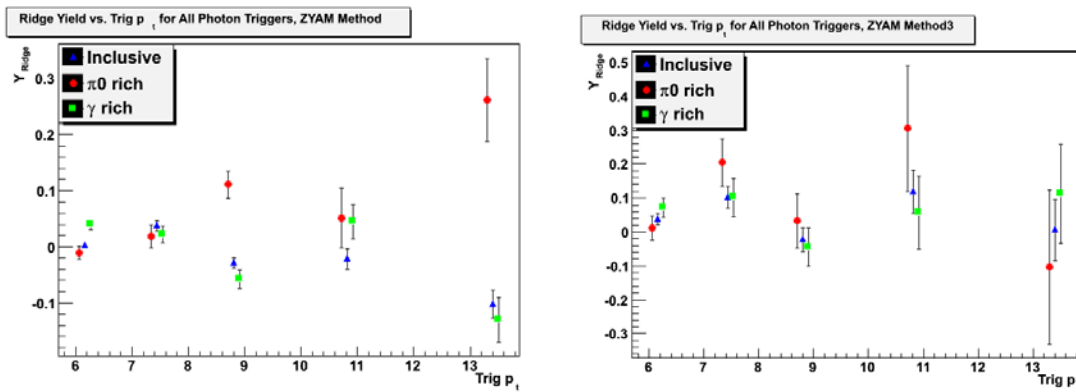


FIG. 3. The “ridge” yields measured in central Au+Au collisions (Run 7), extracted with 2 different methods shown left and right, as a function of trigger  $p_T$  for inclusive photon triggers,  $\pi^0$  triggers, and direct-photon-rich triggers.

the Barrel Shower Maximum Detector (BSMD). The results seem to indicate that there is no significant ridge yield at these high trigger  $p_T$  values, but with large statistical errors. We are currently working on finalizing the systematic errors for these measurements. We are also exploring the possibility of improving the statistical significance using Run-10 Au+Au data.

### III. Photon $v_2$ Measurement:

One of the puzzling conclusions that came from our  $\gamma$ -jet measurement is that there does not seem to be significant path-length dependence to parton energy loss. However, hadrons at high  $p_T$  have been measured to have a positive anisotropy ( $v_2$ ) with respect to the reaction plane, which was explained as being due to larger energy loss for partons traveling through the long part of the reaction zone (out of the reaction plane) than the short path (in the reaction plane). How much of this measured anisotropy is due to a bias of the reaction plane determination, arising from the presence of jets, is also not fully understood yet. We have recently been working on a photon  $v_2$  measurement. Direct photons do not lose energy, and thus should not have a positive  $v_2$ . Neutral clusters from a high- $p_T$   $\pi^0$  can be selected using the transverse shower profile measured in the BSMD, and a direct photon  $v_2$  measurement can be extracted. Figure 4 shows the  $v_2$  measurement for charged hadrons (for  $p_T < 8$  GeV/c) and for inclusive photons,  $\pi^0$ , and direct photons (for  $p_T > 8$  GeV/c).

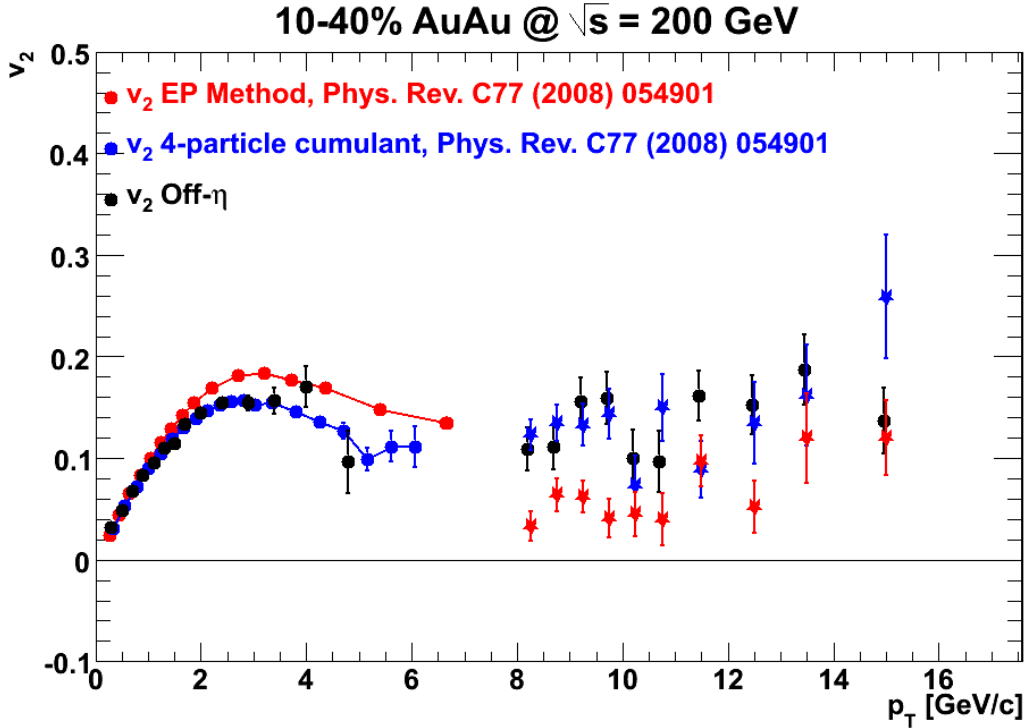


FIG. 4. Azimuthal anisotropy of inclusive photons,  $\pi^0$ ,  $\gamma_{\text{direct}}$ , and charged particles as a function of  $p_T$ .

Although the direct photon  $v_2$  is smaller than that for  $\pi^0$ , it is not zero. This may indicate that even when the reaction plane is determined using low- $p_T$  particles with opposite-sign pseudorapidity relative to the particles measured with respect to the reaction plane (“off- $\eta$ ”), there is a bias in the reaction-plane determination due to the presence of jets. We are currently working on finalizing these results for publication.

#### IV. Simulations for the Muon Telescope Detector

We have been working on simulations exploring the physics goals that can be attained with the STAR upgrade project of the Muon Telescope Detector (MTD). One of these physics goals is to separate  $J/\Psi$  originating from B decays from primordial  $J/\Psi$ , using the MTD to identify muons and the Heavy Flavor Tracker to measure the decay length. Figure 5 shows the reconstructed invariant mass of simulated particles that were embedded into real events. The following particles were embedded in each event.

- $B^+ \rightarrow J/\psi + K^+ \rightarrow \mu^+ + \mu^- + K^+$
- $J/\psi \rightarrow \mu^+ + \mu^-$
- $\eta \rightarrow \mu^+ + \mu^- + \gamma$
- $\Sigma^+ \rightarrow \mu^+ + \mu^- + p$

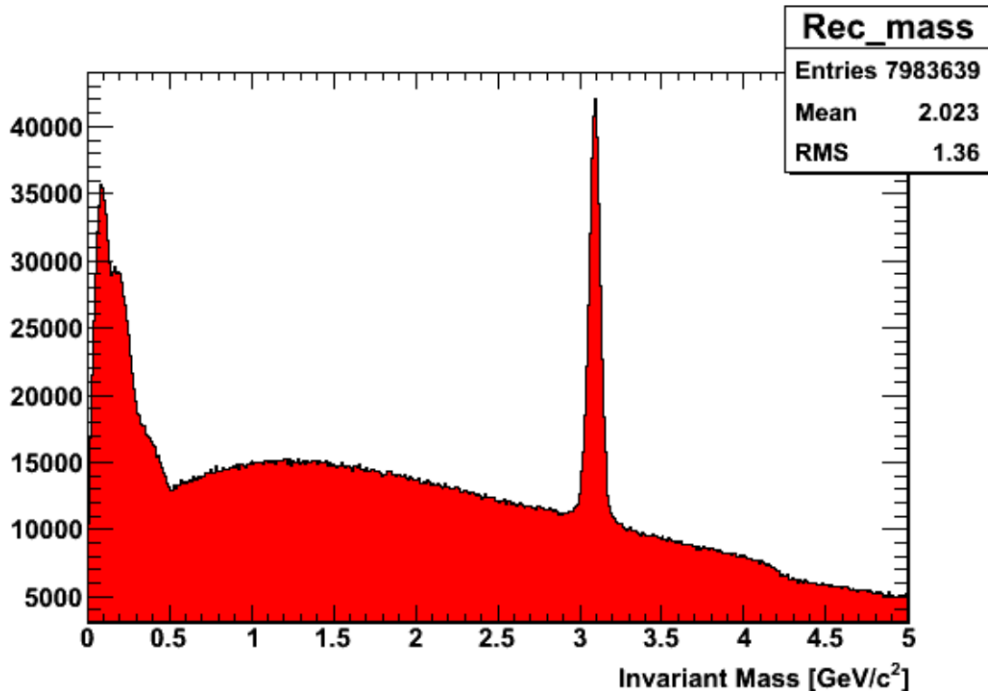


**FIG. 5.** Reconstructed invariant mass for all pairs of reconstructed tracks from simulation (without cuts on particle ID).

We are currently calculating the decay length of the  $J/\psi$  from the primary vertex in order to separate B decays from primordial  $J/\psi$ .

## New trigger logic for the STAR forward meson spectrometer

J. C. Martinez, P. Djawotho, C. A. Gagliardi, and the STAR Collaboration

The STAR Forward Meson Spectrometer (FMS) is a Pb-glass electromagnetic calorimeter covering the forward rapidity region ( $2.5 < \eta < 4$ ) in STAR. It is being used to explore a broad range of spin phenomena in  $pp$  collisions. During RHIC Run 9, the STAR FMS utilized a “cluster trigger”. The trigger selected events that contained a highly localized, high energy deposition. The cluster size was sufficiently small that the trigger preferentially identified events with either a single high energy photon or a very close pair of photons from the decay of a high energy  $\pi^0$ . Higher mass objects, such as  $\eta$  mesons or jet-like events, could only satisfy the trigger when one of the associated photons had sufficient energy to pass the trigger requirements by itself. This led to quite low efficiency for such objects. Furthermore, for the case of the  $\eta$  meson, only very asymmetric  $\eta \rightarrow \gamma\gamma$  decays were selected. The low-energy partner photon is often difficult to reconstruct, which reduced the efficiency even more.  $\eta$  meson decays constitute one of the largest backgrounds in measurements of the transverse single-spin asymmetry for direct photons. Direct photon transverse spin asymmetries are particularly interesting, because they can only arise from the Sivers effect. Thus, it is important to be able to measure  $\eta$  meson yields and asymmetries with good precision.

During Summer, 2010, we designed a new logic scheme for the FMS that replaces the cluster trigger with a combination of “jet patch” (JP) triggers. The JP layout is shown in Fig. 1. Each JP spans  $\frac{1}{4}$  of the entire FMS. There are a total of eight JPs in order to provide significant overlap, thereby eliminating edge-effects in the trigger definition. Studies using PYTHIA events processed through an emulator of the new trigger, which we wrote, indicated that the JPs provide very high efficiency for high-mass objects like energetic  $\eta$  mesons and jet-like events. Nonetheless, we didn’t want to depend solely on the JPs for triggering. Thus, the scheme also included a set of “board sum” (BS) triggers, which play

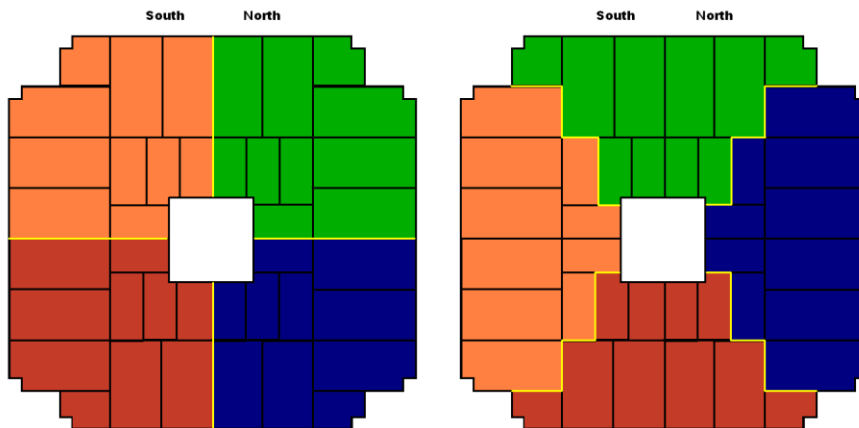


**FIG. 1.** View of the FMS from the STAR collision point, showing the eight overlapping jet patches.

a role analogous to the previous cluster trigger, plus high-tower (HT) triggers for calibration and low-level diagnostic purposes.

The new trigger logic required some recabling within the existing FMS trigger system, plus significant recoding of the trigger FPGAs. The effort required was deemed too large to complete prior to RHIC Run 11. Instead, a partial scheme that included four of the eight JPs, plus the full suite of BS and HT triggers, was installed and has been used during the run. The current plan is to implement the entire new trigger logic scheme before RHIC Run 12.

## Spin physics with STAR at RHIC

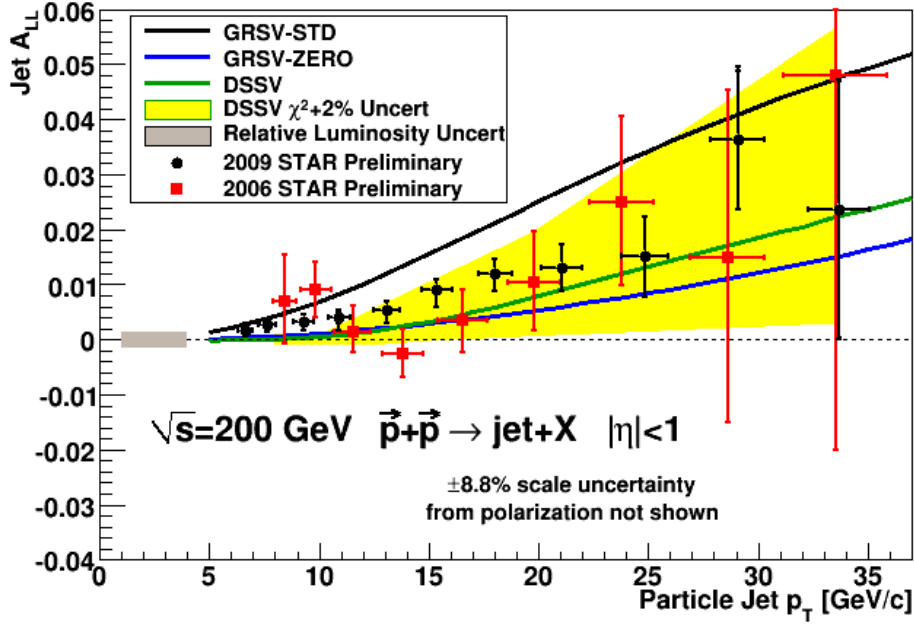
Z. Chang, P. Djawotho, J. L. Drachenberg, C. A. Gagliardi, L. Huo, R. E. Tribble,  
and the STAR Collaboration

Our group continues to play major roles in STAR investigations of both longitudinal and transverse spin phenomena in polarized  $pp$  collisions at RHIC. During the past year, our analysis efforts have focused on the 200 GeV longitudinal spin data that were recorded by STAR during 2009 and 200 GeV transverse spin data that were recorded during 2008. We also led an effort to develop a new trigger logic scheme for the STAR FMS, which is described elsewhere in this report.

One of the primary goals of the RHIC spin program is to determine the gluon contribution to the proton spin. At RHIC energies, jet production at mid-rapidity is dominated by  $gg$  and  $qg$  scattering. This makes the double longitudinal-spin asymmetry  $A_{LL}$  for inclusive jet production a sensitive probe of gluon polarization. In 2009, STAR sampled  $\sim 25 \text{ pb}^{-1}$  of longitudinally polarized  $pp$  collisions, with an average polarization of 58%. Prior to the run, our group initiated a substantial reprogramming of the jet triggers for the Barrel and Endcap Electromagnetic Calorimeters (B/EEMC). This resulted in a 37% increase in jet acceptance compared to the 2006 RHIC run. The STAR DAQ1000 upgrade was also completed prior to the 2009 run. This allowed us to record events at several hundred Hz, with only 5% dead time, compared with 40% dead time at 40 Hz during 2006. We utilized the added flexibility to lower the JP thresholds substantially compared to the 2006 values, thereby significantly increasing the jet trigger efficiency. We also removed the Beam-Beam Counter (BBC) minimum bias coincidence requirement, which had been part of all previous STAR jet triggers. This further increased the efficiency at high jet  $p_T$ , and facilitated a direct measurement of the non-collision background at STAR. The increased jet acceptance and trigger efficiency also help to reduce the trigger bias.

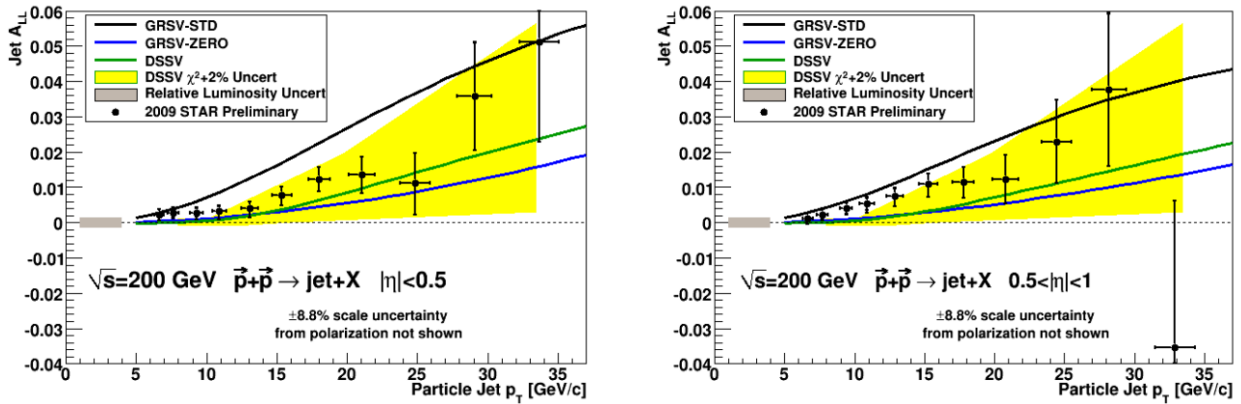
Since the run, we have implemented significant improvements in the STAR jet reconstruction procedures. The electromagnetic calorimeters are  $\sim 1$  hadronic interaction length thick. Many charged hadrons deposit a MIP (minimum-ionizing particle), while others shower and deposit a sizable fraction of their energy while passing through. The strategy adopted in analyses through 2006 was to subtract a MIP from an EMC tower with a charged track passing through. For the 2009 run, we adopted a new procedure. We now subtract up to the full track energy from the struck EMC tower. Detailed PYTHIA+GEANT simulations that we performed demonstrated that this significantly reduces the response to fluctuations from charged hadron showering, and also reduces the average difference between the jet energies at the particle and detector levels. The net benefit comes in the form of an improved overall jet energy resolution of 18%, compared to 23% in the 2006 analysis.

Figure 1 shows the measured inclusive jet  $A_{LL}$  versus jet  $p_T$  for the 2006 ( $-0.7 < \eta < +0.9$ ) and 2009 ( $|\eta| < 1$ ) data, together with theory predictions from GRSV [1] and DSSV [2]. The yellow triangular region in Fig. 1 shows the  $\chi^2+2\%$  uncertainty region identified in the DSSV analysis. The dominant systematic uncertainties in the 2009 measurement originate from differences between the true and reconstructed jet  $p_T$ , the non-uniform trigger sampling of the underlying partonic processes ( $gg$ ,  $qg$ , and  $qq$ ), and relative luminosities. The 2009 data are more precise than the 2006 data by a factor of four



**FIG. 1.** 2006 (red squares) and 2009 (black circles) STAR measurements of the inclusive jet  $A_{LL}$  vs.  $p_T$ . The curves show predictions based upon the GRSV [1] and DSSV [2] polarized parton distributions. The yellow band shows the DSSV  $\chi^2+2\%$  uncertainty region [2].

in the low- $p_T$  bins and a factor of three in the high- $p_T$  bins. The data are sufficiently precise to justify separation into two rapidity regions, thereby permitting detailed comparisons with models for collisions that sample different  $x$  ranges, subprocess mixtures, and average partonic scattering angles. The separation is shown in Fig. 2. In both Figs. 1 and 2, the STAR 2009 inclusive jet results are seen to fall between the predictions from DSSV and GRSV-STD.



**FIG. 2.** STAR 2009 inclusive jet  $A_{LL}$  vs.  $p_T$  for the pseudorapidity regions  $|\eta| < 0.5$  (left panel) and  $0.5 < |\eta| < 1$  (right panel).

DSSV was the first polarized parton distribution fit that included deep-inelastic scattering, semi-inclusive deep-inelastic scattering, and RHIC data on an equal footing [2]. The STAR 2005 and 2006

inclusive jet  $A_{LL}$  measurements played a significant role in constraining  $\Delta g(x)$  in DSSV. The STAR 2009 results draw a narrow road through the previous DSSV error band. As such, they are expected to provide a significant reduction in the present large uncertainty of the gluon polarization in the proton once they are included in a new global analysis.

Another major goal of the RHIC spin program is to unravel the origin of the large transverse single-spin asymmetries that have been seen at forward rapidities at RHIC [3]. The asymmetries have been attributed to the Sivers effect, a correlation between the spin of the incident proton and the transverse momentum of the quark or gluon that experiences the hard scattering, the Collins effect, which arises from the spin-dependent fragmentation of polarized scattered quarks, or a combination of the two. The Sivers effect provides a window into parton orbital motion because it requires interference between amplitudes involving partons with different orbital angular momenta. The Collins effect provides a means to explore quark transversity, the third collinear, leading-twist parton distribution function. (The other two are the unpolarized distribution and the helicity distribution, which is explored in longitudinally polarized collisions.)

We are investigating two-particle correlations in transversely polarized proton collisions from the 2008 RHIC run. By correlating trigger  $\pi^0$ s from the STAR FMS with charged tracks at similar pseudorapidity measured with the STAR FTPC, we can investigate  $A_N$  for two-particle correlations in a kinematic region where we have already measured large  $A_N$  for inclusive pions [3]. Our goal is to

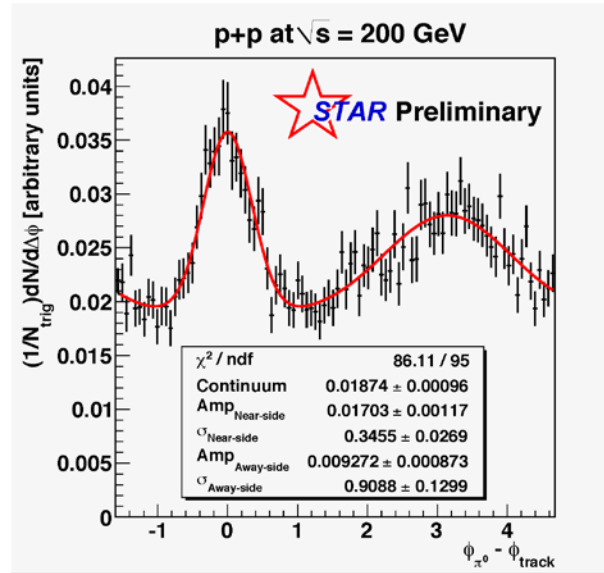


**FIG. 3.**  $\pi^0$ -charged particle correlations in STAR 2008 transversely polarized  $pp$  collisions at 200 GeV.  $\pi^0$ s are required to satisfy the trigger condition and have  $2 < p_T < 5$  GeV/c. Charged particles are required to satisfy  $1 < p_T < 3$  GeV/c. The continuum includes a 12-14% rate-dependent component from pile-up.

measure the interference fragmentation functions (IFF), which are sensitive to quark transversity and closely related to the Collins effect.

Over the past year, we have refined a set of data-driven cuts to optimize the observation of

correlations in the 2008 data. We start from a trigger  $\pi^0$  with  $2 < p_T < 5$  GeV/c. We then correlate it with charged tracks with  $1 < p_T < 3$  GeV/c measured by the FTPC. The resulting distribution is shown in Fig. 3. Separating the continuum background from the correlation signal is a major task. The FTPC is a “slow detector.” The drift time in the FTPC can be up to 50  $\mu$ s. Thus, it is susceptible to pile-up when tracks from other bunch crossings inadvertently get assigned to a collision vertex. This non-physical background should scale with the collision rate. In contrast, physics quantities, such as Gaussian peak width and height, as well as the true contribution to the continuum, should be independent of the rate. To quantify this effect, we have evaluated the correlations for various coincidence rates measured by the BBC. We then fit the resulting distributions with a double-gaussian signal and a continuum contribution linear in rate. We find that  $\sim 86\%$  of the continuum in Fig. 3 is associated with the trigger  $\pi^0$ ; the rest arises from pile-up.

It is useful to understand the behavior of the near-side events to characterize the intra-jet correlations. The invariant mass distributions of events with  $|\Delta\phi| < \pi/3$  show the presence of a modest  $\rho$  peak on an exponentially falling continuum. This peak is suppressed in  $\pi^0$ - $h^-$  correlations relative to  $\pi^0$ - $h^+$  correlations. The presence of the peak serves as a good sanity check, and the fact that the spectrum is not overwhelmed by the  $\rho$  lends confidence to the idea that we are evaluating jet-like events.

To understand the efficiency of the developed cuts in a more robust fashion, we need to analyze simulated tracks embedded in real data. This embedding procedure will also quantify the momentum resolution and reconstruction efficiency in the FTPC. Quality assessment of a sample embedding set is on-going. To perform the spin measurements, we need to understand the spin patterns of the 2008 data. At present, the STAR spin database is not filled for the 2008 run. Efforts to do so are on-going.

- [1] M. Gluck, E. Reya, M. Stratmann, and W. Vogelsang, Phys. Rev. D **63**, 094005 (2001).
- [2] D. de Florian, R. Sassot, M. Stratmann, and W. Vogelsang, Phys. Rev. Lett. **101**, 072001 (2008).
- [3] B.I. Abelev *et al.* (STAR Collaboration), Phys. Rev. Lett. **101**, 222001 (2008).

## TWIST: Measuring the space-time structure of muon decay

C. A. Gagliardi, R. E. Tribble, and the TWIST Collaboration

This past year, TWIST completed its final measurements of the muon decay parameters. We find  $\rho = 0.74977 \pm 0.00012(\text{stat.}) \pm 0.00023(\text{syst.})$ ,  $\delta = 0.75049 \pm 0.00021(\text{stat.}) \pm 0.00027(\text{syst.})$ , and  $P_{\mu\xi} = 1.00084 \pm 0.00029(\text{stat.}) + 0.00165 - 0.00063(\text{syst.})$ , consistent with the Standard Model expectations of  $\frac{3}{4}$ ,  $\frac{3}{4}$ , and 1. The results are summarized in Fig. 1, and have been published in [1].

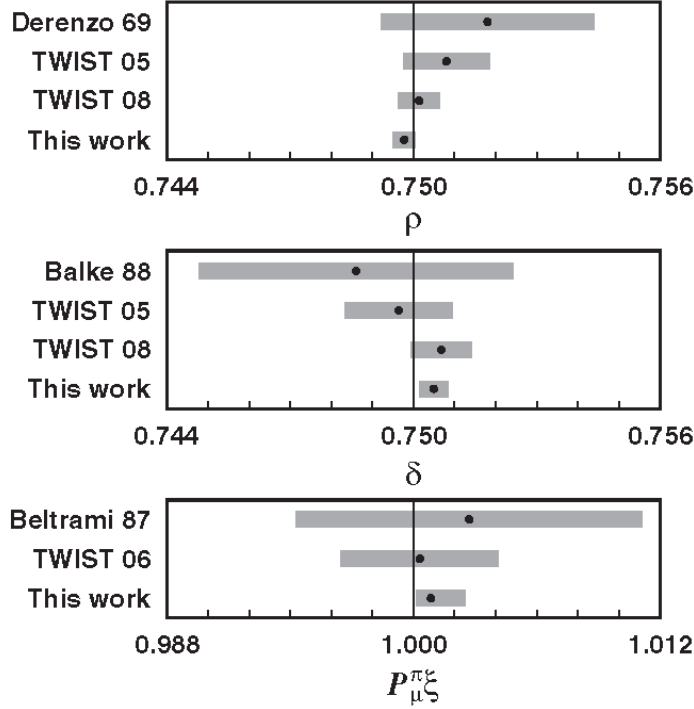


**FIG. 1.** Final TWIST central values and total uncertainties, together with the intermediate TWIST results and the best pre-TWIST measurements. The vertical lines represent the Standard Model values.

Once the results were finalized, our group explored the implications of the measurements within the Left-Right Symmetric (LRS) model [2]. The LRS model assumes parity violation at low energies arises from a mass splitting between (primarily) left- and right-handed bosons  $W_1$  and  $W_2$ . The model parameters include the mass of the heavy  $W_2$  boson, the mixing between the two bosons, the right-handed coupling constant  $g_R$ , and the form of the right-handed CKM matrix. The generalized LRS model allows all of these parameters to be free. The manifest LRS model is a special case where the right-handed coupling constant and CKM matrix are assumed to be equal to their left-handed analogs. In LRS models,  $\delta$  and  $\eta$  retain their Standard Model values, the value of  $\rho$  is determined by the  $W_1 - W_2$  mixing angle  $\zeta$ , and the value of  $P_{\mu\xi}$  is determined by the mixing angle, the heavy boson mass  $m_2$ , the  $V_{ud}^R$  element of the

right-handed CKM matrix, and two CP-violating phases. We developed a method to identify the region of parameter space that is allowed at the 90% level by the TWIST measurements of  $\rho$ ,  $\delta$ , and  $P_{\mu\xi}$ , including the influence of the parameter correlations. The results are shown in Fig. 2. The TWIST measurements provide the most stringent limits to date within generalized LRS models.

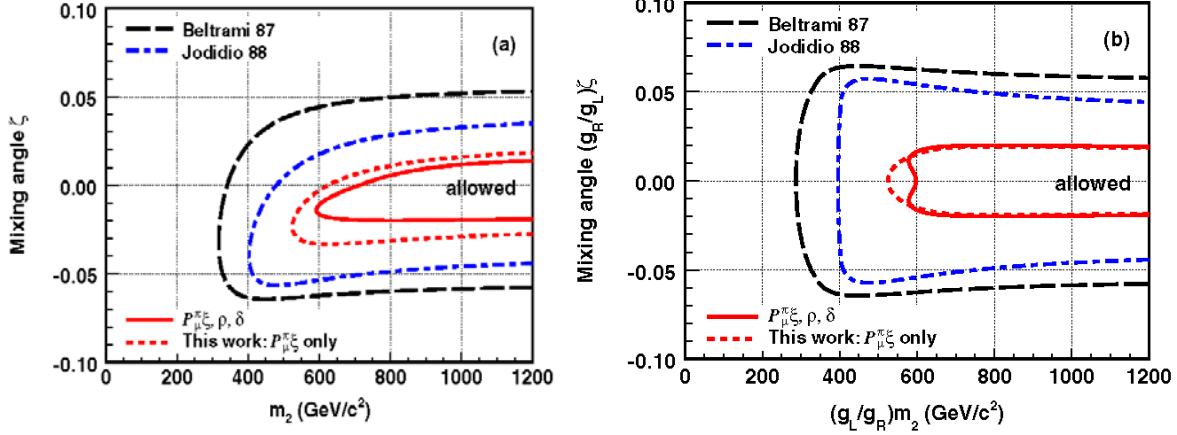


**FIG. 2.** Allowed regions (90% confidence) for the  $W_1 - W_2$  mixing angle and  $W_2$  mass in (left) manifest and (right) generalized LRS models. The red dotted curves show the limits derived using only the final TWIST value for  $P_{\mu\xi}$ . The red solid curves show the limits derived from the final TWIST measurements of  $\rho$ ,  $\delta$ , and  $P_{\mu\xi}$ , including the influence of the parameter correlations.

Our group also updated our previous global analysis of muon decay [3], combining the final TWIST results with a broad range of other measurements. The global analysis sets limits on the weak coupling constants  $g_{\varepsilon\mu}^\Gamma$ , where  $\Gamma$  specifies the space-time structure of the interaction ( $S, V, T$ ), and  $\varepsilon$  and  $\mu$  specify the chirality of the electron and muon, respectively. Table I presents the final 90% confidence limits, together with the pre-TWIST values [4]. The TWIST measurements provide much stronger constraints on  $RR$  and  $LR$  coupling constants that involve right-handed muon interactions. The quantity

**Table I.** 90% confidence limits on the muon decay coupling constants. The second column shows the pre-TWIST limits.

	Ref. [4]	Final TWIST results
$ g_{RR}^S $	$<0.066$	$<0.035$
$ g_{RR}^V $	$<0.033$	$<0.017$
$ g_{LR}^S $	$<0.125$	$<0.050$
$ g_{LR}^V $	$<0.060$	$<0.023$
$ g_{LR}^T $	$<0.036$	$<0.015$
$ g_{RL}^S $	$<0.424$	$<0.420$
$ g_{RL}^V $	$<0.110$	$<0.105$
$ g_{RL}^T $	$<0.122$	$<0.105$
$ g_{LL}^S $	$<0.550$	$<0.550$
$ g_{LL}^V $	$>0.960$	$>0.960$

$Q_R^\mu$  provides the total probability for a muon to decay via a right-handed interaction. We find  $Q_R^\mu < 0.00082$  with 90% confidence, a factor of 6 reduction compared to the pre-TWIST limit.

A report of the final TWIST results has been published in [1]. The collaboration is preparing two long, archival papers. The first will describe the measurement of  $P_{\mu\xi}$ ; the second will describe the measurements of  $\rho$  and  $\delta$ . The collaboration also plans to publish a search for the two-body decay of the muon,  $\mu^+ \rightarrow e^+ + X$ , where  $X$  lives long enough to escape the TWIST detector. The collaboration will disband after those last three papers are published.

- [1] R. Bayes *et al.* (TWIST Collaboration), Phys. Rev. Lett. **106**, 041804 (2011).
- [2] P. Herczeg, Phys. Rev. D **34**, 3449 (1986).
- [3] C.A. Gagliardi, R.E. Tribble, and N.J. Williams, Phys. Rev. D **72**, 073002 (2005).
- [4] B. Balke *et al.*, Phys. Rev. D **37**, 587 (1988); W. Fetscher and H.-J. Gerber, in S. Eidelman *et al.*, Phys. Lett. B **592**, 1 (2004).

**SECTION II**  
**HEAVY ION REACTIONS**

## The nuclear matter free symmetry energy at $0.03 \leq \rho/\rho_0 \leq 0$

L. Qin, K. Hagel, R. Wada, J. B. Natowitz, S. Shlomo, A. Bonasera, G. Roepke,<sup>1</sup> Z. Chen,<sup>2</sup> M. Huang,<sup>2</sup>  
 J. Wang,<sup>2</sup> H. Zheng, S. Kowalski,<sup>3</sup> M. Barbui, M. Rodrigues, K. Schmidt, D. Fabris,<sup>4</sup> M. Lunardon,<sup>4</sup>  
 S. Moretto,<sup>4</sup> G. Nebbia,<sup>4</sup> S. Pesente,<sup>4</sup> V. Rizzi,<sup>4</sup> G. Viesti,<sup>4</sup> M. Cinausero,<sup>4</sup> G. Prete,<sup>5</sup> T. Keutgen,<sup>6</sup>  
 Y. El Masri,<sup>6</sup> and Z. Majka<sup>7</sup>

<sup>1</sup>University of Rostock, FB Physik, Rostock, Germany

<sup>2</sup>Institute of Modern Physics HIRFL, Chinese Academy of Sciences, Lanzhou, 730000, China

<sup>3</sup>Institute of Physics, Silesia University, Katowice, Poland

<sup>4</sup>Dipartimento di Fisica dell'Universita di Padova and INFN Sezione di Padova, Italy

<sup>5</sup>INFN Laboratori Nazionali di Legnaro, Italy

<sup>6</sup>Universit'e Catholique de Louvain, Louvain-la-Neuve, Belgium,

<sup>7</sup>Smoluchowski Institute of Physics, Jagiellonian University, Krakow, Poland

We previously pointed out [ 1, 2] that measurements of nucleon and light cluster emission from the participant matter which is produced in near Fermi Energy heavy ion collisions could be employed to probe the EOS at low density and moderate temperatures where clustering is important. Our data demonstrated a large degree of alpha clustering in matter with average proton fraction,  $Y_p \sim 0.44$ , densities at and below  $\sim 0.05$  times normal nuclear density and temperatures of 4 to 10 MeV. Using these data we derived experimental free symmetry energies in low density nuclear matter [1,2] The analysis employed the isoscaling technique which compares yields for two systems with similar temperatures but different N/Z ratios to determine the differences in chemical potentials and symmetry energy.

The NIMROD multi-detector at Texas A&M University has now been used to extend our measurements of free symmetry energy to higher densities. Clusters production in collisions of 47A MeV  $^{40}\text{Ar}$  with  $^{112,124}\text{Sn}$  and  $^{64}\text{Zn}$  with  $^{112,124}\text{Sn}$  was studied.. Thermal Coalescence model analyses have been

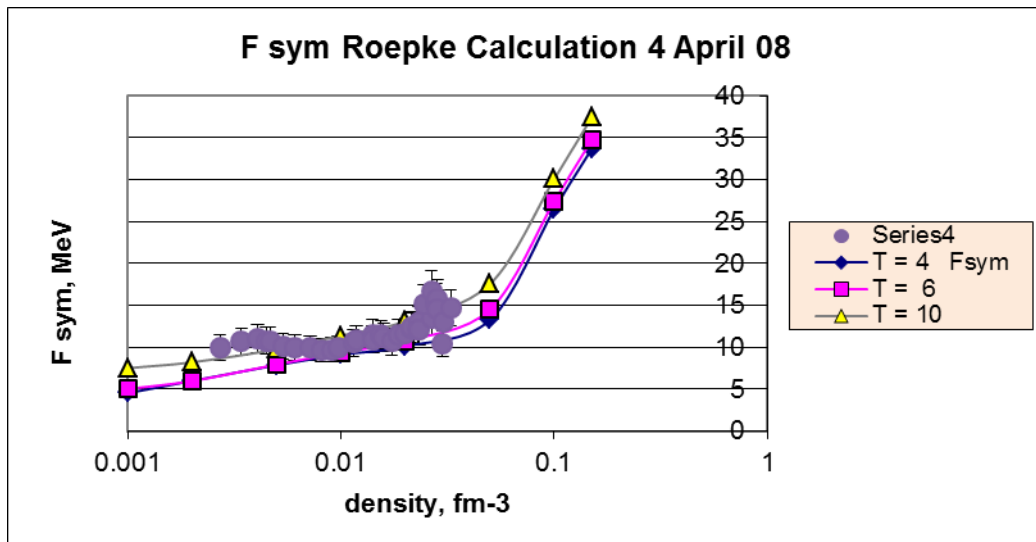


**FIG. 1.** Free symmetry energy vs nuclear density. Lines show values calculated for  $T=4, 6$  and  $10$  MeV. Grey circles indicate experimental data.

employed to derive densities and temperatures. The preliminary results of the measurements are presented in Fig. 1, where they are compared with predictions made using a model developed by G. Roepke and collaborators [3]. This model explicitly treats medium modifications of the cluster binding energies. A paper on this work is in preparation.

[1] S. Kowalski *et al.*, Phys.Rev. C **75**, 014601 (2007).

[2] J.B. Natowitz *et al.*, Phys. Rev. Lett. **104**, 202501 (2010).

[3] G. Roepke *et al.*, Private Communication.

## Laboratory tests of astrophysical equations of state at low densities

L. Qin, K. Hagel, R. Wada, J. B. Natowitz, S. Shlomo, A. Bonasera, G. Roepke,<sup>1</sup> Z. Chen,<sup>2</sup> M. Huang,<sup>2</sup>  
J. Wang,<sup>2</sup> H. Zheng, S. Kowalski,<sup>3</sup> M. Barbui, M. Rodrigues, K. Schmidt, D. Fabris,<sup>4</sup> M. Lunardon,<sup>4</sup>  
S. Moretto,<sup>4</sup> G. Nebbia,<sup>4</sup> S. Pesente,<sup>4</sup> V. Rizzi,<sup>4</sup> G. Viesti,<sup>4</sup> M. Cinausero,<sup>4</sup> G. Prete,<sup>5</sup> T. Keutgen,<sup>6</sup>  
Y. El Masri,<sup>6</sup> and Z. Majka<sup>7</sup>

<sup>1</sup>*University of Rostock, FB Physik, Rostock, Germany*

<sup>2</sup>*Institute of Modern Physics HIRFL, Chinese Academy of Sciences, Lanzhou, 730000, China*

<sup>3</sup>*Institute of Physics, Silesia University, Katowice, Poland*

<sup>4</sup>*Dipartimento di Fisica dell'Universita di Padova and INFN Sezione di Padova, Italy*

<sup>5</sup>*INFN Laboratori Nazionali di Legnaro, Italy*

<sup>6</sup>*Universit'e Catholique de Louvain, Louvain-la-Neuve, Belgium,*

<sup>7</sup>*Smoluchowski Institute of Physics, Jagiellonian University, Krakow, Poland*

Reliable understanding of the nuclear equation of state, EOS, over a wide range of densities and temperatures is crucial in both nuclear science and to our understanding of stellar matter and stellar evolution. In the latter context it is well-known that a valid treatment of the correlations and clusterization in low density matter is a vital ingredient of stellar models. To meet the need for the nuclear input, some well-known extensive calculations and existing tabulations, based on varying effective interactions, were developed and have served as standard input for a wide variety of astrophysical simulations[ [1,2]. More recently some new approaches have produced new predictions [3-9 HORO] While all of the models in use predict strong alpha clustering of the matter at low densities,  $\rho$ , and temperatures,  $T$ , they differ significantly in their quantitative predictions, usually tabulated as alpha mass fractions, at specified  $T$  and  $\rho$ .

Clearly the absolute alpha yields and mass fractions depend upon the model specific nucleon-nucleon interaction assumed and mathematical approximations of a given model. In addition, as all of the treatments assume chemical equilibrium, they also depend upon the number and type of competitive species included in the calculation. In an equilibrium situation, all relevant equilibria must be simultaneously satisfied. Thus, if relevant species are not included the calculated mass fractions of the alpha particles and other nuclei will be in error.

For this reason we do not believe that a direct comparison with calculated alpha mass fractions is the appropriate way to test the models. We choose rather to compare the experimentally derived equilibrium constants for alpha production with those of the models. The model derived equilibrium constants should be independent of the choice of competing species in a particular model.

Specifically we define the equilibrium constant,  $K_C(\alpha)$ , as

$$K_C(\alpha) = \rho_\alpha / [(\rho_p^2)(\rho_n^2)]$$

Where  $\rho_\alpha$ ,  $\rho_p$  and  $\rho_n$  are respectively the densities of alpha particles, protons and neutrons.

Clustering in low density nuclear matter has been investigated using the NIMROD multi-detector. Thermal coalescence models were employed to extract densities,  $\rho$ , and temperatures,  $T$ , for evolving systems formed in collisions of 47A MeV  $^{40}\text{Ar} + ^{112}\text{Sn}$ ,  $^{124}\text{Sn}$  and  $^{64}\text{Zn} + ^{112}\text{Sn}$ ,  $^{124}\text{Sn}$ . The yields of d, t,  $^3\text{He}$  and  $^4\text{He}$  have been determined at  $\rho = .002$  to  $.032$  nucleons/ $\text{fm}^3$  and  $T = 5$  to  $10$  MeV. The experimentally derived equilibrium constants for d, t,  $^3\text{He}$  and  $^4\text{He}$  production are presented in Figure 1. The model comparisons are in progress.

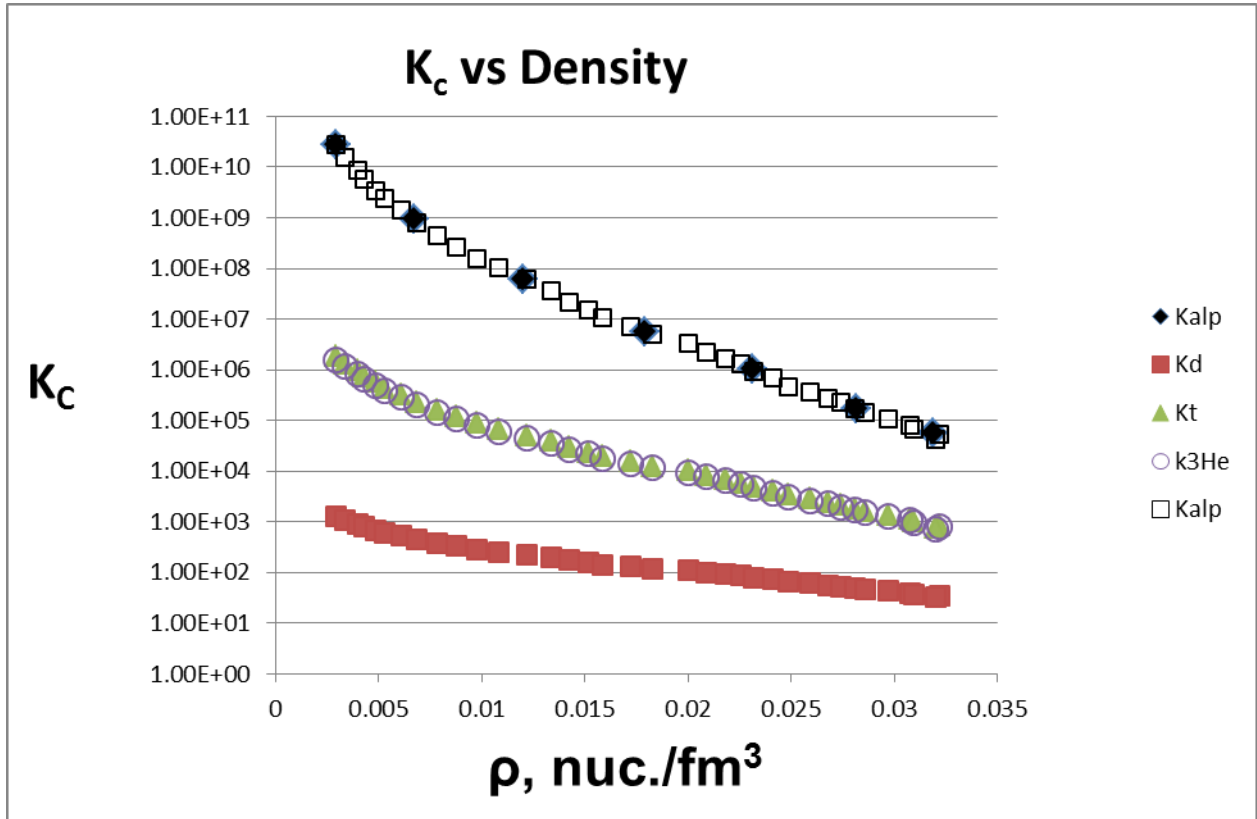


**FIG. 1.** Experimentally derived equilibrium constants for cluster formation at low density and moderate temperature. For the purpose of future comparisons with model calculations we have also interpolated the experimental results to determine the equilibrium constants for alpha particle formation at integral temperatures from 4 to 12 MeV. The values of  $K_C$  for these integral temperatures are indicated by solid diamonds.

- [1] H. Shen *et al.*, Nucl.Phys. **A637**, 435 (1998); Prog. Theor. Phys. **100**, 1013 (1998).
- [2] J.M. Lattimer and F.D. Swesty, Nucl. Phys. **A535** 331 (2001).
- [3] C.J. Horowitz, A. Schwenk Nucl. Phys. **A776**, 55 (2006).
- [4] S. Typel, G. Ropke, T. Klahn, D. Blaschke, and H. H. Wolter, Phys. Rev. C **81**, 015803 (2010).
- [5] M. Hempel and J. Schaffner-Bielich, Nucl. Phys. **A837**, 210-254 (2010)
- [6] G. Shen, C.J. Horowitz, and S. Teige, arXiv:1101.3715
- [7] G. Shen, C.J. Horowitz, and E. O'Connor, arXiv:1103.5174

## Search for heavy and superheavy systems in $^{197}\text{Au} + ^{232}\text{Th}$ collisions near the Coulomb barrier

M. Barbui, K. Hagel, J. B. Natowitz, M. R. D. Rodrigues, K. Schmidt, R. Wada, Z. Majka, H. Zheng,  
M. Barbarino, and A. Bonasera<sup>1</sup>

<sup>1</sup>*INFN Laboratorio Nazionale del Sud, Catania, Italy*

The possibility to produce heavy and superheavy elements in the reaction  $^{197}\text{Au} + ^{232}\text{Th}$  at 7.5 MeV/nucleon has been investigated using the BigSol spectrometer at Texas A&M [1]. This experiment indicated the possibility to produce heavy elements of Z about 100, however a confirmation of this scenario would only come by detecting the high energy alpha particles emitted by the decaying heavy nuclei. In fact, very heavy and superheavy nuclei are expected to decay to stable nuclei through alpha particle chains with energy around or above 10 MeV.

To search for high energy alpha emission, we designed and performed a new experiment, in which the heavy reaction products emitted in the angular range from  $3^\circ$  to  $45^\circ$  are implanted in a catcher foil. The particles emitted by the implanted nuclei are detected using silicon detectors placed in the backward position. A picture of the experimental setup is shown in Fig.1.



**FIG. 1.** Picture of the experimental setup as placed in the reaction chamber. 6 seven strips silicon detectors (Micron Semiconductors design I, thickness  $300\ \mu\text{m}$ ) are placed after the target position, facing the catcher foil. The catcher is a polypropylene layer of thickness  $7.5\ \mu\text{m}$  placed at  $3\ \text{cm}$  from the silicon detectors. The catcher has a central hole to allow the beam to pass through and three additional holes in correspondence of the position of the monitor detectors. A Faraday cup is placed at the end of the line at about  $5\ \text{m}$  from the target. Two different  $^{232}\text{Th}$  targets were placed in the target ladder: one of thickness  $11\ \text{mg}/\text{cm}^2$  and another of thickness  $6.3\ \text{mg}/\text{cm}^2$  followed by a  $^{12}\text{C}$  degrader of thickness  $3\ \text{mg}/\text{cm}^2$ .

A first test run was performed after optimizing the experimental setup. The 7.5 MeV/nucleon  $^{197}\text{Au}$  beam was delivered by the K500 superconducting cyclotron and pulsed at different intervals in order to be able to identify species of different half-life (i.e. 1 ms beam-on, 1 ms beam-off; 10 ms beam-on, 10 ms beam-off or 100 ms beam-on 100 ms beam-off). The events were recorded both in beam-on and beam-off condition. The calibration of the energy signal from the silicon detectors was performed with a  $^{228}\text{Th}$  source before and after the run. Fig. 2 shows a typical spectrum of the  $^{228}\text{Th}$  source. The energy resolution of the detectors is in average 170 keV (FWHM) for the 8.78MeV peak.

The measurements performed with the beam on target show that there is a huge number of events coming from prompt radiations such as high energy neutrons. Once the beam is turned off these events dramatically decrease as shown in Fig.3.

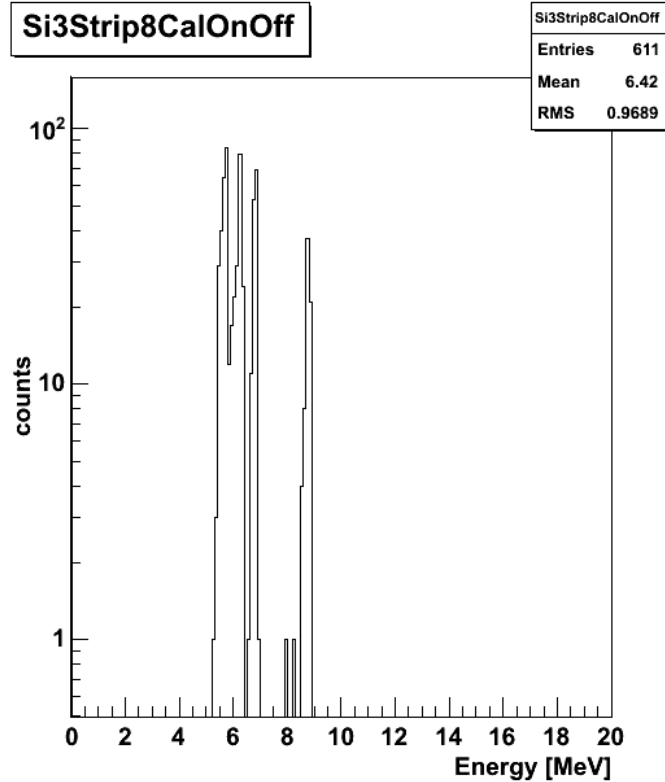


FIG. 2.  $^{228}\text{Th}$  source spectrum

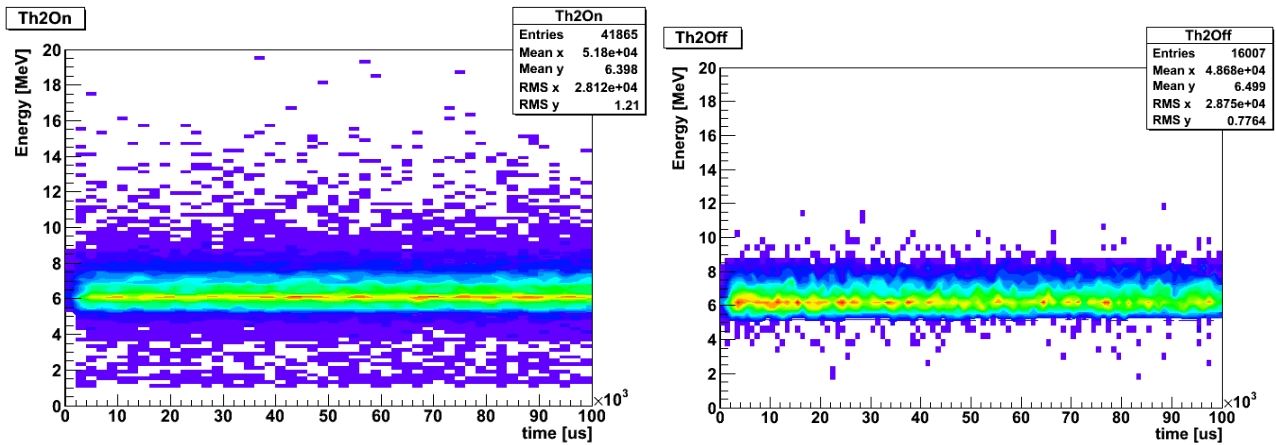


FIG. 3. Energy measured by the Si detectors 3 and 4 as a function of the time in case of beam-on target (left panel) and beam-off (right panel).

A very preliminary analysis of the data measured in the beam-off condition shows several events with energy around and above 10 MeV. The data analysis is still in progress.

A further improvement of the measurement will be possible by adding thin silicon detectors in front of the thick silicon detectors in order to make particle identification and separate alpha particles from other radiation.

[1] M. Barbui *et al.*, INPC 2010 Conference proceedings, J. Phys. Conf. Series (accepted).

## Energy calibration of the $^{40}\text{Ca} + ^{40}\text{Ca}$ data taken on the NIMROD-ISiS array

K. Schmidt, C. Bottosso, J. B. Natowitz, K. Hagel, R. Wada, M. Huang, A. Bonasera, M. Barbui, M. Rodrigues, G. Liu,<sup>1</sup> G. Viesti,<sup>2</sup> S. Moretto,<sup>2</sup> G. Prete,<sup>3</sup> S. Pesente,<sup>2</sup> D. Fabris,<sup>2</sup> Y. El Masri,<sup>4</sup> T. Keutgen,<sup>4</sup> S. Kowalski,<sup>5</sup> and A. Kumar<sup>6</sup>

<sup>1</sup>*Shanghai Institute of Applied Physics, Shanghai, China*

<sup>2</sup>*Dipartimento di Fisica dell'Universita di Padova and INFN Sezione di Padova, Italy*

<sup>3</sup>*INFN Laboratori Nazionali di Legnaro, Italy*

<sup>4</sup>*Universit'e Catholique de Louvain, Louvain-la-Neuve, Belgium,*

<sup>5</sup>*Institute of Physics, Silesia University, Katowice, Poland*

<sup>6</sup>*Nuclear Physics Laboratory, Department of Physics, Banaras Hindu University, Varanasi, India*

The ability to isolate low density matter in near Fermi Energy collisions and the high degree of alpha clustering which is observed suggest that we search for evidence of Bose Condensates which are predicted to occur in the density and temperature range which we explore in near Fermi energy collisions [1-3]. We have initiated a search for evidence of Bose Condensates using the NIMROD array. Our first experiments, carried out at the end of 2008 employed 10, 25, 35 MeV/u beams of  $^{40}\text{Ca}$  and  $^{28}\text{Si}$  incident on  $^{40}\text{Ca}$ ,  $^{28}\text{Si}$ ,  $^{12}\text{C}$  and  $^{180}\text{Ta}$  targets. The first three targets allow an exploration of collisions of alpha conjugate nuclei. In the  $^{180}\text{Ta}$  case the projectile excitation and decay is of primary interest. Before a more sophisticated analysis is performed the mass, charge and energy of detected fragments must be determined.

The identification in mass and charge [4] for all systems is now complete. The energy calibration consists of several steps and the first one is the super-telescope calibration. The Si<sub>1</sub>-Si<sub>2</sub> silicon detectors are "self-calibrating" as we employ range energy tables to established from the punch through points of

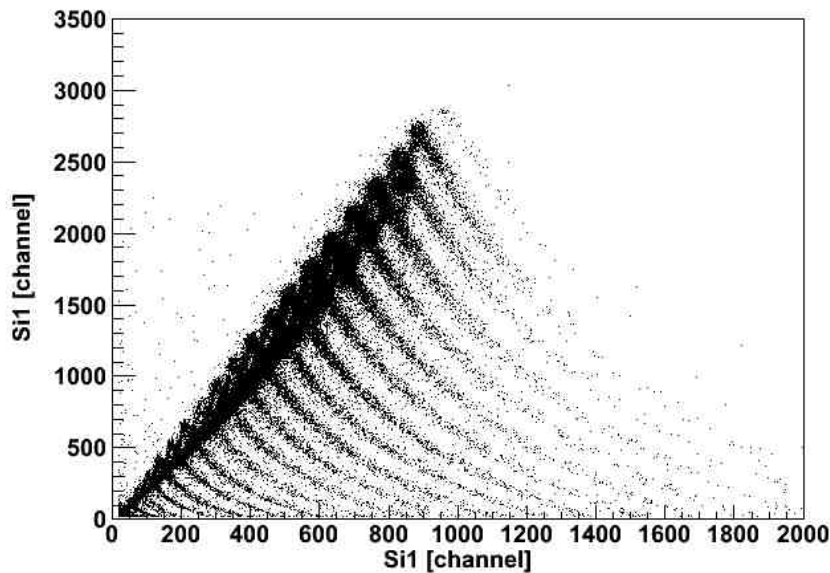


FIG. 1. Si1 signal vs Si2 signal.

various identified species. In Fig. 1 the signals from both silicon detectors of a typical super-telescope are plotted. We note that the position of the punch through points can be very precisely determined.

Once the super-telescope calibrations are established, we calculate the energy deposited in CsI scintillators behind them. Relating the deposited energy to channel numbers allows us to find the calibration parameters of light particles stopped in CsI scintillator. The green low energy points in Fig. 2. show the energy deposited by  $\alpha$  particles in the CsI versus the light output of the Slow signal. The other green, black and red points show the elastic scattering points of p, d, and  $\alpha$  particles on Ca target at energies 25MeV/A, 30MeV/A and 55MeV/A obtained in a later calibration run. We applied the global fit to the spectra, using a formula based on the Tabacaru's prescription [5]:

$$L = a_5 + a_0 \left( E \left( 1 - \frac{a_1 AZ^2}{E} \ln \left( 1 + \frac{E}{a_1 AZ^2} \right) \right) c_1 a_1 AZ^2 \ln \left( \frac{E + a_1 AZ^2}{a_1 a_2 AZ^2} \right) \right) + M;$$

$$c_0 = \frac{a_3}{1 + e^{\frac{a_4}{a_2}}};$$

$$c_1 = \frac{a_3}{1 + e^{-\frac{(E-a_2)}{a_4}}};$$

$$M = -a_0 c_0 a_1 AZ^2 \ln \left( \frac{a_1 AZ^2}{a_1 AZ^2 + a_2} \right).$$

The solid black, red and green lines in Fig. 2. correspond to the modified Tabacaru function for p, d, and  $\alpha$ , respectively. The Tabacaru parameters allow us to transform the light output from the CsI to energy in the scintillator using one function that depends on light output, charge and mass.

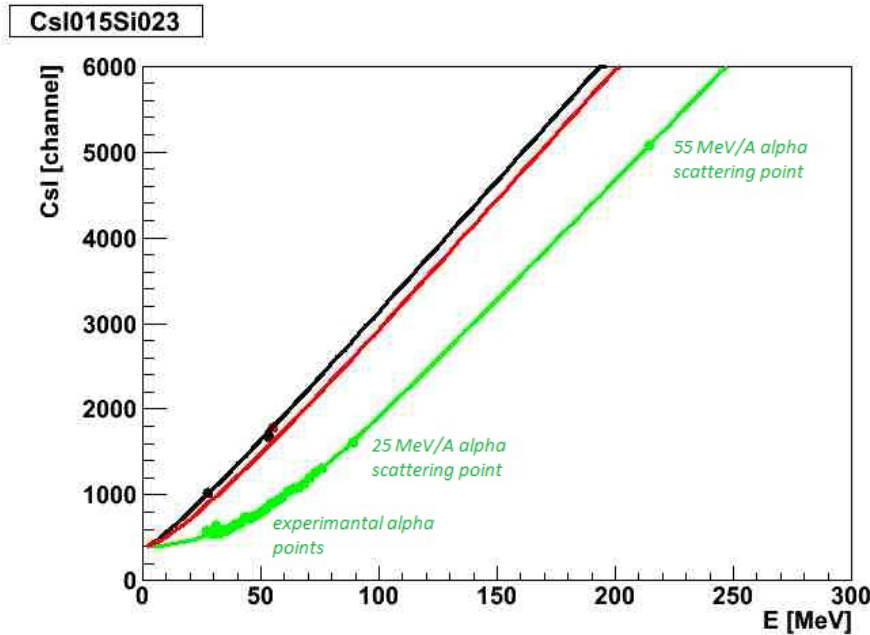


**FIG. 2.** The energy deposited in CsI detectors by p (black points), d (red points) and  $\alpha$  particles (green points) versus CsI slow signal. The solid black, red and green lines correspond to the Tabacaru function for p, d, and  $\alpha$ , respectively.

To determine the energies of light particles detected in the other detectors in the same NIMROD ring, we used the energy spectra of the super-telescopes as a reference spectra and applied a  $\chi^2$  based fitting procedure to determine calibration parameters. In Fig. 3 we show the comparison between the reference energy spectra (black lines) and calibrated spectra (red lines) for protons (left) and alpha particles (right) stopped in the detectors placed in the second Ring of NIMROD. The other rings showed similar results.

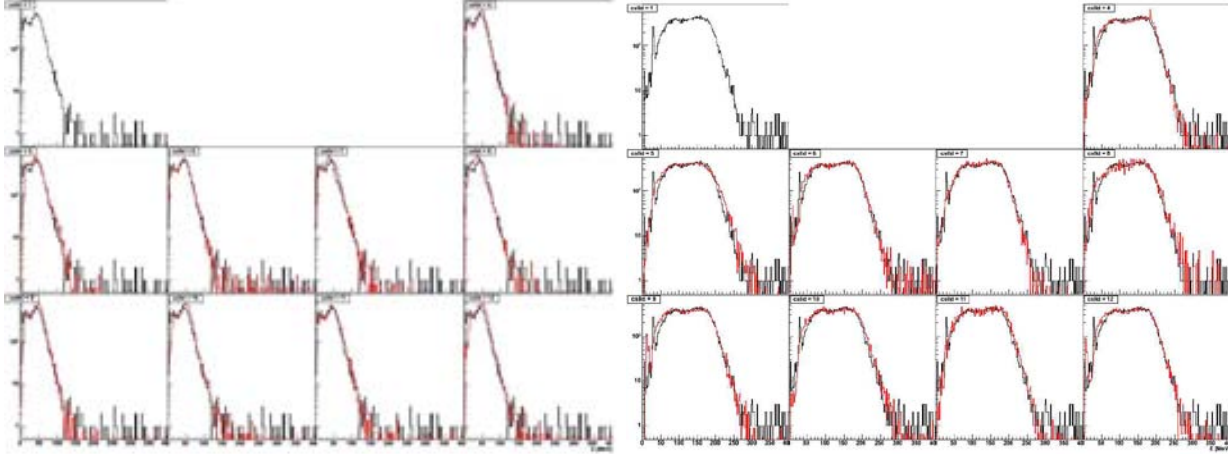


**FIG. 3.** The comparison between the reference energy spectra (black lines) and calibrated spectra (red lines) for protons (left) and alpha particles (right) stopped in the detectors placed in the second Ring of NIMROD array.

The calibration procedure for heavier fragments is in progress. To determine the energy of the heavier fragments we use the energy loss in the silicon detectors to determine the initial energy. The procedure for the heavy fragment calibration is to use the spectra from the super-telescopes as reference spectra and perform the  $\chi^2$  minimalisation to establish the calibration of the other silicon detectors. As soon as the calibration of the heavier fragments is completed, we will begin the advanced analysis.

- [1] Y. Funaki *et al.*, Phys. Rev. C **80**, 064326 (2009).
- [2] G. Roepke *et al.*, Phys. Rev. Lett. **80**, 3177(1998).
- [3] T. Sogo *et al.*, Phys. Rev. C **81**, 064310 (2010).
- [4] C. Bottosso *et al.*, *Progress in Research*, Cyclotron Institute, Texas A&M University (2008-2009), p. II-7, [http://cyclotron.tamu.edu/2009\\_20Progress\\_20Report/2\\_20Heavy\\_20Ion\\_20Reactions/II\\_7\\_calibration\\_20of\\_20the\\_2040car.pdf](http://cyclotron.tamu.edu/2009_20Progress_20Report/2_20Heavy_20Ion_20Reactions/II_7_calibration_20of_20the_2040car.pdf)
- [5] M. Parlog *et al.*, Nucl. Instrum. Methods Phys. Res. **A482**, 693 (2002).

## Neutron yield from d-d reaction in laser induced gas cluster explosions

M. Barbui, A. Bonasera,<sup>1</sup> K. Hagel, J. B. Natowitz, M. R. D. Rodrigues, K. Schmidt, R. Wada, H. Zheng, M. Barbarino, W. Bang,<sup>2</sup> T. Ditmire,<sup>2</sup> G. Dyer,<sup>2</sup> H. Quevedo,<sup>2</sup> and A. Bernstein<sup>2</sup>

<sup>1</sup>*INFN Laboratorio Nazionale del Sud, Catania, Italy*

<sup>2</sup>*University of Texas, Austin, Texas*

Several experiments in the last years have shown that the interaction of intense ultrafast laser pulses with molecular clusters produces the explosion of the clusters with enough kinetic energy to drive nuclear reactions. In case of few nm diameter deuterium clusters, laser pulses with intensities of the order of  $10^{16}$ - $10^{18}$  W/cm<sup>2</sup> can remove the field ionized electrons from the cluster. Consequently the clusters explode due to the Coulomb repulsion of the closely spaced positive ions.

The gas clusters are formed in the expansion in the vacuum of cryogenically pre-cooled and compressed (about 800 psi) D<sub>2</sub> gas. The expansion is regulated by a supersonic nozzle valve.

The d(d,p)T and d(d,n)He<sup>3</sup> nuclear reactions can occur with the same cross-section. The reaction d(d,n)He<sup>3</sup> has been extensively studied, by detecting the characteristic 2.45 MeV neutrons [1] [2]. The study of the reaction d(d,p)T is more difficult because it requires the detection of the 3.02 MeV protons. Thin fast plastic scintillators placed at a proper distance from the reaction point have been used in the past to detect the charged particles produced in laser induced nuclear reactions [3] [4]. CR-39 plastic films [5] or micro-channel plates detectors [6] both coupled to magnetic separators can also serve this purpose.

A first test was performed in March 2011 at University of Texas Petawatt Laser to confirm our capability of measuring the neutrons from the d(d,n)He<sup>3</sup>. Four NE213 neutron detectors were placed at different angles with respect to the laser direction as shown in Figure 1. The average energy of the deuterium ions was measured using a Faraday cup.

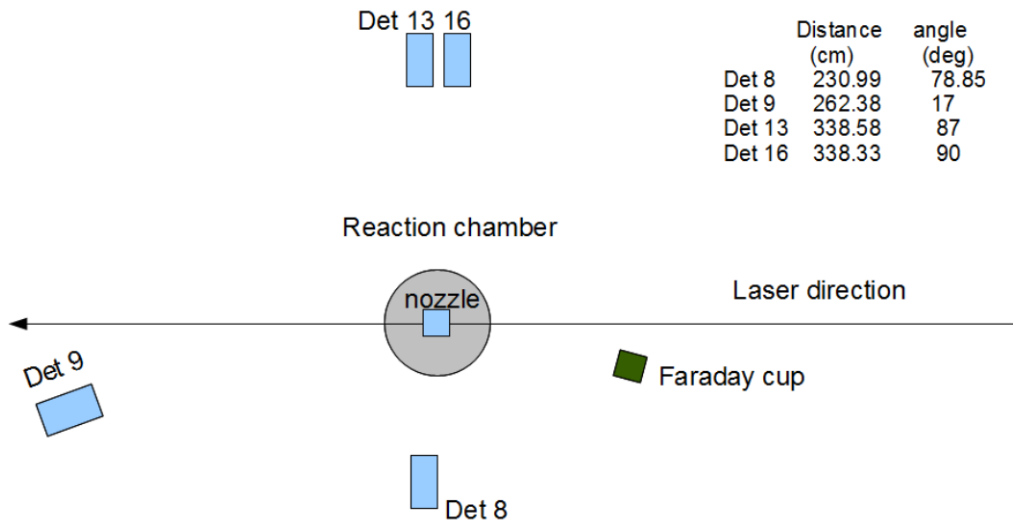


**FIG. 1.** Experimental setup used for the test at UT petawatt laser. The neutron detectors # 8, 9, 16, 13 are liquid scintillators NE213 of cylindrical shape with radius 7 cm and thickness 14 cm. HV=-1800V. The distance from the nozzle and the angle with respect to the laser direction are shown in the picture.

The neutron detectors were calibrated using a  $^{252}\text{Cf}$  source. For the calibration, the signals were amplified by a factor 200 using a fast amplifier (ORTEC FTA820) and recorded using the same flash ADCs used in the experiment (10 ns sampling interval). The time of flight of the neutrons was also measured. In this case the start the signal was given by a silicon detector placed very close to the source and the stop signal by the neutron detector. With a proper window on the time of flight we selected the neutrons in the energy range around 2.45 MeV and plotted the distribution of the amplitudes of the signals, as shown in Figure 2. For every neutron detector, the average of this distribution is used to count how many 2.45 neutrons hit the detector in the real experiment.

Given the thickness of the detectors, we assume a detection efficiency of about 90% for 2.45 MeV neutrons.

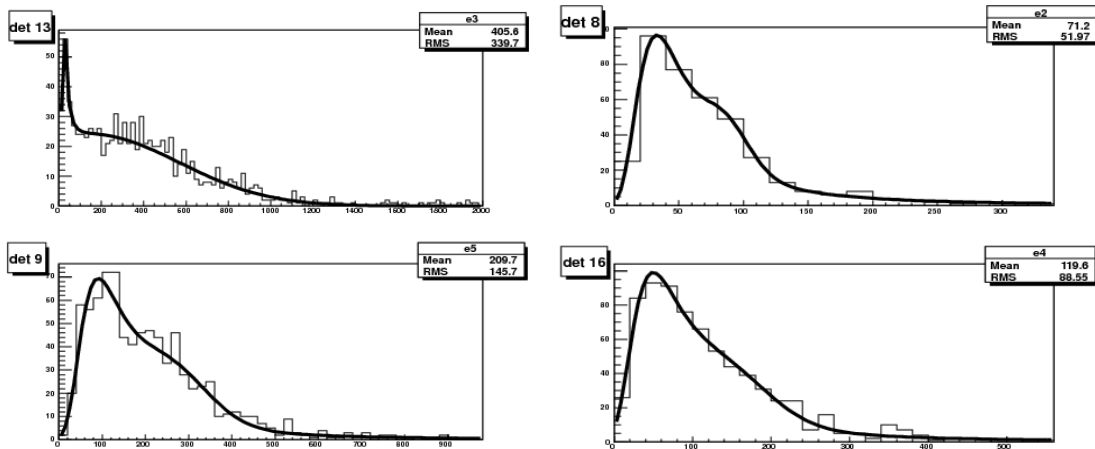


**FIG. 2.** Distribution of the signal amplitudes given by 2.45MeV neutrons in the detectors. The shape of the distribution can be fitted by a Landau + Gauss function.

In the test at UT Petawatt we employed system shots of energy 115 J and duration time 170 fs. A plasma mirror was used in order to reduce the pre-pulse resulting from non-linearities of the laser amplification process. In order to find the best conditions for inducing the nuclear reactions, several positions of the nozzle different from the optimal focus position were tested. The results are reported in Figure 3.

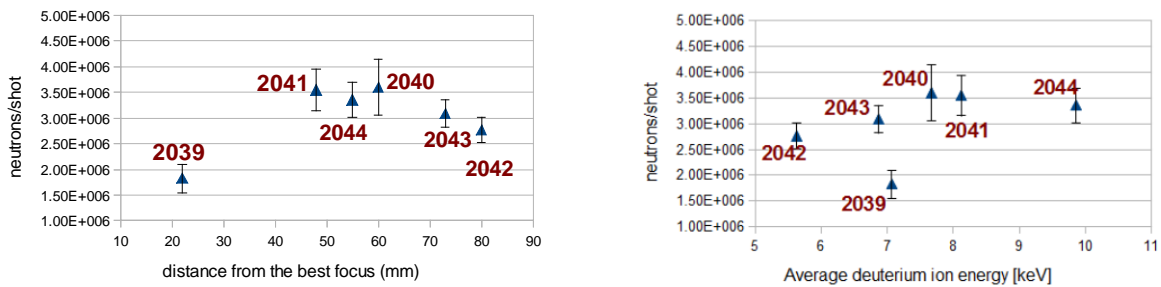


**FIG. 3.** Left panel: neutron yield as a function of the distance of the nozzle from the best focus position. Right panel: neutron yield as a function of the deuterium ions temperature measured with a faraday cup.

The optimal nozzle position was found at about 5-6 cm from the best focus. In this setting we measured a neutron yield of about  $3.5 \times 10^6$  neutrons/shot over  $4\pi$  and an average deuterium ion energy ranging from 7 to 10 keV. Our results are in fair agreement with those obtained in the same experiment by the UT group using plastic scintillator detectors. Comparing the results obtained from detectors 8, 13 and 16 placed at about  $90^\circ$  with respect to the laser direction with the result from detector 9 placed in forward direction we did not observe any anisotropy of the neutron distribution. Figure 4 shows an estimate of the reaction rate (obtained dividing the number of measured neutrons by the number of energetic ions in the Faraday cup) as a function of the average energy of the ions. It is interesting to note that rate is almost constant as the average energy of the ions increases from 7 to about 10 keV.

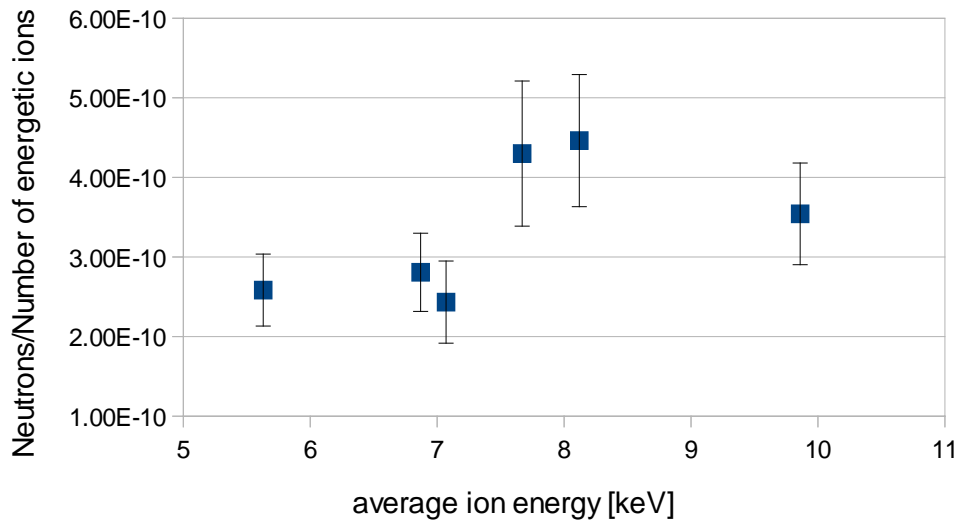


**FIG. 4.** Reaction rate as a function of the average ion energy. To calculate the error bars we assumed an uncertainty of about 15% on the measured number of energetic ions.

- [1] T. Ditmire *et al.*, Nature **386**, 54 (1997).
- [2] J. Zweiback *et al.*, Phys. Rev. Lett. **84**, 2634 (2000) .
- [3] V.W. Slivinsky *et al.*, J. Appl. Phys. **49**, 1106 (1978).
- [4] Tai Ho Tan *et al.*, Nucl. Instrum. Methods **131**, 425 (1975).
- [5] C.K. Li *et al.*, Phys. Plasmas **7**, 2578 (2000).
- [6] K.Harres *et al.*, Rev. Sci. Instrum. **79**, 093306 (2008).

## New gas stopper for heavy element chemistry research

M. C. Alfonso and C. M. Folden III

The periodicity of the heaviest element is of particular interest because relativistic effects increase as  $Z^2$  (proton number). Relativistic effects change the energies of the valence electrons of the atom, which could lead to a significant change in the element's chemical properties. Transactinides, elements where this effect is expected to be the largest, do not exist naturally and are produced via a fusion-evaporation reaction. Before the chemistry of transactinides can be studied, their energy must be degraded to thermal energies (less than 1 eV), since evaporation residues (EVRs) are created with 30-50 MeV of kinetic energy.

Previous experiments have used a combination of Mylar degraders and a gas cell, also known as a recoil transfer chamber (RTC) and gas stopper, filled with helium gas to thermalize EVRs. These gas cells suffer from low efficiency and poor reproducibility due to turbulent gas flow conditions. We have designed a new RTC that has more laminar flow and uses a series of electrodes that create a potential gradient to more efficiently thermalize and transfer these heavy ions to the appropriate chemistry setup. This device will have a series of rings with decreasing potential to pull the stopped particles through; then at the end four concentric spherical electrodes will be used to focus the ions into an extraction nozzle. The electrode design is based on one used at MSU for stopping lighter and more energetic ions [1].

Through a series of simulations, the optimum design for our gas stopper was determined. SRIM [2] and LISE++ [3] were used to predict the expected spatial and energy distributions of the "model" transactinide ion,  $^{257}\text{Rf}$ , out of the Momentum Achromat Recoil Separator (MARS). At the peak of the  $^{208}\text{Pb}(^{50}\text{Ti}, n)^{257}\text{Rf}$  excitation function, the products exit the target with  $39.6 \pm 1.2$  MeV of energy. The predicted vertical and horizontal standard deviation was 8 mm and 12.7 mm, respectively, at the entrance of the gas stopper. These particles have an expected range in Ti of about 4.5  $\mu\text{m}$ . The SRIM predicted energy of the particles after passing through a variable angle degrader and RTC window was about 3.5 MeV. The variable angle degrader will be used to correct for uncertainty in degrader thickness by changing its effective thickness which is dependent on its angle and can be used to change the location of the stopped distribution centroid. The optimum gas cell pressure was determined to be 0.3 atm, it needed to be as large as possible to minimize straggling.

SRIM estimated the stopped distribution of the  $^{257}\text{Rf}$  ions in the longitudinal direction was only  $\sim 5$  cm ( $\pm 3\sigma$ ). This is considerably narrower than the distribution of the particles stopped by the MSU gas stopper ( $>50$  cm), evidence that a shorter gas cell with fewer rings could be used to stop EVRs.

SIMION was used to simulate the trajectory of the thermalized ions due to the ring and spherical electrodes. Included in the simulations was the mobility of the ions in He and collisions between the ions and atoms of the gas. SRIM was used to simulate the stopping width of the ions in the longitudinal direction and angular straggling. The voltage distribution was chosen to emulate MSU's. The equipotential lines of the MSU gas stopper (Fig. 1) suggest that the ions stopped in the first fifth of the gas cell will be defocused due to the grounded beryllium window, so biasing the window was simulated.

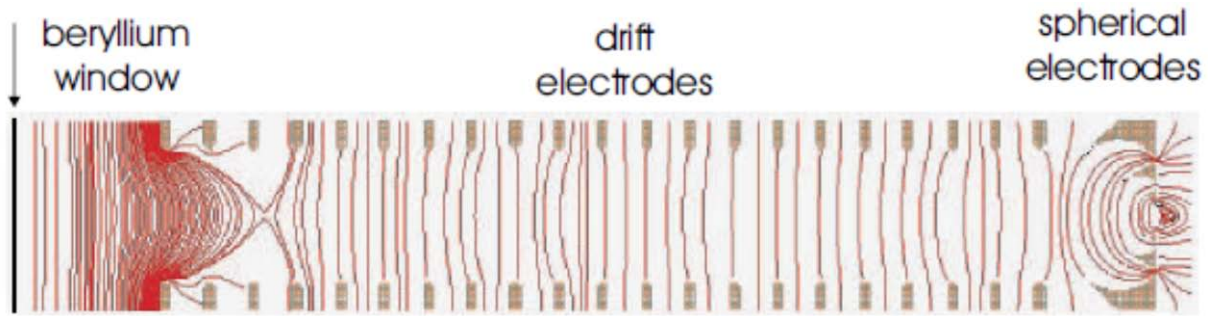


**FIG. 1.** Equipotential lines of the MSU gas stopper determined by SIMION. Ions travel perpendicular to the lines. [4].

It was discovered that a bias difference between the RTC window and 1<sup>st</sup> ring created an extra focusing region (Fig. 2). Also it was observed that equipotential lines bowed more at the center axis (more focusing) if the bias difference between the RTC window and the 1<sup>st</sup> ring was reduced. There is a limit, though, on this difference: If it is too small, the ions will not be guided toward the ring electrodes. Also, for this to work the walls of the chamber have to be the same bias as the window. The outer chamber of this device must be grounded for safety reasons so a two-chamber system is needed. The optimum number of ring electrodes was determined through simulation of gas cells with varying numbers of rings. It was observed that extraction efficiency was independent of ring number. Therefore the minimum number of rings possible was determined. A shorter gas cell has the benefits of decreased extraction time and decreased chance of the ions being neutralized since they go through less gas. It was observed that four rings are optimal; three rings showed signs of reduced focusing (Table I).

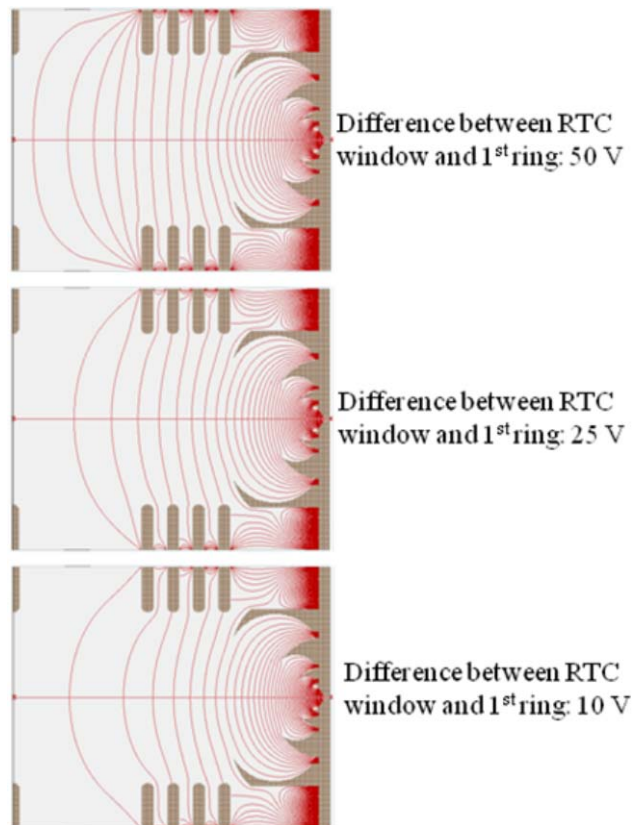


**FIG. 2.** Equipotential lines for gas stoppers with different voltage distribution from the RTC window to the 1<sup>st</sup> ring.

**Table 1.** Simulation results of gas stopper with varying number of rings. As expected, the time-of-flight decreases with the number of rings. Vertical and Horizontal position  $\sigma$  describes the ion distribution at the end of the gas stopper.

	3 rings	4 rings	6 rings
Time-of-Flight	9.6 ms	10.9 ms	13.3 ms
Vertical position $\sigma$	1.30 mm	1.28 mm	1.26 mm
Horizontal position $\sigma$	1.51 mm	1.42 mm	1.42 mm

The gas flow is also very important to the efficient transportation of the ions to the chemistry experiment. The two-chamber system was advantageous to the gas flow (Fig. 3) because the inner chamber could then have a groove-like inlet for the helium gas. Simulations from a computational fluid dynamics program, STAR-CCM+ [5], (Fig. 3) depict this system having a laminar flow that helps focus the ions in the nozzle region. The results from STAR-CCM+ were coupled to the SIMION simulation, resulting in a 65% extraction efficiency. About 34% of the ions were lost in the last 3 mm of the cell; this area will be examined in detail when maximizing the transmission of the actual gas cell.

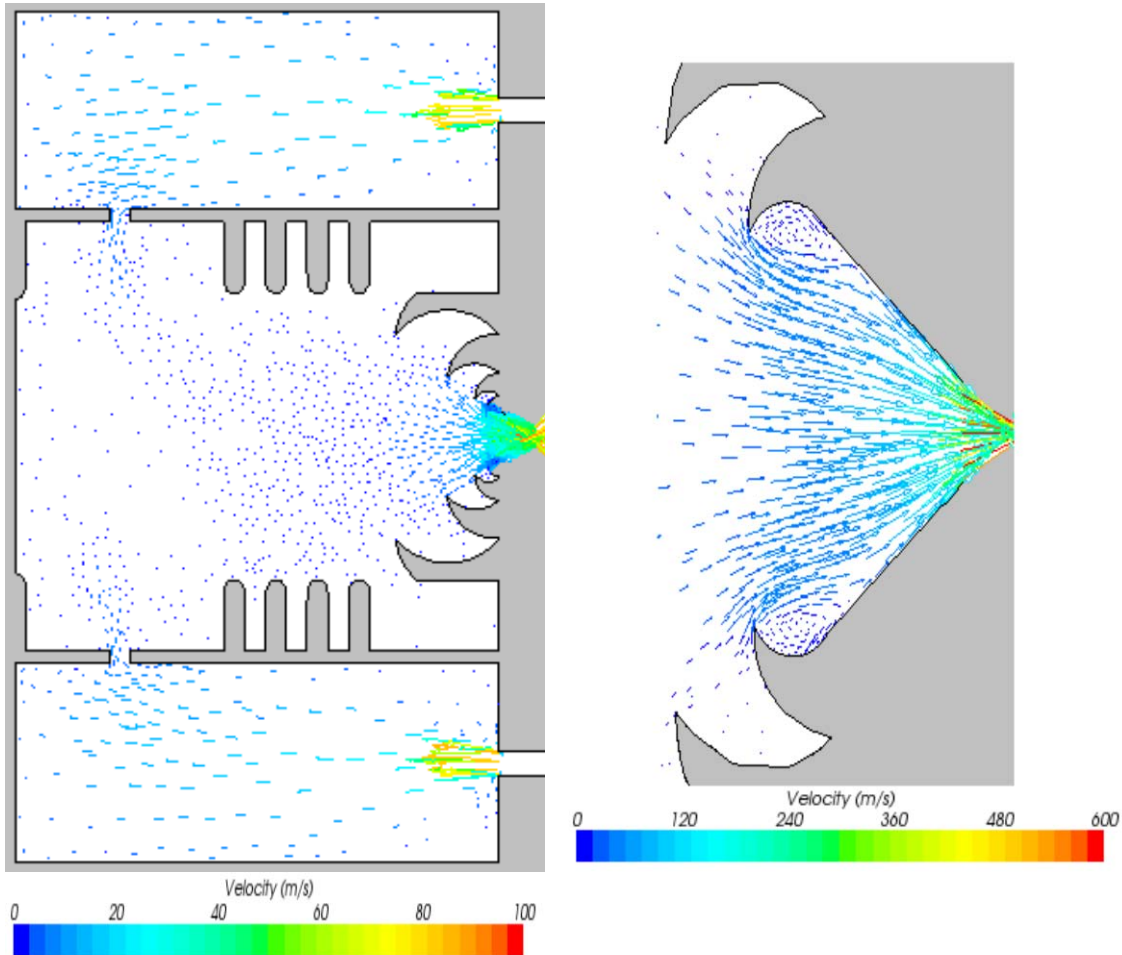


**FIG. 3.** STAR-CCM+ flow simulation with 0.3 atm He in the chamber and vacuum beyond the nozzle.

The design for the RTC for stopping heavy ions is almost finalized (Fig. 4). The flange containing four concentric spherical electrodes will be reused from the decommissioned MSU gas cell. The window material will be  $\sim 2 \mu\text{m}$  Ti foil supported by a wire grid and its vacuum seal will be made using gold o-rings to reduce contaminants produced by rubber o-rings. Once the entire gas cell has been fabricated, the RTC will first be tested with heavy recoils from an alpha-source. The performance will be optimized by varying the bias applied to the RTC window and the voltage drop across the gas stopper. Next, the gas stopper's efficiency will be determined with fusion reactions with high production rates, such as  $^{165}\text{Ho}(^{40}\text{Ar}, 6n)^{199}\text{At}$  and  $^{118}\text{Sn}(^{40}\text{Ar}, 6n)^{152}\text{Er}$ , since MARS has already been optimized in previous experiments for these reactions. Both offline and online tests should be completed by early 2012.

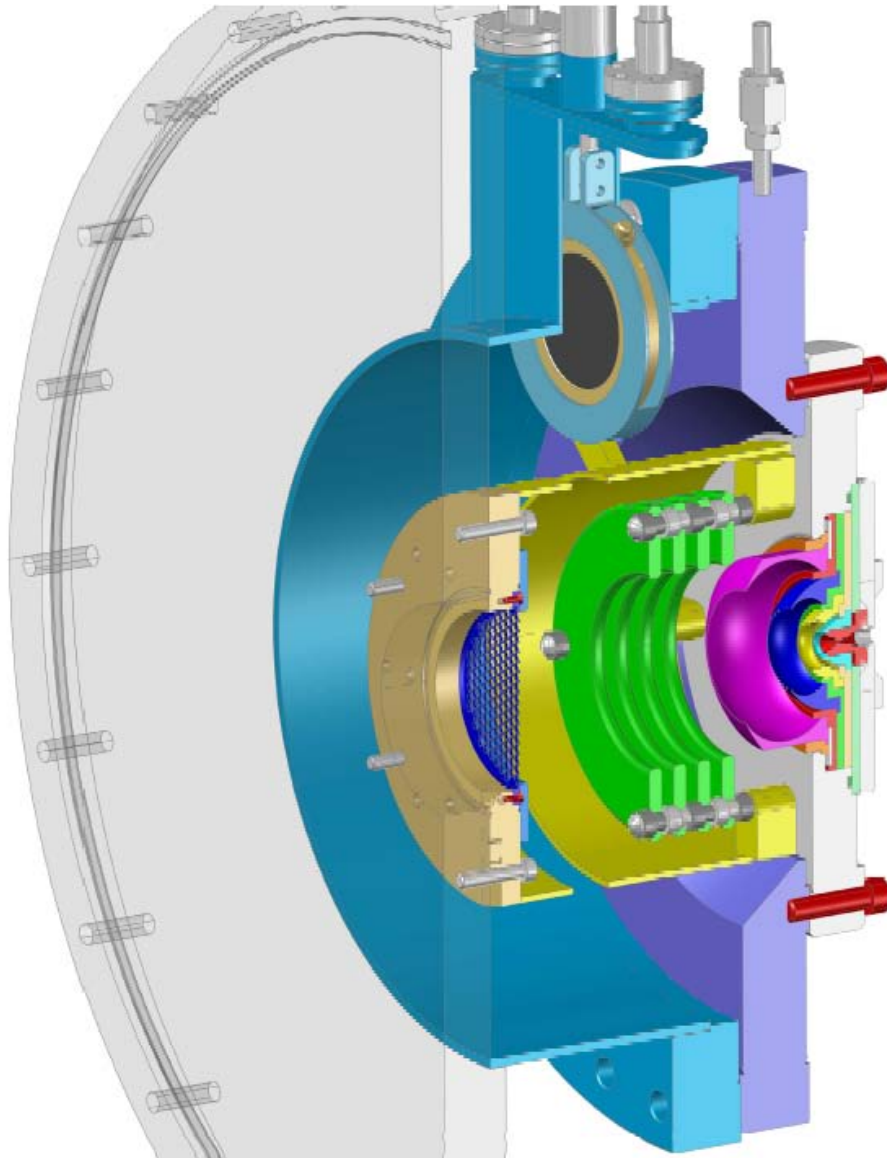


**FIG. 4.** Preliminary design of actual gas stopper (see main text for more detail). The simulated optimum location for the centroid of the stopped distribution is half-way between RTC window and  $1^{\text{st}}$ ; a detector in this location will be used to determine the optimum angle of the variable angle degrader. (Courtesy of Stephen Molitor.)

- [1] L. Weissman, *et al.*, Nucl. Instrum. Methods Phys. Res. **A540**, 245 (2005).
- [2] J.F. Ziegler, Computer Code SRIM-2008, [www.srim.org](http://www.srim.org).
- [3] O.B. Tarasov and D. Bazin, Nucl. Instrum. Methods Phys. Res. **B266**,4657 (2008).
- [4] P.A. Lofy, Ph.D. Thesis, Michigan State University (2003).
- [5] STAR-CCM+ 5.02.010, CD-adapco, [www.cd-adapco.com](http://www.cd-adapco.com).

## Projectile influence on EVR production in $^{48}\text{Ca}$ , $^{54}\text{Cr} + ^{162}\text{Dy}$ fusion-evaporation reactions and its relation to synthesis of element 120

D. A. Mayorov, M. C. Alfonso, T. A. Werke, and C. M. Folden III

While discovery of element 118 is still to be confirmed, pursuits to synthesize an even heavier element are underway [1]. Due to unavailability of targets heavier than Cf, the use of  $^{48}\text{Ca}$  beam for production of new elements, though it has been successful in the past, appears exhausted [2]. A move to heavier beams is a new direction in element discovery and the likely first element to be produced in this way is  $Z = 120$ , for which  $^{54}\text{Cr} + ^{248}\text{Cm}$  is a proposed reaction [3].

Challenges of synthesizing  $Z = 120$  were investigated by analyzing what factors most influence the cross section of the evaporation residue EVR in switching from  $^{48}\text{Ca}$  to  $^{54}\text{Cr}$  projectile in reactions with  $^{162}\text{Dy}$  and the preliminary results are discussed in this report. Reactions of  $^{162}\text{Dy} (^{48}\text{Ca}, 4n) ^{206}\text{Rn}$  and  $^{162}\text{Dy} (^{54}\text{Cr}, 4n) ^{212}\text{Th}$  were chosen as “model” systems for this study due to similar energetics to  $^{48}\text{Ca}$ ,  $^{54}\text{Cr} + ^{248}\text{Cm}$  reactions as shown in Table I. In the experiment, beams of  $^{48}\text{Ca}^{6+}$  (214 MeV) and  $^{54}\text{Cr}^{7+}$  (273 MeV) were accelerated by the K500 cyclotron and interacted with a  $^{162}\text{Dy}$  target having a thickness

**Table I.** Summary of energetics of  $^{48}\text{Ca}$  and  $^{54}\text{Cr}$  reactions on  $^{162}\text{Dy}$  and  $^{248}\text{Cm}$ . Column 4 shows the difference  $E_{\text{cm}} - B$ , where  $E_{\text{cm}}$  is the center of mass projectile energy and  $B$  is the average interaction (representing sum of Coulomb, centripetal, nuclear potentials) barrier height [8].  $E^*_{\text{CN}}$  is the excitation energy of the CN system. Column 6 gives the remaining excitation energy of a nucleus following emission of 4 neutrons each with binding energy  $S_n$ . Values calculated based on estimated projectile energy needed to remove 4 neutrons, leaving the residual nucleus with excitation energy below either the  $S_n$  or  $B_f$ , whichever is lower in energy.

Reaction	Product	N of CN	Energy Above Barrier	$E^*_{\text{CN}}$	$E^*_{\text{CN}} - \Sigma(S_{n,i})$
$^{162}\text{Dy}(^{48}\text{Ca}, 4n)$	$^{206}\text{Rn}$	124	5.46 MeV	48 MeV	15.63 MeV
$^{162}\text{Dy}(^{54}\text{Cr}, 4n)$	$^{212}\text{Th}$	126	10.17 MeV	50 MeV	15.76 MeV
$^{248}\text{Cm}(^{48}\text{Ca}, 4n)$	$^{292}116$	180	9.58 MeV	41 MeV	15.48 MeV
$^{248}\text{Cm}(^{54}\text{Cr}, 4n)$	$^{298}120$	182	12.33 MeV	43 MeV	15.86 MeV

of  $403\text{-}\mu\text{g}/\text{cm}^2$  (deposited onto a  $^{12}\text{C}$  backing). Beam energies were varied using a degrader ladder containing Al foils from  $1.2\ \mu\text{m}$  to  $8.54\ \mu\text{m}$ , plus a blank. Reaction products of interest were separated from unwanted by-products in the Momentum Achromat Recoil Separator [4] based on magnetic rigidity dispersion in the first dipole (D1) and particle velocity in the Wien filter. An excitation function for production of  $^{206}\text{Rn}$  was measured and 84 % upper limit [5] cross sections for the production of  $^{212}\text{Th}$  were calculated following three 10-hour irradiations at center-of-target energies of 244.7, 249.1, and 254.1 MeV (see Fig 1. and Table II). Due to  $^{205}\text{Rn}$  having a nearly identical  $E_{\alpha}$  as  $^{206}\text{Rn}$ , the Rn excitation function is currently treated as the sum of the two isotopes. The contribution of  $^{205}\text{Rn}$  to the peak of the  $^{206}\text{Rn}$  is assumed to be negligible as the 5n peak cross section is estimated to be at 210 MeV. The difference in peak cross section for the 4n product in each reaction is approximately a factor of 6000

( $12.2 \pm 4.0$  mb for  $^{206}\text{Rn}$  and  $\leq 2$   $\mu\text{b}$  for  $^{212}\text{Th}$ ). Using current theoretical models for fusion reactions, reasons leading to the factor of  $\geq 6000$  were assessed.

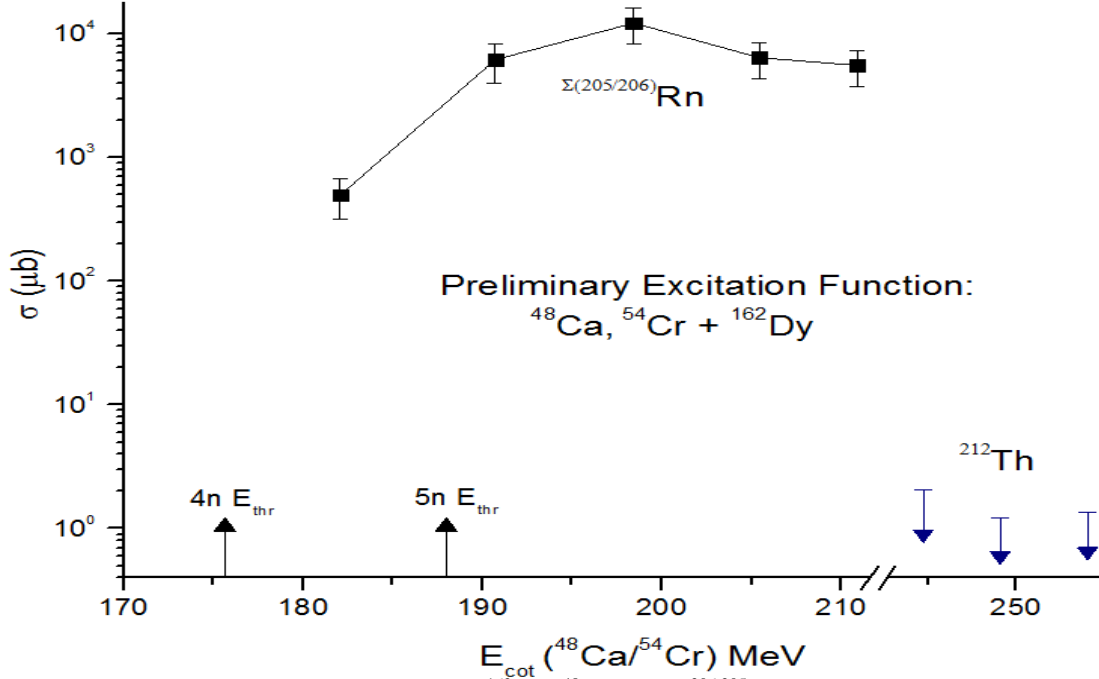


**FIG. 1.** Preliminary excitation function for  $^{162}\text{Dy}$  ( $^{48}\text{Ca}$ , 4-5n)  $^{206,205}\text{Rn}$  and 84% upper limit cross sections for  $^{162}\text{Dy}$  ( $^{54}\text{Cr}$ , 4n)  $^{212}\text{Th}$ .  $E_{\text{cot}}$  is the center-of-target energy. The  $E_{\text{thr}}$  are the threshold energies for the production of  $^{206,205}\text{Rn}$ .

**Table II.** Summary of estimated and measured 4n peak cross sections and estimated  $P_{\text{CN}}$  values in the case of  $^{48}\text{Ca}$  and  $^{54}\text{Cr}$  reactions on  $^{162}\text{Dy}$  and  $^{248}\text{Cm}$ . Values of column 6 were used for Dy reactions, due to their improved predictions for lighter systems (see main text). Values of Column 7 were used for Cm reactions as prescribed by [3, 11]. The measured cross section for  $^{212}\text{Th}$  is an 84% upper limit calculated according to the method described in [4].

Reaction	Product	Z	$\sigma_{\text{EVR}}$ meas.	$\sigma_{\text{EVR}}$ est.	$P_{\text{CN}}$ [13]	$P_{\text{CN}}$ [7]
$^{162}\text{Dy}(^{48}\text{Ca}, 4n)$	$^{206}\text{Rn}$	145.3	12.2 mb	78.5 mb <sup>a</sup>	0.4208	0.1444
$^{162}\text{Dy}(^{54}\text{Cr}, 4n)$	$^{212}\text{Th}$	171.6	$\leq 2$ $\mu\text{b}$ <sup>b</sup>	15.4 $\mu\text{b}$ <sup>a</sup>	0.0037	0.0449
$^{248}\text{Cm}(^{48}\text{Ca}, 4n)$	$^{292}116$	193.6	3.3 pb [16]	1.26 pb <sup>a</sup>	$8.18 \times 10^{-8}$	0.0065
$^{248}\text{Cm}(^{54}\text{Cr}, 4n)$	$^{298}120$	229.0	—	0.01 pb [3]	$1.94 \times 10^{-9}$	0.0011

<sup>a</sup>Estimates were made according to [4-6, 8-9, 11], with accuracy of one to two orders of magnitude.

<sup>b</sup>84% of the distribution lies below the value reported.

Fusion – evaporation cross sections are theoretically modeled by a product of three factors: 1. the cross section corresponding to projectile and target overcoming an interaction barrier and touching ( $\sigma_{\text{cap}}$ ), 2. the probability that the touching di-nuclear system will fuse into a compound nucleus ( $P_{\text{CN}}$ ), and 3. the survival probability of an excited CN against fission ( $P_{\text{sur}}$ ). The value of  $\sigma_{\text{cap}}$  was calculated according to the “diffused barrier formula” as derived in [6]. In cases of very heavy nuclei, the critical angular

momentum formula is used for  $\sigma_{\text{cap}}$ , where  $l_{\text{critical}}$  defines the “cut-off” value of angular momentum above which the CN has no fission barrier [7-8]. To estimate CN survival against fission following multiple de-excitation steps resulting in the emission of neutrons, numerical integration over saddle-point decay channels as discussed in [9] was used. The kinetic energy of the neutrons was assumed to be  $2T$ , where  $T$  is taken as  $(E^*/a)^{1/2}$  and  $a$  is calculated according to the parameterization provided in [10], where saddle-point deformation is considered. Estimates of  $P_{\text{CN}}$  are more challenging, as discussed below. In Table II, the estimated peak cross sections for all reactions of interest in this study are presented.

The greatest uncertainty in theoretical estimates of EVR cross sections lies in making an accurate estimate of  $P_{\text{CN}}$ . Resolving discrepancies in predicated values of  $P_{\text{CN}}$  using different methods is a current field of research [11].  $P_{\text{CN}}$  is known to decrease exponentially with an increase in  $z$ , the Coulomb parameter given by  $Z_1Z_2 / (A_1^{1/3} + A_2^{1/3})$ , severely hindering fusion of symmetric systems [12]. A simple phenomenological expression as a function of  $z$  for  $P_{\text{CN}}$  was reported in [7] with a downside of having discrepancies of one order of magnitude in some cases. This expression is,

$$P_{\text{CN}} = \exp[-\ln(10)\left(\frac{z}{\alpha}\right)^3] \quad \text{Eq. (1)}$$

where  $z$  is the Coulomb parameter and  $\alpha$  is determined by the magnitude of  $E_{\text{cm}} - B$ , where  $E_{\text{cm}}$  is the center-of-mass projectile energy and  $B$  is the interaction barrier (see [7] for details). Another approach for estimating  $P_{\text{CN}}$  cited in [13] considers the fissility of the CN and relates it to a threshold fissility parameter found from fits to a set of hot fusion (generally  $\geq 3n$  products) data. This expression is,

$$P_{\text{CN}} = -0.5 \exp[-c(x_{\text{eff}} - x_{\text{thr}})] \quad \text{Eq. (2)}$$

where  $x_{\text{eff}}$  is the effective fissility descriptive of the degree of deformation required for a nucleus to fission. The parameters  $c$  and  $x_{\text{thr}}$  are extracted from fits to experimental data (see [13] for details).  $P_{\text{CN}}$  values from both calculations are given in Table II. The phenomenological expression is prescribed by [3] for heavier systems such as the Cm reactions, as evidenced by its agreeable predictions for formation cross sections of elements 114 – 118 [14]. For the  $^{162}\text{Dy}$  reactions, the estimates based on CN fissility were used due to its superior predictions in the case of cross sections in [15], where data for  $^{48}\text{Ca} + ^{172,173,176}\text{Yb}$  is reported.

The difference in  $P_{\text{CN}}$  between  $^{162}\text{Dy}$  ( $^{48}\text{Ca}$ , 4n)  $^{206}\text{Rn}$  and  $^{162}\text{Dy}$  ( $^{54}\text{Cr}$ , 4n)  $^{212}\text{Th}$  is predicted according to Eq. (2) to be a factor of 114. Taking the measured production cross sections from the present work for the same reactions and dividing them by the estimated product  $\sigma_{\text{cap}}P_{\text{sur}}$ , estimates of the experimental difference in  $P_{\text{CN}}$  yields a factor of  $\geq 19$ . This treatment is employed realizing that assumptions are made about the level of accuracy in prediction of  $P_{\text{sur}}$ , however this assumption was validated by successfully predicting the survival probabilities of nuclei formed in hot fusion, for which the  $P_{\text{CN}}$  was assumed to be 1 due to the extreme asymmetry in the projectile-target pair [10].

The smaller  $P_{\text{CN}}$  in the less asymmetric  $^{54}\text{Cr}$  reactions, as compared to  $^{48}\text{Ca}$  reactions with the same target, reduces the overall EVR cross sections. This similar effect is observed in calculations using Eq. (1) for  $^{248}\text{Cm}$  ( $^{48}\text{Ca}$ , 4n)  $^{292}\text{116}$  and  $^{248}\text{Cm}$  ( $^{54}\text{Cr}$ , 4n)  $^{302}\text{120}$  where a difference of a factor of 6 in  $P_{\text{CN}}$  is

predicted. However, the survival probability for  $^{302}120$  may be enhanced potentially due its proximity to the  $N = 184$  magic neutron shell. Drawing from the results discussed here, one can expect the  $P_{CN}$  for  $^{54}\text{Cr} + ^{248}\text{Cm}$  to be one to two orders of magnitude lower than for the  $^{48}\text{Ca} + ^{248}\text{Cm}$  reaction [16]. Hence the cross section of 0.01 pb, as predicted in [3], for the synthesis of  $^{298}120$  is quite reasonable. At such a low cross section, the synthesis of element 120 in the  $^{248}\text{Cm} (^{54}\text{Cr}, 4n) ^{302}120$  reaction may not be feasible as it approaches the limits of current production techniques.

- [1] Y.T. Oganessian *et al.*, Phys. Rev. C **79**, 024603 (2009).
- [2] Y.T. Oganessian, J. Phys. G **34**, R165 (2007).
- [3] K. Siwek-Wilczynska, T. Cap, and J. Wilczynski, Int. J. Mod. Phys. E-Nucl. Phys. **19**, 500 (2010).
- [4] R.E. Tribble, R.H. Burch, and C.A. Gagliardi, Nucl. Instrum. Methods Phys. Res. **A285**, 441 (1989).
- [5] K.H. Schmidt, C.C. Sahm, K. Pielenz, and H.G. Clerc, Z. Phys. A **316**, 19 (1984).
- [6] W.J. Swiatecki, K. Siwek-Wilczynska, and J. Wilczynski, Phys. Rev. C **71**, 014602 (2005).
- [7] K. Siwek-Wilczynska, A. Borowiec, I. Skwira-Chalot, and J. Wilczynski, Int. J. Mod. Phys. E **17**, 12 (2008).
- [8] A.J. Sierk, Phys. Rev. C **33**, 2039 (1986).
- [9] W.J. Swiatecki, K. Siwek-Wilczynska, and J. Wilczynski, Phys. Rev. C **78**, 054604 (2008).
- [10] K. Siwek-Wilczynska, I. Skwira, and J. Wilczynski, Phys. Rev. C **72**, 034605 (2005).
- [11] R.S. Naik *et al.*, Phys. Rev. C **76**, 054604 (2007).
- [12] Z.H. Liu and J.D. Bao, Phys. Rev. C **80**, 054608 (2009).
- [13] W. Loveland, Phys. Rev. C **76**, 014612 (2007).
- [14] K. Siwek-Wilczynska, A. Borowiec, and J. Wilczynski, Int. J. Mod. Phys. E-Nucl. Phys. **18**, 1079 (2009).
- [15] C.C. Sahm, H.G. Clerc, K. H. Schmidt, W. Reisdorf, P. Armbruster, F.P. Hessberger, J.G. Keller, G. Münzenberg, and D. Vermeulen, Nucl. Phys. **A441**, 316 (1985).
- [16] Y.T. Oganessian *et al.*, Phys. Rev. C **70**, 064609 (2004).

## Investigation of the de-excitation mechanism in Fermi energy heavy ion collisions

R. Tripathi, A. Bonasera, S. Wuenschel, L. W. May, Z. Kohley, P. Marini, A. McIntosh, G. A. Souliotis, S. Galanopoulos, K. Hagel, D. V. Shetty, K. Huseman, S. N. Soisson, B. C. Stein, and S. J. Yennello

Heavy ion collisions (peripheral and mid-peripheral) in the Fermi energy domain lead to the formation of an excited projectile like source or quasiprojectile. Decay of the excited nuclear system is primarily governed by its excitation energy. A systematic investigation of this aspect requires information about the excitation energy of the decaying system. Reconstruction of a well defined quasiprojectile source provides the opportunity to carry out such a study.

In the present work, fragment yield data from the decay of quasiprojectiles in the reaction  $^{78}\text{Kr} + ^{58}\text{Ni}$  at  $E_{lab}=35$  MeV/nucleon have been analyzed to investigate the dependence of the decay mechanism on excitation energy, which, in turn, provides information about the onset of multi-fragmentation. The study involved the analysis of the data of ‘biggest fragment in the event’, fragment multiplicity and determination of nuclear caloric curves. Nuclear caloric curves were determined using the momentum fluctuation method [1] and the double isotope ratio method [2].

The quasiprojectile source was reconstructed with the condition that sum of the Z of all detected fragments was in the range of 30-34. A quadrupole cut was applied to reject the events dominated by non-equilibrium emission. The excitation energy of the quasiprojectile was determined by a calorimetric method [3]. The

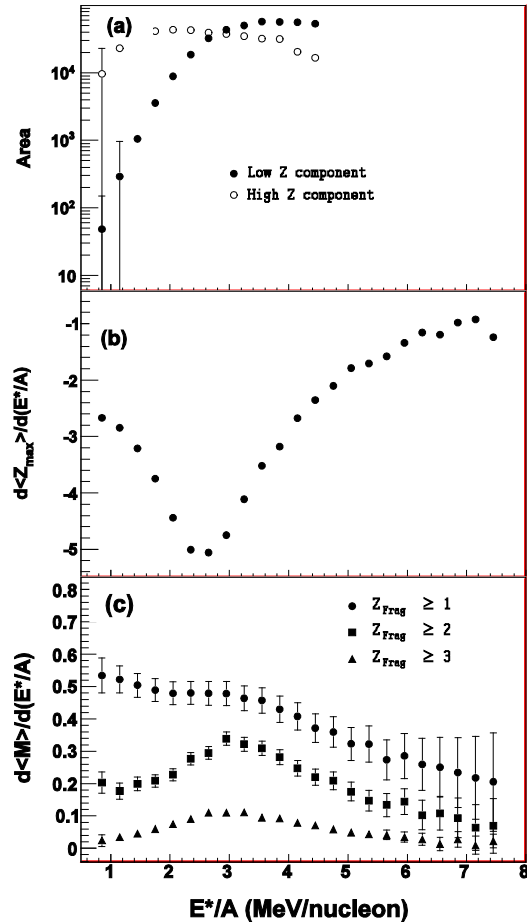


**FIG. 1.** (a) Plot of the contribution from high Z (evaporation) and low Z (fission / multi-fragmentation) components obtained by Gaussian fit to the  $Z_{max}$  distribution. (b) Derivative of  $\langle Z_{max} \rangle$  vs  $E^*/A$  plot (a) Derivative of average multiplicity  $\langle M \rangle$  vs  $E^*/A$  plot.

average excitation energy of the quasiprojectile was about 5 MeV/nucleon. For the present study, the total excitation energy range was divided into bins of 0.3 MeV. An examination of the charge of the biggest fragment in the event  $Z_{max}$  showed that it can be used to distinguish between the evaporation and multi-fragmentation events. It was observed that, in the low excitation energy region, there was also a contribution from fission type of events in addition to evaporation. The  $Z_{max}$  distribution showed two components, namely, evaporation (high  $Z$  component) and fission/multi-fragmentation (low  $Z$  component). Contributions from the two components, obtained from Gaussian fit, are shown as a function of excitation energy in Fig. 1(a). A crossover region around  $E^*/A= 3$  MeV/nucleon can be seen in this figure, beyond which multi-fragmentation events take over. It was not possible to distinguish between the two components above excitation energy of about 4.5 MeV/nucleon. In the same energy range, a minimum in derivative of  $\langle Z_{max} \rangle$  plot (1(b)) can be seen, indicating the onset of multi-fragmentation. This is further confirmed by the maxima in the derivative of multiplicity plot of fragments with  $Z \geq 3$  (1(c)).

In the theoretical calculations by Gross [4], the onset of multi-fragmentation was proposed to be the region of a first order phase transition. The calculations showed a plateau for the source  $A$  around 130, though no plateau was observed for  $A \sim 90$ . Calculations by Bondorf et al. [5] showed a plateau in the caloric curve for  $A \sim 100$  with change in de-excitation mechanism from evaporation to multi-fragmentation. In order to investigate this aspect, caloric curves were determined by the momentum fluctuation method [1] and the double isotope ratio method [2]. Caloric curves determined by the momentum fluctuation method [1] for  $^1\text{H}$ ,  $^2\text{H}$ ,  $^3\text{H}$ ,  $^3\text{He}$ ,  $^4\text{He}$ ,  $^6\text{Li}$ ,  $^7\text{Li}$ ,  $^7\text{Be}$  and  $^9\text{Be}$  are shown in Fig. 2. A plateau in the caloric curve around the onset of multi-fragmentation can be seen for various isotopes except for proton. The temperature values are on the higher side on absolute scale, which may be due to a number of reasons, namely, Coulomb effect, Fermi momentum and classical treatment of momentum

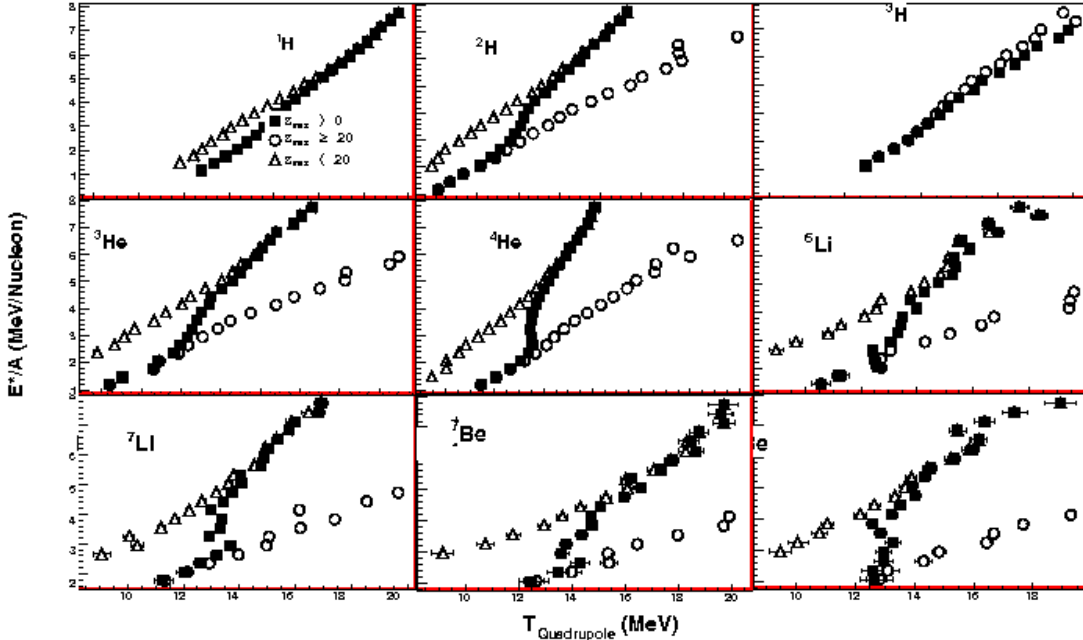


FIG. 2. Plot of nuclear caloric curve obtained by momentum fluctuation method [1].

distribution [6]. The different branches for evaporation and multi-fragmentation can be distinguished by selecting the data with  $Z_{max} \geq 20$  and  $Z_{max} < 20$ . A similar behavior can be seen in the caloric curves obtained from the double isotope ratio method (HeDT and HeLi thermometers), though less pronounced.

Thus, the present study shows various signatures of onset of multi-fragmentation. Observation of the plateau in the caloric curve is consistent with the onset of multi-fragmentation.

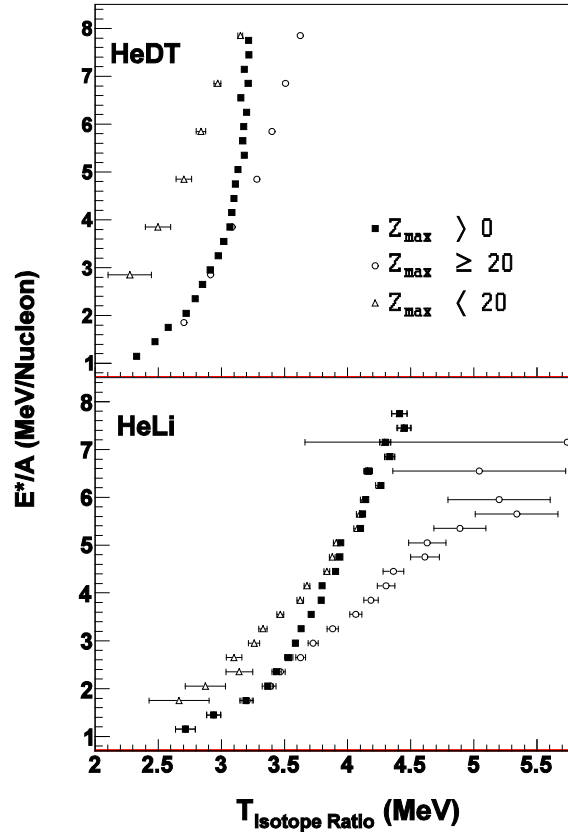


FIG. 3. Plot of nuclear caloric curve obtained by double isotope ratio method [2].

- [1] Wuenschel *et al.*, Nucl. Phys. **A843**, 1 (2010).
- [2] S. Albergo, S. Costa, E. Costanzo, and A. Rubbino, Nuovo Cimento **89**, 1 (1985).
- [3] Wuenschel *et al.*, Phys. Rev. C **79**, 061602 (R) (2009); S. Wuenschel, Ph. D. Thesis, Texas A&M University, 2009.
- [4] D.H.E. Gross and Zhang Xiao-Ze, Nucl. Phys. **A495**, 231c (1985).
- [5] Bondorf *et al.*, Nucl. Phys. **A444**, 460 (1985).
- [6] H. Zheng and A. Bonasera, Phys. Lett. B **696**, 178 (2010).

## Investigation of the role of quasiprojectile isospin in nuclear fragmentation

R. Tripathi, A. Bonasera, S. Wuenschel, L. W. May, Z. Kohley, P. Marini, A. McIntosh, G. A. Souliotis,  
S. Galanopoulos, K. Hagel, D. V. Shetty, K. Huseman, S. N. Soisson,  
B. C. Stein, and S. J. Yennello

In recent studies [1-3], fragment yield data from heavy ion collisions in Fermi energy domain have been analyzed using the Landau free energy approach, which is applicable to the systems in the vicinity of a critical point [4,5]. This approach was extended to interpret the mirror nuclei yield ratios in the fragmentation of quasiprojectile [6]. In the Landau free energy approach, the isospin asymmetry of a fragmenting source, arising from the difference between the neutron and proton chemical potentials, acts as an external field which can modify the fragment yields. A similar dependence of fragment yields on the isospin asymmetry of the quasiprojectile can also be realized in grand-canonical calculations [7]. In the present study, fragment yield data from  $^{78,86}\text{Kr} + ^{58,64}\text{Ni}$  reactions at  $E_{lab}=35$  MeV/nucleon were analyzed within the framework of Landau free energy approach to investigate the role of quasiprojectile isospin.

Experiments were performed using a  $^{78,86}\text{Kr}$  beam from K500 superconducting cyclotron at the Cyclotron Institute, Texas A&M University. Fragments were measured using the  $4\pi$  charged particle array NIMROD, which was surrounded by the TAMU neutron ball to detect free neutrons. Details about the experiment and the procedure to determine the fragment yields can be found in Ref [8,9]. In the present analysis, yields of fragments arising from the fragmentation of quasiprojectiles having  $Z$  in the range of 30-34 have been used. Limits were placed on the deformation of the quasiprojectile through a quadrupole cut to minimize the contribution from events dominated by non-equilibrium emission [8,9]. The isospin asymmetry ( $m_s$ ) of the quasiprojectile was calculated on an event-by-event basis from the  $A$  and  $Z$  of the detected fragments. The  $m_s$  values were corrected for free neutrons using the neutron data from TAMU neutron ball [9,10]. Since the analysis required  $A$  as well as  $Z$  of the detected fragments, only the events with full isotopic identification were included in the analysis. Fragment yield data in the  $m_s$  range of -0.03 to 0.21 were divided into four  $m_s$  bins, each of width 0.06. The mean  $m_s$  values corresponding to these  $m_s$  bins were 0.01, 0.06, 0.11 and 0.17.

According to the modified Fisher model [11-13] the fragment yield is given by

$$Y = y_0 A^{-\tau} e^{-\frac{F}{T}A} \quad (1)$$

where  $F/T$  is free energy per nucleon normalized with respect to the temperature  $T$ .  $A$  is mass number,  $\tau$  is a critical exponent and  $y_0$  is a constant. In ref [1,11], it was shown that  $F/T$  is dominated by the symmetry free energy in the vicinity of a critical point, which can be expressed by the following expression, within the framework of Landau free energy approach

$$\frac{F(m)}{T} = \frac{1}{2}am^2 + \frac{1}{4}bm^4 + \frac{1}{6}cm^6 - \frac{H}{T}m + O(m^8) \quad (2)$$

where  $m$  is an order parameter and  $H$  is an external field. In the studies of ref. [1-3],  $m$  was identified as the isospin asymmetry of a fragment and the external field  $H$  was related to the isospin asymmetry of the source ( $m_s$ ).  $a$ ,  $b$  and  $c$  are fit parameters [1,4].  $F/T$  values of  $N=Z$  nuclei, particularly of lighter isotopes calculated using eq. 1 after normalizing with respect to the yield of  $^{12}\text{C}$  as was done in ref. [1,6], showed significant deviation from the plot of  $F/T$  values of  $N\neq Z$  nuclei. Based on liquid drop mass formula, a coefficient to correct for the odd-even effect was obtained from the analysis of  $N=Z$  nuclei. This analysis also gave the value of constant  $y_0$  which was used in Eq. 1 for the calculation of  $F/T$  without normalizing with respect to the yield of  $^{12}\text{C}$ . The plots of  $F/T$  values for different  $m_s$  bins are shown in Fig. 1. Solid lines are fit to the free energy data using Landau equation as given by Eq. 2 with  $a$ ,  $b$ ,  $c$  and  $H/T$  as free

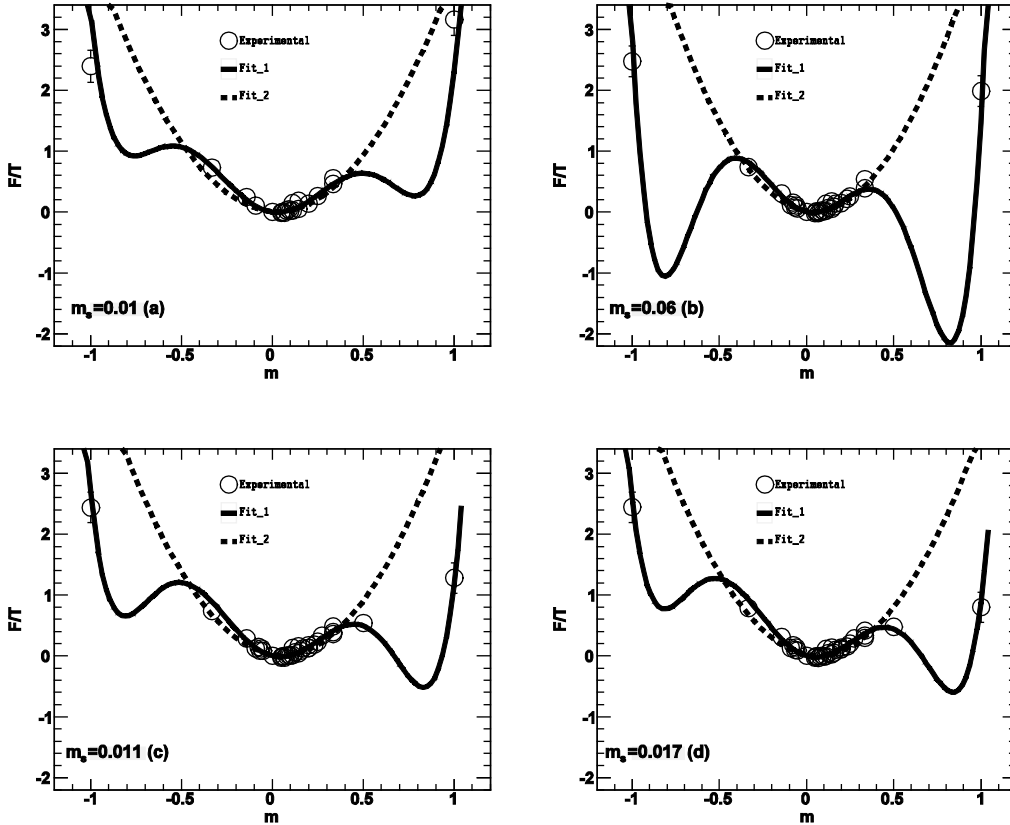


**FIG. 1.** Plot of  $F/T$  calculated from fragment yields for  $m_s=0.01$  (a),  $0.06$  (b),  $0.11$  (c) and  $0.17$  (d).

parameters. Dashed lines are fit using only first and last term of Eq. 2. It can be seen from the figure that the Landau equation provides a better fit to the free energy data. The three minima in the free energy plot indicate the system to be in the regime of a first order phase transition, however, it is difficult to draw any definitive conclusion on this aspect due to the absence of data points at large  $m$  values. The fit parameters  $a$ ,  $b$ ,  $c$  and  $H/T$  are plotted as a function of  $m_s$  in Fig. 2. The parameters  $a$ ,  $b$  and  $c$  do not show any significant dependence on  $m_s$ . The parameter  $H/T$  which is related to the isospin asymmetry of the source shows a systematic increase with increasing  $m_s$ . This demonstrates the role of quasiprojectile isospin in governing the fragment yields in nuclear fragmentation. In earlier studies [2,6], it has been

shown that the position of the central minimum of the fit ( $\varepsilon_0$ ) is equal to  $(H/T)/a$ . The  $\varepsilon_0$  values, calculated using the parameter  $H/T$  and  $a$ , were observed to be in reasonable agreement with the average isospin asymmetry of fragments  $\langle m_f \rangle$ .

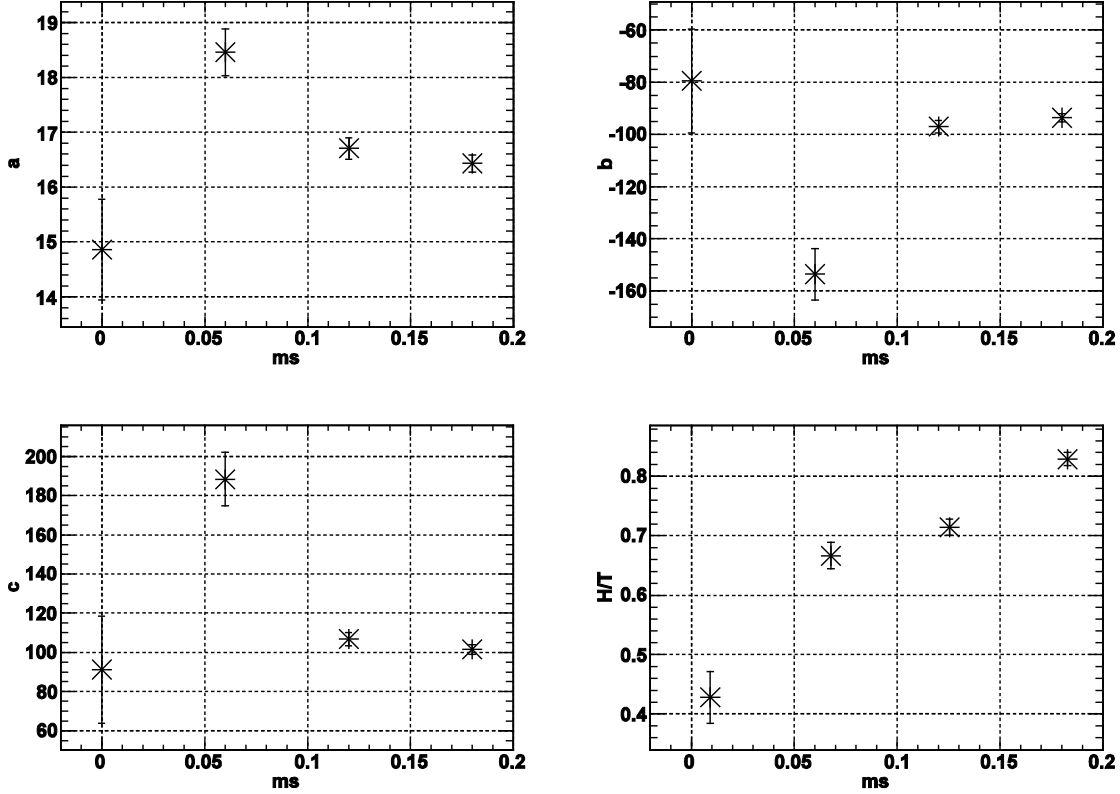


FIG. 2. Plot of fit parameters  $a$ ,  $b$ ,  $c$  and  $H/T$  as a function of quasi-projectile isospin  $m_s$ .

In summary, Landau free energy approach was successfully used to explain fragment yield data, indicating the system to be in the vicinity of a critical point. The analysis demonstrated the role of quasiprojectile isospin in governing the fragment yields.

- [1] A. Bonasera *et al.*, Phys. Rev. Lett. **101**, 122702 (2008).
- [2] M. Huang *et al.*, Phys. Rev. C **81**, 044618 (2010).
- [3] M. Huang *et al.*, Nucl. Phys. **A847**, 233 (2010).
- [4] K. Huang, *Statistical Mechanics*, 2<sup>nd</sup> Edition (Wiley and Sons, New York, 1987).
- [5] L.D. Landau and E.M. Lifshitz, *Statistical Physics*, 3<sup>rd</sup> Edition (Pergamon, New York, 1989).
- [6] R. Tripathi *et al.*, Phys. Rev C (In Press); arXiv :1010.2227v 1.
- [7] T.X. Liu *et al.*, Phys. Rev. C **76**, 034603 (2007).
- [8] S. Wuenschel *et al.*, Phys. Rev. C **79**, 061602 (2009).
- [9] S. Wuenschel, Ph. D. Thesis, Texas A& M University, 2009.
- [10] S. Wuenschel *et al.*, Nucl. Instrum. Methods Phys. Res. **A604**, 578 (2009).

- [11] A. Bonasera, M. Bruno, C.O. Dorso, and P.F. Mastinu, Riv. Nuovo Cimento **23**, 1 (2000).
- [12] R.W. Minich *et al.*, Phys. Lett. B **118**, 458 (1982).
- [13] M.E. Fisher, Rep. Prog. Phys. **30**, 615 (1967).

## Isoscaling studies in $^{86}\text{Kr}+^{112,124}\text{Sn}$ , $^{197}\text{Au}$ reactions at $E_{lab}=30$ MeV/nucleon

R. Tripathi, B. C. Stein, Z. Kohley, L. W. May, P. Marini, A. Bonasera, G. A. Souliotis, S. Wuenschel, S. Galanopoulos, D. V. Shetty, K. Huseman, S. N. Soisson, and S. J. Yennello

Isoscaling of fragment yields from similar sources of nearly same temperature, but different isospin asymmetry ( $m_s$ ), provides information about the nuclear symmetry energy [1-3]. Information about the nuclear symmetry energy would help in constraining the asymmetric part of the nuclear equation of state (EOS), which has important implications in nuclear physics and astrophysics [4-5].

In the present work, isoscaling studies have been carried out using fragment yield data from the fragmentation of projectile like source (quasiprojectile) in the reactions  $^{86}\text{Kr}+^{112,124}\text{Sn}$ ,  $^{197}\text{Au}$ . The values of isospin asymmetry ( $m=(N-Z)/A$ ) for the projectile, target and composite system for different reactions are given in the Table I.

**Table I.** Isospin asymmetry ( $m$ ) for different reactions.

Reaction	$m=(N-Z)/A$		
	Projectile	Target	Composite system
$^{86}\text{Kr}+^{112}\text{Sn}$	0.163	0.107	0.131
$^{86}\text{Kr}+^{124}\text{Sn}$		0.194	0.181
$^{86}\text{Kr}+^{197}\text{Au}$		0.198	0.187

It can be seen from the table that  $m$  values for the composite system of  $^{86}\text{Kr}+^{124}\text{Sn}$  and  $^{86}\text{Kr}+^{197}\text{Au}$  reactions are close. Thus, any difference in the isospin asymmetry of the quasiprojectile in the two reactions would indicate a Coulomb effect in  $N/Z$  equilibration.

Experiments were carried out at the K500 superconducting cyclotron at the Cyclotron Institute, Texas A&M University. Fragments were detected using the FAUST detector array, which consists of 68 Si-CsI telescopes and covers  $1.6^\circ$  to  $45^\circ$  in the forward hemisphere. Free neutrons were not detected in these measurements. The detector thresholds and angular acceptance provide a preference for the fragments from the projectile like source or quasiprojectile by rejecting majority of slow moving target-like products. The  $E-\Delta E$  spectra from FAUST array were linearized using a point to curve method and calibrated using the existing calibration data of FAUST.

The average isospin asymmetry value of fragments ( $\langle m_f \rangle$ ), calculated from the  $m$  values of the detected fragments, was 0.035, 0.047, 0.047 for  $^{86}\text{Kr}+^{112}\text{Sn}$ ,  $^{86}\text{Kr}+^{124}\text{Sn}$  and  $^{86}\text{Kr}+^{197}\text{Au}$  reactions, respectively. Similar  $\langle m_f \rangle$  values for the last two reactions suggest that the process of  $N/Z$  equilibration is mainly governed by the isospin difference between the projectile and the target nuclei and Coulomb

effect is not very significant. According to the isoscaling relation, the ratio of fragment yields for a given  $Z$  from two different reaction systems is given as [2,3]

$$R_{21} = \ln\left(\frac{Y_2}{Y_1}\right) \propto \alpha N \quad (1)$$

where  $N$  is neutron number and  $\alpha$  is an isoscaling parameter which is equal to  $-(4C_{sym}/T)\Delta$  [2].  $C_{sym}$  is the symmetry energy coefficient and  $T$  is the temperature of the system. In the present study,  $\Delta$  is taken as the difference in  $\langle m_p \rangle$  for the two reactions. In order to determine  $\alpha$  values,  $R_{21}$  values were calculated by taking the ratio of fragment yields in the reactions  $^{86}\text{Kr}+^{124}\text{Sn}$  and  $^{86}\text{Kr}+^{197}\text{Au}$  with respect to  $^{86}\text{Kr}+^{112}\text{Sn}$  reaction. Plots of  $R_{21}$  values calculated for  $^{86}\text{Kr}+^{124}\text{Sn}/^{86}\text{Kr}+^{112}\text{Sn}$  along with the fitted lines for  $Z=4-13$  are shown in Fig. 1. The behavior of fragments with  $Z \leq 3$  was not consistent, possibly, due to the contribution from pre-equilibrium and neck emission.

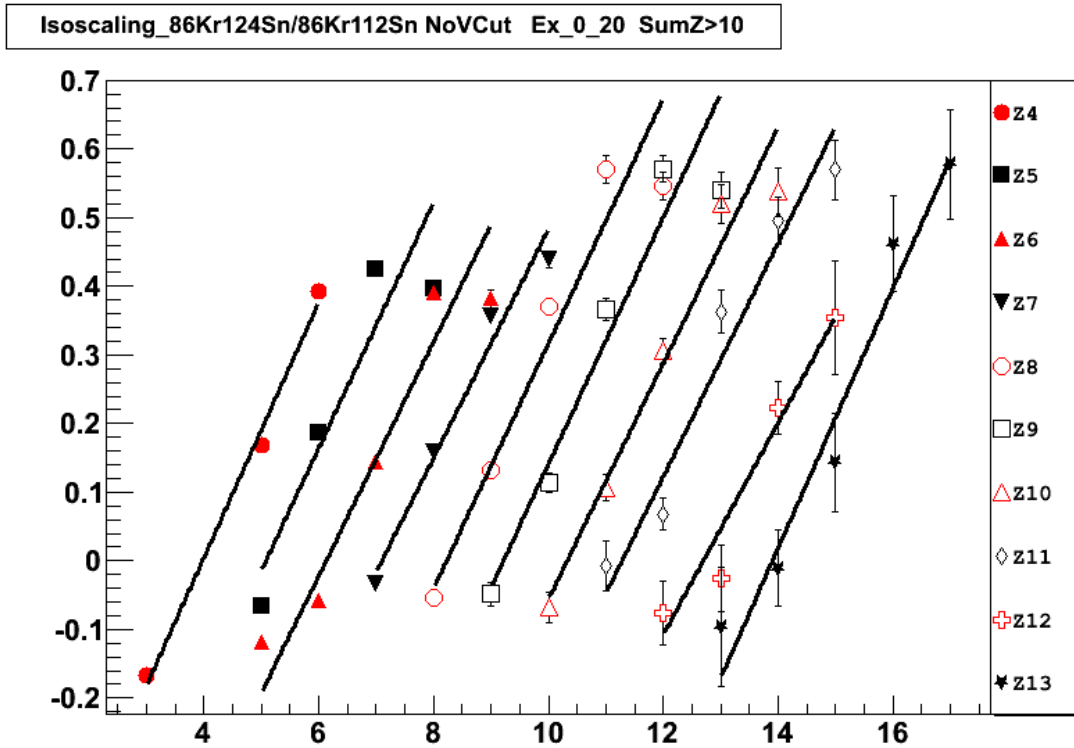


FIG. 1. Plot of  $R_{21}$  for  $^{86}\text{Kr}+^{124}\text{Sn}/^{86}\text{Kr}+^{112}\text{Sn}$ .

In Fig. 2,  $\alpha$  values, obtained as slopes of linear fits to  $R_{21}$  values for  $^{86}\text{Kr}+^{124}\text{Sn}/^{86}\text{Kr}+^{112}\text{Sn}$ ,  $^{86}\text{Kr}+^{197}\text{Au}/^{86}\text{Kr}+^{112}\text{Sn}$  and  $^{86}\text{Kr}+^{197}\text{Au}/^{86}\text{Kr}+^{124}\text{Sn}$  are shown. The error weighted average values of  $\alpha$  for these reaction pairs were  $0.177 \pm 0.008$ ,  $0.175 \pm 0.024$  and  $-0.002 \pm 0.024$  respectively. The close agreement between the  $\alpha$  values for the first two reaction pairs further suggests similar isospin asymmetry of the fragmenting sources in  $^{86}\text{Kr}+^{124}\text{Sn}$  and  $^{86}\text{Kr}+^{197}\text{Au}$  reactions, which is also the reason

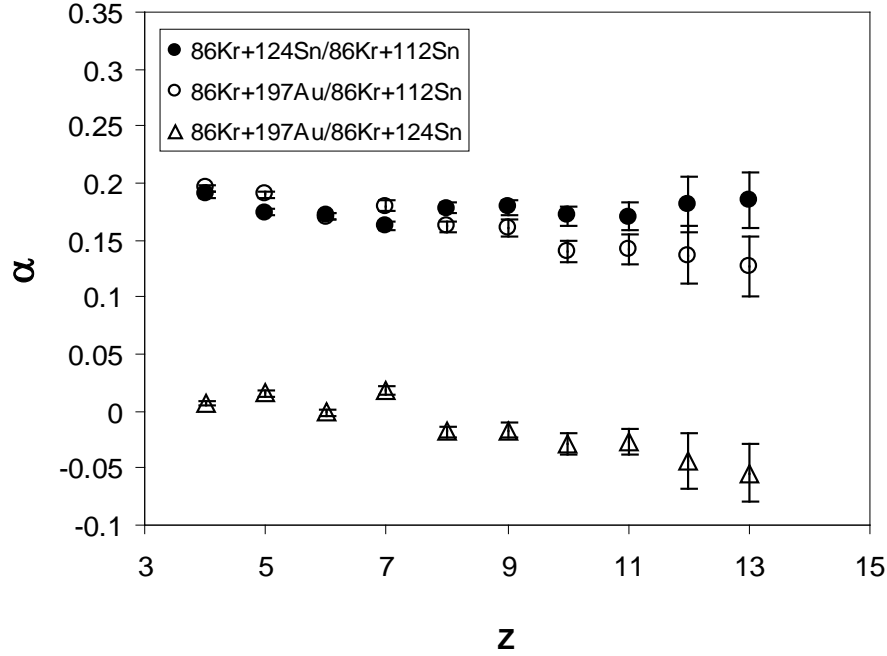


FIG. 2. Plot of  $\alpha$  values vs.  $Z$  for different pairs of reactions.

for negligibly small  $\alpha$  values for the third pair. For  $Z > 9$ , a systematic difference between the  $\alpha$  values for  $^{86}\text{Kr} + ^{124}\text{Sn} / ^{86}\text{Kr} + ^{112}\text{Sn}$  and  $^{86}\text{Kr} + ^{124}\text{Sn} / ^{86}\text{Kr} + ^{112}\text{Sn}$  pairs needs further investigation. In Fig. 3,  $C_{Sym}/T$  values calculated using average  $\alpha$  values are shown as a function of apparent excitation energy [1] of the fragmenting source. As seen in Fig. 3, decrease in  $C_{Sym}/T$  with increasing excitation energy has also been reported in recent isoscaling studies [1,6,7]. Further work is going on to determine the temperature of the system, in order to extract information about  $C_{Sym}$ .

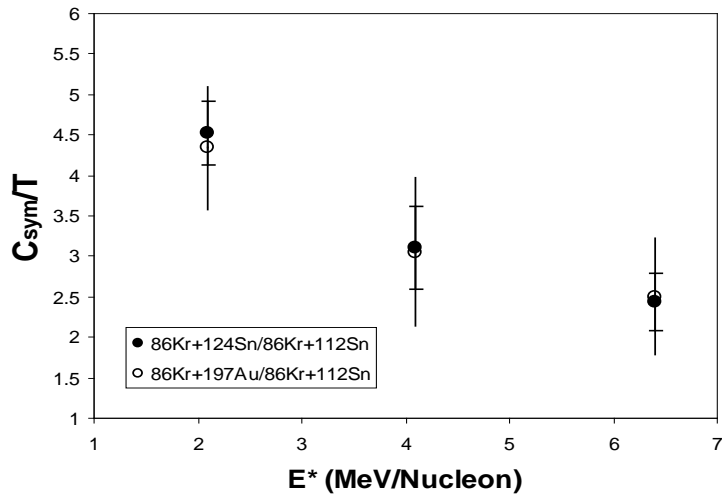


FIG. 3. Plot of  $C_{Sym}/T$  vs. excitation energy of the source.

In summary, isoscaling studies showed formation of projectile-like fragmenting sources with similar isospin asymmetry in  $^{86}\text{Kr}+^{124}\text{Sn}$  and  $^{86}\text{Kr}+^{197}\text{Au}$  reactions which have significantly different Coulomb repulsion in the entrance channel.  $C_{\text{sym}}/T$  values determined from the isoscaling parameter  $\alpha$  showed a systematic decrease with increasing excitation energy of the fragmenting source.

- [1] S. Wuenschel *et al.*, Phys. Rev. C **79**, 061602 (2009).
- [2] M.B. Tsang *et al.*, Phys. Rev. C **64**, 054615 (2001) .
- [3] A. Ono *et al.*, Phys. Rev. C **68**, 051601 (2003).
- [4] B.A. Brown, Phys. Rev. Lett. **85**, 5296 (2000) .
- [5] J.M. Lattimer *et al.*, Astrophys. J. **550**, 426 (2001).
- [6] G.A. Souliotis *et al.*, Phys. Rev. C **75**, 011601 (2007).
- [7] G.A. Souliotis *et al.*, Phys. Rev. C **73**, 024606 (2006).

## Source reconstruction and caloric curves in $^{70}\text{Zn} + ^{70}\text{Zn}$ at $E/A = 35\text{MeV}$

A. B. McIntosh, A. Bonasera, S. Galanopoulos, K. Hagel, L. Heilborn, Z. Kohley,  
P. Marini, L. W. May, A. Raphelt, D. V. Shetty, W. B. Smith, S. N. Soisson,  
G. A. Souliotis, B. C. Stein, R. Tripathi, S. Wuenschel, and S. J. Yennello

Preliminary caloric curves have been extracted for reconstructed quasi-projectile sources in collisions of  $^{70}\text{Zn} + ^{70}\text{Zn}$  at  $E/A = 35\text{MeV}$ .

Charged particles and free neutrons were measured in the NIMROD-ISiS  $4\pi$  detector array. Charged particles were isotopically identified up to  $Z=17$ . A series of constraints are placed on the events to select events with a well-measured, equilibrated quasi-projectile source. This is done using the method developed by S. Wuenschel et al. [1]. First, non-equilibrium particle production is suppressed by considering the parallel velocity of charged particles relative to the projectile-like fragment (the heaviest charged particle in the event). Only those within a specific tolerance of this velocity are included in the reconstruction. Second, the charge of the reconstructed quasi-projectile is required to be between 25 and 30 inclusive to ensure near-complete measurement of the quasi-projectile. Third and finally, since we seek an equilibrated source, which should be spherical on average, the quadrupole deformation is restricted to be  $-1 \leq \log Q \leq 1$  where  $Q = \Sigma p_z^2 / 2\Sigma p_t^2$ . The excitation energy of this reconstructed quasi-projectile source is calculated as the sum of three things: the measured charged particle transverse kinetic energy, an average neutron kinetic energy (time the number of free neutrons), and the negative of the  $Q$ -value of the breakup. This reconstruction (series of “source cuts”) was implemented in a transparent and modular fashion, allowing easy adaptation to other data-sets and inclusion in future analysis routines.

The temperature of the quasi-projectiles has been extracted from the momentum quadrupole fluctuations as described by Zheng and Bonasera both in the classical approximation, and considering the fermionic nature of the nuclei [2]. Preliminary caloric curves are shown in Figure 1 for selected charged particles. As expected, the classical and quantum temperatures are in agreement at low excitation energy. As the excitation energy increases, both the quantum and classical temperatures increase monotonically, with the quantum temperature rising less rapidly than the classical as expected.

In the near future, the caloric curves will be investigated to understand how they depend on reaction mechanism and isotopic composition. The reaction mechanism evolution has been shown to influence the caloric curve [3]. In this data, we can select on the reaction mechanism both through collision violence [4], and through the size of the projectile-like fragment. Moreover, the impact of the isotopic composition of the emitting source on the caloric curves will be investigated. It is possible that by selecting on the composition of isotopically-resolved reconstructed quasi-projectiles rather than the composition of the initial system, an isospin dependence of the caloric curves may be observed.

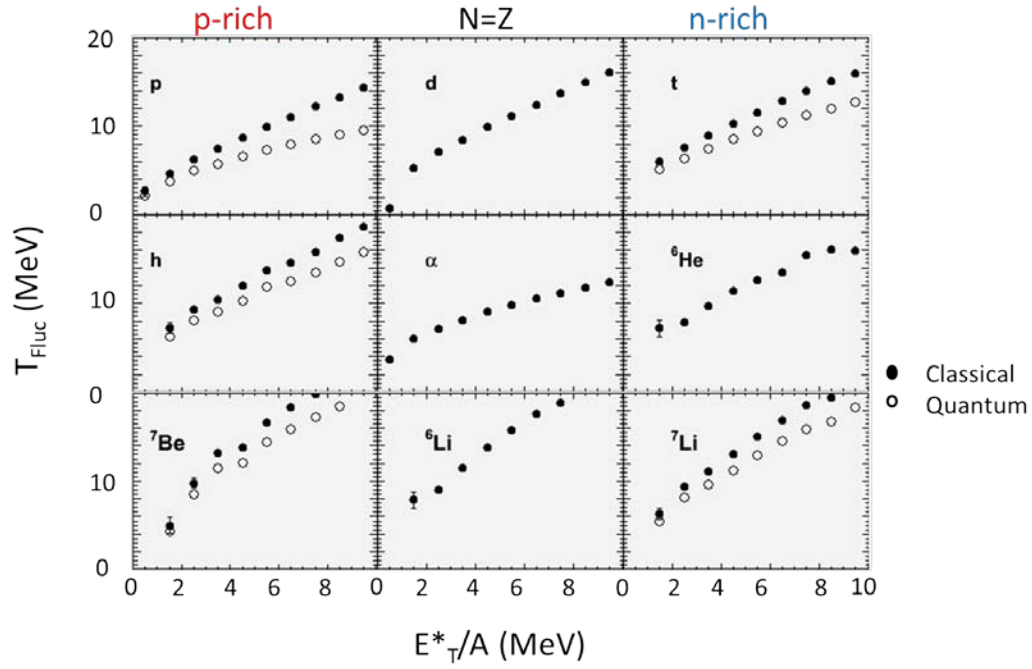


**FIG. 1.** Caloric curves for light charged particles and intermediate mass fragments produced in  $^{70}\text{Zn} + ^{70}\text{Zn}$  collisions at  $E/A = 35\text{MeV}$ .

- [1] S. Wuenschel *et al.*, Nucl.Phys. **A843**, 1 (2010).
- [2] H. Zheng and A. Bonasera, Phys. Lett. B **696**, 178 (2011).
- [3] R. Tripathi *et al.*, Phys. Rev. C **83**, 054609 (2011).
- [4] Z. Kohley, Ph.D. Thesis, Texas A&M University, 2010

## Isoscaling, isobaric yield ratio and the symmetry energy: interpretation of the results with SMM

P. Marini, A. Botvina, A. Bonasera, Z. Kohley, L. W. May, R. Tripathi,  
S. Wuenschel, and S. J. Yennello

Significant theoretical and experimental works [1-3] have been devoted to the study of the nuclear symmetry energy ( $E_{sym}$ ), which is essential for understanding not only the structure of radioactive nuclei [4], but also many important issues in astrophysics [5]. The value of the symmetry energy has been well constrained only at normal nuclear density and zero temperature. Heavy ion collisions remain the most powerful way to study the nuclear matter behavior in extreme conditions of temperature and density that can otherwise be encountered only in astrophysical environments, like supernova explosions and neutrons stars.

Several observables in heavy ion collisions are known to be affected by the symmetry energy ( $E_{sym}$ ), but quantitative information is difficult to extract, due to secondary decay of excited primary fragments, which can distort signatures contained in primary fragment observables. When experimentally determining the symmetry energy two important considerations are the degree of confidence which can be accorded to the estimation and the way in which the secondary decay processes impact the currently used observables. Indeed most of the primary fragments produced in Fermi-energy heavy-ion reactions are expected to be in an excited state when they are formed, while the majority of the experimentally detected fragments are in their ground states. Previous works [6, 7] have evaluated the excitation energies of the primary fragments and demonstrated that secondary decay is important.

In this respect we are investigating the effect of the secondary decay as predicted by the Statistical Multifragmentation Model (SMM) [8] on the symmetry energy coefficient extracted by the isoscaling and isobaric yield methods. Isoscaling [9] has been observed for a variety of reaction mechanisms that are dominated by phase space, including evaporation, multifragmentation, and deep inelastic scattering under the condition of statistical emission. Its statistical interpretation links the isoscaling parameter  $\alpha$  to the symmetry energy coefficient  $C_{sym}$  [9-12].

$$\alpha = \frac{4C_{sym}}{T} \left[ \left( \frac{Z}{A} \right)_1^2 - \left( \frac{Z}{A} \right)_2^2 \right] \quad (1)$$

where  $T$  is the temperature and the  $Z/A$  values correspond to the proton fraction of the most probable primary isotope produced in two similar sources with different proton-to-neutron ratios.

Recently a different method based on the Modified Fisher Model [13] has been suggested [14-16], which allows one to extract  $C_{sym}$  from the yield ratio between two pairs of isobars differing by 2 units in  $I=N-Z$  and produced by the same source. The two methods have been applied to secondary fragments from  $^{78,86}\text{Kr} + ^{58,64}\text{Ni}$  at 35A MeV reactions, taken on the NIMROD-ISiS array. The details of the experiment and of the analysis can be found in Ref. [17] and [18], respectively. A comparison to models is now needed to constrain  $E_{sym}$ .

The Statistical Multifragmentation Model (SMM) [8] has been widely used for interpreting experimental data on multiple fragment production in different nuclear reactions and to extract information on the symmetry energy starting from secondary fragments. Isotopic yields of fragments (N,Z) emitted in the multifragmentation of the quasi-projectile simulated by SMM have been determined for both the quasi-projectile sources ( $^{78}\text{Kr}$  and  $^{86}\text{Kr}$ ).  $C_{sym}/T$  has been extracted from the isoscaling parameter  $\alpha$  using as  $Z/A$  the values corresponding to the neutron richness of the neutron-rich and neutron-poor sources, respectively. The isobaric yield ratio method instead provides a direct estimation of  $C_{sym}/T$  for each source.

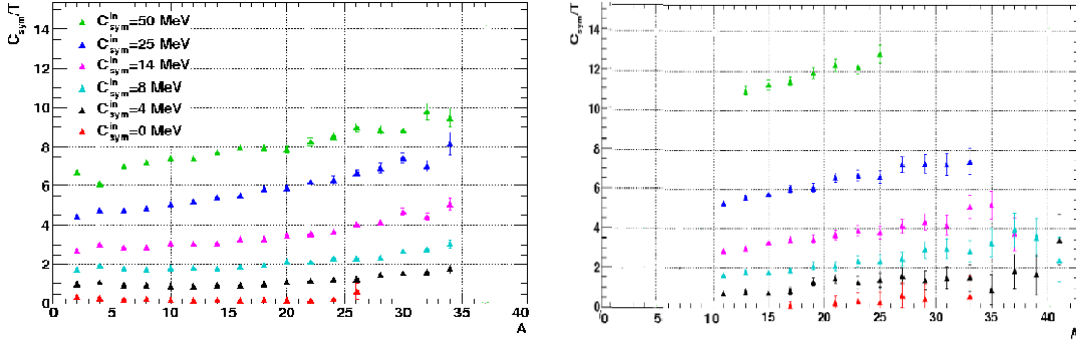


**FIG. 1.**  $C_{sym}/T$  values as a function of the fragment mass number ( $A=2Z$  for the isoscaling method) extracted from the isoscaling (left) and isobaric yield ratio (right) methods for hot fragments.

For hot fragments (i.e. before the secondary de-excitation) the behaviour of  $C_{sym}/T$  as a function of the fragment mass  $A$  for a chosen source excitation energy (5 AMeV) and input symmetry energy coefficient (25 MeV) is shown in fig.1.  $C_{sym}/T$  shows the same behavior as function of  $A$ , even for other values of source excitation energy (3, 4 and 7 AMeV) and input symmetry energy values  $C_{sym}$  (4, 8 and 14 MeV). The increasing trend is observed independently on the method used to determine  $C_{sym}/T$ . Attempts to physically interpret this trend have been done by varying the source size, to eventually figure out finite size effects, by isolating the Coulomb contribution ( $C_{sym} = 0$ ) and by selecting a narrow hot fragment excitation energy window.

Ideally, primary fragments should be detected to extract information on  $C_{sym}$  as will be shown later, but experimentally only cold fragments can be detected and, unless we rely on models to reconstruct primary quantities, information has to be extracted from secondary fragments (i.e. after de-excitation). The behavior of  $C_{sym}/T$  extracted with isoscaling and isobaric yield ratio methods as a function of the fragment mass for secondary fragments is plotted in fig.2. The same trend has been observed varying the source excitation energy and the symmetry energy input parameter. In the figure results obtained applying GEMINI to hot fragments generated by SMM are also plotted. It turns out that the de-excitation processes in SMM and GEMINI favour the production of different isobars. Indeed for  $C_{sym}/T$  to be estimated for a given isobars  $A$ , fragments with  $N-Z=3, 1, -1$  have to be produced by the code. For  $15 < A < 25$  the production of all the three isobars is damped in SMM code, while fragments produced by GEMINI have  $A < 28$ .  $C_{sym}/T$  obtained with the isoscaling method applied to SMM cold

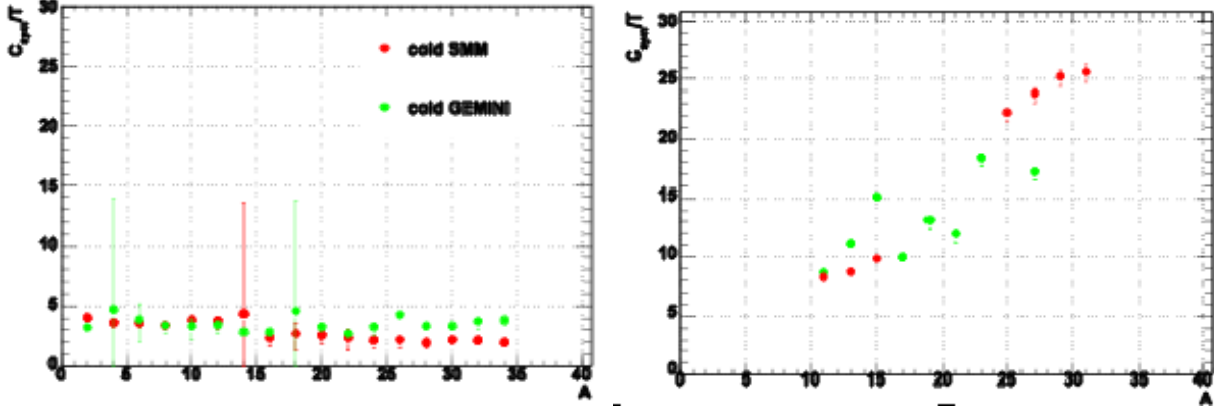


**FIG. 2.**  $C_{sym}/T$  values as a function of the fragment mass number ( $A=2Z$  for the isoscaling method) extracted from the isoscaling (left) and isobaric yield ratio (right) methods for cold fragments. In green the values obtained applying the two methods to fragments produced by SMM and de-excited by GEMINI are plotted.

fragments shows a gap between  $Z=7$  and  $Z=8$ , which is due to the change in de-excitation mechanism implemented in SMM for  $A=16$ . We observe a flat behavior of  $C_{sym}/T$  as a function of  $2Z$  ( $=A$ ) for isoscaling-extracted results, while  $C_{sym}/T$  increases as a function of  $A$  for isobaric yield method-extracted values. A possible interpretation of the two different trends may be that the secondary decay effects are minimized (or cancels out) when taking the ratio of the same isotope produced in similar sources, as done in the isoscaling method. On the contrary the effects do not cancel out when considering the ratio of two isobars produced by the same source. The opposite is true when considering the effect of the particle identification thresholds on the computation of the yield ratios. Moreover we would like to stress that  $C_{sym}/T$  can be directly extracted from the isobaric yield ratio method only if the second order approximation of the Lanadau free energy per particle as a function of the relative isospin asymmetry  $m=(N-Z)/A$  is valid [18]. If higher order terms are significant, they have to be taken into account in the estimation of  $C_{sym}/T$ . We are currently working to estimate their contribution.

The correlation of the extracted  $C_{sym}$  ( $C_{symout}$ ) with the input  $C_{sym}$  ( $C_{symin}$ ) are plotted in fig.3 and fig. 4 for both hot and cold fragments, respectively. As a measure of the temperature we have used the microcanonical temperature estimated by the SMM code. Other estimations of the temperature could be performed, using for example the particle kinetic energy spectra or the momentum fluctuations. In both cases we should disentangle the Coulomb contribution to the kinetic energy and momentum fluctuations, respectively, from the temperature contribution, but the Coulomb interaction can not be turned off without affecting also the partition configuration in SMM.

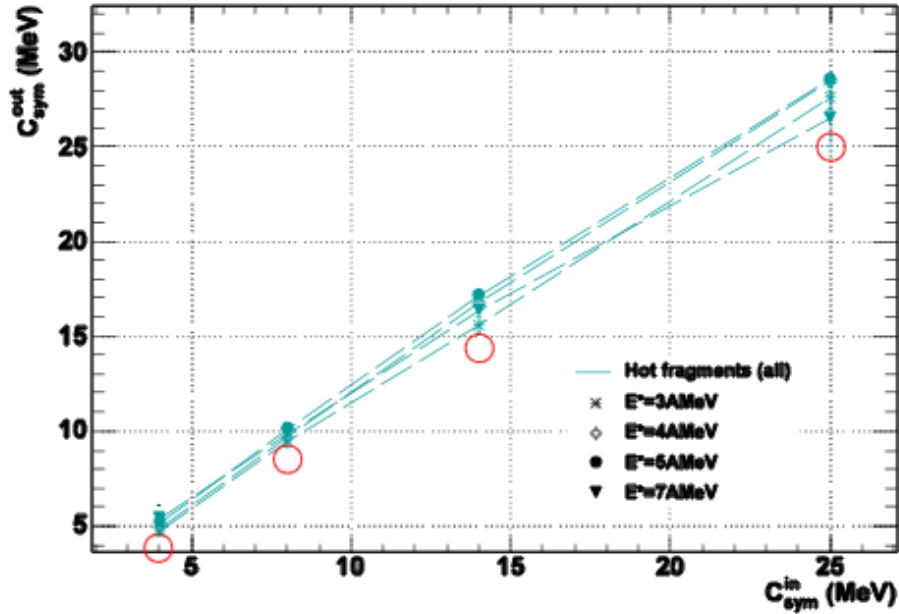


FIG. 3. Correlation between the SMM input symmetry energy coefficient value ( $C_{sym}^{in}$ ) and the symmetry energy coefficient value determined by the analysis of hot fragments.

The  $C_{sym}^{out}$  values extracted from hot fragments are in good agreement with the input values  $C_{sym}^{in}$ , suggesting that information on  $C_{sym}$  can be extracted from primary fragments. The correlation for values extracted from isoscaling analysis is significantly damped for excitation energy above 3 MeV/nucleon by the secondary de-excitation. The correlation for values extracted with the isobaric yield ratio method is present but the output values are in disagreement with the input values of a factor of 2-3. A possible reason could be the estimation of the temperature used to determine  $C_{sym}$ , but work is still in progress on this issue.

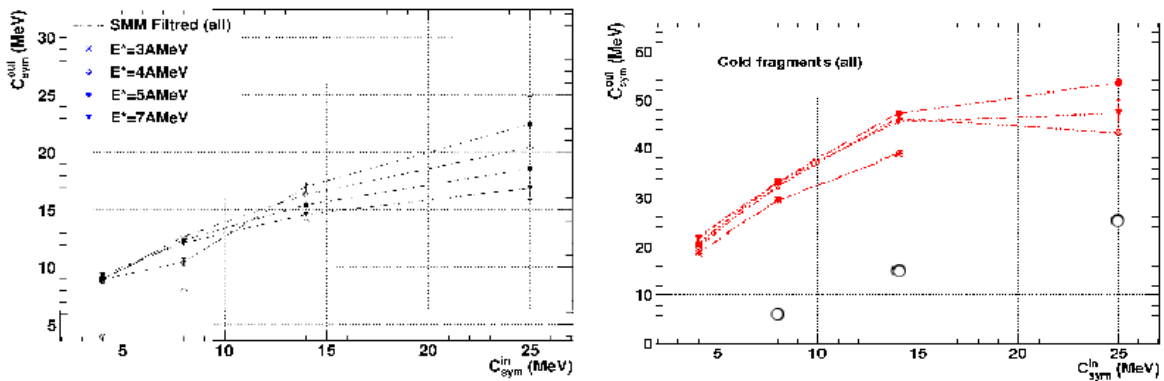


FIG. 4. Correlation between the SMM input symmetry energy coefficient value ( $C_{sym}^{in}$ ) and the symmetry energy coefficient value determined by the isoscaling (left) and the isobaric yield ratio (right) methods for cold fragments.

[1] D.V. Shetty *et al.*, Phys. Rev. C **76**, 024606 (2007).

- [2] B.A. Li *et al.*, Phys. Rep. **464**, 113 (2008).
- [3] V. Baran *et al.*, Phys. Rep. **410**, 335 (2005); and references therein.
- [4] B.A. Brown *et al.*, Phys. Rev. Lett. **85**, 5296 (2000).
- [5] J.M. Lattimer *et al.*, Astrophys. J. **550**, 426 (2001).
- [6] S. Hudan *et al.*, Phys. Rev. C **67**, 064613 (2003).
- [7] N. Marie *et al.*, Phys. Rev. C **58**, 256 (1998).
- [8] J.P. Bondorf *et al.*, Phys. Rep. **257**, 133 (1995).
- [9] M.B. Tseng *et al.*, Phys. Rev. Lett. **86**, 5023 (2001).
- [10] G. Chauduri *et al.*, Nucl. Phys. **A813**, 293 (2008); and references therein.
- [11] A.S. Botvina *et al.*, Phys. Rev. C **65**, 044610 (2002).
- [12] A. Ono *et al.*, Phys. Rev. C **68**, 051601(R) (2003).
- [13] R.W. Minich *et al.*, Phys. Lett. B **118**, 458 (1982).
- [14] M. Huang *et al.*, Phys. Rev. C **81**, 044618 (2010).
- [15] M. Huang *et al.*, Nucl. Phys. **A847**, 233 (2010).
- [16] M. Huang *et al.*, Phys. Rev. C **81**, 044620 (2010).
- [17] S. Wuenschel *et al.*, Phys. Rev. C **79**, 061602 (R) (2009).
- [18] P. Marini *et al.*, Phys. Rev. C (submitted).

## Constraining the symmetry energy at supra-saturation densities with measurements of neutron and proton elliptic flow - the Microball at GSI

P. Marini, P. Cammarata, L. Heilborn, L. May and S. J. Yennello for the ASY-EOS Collaboration

Understanding the equation-of-state of asymmetric nuclear matter is of fundamental importance and underpins our knowledge of many aspects of nuclear physics and astrophysics. The equation-of-state of asymmetric matter at supra-saturation densities has very few experimental constraints [1]. This is the domain with the greatest theoretical uncertainties and the largest impact on the understanding of neutron stars [2]. The behaviour of the symmetry energy at supra-saturation densities can only be explored in terrestrial laboratories by using relativistic heavy-ion collisions of isospin asymmetric nuclei.

A measure of the neutron and proton direct and elliptic flows, neutron-proton yield ratios and light-fragment flows and ratios in  $^{197}\text{Au}+^{197}\text{Au}$ ,  $^{96}\text{Ru}+^{96}\text{Ru}$  and  $^{96}\text{Zr}+^{96}\text{Zr}$  at 400 MeV/u reactions has been conducted at GSI by the ASY-EOS collaboration. We focused on the difference between the neutron and proton flows, so that the influence of the isoscalar potential, which acts equally on neutrons and protons, is minimized, whereas the effects of the symmetry potential, which has opposite effects on neutrons and protons, are maximized. The experiment has been specifically designed to constrain the symmetry energy at density around 2-3 times the normal density and has been intended as a start of a program of measurements to constrain the equation of state of asymmetric nuclear matter using both stable and rare isotope beams at the present GSI facility and in the future at FAIR.

Neutrons and protons were detected and identified by LAND [3] while the modulus and the orientation of the impact parameter were measured by coupling the forward rings of CHIMERA[4] and the ALADIN-Time of flight wall [5]. Light fragments were detected by the Krakow telescope. The experiment was performed in air. Moreover, the Ru target was an oxide, thus the discrimination of the desired reactions versus those occurring on light elements was crucial for the analysis. The discrimination of reactions occurring in air from reactions occurring in the target was enabled by the Microball [6]. It was based on the backward emitted multiplicity, which is expected to be different in the two cases, according to a UrQMD simulation.

The Microball was located in a light-tight box, 40cm downstream of the beam-pipe end. The target was mounted inside the Microball, using a special target holder able to slide inside the detector, so that the Microball was covering angles from 60 to 172°. Only 4 rings of the Microball have been used during the experiment, in order not to shadow other detectors. A halo detector was located in front of the Microball to detect particles coming from upstream. Moreover, an aluminium shield was protecting the Microball from  $\delta$  electrons produced by the interaction of the beam in air. The Microball also has a thin aluminium foil in the inner side shielding the detector from electrons produced in the target region. A lead shield was placed in front of the Microball, upstream and outside the box, 5cm downstream of the beam-pipe, to stop fragments produced upstream.

Data with and without a target have been collected during the experiment. A preliminary analysis performed online has shown that the detected multiplicity in the Microball is different in the two cases, as shown in fig. 1 giving us confidence in the capability of the Microball to discriminate the two reactions. The ratio of the number of events normalized to the beam current appears to be around 50%.

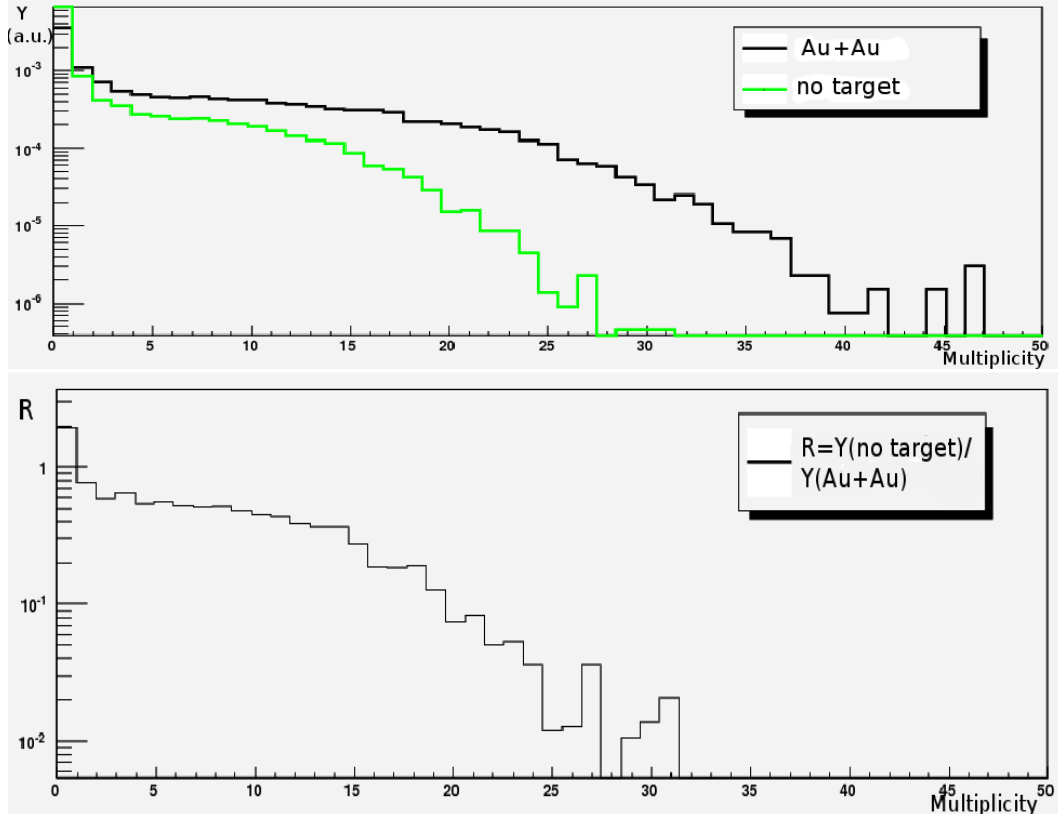


**FIG. 1.** Normalized multiplicity distributions for runs with (black) and without (green) target (top panel). In the bottom panel the ratio of the normalized yields is shown.

An even better discrimination of the two kind of reactions can be achieved looking at the multiplicity correlation with CHIMERA. Indeed events in which the reaction occurred in air present a much lower multiplicity in both the Microball and CHIMERA, as can be seen in fig. 2.

The unexpected high multiplicity observed in the Microball during runs with no target may be attributed to some noise in our detectors and/or to reactions occurring upstream. The off-line analysis will be able to compensate for these noise problems. The halo detector will provide a useful veto in our analysis to remove events in which particles hitting the Microball where produced upstream. Time-of-flight and energy measurements have also been performed in the Microball.

The calibrations of the detectors and the data analysis are now in progress by members of the ASY-EOS collaboration.

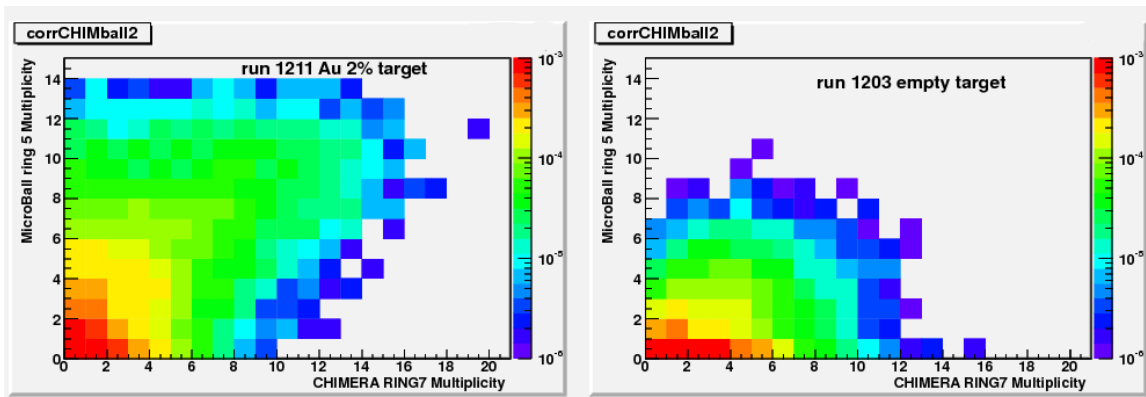


**FIG. 2.** Multiplicity correlations between CHIMERA and the Microball for runs with (left) and without (right) target.

- [1] B.A. Brown *et al.*, Phys. Rev. Lett. **85**, 5296 (2000).
- [2] J.M. Lattimer *et al.*, Astrophys. J. **550**, 426 (2001).
- [3] T. Blaich *et al.*, Nucl. Instru. Methods Phys. Res. **A314**, 136 (1992).
- [4] S. Aiello *et al.* Nucl. Phys. **A583**, 461 (1995).
- [5] J. Hubele *et al.*, Z. Phys. A **340**, 263 (1991) and Refs. Therein.
- [6] D.G. Sarantites *et al.*, Nucl. Instrum. Methods Phys. Res. **A381**, 418 (1996).

## Constraining the symmetry energy with isotopic yield distributions

P. Marini, G. Souliotis, A. Bonasera, S. N. Soisson, R. Tripathi, L. W. May,  
A. McIntosh and S. J. Yennello

In the past few years the importance of the symmetry energy term in the nuclear equation of state has stimulated a growing interest in isospin effects in nuclear reactions. Understanding the properties of asymmetric nuclear matter both at normal densities and at densities away from the saturation density has an important impact on the study of the nuclear structure close to the drip lines [1] and of astrophysical processes [2].

The study of the multifragmentation process in violent heavy ion collisions at Fermi energies is important for the investigation of the symmetry energy. Indeed the isotopic distribution of fragments produced in such collisions is governed by the free energy at the density and temperature of the fragmenting source. Thus, information on the free symmetry energy can be extracted from the isotopic yield distributions.

The production of fragments up to  $Z=7$ , detected in FAUST, from a range of isotopically identified quasi-projectiles obtained in the  $^{32}\text{S}+^{112}\text{Sn}$  has been studied by S. Soisson [3]. By looking at the fragment isotopic distributions it has been shown that, within the adopted Statistical Multifragmentation Model picture, the symmetry energy of the primary hot fragments produced from the decay of neutron-rich sources appears to be considerably lower than the symmetry energy of the same fragments produced from neutron-poor sources.

We have extended the analysis to heavier fragments produced in  $^{78,86}\text{Kr}+^{58,64}\text{Ni}$  at 35MeV/nucleon reactions and detected with NIMROD+ISiS apparatuses, located in the Neutron Ball. A stringent selection of the events has allowed the reconstruction of the quasi-projectile, obtaining events, on average, spherical, with a total detected charge  $36 \leq Z \leq 34$ . Moreover, particles not produced from projectile-like sources have been removed from the analysis [4,5].

The quasi-projectile (QP) mass distributions sorted by excitation energy show the same trend observed in  $^{32}\text{S}+^{112}\text{Sn}$ : increasing the QP excitation energy, the QP mass distribution broadens, as shown in fig. 1. We should notice that in our analysis free neutrons have been included in the QP mass and excitation energy determination, while they were not included in the previous analysis.

The fragment charge distribution of the reconstructed sources  $^{71}\text{Kr}$  to  $^{89}\text{Kr}$

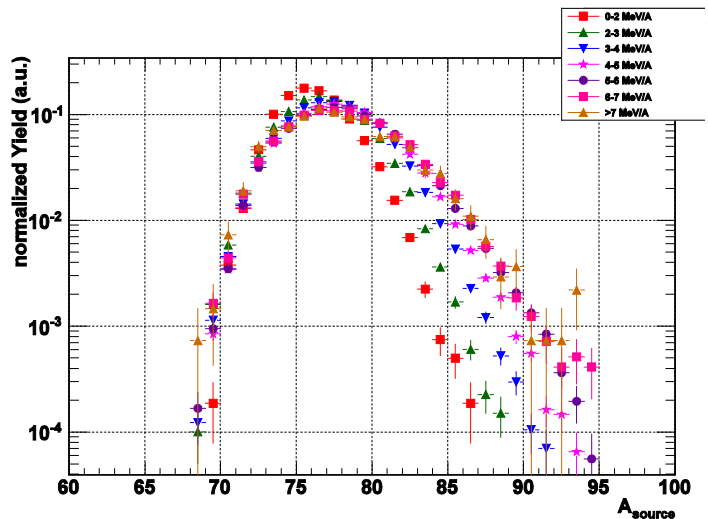
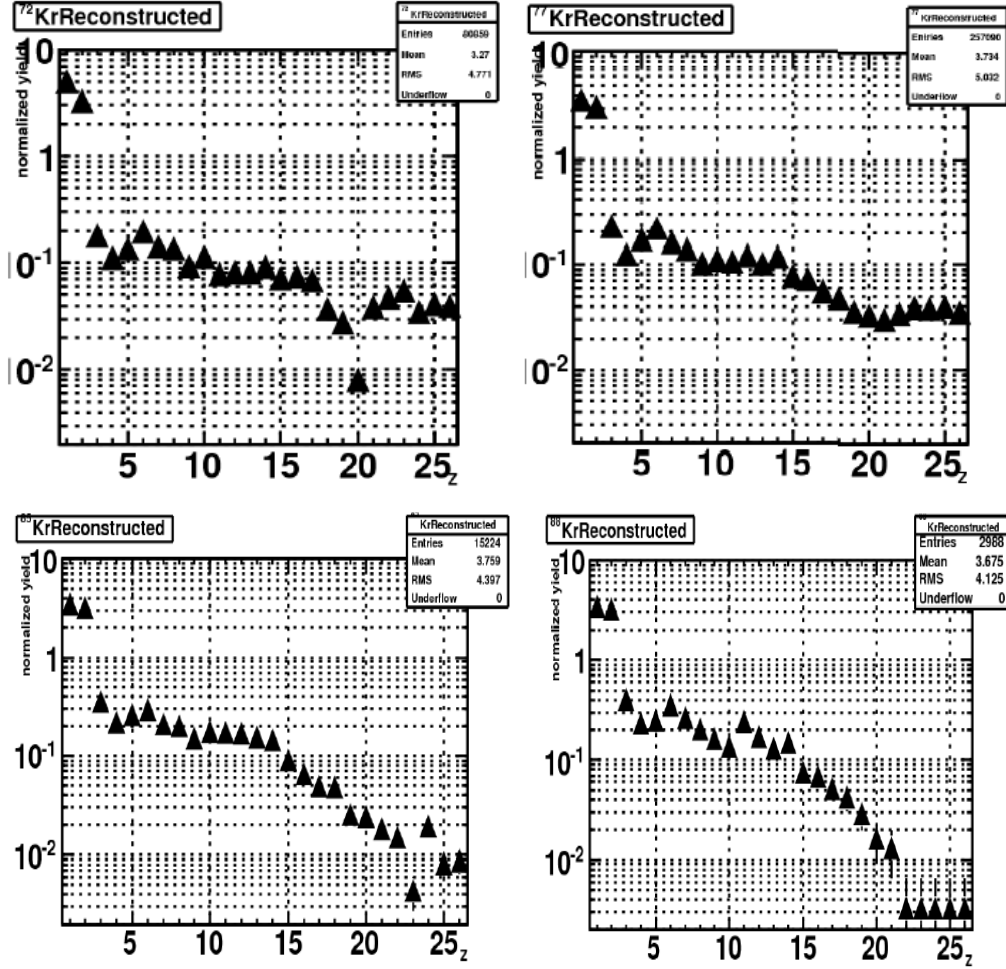


FIG. 1. Mass distribution of  $Z=36$  quasi-projectile sources in seven excitation energy ranges.

( $\frac{N-Z}{A} = -0.014 - 0.19$ ) do not show the odd-even behavior observed for the lighter neutron poor QP source  $^{27}\text{S}$  ( $\frac{N-Z}{A} = -0.185$ ), as shown in fig. 2. A possible reason could be the higher mass of the Kr source or the smaller  $\frac{N-Z}{A}$  asymmetry of the most n-poor Kr source.



**FIG. 2.** Normalized fragment charge distribution for the multifragmentation of the  $^{72}\text{Kr}$  (top left),  $^{77}\text{Kr}$  (top-right),  $^{85}\text{Kr}$  (bottom-left) and  $^{88}\text{Kr}$  (bottom-right). The yields are normalized to the total number of sources of the corresponding mass.

In agreement with previous studies and the S case, the fragment charge distributions change shape with the increase of the source excitation energy, moving from a U-shape to an exponential-like distribution. No odd-even effect is observed in the Kr case for the neutron-poor sources at low excitation energy, as shown in fig. 3. The average neutron-proton ratio of the produced fragments is found to be correlated to the neutron richness of the source, as shown in [3].

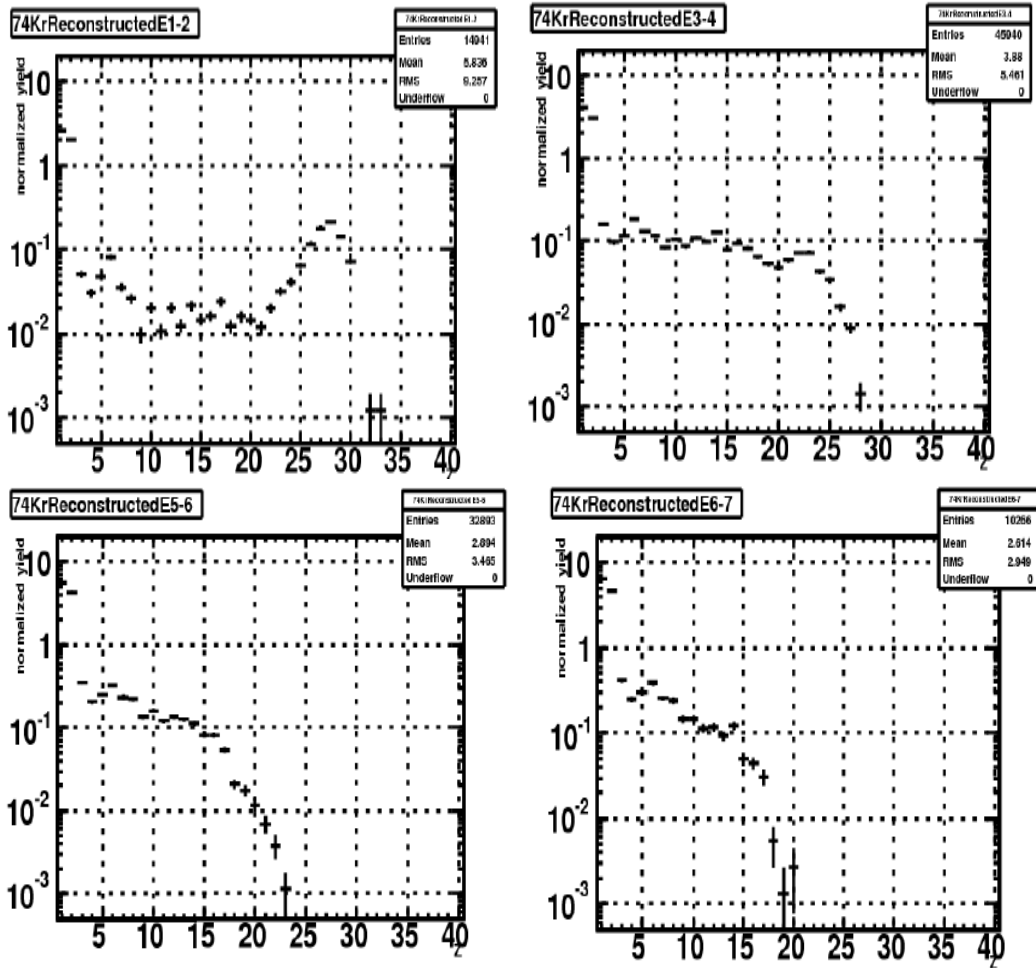


FIG. 3. Fragment charge distribution for the reconstructed source  $^{74}\text{Kr}$  for 4 excitation energy bins: 1-2 (top left), 3-4 (top-right), 5-6 (bottom-left) and 6-7 (bottom-right). The yields are normalized to the total number of sources of the corresponding mass in the given excitation energy bin.

A comparison of these results and of the isotopic yield of heavy fragments ( $Z > 8$ ) with the Statistical Multifragmentation Model is in progress. In particular, it will be interesting to verify if for sources larger than S produced in reactions involving a higher mass projectile (such as the Kr+Ni reactions that we are analysing) lower symmetry energy coefficients are needed to reproduce the distributions of fragments produced in n-rich sources.

- [1] B.A. Brown *et al.*, Phys. Rev. Lett. **85**, 5296 (2000).
- [2] J.M. Lattimer *et al.*, Astrophys. J. **550**, 426 (2001).
- [3] S.N. Soisson, Ph.D. Thesis, Texas A&M University, 2011.

- [4] S. Wuenschel *et al.*, Nucl. Phys. **A843**, 1 (2010); S. Wuenschel, Ph.D. Thesis, Texas A&M University, 2009.
- [5] P. Marini *et al.*, Phys. Rev. C (submitted).

## Observed suppression of fermionic fluctuations in heavy-ion reactions

B. C. Stein, Hua Zheng, Aldo Bonasera, and S. J. Yennello

Recently Zheng and Bonasera have proposed a new temperature and density calculation to be used for nuclear fragmentation studies [1, 2]. This thermometer treats the quantum nature of the system distinguishing it from the classically based methods previously available. The calculation uses the particle quadrupole fluctuations and normalized variance of the particle multiplicity per event to calculate the temperature. Full details of the calculation can be found in the above references. The necessity of a quantum treatment, however, can be shown experimentally through effects on the normalized variance used in the temperature calculation.

Data was used from the 2005-2006 FAUST campaign [3]. The 45 MeV/A  $^{32}\text{S} + ^{112}\text{Sn}$  reaction system was chosen because it has the highest statistics. FAUST is a forward array of 68, 300  $\mu\text{m}$  Silicon / 2.5 cm CsI (TI) telescopes [4]. The thickness of the silicon detectors bias the data toward fragments emitted from the projectile like source in peripheral reactions. Projectile like sources were selected by summing the charge of each particle detected in each event and selecting events with a sum charge equal to that of the incident beam ( $Z=16$ ). Events with particles that could not be fully isotopically identified were excluded. An event selection requiring the sum of the mass number of the detected fragments to be equal to the incident beam has been performed. This keeps the size of the fragmenting system constant.

The excitation energy was calculated through calorimetry as defined in Equation 1. Notice that only the portion of the kinetic energy transverse to the beam direction is used in this calculation to reduce any dynamic contribution to the kinetic energy from the interaction with the target. The resulting sum kinetic energy is then multiplied by 3/2. In effect this estimates the Z-axis contribution to the sum kinetic energy as the average of the other two axes.

$$E_{xy}^* / A = \left(\frac{3}{2}\right) \frac{\sum_{i=0}^{CP_{mult}} KE_{xy} - Q_{rxn}}{\sum_{i=0}^{CP_{mult}} A_{fragment}} \quad (1)$$

The data was broken in to 12  $E_{xy}^*$  bins of 0.5 MeV/A. The central values of these bins ranged from 0.5 to 7 MeV per nucleon. Figure 1 shows the normalized variance of the fragment multiplicity per event for three different fermionic particles for each of the above excitation energy bins.

The reduction of the normalized variance below 1 is expected for fermions and is the result of Pauli blocking. This effect is most pronounced for the protons and reduced for the two  $A=3$  fragments. This is also understood, as Pauli blocking should be reduced for composite particles. In a classical system, we would expect the normalized variance to be equal to 1 across all excitation bins. The trend observed in figure 1 agrees qualitatively with the model calculations of Zheng and Bonasera although their calculations were performed for a different reaction system.

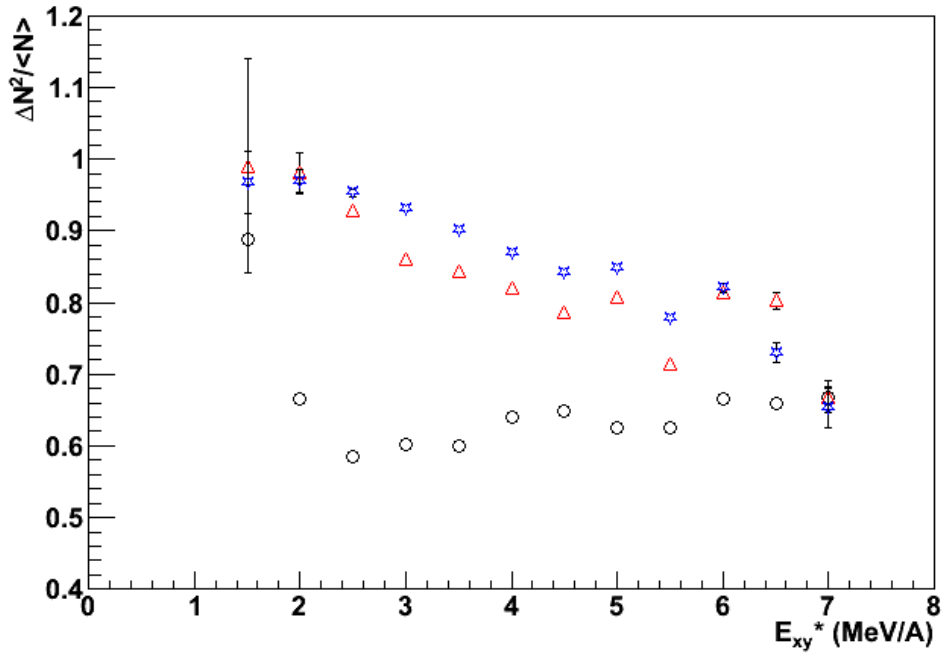


**FIG. 1.** Normalized variance by particle type versus excitation per nucleon. The open circles, triangles, and stars represent the protons, tritons, and  $^3\text{He}$  respectively. The excitation has been calculated using the transverse kinetic energy as discussed in the text. Statistical error on the normalized variance is plotted. The  $E_{xy}^*$  bins are 0.5 MeV/A in width.

Another temperature calculation based on event particle quadupole fluctuations, but classically derived, was previously proposed by Wuenschel and Bonasera [5]. For comparison the proton

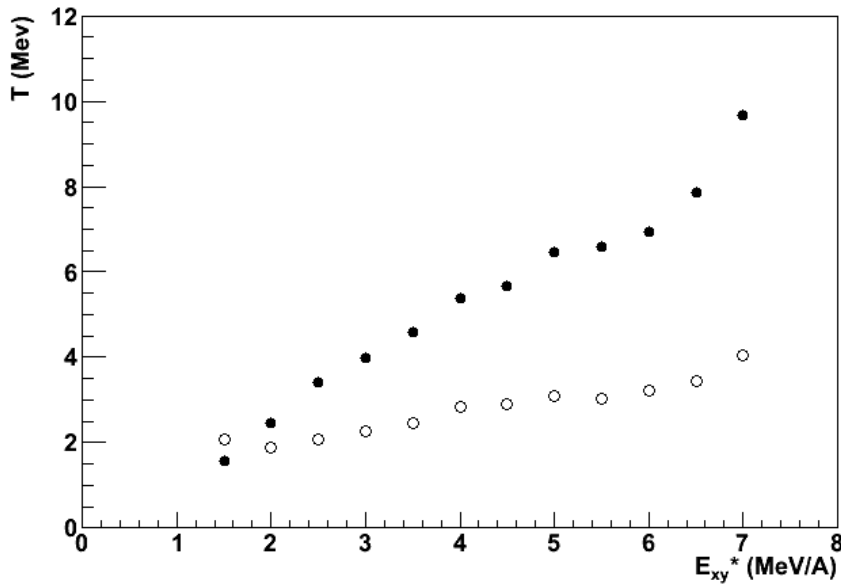


**FIG. 2.** Proton temperature calculated with both a classical (closed circles) and quantum (open circles) calculation. Notice the significant reduction in the calculated temperature of the quantum calculation over that of the classical, particularly at high excitation. Statistical error for the temperature is plotted (though the error bars remain smaller than the individual points). The  $E_{xy}^*$  bins are 0.5 MeV/A in width.

temperature from each calculation is plotted with the above event selection in figure 2. The classical and quantum temperatures are the closed and open circles respectively. There is a significant decrease in the temperature calculated by the quantum method over that of the classical, especially at higher event excitation.

Together the results suggest the importance of a quantum treatment of temperature for heavy ion reactions. Future work will include the expansion of the project to include the investigation of bosons type fragments as well as direct comparison with the CoMD model used in references [1,2].

- [1] Hua Zheng and Aldo Bonasera, *Phys. Lett. B* **696**, 178 (2011).
- [2] Hua Zheng and Aldo Bonasera, arXiv: 1105.0563v1; Hua Zheng and Aldo Bonasera, *Progress in Research*, Cyclotron Institute, Texas A&M University (2010 – 2011), p ??-??.
- [3] B.C. Stein *et al.*, *Progress in Research*, Cyclotron Institute, Texas A&M University (2007 – 2008), p II-30.
- [4] F. Gimeno-Nogues *et al.*, *Nucl. Instrum. Methods Phys. Res.* **A399**, 94 (1997).
- [5] S. Wuenschel *et al.*, *Nucl. Phys.* **A843**, 1 (2010).

## Isospin diffusion and equilibration in heavy-ion reactions

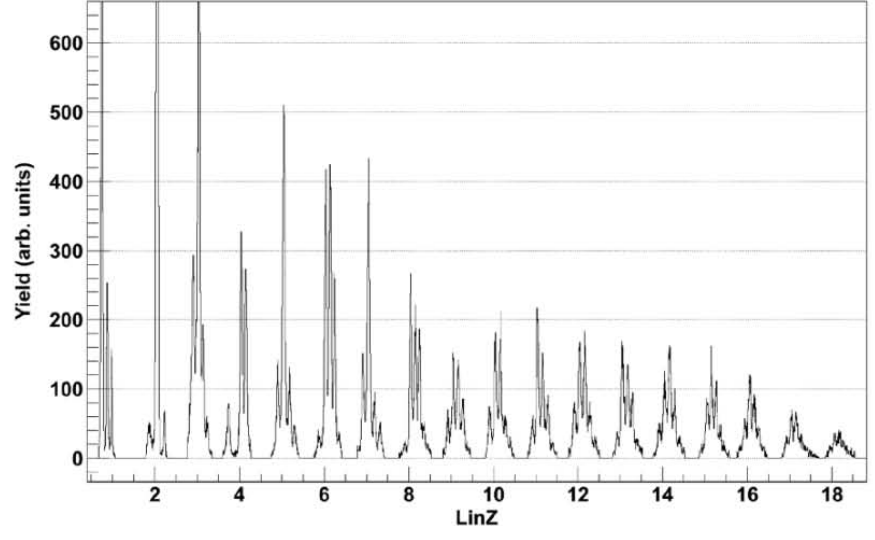
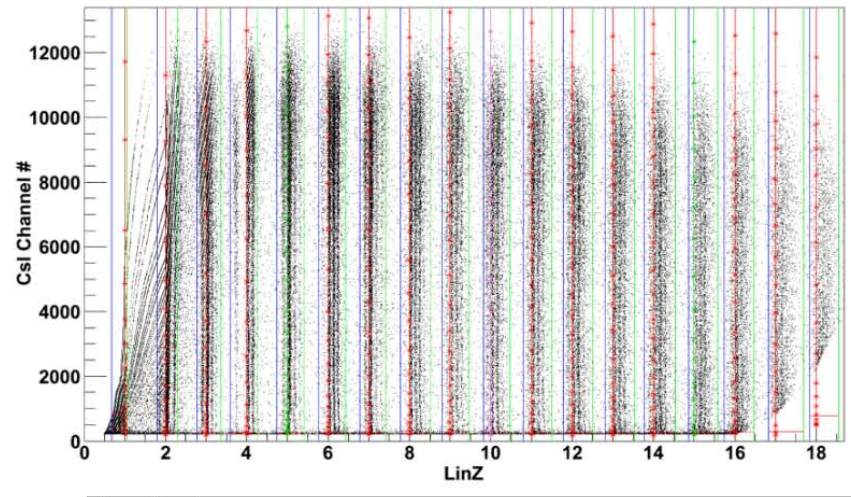
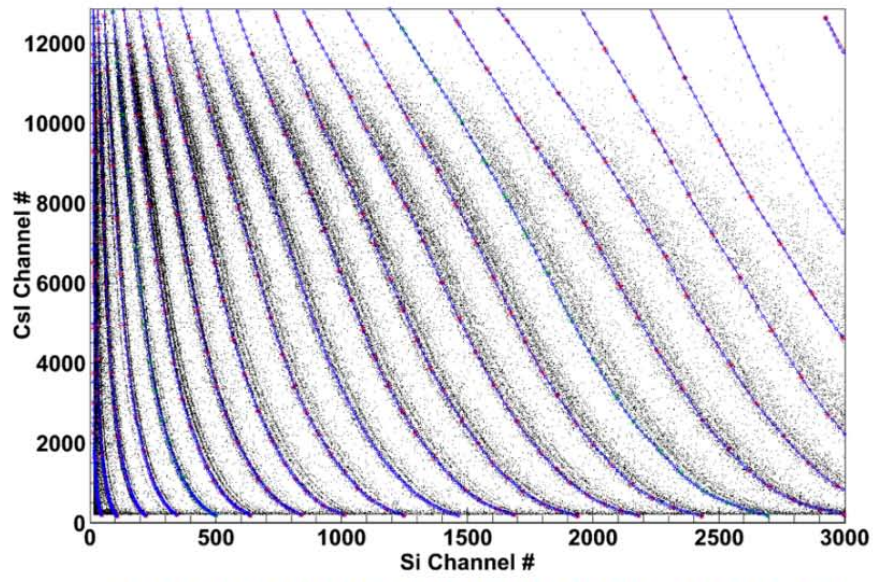
L. W. May, Z. Kohley, S. Behling G. Bonasera, J. Erchinger, L. Heilborn, P. Marini, A. McIntosh, A. Raphelt, G. Souliotis, B. Stein, R. Tripathi, T. Werke, and S. J. Yennello

The nuclear Equation of State (EoS) is an important component to our understanding of astrophysical events like supernovae and neutron star composition as well as more terrestrial matters such as explaining the distribution of the elements and isotopes in the world resultant from the Big Bang. The nuclear symmetry energy, which describes the behavior of nuclear material as you move away from  $N=Z$  symmetric nuclear matter, is currently one of the least constrained portions of the nuclear EoS. Two suggested probes for this are isospin diffusion and isospin equilibration. Isospin diffusion is a driving force for the exchange of nucleons between projectile and target in a reaction where there is differential  $N/Z$  content and is defined as  $D_q^I = -ct \left( \frac{\partial \mu_q}{\partial I} \right)_{\rho, T}$  where  $I = \frac{\rho_n - \rho_p}{\rho_{Tot}} = \frac{N - Z}{A}$  and  $q$  can be either

protons or neutrons. This isospin diffusion parameter,  $D$  in the equation above, describes the isospin dependent change in the chemical potential in nuclear matter and can be linked back to the symmetry energy. By looking at the nucleon transport between isospin asymmetric nuclei in Fermi energy heavy-ion collisions, using symmetric collisions as a reference, we can observe the un-equal mixing of  $N/Z$  content between nuclei in order to understand the diffusion that takes place in the reaction.

Isotopically identified fragments and neutron multiplicities were measured from the reactions of 35 MeV/nucleon  $^{70}\text{Zn}$ ,  $^{64}\text{Ni}+^{64}\text{Zn}$  and  $^{64}\text{Zn}+^{70}\text{Zn}$ ,  $^{64}\text{Ni}$ . These will be complimented by three previously obtained reactions on the same detector array: 35 MeV/nucleon  $^{70}\text{Zn}+^{70}\text{Zn}$ ,  $^{64}\text{Zn}+^{64}\text{Zn}$  and  $^{64}\text{Ni}+^{64}\text{Ni}$ . In addition, several reactions were collected for use in calibrating the detector. These calibration beams are 25 MeV/nucleon  $^4\text{He}+^{197}\text{Au}$ , 30 MeV/nucleon  $p\text{-d}+^{197}\text{Au}$ , 35 MeV/nucleon  $^{20}\text{Ne}+^{197}\text{Au}$ , 55 MeV/nucleon  $p\text{-p}$ ,  $^4\text{He}+^{197}\text{Au}$ , 35 MeV/nucleon  $^{35}\text{Cl}+^{64}\text{Zn}$  and 35MeV/nucleon  $^{70}\text{Zn}+^{70}\text{Zn}$  where the last system will be used to double check the energy calibrations against the symmetric systems from the previous campaign. With the addition of the previously acquired systems, a complete data set of 7 reaction systems will be formed and used to perform the isospin equilibration analysis.

The NIMROD-ISiS array is a  $4\pi$  charged particle array that consists of 228 detector telescopes covering the complete solid-angle in  $\phi$  and from  $3.6^\circ$ - $167^\circ$  in  $\theta$ . Each telescope is composed of a silicon detector (150 or 300  $\mu\text{m}$  thickness) followed by a CsI(Tl) crystal connected to a photomultiplier tube. This Si-CsI combination allows for the identification of charged particles by energy loss in the detectors via  $\Delta E$ - $E$  plots. A linearization, as shown in figure 1, is performed where lines are drawn to match the curves seen in the  $\Delta E$ - $E$ . These lines are then straightened and projected on the x-axis to give mass distributions of the particles detected. These distributions can then be fit with Gaussian curves to separate and identify particle charge and mass. Particle identification and energy calibration is underway.



## Investigation of the affect of a Coulomb force on velocity distributions in multifragmentation

L. Heilborn, G. Souliotis, S. Soisson, P. Cammarata, P. Marini, L. W. May, A. McIntosh,  
A. Raphelt, B. Stein, and S. Yennello

The relationship between the N/Z of the fragmenting source and the nature of its subsequent fragmentation was studied in the reaction of  $^{32}\text{S}$  with  $^{112}\text{Sn}$  at 45 MeV/nucleon. Isotopically resolved LCP and IMF were measured with the Forward Array Using Silicon Technology (FAUST) [1]. The velocity distribution of  $^7\text{Li}$  was observed to be asymmetric and backward peaked in the frame of the moving QP [2].

The velocity of the QP frame was determined by the velocity of the reconstructed QP, which consisted of all detected fragments in a given event. We observed a clear shift in the peak of the velocity distributions of the emitted Light Charged Particles (LCPs) towards the QT as the particles of a given Z become more neutron-rich, as shown left to right across a row in Figure 1. The magnitude of the shift decreases with increasing mass of the fragments. Some dependence of the positions of the peaks of these distributions on the distance between the QP and QT was proposed due to the Coulomb interaction. Previous work has utilized average velocities to probe the time between collision of the projectile and target and the break-up of the QP [3].

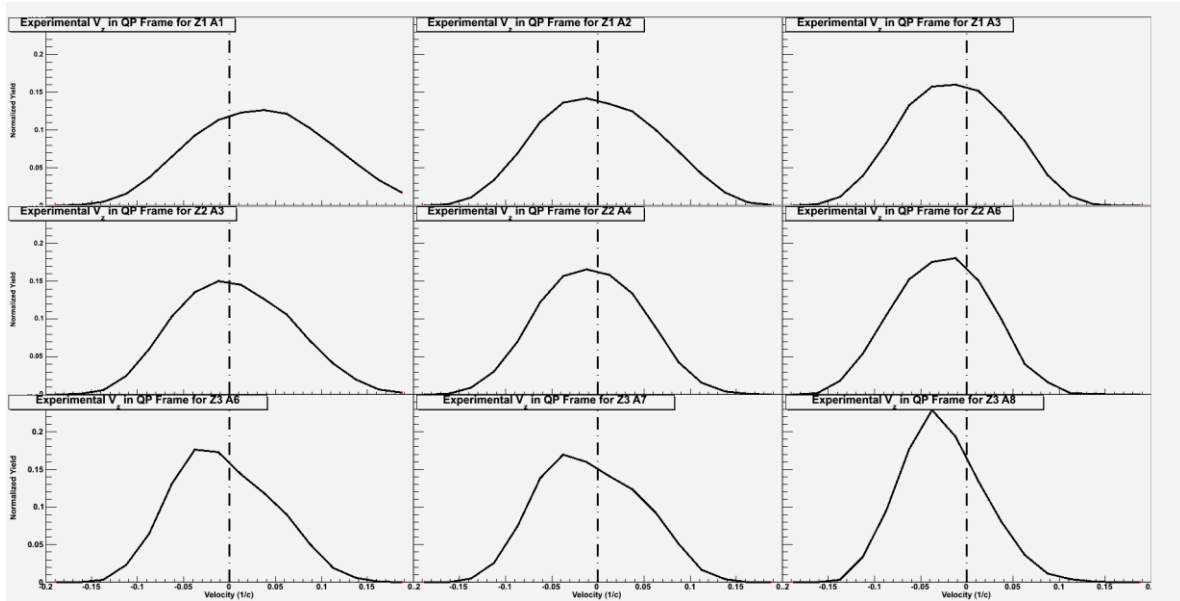


**FIG. 1.** Experimental velocity distributions of emitted fragments in the QP direction, in the QP frame (indicated by the dashed line).

In order to investigate the velocity distributions of the emitted fragments and their possible relationship to timing, DIT/SMM code for the system was run for different distances between the QP and the QT at the time of breakup. The Deep-Inelastic Transfer (DIT) creates an excited QP.<sup>4</sup>The Statistical

Multifragmentation Model (SMM) simulates the multifragmentation of this excited QP.<sup>5</sup> The unfiltered DIT/SMM data was mostly Gaussian in shape. The peaks of the velocity distributions of emitted fragments in the beam direction in the QP frame were shifted towards the QT (negative in the QP frame) at close proximity, but shifted forward with increasing distance between the QP and QT (“proximity”), as shown in figure 2.

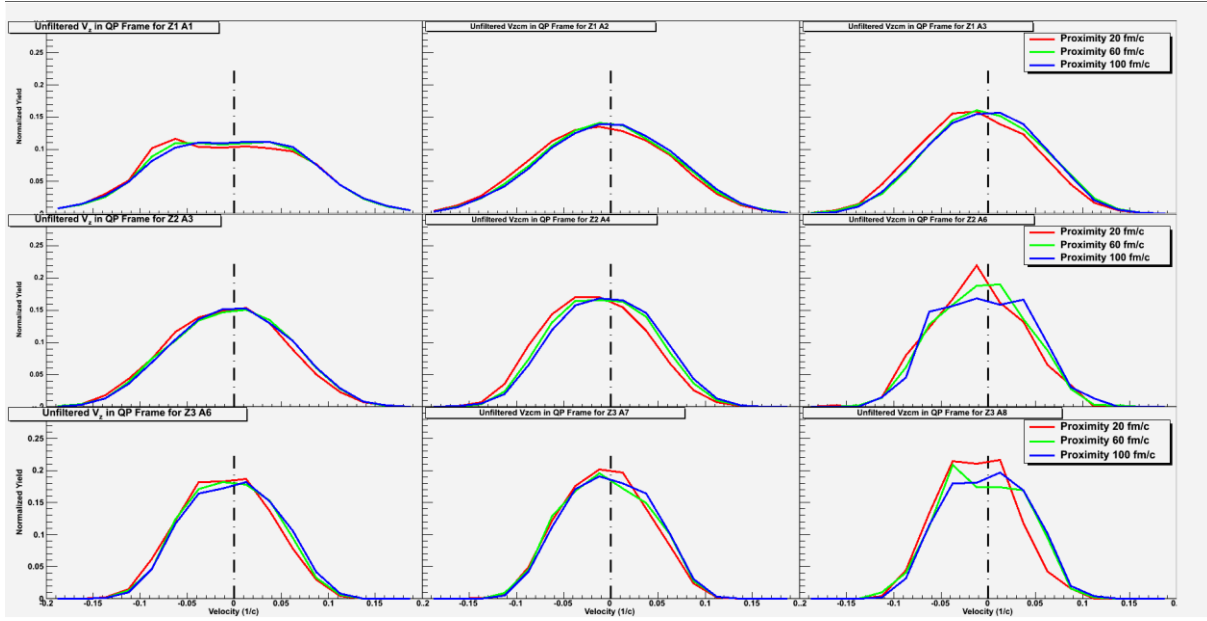


**FIG. 2.** Velocity distributions of emitted fragments in the QP direction, in the QP frame (indicated by the dashed line), generated from DIT/SMM.

The proximity effect was seen most clearly in the alpha particle distribution. The left panel of figure 3 shows the gradual shifting of the mode of the velocity of the alpha particles towards the velocity of the QP frame as the proximity increases. The FAUST software filter takes into account the geometry and energy thresholds of the apparatus. It results in a shift of the alpha velocity distribution in the beam direction of the QP frame to be more centered around zero, and obfuscated the shift in velocity distribution between the different proximities between the QP and QT. The distribution also narrowed after the application of the filter, as the right panel in figure 3 demonstrates. This shift is likely related to the omission of back-emitted particles from the QP frame.

The proximity of the QP to the QT at the time of breakup in SMM does affect the distribution of fragments in the QP frame. However, the effect is diminished when the experimental filter is applied. None of the proximity options shown scaled to the shapes of the originally observed distributions of <sup>7</sup>Li and other LCPs from the experimental data. Investigation of the source of the asymmetric velocity distributions of fragments is ongoing.

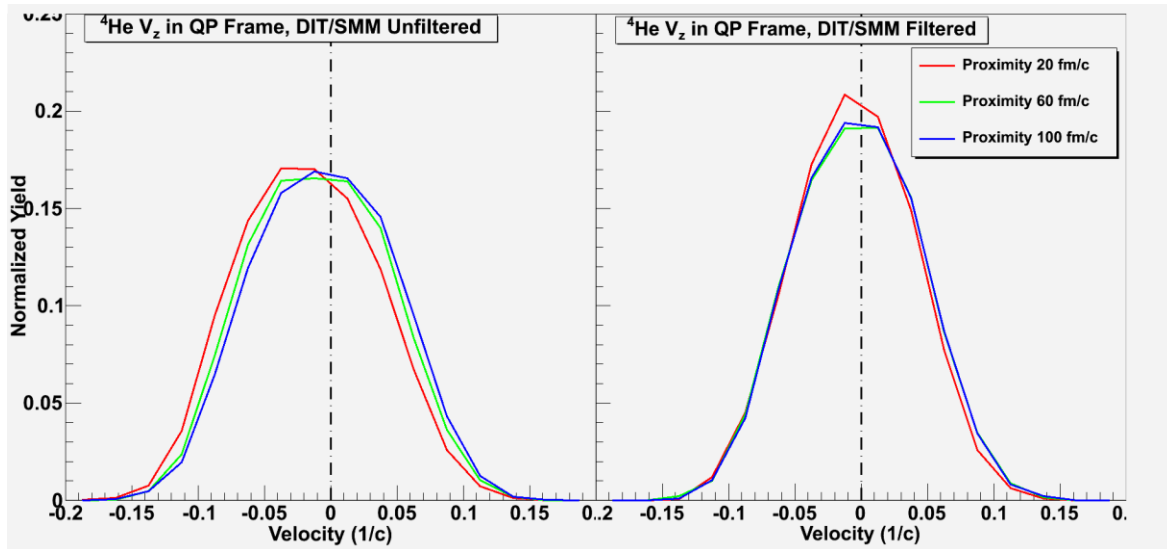


**FIG. 3.** The effect of the FAUST filter on the velocity distribution of alpha particles in the QP direction, in the QP frame. The “Proximity” in the legend refers to the distance in time between the QT and QP at the time of the break-up of the QP.

- [1] F. Gimeno-Nogues *et al.*, Nucl. Instrum. Methods Phys. Res. **A399**, 1 (1997).
- [2] S. Soisson, Ph.D. Thesis, Texas A&M University, 2010.
- [3] R. Charity *et al.*, Phys. Rev. C **52**, 3126 (1995).
- [4] L. Tassen-Got and C. Stephan, Nucl. Phys. **A524**, 121 (1991).
- [5] A. Botvina *et al.*, Nucl. Phys. **A475**, 663 (1987).

## Studies on antisymmetrized molecular dynamics (AMD) and isoscaling

A. Raphelt, Z. Kohley, P. Cammarata, P. Marini, L. W. May, A. McIntosh, and S. J. Yennello

Isoscaling was performed on nuclear collisions of  $^{70}\text{Zn}+^{70}\text{Zn}$  and  $^{64}\text{Zn}+^{64}\text{Zn}$  at 35 MeV/A from experimental data and from simulations by antisymmetrized molecular dynamics (AMD). The AMD model has two forms, the Gogny and the Gogny-AS. At high densities, the symmetry energy of the Gogny force decreases while the Gogny-AS force increases. AMD was simulated for various reactions for 300 fm/c for both forces, and up to 3000 fm/c for the Gogny-AS force. After 300 fm/c, Gemini was applied to AMD in order to de-excite the fragments. For the AMD data, all events were used in the isoscaling. For the experimental data, all events with isotopic identification and multiplicity greater than two were used. All isotopes of elements through sulfur were used in isoscaling and only central collisions were studied except where indicated. In isoscaling, the parameter  $\alpha$ , related to the neutron content of the fragmenting source, can be extracted. A plot was made to show the change of the  $\alpha$  parameter with impact parameter. The impact parameter can be extracted from the AMD simulations and was approximated by Kohley for his experimental data. The  $\alpha$  parameter was extracted from the isoscaling of the  $^{70}\text{Zn}+^{70}\text{Zn}/^{64}\text{Zn}+^{64}\text{Zn}$ . Here it can be seen in Figure 1 that as the impact parameter increases, the  $\alpha$  parameter also increases.

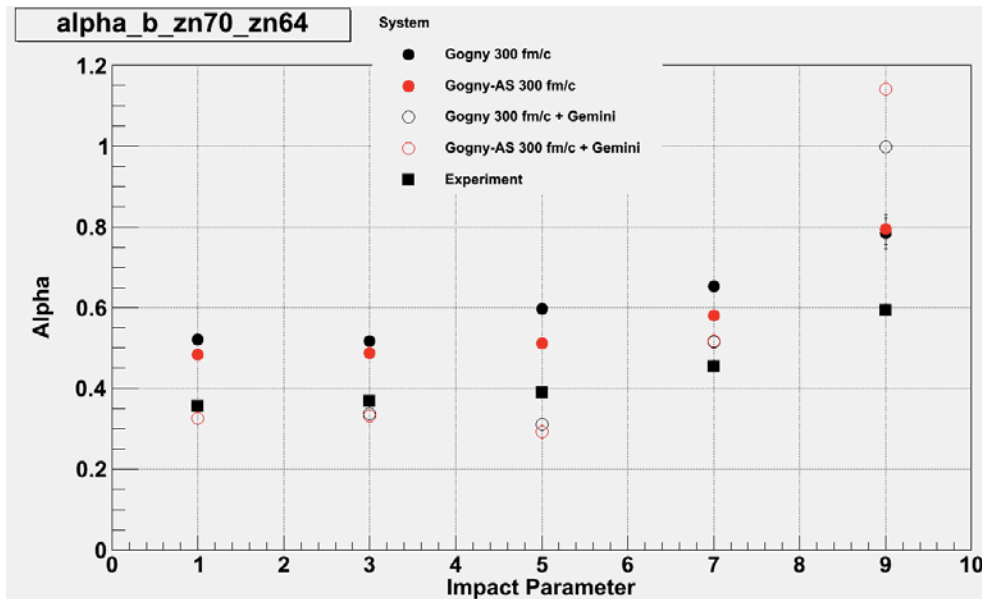


FIG. 1. The  $\alpha$  parameter vs. impact parameter.

A plot of excitation energy vs time is shown in Figure 2 in order to look at the change in excitation energy of the fragments from the reaction as it progresses in time. The Gogny-AS form of AMD was simulated for the reaction of  $^{70}\text{Zn} + ^{70}\text{Zn}$  from 0 to 3000 fm/c. The excitation energy of the experimental reaction was calculated as the sum of the excitation energy of the fragments. The excitation energy was plotted by splitting the fragments from the reaction into various groups based on their charge.

Fig. 2 shows that as the reaction proceeds to 3000 fm/c, the excitation energy for the reaction decreases initially, but then reaches a plateau at some  $E^*/A$  value for each fragment size. This is interesting because by 3000 fm/c, the reaction should be complete and fragments should have cooled through de-excitation channels so that there is no excitation energy left. The AMD model does not seem to show the fragments de-exciting completely.

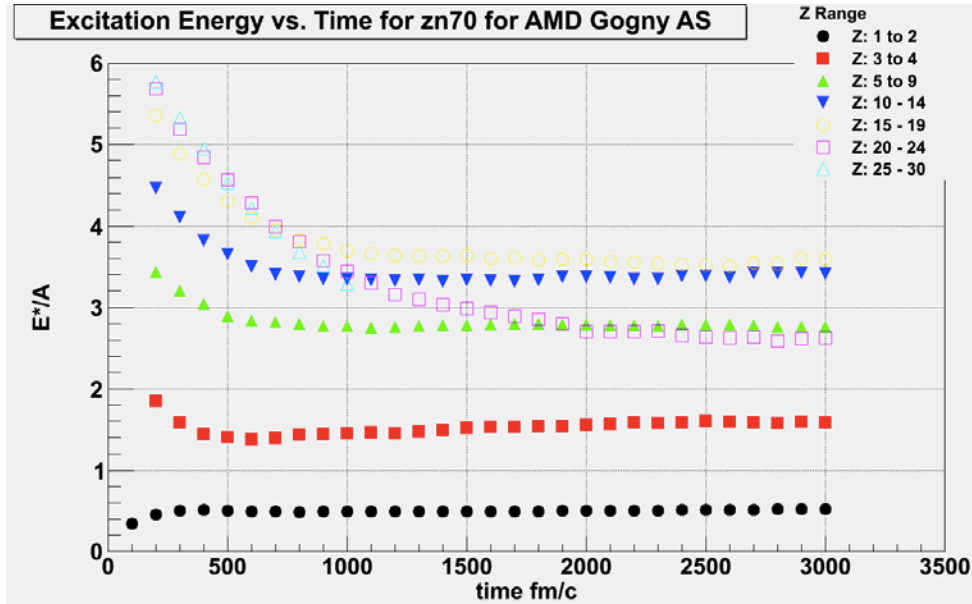


FIG. 2. Excitation energy vs. time.

Figure 3 shows how the isoscaling parameter,  $\alpha$ , from the system of  $^{70}\text{Zn}+^{70}\text{Zn}/^{64}\text{Zn}+^{64}\text{Zn}$  changes as a function of time. Values of  $\alpha$  for AMD are shown along with the values from a simulation

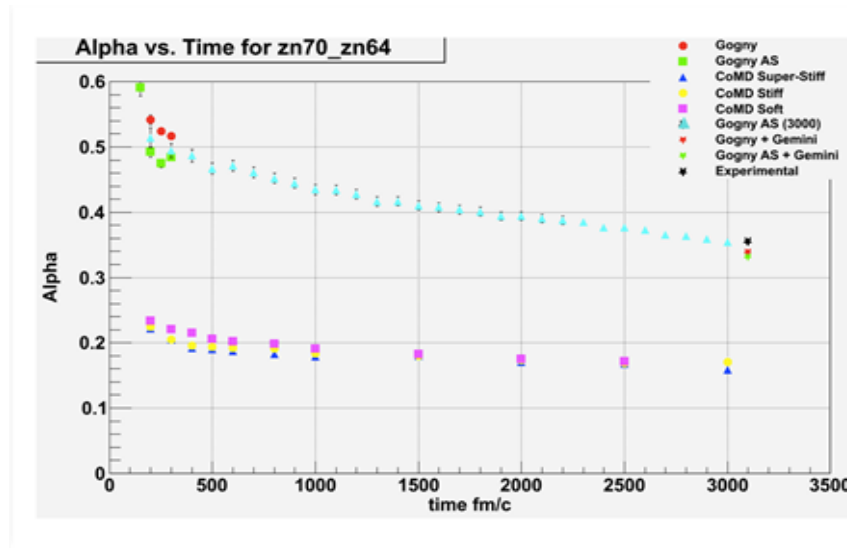


FIG. 3. The  $\alpha$  parameter vs time.

using constrained molecular dynamics (CoMD). The experimental data and the AMD data with Gemini

applied are plotted at 3100 fm/c in order to position them after the final time-step of the simulated data. In this plot, the AMD Gogny-AS values decrease with time and approach the same final  $\alpha$  value as the experimental data. Also, the AMD with Gemini data lie very close to the experimental point as well. This agreement between the model and the experimental values of  $\alpha$  indicates the utility of isoscaling on AMD simulated data.

[1] A. Ono *et al.*, Phys. Rev. C **68**, 051601 (2003).

[2] D.V. Shetty *et al.*, Phys. Rev. C **70** 011601(R) (2004).

**Production of neutron-rich nuclides in peripheral collisions of  $^{86}\text{Kr}$  (15 MeV/nucleon) projectiles with  $^{64}\text{Ni}$ ,  $^{58}\text{Ni}$  and  $^{124}\text{Sn}$ ,  $^{112}\text{Sn}$  targets**

G. A. Souliotis, M. Veselsky, S. Galanopoulos, Z. Kohley, L. May, D. V. Shetty, B. C. Stein,  
and S. J. Yennello

A large part of our recent efforts has been directed to the production and separation of RIBs in peripheral collisions below the Fermi energy. High intensity beams at this energy range are expected from the refurbished K150 cyclotron and can be exploited for the production of RIBs with the aid of a large-bore superconducting solenoid as a preseparator before a heavy-ion gas stopper [1]. Our recent measurements and simulations indicate that the application of the deep-inelastic transfer mechanism [2,3,4] appears to be a very effective way to obtain neutron-rich rare isotopes at the K150 energies.

Aiming at obtaining systematics on production rates, we performed a series of measurements with a 15 MeV/nucleon  $^{86}\text{Kr}$  beam striking targets of  $^{64}\text{Ni}$ ,  $^{58}\text{Ni}$  and  $^{124}\text{Sn}$ ,  $^{112}\text{Sn}$ . The projectile fragments were collected and identified using the MARS recoil separator applying the techniques developed and documented in [2,3]. The Kr beam was sent on the primary target location of MARS with an inclination of  $4^\circ$ . After interaction with the target, the fragments traversed a PPAC at the intermediate image location (for position/Bp measurement and START time information) and then they were focused at the end of the device passing through a second PPAC (for image size monitoring and STOP time information). Finally the fragments were collected in a  $5 \times 5 \text{ cm}^2$   $\Delta E$ -E Si detector telescope (60 and 1000  $\mu\text{m}$  thickness). Following standard techniques of Bp- $\Delta E$ -E-TOF (magnetic rigidity, energy-loss, residual energy and time-of-flight, respectively), the atomic number Z, the mass number A, the velocity and the ionic charge of the fragments were obtained on an event-by-event basis (see, e.g., [3]). Data were obtained in a series of magnetic rigidity settings of the spectrometer to cover the energy and charge state distributions of the fragments. In order to obtain total cross sections from the measured yields at  $4^\circ$ , we used a model approach as described in our previous works [2,3,4]. First we performed calculations of the yields with the codes DIT [5] for the primary interaction stage and GEMINI [6] for the deexcitation stage of the reaction. We then performed filtering of the DIT/GEMINI results for the limited angular acceptance of the spectrometer and the Bp range covered in the measurements. We used the ratio of the filtered to unfiltered simulations to correct the measured data (obtained in the limited angular acceptance of the spectrometer) and extract total production cross sections for each projectile-like fragment.

Figure 1 shows the cross sections of projectile-like fragments of elements  $Z=35-30$  from the reactions  $^{86}\text{Kr}$  (15 MeV/nucleon) +  $^{64}\text{Ni}$ ,  $^{58}\text{Ni}$  (black and red points, respectively). Similarly, figure 2 shows the cross sections of projectile-like fragments of elements  $Z=35-30$  from the reactions  $^{86}\text{Kr}$  (15 MeV/nucleon) +  $^{124}\text{Sn}$ ,  $^{112}\text{Sn}$  (black and red points, respectively). The results indicate that along with proton-removal products, neutron-pickup products are produced in substantial yields, as expected from a deep-inelastic transfer mechanism at these energies [2,3,4]. Especially for the present 15 MeV/nucleon data, we observe enhanced cross sections of neutron pick-up products near the projectile. We are currently working on detailed simulations of the cross sections using an improved version of the DIT model approach [4], as well as, the CoMD code [8].

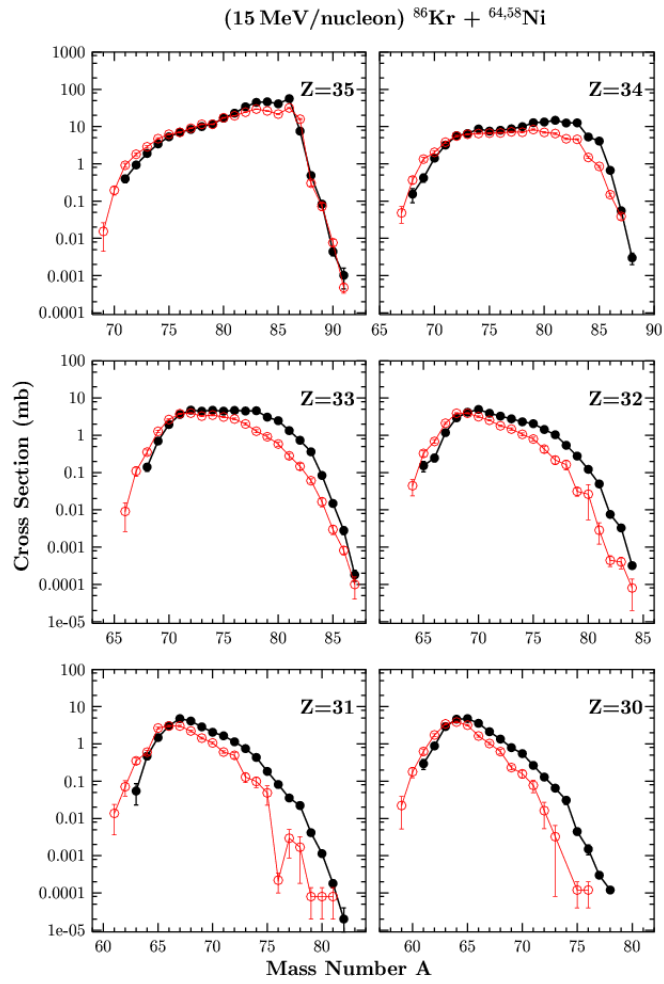


**FIG. 1.** Cross sections of projectile-like fragments of elements  $Z=35-30$  from the reactions  $^{86}\text{Kr}$  (15 MeV/nucleon) +  $^{64}\text{Ni}$  (black points) and  $^{86}\text{Kr}$  (15 MeV/nucleon) +  $^{58}\text{Ni}$  (red points).

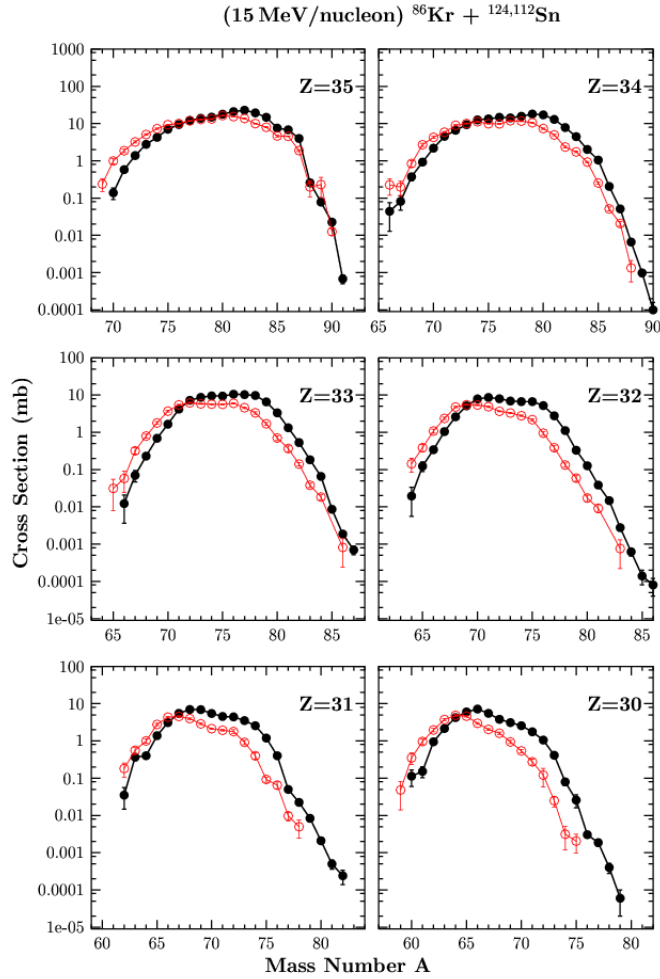


**FIG. 2.** Cross sections of projectile-like fragments of elements  $Z=35-30$  from the reactions  $^{86}\text{Kr}$  (15 MeV/nucleon) +  $^{124}\text{Sn}$  (black points) and  $^{86}\text{Kr}$  (15 MeV/nucleon) +  $^{112}\text{Sn}$  (red points).

- [1] *A Proposed Facility Upgrade for the Texas A&M University Cyclotron Institute* (College Station, Texas), <http://cyclotron.tamu.edu>.
- [2] G.A. Souliotis *et al.*, Phys. Rev. Lett. **91**, 022701 (2003)
- [3] G.A. Souliotis *et al.*, Nucl. Instrum. Methods Phys. Res. **B204**, 166 (2003).
- [4] M. Veselsky, G.A. Souliotis, Nucl.Phys. **A765**, 252 (2006).
- [5] L. Tassan-Got, Nucl. Phys. **A524**, 121 (1991).
- [6] R. Charity, Nucl. Phys. **A483**, 391 (1988).
- [7] K. Suemmerer *et al.*, Phys. Rev. C **61**, 034607 (2000).
- [8] M. Papa *et al.*, Phys. Rev. C **64**, 024612 (2001).

**SECTION III**  
**NUCLEAR THEORY**

## Astrophysical $S$ factor for the $^{15}\text{N}(p,\gamma)^{16}\text{O}$ reaction

A. M. Mukhamedzhanov, M. La Cognata,<sup>1</sup> and V. Kroha<sup>2</sup>

<sup>1</sup>*Universit`a di Catania and INFN Laboratori Nazionali del Sud, Catania, Italy*

<sup>2</sup>*Nuclear Physics Institute, Czech Academy of Sciences, 250 68 Rez, Czech Republic*

The  $R$ -matrix approach has proved to be very useful in extrapolating the astrophysical factor down to astrophysically relevant energies, since the majority of measurements are not available in this region. However, such an approach has to be critically considered when no complete knowledge of the reaction model is available. To get reliable results in such cases one has to use all the available information from independent sources and, accordingly, fix or constrain variations of the parameters. In this paper we present a thorough  $R$ -matrix analysis of the  $^{15}\text{N}(p,\gamma)^{16}\text{O}$  reaction, which provides a path from the CN cycle to the CNO bi-cycle and CNO tri-cycle. The measured astrophysical factor for this reaction is dominated by resonant capture through two strong  $J^\pi=1^-$  resonances at  $E_R = 312$  and  $962$  keV and direct capture to the ground state. Recently, a new measurement of the astrophysical factor for the  $^{15}\text{N}(p,\gamma)^{16}\text{O}$  reaction has been published [1]. The analysis has been done using the  $R$ -matrix approach with unconstrained variation of all parameters including the asymptotic normalization coefficient (ANC). The best fit has been obtained for the square of the ANC  $C^2 = 539 \text{ fm}^{-1}$ , which exceeds the previously measured value by a factor of  $\approx 3$ . We have performed a new  $R$ -matrix analysis of the Notre Dame–LUNA data with the fixed within the experimental uncertainties square of the ANC  $C^2 = 200.34 \text{ fm}^{-1}$ . Rather than varying the ANC we add the contribution from a background resonance that effectively takes into account contributions from higher levels. Altogether we present ten fits, seven unconstrained and three constrained. For the unconstrained fit with the boundary condition  $B_c = S_c(E_2)$ , where  $E_2$  is the energy of the second level, we get  $S(0) = 39.0 \pm 1.1 \text{ keVb}$  and normalized  $\chi^2 = 1.84$ , i.e., the result which is similar to LeBlanc *et al.* From all our fits we get the range  $33.1 \leq S(0) \leq 40.1 \text{ keVb}$ , which overlaps with the result of LeBlanc *et al.* We address also the physical interpretation of the fitting parameters. The paper has been published in Phys. Rev. C.

[1] P. J. LeBlanc *et al.*, Phys. Rev. C **82**, 055804 (2010).

## High accuracy $^{18}\text{O}(p,\alpha)^{15}\text{N}$ reaction rate at AGB nucleosynthesis relevant temperatures

M. La Cognata,<sup>1</sup> C. Spitaleri,<sup>1</sup> and A. M. Mukhamedzhanov

<sup>1</sup>*INFN Laboratori Nazionali del Sud & DMFCI Università di Catania, Catania, Italy*

The  $^{18}\text{O}(p,\alpha)^{15}\text{N}$  reaction is of great importance in several astrophysical scenarios, as it influences the production of key isotopes such as  $^{19}\text{F}$ ,  $^{18}\text{O}$  and  $^{15}\text{N}$ . Fluorine is synthesized in the intershell region of asymptotic giant branch stars, together with s-elements, by  $\alpha$  radiative capture on  $^{15}\text{N}$ , which in turn is produced in the  $^{18}\text{O}$  proton-induced destruction. Peculiar  $^{18}\text{O}$  abundances are observed in R-Coronae Borealis stars, having  $^{16}\text{O}/^{18}\text{O} \leq 1$ , hundreds of times smaller than the galactic value. In the framework of the double degenerate scenario, a quantitative account of such abundances can be provided if H-rich material is ingested and the  $^{18}\text{O}(p,\alpha)^{15}\text{N}$ ,  $^{18}\text{O}(p,\alpha)^{15}\text{N}(p,\alpha)^{12}\text{C}$  chain is activated, thus reducing  $^{18}\text{O}$  overproduction. Finally, there is no definite explanation of the  $^{14}\text{N}/^{15}\text{N}$  ratio in presolar grains formed in the outer layers of asymptotic giant branch stars. Again, such an isotopic ratio is influenced by the  $^{18}\text{O}(p,\alpha)^{15}\text{N}$  reaction that might increase the  $^{15}\text{N}$  yield during non-convective mixing episodes. In this work, a high accuracy  $^{18}\text{O}(p,\alpha)^{15}\text{N}$  reaction rate is proposed, based on the simultaneous fit of direct measurements and the results of a new Trojan Horse experiment. Indeed, current determinations are uncertain because of the poor knowledge of the resonance parameters of key levels of  $^{19}\text{F}$ . In particular, we have focused on the study of the broad 660 keV  $\frac{1}{2}^+$  resonance corresponding to the 8.65 MeV level of  $^{19}\text{F}$ . Since  $\Gamma \sim 100\text{-}300$  keV, it determines the low-energy tail of the resonant contribution to the cross section and dominates the cross section at higher energies. We get a factor of 2 larger reaction rate above  $T \sim 0.5 \times 10^9$  based on our new improved determination of its resonance parameters compared to previous estimations, which could strongly influence present-day astrophysical model predictions. This work has been published in *Astrophysical Journal*.

## Low-energy d+d fusion reactions via the Trojan horse method

A. Tumino,<sup>1,2</sup> C. Spitaleri,<sup>1</sup> A. M. Mukhamedzhanov, S. Typel,<sup>3,4</sup> M. Aliotta,<sup>5</sup> V. Burjan,<sup>6</sup>  
M. Gimenez del Santo,<sup>7</sup> G. G. Kiss,<sup>1,8</sup> V. Kroha,<sup>6</sup> Z. Hons,<sup>6</sup> M. La Cognata,<sup>1</sup> L. Lamia,<sup>1</sup>  
J. Mrazek,<sup>6</sup> R. G. Pizzone,<sup>1</sup> S. Piskor,<sup>6</sup> G. G. Rapisarda,<sup>1</sup> S. Romano,<sup>1</sup> M. L. Sergi,<sup>1</sup> and R. Sparta<sup>1</sup>

<sup>1</sup>*Laboratori Nazionali del Sud - INFN and DMFCI Universit\_a di Catania, Catania, Italy*

<sup>2</sup>*Universit\_a degli Studi di Enna "Kore", Enna, Italy*

<sup>3</sup>*Excellence Cluster Universe - Technische Universit\_at Munchen, Garching, Germany*

<sup>4</sup>*GSI Helmholtzzentrum f\_ur Schwerionenforschung GmbH - Theorie Darmstadt Germany*

<sup>5</sup>*School of Physics and Astronomy - University of Edinburgh; SUPA, United Kingdom*

<sup>6</sup>*Nuclear Physics Institute of ASCR - Rez near Prague, Czech Republic*

<sup>7</sup>*Departamento de Fisica Nuclear - Universidade de Sao Paulo, Sao Paulo, Brasil*

<sup>8</sup>*ATOMKI - Debrecen, Hungary*

The bare nucleus S(E) factors for the  $^2\text{H}(d,p)^3\text{H}$  and  $^2\text{H}(d,n)^3\text{He}$  reactions have been measured for the first time via the Trojan Horse Method off the proton in  $^3\text{He}$  from 1.5 MeV down to 2 keV. This range overlaps with the relevant region for Standard Big Bang Nucleosynthesis as well as with the thermal energies of future fusion reactors and deuterium burning in the PreMain Sequence phase of stellar evolution. This is the pioneering experiment in quasi free regime where the charged spectator is detected. Both the energy dependence and the absolute value of the S(E) factors deviate by more than 15% from available direct data with new S(0) values of  $57.4 \pm 1.8$  MeVb for  $^3\text{H}+p$  and  $60.1 \pm 1.9$  MeVb for  $^3\text{He}+n$ . None of the existing curves is able to provide the correct slope of the new data in the full range, thus calling for a revision of the theoretical description. This has consequences in the calculation of the reaction rates with more than a 25% increase at the temperatures of future fusion reactors. This work has been published in Phys. Lett. B.

## New theory of deuteron stripping to bound states and resonances

A. M. Mukhamedzhanov

Production of unstable nuclei close to proton and neutron drip lines has become possible in recent years, making deuteron stripping reactions (d,p) and (d,n) on these nuclei (in inverse kinematics) not only more and more feasible as beam intensity increasing but also a unique tool to study unstable nuclei and astrophysical (n, $\gamma$ ) and (p, $\gamma$ ) processes. The deuteron stripping reactions populating resonance states of final nuclei are important and most challenging part of reactions on unstable nuclei. If for nucleon transfer reactions populating bound states for about fifty years experimentalists used the DWBA, which is now gradually being replaced by more advanced approaches like adiabatic DWBA (ADWBA), coupled reaction channels (CRC) and the coupled channels in Born approximation (CCBA) available in FRESKO code, an adequate theory for transfer reactions to resonance states yet to be developed. There are two main reasons for absence of the practical theory of stripping to resonance states which can be used by experimental groups. First one is the numerical problem of the convergence of the DWBA matrix element when the full transition operator is included. However, it is only a technical problem. The second pure scientific unsolved problem is what spectroscopic information can be extracted from the analysis of transfer reactions populating the resonance states. It was always a temptation to develop the theory of stripping into resonant states which is fully similar to stripping to bound states. The theory of the deuteron stripping into bound and resonance states  $A(d,p)B$  based on the surface formulation of the reactions has been developed. In this approach the reaction amplitude is parameterized in terms of the reduced width amplitudes (asymptotic normalization coefficients (ANCs)) and boundary conditions, i.e. the same parameters, which are used in the conventional R-matrix method for analysis of binary reactions. Thus, new theory leads to generalization of the R-matrix method for stripping reactions. This theory provides a new tool to experimentalists, which allow them to analyze stripping reactions and binary resonance reactions using the same R-matrix parameters. The theory includes continuum discretized coupled channel approach. Different examples are presented.

## Reexamination of the astrophysical S factor for the $\alpha+d \rightarrow {}^6\text{Li}+\gamma$ reaction

A. M. Mukhamedzhanov, L. D. Blokhintsev,<sup>1</sup> and B. F. Irgaziev<sup>2</sup>

<sup>1</sup>*Skobeltsyn Institute of Nuclear Physics, Moscow State University, Moscow, Russia*

<sup>2</sup>*GIK Institute of Engineering Sciences and Technology, Topi, Pakistan*

Recently a new measurement of the  ${}^6\text{Li}$ (A 150 MeV) dissociation in the field of  ${}^{208}\text{Pb}$  has been reported in [1] to study the radiative capture  $\alpha+d \rightarrow {}^6\text{Li}+\gamma$  process. However, the dominance of the nuclear breakup over the Coulomb one prevented from obtaining the information about the  $\alpha+d \rightarrow {}^6\text{Li}+\gamma$  process from the breakup data. The astrophysical  $S_{24}(E)$  factor has been calculated within the  $\alpha$ -d two-body potential model with potentials determined from the fits to the  $\alpha$ -d elastic scattering phase shifts. However, the scattering phase shift itself, according to the theorem of the inverse scattering problem, doesn't provide a unique  $\alpha$ -d bound state potential, which is the most crucial input when calculating the  $S_{24}(E)$  astrophysical factor at astrophysical energies. In this work we emphasize an important role of the asymptotic normalization coefficient (ANC) for  ${}^6\text{Li} \rightarrow \alpha+d$  which controls the overall normalization of the peripheral  $\alpha+d \rightarrow {}^6\text{Li}+\gamma$  process and is determined by the adopted  $\alpha$ -d bound state potential. Since the potential determined from the elastic scattering data fit is not unique, the same is true for the ANC generated by the adopted potential. However, a unique ANC can be found directly from the elastic scattering phase shift, without invoking intermediate potential, by extrapolation the scattering phase shift to the bound state pole [2].

We demonstrate that the ANC previously determined from the  $\alpha$ -d elastic scattering s-wave phase shift in [2] and confirmed by the abinitio calculations [3], gives  $S_{24}(E)$ , which is at low energies about 38% lower than the one reported in [1]. We recalculate also the reaction rates, which are also lower than those obtained in [1]. This paper has been published in Phys. Rev. C.

[1] F. Hammache *et al.*, Phys. Rev. C **82**, 065803 (2010).

[2] L.D. Blokhintsev *et al.*, Phys. Rev. C **48**, 2390 (1993).

[3] P. Navratil and Quaglioni, Phys. Rev. C **83**, 044609 (2011).

## **Unitary correlation in nuclear reaction theory: Separation of nuclear reactions and spectroscopic factors**

A. M. Mukhamedzhanov and A. S. Kadyrov<sup>1</sup>

<sup>1</sup>*ARC Centre for Antimatter-Matter Studies, Curtin University, GPO Box U1987, Perth, WA 6845, Australia*

Future exact many-body theory will allow us to calculate nuclear reactions based on the adopted NN and many-body nuclear potentials. But NN potentials are not observable and there are infinite number of the phase-equivalent NN potentials related via finite-range unitary transformations. We show that asymptotic normalization coefficients, which are the amplitudes of the asymptotic tails of the overlap functions are invariant under finite-range unitary transformations but spectroscopic factors are not. We prove also that the exact amplitudes for the (d,p), (d,pn) and (e,e'p) reactions determining the asymptotic behavior of the exact scattering wave functions in the corresponding channels, in contrast to spectroscopic factors, are invariant under finite-range unitary transformations. Moreover, the exact reaction amplitudes are not parametrized in terms of the spectroscopic factors and nuclear reactions in the exact approach cannot provide a tool to determine spectroscopic factors which are not observable. We call it separation of the exact reaction theory and SFs. This work has been published in Phys. Rev. C.

## Density and temperature of fermions and bosons from quantum fluctuations

Hua Zheng and Aldo Bonasera<sup>1</sup>

<sup>1</sup>*Laboratori Nazionali del Sud, INFN, via Santa Sofia, 62, 95123 Catania, Italy*

In recent years, the availability of heavy-ion accelerators which provide colliding nuclei from a few MeV/nucleon to GeV/nucleon and new and performing  $4\pi$  detectors, has fueled a field of research loosely referred to as Nuclear Fragmentation. Fragmentation experiments could provide information about the nuclear matter properties and constrain the equation of state (EOS) of nuclear matter [1]. Even though a large variety of experimental data and refined microscopic models exist, to date it does not exist a method to determine densities and temperatures reached during the collisions, which takes into account the genuine quantum nature of the system. In this work we discuss some properties at finite temperatures assuming either a classical gas or a quantum system (Fermions or Bosons). We show that at the densities and temperatures of interest the classical approximation is not valid. We base our method on fluctuations estimated from an event-by-event determination of fragments arising from the energetic collision. We also include quadrupole fluctuations to have a direct measurement of densities and temperatures for subatomic systems for which it is difficult to obtain such informations in a direct way. We also suggest a method for calculating an excitation energy which should minimize collective effects and could be applied when a limited information is available, for example if only light cluster are measured. We apply the proposed method to microscopic CoMD approach [2] which includes fermionic statistics.

A method for measuring the temperature was proposed in [3] based on momentum fluctuations of detected particles. A quadrupole  $Q_{xy} = \langle p_x^2 - p_y^2 \rangle$  is defined in a direction transverse to the beam axis (z-axis) to minimize non equilibrium effects and the average is performed, for a given particle type, over events. Such a quantity is zero in the center of mass of the equilibrated emitting source. Its variance is given by the simple formula:

$$\sigma_{xy}^2 = \int d^3p (p_x^2 - p_y^2)^2 f(p) \quad (1)$$

Where  $f(p)$  is the momentum distribution of particles. In [3] a classical Maxwell-Boltzmann distribution of particles at temperature  $T_{cl}$  was assumed which gives  $\sigma_{xy}^2 = \bar{N}4m^2T_{cl}^2$ ,  $m$  is the mass of fragment.  $\bar{N}$  is the average number of particles which could be conveniently normalized to one. In heavy ion collisions, the produced particles do not follow classical statistics thus the correct distribution function must be used in eq. (1). Protons(p), neutrons(n), tritium(t) ect. follow the Fermi-Dirac statistics while, deuterium(d), alpha( $\alpha$ ), ect. should follow the Bose-Einstein statistics. In this work, we will concentrate on fermions and bosons respectively, in particular p and n for fermions and d and  $\alpha$  for bosons which are abundantly produced in the collisions thus carrying important information on the densities and temperatures reached.

For fermions, we use a Fermi-Dirac distribution  $f(p)$  and expanding to  $O(\frac{T}{\epsilon_f})^4$ , where  $\epsilon_f = \epsilon_{f0}(\frac{\rho}{\rho_0})^{\frac{2}{3}} = 36(\frac{\rho}{\rho_0})^{\frac{2}{3}}$  MeV is the Fermi energy of nuclear matter, we get [4]

$$\sigma_{xy}^2 = \bar{N}[\frac{16m^2\epsilon_f^2}{35}(1 + \frac{7}{6}\pi^2(\frac{T}{\epsilon_f})^2 + O(\frac{T}{\epsilon_f})^4)] \quad (2)$$

This result is in evident contrast with the classical one: even at zero T and ground density  $\rho_0$ , quadrupole fluctuations arise from the Fermi motion. The quadrupole fluctuations depend on temperature and density through  $\epsilon_f$ , thus we need more information in order to be able to determine both quantities.

Within the same framework we can calculate the fluctuations of the p, n multiplicity distributions. These are given by [4]:

$$\frac{\langle(\Delta N)^2\rangle}{\bar{N}} = \frac{3}{2} \frac{T}{\epsilon_f} + O\left(\frac{T}{\epsilon_f}\right)^3 \quad (3)$$

Substitute eq. (3) into eq. (2) gives the Fermi energy in terms of quadrupole and multiplicity fluctuations which can be measured in experiments. Knowing the Fermi energy we obtain the quantum temperature from eq. (3).

For bosons, we use a Bose-Einstein distribution  $f(p)$  for a particle of spin  $s$ , and expanding near the critical temperature  $T_c = \frac{2\pi}{[2.612(2s+1)]^{2/3}} \frac{\hbar^2}{m} \rho^{2/3}$  at a given density  $\rho$ , we get [4]:

$$\sigma_{xy}^2 = \bar{N} (2mT)^2 \frac{g_7(1)}{g_3^2(1)} \quad (T < T_c) \quad (4)$$

$$\sigma_{xy}^2 = \bar{N} (2mT)^2 \frac{g_7(z)}{g_3^2(z)} \quad (T > T_c) \quad (5)$$

where the  $g_n(z)$  functions are well studied in the literature [4] and  $z = e^{\mu/T}$  is the fugacity which depends on the critical temperature for Bose condensation and thus on the density of the system and the chemical potential  $\mu$  [4]. The quadrupole fluctuations depend on temperature and density through  $T_c$ , thus we need more information in order to be able to determine both quantities for  $T > T_c$ .

Within the same framework we can calculate the fluctuations of the d,  $\alpha$  multiplicity distributions. These are given by [4]:

$$\frac{\langle(\Delta N)^2\rangle}{\bar{N}} = \left(\frac{T}{T_c}\right)^{3/2} \left[1 + \left(\frac{T}{T_c}\right)^{3/2}\right] \quad (T < T_c) \quad (6)$$

$$\frac{\langle(\Delta N)^2\rangle}{\bar{N}} = 0.921 \frac{\left(\frac{T}{T_c}\right)^3}{\left[1 - \left(\frac{T}{T_c}\right)^{3/2}\right]^2} \quad (T > T_c) \quad (7)$$

Fluctuations are larger than the average value and might diverge near the critical point, eq. (7), in the indicated approximations. Interactions and finite size effects will of course smoothen the divergence [4]. These results are very important and could be used to pin down a Bose condensate.

Two solutions are possible depending whether the system is above or below the critical temperature for a Bose condensate. Below the critical point, eq. (4) can be used to calculate T and then eq. (6) gives the critical temperature and the corresponding density. Above the critical point it is better to estimate the chemical potential which, in the same approximation, is given by:

$$\frac{-\mu}{T} = \frac{1}{2} \frac{1}{\frac{\langle(\Delta N)^2\rangle}{\bar{N}}} \quad (T > T_c) \quad (8)$$

Notice the similarity between eq. (3) and eq. (8), where the Fermi energy is substituted by the chemical potential. From this equation we can estimate the  $g_n$  functions entering eq. (5) and obtain the value of T. Using such a value in eq. (7), gives  $T_c$  and the density  $\rho$ .

To illustrate the strength of our approach we simulated  $^{40}\text{Ca}+^{40}\text{Ca}$  heavy ion collisions at fixed impact parameter  $b=1$  fm and beam energies  $E_{\text{lab}}/A$  ranging from 4 MeV/A up to 100 MeV/A. Collisions were followed up to a maximum time  $t = 1000$  fm/c in order to accumulate enough statistics. Particles emitted at later times (evaporation) could affect somehow the results and this might be important especially at the lowest beam energies. The choice of central collisions was dictated by the desire to obtain full equilibration. This however, did not occur especially at the highest beam energies due to a partial transparency for some events. For this reason the quadrupole in the transverse direction, eq. (1), was chosen. Furthermore, in order to correct for collective effects as much as possible, we defined a ‘thermal’ energy as:

$$\langle \frac{E_{\text{th}}}{A} \rangle = \frac{E_{\text{cm}}}{A} - \left[ \langle \frac{E_{\text{object}}}{N_{\text{object}}A_{\text{object}}} \rangle - \frac{3}{2} \langle \frac{E_{\text{object xy}}}{N_{\text{object}}A_{\text{object}}} \rangle \right] - Q_{\text{value}} \quad (9)$$

where  $\langle \frac{E_{\text{object}}}{N_{\text{object}}A_{\text{object}}} \rangle$  and  $\langle \frac{E_{\text{object xy}}}{N_{\text{object}}A_{\text{object}}} \rangle$  are the average total and transverse kinetic energies per particle of object  $A_{\text{object}}$ , eg.  $A_{\text{object}}=1$  for proton,  $A_{\text{object}}=4$  for  $\alpha$ .  $Q_{\text{value}} = \frac{N_{\text{object}}}{N_{\text{object}}} 8 \text{ MeV}$ . 8 MeV is the average binding energy of a nucleon,  $N_{\text{object}}$  the total objects of the system and  $\overline{N_{\text{object}}}$  the average number of objects emitted at each beam energy. For a completely equilibrated system, the transverse kinetic energy (times 3/2) is equal to the total kinetic energy and the term in the square bracket cancels.

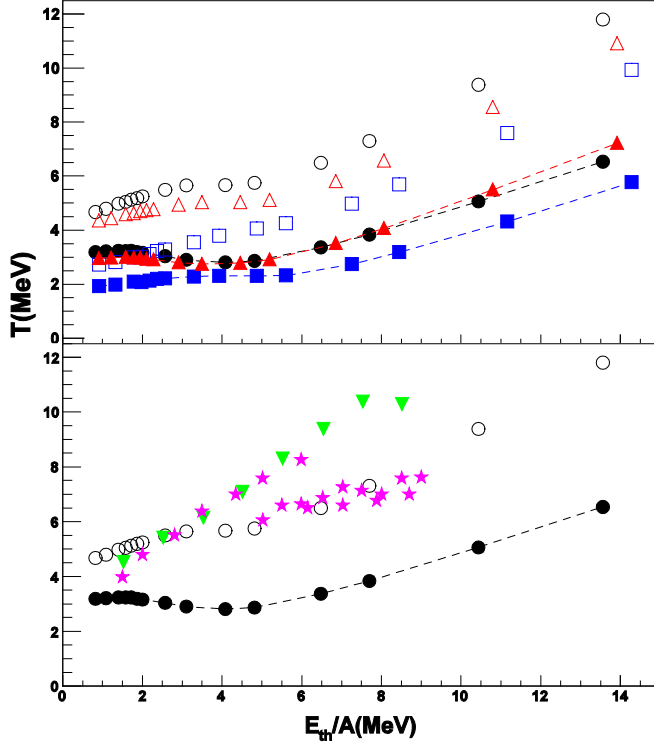


**FIG. 1.** Temperature versus thermal energy per particle derived from quantum fluctuations (full symbols joined by dashed lines) compared to the classical case (open symbols). (Top) Circles refer to protons, squares to neutrons and triangles to protons and neutrons. (Bottom) Same as above for protons. Data: down triangles from classical quadrupole fluctuations [3], star symbols from particle ratios [5].

All the center of mass energy,  $\frac{E_{cm}}{A}$ , is converted into thermal energy (plus the  $Q_{value}$ ). In the opposite case, say an almost complete transparency of the collision, the transverse energy would be negligible and the resulting thermal energy would be small. Our approximation will account for some corrections, and this will become more and more exact when many fragment types are included in eq. (9) [3].

In fig. 1 (top) we plot the estimated temperatures for fermions at various ‘thermal’ energies both for the quantum (full symbols) and classical approximations (open symbols). As we see the quantum case is systematically lower than the classical one. We also notice a difference if the  $T$  are estimated from the proton distributions (circles) or neutrons (squares) or the sum of the two (triangles). This is clearly a Coulomb effect which gets smaller as expected at higher energies.

In fig. 2 we plot the ratio  $\frac{T}{\epsilon_f}$  directly obtained from eq. (3), versus reduced density which is obtained from eqs. (2) and (3). The highest  $\frac{T}{\epsilon_f}$  corresponds to the lowest beam energy as well and gives the lowest density, especially for the neutrons case. The top energy scale in the figure is for illustration purposes only and it refers to the neutron case. In fact at the same beam energy, p and pn might measure a different  $\frac{T}{\epsilon_f}$  ratio respect to n. This result might be surprising at first, but it simply tells us that at the lowest energies nucleons from the surface of the colliding nuclei come into contact. Those nucleons are located in a low density region, especially neutrons which do not feel the Coulomb field. Thus this is the average density explored by the participant nucleons. With increasing beam energy, the overlapping region

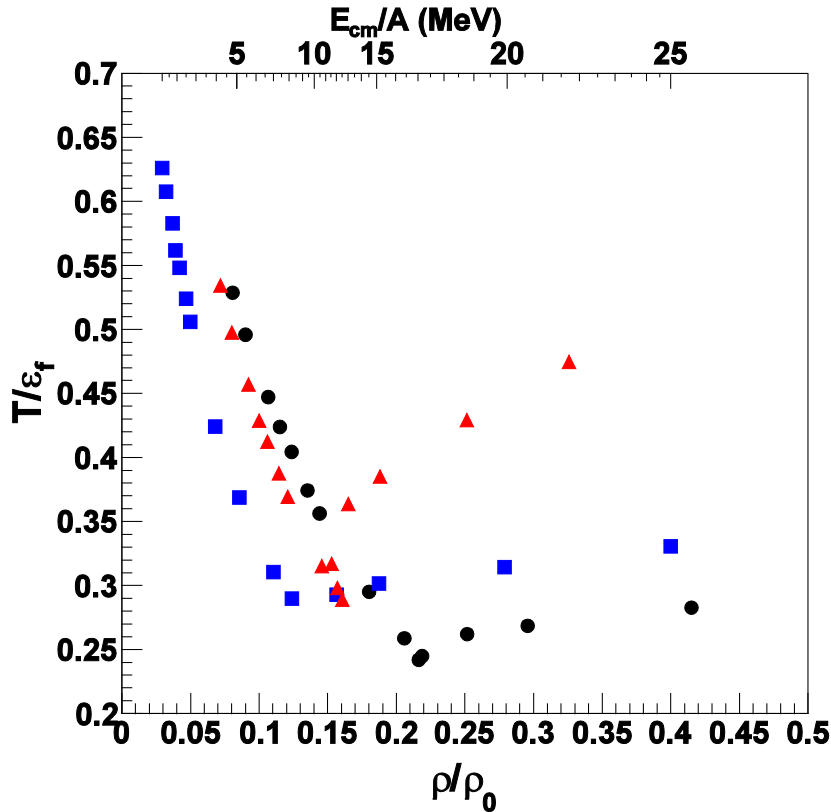


**FIG. 2.** Temperature divided the Fermi energy versus density normalized to the ground state one derived from quantum fluctuations, eqs. (1)-(3). Symbols as in Fig. 1. The top energy scale refers to the neutron case.

increases and more and more fermions are emitted. At about  $E_{\text{lab}}/A \approx 20 \text{ MeV}/A$  a large number of nucleons are excited and the emission from surface becomes a volume emission. It is important to stress that the ratio plotted in fig. 2 is always smaller than one which confirms the approximations used in eqs. (1)-(3).

In fig. 3 we plot the reduced variances versus excitation energy per particle. The Boson results are given by the full symbols, top panel. As we see in the figure,  $\alpha$  normalized fluctuations are generally larger than d-fluctuations. As we will show below, this implies that those particles might explore different regions of densities and temperatures. In both cases, fluctuations are large and, in some cases, above Poissonian for  $\alpha$ 's. In order to understand if a Bose condensate occurs in the model (and in the future in experiments) it is instructive to compare the Boson normalized fluctuations to those of Fermions. In fig. 3 (bottom panel), normalized Fermion fluctuations are given. As we see the normalized fluctuations of p and n are much smaller than 1 at variance with the Boson case, which would suggest a condensate. However, heavier Fermion clusters such as  ${}^3\text{He}$  and tritons, display fluctuations larger than d and smaller than  $\alpha$ . These facts are important to understand what is happening in the model and eventually search for an experimental confirmation. Notice in fig. 3 the occurrence of a minimum at a similar excitation energy for p, n and d but not for heavier clusters. This will have an effect on the EOS as we will show below.

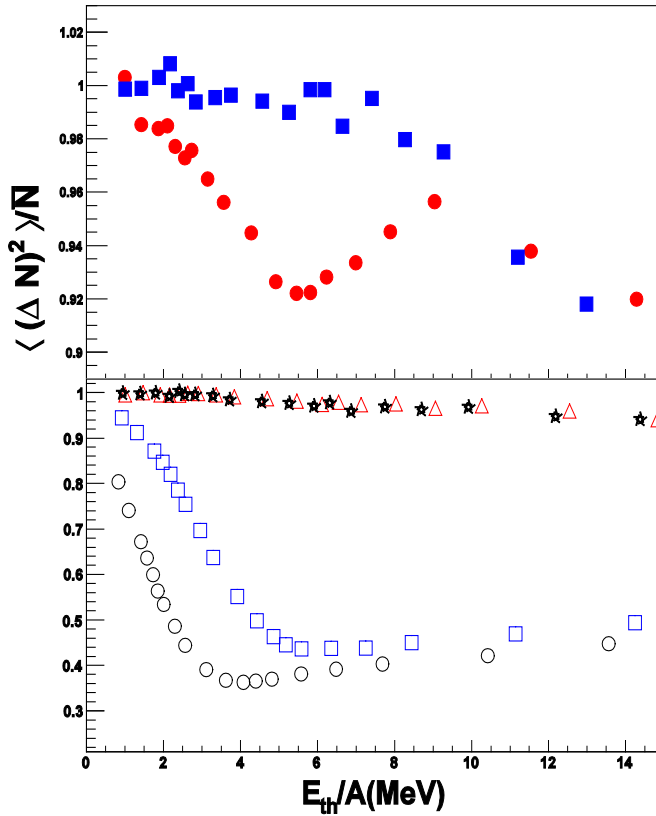


**FIG. 3.** Normalized variance versus excitation energy per nucleon. (Top panel) CoMD results for d (full circles) and  $\alpha$  particles (full squares). For comparison the normalized fluctuations for fermions (bottom panel). (Open) Circles, squares and triangles refer to protons, neutrons and tritons, stars refer to  ${}^3\text{He}$ . Notice the change of scales in the two panels.

It is interesting to discuss the densities ‘seen’ by the different Bosons during the reaction. A plot of density (divided by then ground state density) versus temperature (divided by the critical temperature for a condensate) is given in fig. 4. Notice the peculiar behavior of d and  $\alpha$  clusters. While the latter are formed at a constant reduced density but at different densities for each beam energy, the deuterons are formed always at a very small (constant) density but at different reduced temperatures. As we noticed above two effects are at play. The first is that there is no Pauli blocking for nucleons inside the clusters, the second is the different binding energies. Since d are over bound in the model (about 7 MeV) we expect that even smaller densities will be ‘seen’ in the data, the opposite we expect for  $\alpha$ . These features remind of Mott transitions and in particular suggest that different particle types might be sensitive to different regions of the nuclear EOS as already noticed for Fermions [6, 7].

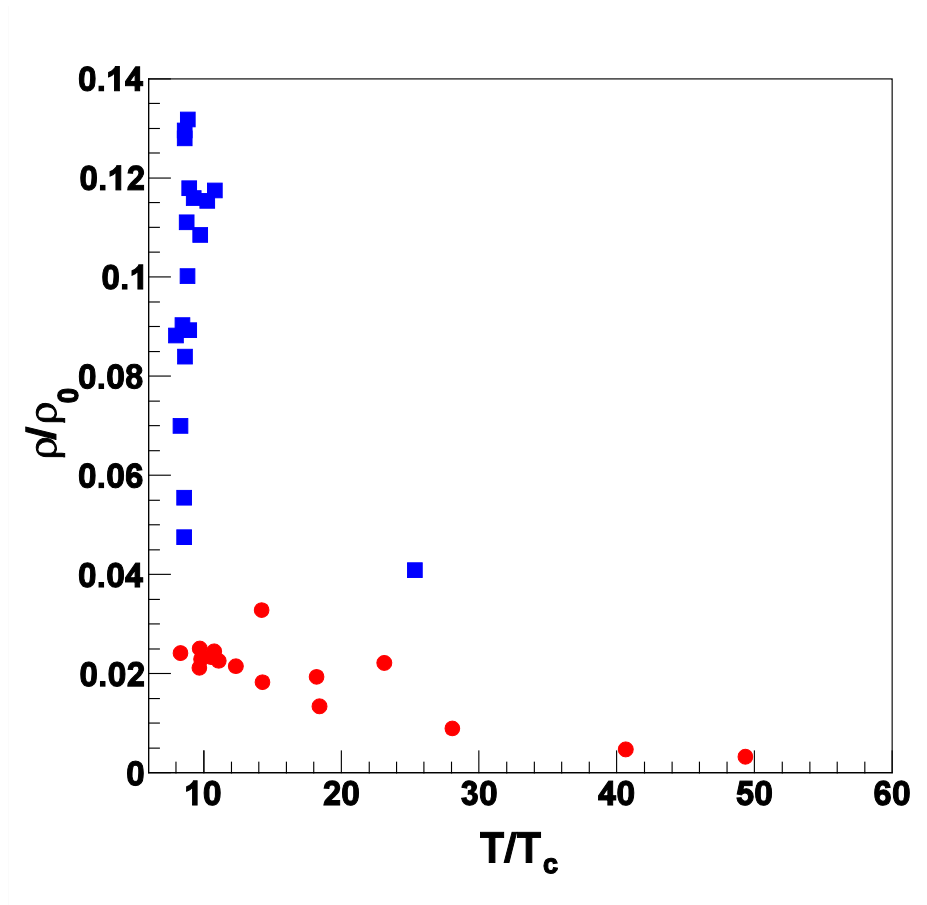


FIG. 4. Reduced density versus reduced temperature for Bosons. Symbols as in fig. 3.

In conclusion, we have addressed [6, 8] a general method for deriving densities and temperatures of fermions and bosons. In the framework of Constrained Molecular Dynamics model, which includes Fermi Statistics, we have discussed collisions of heavy ions below 100 MeV/A and obtained densities and temperatures at each bombarding energy. The results we have obtained here in a model case confirm that the classical approximation is unjustified. We have seen in this work that different particles like (p, n, d,

$\alpha$ ) explore different density and temperature regions. Open problems such as Mott transition, Bose condensate, pairing ect. in low density matter might be addressed through a detailed study of the EOS.

- [1] L.P. Csernai, *Introduction to Relativistic Heavy Ion Collisions*, (Wiley, New York, 1994).
- [2] A. Bonasera, Phys. Rev. C **62**, (R) (2000); M. Papa, T. Maruyama, A. Bonasera, Phys. Rev. C **64** 024612 (2001); A. Bonasera, Nucl. Phys. **A681**, 64c (2001); S. Terranova, A. Bonasera, Phys. Rev. C **70**, 024906 (2004); S. Terranova, D. M. Zhou, A. Bonasera, Eur. Phys. J. A **26**, 333 (2005).
- [3] S. Wuenschel *et al.*, Nucl. Phys. **A843**, 1 (2010).
- [4] L. Landau, F. Lifshits, *Statistical Physics*, (Pergamon, New York, 1980); K. Huang, *Statistical Mechanics*, second edition, (John Wiley and Sons, New York, 1987).
- [5] J.B. Natowitz *et al.*, Phys. Rev. C **65**, 034618 (2002).
- [6] H. Zheng and A. Bonasera, Phys. Lett. B **696**, 178 (2011).
- [7] J.B. Natowitz *et al.*, Phys. Rev. Lett. **104**, 202501(2010).
- [8] H. Zheng and A. Bonasera, arXiv: 1105. 0563[nucl-th]

## Charmonium production and elliptic flow in relativistic heavy ion collisions

T. Song, C. M. Ko, S. H. Lee,<sup>1</sup> and J. Xu

<sup>1</sup>*Institute of Physics and Applied Physics, Yonsei University, Seoul 120-749, Korea*

We have studied the nuclear modification factor  $R_{AA}$  and elliptic flow  $v_2$  of  $J/\psi$  in relativistic heavy ion collisions [1] in a two-component model [2] that includes contributions from both initial hard nucleon-nucleon scattering and regeneration in the quark-gluon plasma. For the expansion dynamics of produced hot, dense matter, we have introduced a schematic fireball model with its transverse acceleration determined from the pressure gradient inside the fireball and azimuthally anisotropic expansion parameterized to reproduce measured  $v_2$  of light hadrons. We have assumed that light hadrons freeze out at the temperature of 120 MeV while charmonia freeze out at 160 MeV, similar to the kinetic and chemical freeze-out temperatures in the statistical model, respectively. For the properties of charmonia in the quark-gluon plasma, we have used the screening mass between their charm and anticharm quarks and their dissociation cross sections given by the perturbative QCD (pQCD) calculations in the leading order and up to the next-to-leading order, respectively [3]. For the relaxation time of charm and anticharm quarks in the quark-gluon plasma, we have also used the one calculated in the leading-order pQCD [2]. Modeling the effect of higher-order corrections in pQCD by introducing multiplicative factors to the dissociation cross section of charmonia and the elastic scattering cross section of charm and anticharm quarks, we have found that this effect is small for the  $R_{AA}$  of  $J/\psi$  as they suppress the number of initially produced  $J/\psi$  but enhance the number of regenerated ones as shown in the left window of Fig. 1. The higher-order corrections increase, however, the  $v_2$  of  $J/\psi$  as shown in the

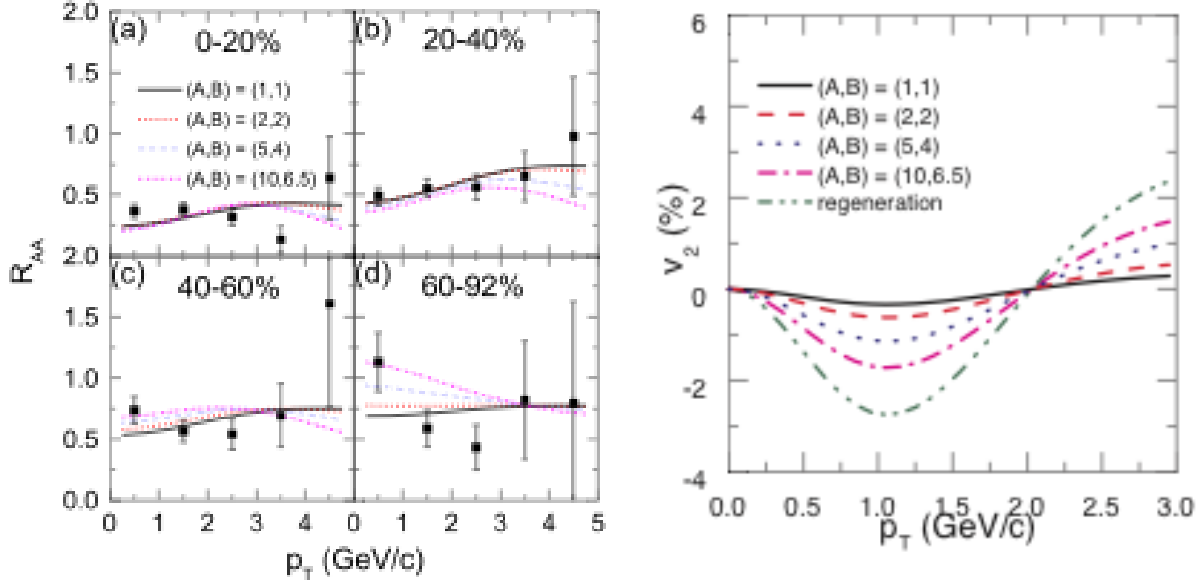


**FIG. 1.** Charmonium nuclear modification factor  $R_{AA}$  in collisions of 0-20% (a), 20-40% (b), 40-60% (c) and 60-92% (d) centralities (left window) and elliptic flow  $v_2$  (right window) as functions of transverse momentum for different multiplicative factors  $(A,B) = (1,1)$ ,  $(2,2)$ ,  $(5,4)$  and  $(10,6.5)$  to the  $J/\psi$  dissociation and charm quark scattering cross sections.

right window of Fig. 1. Our results suggest that the  $v_2$  of  $J/\psi$  can play an important role in discriminating between  $J/\psi$  production from initial hard collisions and from regeneration in the quark-gluon plasma.

[1] T. Song, C.M. Ko, S.H. Lee, and J. Xu, Phys. Rev. C **83**, 014914 (2011).

[2] T. Song, W. Park, and S.H. Lee, Phys. Rev. C **81**, 034914 (2010).

[3] Y. Park, K.I. Kim, T. Song, S.H. Lee, and C.Y. Wong, Phys. Rev. C **76**, 044907 (2007).

## Density matrix expansion for the isospin- and momentum-dependent MDI interaction

J. Xu and C. M. Ko

Using the density matrix expansion [1,2], we have obtained an effective zero-range Skyrme-like interaction with density-dependent parameters [3] from the finite-range exchange interaction of the isospin- and momentum-dependent MDI interaction [4] that has been extensively used in studying isospin effects in intermediate-energy heavy-ion collisions [5] as well as the properties of hot nuclear matter [6] and neutron star matter [7]. We have then used the resulting interaction to determine the transition density and pressure at the inner edge of neutron star crusts based on the linearized Vlasov equation for the neutron star matter. From the latest constraint  $L = 58 \pm 18$  MeV on the density slope of the nuclear symmetry energy [8], the transition density and pressure are constrained within  $0.050 \text{ fm}^{-3} < \rho_t < 0.071 \text{ fm}^{-3}$  and  $0.12 \text{ MeV/fm}^3 < P_t < 0.31 \text{ MeV/fm}^3$  for  $T=0$  MeV, and  $0.038 \text{ fm}^{-3} < \rho_t < 0.070 \text{ fm}^{-3}$  and  $0.06 \text{ MeV/fm}^3 < P_t < 0.30 \text{ MeV/fm}^3$  for  $T=1$  MeV as shown in Fig. 1. Although the transition density is smaller at fixed  $L$  compared to previous results, which leads to a smaller crustal fraction of the moment of inertia for neutron stars and an even stricter constraint on the masses and radii of neutron stars, the upper limit values of  $\rho_t$  and  $P_t$  are larger because of the smaller values of  $L$ . The final constraint on the neutron star mass-radius relation is expected to be similar to that in the previous work.

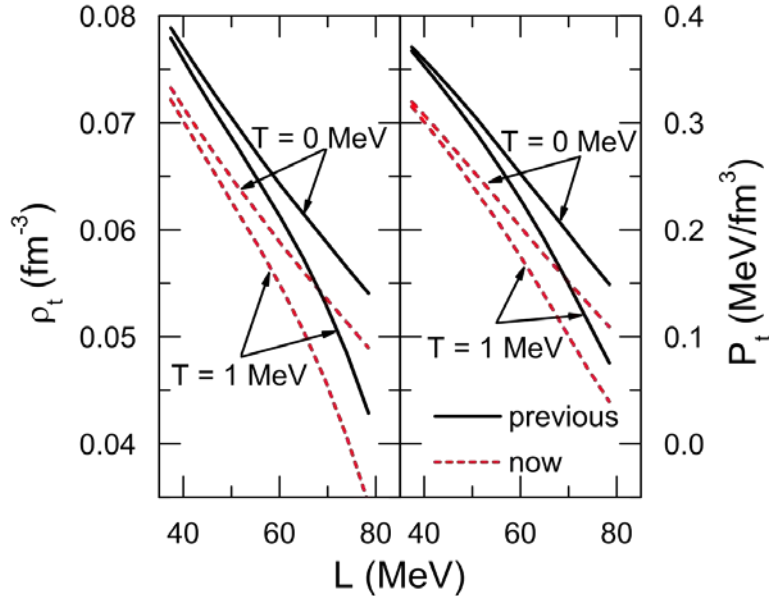


**FIG. 1.** The transition density  $\rho_t$  and pressure  $P_t$  at the inner edge of neutron star crust as functions of the density slope parameter  $L$  of the nuclear symmetry energy for  $T=0$  MeV and  $T=1$  MeV from the MDI interaction [4] (solid lines) and from its density matrix expansion (dashed lines) [3].

[1] J.W. Negele and D. Vautherin, Phys. Rev. C **5**, 1472 (1972).

- [2] D.W. Sprung, M. Vallieres, X. Campi, and C.M. Ko, Nucl. Phys. **A253**, 1 (1973).
- [3] J. Xu and C.M. Ko, Phys. Rev. C **82**, 044311 (2010).
- [4] C.B. Das, S. Das Gupta, C. Gale, and B.A. Li, Phys. Rev. C **67**, 034611 (2003).
- [5] L.W. Chen, C.M. Ko, and B.A. Li, Phys. Rev. Lett. **94**, 032701 (2005).
- [6] J. Xu, L.W. Chen, B.A. Li, and H.R. Ma, Phys. Rev. C **77**, 014302 (2008).
- [7] J. Xu, L.W. Chen, B.A. Li, and H.R. Ma, Phys. Rev. C **79**, 035802 (2009).
- [8] L.W. Chen, C.M. Ko, B.A. Li, and J. Xu, Phys. Rev. C **82**, 024321 (2010).

## Dilepton production in schematic causal viscous hydrodynamics

T. Song, K. C. Han, and C. M. Ko

We have derived a set of schematic equations from the causal viscous hydrodynamics of Israel-Stewart for central relativistic heavy-ion collisions by assuming that not only the energy density, pressure and entropy density but also the azimuthal and space-time rapidity components of the shear tensor are uniform in the produced fire-cylinder [1]. Solving these equations using the massive quasi-particle model for the equation of state of the quark-gluon plasma (QGP) and the resonance gas model for that of the hadronic matter, we have found that the shear viscosity slightly delays the cooling of produced hot matter and enhances somewhat its transverse expansion. Including the shear viscosity also significantly increases the particle distributions at high transverse momentum ( $p_T$ ), compared with those in the ideal hydrodynamics. Using this model, we have investigated thermal dilepton production in relativistic heavy-ion collisions by including contributions from the dominant quark-antiquark and pion-pion annihilations as well as rho meson decay after freeze out. Because of the viscous effect, the dilepton  $p_T$  spectrum is enhanced at high  $p_T$  as shown in the left window Fig. 1. For the invariant mass spectrum of dileptons, we have found that it differs very little from that in the ideal hydrodynamics. We have also studied the effect of viscosity on the transverse mass scaling of thermal dileptons from the QGP, i.e., the yield is independent of  $p_T$  for fixed dilepton transverse mass  $M_T = (M_2 + p_T^2)^{1/2}$ , that has been previously predicted in the ideal hydrodynamics with massless quarks and gluons [2]. As shown in the right window of Fig. 1, our results show that the  $M_T$  scaling still holds in the ideal hydrodynamics even if the QGP is composed of massive quarks and gluons resulting from their strong couplings, but is broken in the viscous hydrodynamics due to the enhancement in the number density of quarks and antiquarks at high  $p_T$  by the viscous effect.

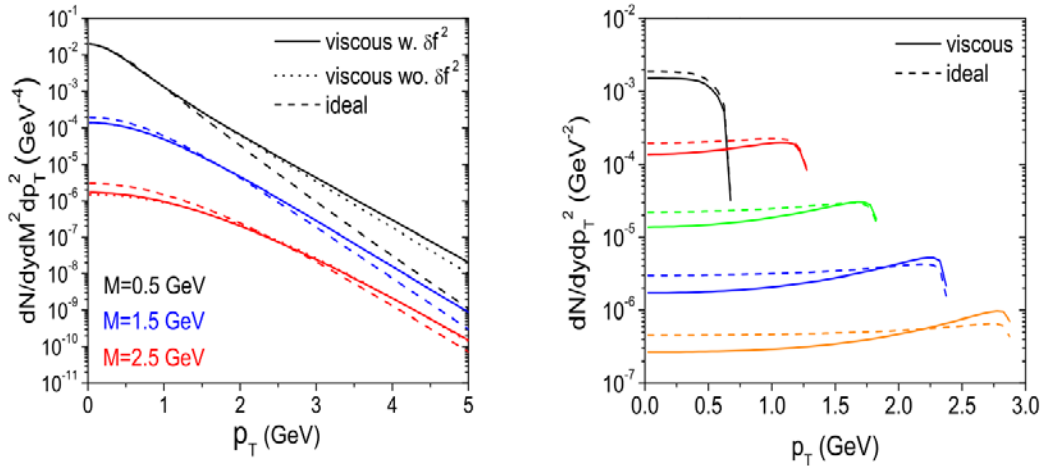


**FIG. 1.** Left window: Dilepton transverse momentum spectra from viscous (solid line) and ideal hydrodynamics (dashed line). Right window: Transverse momentum dependence of dileptons from QGP with transverse mass  $M_T = 1, 1.5, 2, 2.5$  and  $3$  GeV from top to bottom. Dashed and solid lines are, respectively, from ideal and viscous hydrodynamics.

- [1] T. Song, K.C. Han, and C.M. Ko, Phys. Rev. C **83**, 024904 (2011).
- [2] M. Asakawa, C.M. Ko, and P. Levai, Phys. Rev. Lett. **70**, 398 (1993).

## Effects of triangular flow on di-hadron azimuthal correlations in relativistic heavy ion collisions

J. Xu and C. M. Ko

We have investigated [1] the di-hadron azimuthal angular correlations triggered by emitted jets for Au+Au collisions at  $\sqrt{s_{NN}}=200$  GeV and impact parameter  $b=8$  fm in a multiphase transport (AMPT) model with string melting [2]. Although the total di-hadron correlations show only a single away-side peak besides a peak at the near side, a double peak structure appears at the away side after the subtraction of the background correlations due to the hadron elliptic flow as shown in the left window of Fig. 1. We have found that both the near-side peak and away-side double peaks in the di-hadron correlations are sensitive to the hadron triangular flow as they are enhanced (suppressed) when we only consider events of large (small) hadron triangular flow. Moreover, the away-side double peaks change into a single peak with broad shoulders on both sides after the subtraction of background correlations due to both hadron elliptic and triangular flows as shown in the right window of Fig. 1. After further subtracting background correlations due to anisotropic flow up to the 5th order, the away side of the di-hadron correlations becomes essentially a single peak. Although other effects, such as jet deflections and Mach cone shock waves [3], on di-hadron correlations are appreciable in central collisions, our study indicates that the away-side double peaks may be dominated by the triangular flow in mid-central collisions.

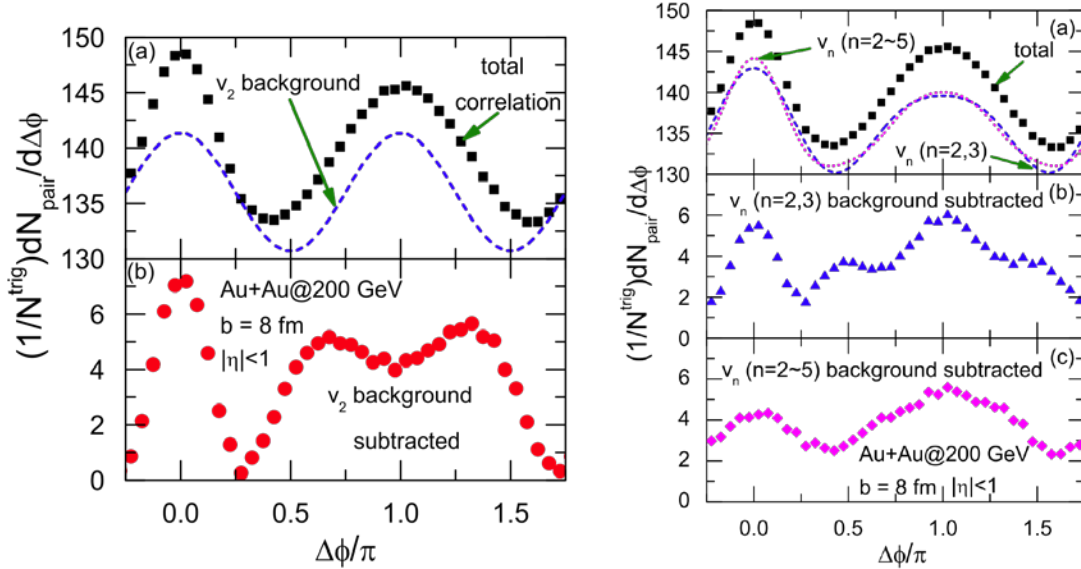


**FIG. 1.** Left window: Di-hadron azimuthal angular correlations per trigger particle before (panel (a)) and after (panel (b)) subtracting background correlations due to the hadron elliptic flow shown by the dashed line in panel (a). Right window: Same as left window before (panel (a)) and after subtracting background correlations due to both hadron elliptic and triangular flows (panel (b)) shown by the dashed line in panel (a) and due to anisotropic flows up to the 5th order (panel (c)) shown by the dotted line in panel (a).

[1] J. Xu and C.M. Ko, Phys. Rev. C **83**, 021903(R) (2011).

[2] Z.W. Lin, C.M. Ko, B.A. Li, B. Zhang, and S. Pal, Phys. Rev. C **72**, 064901 (2005).

[3] G.L. Ma and X.N. Wang, Phys. Rev. Lett. **106**, 162301 (2011).

## Identifying multiquark hadrons from heavy ion collisions

S. Cho,<sup>1</sup> T. Furumoto,<sup>2,3</sup> T. Hyodo,<sup>4</sup> D. Jido,<sup>2</sup> C. M. Ko, S. H. Lee,<sup>1</sup> M. Nielsen,<sup>5</sup>  
A. Ohnishi,<sup>2</sup> T. Sekihara,<sup>2,6</sup> S. Yasui,<sup>7</sup> and K. Yazaki<sup>2,3</sup>

<sup>1</sup>*Institute of Physics and Applied Physics, Yonsei University, Seoul 120-749, Korea*

<sup>2</sup>*Yukawa Institute for Theoretical Physics, Kyoto University, Kyoto 606-8502, Japan*

<sup>3</sup>*RIKEN Nishina Center, Hirosawa 2-1, Wako, Saitama 351-0198, Japan*

<sup>4</sup>*Department of Physics, Tokyo Institute of Technology, Meguro 152-8551, Japan*

<sup>5</sup>*Instituto de Fisica, Universidade de Sao Paulo, C.P. 66318, 05389-970 Sao Paulo, SP, Brazil*

<sup>6</sup>*Department of Physics, Graduate School of Science, Kyoto University, Kyoto 606-8502, Japan*

<sup>7</sup>*Institute of Particle and Nuclear Studies, High Energy Accelerator Research Organization (KEK), 1-1, Oho, Ibaraki 305-0801, Japan*

Using the coalescence model for hadron production [1], we have found that the yields of hadrons produced in heavy ion collisions are strongly affected by their internal structures [2]. As shown in Fig. 1, for the ratios of hadron yields at RHIC in the coalescence model to those in the statistical model [3], compared to hadrons with normal quark numbers, we have found that the yields of exotic hadrons are typically an order of magnitude smaller when they are compact multi-quark states and a factor of two or more larger when they are loosely bound hadronic molecules. We have further found that due to the appreciable numbers of charm and bottom quarks produced in heavy ion collisions at RHIC and even larger numbers expected at LHC [4], some of the newly proposed heavy exotic states such as  $\bar{D}N$  and  $\bar{D}NN$  [5] could be produced and realistically measured in these experiments. Studying hadron production in relativistic heavy ion collisions thus provides a promising new method to resolve the longstanding challenge in hadron physics of identifying hadronic molecular states and/or hadrons with multi-quark components either with or without exotic quantum numbers.

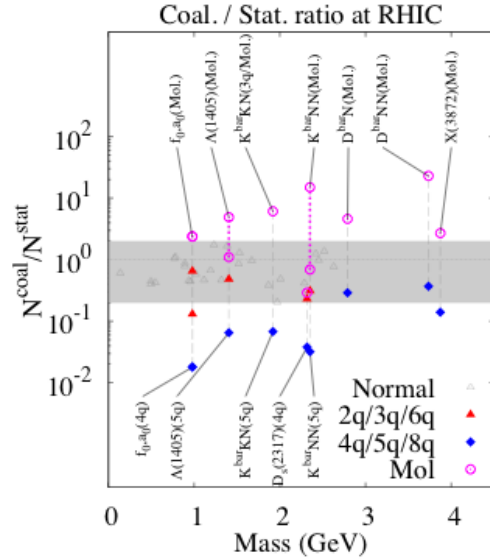


**FIG. 1.** Ratios of hadron yields at RHIC in the coalescence model to those in the statistical model for normal hadrons (gray band), hadronic molecules (above gray band), and multi-quark states (below grey band).

[1] V. Greco, C.M. Ko, P. Levai, Phys. Rev. Lett. **90**, 202302 (2003).

[2] S. Cho, T. Furumoto, T. Hyodo, D. Jido, C.M. Ko, S.H. Lee, M. Nielsen, A. Ohnishi, T. Sekihara, S. Yasui, and K. Yazaki, Phys. Rev. Lett. **106**, 212001 (2011).

[3] A. Andronic, P. Braun-Munzinger, and J. Stachel, Nucl. Phys. **A772**, 167 (2006).

- [4] B.W. Zhang, C.M. Ko, and W. Liu, Phys. Rev. C **77**, 024901 (2008).  
[5] S. Yasui and K. Sudoh, Phys. Rev. D **80**, 034008 (2009).

## Pb-Pb collisions at $\sqrt{s_{NN}} = 2.76$ TeV in a multiphase transport model

J. Xu and C. M. Ko

We have studied [1] the multiplicity and elliptic flow of charged particles produced in Pb-Pb collisions at center of mass energy  $\sqrt{s_{NN}} = 2.76$  TeV from the Large Hadron Collider in a multiphase transport (AMPT) model [2]. With the standard parameters in the HIJING model [3], which is used as initial conditions for subsequent partonic and hadronic scatterings in the AMPT model, the resulting multiplicity of final charged particles at mid-pseudorapidity is consistent with the experimental data measured by the ALICE Collaboration as shown in the left window of Fig. 1. This value is increased by about 25% if we turn off the final-state partonic and hadronic scatterings. Because of final-state scatterings, particular those among partons, the final elliptic flow of charged hadrons is also consistent with the ALICE data as shown in the right window of Fig. 1, if we use a smaller but more isotropic parton scattering cross section than previously used in the AMPT model for describing the charged hadron elliptic flow in heavy ion collisions at the Relativistic Heavy Ion Collider. We have further found that the transverse momentum spectra of charged particles as well as the centrality dependence of their multiplicity density and the elliptic flow are also in reasonable agreement with the ALICE data. Moreover, we have made predictions on the multiplicities, transverse momentum spectra and elliptic flows of identified hadrons such as protons, kaons and pions.

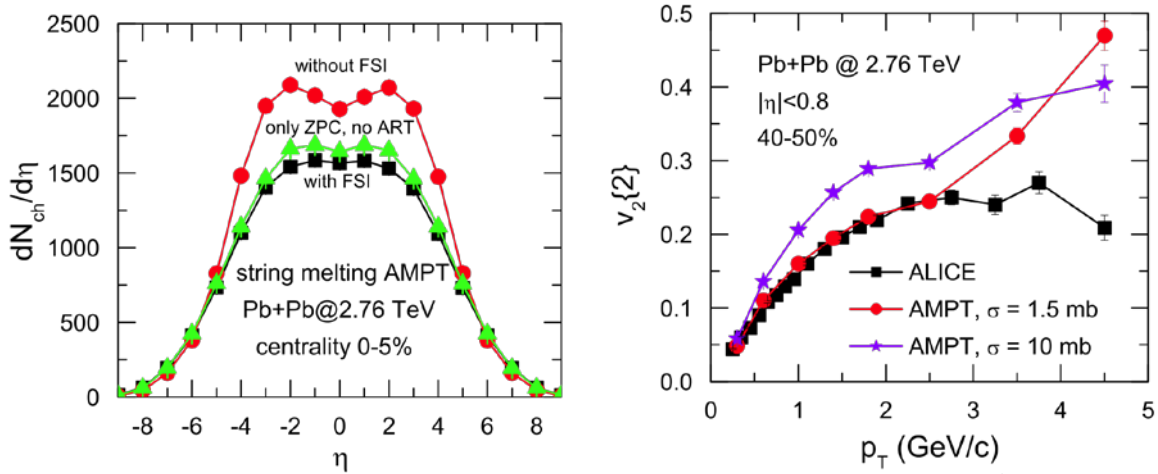


**FIG. 1.** Left window: Pseudorapidity distribution of charged particles in Pb-Pb collisions at  $\sqrt{s_{NN}} = 2.76$  TeV and centrality of 0-5% from the AMPT model with both final-state partonic and hadronic scatterings (filled squares), with only partonic scatterings (filled triangles), and without final-state interactions (filled circles). Right window: Transverse momentum dependence of the elliptic flow obtained from the two-particle cumulant method for charged particles in the same reaction as in the left window at 40-50% centrality from the AMPT model with string melting using a parton scattering cross section of 1.5 mb (filled circles) or 10 mb (filled stars). Corresponding experimental data from Ref.[4] are shown by filled squares.

[1] J. Xu and C.M. Ko, Phys. Rev. C **83**, 034904 (2011).

[2] Z.W. Lin, C.M. Ko, B.A. Li, B. Zhang, and S. Pal, Phys. Rev. C **72**, 064901 (2005).

[3] X.N. Wang and M. Gyulassy, Phys. Rev. D **44**, 3501 (1991).

[4] K. Amodt *et al.* (ALICE Collaboration), Phys. Rev. Lett. **105**, 252302 (2010).

## Determining the proton and neutron transition matrix elements from Coulomb-nuclear interference in hadron inelastic scattering

S. Shlomo, M. R. Anders, and M. R. D. Rodrigues

Experimental determination of nuclear transition strengths provides sensitive test on nuclear structure calculations. Measurements of the lifetimes and electromagnetic excitations of nuclear states lead to quite accurate values for the proton multipole matrix element  $M_p$ , which is related to the reduced electric transition probability by  $B(EL) = M_p^2$ . Excitations of nuclear states by hadron inelastic scattering allows us to study the isospin character of the transition and deduce the neutron multipole matrix element  $M_n$ , as well as  $M_p$ . This is done by varying the experimental parameters, so that a significant interference between the nuclear and Coulomb excitations occurs, and studying the effect of the nuclear-Coulomb interference on the angular distribution of the excitation cross section. We note that the Coulomb interaction between the probe and the target nucleus contributes to both the isoscalar and isovector transitions. Similarly, for a probe with isospin  $T > 0$ , such as a proton, the nuclear interaction also contributes to both isoscalar and isovector transitions. Using an isoscalar probe (with  $T = 0$ ), such as deuteron (d), alpha particle ( $\alpha$ ) and  ${}^6\text{Li}$ , to investigate isoscalar transitions, one exploits the destructive interference between the nuclear and the Coulomb amplitudes and thereby extract the values of  $M_p$  and  $M_n$  and their ratio  $M_n/M_p$ . Note that for a target nucleus with different neutron and proton density distributions, the nuclear interaction due to an isoscalar probe also contributes to an isovector transition.

In this work we consider the excitation of low lying isoscalar multipole states, such as the  $2^+$  and  $3^-$ , excited by the isoscalar probes d,  $\alpha$  and the  ${}^6\text{Li}$  nucleus. In particular, we take a closer look at the recent analysis of experimental data on the excitation cross sections of the isoscalar low lying  $2^+$  and  $3^-$  in the isotopes of Ge, Mo, Ru, and Pd within the distorted wave Born approximation (DWBA). The analyses of these cross sections were carried out by employing the deformed potential (DP) model resulting with values of  $M_n/M_p$  which are significantly smaller than the corresponding  $N/Z$  expected from the simplified collective model. We reanalyze [1] these data within the deformed potential (DP) model and within the implicit folding model (IFM) employing realistic neutron and proton density radial moments and discuss the sensitivity of the results to model assumptions. We note that the folding model approach [FM] to the evaluation of optical potentials and transition potentials is quite successful in describing hadron (h)-nucleus scattering. The main advantage of this approach is that it provides a direct link to the description of h particle scattering reactions based on ground state nucleon density and transition density.

[1] S. Shlomo, M.R. Anders, and M.R. D. Rodrigues, in preparation

## Isoscalar and isovector giant resonances in $^{40}\text{Ca}$ and $^{48}\text{Ca}$

M. R. Anders, S. Shlomo, T. Sil,<sup>1</sup> D. H. Youngblood, Y.-W. Lui, and Krishichayan

<sup>1</sup>*Indian Institute of Information Technology Design and Manufacturing, Kancheepuram,  
Chennai 600 036, Tamil Nadu, India.*

The study of collective modes in nuclei has been the subject of extensive theoretical and experimental studies during several decades, since it contributes significantly to our understanding of bulk properties of nuclei, their non-equilibrium properties and properties of the nuclear force. Of particular interest is the equation of state (EOS), an important ingredient in the study of properties of nuclei at and away from stability, structure and evolution of compact astrophysical objects, such as neutron stars and core-collapse supernovae, and of heavy-ion collisions. To extend our knowledge of the EOS beyond the saturation point of the symmetric NM (SNM), an accurate value of the NM incompressibility coefficient  $K_{NM}$  is needed. An accurate value of the density dependence of the symmetry energy coefficient,  $J$ , is needed for the EOS of asymmetric NM. In this work we consider the high sensitivity of the strength function distributions of giant resonances to bulk properties of NM, such as  $K_{NM}$  and  $J$ . It is well known that the energies of the compression modes, the isoscalar giant monopole resonance (ISGMR) and isoscalar giant dipole resonance (ISGDR), are very sensitive to the value of  $K_{NM}$ . Also the energies of the isovector giant resonances, in particular, the isovector giant dipole resonance (IVGDR), are sensitive to the density dependence of  $J$ , commonly parameterized in terms of the quantities  $L$  and  $K_{sym}$ , which are directly related to the derivatives and the curvature of  $J$  at the saturation density. Furthermore, information on the density dependence of  $J$  can also be obtained by studying the isotopic dependence of strength functions, such as the difference between the strength functions of  $^{40}\text{Ca}$  and  $^{48}\text{Ca}$ . We note that the value of the neutron-proton asymmetry parameter  $\delta = (N-Z)/A$  increases from  $^{40}\text{Ca}$  to  $^{48}\text{Ca}$  by a value of 0.167 which is significantly larger than the change of 0.087 between  $^{112}\text{Sn}$  and  $^{124}\text{Sn}$ .

In this work we adopt the microscopic approach of fully self consistent Hartree-Fock (HF) based random phase approximation (RPA), with specific interactions. It is important to note that ground state properties of nuclei can be well described by HF approximation, using an effective nucleon-nucleon interaction, such as the Skyrme type interaction, with parameters obtained by a fit to a selected set of experimental data on binding energies or radii of nuclei. It has also been demonstrated that HF-based RPA nicely reproduces the properties of low lying collective states as well as of giant resonances. We have carried out fully self-consistent Hartree-Fock (HF) based RPA calculations of the isoscalar ( $T = 0$ ) giant monopole resonance (ISGMR), dipole (ISGDR), quadrupole (ISGQR), and the octopole (ISGOR) strength functions, and for the isovector ( $T = 1$ ) giant monopole resonance (IVGMR), dipole (IVGDR), quadrupole (IVGQR) and octopole (IVGOR) strength functions, for  $^{40}\text{Ca}$  and for  $^{48}\text{Ca}$ , using a wide range of over 15 commonly employed Skyrme type interaction. These interactions, which were fitted to ground state properties of nuclei are associated with a wide range of nuclear matter properties such as incompressibility coefficient  $K_{NM} = 200 - 255$  MeV, symmetry energy  $J = 27 - 37$  MeV and effective mass  $m^* = 0.6 - 1.0$ . We compare the theoretical values to the available experimental data on the

isoscalar and isovector giant resonances in  $^{40}\text{Ca}$  and  $^{48}\text{Ca}$  and discuss our results, considering, in particular, the issue of self consistency and the sensitivity of the giant resonances energies to various bulk properties of NM.

[1] M.R. Anders *et al*, in preparation.

## Isoscalar giant monopole resonance in $^{48}\text{Ca}$

Y. -W. Lui, D. H. Youngblood, S. Shlomo, X. Chen,<sup>1</sup> Y. Tokimoto,<sup>2</sup> Krishichayan,  
M. Anders, and J. Button

The location of the isoscalar giant monopole resonance (ISGMR) is important because it can be directly related to the incompressibility coefficient of nuclear matter (NM), an important ingredient in equation of state (EOS) of NM. In recent years, studies of the isotope dependence and the extraction of the symmetry term  $K_\tau$  are mostly concentrated in heavy nuclei, especially in Sn isotopes where the neutron excess ratio  $(N-Z)/A$  value changes from 0.107 in  $^{112}\text{Sn}$  to 0.194 in  $^{124}\text{Sn}$ . This gives a relative large deviation in the isotope dependence. However, in the calcium isotopes,  $(N-Z)/A$  is 0 in  $^{40}\text{Ca}$  and 0.167 in  $^{48}\text{Ca}$ , a much larger variation than in the Sn isotopes, even though the neutron excess in  $^{48}\text{Ca}$  is not as large as in  $^{124}\text{Sn}$ . Thus a study of  $^{40-48}\text{Ca}$  might provide a more precise determination of the symmetry coefficient  $K_\tau$ .

We have carried out fully self-consistent Hartree-Fock based RPA calculations for the  $^{40}\text{Ca}$  and the  $^{48}\text{Ca}$  isotopes, with commonly used Skyrme type interactions, and compare the results with the recent experimental data obtained at our Institute [1]. We emphasize, in particular, the importance of self-consistency.

The microscopic mean-field based RPA provides a good description of collective states in nuclei. It is common to calculate the RPA states  $|n\rangle$  with the corresponding energies  $E_n$ , and obtain the strength function

$$S(E) = \sum_n |\langle 0|F|n\rangle|^2 \delta(E-E_n),$$

for a certain single particle scattering operator  $F = \sum f(i)$ , and then determine the energy moments

$$m_k = \int E^k S(E) dE.$$

The constrained energy,  $E_{\text{con}}$ , centroid energy,  $E_{\text{cen}}$ , and the scaling energy,  $E_s$ , of the resonance are then obtained from

$$E_{\text{con}} = (m_1/m_0)^{1/2}, \quad E_{\text{cen}} = m_1/m_0, \quad E_s = (m_3/m_1)^{1/2}.$$

The energy moment  $m_1$  can also be calculated using the Hartree-Fock (HF) ground state wave function, leading to an energy weighted sum rule (EWSR). In a fully self-consistent mean-field calculation of the response function, one adopts an effective two-nucleon interaction  $V$ , usually fitted to ground states properties of nuclei, and determines the mean-field. Then, the random-phase approximation

---

<sup>1</sup> Present Address: Department of Chemistry, Washington University at St. Louis, St. Louis, MO 63130.

<sup>2</sup> Present Address: Higashi-Korien-cho 12-9, Neyagawa-shi, Osaka, 572-0081 Japan.

(RPA) calculation is carried out with all the components of the two-body interaction using a large configuration space. In this sense, the calculations are fully self-consistent.

In Figure 1 we compare the measured centroid energies in  $^{40,48}\text{Ca}$  to our results from HF-based RPA calculations using the Skyrme type, SGII, SKM\*, KDE0 and SK255 interactions. The selected Skyrme interactions are associated with a wide range of nuclear matter [NM] incompressibility coefficients  $K = 215 - 255$  MeV and a wide range of NM symmetry energy coefficients  $J = 27 - 37$  MeV.

In Figure 1 we show the centroid energies as a function of  $K_{\text{NM}}$ . As can be seen in Fig. 1b, for  $^{48}\text{Ca}$ , the centroid obtained with SKM\* is in agreement with the data, while that for KDE0 is slightly outside the errors while those for the other two interactions are a few hundred keV outside the errors. For  $^{40}\text{Ca}$  (Fig. 1a) the centroid obtained with SkM\* is high and  $\sim 600$  keV outside the errors, while those for the other interactions are yet higher and over an MeV outside the errors.

Whereas in the Sn isotopes the ISGMR energy decreases with increasing mass, the measured  $^{48}\text{Ca}$  centroid energy is higher than that for  $^{40}\text{Ca}$ . The measured centroid energy for  $^{40}\text{Ca}$  is 0.7 MeV below that of  $^{48}\text{Ca}$ . The energies of the ISGMR in  $^{48}\text{Ca}$  obtained in our fully self-consistent calculations using various Skyrme type interactions are all 0.7 to 1.2 MeV below those of  $^{40}\text{Ca}$  (Fig. 1c). It is well known that the effects of self-consistency violation associated with neglecting the particle-hole spin-orbit and Coulomb interactions in HF-based RPA calculations can shift giant resonance energies by hundreds of keV. Neglecting the particle-hole Spin-orbit and Coulomb interactions in the RPA calculations give  $^{48}\text{Ca}$

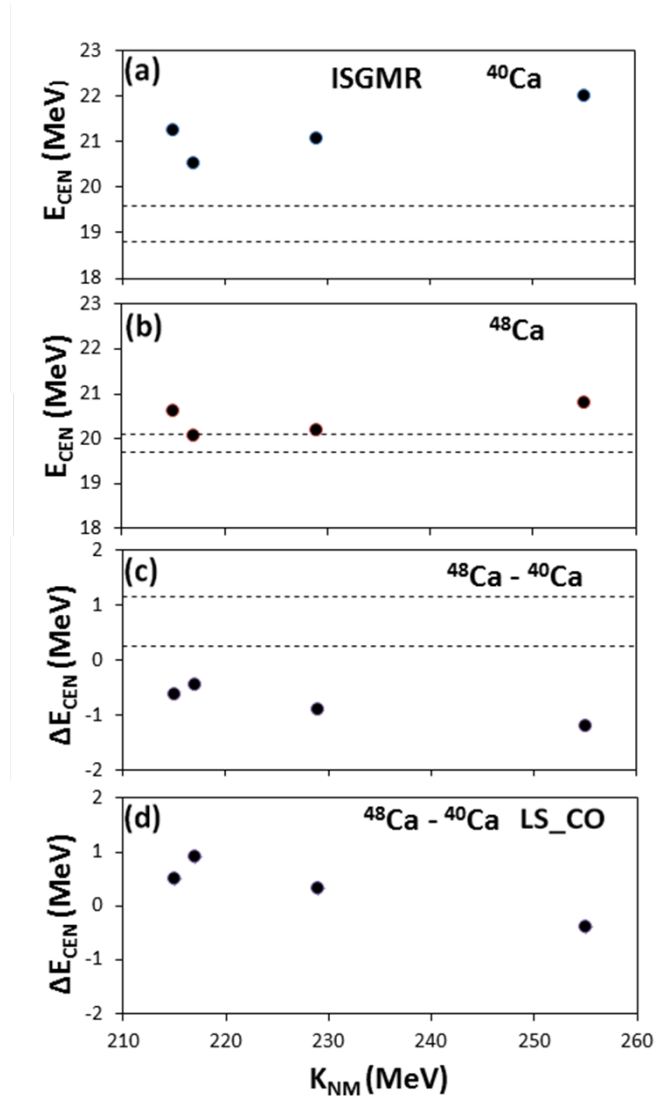


**FIG. 1.** Comparison of experimental data of the centroid energies  $E_{\text{cen}}$  of  $^{40}\text{Ca}$  (a),  $^{48}\text{Ca}$  (b), and the energy difference between  $^{48}\text{Ca}$  and  $^{40}\text{Ca}$  (c), shown as the regions between the dashed lines, with the results of fully self consistent HF based RPA calculations (full circles), using the SGII, SKM\*, KDE0, and SK255 Skyrme type interactions having nuclear matter incompressibility coefficients  $K_{\text{NM}} = 215, 217, 230,$  and  $255$  MeV, respectively. The results obtained with violation of self-consistency by the neglecting the Coulomb and the spin orbit interactions in the RPA calculations, are shown in (d). The energies shown were calculated over the experimental excitation energy range of 9.5 - 40 MeV.

energies higher relative to  $^{40}\text{Ca}$  than those that include these interactions by 0.4 to 1.2 MeV. Leaving out these interactions, the predicted ISGMR centroid energies (Fig. 1d) in  $^{48}\text{Ca}$  are higher than those in  $^{40}\text{Ca}$  by  $\Delta E_{\text{cen}} = 0.5, 0.3$  and  $1.0$  MeV for the SGII, KDE0 and SkM\* interactions, and SK255 gives a  $^{48}\text{Ca}$  energy below  $^{40}\text{Ca}$  by 0.4 MeV.

In summary, the experimental value for the centroid energy in ISGMR in  $^{48}\text{Ca}$  is larger than that in  $^{40}\text{Ca}$  by about 0.7 MeV, whereas self consistent HF-RPA calculations predict a lower centroid energy in this neutron rich Ca isotope. Moreover, the HF based RPA calculations do not reproduce the strength distributions, and it would be interesting to extend them beyond the RPA to include coupling to more complex configurations.

[1] Y.-W. Lui, D.H. Youngblood, S. Shlomo, X. Chen, Y. Tokimoto, Krishichayan, M. Anders and J. Button, Phys. Rev. C **83**, 044327 (2011).

## Event-by-event jet quenching

R. J. Fries, R. Rodriguez, and E. Ramirez

We have investigated the role of fluctuations and inhomogeneities on hard probes in nuclear collisions. Many jet quenching calculations in the past have used “averaged” events in which the density of the fireball is a smooth function of the coordinates. However, it has become increasingly clear that initial fluctuations of the positions of the nucleons inside the nuclei, and fluctuations of the nucleon-nucleon cross section can lead to very inhomogeneous fireballs. At the same time the position of the hard processes can be correlated in a non-trivial way with hot spots (i.e. local maxima of the density) in the fireball.

We have used our software package PPM to propagate quarks and gluons created in hard processes through the background fireball. Here we compared runs of PPM averaged over many individual events (i.e. spatial distributions of the fireball density and the distribution of hard processes) created with the Glauber event generator GLISSANDO [1], with runs using smooth events from an averaging of 500,000 GLISSANDO events. The latter resembles the current state-of-the-art in the field while the former is the more realistic scenario for comparison with data.

We have found that comparison of data on the nuclear modification factor  $R_{AA}$  to calculations from smooth fireballs leads to values of the quenching strength  $q$  which are above the real value. In the ASW energy loss model the error could be as large as 50%. If the size of fluctuations is taken to be a priori unknown this introduces a 50% uncertainty on the extraction of  $q$  from data. After adjusting  $q$  to fit event-by-event  $R_{AA}$  we arrive at a consistent picture in which both the momentum and centrality dependence of single hadron suppression data from the Relativistic Heavy Ion Collider (RHIC) can be described. We observe that residual deviation remains for both elliptic flow and di-hadron correlations, opening the possibility to distinguish different fluctuations strengths and therefore conduct something close to a true spatial tomography of the fireball. We have defined a correlation function  $R(x,y)$  between fluctuations of hard processes and the surrounding fireball. Hard probes are sensitive to the integral of  $R$  taken along the trajectory of a hard probe. In principle  $R$  can be constrained from data and can provide tomographic information.

This project has been finished and results have been published in Physics Letters B [2]. Figure 1 shows a typical result for  $R_{AA}$ .

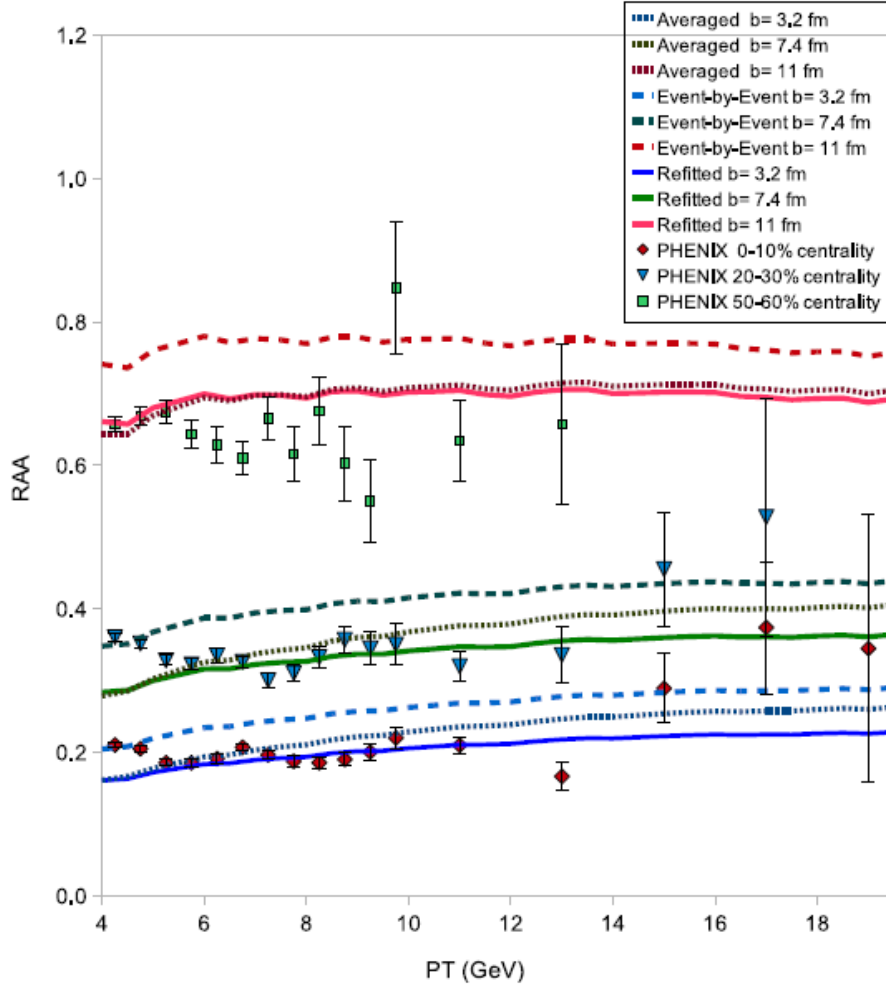


**FIG. 1.**  $R_{AA}$  at RHIC (data from the PHENIX experiment) calculated for 3 different centralities (or impact parameters) and with 3 different methods (averaged event, event-by-event with  $q$  as extracted from averaged event, event-by-event with  $q$  adjusted to fit  $R_{AA}$  data)

- [1] W. Broniowski, M. Rybczynski, and P. Bozek, *Comp. Phys. Comm.* **180**, 69 (2009).  
 [2] R. Rodriguez, R.J. Fries, and E. Ramirez, *Phys. Lett. B* **693**, 108 (2010).

## The initial state of high energy nuclear collisions

R. J. Fries and G. Chen

The initial state of nuclear collisions at very high energies is thought to be a phase of QCD called the Color Glass Condensate (CGC). A key problem in our understanding of relativistic heavy ion collisions is the question how this color glass evolves into a thermalized plasma of quarks and gluons (QGP). We have embarked on a project to calculate the energy momentum tensor in nuclear collisions at early times based on a classical description of the color glass condensate (the McLerran-Venugopalan model).

We use an expansion of the classical gluon field around the time of collision ( $t=0$ ). In the last year we have used previously obtained expressions for the components of the energy momentum tensor for fixed color sources  $\rho_i$  in the colliding nuclei and have developed the techniques to compute the expectation value under realistic conditions (the  $\rho_i$  cannot be observed and on average  $\langle\rho_i\rangle=0$  since the nuclei are color neutral). We can now evaluate n-point functions of gluon fields,  $\langle A(x)A(y)\rangle$ ,  $\langle A'(x)A(y)\rangle$ ,  $\langle A'(x)A'(y)\rangle$ , etc. ( $A'$  denotes the gradient of the gluon field) within an infrared-safe generalization of the McLerran-Venugopalan framework. This allows us to finally compute the transverse dynamics of the early gluon field with interesting consequences.

Some of the surprise findings are directed flow (known as  $v_1$  in heavy ion collisions) and global angular momentum emerging from these coherent gluon fields. They add to the radial and elliptic flow from coherent gluon fields which had been identified earlier. We are currently exploring the energy momentum tensor up to 4<sup>th</sup> order in the early time expansion. This energy momentum tensor will be used as input for a further hydrodynamic evolution of the fireball.

## Charmonium production in heavy-ion collisions at the large hadron collider

X. Zhao and R. Rapp

Charmonium has been suggested as a probe of deconfinement in the hot/dense medium created in relativistic heavy-ion (A-A) collisions: once charmonia dissolve as a result of color-Debye screening in the Quark-Gluon Plasma (QGP) their yields in A-A collisions ought to be suppressed compared to the superposition of individual nucleon-nucleon collisions.  $J/\psi$  suppression was indeed observed, first in Pb-Pb collisions at SPS at CERN and later in Au-Au collisions at RHIC at BNL. However, the finally observed charmonia may “regenerate” during the collision, by recombination of charm and anti-charm quarks in the later stages of the medium evolution. At RHIC, an increase of  $c$ -bar production leads to a larger regeneration component, but the observed (lack of) suppression renders it difficult to establish unambiguously. A more sensitive test of regeneration becomes possible at the even higher energies at the LHC, where  $c$ -bar pairs are produced abundantly, which could result in significantly less suppression of observed the  $J/\psi$  yield compared to RHIC and SPS, contrary to the expectation of stronger suppression.

In our previous work [1] we have employed a thermal rate-equation approach to describe the evolution of charmonium yields in the thermalized medium formed in A-A collisions. The main inputs to the rate-equation are the in-medium charmonium reaction rates and the equilibrium limit which is governed by the charmonium and open-charm masses. The dissociation rate is evaluated using perturbative QCD assuming charmonia to be loosely bound states in the deconfined medium; detailed balance has been applied to obtain the formation rate (regeneration processes). These rates are sensitive to the in-medium charmonium binding energies, which are extracted from in-medium T-matrix calculations [2] with input potentials inferred from lattice-QCD. The current ambiguity in using free (F) or internal energies (U) as potential (V) has been bracketed by two limiting scenarios, assuming  $V=F$  or  $V=U$ , leading to either weak or strong  $J/\psi$  binding in the QGP, respectively. An important aspect in our approach of Ref. [1] is that we have verified the consistency between the resulting charmonium spectral functions with Euclidean current-current correlators computed in thermal lattice QCD. Essentially two tunable parameters remain: the strong coupling constant,  $\alpha_s$  (controlling the reaction rate) and the thermal charm-quark relaxation time,  $\tau_c$  (affecting the regeneration yields). They have been adjusted in an overall fit to the observed inclusive  $J/\psi$  yields at SPS and RHIC which can be fairly well reproduced. In the present work [3] we apply this approach at the LHC, to predict inclusive  $J/\psi$  yields in Pb-Pb collisions at  $\sqrt{s}=2.76\text{A TeV}$  without adjusting parameters.

The initial condition of the rate equation is estimated from  $J/\psi$  yields in p-p collisions scaled by the number of collisions in A-A and augmented with cold-nuclear-matter (CNM) effects. For p-p we use  $d\sigma^{J/\psi}/dy=4\mu\text{b}$  and  $d\sigma^{cc}/dy=0.75\text{mb}$ . Since the nuclear absorption and Cronin effects are expected to be small at LHC, the only considered CNM effect is nuclear shadowing. The charged-particle multiplicity of the fireball expansion has been adjusted to first LHC data,  $dN_{ch}/d\eta=1600$ , which yields an initial QGP temperature of  $\sim 600\text{MeV}$ .

We first present the results for the centrality dependence of inclusive  $J/\psi$  yields without shadowing in Fig.1 (feeddown from  $\chi_c$ ,  $\psi'$  and B mesons are included). The total yields are found to be similar for the  $V=F$  and  $V=U$  scenarios. In both scenarios the regeneration component dominates in central collisions. The total yields remain below one and are much smaller than the predictions from the statistical model.

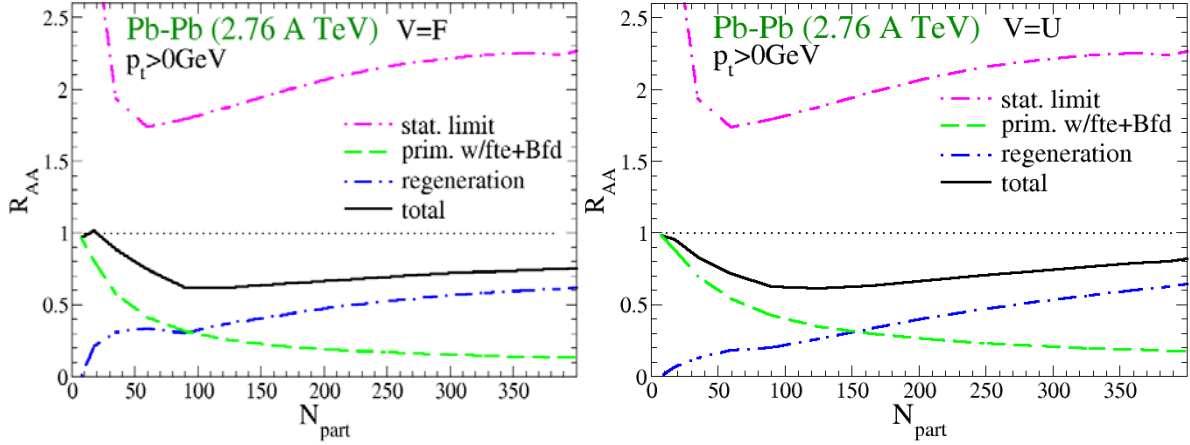


**FIG. 1.** Centrality dependence of the  $J/\psi$  nuclear modification factor at LHC without nuclear shadowing on either  $J/\psi$  or  $c$ - $\bar{c}$ . Left panel: weak binding scenario ( $V=F$ ); right panel: strong binding scenario ( $V=U$ ).

A more realistic prediction for  $J/\psi$  production at LHC includes nuclear shadowing effects on both primordial  $J/\psi$  and  $c$ - $\bar{c}$ , cf. left panel of Fig. 2. Nuclear shadowing suppresses both primordial and regeneration components so that the total  $R_{AA}$  is reduced to  $\sim 0.45$ . It is approximately constant with centrality for  $N_{part} > 100$  due to the interplay of primordial and regeneration components. These predictions are in good agreement with recent ALICE data (which, however, are for forward rapidity). At high  $p_t > 6.5$  GeV, where the regeneration contribution is negligible, our results agree fairly well with ATLAS data [5], cf. right panel of Fig. 2.

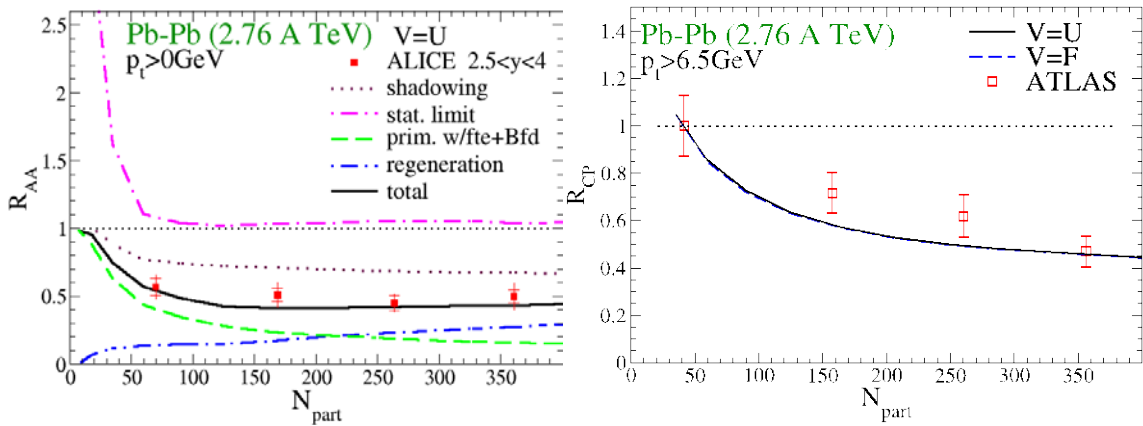


**FIG. 2.** Left panel: Centrality dependence of the  $J/\psi$  nuclear modification factor in the strong binding scenario ( $V=U$ ) including nuclear shadowing, compared to ALICE data [4]; right panel: centrality of the  $J/\psi$  central-to-peripheral ratio ( $R_{CP}$ ) for  $p_t > 6.5$  GeV (no shadowing), compared to ATLAS data [5].

The agreement of our calculations with LHC data support the picture that charmonia produced in heavy-ion collisions are from both primordial production and  $c$ - $\bar{c}$  recombination.

- [1] X. Zhao and R. Rapp, Phys. Rev. C **82**, 064905 (2010).
- [2] F. Riek and R. Rapp, Phys. Rev. C **82**, 035201 (2010).
- [3] X. Zhao and R. Rapp, Nucl. Phys. **A859**, 114 (2011).
- [4] G. Martinez-Garcia *et al.* (ALICE Collaboration), LANL e-print arXiv:1106.5889 [nucl-ex]
- [5] G. Aad *et al.* (ATLAS Collaboration), Phys. Lett. B **697**, 294 (2011).

# Scaling of elliptic flow, recombination and sequential freeze-out of hadrons in heavy-ion collisions

Min He, Rainer J. Fries, and Ralf Rapp

Quark recombination has been identified as an efficient particle production mechanism for hadrons with intermediate transverse momentum  $p_T$  in ultrarelativistic heavy-ion collisions [1]. In particular, it explained the constituent-quark number scaling of elliptic flow of mesons and baryons at  $2 < p_T < 6$  GeV:  $v_2(p_T) = n_q v_2^q(p_T/n_q)$ , where  $n_q$  is the number of valence quarks contained in a hadron. However, the conventional quark recombination models suffer the drawback of energy non-conservation and thus their application is limited to intermediate  $p_T$ . In the present work [2], we employ the Resonance Recombination Model (RRM) [3] to investigate the scaling properties of elliptic flow in the low- $p_T$  regime where particles are in (or close to) equilibrium. Since the RRM satisfies energy conservation and detailed balance, it provides an equilibrium mapping from quark distributions to the formed hadron distributions, as shown in Fig. 1.

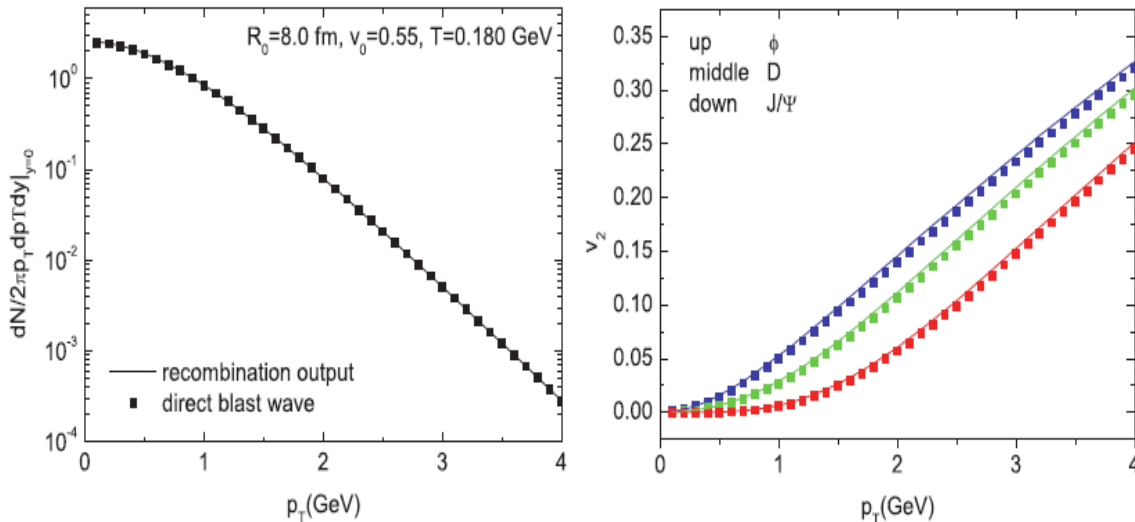


**FIG. 1.** Equilibrium mapping from quark to meson distributions as realized in RRM [2]. Left panel: phi-meson  $p_T$  spectrum. Right panel: phi, D and Jpsi-meson  $v_2$ . The solid lines are direct blast wave calculations and the symbols are output of RRM calculations.

Based on this equilibrium mapping in RRM, we extract the quark distributions around hadronization (see Fig. 2) from an empirical fireball source which is parameterized according to the multi-strange hadron spectra in semi-central Au-Au collisions at RHIC. Multi-strange hadrons are believed to freeze out close to hadronization since their hadronic cross sections are believed to be small [4] and thus their observed spectra reflect the source information at  $T_c \sim 180$  MeV.

In contrast to multi-strange hadrons, bulk particles (pions, kaons and protons) freeze out much later owing to efficient hadronic (elastic) resonant interactions. We show that the bulk-particle spectra

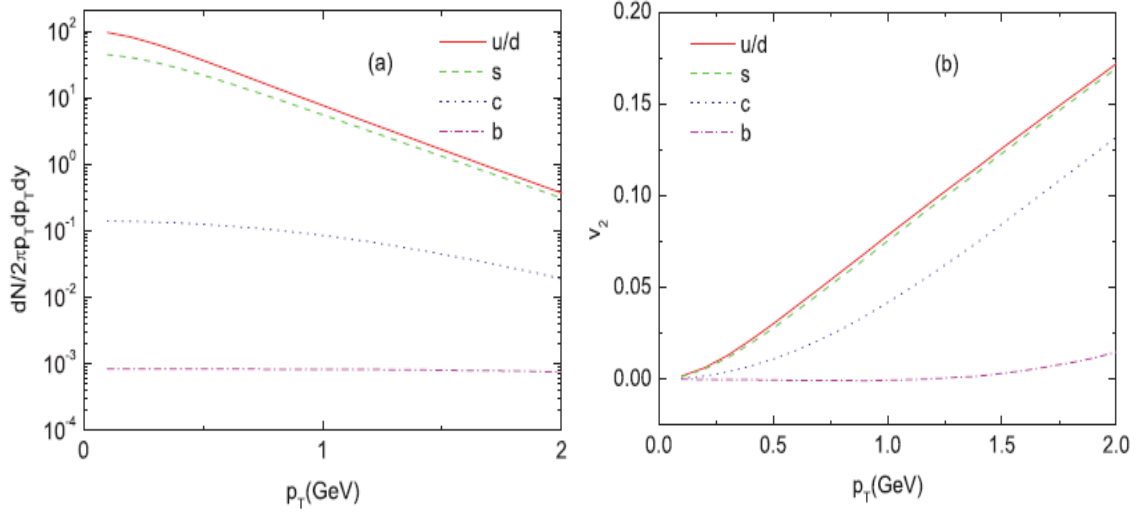


**FIG. 2.** Extracted equilibrium quark distributions from empirical fits of multi-strange hadron spectra at hadronization with  $T_c \sim 180$  MeV. Left panel: quark spectra. Right panel: quark  $v_2$ .

can be fitted fairly well at  $T_{\text{kin}} \sim 110$  MeV with a source of larger flow [2]. Based on this sequential freeze-out scenario, we verify that the resulting elliptic flow of various hadrons from empirical fits exhibit transverse-kinetic energy ( $KE_T$ ) and valence-quark number scaling [2], see Fig. 3. We thus conclude that elliptic-flow scaling in the low- $p_T$  regime bridges equilibrium hydrodynamics and quark recombination.

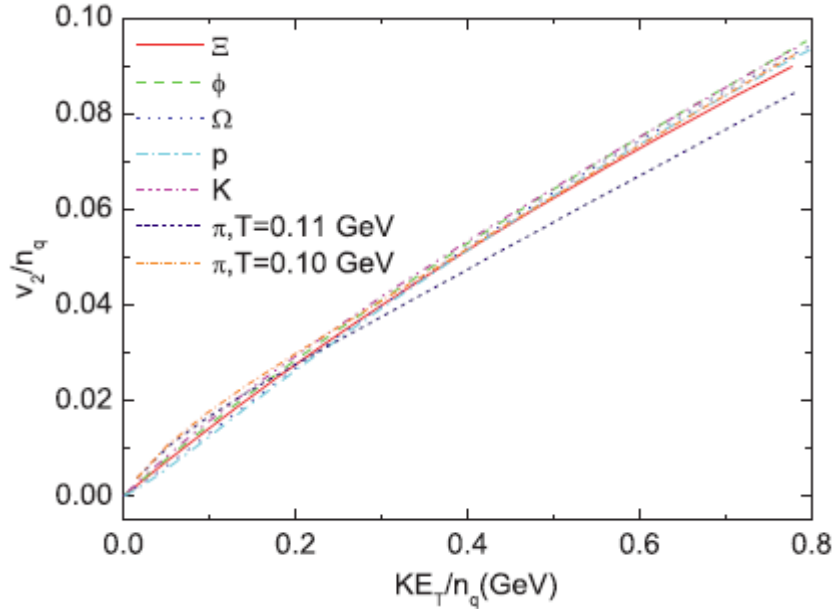


**FIG. 3.**  $KE_T$  and  $n_q$  scaling of  $v_2$  for different hadrons obtained within the sequential freeze-out scenario. A slightly later freeze-out for pions at  $T=100$  MeV further improves the scaling.

- [1] R.J. Fries, B. Muller, C. Nonaka, and S.A. Bass, Phys. Rev. C **68**, 044902 (2003); V. Greco, C.M. Ko, and P. Levai, Phys. Rev. C **68**, 034904 (2003).
- [2] Min He, Rainer J. Fries, and Ralf Rapp, Phys. Rev. C **82**, 034907 (2010).
- [3] L. Ravagli and R. Rapp, Phys. Lett. B **655**, 126 (2007).
- [4] B. Mohanty and N. Xu, J. Phys. G **36**, 064022 (2009).

# Self-consistent evaluation of charm and charmonium properties in the quark-gluon plasma

F. Riek and R. Rapp

Heavy quarks are versatile probes of the medium created in ultrarelativistic heavy-ion collisions. The diffusion of a single heavy quark is sensitive to the transport properties of the medium and the spectrum of heavy quarkonia to Debye screening of the color force in bound-state formation. The large heavy-quark (HQ) mass,  $m_Q \gg T$ , implies that the 4-momentum transfers in these interactions are dominantly spacelike, i.e., potential-like. In Ref. [1] we have constructed a potential-based thermodynamic T-matrix approach to describe HQ diffusion and quarkonia in the quark-gluon plasma (QGP) in a common framework. With input potentials taken from lattice-QCD (IQCD) computations of the HQ free energy and relativistic (kinematic) corrections, a fair description of the vacuum quarkonium and heavy-light meson spectrum can be obtained. Using in-medium HQ free (or internal) energies to calculate heavy-heavy and heavy-light quark T-matrices, one finds that (i) the resulting quarkonium spectral functions are approximately compatible with Euclidean correlation functions computed in IQCD, and (ii) the thermal HQ relaxation time is substantially reduced compared to perturbative calculations.

In the present work [2] we have gone beyond Ref. [1], treating the HQ sector self-consistently by calculating the HQ self-energy from the heavy-light T-matrix and vice versa via numerical iteration. Going beyond the quasiparticle approximation, we also obtain the quarkonium zero modes from applying the Matsubara formalism to the 2-body Q-Qbar Greens function in the T-matrix equation. This enables a parameter-free inclusion of the zero-mode contribution in the Euclidean quarkonium correlators as well as a calculation of the HQ susceptibility which for the first time includes finite-width effects.

In Fig. 1 we compare our result for the correlator ratio in the S-wave charmonium channel (using the internal energy as potential) to unquenched IQCD data, showing fair (albeit not perfect) agreement. The underlying spectral function is characterized by a “melting” of the  $J/\psi$  peak at ca.  $1.5 T_c$ . This is somewhat lower than in previous calculations, mostly due to the rather large charm-quarks widths of ca. 200 MeV (the single HQ transport properties are essentially unchanged, with a thermalization time of

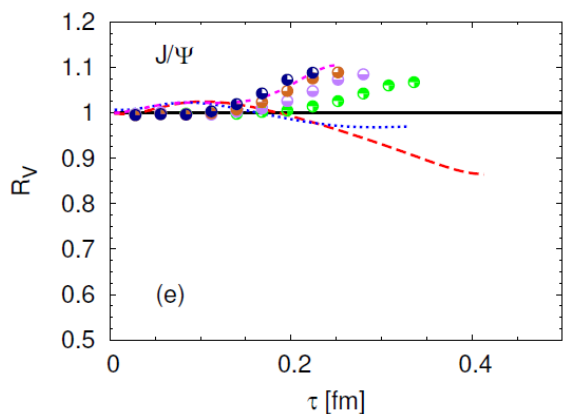


**FIG. 1.** Euclidean  $J/\psi$  correlator ratios calculated using the internal energy (U), compared to IQCD “data” [3].

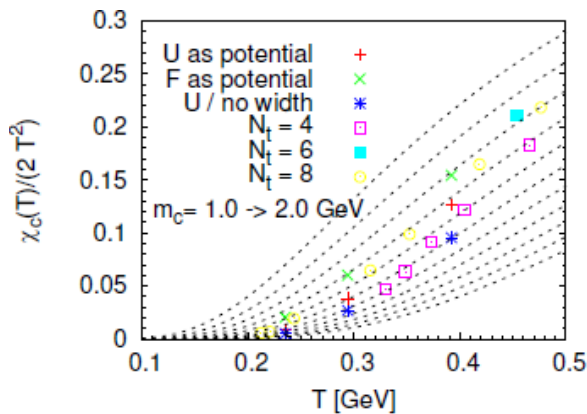


**FIG. 2.** Heavy-quark susceptibility calculated from the quarkonium zero modes, compared to IQCD computations with different number of Euclidean-fine points,  $N_t$  [4].

around 5fm/c). The extraction of the HQ susceptibility, shown in Fig. 2, reiterates the importance of width effects which can compensate for an increase in the HQ mass. Again, the self-consistent results are in fair agreement with thermal IQCD computations.

- [1] F. Riek and R. Rapp, Phys. Rev. C **82**, 035201 (2010).
- [2] F. Riek and R. Rapp, New J. Phys. **13**, 045007 (2011).
- [3] G. Aarts et al., Phys. Rev. D **76**, 094513 (2007).
- [4] P. Petreczky, P. Hegde and A. Velytsky, PoS **LAT2009**, 159 (2009).

## Thermal relaxation of charm in hadronic matter

Min He, Rainer J. Fries, and Ralf Rapp

Heavy-flavor hadrons can serve as a direct probe for the hot and dense matter created in ultra-relativistic heavy ion collisions (URHICs) [1]. Recently, heavy-quark diffusion and thermalization in the quark-gluon plasma (QGP) have been subject of intense studies [1,2]. Heavy-quark interactions with the QGP medium can be characterized by transport coefficients, i.e., a thermal relaxation rate or spatial diffusion coefficient, as calculated, for example by a non-perturbative T-matrix approach [3]. However, a complete description of heavy-flavor probes in URHICs requires to account for the effect of the hadronic phase on heavy-flavor transport.

In the present work [4], we calculate the thermal relaxation rate of open-charm (D) mesons in hot and dense hadronic matter using empirical elastic scattering amplitudes. D-meson interactions with thermal pions are approximated by  $D^*$  resonances, while scattering off other hadrons (K, eta, rho, omega,  $K^*$ , N, Delta) is evaluated using vacuum scattering amplitudes as available in the literature based on effective Lagrangians and constrained by realistic spectroscopy. Fig.1 shows the empirical cross sections of D-meson scattering off various hadrons

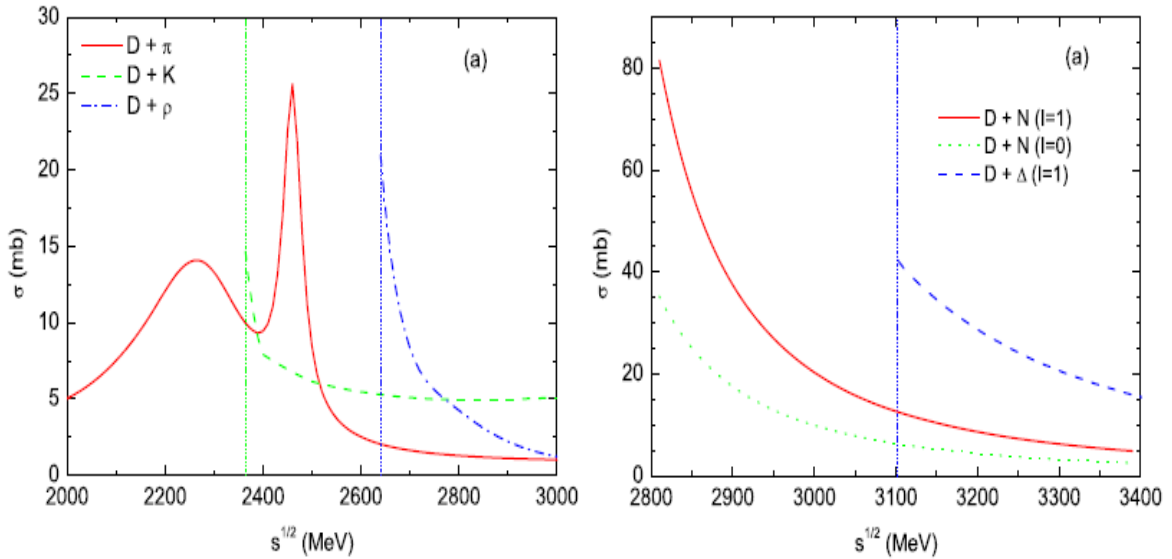


**FIG. 1.** Empirical cross sections of D-meson scatterings off mesons (left) and baryons (right).

The resulting D-meson thermal relaxation rate is shown in the left panel of Fig. 2. At  $T=180$  MeV, it turns out to be comparable to the charm-quark relaxation rate in the QGP as calculated by the T-matrix approach [3], indicative for a “quark-hadron duality”. Under RHIC conditions, with off-equilibrium chemical potentials, the average D-meson relaxation rate of  $A \sim 0.04/\text{fm}$  translates into a relaxation time of  $\sim 25$  fm/c. For a hadronic evolution lasting for  $\sim 5$  fm/c, the D-meson spectrum is expected to be modified by  $\sim 20\%$ .

The D-meson spatial diffusion coefficient  $D_s=T/(m_D A)$  is displayed in the right panel of Fig. 2. When normalized to the medium's thermal wavelength,  $1/(2\pi T)$ ,  $D_s$  decreases with temperature and reaches a value of  $\sim 5$  at  $T=180$  MeV. Again, this is surprisingly close to the T-matrix results for charm quarks in the QGP phase [3], and together with those results, suggests a minimum across the hadron-to-quark transition. This behavior is analogous to a widely discussed transport coefficient characterizing the fluidity of the matter, i.e. the ratio of shear viscosity to entropy-density,  $\eta/s$ . Specifically, our value for  $D_s$  translates into  $\eta/s \sim (2-5)/4\pi$  at  $T=180$  MeV, not far from the postulated lower quantum bound of  $1/4\pi$  from AdS/CFT correspondence.

Our findings may help improve the theoretical accuracy in heavy-flavor phenomenology for the upcoming precision measurements at RHIC and LHC.

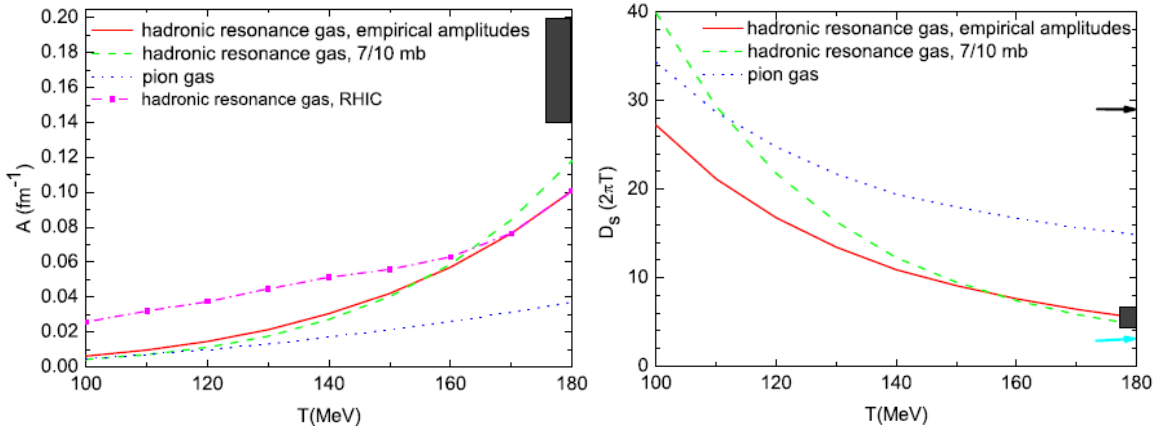


**FIG. 2.** Left panel: D-meson thermal relaxation rate as a function of temperature in a hadron gas. Right panel: D-meson spatial diffusion coefficient in units of the thermal wavelength  $1/(2\pi T)$ ; to the right, estimates for charm-quark diffusion in the QGP are indicated (filled box: T-matrix approach at  $1.2T_c$ , lower arrow: AdS/CFT correspondence, upper arrow: perturbative QCD).

- [1] R. Rapp, H. van Hees, in: R. Hwa, X.N. Wang (Eds.), Quark-Gluon Plasma, vol. 4, World Scientific, Singapore, 2010, p. 111, arXiv:0903.1096 [hep-ph].
- [2] H. van Hees and R. Rapp, Phys. Rev. C **71**, 034907 (2005); G. D. Moore and D. Teaney, Phys. Rev. C **71**, 06 4904 (2005).
- [3] F. Riek and R. Rapp, Phys. Rev. C **82**, 035201 (2010); New J. Phys. **13**, 045007 (2011).
- [4] Min He, Rainer J. Fries, and Ralf Rapp, Phys. Lett. **B 701**, 445 (2011).

## Hartree-Fock-Bogoliubov calculations of the isospin-symmetry-breaking correction in superallowed Fermi beta decay

I. S. Towner and J. C. Hardy

For accurate work, an isospin-symmetry breaking correction of between 0.5 % and 1.5 % is applied to ft values of nuclear beta decay. The correction is nucleus dependent and its evaluation dependent on nuclear-structure models. For convenience, the correction is divided into two components:  $\delta_C = \delta_{C1} + \delta_{C2}$ , where  $\delta_{C1}$  arises from inserting charge-dependent terms into the Hamiltonian employed in a shell-model calculation, while  $\delta_{C2}$  – the larger term – depends on radial-function differences between the proton and neutron involved in the beta transition. These radial functions are taken to be eigenfunctions of either a Saxon-Woods (SW) or a mean-field Hartree-Fock (HF) potential with adjustments to ensure that the radial functions have the appropriate asymptotic behavior.

To date, all HF calculations have been performed with the Skyrme parameterization of the nucleon-nucleon interaction. The computations assume spherical symmetry, which for open-shell nuclei is imposed by making the “filling approximation”. Briefly, for partially filled orbitals a shell-model calculation is performed first to find the orbit occupancy. This occupancy is then imposed on the HF calculation and kept fixed during the HF iterations. An alternative strategy is to add a pairing term to the Skyrme interaction. At the end of each HF iteration, the standard pairing equations are solved to obtain the occupation probabilities, which are then returned to the HF code for the next iteration. This is known as a Hartree-Fock-Bogoliubov (HFB) procedure. In HF, the total energy of the nucleus is minimized subject to variations in the single-particle wave functions. In HFB, the total energy is minimized not only subject to variations in the single-particle wave functions, but also to variations in their occupation probabilities.

We take the form of the pairing interaction to be a delta function whose strength,  $V_0$ , is adjusted to reproduce the odd-even mass difference,  $E_\alpha$ , where alpha denotes the valence orbital. However, a problem arose whenever the proton or neutron number corresponded to a closed sub-shell, because in this case the value of the pairing strength fell below a certain “critical value” and no superconducting solution could be found for the pairing equations. In this situation the occupation probability is constrained to be either 1 or 0, fully occupied or completely unoccupied. By contrast, the shell model produces solutions at sub-shell closures where the occupation probabilities are not just 1 or 0. To get such a result from a pairing model, we have to insist that the pairing strength be above the critical value. In such cases we fix the pairing strength, not to reproduce the odd-even mass difference, but to produce a “gap energy”,  $\Delta_\alpha$ , of order 1 MeV. Fortunately, in the computation of the isospin-symmetry breaking correction, the dependence of  $\delta_{C2}$  on the pairing strength is very weak, and a precisely determined value is not required.

Our procedure for obtaining the isospin-symmetry breaking correction,  $\delta_{C2}$ , is essentially the one described in Ref. [1] except that HFB rather than HF calculations were performed. Results for one choice of the Skyrme interaction, SkM\*, are given in Table I. It is seen that the addition of a pairing term has only a small impact on  $\delta_{C2}$ . The average percentage shift between HF and HFB calculations was around 3%. In all cases, the shift is smaller than the error we assigned when we published our HF  $\delta_{C2}$

values in 2009 [1]. It is clear that no serious error has been made in our published work through the omission of pairing in the HF procedure.

**Table I.** Results of Hartree-Fock (HF) and Hartree-Fock-Bogoliubov (HFB) calculations with the Skyrme force, SkM\*, for the isospin-symmetry-breaking correction,  $\delta_{C2}$ . The columns headed by  $E_\alpha$  contain the quasi-particle energies in MeV determined from odd-even mass differences; those headed by  $V_0$  contain the adjusted strengths of the pairing delta function in MeV fm<sup>3</sup> units, and  $\Delta_\alpha$  are the resulting gap energies in MeV. Quantities marked with a dagger represent sub-shell closures.

Nucleus	$\alpha$	$E_\alpha^p$	$E_\alpha^n$	$V_0^p$	$V_0^n$	$\Delta_\alpha^p$	$\Delta_\alpha^n$	$\delta_{C2}^{HFB}$	$\delta_{C2}^{HF}$	% Diff.
<sup>10</sup> C	$p_{3/2}$	2.10	2.57	337	362	1.88	2.57	0.196	0.206	4.9
<sup>14</sup> O	$p_{1/2}$	1.34	1.62	350	375 <sup>†</sup>	1.35	1.03 <sup>†</sup>	0.227	0.245	7.4
<sup>18</sup> Ne	$d_{5/2}$	1.66	1.95	290	433 <sup>†</sup>	1.21	0.98 <sup>†</sup>	0.191	0.194	1.6
<sup>22</sup> Mg	$d_{5/2}$	1.87	2.15	273	320	1.86	2.01	0.212	0.243	12.8
<sup>26</sup> Si	$d_{5/2}$	1.62	1.88	247	288	1.25	1.78	0.341	0.335	1.8
<sup>30</sup> S	$s_{1/2}$	0.83	1.07	272	325 <sup>†</sup>	0.82	1.05 <sup>†</sup>	0.521	0.536	2.8
<sup>34</sup> Ar	$d_{3/2}$	1.19	1.39	305	350 <sup>†</sup>	1.05	1.34 <sup>†</sup>	0.492	0.498	1.2
<sup>38</sup> Ca	$d_{3/2}$	1.35	1.53	289	311	1.20	1.53	0.604	0.598	1.0
<sup>42</sup> Ti	$f_{7/2}$	1.34	1.56	237	335 <sup>†</sup>	0.88	1.05 <sup>†</sup>	0.546	0.538	1.5
<sup>26</sup> Al	$d_{5/2}$	1.62	1.88	270	288	1.54	1.45	0.374	0.418	10.5
<sup>34</sup> Cl	$d_{3/2}$	1.19	1.39	345 <sup>†</sup>	303	1.00 <sup>†</sup>	1.20	0.655	0.623	5.1
<sup>38</sup> K	$d_{3/2}$	1.35	1.53	290	306	1.35	1.36	0.677	0.672	0.7
<sup>42</sup> Sc	$f_{7/2}$	1.34	1.56	310 <sup>†</sup>	279	1.06 <sup>†</sup>	1.07	0.634	0.643	1.4
<sup>46</sup> V	$f_{7/2}$	1.63	1.83	274	295	1.43	1.79	0.549	0.545	0.7
<sup>50</sup> Mn	$f_{7/2}$	1.29	1.48	246	260	1.29	1.44	0.595	0.590	0.8
<sup>54</sup> Co	$f_{7/2}$	1.13	1.35	230	245	0.98	0.90	0.647	0.649	0.3
<sup>62</sup> Ga	$p_{3/2}$	1.13	1.33	286	290	1.13	1.24	0.951	0.942	1.0
<sup>66</sup> As	$f_{5/2}$	1.15	1.68	300 <sup>†</sup>	272	0.73 <sup>†</sup>	0.98	1.135	1.122	1.2
<sup>70</sup> Br	$f_{5/2}$	1.50	1.87	287	295	1.29	1.63	1.230	1.165	5.6
<sup>74</sup> Rb	$f_{5/2}$	1.40	1.73	285	289	1.41	1.74	1.385	1.322	4.8

[1] J.C. Hardy and I.S. Towner, Phys. Rev. C **79**, 055502 (2009).

## **SECTION IV**

# **ATOMIC, MOLECULAR AND MATERIALS SCIENCE**

## Kinetic energy release in the dissociations of doubly and triply charged molecular ions

V. Horvat and R. L. Watson

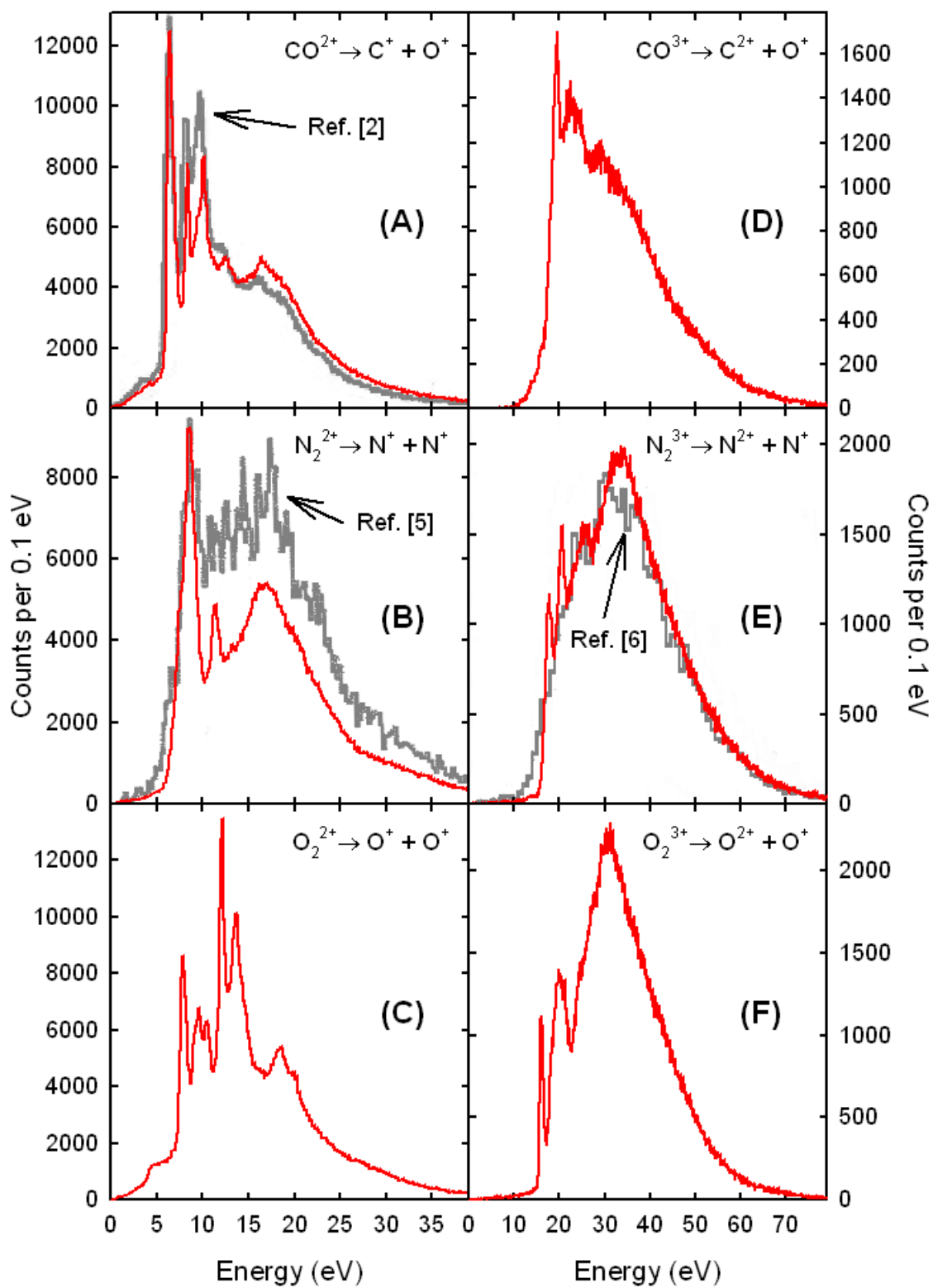
A system for 3D recoil-ion momentum spectroscopy (RIMS) [1] was used to measure the spectra of kinetic energy release (KER) in the dissociations of doubly and triply charged ions of CO, N<sub>2</sub>, and O<sub>2</sub> molecules produced by bombardment of neutral molecules with 2.5 MeV/u Xe<sup>34+</sup> projectiles. Similar results are expected for any collision system in which  $Q_p / v_p \gg 1$  and  $v_p \gg 1$ , where  $Q_p$  is the projectile charge and  $v_p$  is the projectile speed relative to the molecule, expressed in atomic units. Negligible dependence on the projectile species and energy in this collision regime is a result of the fact that for large values of  $Q_p / v_p$  the projectile interacts with the target at large average (or most probable) impact parameter  $b$ . If  $Q_p / v_p$  is increased,  $b$  increases as well, so that  $Q_p / v_p b$  remains nearly constant and the net effect of the Coulomb interaction remains unchanged. Additionally, at large impact parameters, other available ionization mechanisms (such as single and multiple electron capture) can be neglected compared to direct Coulomb ionization (DI).

Figure 1 shows (by the thin red lines) the KER spectra obtained in the present work for the following reactions:

- (A)  $\text{CO}^{2+} \rightarrow \text{C}^+ + \text{O}^+$ ,
- (B)  $\text{N}_2^{2+} \rightarrow \text{N}^+ + \text{N}^+$ ,
- (C)  $\text{O}_2^{2+} \rightarrow \text{O}^+ + \text{O}^+$ ,
- (D)  $\text{CO}^{3+} \rightarrow \text{C}^{2+} + \text{O}^+$ ,
- (E)  $\text{N}_2^{3+} \rightarrow \text{N}^{2+} + \text{N}^+$ , and
- (F)  $\text{O}_2^{3+} \rightarrow \text{O}^{2+} + \text{O}^+$ .

Also shown in Figure 1 are the corresponding best-available KER spectra obtained by other authors under similar conditions (i.e., in the strong interaction regime with fast heavy ion projectiles and measured by means of RIMS). Such results are very scarce; virtually limited to just two groups. A survey of the available results is presented in Table I. Evidently, KER spectra for dissociations C, D, and F have not been presented previously.

The KER FWHM resolution of the present system was assessed by a propagation of errors procedure applied to each event based on the measured resolution of the molecular-fragments' times of flight and that of their impact positions on the detector. The results obtained for the dissociations (A) and (D) are shown in Figure 2. It is evident that the KER FWHM resolution has a distribution that depends on the KER value. Furthermore, it was found that all of these distributions are effectively bounded by lines representing a direct proportionality between the minimum or maximum KER FWHM resolution and the square root of the corresponding KER (see the black lines in Figure 2). The constants of proportionality (in eV<sup>1/2</sup>) were found to be 0.106 and 0.198 for dissociation (A) and 0.130 and 0.342 for dissociation (D). Therefore, in the region between the peaks in the KER spectra [6 - 20 eV for (A) and 19 - 30 eV for (D)] the KER FWHM resolution ranges between 0.26 eV and 0.88 eV and between 0.56 eV and 1.9 eV, respectively. However, it should be noted that most of the events in the peaks have KER



**FIG. 1.** Total kinetic energy release (KER) spectra for the dissociations (A)  $\text{CO}^{2+} \rightarrow \text{C}^+ + \text{O}^+$ , (B)  $\text{N}_2^{2+} \rightarrow \text{N}^+ + \text{N}^+$ , (C)  $\text{O}_2^{2+} \rightarrow \text{O}^+ + \text{O}^+$ , (D)  $\text{CO}^{3+} \rightarrow \text{C}^{2+} + \text{O}^+$ , (E)  $\text{N}_2^{3+} \rightarrow \text{N}^{2+} + \text{N}^+$ , and (F)  $\text{O}_2^{3+} \rightarrow \text{O}^{2+} + \text{O}^+$ . Spectra obtained in the present work are shown by the red lines, while the best-available spectra obtained previously by other authors under similar conditions (as specified in the text) are shown by the gray lines.

**Table I.** Survey of the available KER spectra for the dissociation of doubly and triply charged ions of CO, N<sub>2</sub> and O<sub>2</sub> molecules, measured in the strong collision regime by means of recoil-ion momentum spectroscopy.

Beam energy (MeV/u)	Beam Species	Beam Charge State	Projectile speed Vp(au)	Somerfeld parameter Qp/vp	Target	KER spectra shown	Ref.
8.0	Ni	24+	18	1.3	CO	C <sup>+</sup> O <sup>+</sup>	[2]
3.6	Xe	21+	12	1.7	CO	C <sup>+</sup> O <sup>+</sup>	[3]
2.5	Xe	34+	10	3.4	CO	C <sup>+</sup> O <sup>+</sup> , C <sup>2+</sup> O <sup>+</sup>	Present
5.9	Xe	17+	15	1.1	N <sub>2</sub>	N <sup>+</sup> N <sup>+</sup>	[4]
5.9	Xe	43+	15	2.8	N <sub>2</sub>	N <sup>+</sup> N <sup>+</sup>	[5]
4.7	Bi	26+	14	1.9	N <sub>2</sub>	N <sup>+</sup> N <sup>+</sup>	[5]
4.7	Bi	57+	14	4.2	N <sub>2</sub>	N <sup>+</sup> N <sup>+</sup>	[5]
3.6	Xe	40+	12	3.3	N <sub>2</sub>	N <sup>+</sup> N <sup>+</sup> , N <sup>2+</sup> N <sup>+</sup>	[6]
2.5	Xe	34+	10	3.4	N <sub>2</sub>	N <sup>+</sup> N <sup>+</sup> , N <sup>2+</sup> N <sup>+</sup>	Present
5.9	Xe	18+	15	1.2	O <sub>2</sub>	n/a*	[7]
5.9	Xe	43+	15	2.8	O <sub>2</sub>	n/a*	[7]
2.5	Xe	34+	10	3.4	O <sub>2</sub>	O <sup>+</sup> O <sup>+</sup> , O <sup>2+</sup> O <sup>+</sup>	Present

\*See the text

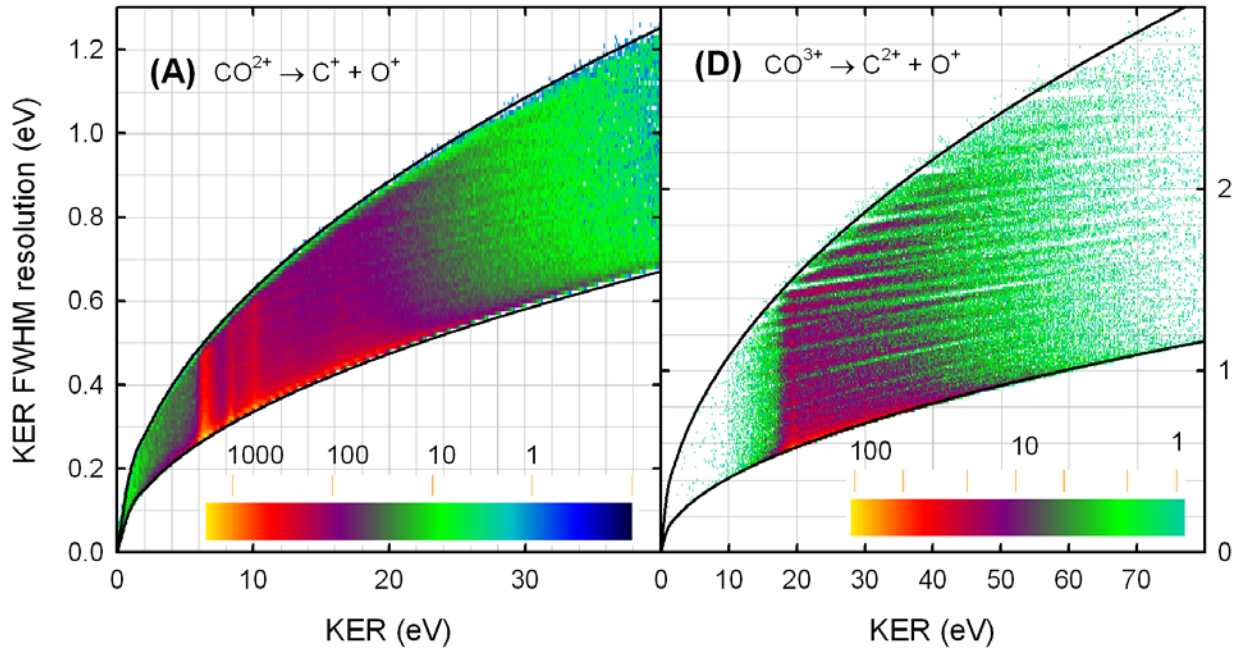


**FIG. 2.** Two-dimensional histograms of KER FWHM resolution versus KER for the dissociations (A)  $\text{CO}^{2+} \rightarrow \text{C}^+ + \text{O}^+$  and (D)  $\text{CO}^{3+} \rightarrow \text{C}^{2+} + \text{O}^+$ . The boundaries delineated by the black lines represent upper and lower limits that are described in the text.

FWHM closer to the lower limit. This is especially true for the peak at 6.4 eV in Figure 1 (A), for which

the lower limit of the KER FWHM resolution is about 0.26 eV. This resolution is comparable to or better than that obtained in the previously published measurements under similar conditions.

For dissociation (B), Figure 1 (B) compares the present KER spectrum with a spectrum obtained using 5.9 MeV/u Xe<sup>43+</sup> projectiles [5]. While the KER resolution of the two spectra seems comparable, the rather poor statistics of the spectrum from Ref. 5 does not allow for a detailed comparison. It is noticeable, though, that the high-energy side of the spectrum from Ref. 5 displays significantly higher intensity relative to the low-energy peak.

For dissociation (E), Figure 1 (E) compares the present KER spectrum with the only available KER spectrum measured by other authors under similar conditions. The latter spectrum was obtained using 3.6 MeV/u Xe<sup>40+</sup> projectiles [6]. Apparently, the KER resolution of Ref. 6 was too poor to observe the triple peak structure displayed by the present data. Other than that, the overall shape of the spectrum appears to be essentially the same.

As noted above, no other published spectra obtained under similar conditions were found for dissociations (C), (D) and (F). However, such measurements were reported for dissociations (C) and (F) [7], but it was stated that no significant structure was observed. The energies of peak channels observed in the KER spectra for dissociations (D), (E), and (F) in the present work are given in Table II.

**Table II.** Energies (eV) of peak channels in the present KER spectra for the dissociation of triply charged ions of CO, N<sub>2</sub> and O<sub>2</sub> molecules.

Reaction	Peak channel energy (eV)
CO <sup>3+</sup> → C <sup>2+</sup> + O <sup>+</sup>	19.5
	22.5
	29.4
N <sub>2</sub> <sup>3+</sup> → N <sup>2+</sup> + N <sup>+</sup>	17.8
	20.7
	25.2
	24.5
O <sub>2</sub> <sup>3+</sup> → O <sup>2+</sup> + O <sup>+</sup>	15.9
	19.8
	31.2

The spectra shown in Figure 1 (D-F) are believed to be the best available at the present time. A detailed analysis of these spectra will require extensive calculations of the potential energy curves for the parent molecular ions.

[1] R.L. Watson and V. Horvat, *Progress in Research*, Cyclotron Institute, Texas A&M University (2009-2010), p. IV-1.

- [2] L. Adoui, M. Tarisien, J. Rangama, P. Sobocinsky, A. Cassimi, J.-Y. Chesnel, F. Frémont, B. Gervais, A. Dubois, M. Krishnamurty, Sanjay Kumar, D. Mathur, *Physica Scripta* T92, 89 (2001).
- [3] U. Werner, B. Siegmann, and R. Mann, GSI Scientific Report, 282 (2004).
- [4] U. Brinkmann, A. Reinköster, B. Siegmann, U. Werner, H.O. Lutz , R. Mann, GSI Scientific Report 99 (1998).
- [5] B. Siegmann, U. Brinkmann, C. Haumann, U. Werner, H.O. Lutz , R. Mann, GSI Scientific Report (1999) 101.
- [6] U. Werner, B. Siegmann, and R. Mann, GSI Scientific Report 282 (2007).
- [7] U. Werner, B. Siegmann, R. Mann, N.M. Kabachnik, and H.O. Lutz, *Physica Scripta* T92, 244 (2001).

## **SECTION V**

# **SUPERCONDUCTING CYCLOTRON, INSTRUMENTATION, AND RIB UPGRADE**

## **K500 operations and development**

D. P. May, G. J. Kim, H. L. Clark, and F. P. Abegglen

### **Introduction**

During the 2010-2011 reporting period a total of 34 different beams, including 10 newly developed beams, were used for experiments, and there were a total of 49 beam tunings for these experiments. The SEE program is treated separately in this progress report.

### **Ion Sources**

Before the January shut-down ECR1 began to be plagued with leaks, probably caused by x-ray damage, developing in the Poly-Flo tubing that supplies cooling water to the plasma chamber. Also, degradation of the voltage-holding ability of ECR1 was beginning to be a problem. During the shutdown ECR1 was opened for examination, and it was found that there had been no further deterioration in the damaged spot that had developed over a plasma flute on the aluminum wall. The plasma chamber was then pulled from within the axial coils so that all the poly-Flo tubing could be replaced. After it was withdrawn, examination of the G-10 flange used for support and insulation of the plasma chamber on its extraction end revealed a spark track which was subsequently repaired. This whole operation was complicated by the contamination of the chamber by  $^{14}\text{C}$  which had been extensively used for beams. After reassembly ECR1 has exhibited much improved voltage-holding and has continued to perform well.

### **Cyclotron Beams**

New beams of  $^3\text{He}$  at 33 AMeV,  $^{11}\text{B}$  at 26 AMeV,  $^{27}\text{Al}$  at 25 AMeV,  $^{28}\text{Si}$  at 45 AMeV,  $^{30}\text{Si}$  at 18 AMeV,  $^{38}\text{Ar}$  at 25 and 29 AMeV,  $^{40}\text{Ar}$  at 5.5 AMeV,  $^{40}\text{Ca}$  at 35 AMeV, and  $^{64}\text{Zn}$  at 40 AMeV were developed for experiments.

### **Operations**

For the period April 1, 2010 through March 31, 2011, the operational time is summarized in Table I, while Table II lists how the scheduled time was divided. In April it was necessary to use one week of unscheduled maintenance for repairs to the Sullair helium compressor in the helium refrigeration system. In September maintenance was devoted to implementing the new interlock system and merging the K500 and K150 control systems. At the same time the K500 control room was dismantled to make way for construction on the ion-guide cave described elsewhere in this progress report. Since that time tuning of the K500 has been divided among three widely separated stations. In November, breakdown of the K500 inflector high voltage was addressed by repairing a vacuum leak through a seal on the inflector

shaft. As a consequence the vacuum in the K500 improved substantially, from the low  $10^{-7}$  torr range to the mid  $10^{-8}$  torr range.

**TABLE I.** 2010-2011 Operational Time

<b>Time</b>	<b>Hrs.</b>	<b>%Time</b>
Beam on target	6537.00	<b>87.9</b>
Tuning, optics, set-up	49.00	<b>0.7</b>
Beam development	224.75	<b>3.0</b>
Scheduled maint.	211.50	<b>2.8</b>
Unscheduled maint.	417.75	<b>5.6</b>
Idle time	0.00	<b>0.0</b>
<b>Total</b>	<b>7440.00</b>	<b>100.0</b>

**TABLE II.** 2010-2011 Scheduled Beam Time.

<b>Time</b>	<b>Hrs.</b>	<b>%Time</b>
Nuclear physics	1859.75	<b>26.3</b>
Nuclear chemistry	1540.00	<b>21.8</b>
Atomic physics	95.50	<b>1.4</b>
Outside collaboration	0.00	<b>0.0</b>
Outside users	3340.50	<b>47.3</b>
Beam development	224.75	<b>3.2</b>
<b>Total</b>	<b>7228.50</b>	<b>100.0</b>

**Texas A&M cyclotron radiation effects facility**  
**April 1, 2010 – March 31, 2011**

H. L. Clark, J. Brinkley, G. Chubarian, V. Horvat, B. Hyman, B. Roeder, and G. Tabacaru

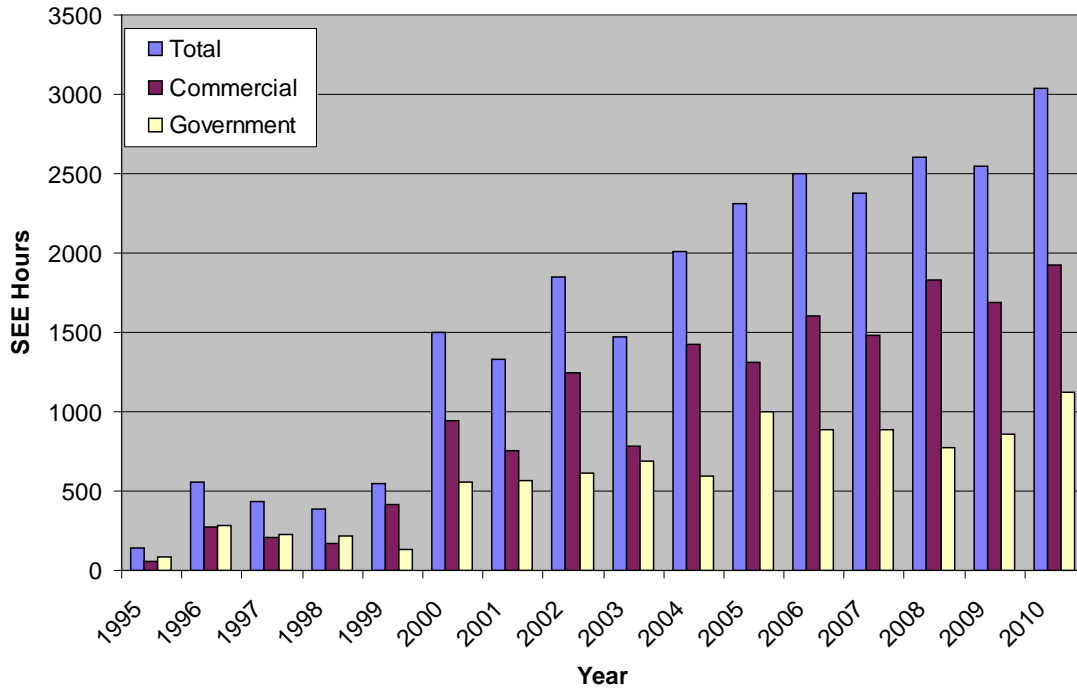
The activity of the Radiation Effects Facility (REF) increased dramatically over the previous reporting year. In this reporting period, the facility was used for 3,042 hours, which is a ~19% increase over the 2,552 hours used in the 2009-2010 reporting period and surpasses the record of 2,600 hours from 2008-2009. Users of the facility (and hours used) over the past year were: NASA GSFC (367), NAVSEA (345.25), SEAKR (335), Xilinx Corp (284), Lockheed Martin (203.5), Intersil (165), Boeing Research & Technology (144), Aeroflex Corp (130.25), NASA JPL (106.5), Boeing Satellite Systems (89), BAE Systems (87.5), Stapor Research Corp (80), HIREX - France (73), Honeywell Corp (68), Ball Aerospace (67), International Rectifier (65), Silicon Turnkey (55.5), National Semiconductor (43.5), Northrop Grumman (39.25), Georgia Tech (32), Air Force (30.5), Microsemi Lawrence (30), General Dynamics (25), JD Instruments (24), VPT Inc (24), OptiComp Corp (21), University of Idaho (20), NASA JSC (16), SOREQ - Israel (16), Thales Alenia - France (16), Data Device Corp (12.5), Radiation Assured Devices (10), Silicon Space Technologies (9) and SunTronics (8). New users included Boeing Research & Technology, HIREX – France, OptiComp Corp and Thales Alenia - France.

Table I compares the facility usage by commercial and government customers. The ratio from this reporting year (63% to 37%) is similar to the trend seen in previous reporting periods and commercial hours still dominate (see Fig 1). Commercial hours increased by 14% and government hours

**TABLE I.** Radiation Effects Facility usage by commercial and government customers for this and previous reporting years.

Reporting Year	Total Hours	Commercial Hours (%)	Government Hours (%)
2010-2011	3,042	1,922(63%)	1,121(37%)
2009-2010	2,551	1,692 (66%)	859 (34%)
2008-2009	2,600	1,828 (70%)	772 (30%)
2007-2008	2,373	1,482 (62%)	891 (38%)
2006-2007	2,498	1,608 (64%)	890 (36%)
2005-2006	2,314	1,314 (57%)	1,000 (43%)
2004-2005	2,012	1,421 (71%)	591 (29%)
2003-2004	1,474	785 (53%)	689 (47%)
2002-2003	1,851	1,242 (67%)	609 (33%)
2001-2002	1,327	757 (57%)	570 (43%)
2000-2001	1,500	941 (63%)	559 (37%)
1999-2000	548	418 (76%)	131 (24%)
1998-1999	389	171 (44%)	218 (56%)
1997-1998	434	210 (48%)	224 (52%)
1996-1997	560	276 (49%)	284 (51%)

increased by 30% over hours from 2009-2010. 15 and 25 MeV/u Kr and Xe were most utilized as well as 15 MeV/u Au. No new beams were added to SEELine users list. Much of the testing conducted at the facility continues to be for defense systems by both government and commercial agencies. It is expected that the facility will continue to be as active in future years.



**FIG. 1.** Radiation Effects Facility usage by commercial and government customers for this and previous reporting years. Despite the increase in total hours by 19%, the ratio from this reporting year (63% to 37%) is similar to the trend seen in previous reporting periods where commercial hours still dominate.

## Cyclotron computing

R. Burch and K. Hagel

Our mission is to provide the Cyclotron Institute personnel the computational and network resources necessary to execute their research programs. This past year we increased the Institute's computing capacity by adding two additional computational servers to the lab's cluster, four computational servers to sjy-group's cluster, and two computational servers to the star-group's cluster. We also upgraded the mail, backup, and vm servers. We are continuing the pursuit of virtualizing<sup>1</sup> administrative servers to allow us to better utilize server room rack space, power and cooling by reducing our physical machine count. Procedures to build and deploy these virtual machines are still under development.

The Institute's computational power was greatly enhanced by retiring two machines and adding four new machines to the lab computational cluster, increasing our capacity from 80 to 128 concurrent jobs, while sjy-group's cluster, with four new machines went from 58 to 132 concurrent jobs, and star-group's cluster, retiring three and adding two new machines, went from 14 to 56 concurrent jobs. The server room's concurrent job capacity increase of 110 to 316 jobs (223%) allows research groups to execute computational jobs in a more timely manner. Each new server included a minimum of 16GByte RAM enable jobs with larger memory requirements to execute more efficiently.

Responding to user comments, we analyzed the mail server/mail client responsiveness and in the process we identified a bottleneck. The server was unable to place user mailboxes fully in memory and so swapped parts of the mailbox to disk which slowed the processing considerably and delayed delivery for all users. Quadrupling the memory of the mail server allowed the server to place user mailboxes, some approaching 1GByte, fully into system memory, hence removing the bottleneck and speeding mail retrieval.

During the past year, one drive on the home disk fileserver failed. The RAID system worked as advertised and removed the failed drive and activated the hot spare, transparent to our users. On a day of our choosing, we installed the replacement drive into the RAID system and provisioned it as a hot spare. With this experience, we re-provisioned disks on our test vm server as a RAID system. We also added two 1TByte user data disks to our cluster.

As the institute adds new research groups and personnel, the quantity of data requiring backup increases. We found that we were growing short on backup disk space and therefore replaced the two 500GByte drives with two 1TByte drives to cover the institute's continuing data growth. We also replaced the USB2 offsite backup drive with an eSATA drive which is considerably faster, accomplishing the backup in nominally 4 hours instead of the previous 6 hours. This change resulted in fewer backup failures due to the previous backup not completing before a new backup would start.

The enhancements and general maintenance allows us to supply the Institute with the resources it needs to execute its mission by increasing our computational and data serving capacity while enhancing

backup capacity, eliminating slow mail service, and provisioning RAID setups for critical servers. Additionally, we plan to push to deploy a VM infrastructure this coming year.

[1] R. Burch and K. Hagel, Progress in Research, Cyclotron Institute, Texas A&M University (2009-2010), p. V-5.

## Cyclotron Institute upgrade project

H. L. Clark, F. Abegglen, G. Chubarian, G. Derrig, G. Kim, D. May, and G. Tabacaru

On January 3, 2005 the Cyclotron Institute Upgrade Project (CIUP) began with the approval of the CIUP management plan by the Department of Energy Nuclear Physics Office. The project will extend at least to the second quarter of calendar year 2012. When completed, the upgraded facility will provide high-quality re-accelerated secondary beams in a unique energy range in the world. Funding for the upgrade comes from several sources: the Department of Energy, matching support from TAMU, the Robert A. Welch Foundation and beam time sales for testing electronics components at the Cyclotron Institute.

The CIUP is divided into three major tasks: (1) Re-commission of the existing K150 (88") cyclotron and refurbish beam lines; (2) Construct light-ion and heavy-ion guides and produce 1+ radioactive ions; (3) Transport and charge boost radioactive ions and accelerate in the K500 cyclotron.

As detailed in the Management Plan, effort made during this year on Task 1 included,

- Construction of equipment for the K150 high vacuum system,
- Development of the negative ion source,
- Development of high intensity proton and deuteron beams, and
- Installation of the radiation monitoring system for the K150 and K500 cyclotron vaults and experimental caves.

Progress was also made on Tasks 2 and 3. This included,

- Procurement and installation of the radiation shielding for the ion guide cave,
- Construction of the Heavy Ion Guide gas cell and transport system, and
- Assembly and installation of the n+ transport system. Below we report on a few of the accomplishments listed above.

### K150 Cyclotron Development

In this reporting period, we successfully injected, accelerated, and strip extracted 20 and 30 MeV H<sup>-</sup> and 10 AMeV D<sup>-</sup> beams from the K150 cyclotron. We then were able to deliver the first K150 beams, namely 30 MeV protons and 10 AMeV deuterons, to three different experiments.

The H<sup>-</sup> source was installed in Feb. 2010 as was reported in the last progress report. In addition, a 3.5" einzel lens was installed just below the 90° analyzing magnet in order to make the H<sup>-</sup> beam transport consistent with the existing injection scheme from the ECR2 beams into the cyclotron. To accelerate H<sup>-</sup> beams, the polarities of the main magnet and all the trim coils were reversed, so that the H<sup>-</sup> beams would circulate in the same direction as the normal, positively charged beams. Then to strip extract the H<sup>-</sup> beams, a stripper foil system and a corrector dipole were installed as shown in Fig. 1. The stripper system allows the foil to be positioned with range of 2" in radius and 3 degree in azimuth about the nominal stripping point at 38" and 120° (0° being along the dee lip pointing South). Finally, the H<sup>-</sup>

corrector dipole bends the stripped beam, which after going through the foil peeled away, by about 15-18 degrees into the exit beam line.

First  $H^-$  and  $D^-$  beams were developed in May and June of 2010. The very first trial beam was 20 MeV  $H^-$ , having accelerated the 20 MeV protons before. After injecting the beam onto the mirror inflector and then finding the beam on the beam probe, the accelerated  $H^-$  beam was stripped and extracted onto FC01, a faraday cup located just after the  $H^-$  corrector dipole. Finding the proper stripper position and the  $H^-$  corrector value took some effort to optimize, but we were able to obtain about  $7 \mu A$  on FC01.

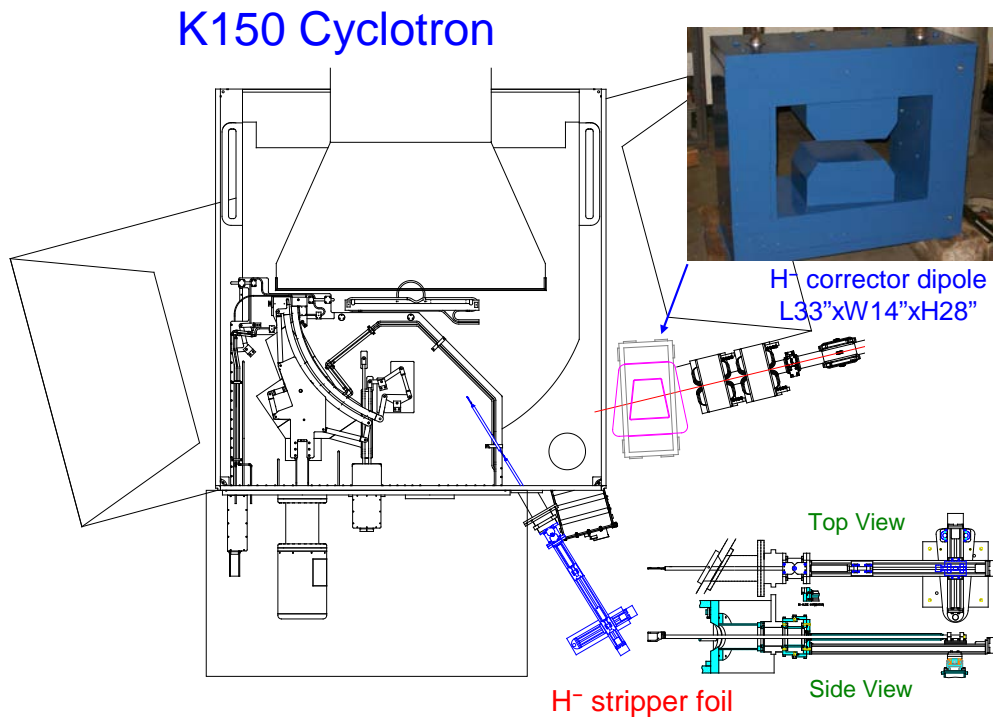


**FIG. 1.** Strip extraction for  $H^-$  beams. A stripper foil system and a small dipole were added to produce very efficient strip extraction for the  $H^-$  beams.

The next beam was 30 MeV  $H^-$ . And after a few days of tuning the beam, including the source and the beam buncher, we were able to achieve  $17 \mu A$  of extracted beam on FC01, meeting another milestone for the K150 cyclotron. We actually topped  $24 \mu A$  on FC01; however, the beam current declined over time due to deteriorating vacuum in the cyclotron due to beam and RF heating. The fleeting  $24 \mu A$  was obtained just after unblocking the beam with an injection line cup, which was blocked to cool the cyclotron vacuum over several minutes. We believe that this vacuum problem would slowly improve as the cyclotron becomes conditioned over time.

We also worked on two deuterium beams, at 10 and 20 AMeV, using the same  $H^-$  source with deuterium gas instead of hydrogen gas. We were able to accelerate and extract  $1.2 \mu A$  of 10 AMeV deuterons on FC01. However, for the 20 AMeV  $D^-$ , we were able to accelerate, but were unable to find

the extracted beam on FC01. Next time, we plan to take smaller energy steps in developing higher energy beams.

The developed  $H^-$  and  $D^-$  beams were used in actual experiments by three separate groups in Nov. and Dec. 2010. The 30 MeV proton beam was used by Sobotka (Washington Univ. in St. Louis) and Youngblood in the MDM cave, and the 10 AMeV deuteron beam by Natowitz in the K150 vault at the end of Heavy Ion Guide line. The first K150 beam transport to the experimental areas was difficult, just because the beamlines were new and unfamiliar. More detailed accounts of the first beam transport of the K150 beams are given below. After the beams were delivered to the experimenters, each group used the beam for about 10 hours per day for a few days; the source and the beam ran very stably during the runs.

In developing the 30 MeV  $H^-$  beam and also in trying to meet the 14  $\mu A$  extraction milestone, the following numbers have been collected from May 2010.

- 1) The  $H^-$  source provided up to 800  $\mu A$  at ILC02.
- 2) Injection efficiencies from ILC02 to inflector cup were 30-50%.
- 3) Beam acceptance into cyclotron is defined as the ratio of the beam current on the beam probe at 10", BP(10") to the beam current on ILC02. Since only a small area of the mirror inflector properly deflects the beam into cyclotron, whereas the entire mirror electrode can collect the beam, the ratio of the beam current from the inflector to BP(10") is not a direct measure of the beam acceptance. The above definition of the beam acceptance into the cyclotron obviously includes beam injection efficiencies. The beam acceptance ranged from 2-3% (without bunching). The bunching was not very effective for intense beams, it enhanced by only about 30%, whereas for 10% of the full beam, the bunching factor was 370%. The space charge effects on the buncher and the inflector seem dramatic; the mirror inflector operates by slowing the beam down and speeding it up on the way out, and a slow beam is more susceptible to space charge effects, and so having a spiral inflector would help here.
- 4) The internal transmission from 10" to 38" was 80-90%.
- 5) Strip extraction efficiencies, as measured as the ratio of the beam current on FC01 over BP(38"), ranged from 70-80%.
- 6) Recall that we topped 24  $\mu A$  on FC01 (however briefly), which we summarize as:  
 $24 \mu A = 800 \mu A \times 1.3 \times 0.034 \times 0.80 \times 0.85$  This translates into the throughput for the intense beam production, from ILC02 to FC01, at only 3%.

The K150 cyclotron and its beamlines are shown in Fig. 2. As was mentioned previously that first K150 beams were delivered to three separate experiments in late 2010; beams have been transported to the MDM cave and to the Heavy Ion Guide line (inside the K150 vault).

For the K150 beamlines, a big challenge was how to control the beam divergence in transporting large emittance beams from the K150 cyclotron. Using TRANSPORT, the beamlines were designed to transport  $24 \pi$  mm-mrad emittance beams, utilizing two sets of quadrupole doublets configured for point-to-parallel and then parallel-to-point focusing scheme. By dividing the usual two large angular kicks

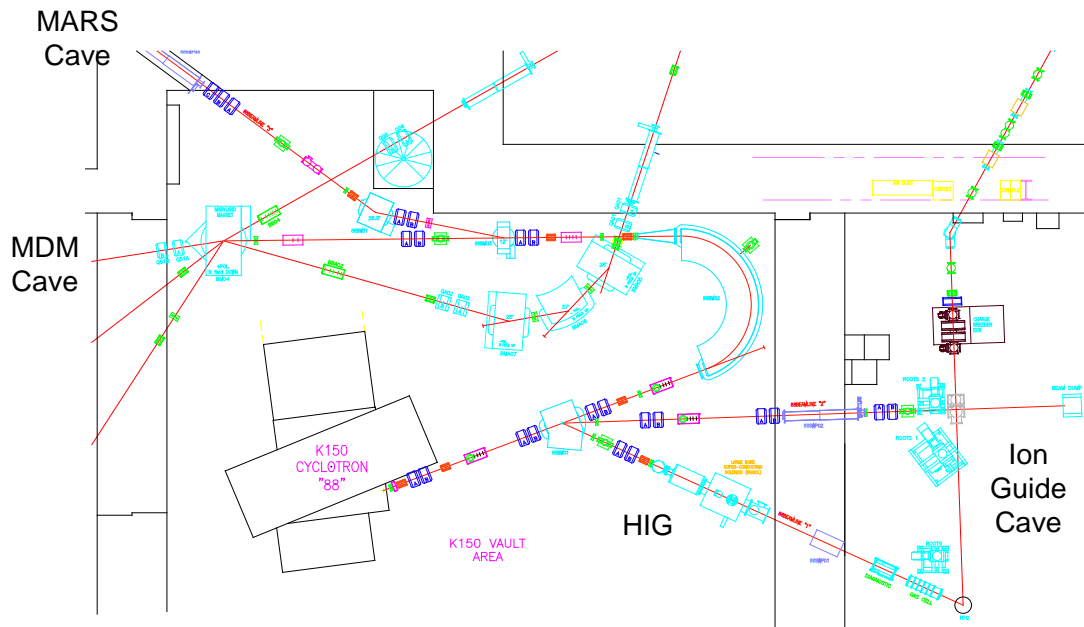


**FIG. 2.** New K150 beam lines.

from a quadrupole doublets into four gentle kicks using two pairs of doublets, we wanted to control the beam divergence through the beamlines. However in practice, this scheme became complicated due to couplings of four quadrupoles from two doublets.

Having a field calibration for the quadrupoles (we used a TOSCA calculation) has helped to get close to the proper values on the quadrupoles, however, we need more experience with the K150 beamlines as well as working with the larger emittance K150 beams.

### Ion Guide Cave Radiation Shielding System

The design for the beam dump and shielding structure was approved by a review panel in March 2007. Following the guidance of the review panel, the shielding system of the Ion Guide cave (see Fig 3.) was studied with additional concrete shielding around and above the beam dump. The extra beam dump shielding and an extra layer of 18" thick roof planks were found to reduce the secondary radiation inside and outside the cave by two orders of magnitude. The cost for the additional shielding is within the budget of the project and has been implemented.

The beam dump (to stop the intense proton beams from the light ion guide) will be made from pure aluminum (to stop the beam) surrounded by thick concrete walls (to retain secondary radiation produced by the aluminum). Heat from the beam will be removed by water cooling the aluminum with a purchased cooling unit. Aluminum quoted to be 99.98% pure was cast into one solid block and then machined into shape. A second aluminum beam dump has been machined as well.

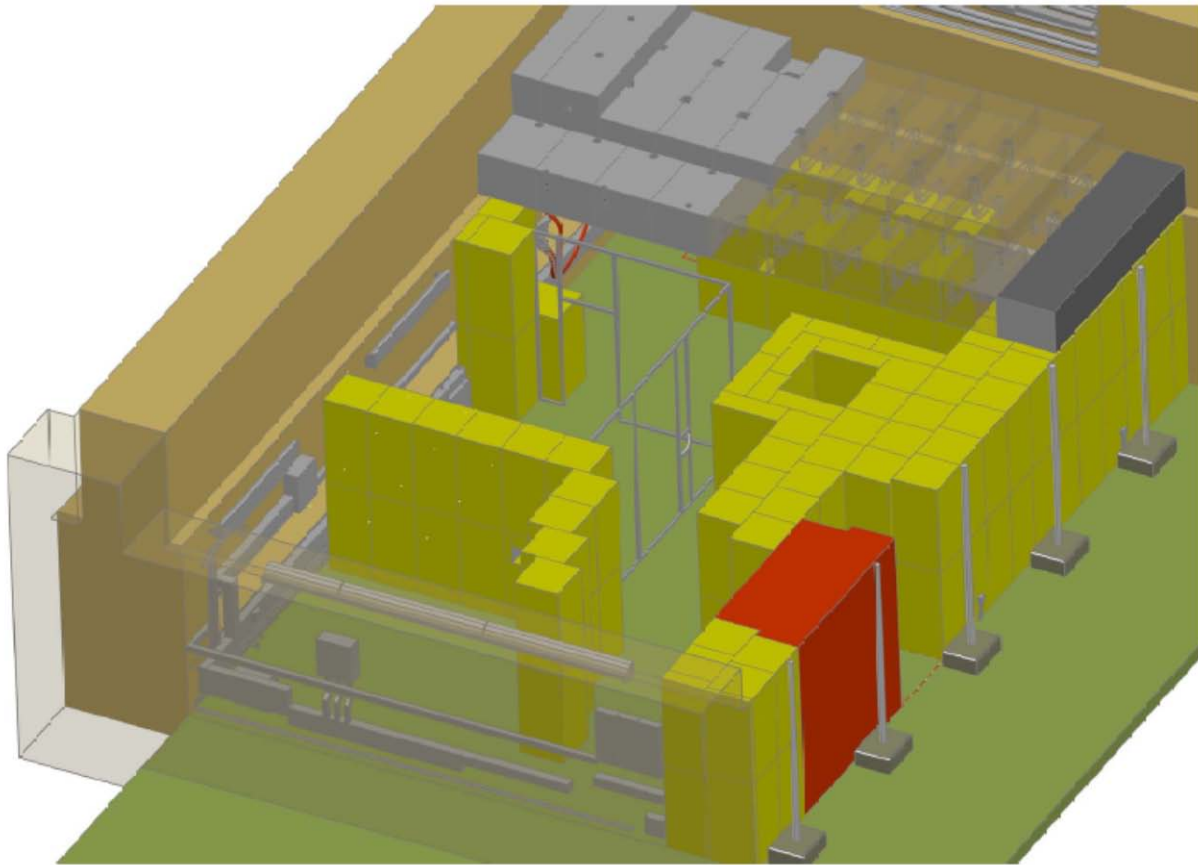


**FIG. 3.** Ion Guide Cave Radiation Shielding system was completed in February 2011 and tested in March 2011.

Preparation of the Ion Guide cave was completed in September 2010 and included the complete removal of the office building on top of the roof planks. The CB-ECR ion source and Light Ion Guide were dismantled and/or covered to protect them during the installation of the Radiation Shielding system. The majority of the shielding system (wall block, wall panels and roof planks) arrived as scheduled and was installed in November and December 2010. The four remaining wall blocks were installed and the end walls poured in early March 2011.

In late March 2011, the beam dump and radiation shielding system were tested and were found to perform as according to design. Beams of 30 MeV protons at intensities of  $10 \mu\text{A}$  were stopped on the beam dump in the ion guide hall. The leakage of secondary radiation from the cracks and passageways in the radiation shielding system were carefully measured and documented. No major leakage points were discovered. The results of the test will be reported in another progress report.

## Shielding evaluation for the light ion guide and heavy ion guide

G. Tabacaru, H. L. Clark, G. Chubaryan, G. Derrig, F. P. Abegglen, and L. Rodriguez

The Upgrade Project at Cyclotron Institute arrived at the stage where the hall accommodating the Light Ion Guide (LIG) and the Heavy Ion Guide (HIG), the new radioactive beam production devices, is being prepared for the final configuration. This new hall will include the primary beam dump [1] bunker; consequently, careful design of the shielding is required. During the normal operation, the primary beam will be stopped into a high purity aluminum stopper. The stopper is embedded in a box-like structure with the dimensions of 31.7" x 41.5" x 19.7" with walls made from concrete, 4" thick borated polyethylene and 2" thick steel. This box is installed inside a concrete bunker, it rests on a concrete brick base and it is surrounded by several concrete wall panels with the approximate dimensions of 10' tall, 45" or 30" wide and 15" thick. On the top of the beam dump box three large concrete blocks fill the void in the ceiling of the cave.

The roof of the hall consists in two layers of concrete roof planks: the first layer (the original one) is 39" wide and 30" thick with serpentine channels for ventilation and cable conduit; the second one is a new addition to the hall and is only 15" thick with the same 39" wide. The second layer is placed staggered on the top of the first one in order to cover the cracks from the first layer of roof planks. At the

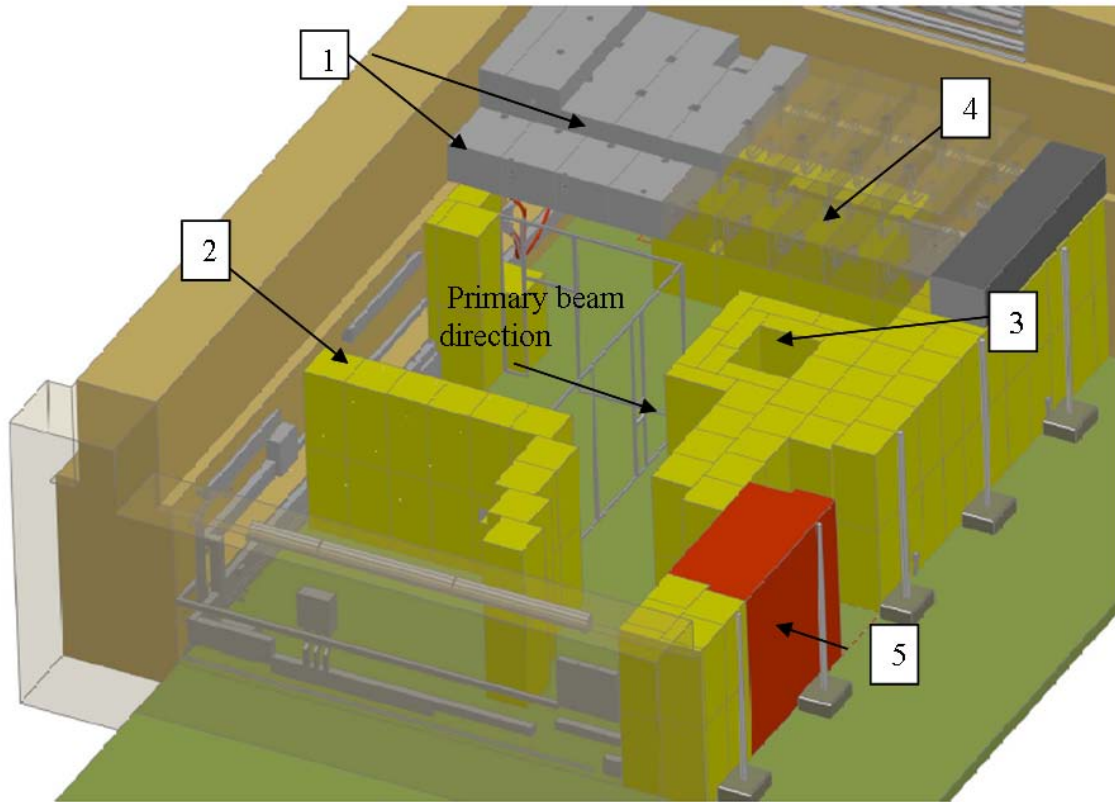


**FIG. 1.** View of the Light Ion Guide (LIG) and the Heavy Ion Guide (HIG) hall. 1. First and second layer of roof planks. 2. Separation wall between LIG and HIG areas. 3. Concrete bunker. The concrete blocks filling the void are missing. 4. Separation wall in the LIG for area for the vertical injection line. 5. Concrete sliding door.

positions of the ventilation openings from the first layer, square openings are present in the second layer. Figure 1 represents a view of the hall.

Inside the hall two new walls were built: one separates the LIG area from the HIG area, and the second one separates the vertical injection line from the rest of the cave. The two walls have the role in reducing the neutron and gamma flux in the HIG area, where electric equipment sensitive to radiation will be located and above the LIG area at the vertical injection line penetration location where human personnel might be present.

This shielding design was studied throughout the years using Monte-Carlo type radiation transport codes MCNPX [2] and PHITS [3], coupled essentially with Los Alamos Natl. Lab. libraries. The simulations are time consuming and different approaches of the problem were considered in order to minimize the calculation time and to have reasonable results with reasonable errors. Two types of simulations were performed: one covers the situation where the primary beam is stopped inside the concrete bunker (normal operation) and one covers the unfortunate situation when the primary beam is stopped outside the bunker. The last situation could appear, for example, in the case when magnetic elements in the beam line fail to operate and the beam takes other trajectories, being stopped in the beam pipe walls. This last case was studied in detail and also recently some few measurements were performed.

In the following we will report neutron calculated equivalent dose at 8 locations above the experimental hall; they are compared with recent performed measurements. The MCNPX calculations consider a 30 MeV proton beam with an intensity of 10  $\mu$ A stopped in an aluminum block outside the

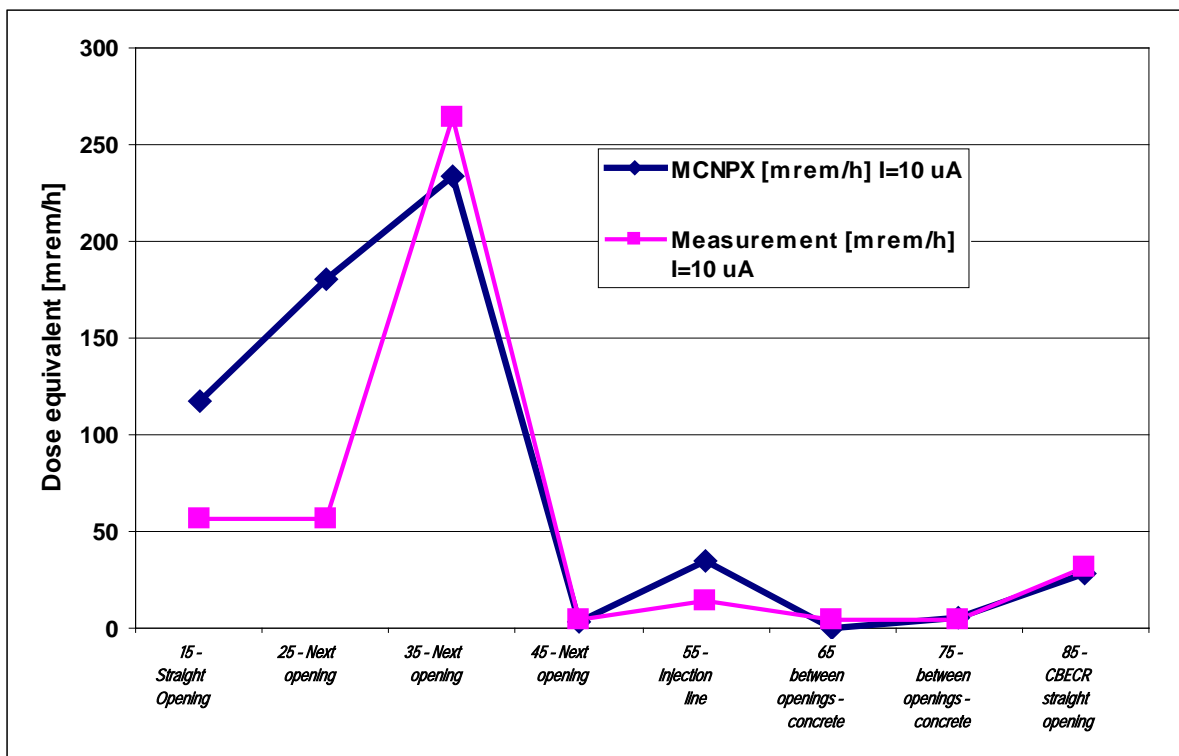


**FIG. 2.** Comparison between calculated dose equivalent (blue) and measured dose equivalent (magenta) for neutrons at 8 locations above the LIG area. The largest dose is measured and calculated at the beam stopper location.

concrete bunker. The measured current on the block was 10  $\mu\text{A}$  as well. Figure 2 presents the calculated dose equivalent in mrem/h in comparison with the measured dose equivalent using a Neutron Survey Meter (model REM 500 by Health Physics Instruments [4]). The calculations follow very well the measurements, the highest measured dose being at the stopper location. It is also remarkable the fact that some of the measured values are in very good agreement with the calculated one showing the power of prediction of the MCNPX code.

The measurements showed the necessity of declaring an exclusion zone above the LIG area. As the calculations predicted, in the vast majority, the neutrons escaping from the hall follow the serpentine ventilation channels contributing to a dose enhancement immediately above the square opening in the second layer of roof planks. Polyethylene or other hydrogenous materials together with steel will be used to cover the openings aligned with the primary beam line. Outside the walls neutrons were not detected; however higher gamma doses were measured at the joint between the wall and the roof planks.

Overall the shielding will protect human personnel from exposure, but a few precautions need to be considered when accessing the location above the LIG area. Future plans include new measurements with the primary beam stopped inside the concrete bunker (normal operation) and an activation / cooling analysis.

- [1] G. Tabacaru and H.L. Clark, Progress in Research, April 1, 2006 – March 31, 2007, Cyclotron Institute, [http://cyclotron.tamu.edu/2007%20Progress%20Report/5%20Superconducting%20Cyclotron%20and%20Instrumentation/V\\_21\\_shielding.pdf](http://cyclotron.tamu.edu/2007%20Progress%20Report/5%20Superconducting%20Cyclotron%20and%20Instrumentation/V_21_shielding.pdf)
- [2] <http://mcnpx.lanl.gov>
- [3] K. Niita *et al.* PHITS: Particle and Heavy Ion Transport code System, Version 2.23, JAEA-Data/Code 2010-022 (2010)
- [4] [http://www.fwt.com/hpi/hpi\\_rem500ds.htm](http://www.fwt.com/hpi/hpi_rem500ds.htm)

## Active bases in NIMROD

K. Hagel, A. J. Henryson and T. Cowden

Scientists using multidetector arrays that employ scintillating detectors with photomultiplier tubes (PMT) must decide what type of voltage divider to use in order to collect the signal from the PMT. On the one hand are the so called passive bases which are simply resistor chains with the resistance tuned to provide the proper voltage for the proper dynode. Such bases have the advantage of simplicity. However, the voltage over the later stage dynodes drops when the PMT detects a photon, thus changing the voltage divide ratio and hence affecting the eventual signal from the PMT. A further drawback of such passive bases is that when the rate of detected photons is high, the voltage can sag as well causing a count rate dependent output from the PMT. It is possible to compensate for this effect by suitably choosing a resistor series that allows a large enough current that the relative drop of the voltage is very small. This is usually of the order of a milliamp. This requires the use of power supplies which can supply at least that much current. Such power supplies are typically more expensive. Heat from the increased power can also be an issue.

Another approach is to use so called active bases. Such bases are also voltage dividers, but they employ Field Effect Transistors (FETs) which restore the sagging voltage by opening the gate when the voltage sags. This leads to stability relative to the counting rate. Because the voltage is restored when it sags, the amount of current required is much less leading to less heat load and hence less stringent requirements for cooling. Active bases have been employed INDRA [1] and the design and performance of them has been detailed in that reference.

We have to date employed passive bases in NIMROD [2]. This was possible because the high voltage power supply that was available supported high current. In addition, because of the forward silicon detectors, NIMROD demands a low counting rate removing the problem of count rate dependent gains resulting from passive bases. Due to various upgrades, it has become necessary to upgrade the HV power supply that is used in NIMROD. In order to find the most cost effective solution, we have developed active bases for the various PMTS used in NIMROD. These developed bases are based on the active bases employed in INDRA [1].

The bases were tested in several test runs where we used some available CsI detectors with the newly designed active bases. Figure 1 shows the results of a run with 20 MeV deuterons incident on a Gold target. We note the deuteron elastic peak at 25000 in fast (x-coordinate). We note a very good separation of deuterons from protons down to less than 4 MeV. Triton and  $^3\text{He}$  lines are absent due to kinematics in this reaction system. The line of alpha-particles is very well separated and extends as far as it is kinematically allowed.

As the test described used a very low energy  $^2\text{H}$  beam, we plan a “final” test of the new active bases in NIMROD using a typical beam for experiments performed in NIMROD. One active base will be implemented in each ring. Assuming a positive result, we will construct the rest of the bases before the next production experiment.

hFastVsSlow

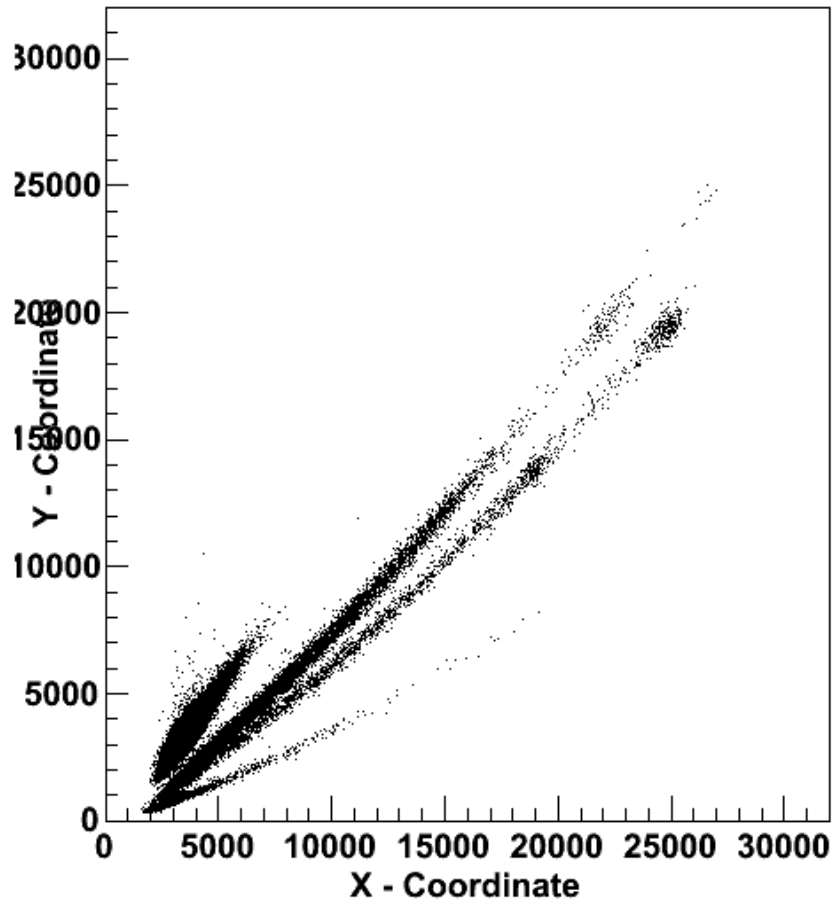


FIG. 1. Fast vs slow plot showing the performance of the active base.

[1] J. Pouthas *et al.*, Nucl. Instrum. Methods Phys. Res. **A369**, 222 (1996).

[2] S. Wuenschel, *et al.*, Nucl. Instrum. Methods Phys. Res. **A604**, 578 (2009).

**Experimental and theoretical cross section study for production of medically important radioisotopes  $^{52}\text{Mn}$ ,  $^{51}\text{Cr}$  and  $^{46,47}\text{Sc}$**

A. Alharbi, M. McCleskey, B. Roeder, A. Spiridon, E. Simmons,  
L. Trache, and R. E. Tribble

The production of  $^{52}\text{Mn}$ ,  $^{51}\text{Cr}$ ,  $^{46}\text{Sc}$  and  $^{47}\text{Sc}$  radioisotopes of considerable interest for the application in nuclear medicine for PET imaging, cancer treatment, monoclonal antibodies and radio-immunotherapy[1,2], as shown in Table I, were investigated by alpha bombardment of natural Vanadium target up to  $E_\alpha= 25 \text{ MeV/u}$  and currents of about 50 nA.

**Table I.** The significant applications for the studied radioisotopes.

<b>Radioisotope</b>	<b>Applications</b>
$^{52}\text{Mn}$	PET scanning.
$^{51}\text{Cr}$	Cell labeling and dosimetry.
$^{46}\text{Sc}$	Regional blood flow studies, PET imaging.
$^{47}\text{Sc}$	Cancer treatment/diagnostics, monoclonal antibodies, radio-immunotherapy.

The experimental excitation function and yield for the reaction shown in Table II were measured using the stacked foil irradiation technique followed by HPGe  $\gamma$ -ray analysis and then compared with earlier measured and published values when possible.

Two irradiation processes were carried out using an Aluminum target holder that acts as Faraday

**Table II.** The contributing reactions and the decay data of the investigated radioisotopes [3].

<b>Nuclide</b>	<b>Half life</b>	<b>Principal contributing reactions</b>	<b>Q-value MeV</b>	<b><math>E_\gamma</math> keV</b>	<b><math>I_\gamma</math> %</b>
$^{54}\text{Mn}$	312.2 d	$^{51}\text{V}(\alpha, n)$	-2.31	834.8	99.9
$^{52}\text{Mn}$	5.71 d	$^{51}\text{V}(\alpha, 3n)$	-23.42	1434.1	98.2
$^{51}\text{Cr}$	27.7 d	$^{51}\text{V}(\alpha, p3n)$	-29.85	320.2	9.83
$^{48}\text{V}$	16.2 d	$^{51}\text{V}(\alpha, \alpha 3n)$	-31.94	944.3	7.75
$^{48}\text{Sc}$	43.66 h	$^{51}\text{V}(a, a2pn)$	-58.61	1037.5	97.5
$^{47}\text{Sc}$	3.42 d	$^{51}\text{V}(\alpha, 2\alpha)$	-10.32	159.4	68.0
$^{46}\text{Sc}$	83.86 d	$^{51}\text{V}(\alpha, 2\alpha n)$	-20.96	889.2	99.9

cup to measure the beam intensity. The alpha particles beam extracted from the K500 superconducting cyclotron have been used to irradiate a multi-target stack made of the targets shown in Table III.

**Table III.** The used specifications and roles of the used targets.

Target	Purity %	Thickness ( $\mu\text{m}$ )	Number of used foils	Role
$^{nat}\text{V}$	99.8+	80	21	Target for medical radioisotope production
$^{nat}\text{Ti}$	99.6+	25	10	Monitoring and degrading
$^{nat}\text{Al}$	99.99	50, 59, 100	23	Monitoring and degrading

Different monitor reactions such as:  $^{27}\text{Al}(p,x)^{22,24}\text{Na}$ ,  $^{nat}\text{Cu}(p,x)^{62,63,65}\text{Zn}$ ,  $^{nat}\text{Ti}(\alpha,x)^{51}\text{Cr}$ ,  $^{nat}\text{Al}(\alpha,x)^{22,24}\text{Na}$ , and  $^{nat}\text{Cu}(\alpha,x)^{66,67}\text{Ga}$ ,  $^{65}\text{Zn}$  [4,5] were studied by inserting the monitor foils in different positions along the stack to determine the beam current. The chosen irradiation geometry allows the beam to pass through every foil. The secondary effect of the background neutrons on each target was checked by foils placed in the stack far beyond the range of the fully stopped proton beam.

The radioactivity of the residual nuclei in the activated foils was measured using one HPGe  $\gamma$ -ray detector (70% relative efficiency). Each foil was recounted after different cooling times to avoid disturbance by overlapping  $\gamma$ -lines from undesired sources and in order to accurately evaluate cross-sections for cumulative formation of the corresponding longer-lived daughter radionuclide. The detector-source distance was kept large enough to keep the dead time below 5% and to assure the same geometry. From the decay rates of the radioactive products and the measured beam current, the cross sections for the nuclear reactions were determined using the well-known activation formula [6]. Figure 1 show two excitation functions from the measured cross-sections.

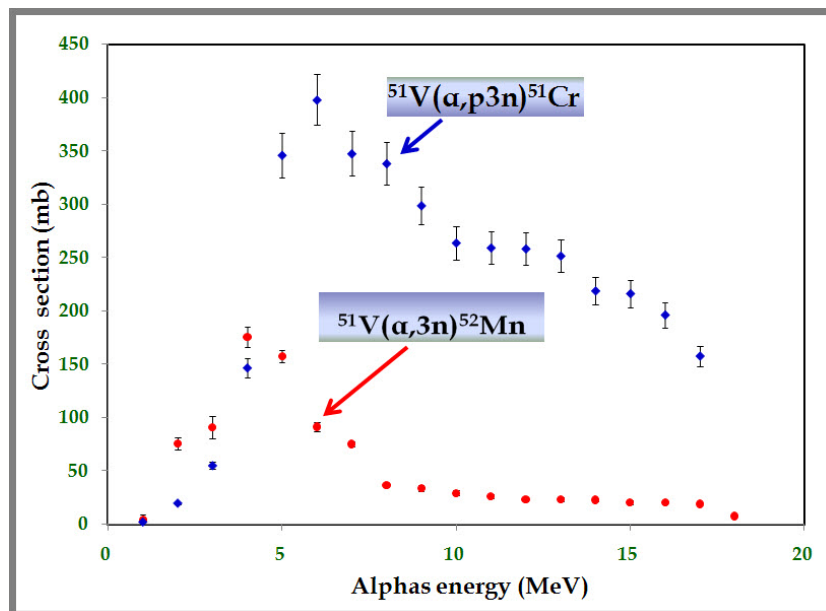


**FIG. 1.** Excitation function of the  $^{51}\text{V}(\alpha, 3n)^{52}\text{Mn}$  and  $^{51}\text{V}(\alpha, p3n)^{51}\text{Cr}$  reactions.

A consistency check of all experimental data was carried out using nuclear model calculations via two different codes. The first is EMPIRE II [7], which is accounting for the major nuclear reaction mechanisms, including the Optical Model (OM), the Multi-step Compound, Exciton Model, full featured Hauser-Feshbach Model, with a comprehensive parameter library mainly covering nuclear mass, OM data, discrete levels and decay schemes. The second code is TALYS [8] which is a software package which provides a simulation of nuclear reactions that takes in consideration a huge database for nuclear structure and model parameters, mostly based on the IAEA reference input parameter library.

We are finalising the data analysis and the constructed excitation functions will be compared with the available previously published data to be able to derive reproducible and recommended cross section values for the different reactions.

- [1] S.M. Qaim, Use of cyclotron in medicine, *Radiation Physics and Chemistry*, **71**, 917 (2004).
- [2] R.M. Lamberecht, Positron emitting radionuclides-present and future status, Proceedings second international symposium on radiopharmaceuticals. Seattle, Washington, March, 1979 (The Society of Nuclear Medicine Inc., New York).
- [3] T-16, Nuclear Physics Group, [Theoretical Division](#) of the Los Alamos National Laboratory (1997). Nuclear Information Service, Los Alamos, USA. Available online: <http://t2.lanl.gov/data/data.html>
- [4] F. Tárkányi *et al.*, (2001): Beam Monitor reactions. IAEA-TECDOC-1211. IAEA, (2001) Vienna, p. 49.
- [5] K. Gull, A. Hermanne, M.G. Mustafa, F.M. Nortier, P. Oblozinsky, S.M. Qaim, B. Scholten, Yu Shubin, S. Takács, T.F. Tárkányi, and Y. Zhuang, Charged particle cross-section database for medical radioisotope production: diagnostic radioisotopes and monitor reactions, Final Report of a Co-ordinated Research Project, IAEA-TECDOC-1211, IAEA, (2001) Vienna, Austria.
- [6] F. Helus, Lelio G. Colombetti, Radionuclides Production, CRC Press Inc., (1980) Boca Raton, Florida.
- [7] M. Herman, EMPIRE-II Statistical Model Code for Nuclear Reaction Calculations, (Londri), IAEA, (2005) Vienna, Austria, March, Version 2.19; <http://www-nds.iaea.org/empire/>, 2005.
- [8] A.J. Koning, S. Hilaire, and M.C. Duijvestijn, Proceeding Int. Conf. Nucl. Data for science and Technology, Nice, France, April, 2007, edited by O. Bersil-Ion, F. Gunsing, E. Bauge, R. Jacqmin, and S. Leray, (EDP Sciences 2008), p. 211.

## Production cross-sections of medical radioisotopes from proton bombardment of $^{nat}\text{Mo}$

A. Spiridon, A. A. Alharbi,\* M. McCleskey, A. Banu,<sup>†</sup> G. Tabacaru, B. Roeder,  
E. Simmons, L. Trache, and R. E. Tribble

This In 2009 a research program was started at the Cyclotron Institute to study the production of medical radioisotopes using beams of protons, alphas and helium-3 from the K500 superconducting cyclotron. Radioactive nuclides are mainly used in medicine for diagnostic (PET and SPECT imaging) and therapeutic (radiopharmaceuticals and brachytherapy) purposes.

There have been 8 experiments performed as part of this program. The present work will focus on results of the analysis of the first experiment in the series. The motivation for it was two-fold. First, it was a study of the excitation function of  $^{99m}\text{Tc}$ , commonly used in SPECT imaging, and of the potential for medical applications of the other residual radioisotopes. Second, it was a test on the effectiveness of the setup and the viability of the production mechanism as an alternative to nuclear reactors and generators.

The analysis was based on the activation technique. A stack of Mo, Cu and Al foils was irradiated with a beam of protons with energy of 40 MeV/n. The gammas emitted from the activated foils were measured after a short cooling down period with a HPGe detector. A detailed description of the experimental set-up, procedure and the analysis steps can be found in a previous work [1]. The Cu and Al foils were used for energy degrading and beam normalization purposes. Figure 1 shows the beam energy after each foil as well as the order in the stack.

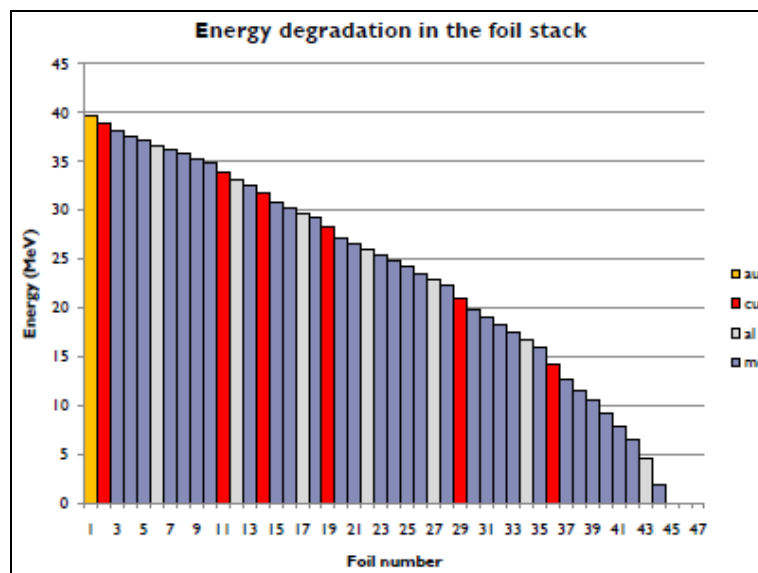
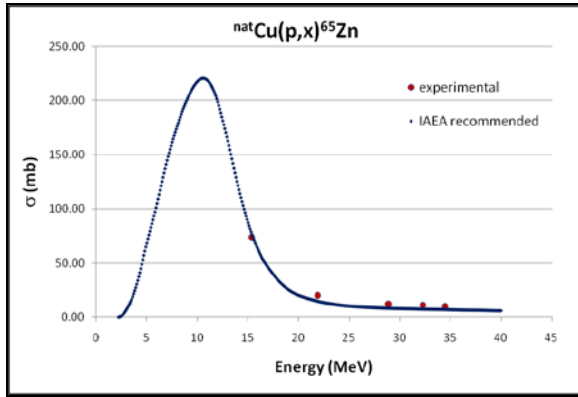


FIG. 1. Energy degradation through the stack and foil composition.

\* Fulbright Fellow 2009. Permanent address: Physics Department, Faculty of Sciences, Princess Nora Bint Abdul Rahman University, Riyadh, Saudi Arabia.

<sup>†</sup> Present address: Department of Physics and Astronomy, James Madison University, Harrisonburg, VA.

The beam normalization was done solely with the Cu foils as Al didn't yield sufficient data. Figures 2 and 3 show the excitation functions for the  $^{nat}\text{Cu}(p,x)^{65}\text{Zn}$  and  $^{nat}\text{Cu}(p,x)^{62}\text{Zn}$ . The blue dots indicate the recommended values dictated by the International Atomic Energy Agency. Our data showed good agreement for the  $^{nat}\text{Cu}(p,x)^{65}\text{Zn}$  reaction. However, for the  $^{nat}\text{Cu}(p,x)^{62}\text{Zn}$  reaction, our numbers were not very consistent with the recommended data. This turned out to be the main source of uncertainty for our measurements.



**FIG. 2.** Comparison between experimental and IAEA recommended cross-section values for  $^{nat}\text{Cu}(p,x)^{65}\text{Zn}$ .

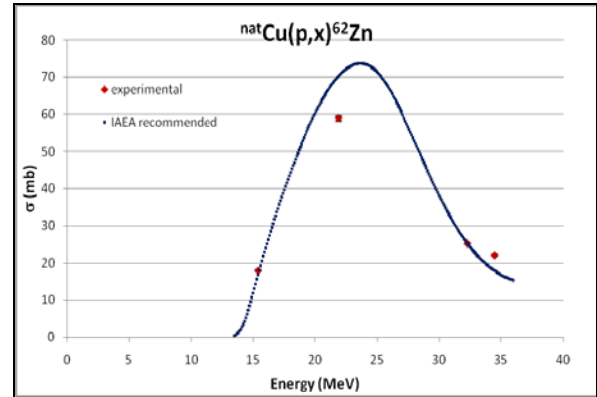


**FIG. 3.** Comparison between experimental and IAEA recommended cross-section values for  $^{nat}\text{Cu}(p,x)^{62}\text{Zn}$ .

The cross-sections for the various nuclear reactions  $^{nat}\text{Mo}(p,x)$  were determined with the usual activation formula [2] and then compared with available previously published results and with calculations done with the code TALYS [3]. Given the space restrictions, here results will be shown only for the medical radioisotopes  $^{99m}\text{Tc}$  and  $^{94g}\text{Tc}$ .

**A.  $^{nat}\text{Mo}(p,x)^{99m}\text{Tc}$**  - The radionuclide  $^{99m}\text{Tc}$  is used mainly in single photon emission computed tomography (SPECT). It has a half-life of  $\sim 6$  h and low energy gamma emission preferable for medical imaging. The production cross-section was determined through the analysis of the 140.5 keV gamma peak. There are two main processes contributing to its production. One is the reaction  $^{100}\text{Mo}(p,2n)^{99m}\text{Tc}$  and the other is  $^{100}\text{Mo}(p,pn)^{99}\text{Mo} \rightarrow ^{99m}\text{Tc}$ . Figure 4 shows the results compared to previous published data and simulated values. In the energy range 12 – 22 MeV results are consistent with the calculations but lower than previous data. Above 22 MeV the contributions from  $^{99}\text{Mo}$  (140.51 keV) and  $^{90}\text{Nb}$  (141.18 keV) couldn't be separated well enough so the cross-section values are higher than the calculation.

**B.  $^{nat}\text{Mo}(p,x)^{94g}\text{Tc}$**  - The radionuclide  $^{94g}\text{Tc}$  has a half-life of  $\sim 5$  h and a mean positron energy of 358.3 keV. It has been studied for potential applications in positron emission tomography (PET) together with the isomeric state  $^{94m}\text{Tc}$ . The latter has a half-life of 52 min, so it couldn't be studied here as it was mostly decayed by the time measurements started. The gamma line used in the analysis was the independent 702.6 keV line. Figure 5 shows the results, again compared with previous research and calculations. There is good agreement within the error bars with previous works. The calculations yielded higher values as TALYS considered the ground and isomeric states together. The red arrows and labels indicate the contributing production reactions.

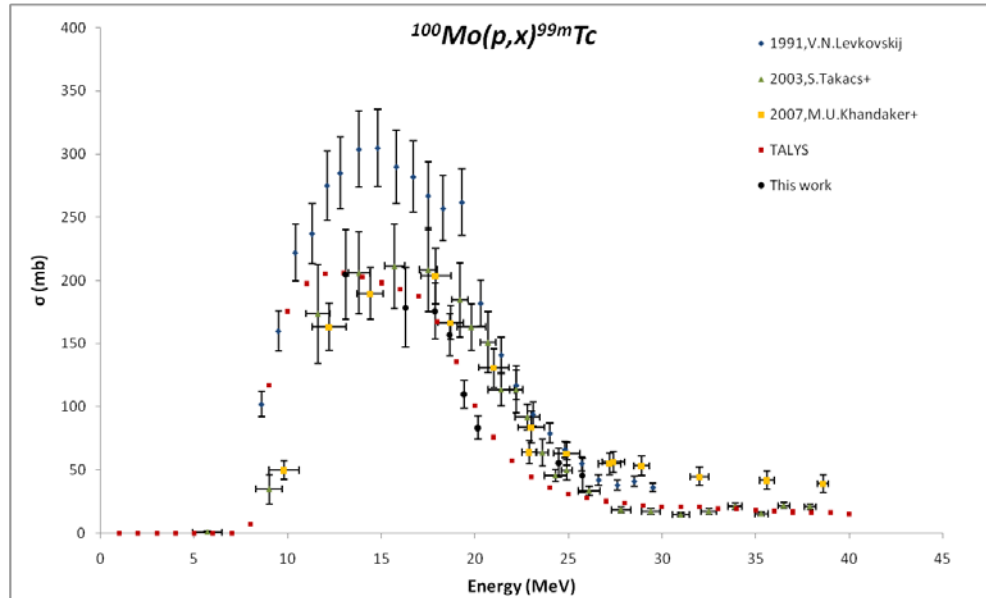


FIG. 4. Excitation function of the reaction  $^{100}\text{Mo}(p,x)^{99m}\text{Tc}$ .

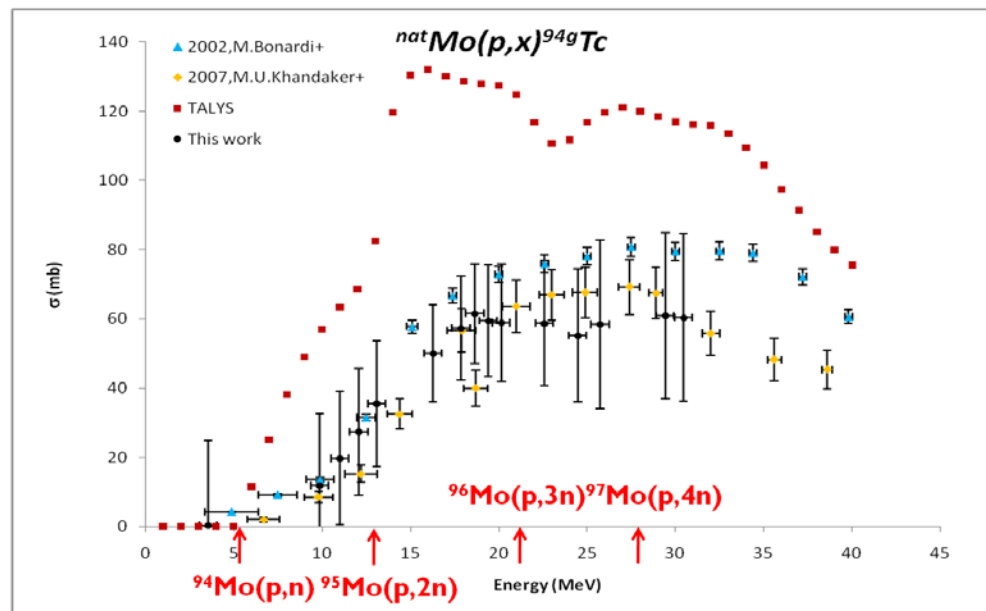


FIG. 5. Excitation function of the reaction  $^{nat}\text{Mo}(p,x)^{94g}\text{Tc}$ .

To summarize, Mo foils were irradiated with protons to test the production of medical radioisotope  $^{99m}\text{Tc}$  using a cyclotron beam as an alternative method to the currently used  $^{99}\text{Mo}/^{99m}\text{Tc}$  generator. The measured excitation function for  $^{99m}\text{Tc}$  was in relatively good agreement with model

calculations. However, there are significant discrepancies among available works including this one, which indicates the need for more data before this production method can be considered viable.

The  $^{96}\text{Tc}$  and  $^{95\text{m}}\text{Tc}$  excitation functions, not presented here, were measured to test the reliability of the data. They were found slightly higher than the calculations but were in good agreement with previous works. Both are being used in radiochemical and animal studies. The radioisotope  $^{94\text{g}}\text{Tc}$  was studied for its potential application in PET studies and was found in good agreement with previous works.

The main source of uncertainty in the experiment came from beam normalization, ~20%. Other sources included statistical uncertainties of up to ~9% and uncertainties from gamma line intensity (2%), detector efficiency (1-4%) and foil thickness determination (2%).

As a test experiment, it proved that the used set-up was working and it revealed improvements necessary to be made for the following experiments in order to minimize uncertainties and increase the reliability of the data.

- [1] A.A. Alharbi *et al.*, *Progress in Research*, Cyclotron Institute, Texas A&M University (2009 -2010), p. V-19.
- [2] G. Gilmore, J.D. Hemingway, *Practical Gamma-Ray Spectrometry*, John Wiley & Sons, England, 1995, p. 17.
- [3] [www.talys.eu](http://www.talys.eu)
- [4] S. Takacs, *et al.*, *J. Radioanal. Nucl. Chem.* **257**, 195 (2003).
- [5] M. Bonardi, C. Birattari, F. Groppi, E. Sabbioni, *Appl. Radiat. Isot.* **57**, 617 (2002).
- [6] V.N. Levkovskij, *Middle Mass Nuclides (A = 40–100) Activation Cross-sections by Medium Energy (E = 10–50 MeV) Protons and Alpha Particles (Experiment and Systematics)*, (Inter-vesi, Moscow, 1991).

## First in-beam commissioning test of AIDA

T. Davinson,<sup>1</sup> Z. Liu,<sup>1</sup> J. P. Wallace,<sup>1</sup> P. J. Woods,<sup>1</sup> R. D. Page,<sup>2</sup> P. J. Coleman-Smith,<sup>3</sup> I. Lazarus,<sup>3</sup>  
S. Letts,<sup>3</sup> V. F. E. Pucknell,<sup>3</sup> J. Simpson,<sup>3</sup> D. Braga,<sup>4</sup> S. L. Thomas,<sup>4</sup> L. Trache, A. Alharbi,

A. Banu, M. McCleskey, B. Roeder, E. Simmons, A. Spiridon, and R. E. Tribble

<sup>1</sup>*School of Physics & Astronomy, University of Edinburgh, Edinburgh, UK*

<sup>2</sup>*Department of Physics, University of Liverpool, Liverpool, UK*

<sup>3</sup>*Nuclear Physics Group, STFC Daresbury Laboratory, Daresbury, Warrington, UK*

<sup>4</sup>*Microelectronics Group, STFC Rutherford Appleton Laboratory, Chilton, Didcot, UK*

This The Advanced Implantation Detector Array (AIDA) [1] is a state of the art detector system designed for the study of the radioactive decay of exotic nuclei at the SuperFRS, FAIR and other applications, for example, reaction studies with radioactive ion beams. AIDA has been designed and developed by a collaboration between the University of Edinburgh (the lead research organisation), the University of Liverpool and the STFC Daresbury and Rutherford Appleton Laboratories. High-energy, exotic nuclei will be implanted into a multi-plane double-sided silicon strip detector (DSSSD) system. Subsequent correlated radioactive decays are detected by the DSSSDs and surrounding neutron and gamma-ray detector systems. To instrument the DSSSDs a 16-channel application specific integrated circuit (ASIC) has been developed. The ASIC provides asynchronous readout, selectable gain (20MeV or 1GeV FSR) and a novel overload recovery circuit providing high energy (20GeV FSR) operation and sensitivity to fast, low-energy decays. To provide a fully integrated ASIC control and data acquisition system a front end electronics (FEE) module has been produced which incorporates readout of four ASICs (64 channels) via an analogue multiplexor (MUX) and 1MHz, 16-bit and 50MSPS 14-bit sampling ADCs using a Xilinx Virtex 5 FPGA incorporating a PowerPC 604 CPU running Linux and Gbit ethernet interface.

A system consisting of an MSL Type W(DS)-1000 DSSSD and prototype AIDA FEE and ASIC hardware was tested with beta-delayed protons from <sup>33</sup>Ar ions produced by 40MeV/u <sup>36</sup>Ar incident on a cryogenic, 2 bar H<sub>2</sub> target and selected by MARS. This enabled the prototype AIDA hardware to be tested with high energy ions for the first time. A range of systematic tests were performed and implant-decay event correlation using an internal clock was demonstrated. It should be emphasised that it is difficult to reproduce such tests in bench tests or computer simulations due to the complexity of the DSSSD, ac coupling, bias network and ASIC input interactions, and that these tests therefore provided unique information. As a direct consequence of these tests, significant design revisions of the AIDA ASIC input stage, FEE power distribution and regulation network, and FPGA VHDL hardware have been undertaken. Production runs of the AIDA ASIC and FEE hardware are now reaching completion and we expect commissioning tests of the production hardware to be performed in the second half of 2011.

- [1] D. Braga *et al.*, *AIDA: A 16-channel amplifier ASIC to read out the advanced implantation detector array for experiments in nuclear decay spectroscopy*, IEEE NSS 2009 IEEE pp.1924; doi:10.1109/NSSMIC.2009.5402153

## Design and use of a new implantation station for beta-delayed decay experiments

E. Simmons, M. McCleskey, and L. Trache

Several experiments involving beta-delayed proton- and alpha-decays have been studied by our group, with collaborators, using the Momentum Achromat Recoil Spectrometer (MARS) at TAMU. So far,  $^{23}\text{Al}$ ,  $^{31}\text{Cl}$ ,  $^{20}\text{Mg}$ ,  $^{20}\text{Na}$  have been investigated and most recently  $^{27}\text{P}$ . Investigation of beta-delayed proton decay is being used as an indirect method to study astrophysical reactions that would otherwise be beyond our current capabilities to study directly in the laboratory. What are of interest are resonances in the proton-capture cross sections. We study them by decay spectroscopy, measuring simultaneously beta-delayed protons and gammas.

The experimental technique developed by our group to effectively do these experiments involves implanting the parent nucleus ( $^{23}\text{Al}$ ,  $^{31}\text{Cl}$ ,  $^{20}\text{Mg}$  or  $^{27}\text{P}$ ) in the center of a thin Si detector (referred to as the proton (or alpha) detector). One, or in some cases two HpGe detectors are used, placed on either side of the proton detector, at 90 degrees to the beam axis. A telescope setup is used for the Si detector arrangement; a thin (45-65  $\mu\text{m}$ ) double sided Si strip detector (DSSSD), the p-detector, sandwiched between two thick (300 $\mu\text{m}$  to 1 mm) Si detectors (referred to here as the  $\beta$ -detectors) allows us to measure protons (or alphas). The beta-detectors help to reduce the background in the analysis. The precise implantation, in the middle of a very thin detector, can be obtained due to the combination of good momentum control in MARS and of the ability to controllably change the angle of an Al degrader foil that is placed inside the implantation station, right in front of the Si detectors. Pulsing the beam from the cyclotron allows us to measure, simultaneously, the  $\beta$ -p and  $\beta$ - $\gamma$  coincidences. See Fig. 1 for a general layout used for these experiments.

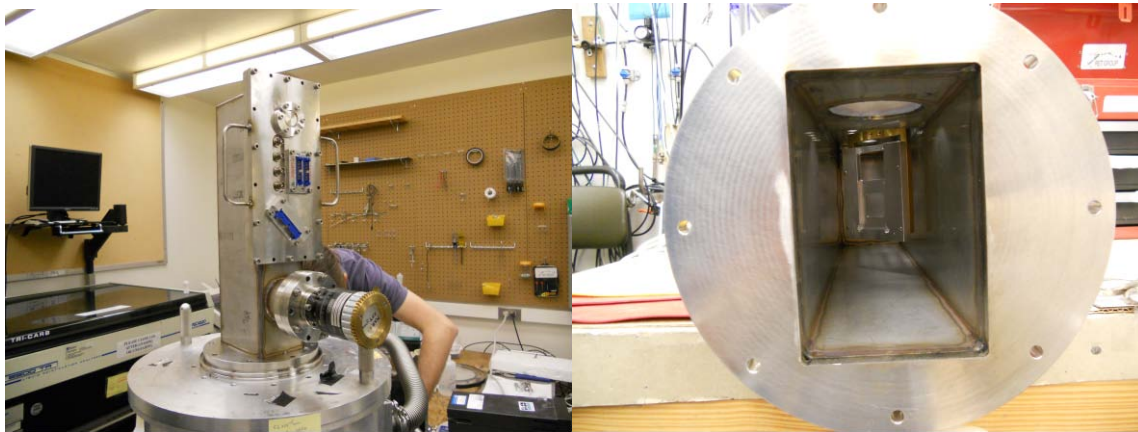


**FIG. 1.** New Implantation Station. Picture on the right shows the view point of the beam.

A new implantation-decay station was designed and built this year, replacing the one used before in the  $^{23}\text{Al}$  and  $^{31}\text{Cl}$  decay studies. First and foremost we wanted to be able to move the HpGe detectors in

even closer to the Si detectors where the implantation and decay occur. This decrease in distance alone (3" to 2") results in an approximate 50% increase in solid angle (when using two HpGe's). Changing from a cylindrical chamber to a rectangular one also allows the HpGe's to be placed flush with the chamber side. Originally we wanted to make this new chamber entirely out of Aluminum, but due to the way in which it had to be welded (tight corners) and the dimensions of the actual welding tools, it was not physically possible to make unless we used stainless steel. Estimates showed that, at the energies we are interested in, the change in material does not cost us that much in efficiency (for example, 70% (SS) verses 85% (Al) transmission for 200 keV photons, and the higher the gamma-ray energy, the more equal the transmissions become).

The change from 6" diameter chamber to a rectangular chamber 4" wide and 6" tall required a complete rearrangement of water pipes used for cooling the detector telescope and of electric feed through locations. Attention was paid to make sure that no cables or pipes would be in the path of the beam either as a hindrance or as a potential for scattering. The inclusion of the rotating degrader motor (interchangeable with the old implantation station) made this a complete, self contained chamber. As before, the Si detectors are placed at a 45 degree angle to the path of the beam in order to increase the amount of Si the beam encounters and simplify the gamma-ray transmission to the Ge detectors. This chamber design also allows for either the BB2 or the W1 type DSSD detectors to be used for the proton detector (both made by Micron Semiconductor). Also, a beta detector can be placed on either side of the proton detector without coming in contact with the side of the chamber. All Si detectors, as before, are attached to a brass stand that is cooled by flowing cool water through pipes that are welded to the back of this stand. This brass stand is placed on a plastic part that is then secured to the top plate of the chamber in order to try to maintain electrical isolation (even though the detector cables go through the BNC feed through connections). Handle bars were added to the top plate to make it easier to remove and change detectors throughout the experiment.

At the same time a new stand was designed and built to permit two HpGe gamma-ray detectors to be positioned easily, in a close and reproducible geometry.

In November 2010 the most recent beta-delayed proton decay experiment ( $^{27}\text{P}$ ) used successfully this implantation station. Analysis of the data is underway, and so far the improvement in efficiency is clear. It is hoped that future experiments required proton detections in addition to gamma spectroscopy will find this implantation station useful.

## TABS – an ASIC-based electronics system at Texas A&M

M. McCleskey, J. Elson,<sup>1</sup> L. G. Sobotka,<sup>1</sup> L. Trache, J. Blackmon,<sup>2</sup> M. Matos,<sup>2</sup> B. Roeder,  
E. Simmons, A. Spiridon, and R. E. Tribble

<sup>1</sup>*Departments of Chemistry and Physics, Washington University, St. Louis, MO*

<sup>2</sup>*Department of Physics, Louisiana State University, Baton Rouge, LA*

A high density electronics readout system has recently been tested in beam at the Texas A&M Cyclotron Institute as part of a broader effort to develop a silicon strip detector array and associated readout system for the SAMURAI spectrometer [1] at RIBF at RIKEN. This project is a collaborative effort amongst groups at Washington University, Louisiana State University, Texas A&M University and RIKEN Nishina Center. For this test a TTT silicon strip detector provided by Micron Semiconductor was used. The design requirements for the SAMURAI-Si detector project require a position sensitive detector able to detect breakup products before they enter the spectrometer. Because the typical breakup products will be a proton in coincidence with a heavy ion, a large dynamic range is needed. In order to achieve sufficient position resolution, a high strip density and thus a large number of channels is required.

The electronic system (Texas A&M ASIC-Based System – TABS) was designed and made by the WU group based on the HINP16C application-specific integrated circuit (ASIC) [2] and can support up to 512 channels on the motherboard. The motherboard has slots for 16 chipboards, and each chipboard supports two HINP16C chips, 16 channels each. Currently the system is half complete, supporting 256 channels. The motherboard is mounted in an aluminum box bolted directly to an ISO200 flange on the vacuum chamber which allows for short cables between the detector and electronic system. It is designed as a prototype for the complete system that will be delivered for RIKEN.

The Micron TTT2-300 detector is one of the designs being considered for the SAMURAI-Si project. It is a 10cm x 10cm x 300 $\mu$ m thick silicon strip detector. It has 128 strips on each side, giving a <0.8 mm strip pitch. Two detectors were provided by Micron Semiconductor Ltd., one N-type and one P-type. Due to large leakage current in the P-type detector, the N-type was used for the in-beam test. The

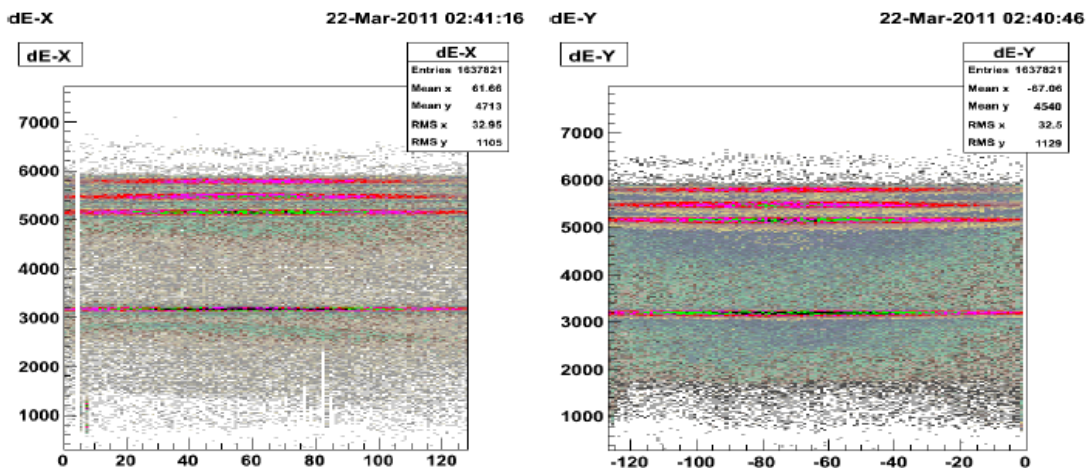


FIG. 1.  $\alpha$  source calibration of the TTT detector.

detector is placed in a 5-way NW200 cross. A similar cross was purchased for testing purposes at WU. Prior to being tested in beam, the N-type detector was tested with pulser and sources at WU and the resolution was found to be around 45 keV at the 5.5 MeV alpha line of  $^{241}\text{Am}$ , and the threshold at about 400 keV. Calibrations of the X and Y sides of the TTT using a mixed  $\alpha$  source are shown in Figures 1 and 2.

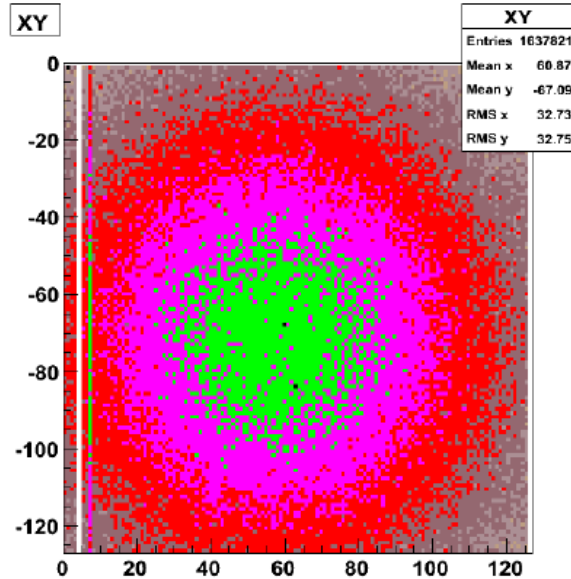


FIG. 2. XY distribution with the  $\alpha$  source.

The control of the chips is performed via a Jtec Xilinx logic module (XLM). This unit both handles communication with the chips and also digitizes the analog output. Control of the XLM is by VME-USB using the NSCL Readout program. Online data viewing was done in ROOT.

A 48 MeV/nucleon  $^{24}\text{Mg}$  beam was selected for the in-beam test in March 2011. Because the range of the charge-sensitive amplifiers on the ASIC chips is 0-70 MeV for the high gain setting, a fragmentation reaction was used to get a beam that would deposit a suitable amount of energy in the TTT. The fragmentation was done using a 150  $\mu\text{m}$  Be foil at the primary target position of the MARS beamline. Because of the large variety of fragmentation products produced, the entire range of the readout system was able to be tested with the same beam. The vertical dipole D3 was set to place the N=Z line in the center of the detector. A 1 mm thick silicon detector was placed behind the TTT to get  $E_{\text{res}}$  for particle identification.

The fragmentation beam on the usual MARS target detector is shown in Fig. 3, along with the beam on the TTT detector.  $\Delta E - E_{\text{res}}$  on the TTT is shown in Fig. 4.

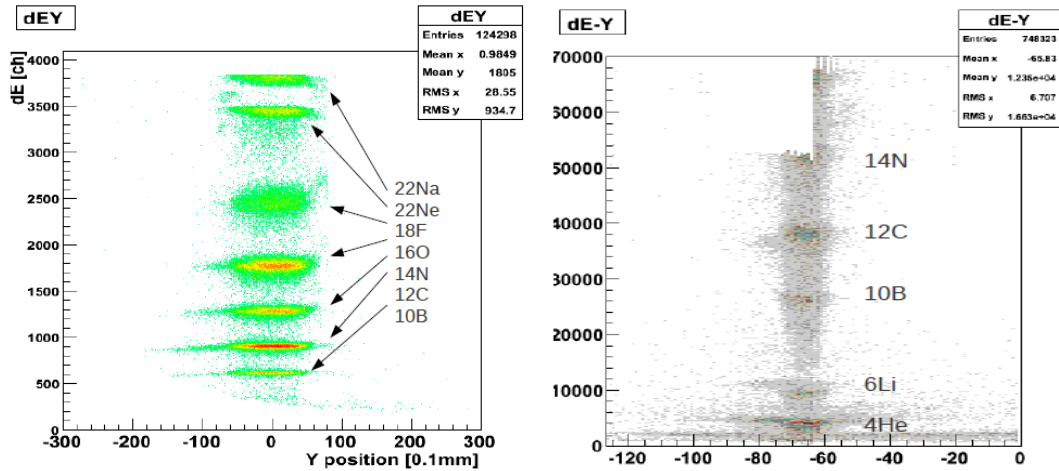


FIG. 3. Beam on the MARS target detector (left) and TTT (right).

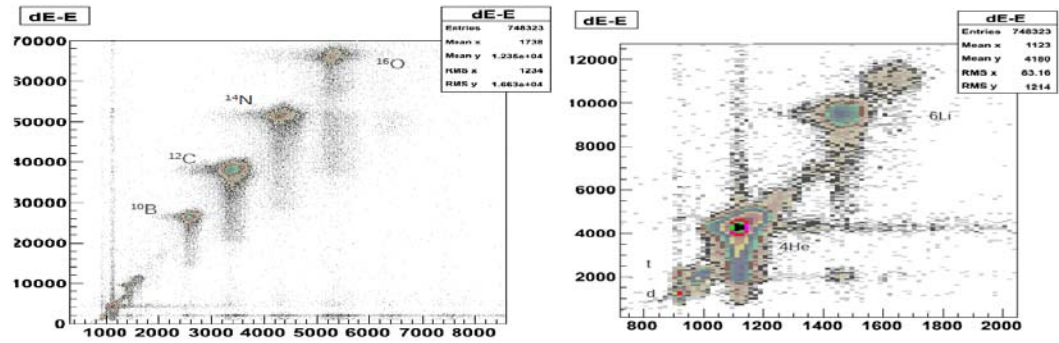


FIG. 4.  $\Delta E-E_{res}$  in the TTT detector. particles as low as deuterons were identified ( $\sim 1$  MeV deposited in TTT).

During the in beam test a cross talk problem was observed that involved high energy signals ( $>60$  MeV) causing small ( $\sim 1$  MeV) signals in the other chip on the same board. A modification to the chipboards has since been performed at WU to address this problem, raising the threshold where the problem may occur to 120 MeV, and a future beam test will be needed to test this as well as to look to push thresholds lower and to attempt to observe low energy signals from protons in coincidence with large energy signals from heavy ions.

[1] T. Kobayashi *et al.*, “Large-Acceptance Multi-Particle Spectrometer SAMURAI” – proposal, RIKEN 2008.

[2] G.L. Engel *et al*, Nucl. Instrum. Methods Phys. Res. **A573** , 418 (2007).

## AstroBox – a new type of low energy proton detector

E. Simmons, M. McCleskey, A. Spiridon, L. Trache, B. Roeder, R. E. Tribble

E. Pollacco,<sup>1</sup> M. Kebbiri,<sup>1</sup> and G. Pascovici<sup>2</sup>

<sup>1</sup>*Service de Physique Nucleaire, CEA Saclay, France*

<sup>2</sup>*Institut fuer Kernphysik der Universitaet zu Koeln, Cologne, Germany*

We worked hard in the last four years to measure very low proton energies from  $\beta$ -delayed proton decays, motivated by our interest in nuclear astrophysics (NA) studies. In many reactions important in H-burning involving radiative proton capture on sd-shell nuclei or heavier, resonances dominate. We aim at evaluating their contribution by studying these resonances and their properties (energy, spin and parity, resonance strength) by populating them from the beta decay of exotic nuclei that we produce and separate with MARS. These are excited states above the proton threshold in daughter nuclei that may decay by gamma-rays or by proton emission. Only the states within the Gamow window are important in NA, and this means very low proton energies: below 200-300-400 keV, depending on the temperature of the stellar process. Our first solution was to implant the proton emitting nuclei in very thin (use used 45-65  $\mu\text{m}$ ) double sided Si strip detectors [1]. With this technique we could measure efficiently and without much background protons with energies  $E_p=400-1500$  keV and we could reach as low as  $E_p=200$  keV from the decay of  $^{23}\text{Al}$  through a careful subtraction of the important background created at low energies by the positrons from the  $\beta$  continuum [2]. However, the very large background in the 100-300 keV energy region and the limited resolution did impair our searches for states with small proton branchings. We realized recently an important breakthrough by using a new type of proton detector that we call AstroBox. It is based on a gas detector using micromegas [3] electron amplifiers and was designed and assembled together with specialists at CEA Saclay. The micromegas were produced at CERN. The principle of the measurement remains similar with the one used with Si detectors: the source nuclei are stopped (“implanted”) in the active volume of the detector (with the detector turned off) for a period equal to about two half-lives, after which the beam is turned off and the detector is turned on for the same period. The central detector, 5 mm in diameter, is surrounded by an ‘outer’ detector, 10 cm OD, split in four sectors (which may be connected into two or even one signal only). In March 2011 we have did the first test of the detector and its working principle, using the same  $\beta$ -delayed proton emitter  $^{23}\text{Al}$ . Figure 1 shows a summary of results. The left side shows a 2-dimensional spectrum of the center detector and of the detector surrounding it (outer), which was used to tune the implantation in the source in the desired space. The right hand side shows a proton spectrum measured in the center detector. It shows a spectacular reduction of the beta background, which was restricted to energies below  $E_p\sim 80$  keV, a good separation of the proton peaks around 200-270 keV observed before [2], and an improved resolution. While we can confirm the observations made in Ref. 2, due to this much reduced background and the better resolution, we could also clearly observe the proton peak corresponding to the proton decay of the isobaric analog state of  $^{23}\text{Al}$ . We note that this decay is isospin forbidden in first order, a fact that results in a very weak proton branching, and its observation can give information about isospin mixing in these nuclei.

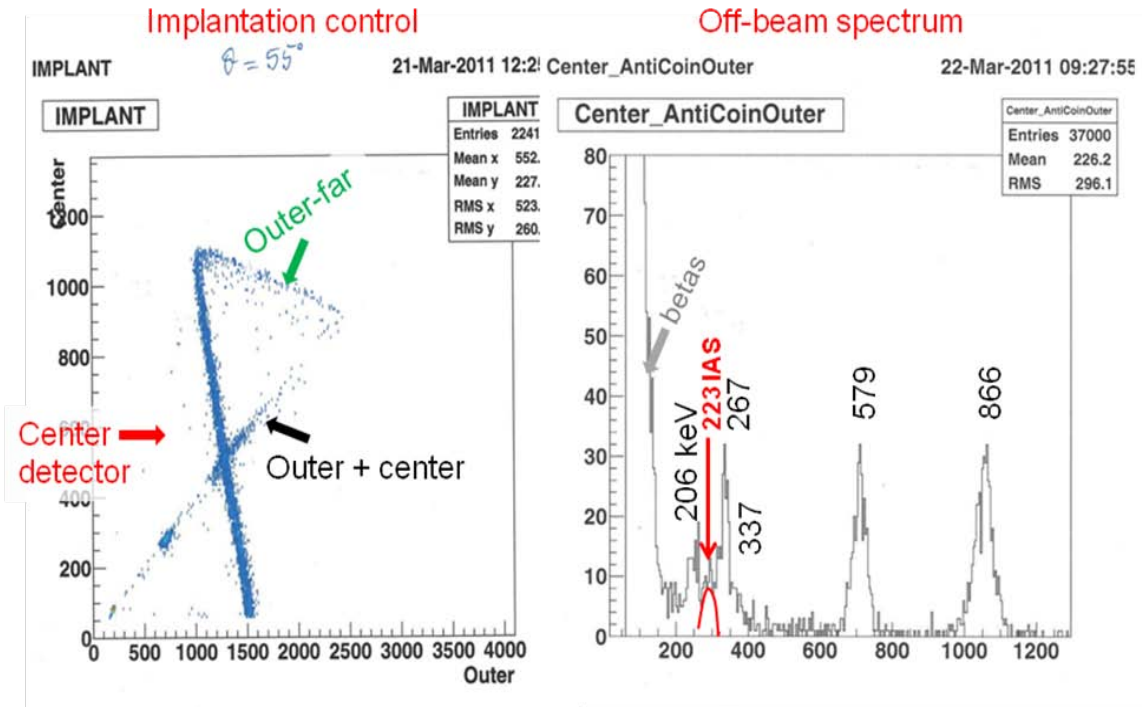


**FIG. 1.** Summary of the two phases of the experiment. On the left the implantation control phase, showing that most of  $^{23}\text{Al}$  is implanted in the center region. Right side: proton spectrum from the decay of  $^{23}\text{Al}$ . It was obtained in about 2 hours of beamtime. The energies marked are in keV.

- [1] L. Trache *et al.*, *Progress in Research*, Cyclotron Institute, Texas A&M University (2006-2007), p.I-29; <http://cyclotron.tamu.edu/2007%20Progress%20Report/index.html>
- [2] A. Saastamoinen, L. Trache, A. Banu *et al.*, *Phys. Rev. C* **83**, 045808 (2011).
- [3] Y. Giomataris, Ph. Rebourgeard, J.P. Robert, and G. Charpak, *Nucl. Instrum. Methods Phys. Res.* **A376**, 29 (1996).

## SAMURAI TPC: Conceptual design of a time projection chamber

A. B. McIntosh, J. Barney, J. Dunn, J. Gilbert, T. Isobe, K. Klein,  
M. Famiano, F. Lu, W. G. Lynch, N. W. Maass, T. Murakami,  
R. Olsen, A. Taketani, M. B. Tsang, and S. J. Yennello

A conceptual design for a new time projection chamber, the SAMURAI TPC, has been developed. The utility of the device and some specifications have been previously described [1]. Design considerations, sketches and detailed 3D mechanical drawings are posted and archived online [2]. The conceptual design was produced using Autodesk Inventor 2011.

An exploded view of the SAMURAI TPC conceptual design is shown in Figure 1. The TPC is largely based on the original “EOS” (equation-of-state) TPC [3]. The TPC will consist of a main volume of detection gas (P10) at one atmosphere enclosed in a field cage 144.4cm long, 96.4cm wide and 53.3cm

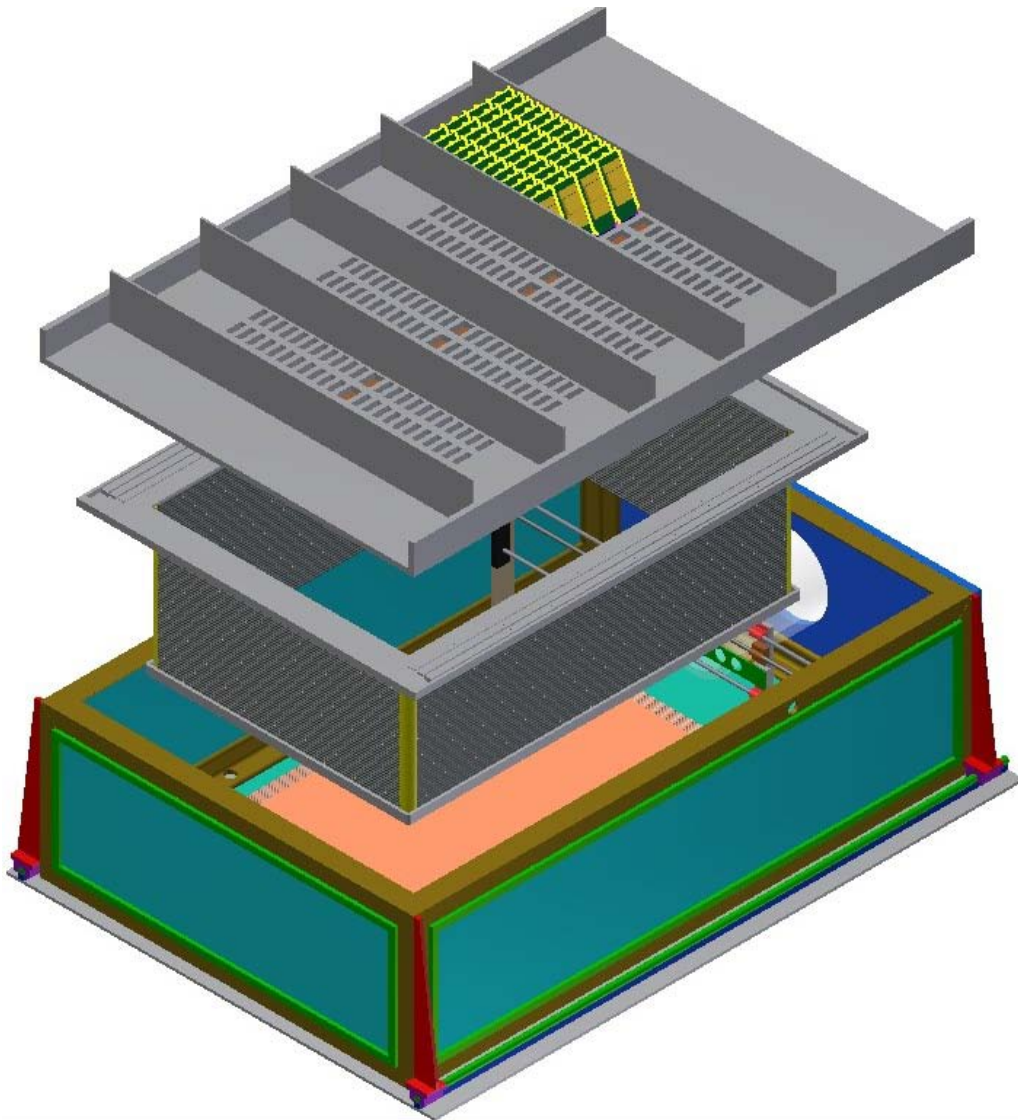


**FIG. 1.** Exploded view of the SAMURAI TPC conceptual design.

high. A uniform electric field of  $\sim 375\text{V/cm}$  will be maintained with 1cm wide copper strips on the field cage held at the appropriate potentials. Electrons liberated by the passage of energetic charged particles through the gas will drift past a gating wire grid and Frisch wire grid; amplification will occur at a third plane of wires. The signal will be measured on a pad plane with dimensions of 134.4cm x 86.4cm; each of the 12096 pads will be 1.2cm x 0.8cm in size. The liquid-cooled electronics to read out and digitize the signals from the pads will be located directly above the pad plane. The field cage will be surrounded by inert gas ( $\text{N}_2$ ) at zero differential pressure. A motorized target-ladder mechanism will be located immediately upstream of the field cage. The walls of the TPC will be made as thin as possible to allow downstream measurement of neutrons and very energetic charged particles. For calibration purposes, a laser and beam-splitting system will be included. Light charged particles and charged pions will be measured and identified via energy-energy loss and magnetic rigidity in a magnetic field of approximately one Tesla. The spatial resolution of the TPC will be sufficient to simultaneously resolve up to 200 particle tracks.

The conceptual design was completed on schedule by May 15, 2011. The conceptual design underwent a thorough review, and the minor revisions necessary are nearly complete. A full detailed design is expected to be complete by August 15, 2011. Construction of the TPC will commence at the TAMU Cyclotron Institute soon after. Development of some of the sensitive detector components will be conducted at Michigan State University.

Following its completion and testing, the SAMURAI TPC will be installed in the SAMURAI magnet at the RIKEN laboratory in Wako Japan. There it will be used for experiments to constrain the density dependence of the asymmetry energy in the nuclear equation of state at supra-saturation density through measurements of pion production and through flow of light particles.

[1] [http://rarfaxp.riken.go.jp/RIBF-TAC05/10\\_SAMURAI.pdf](http://rarfaxp.riken.go.jp/RIBF-TAC05/10_SAMURAI.pdf)

[2] <http://groups.nscf.msu.edu/hira/sep/sepwiki/doku.php/start>

[3] H. Wieman *et al.*, Nucl. Phys. **A525**, 617c (1991).

# Delta-ray simulations for the SAMURAI-Si project at RIKEN

Brian Roeder

## I. Introduction

The Superconducting Analyzer for Multi-particle from RAdio Isotope beams (SAMURAI) is a large acceptance spectrometer currently under construction at the RIBF facility at RIKEN, Japan [1]. It will consist of a large-gap superconducting magnet with 7 Tm of bending power. Among the experiments planned with this new device are proton breakup reactions with proton-rich exotic beams, exciting proton unbound states in these nuclei with  $(\gamma,p)$  reactions induced by virtual photons. These are of interest to nuclear astrophysics as they play an important role in nucleosynthesis processes, such as the rp-process.

The invariant mass method will be used. In this method, the kinetic energies and scattering angles of the breakup products must be measured to high precision in order to obtain information about the relative angle and energy ( $E_{rel}$ ) between the particles, and relate to the reaction mechanism. A resolution of  $\sim 0.2$  MeV at  $E_{rel} = 1.0$  MeV is desired, and this can be obtained if the resolution of the opening angle between the proton and the heavy-ion residual has a resolution of  $\Delta \theta_{pen} \sim 2$  mrad. However, this precision is difficult to reconstruct after the breakup reaction products have been separated by SAMURAI and detected in the focal plane detectors. A more precise measurement of the opening angle is possible if silicon strip detectors are placed after the reaction target, but before the SAMURAI spectrometer.

Simulations with the GEANT4 package [2] were conducted in order to determine a possible arrangement for placing silicon detectors in the setup for the  $(\gamma,p)$  reaction measurements. In these calculations, the detection efficiencies and resolutions were compared for two types of silicon strip detectors: the GLAST single-sided strip detector (SSSD), manufactured by Hamamatsu, and the TTT double-sided strip detector (DSSD), manufactured by Micron Semiconductor Ltd. In addition, possible experimental difficulties, such as the effect of delta-ray electrons on the measurement, were investigated with these simulations.

## II. Simulations of the detection efficiency and resolution

The design specifications for the silicon detectors associated with the  $(\gamma,p)$  reaction setup for SAMURAI require that the silicon detector setup should have close to 100% efficiency for detection of proton-Heavy Ion (p-HI) pairs with  $E_{rel} < 1$  MeV. This corresponds to having an angular coverage of about  $3.6^\circ$  in the lab for most experiments with secondary beams at 250 MeV/u. For a hypothetical Si detector with  $10 \text{ cm} \times 10 \text{ cm}$  of surface coverage, a simple calculation shows that the Si detectors can be placed up to 80 cm away from the breakup reaction target and still satisfy the efficiency requirement. The TTT-DSSD detectors have  $9.73 \text{ cm} \times 9.73 \text{ cm}$  of surface coverage, while the GLAST-SSSD detectors have  $8.75 \text{ cm} \times 8.75 \text{ cm}$  of surface coverage. The 100% detection efficiency requirement can be still be satisfied by the GLAST-SSSD detectors if they are placed up to 70 cm away from the target.

To verify the assumptions of the simple calculations mentioned above, a simulation of the proposed Si-detector setup was conducted with GEANT4. In the simulation, the breakup reactions  ${}^9\text{C} \rightarrow {}^8\text{B}+p$  and  ${}^{57}\text{Cu} \rightarrow {}^{56}\text{Ni}+p$  at 250 MeV/u were investigated. A target of  ${}^{208}\text{Pb}$  with areal density of 10 mg/cm<sup>2</sup> was assumed. Two Si detectors of each type were placed at 50 cm and 80 cm from the  ${}^{208}\text{Pb}$  target. The detection efficiency was simulated with the requirement that both the proton and heavy ion should be detected by both detectors in each event, and thus the detection efficiency was limited by the detector that was placed the farthest downstream from the reaction target. The results of these simulations for the two reactions and two detector types are shown in Figure 1. Both detectors satisfy the efficiency requirement for the  ${}^{57}\text{Cu} \rightarrow {}^{56}\text{Ni}+p$  reaction, but a larger opening angle in the case of the  ${}^9\text{C} \rightarrow {}^8\text{B}+p$  reaction leads to lower detection efficiency (the “simple” calculation above assumed that  $M_{\text{HI}} \gg M_{\text{proton}}$ ). This problem can be corrected if the detectors are simply moved closer to the target as required by the experiment.

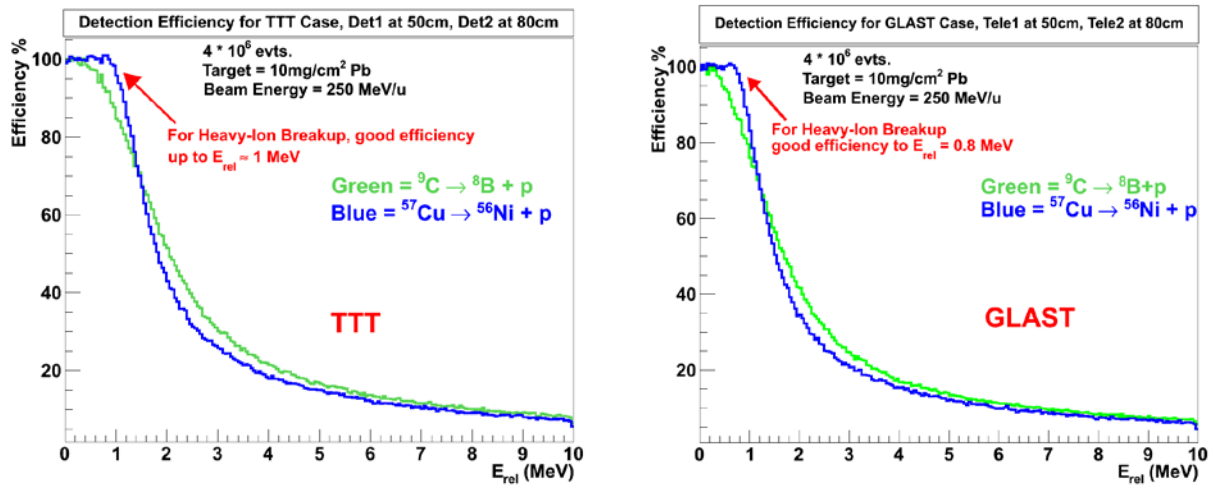


**FIG. 1.** Results of the breakup reaction detection efficiency simulations for the case where the TTT-DSSD or GLAST-SSSD detectors were placed at 50 cm and 80 cm downstream of the reaction target. Both types of detectors had close to 100% efficiency for the heavy-ion ( ${}^{57}\text{Cu}$ ) breakup, whereas the efficiency was reduced for light-ion ( ${}^9\text{C}$ ) breakup case.

GEANT4 simulations were also carried out to investigate if the detectors satisfied the design specifications for the resolution of  $E_{\text{rel}}$ . Since both detectors have strip pitches of  $< 1$  mm, the 2 mrad angular resolution is possible. In practice, the simulations show that for both types of detectors, the resolution of  $E_{\text{rel}}$  is mainly limited by the thickness of the reaction target and not by the strip pitch of the detectors.

### III. The Effect of Delta Electrons

In order to maximize the detection efficiency for the breakup reactions at  $E_{\text{rel}} < 1$  MeV, the silicon detectors should be placed along the beam axis after the reaction target. This implies that the un-

reacted beam and the reaction products from the breakup reactions will interact with the silicon detectors. As these charged ions pass through the reaction target and silicon detectors, they will scatter atomic electrons from the material, creating delta-rays ( $\delta$ -rays). At 250 MeV/u, the maximum kinetic energy of elastically scattered electrons is  $(4m_e/M_{\text{beam}})*E_{\text{beam}}$ , corresponding to  $E_e \approx 550$  keV. Electrons passing through silicon deposit  $1.66 \text{ MeV}/(\text{g}/\text{cm}^2)$  [3]. Thus,  $\delta$ -rays with  $E_e = 550$  keV passing through  $300 \mu\text{m}$  of silicon, the proposed thickness of the Si detectors for the  $(\gamma, p)$  experiments, would deposit about 116 keV, not including the electron angle of incidence or the multiple scattering in the silicon. For comparison, a 250 MeV proton from the breakup reaction deposits around  $\approx 200$  keV as it passes through a detector with that thickness. Since the energy deposits for the  $\delta$ -rays and the protons are both relatively low in energy, the  $\delta$ -rays could cause “cross-talk” and false proton events in the silicon detectors. Simulations of the  $\delta$ -ray energy and production were also carried out with GEANT4 using the standard EM models for ionization and electron multiple scattering. In these simulations, the number of  $\delta$ -rays scattered from the first silicon detector downstream of the reaction target and detected in the second silicon detector was investigated. First, the distance between the two detectors was varied. This distance is important because for the GLAST-SSSD solution, silicon detector telescopes with two detectors that are close together (within 2 cm) are needed to give simultaneous x and y position measurements for the reaction products (the TTT-DSSD detectors give x and y position measurements within one detector). Summaries of the results of these simulations are given in table 1 and figure 2. In figure 2, it is seen that the number of  $\delta$ -rays detected in the second Si detector decreases roughly exponentially with distance. For this reason, having the Si detectors close together, such as would be the case with the GLAST-SSSD telescopes, should be avoided as there will be too many false events generated by the  $\delta$ -rays.

**Table I.** Summary of the simulation results for the  $\delta$ -rays

Distance between dets.	$\delta$ -rays/1000 evts.	$\langle n_\delta \rangle$ /event	$\langle E_\delta \rangle$ /event
2 cm	26513	27	115 keV
10 cm	8894	8.9	113 keV
25 cm	1856	1.9	110 keV
50 cm	474	0.47	115 keV

Other solutions for reducing  $\delta$ -rays were tried in the simulations. One solution was to modify the silicon detector by making a hole in the middle of the detector for the beam to pass through. While this solution would reduce the number of  $\delta$ -rays produced, it was also found to reduce the detection efficiency for the breakup reactions, especially for the heavy-ion cases of interest like  $^{57}\text{Cu} \rightarrow ^{56}\text{Ni}+p$  where the  $\theta_{\text{open}}$  would be within the detector hole for small  $E_{\text{rel}}$ . Another solution was to place a material in between the Si detectors to absorb or deflect the  $\delta$ -rays. Thin ( $15\mu\text{m}$ ) sheets of materials like Ta were effective in reducing the  $\delta$ -rays that triggered the second Si detector, but these sheets also degraded the resolution of the  $E_{\text{rel}}$ . So, maximizing the distance between the Si detectors seems to be the best way to minimize the effect of  $\delta$ -rays on the breakup reaction measurement while not sacrificing detector efficiency and/or resolution.

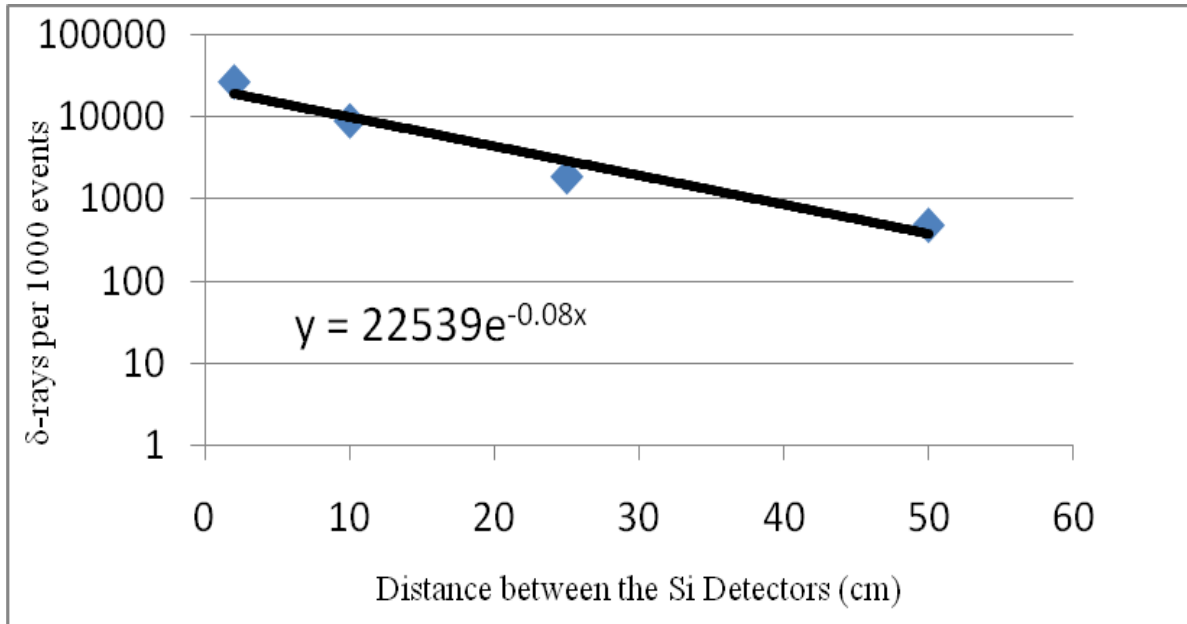


**FIG. 2.** Variation of the number of  $\delta$ -rays seen in the second, downstream Si detector generated from the interaction of the beam with the first silicon detector. The number of  $\delta$ -rays detected decreases roughly exponentially with distance.

#### IV. Conclusion

In conclusion, a GEANT4 simulation for the  $(\gamma,p)$  reaction setup with the SAMURAI spectrometer at RIKEN has been developed to investigate the properties of the proposed silicon detector setup. With this simulation, the setup was found to satisfy the design specifications for detection efficiency and resolution for the breakup reactions. However, significant numbers of  $\delta$ -rays with kinetic energies large enough to impact the quality of the measurement were also produced as the ions interacted with the detectors in the simulation. While several methods for reducing the effect of the  $\delta$ -rays on the measurement were tried, the best way found so far has been to keep the detectors some distance apart, such as, for example 30 cm. Given this constraint, the silicon detector setup with SSSD telescopes is not a valid solution. In general, to provide x-y position measurements, while allowing that a reasonable distance is also needed between the detectors, double sided silicon strip detectors (DSSSD) should be used.

- [1] Large-Acceptance Multi-Particle Spectrometer SAMURAI Construction Proposal, version 2010.
- [2] GEANT4 version 4.9.4, S. Agostinelli *et al.*, Nucl. Instrum. Methods Phys. Res. **A506**, 250 (2003).
- [3] M. Pindo, Nucl. Instrum. Methods Phys. Res. **A395**, 360 (1997).

## The Wiener VME-USB controller for data acquisition: A status report

Kris Hagel and Brian Roeder

This year, we have developed and commissioned a new data acquisition system for the Cyclotron Institute based on the Wiener VME-USB control module, model VM-USB [1]. The VM-USB replaces the SBS controller and CES model CBD-8210 trigger module that were previously used to control the data acquisition system. This upgrade was necessary because the CES trigger module is no longer manufactured. The VM-USB was chosen because of its flexibility, autonomous data acquisition capabilities, and USB 2.0 computer interface. For most of the data acquisition used in the lab, these features will allow the development of systems with less acquisition downtime. However, migration to the new system will require users to move away from the data acquisition with CAMAC modules as a similar VME-CAMAC interface has not yet been implemented in our system.

The VM-USB controller has been integrated into the existing data acquisition software at the Cyclotron Institute. Separate protocols in the “Transport Manager” program allow the user to choose at startup either the VM-USB or the previous SBS controller for backwards compatibility. It can be used currently with an assortment of VME electronics modules, including the Mesytec 32-channel VME ADCs, CAEN 128-channel TDC V1190, CAEN 16-channel dual-range QDC V965, SIS 3820 32-channel VME scaler and other VME modules.

The user will notice a few changes in the frontend and backend DAQ programming for the VM-USB when compared with the SBS controller. First, to take advantage of the data transfer rates of the USB 2.0 interface with the frontend control computer, the VM-USB uses a set of user-defined command stacks to carry out the readout of the data event-by-event. These command stacks are set up by the user in the “Frontend::Init()” method such that the modules are read out event-by-event in the order that they are defined in the Init() method. Once the command stack and readout order is defined, the VM-USB is triggered to execute the command stack (i.e. read out the data) by a NIM trigger pulse going into the front panel LEMO input “I1”. During the data digitization and readout process, an inhibit NIM logic signal is output from the “O1” LEMO connector on the VM-USB module. The data read out in that event are stored in an onboard data buffer on the VM-USB that can hold up to 28 kB of data. When the data buffer is full, the VM-USB dumps the stored information, which may contain many individual events, to the control computer where it can be analyzed as online data and/or recorded to a file. Converting, reading out, and transferring data in this way have been observed to improve the downtime of the DAQ system by about ~3x for a typical experimental setup (e.g. 50  $\mu$ s for the VM-USB versus 150  $\mu$ s for the same setup with the SBS controller). The remaining downtime of the DAQ arises mostly from the conversion time of the DAQ modules.

In the TAMU DAQ software, the readout commands for a given VME module are added to the command stack in the “Frontend::Init()” method by using a C++ class constructor similar to the following (for the Mesytec ADC):

```
CycMesytecMadc32Module*Adc = new CycMesytecMadc32Module(GetVmeUsbStack(0), VMEaddress)
```

where the readout commands are added to the event-by-event readout stack “0” with the function “GetVmeUsbStack(0)”. If a given VME module is to be read out event-by-event, its commands should be added to stack “0”. Once created, the module can be set up with the same initialization commands that were available when the SBS controller was used. In general, a readout delay should be also be added to the stack with the function “SetReadoutStartDelay(x)” (where “x” is the number of microseconds to wait) such that the readout of the VME modules does not begin before the digitization is completed. The amount of time to wait depends on the number of channels and/or number of modules to be read out. By contrast, a module that is initialized in the “Frontend::Init()” method, but should not be read event-by-event, should be defined as being added to stack “-1”. An example of this type of module is the CAEN V812B VME CFD, which is declared in the “Frontend::Init()” method as follows:

```
CycCaenV812BModule* Cfd = new CycCaenV812BModule(GetVmeUsbStack(-1),VMEaddress).
```

The last type of module to be read out would be a scaler such as the SIS 3820 VME scaler. While this module can also be read out event-by-event by adding it to command stack “0”, typically a timed readout of this module is desirable, such as, every 10 seconds. In this case, the module should be added to stack “1”. In addition, the command “SetScalerReadFrequency(x)” (where “x” is the number of seconds) is invoked to set the time in seconds between scaler readouts, as before in the SBS DAQ system. Up to 8 command stacks can be programmed on the VM-USB, but to date only stacks “0” and “1” are implemented. The other stacks operate on interrupt vectors and will be implemented as needs arise.

Once the command stack “0” is defined, no further functions need to be added to the “Frontend” class for the “Transport Manager”. While the functions “Frontend::Event()”, “Frontend::Begin()”, “Frontend::End()” and “Frontend::ReadScalers()” still exist in the Frontend class, VME commands defined inside these methods are ignored because the readout of the modules is controlled by commands in the “stack”. For this reason, is not possible to observe the raw data being read out from the VME modules in the Frontend part of the program as was available with the SBS VME controller. If the user wishes to observe the raw digitized data from the VME modules, one must unpack the data in the backend analysis part of the DAQ code and display the raw data from the data buffer there.

For the analysis part of the TAMU DAQ system, the data buffers from the VM-USB are unpacked online or from the data file by the “Analysis Manager” program in the same way as they were from the SBS controller. To differentiate data coming from SBS controller type data files and VM-USB type data files, the VM-USB event-by-event data buffers are recorded with EventType=6 and EventSubType=1, and the VM-USB scaler data buffers are recorded with EventType=6 and EventSubType=2. However, the user should be careful to unpack the data as defined by the readout data word order for a given module. For example, the data word order for the Mesytec VME ADC begins with a “header” word, followed by “data” words containing digitized data from channels that were above the ADC threshold and then finally a “trailer” finishes the data word from the ADC for that event. Further information about the data word unpacking is often available in the module manual. This approach

differs from the SBS VME controller because the user could, in principle, choose only to record “important” data words and discard the rest.

The TAMU DAQ system with the VM-USB controller was tested in an experiment in June 2010. In that experiment,  $^{37}\text{K}$  was produced with MARS with the  $p(^{38}\text{Ar}, ^{37}\text{K})2n$  at 29 MeV/u. To compare the two systems, the  $^{37}\text{K}$  production rate was measured in two separate runs: one with the SBS controller and an existing DAQ control computer, and one with the VM-USB controller and a new DAQ control computer with a USB 2.0 input. All other parts of the readout electronics were the same for the two runs. In this simple test, the same  $^{37}\text{K}$  production rate of  $\sim 500$  eV/nC was measured for both runs. This indicated that the two DAQ systems gave the same results for comparable measurements. Following this test run, the VM-USB has been successfully used as the DAQ VME controller in several experiments.

In conclusion, the Wiener VM-USB control module has been integrated into the TAMU DAQ system and the TAMU DAQ software. It has been used to read out most of the existing VME DAQ modules at the Cyclotron Institute. The improvements in acquisition readout time and low cost make the new control module a suitable replacement for the old control system that utilized the SBS VME control module.

[1] For more information about the Wiener VM-USB controller, see the manual at:

[http://www.wiener-d.com/Support/XXUSB/Manual\\_VM-USB\\_3\\_3.pdf](http://www.wiener-d.com/Support/XXUSB/Manual_VM-USB_3_3.pdf).

## Diffusion of $^{18,19}\text{Ne}$ out of mylar tape

V. E. Jacob and J. C. Hardy

Several years ago we successfully measured the half life of  $^{34}\text{Ar}$  ( $t_{1/2} = 0.84$  s) [1]. Although argon is a noble gas with the potential to diffuse out of the detection region during the measurement, we demonstrated with  $^{35}\text{Ar}$  ( $t_{1/2} = 1.775$  s) that measurable diffusion did not occur over a 35-second period. With that result in mind we sought to measure the half life of another noble gas:  $^{18}\text{Ne}$  ( $t_{1/2}=1.7\text{s}$ ). To check for possible diffusion of implanted neon ions out of the Mylar tape of our fast tape-transport system we began by measuring the decay of  $^{19}\text{Ne}$ . We hoped to be able to put an upper limit on the loss of neon by measuring its half-life and comparing our result to the well-known half-life,  $t_{1/2} = 17.219(17)$  s [2]. We produced  $^{19}\text{Ne}$  using the  $^1\text{H}(^{19}\text{F}, 2n)$  reaction and collected it via MARS, the tape-transport system and our  $4\pi$  proportional gas counter as described in Ref. [1]. We collected each sample on tape for 1.5 s and observed its decay for 150 s. Figure 1 presents the experimental spectrum (red) actually obtained along with the expected  $^{19}\text{Ne}$  exponential. The difference between the two curves clearly identifies the presence of significant diffusion of the radioactive gas during the 150-s detection time.

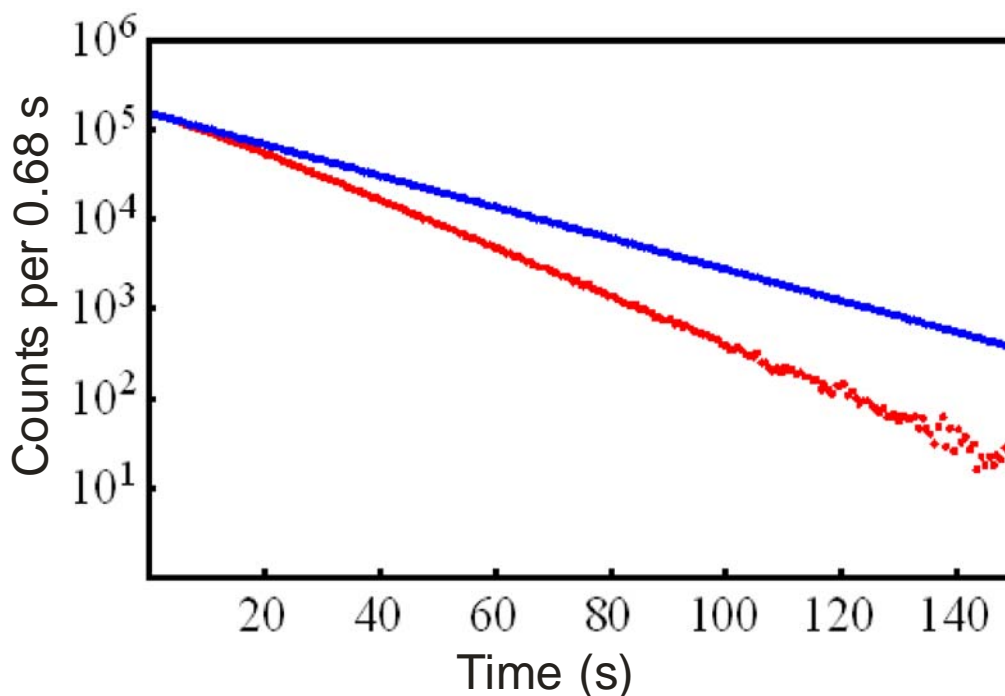


**FIG. 1.** Observed (red) versus expected (blue)  $^{19}\text{Ne}$  ( $t_{1/2} = 17$  s) decay. The contribution of the diffusion losses significantly “speeds up” the observed decay.

If we are to have any hope of extracting a half-life from such a measurement on neon, we need to consistently account for the diffusion process. In our experiments, we prepare the sources by implanting radioactive ions in a 76- $\mu\text{m}$ -thick Mylar tape; then the radioactivity is moved to the center of a  $4\pi$  proportional counter where we observe the decay and ultimately multiscale it. The source consists of an

almost uniform distribution with the shape of a 1.5-cm-diameter disk, 20  $\mu\text{m}$  thick and located in the middle of the tape. The  $4\pi$  proportional gas counter is split in two halves that enclose the tape, having an air gap of about 1 mm between the halves.

To try to understand neon diffusion out of our detection system, we calculated the diffusion of (non-radioactive) neon atoms in the Mylar tape and detector air-gap. For the source geometry, the in-tape-diffusion is essentially a 1-dimensional process in the direction perpendicular to the tape. A source with a original rectangular distribution in the direction perpendicular to the tape (as in our implanted source) evolves toward a bell shape that broadens and reaches the tape edges. Figure 2 shows the expected modification of the concentration of Ne atoms after 3.5 s, assuming them to be uniformly implanted in the middle of the tape over a depth range of 20  $\mu\text{m}$ ; the diffusion coefficient of neon in Mylar ( $2.16 \times 10^{-10} \text{ m}^2/\text{s}$ ) was taken from [4].

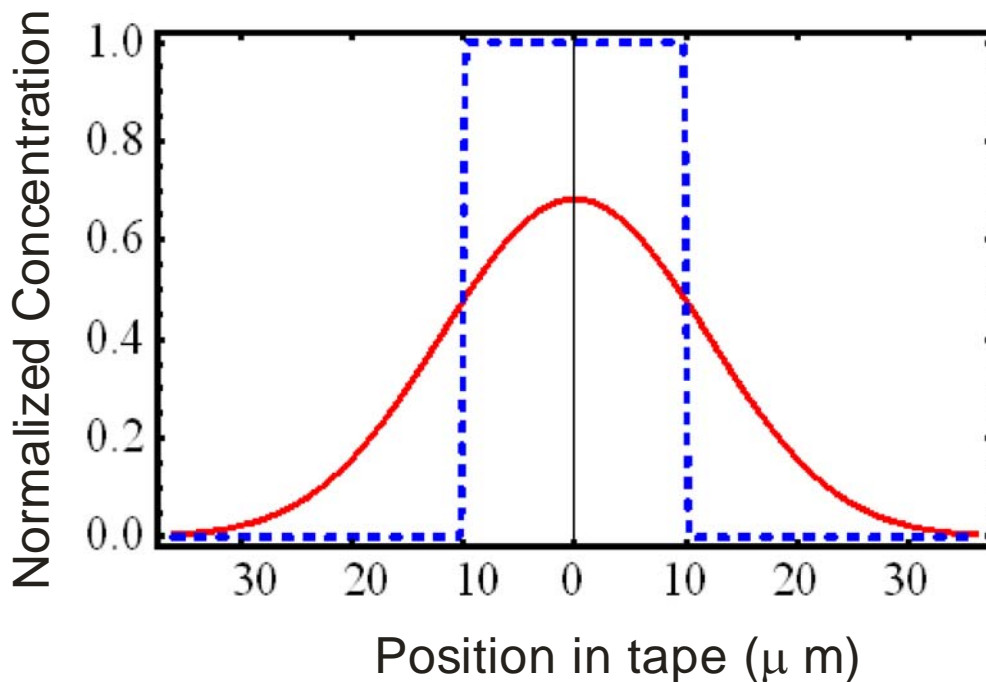


**FIG. 2.** Diffusion-induced redistribution of uniformly implanted Ne ions in the direction perpendicular to the tape. The abscissa extends over the whole thickness of the Mylar tape (76  $\mu\text{m}$ ). The blue dashed curve corresponds to the initial distribution; the red curve is the calculated distribution after a 3.5 s diffusion time.

Once the neon atoms reach the Mylar-air interface, the neon diffusion in air proceeds extremely fast: the diffusion coefficient of neon in air ( $1.89 \times 10^{-5} \text{ m}^2/\text{s}$ ) [5] is 5 orders of magnitude higher than it is in Mylar. Thus the only real cause for a neon presence in the air gap of our proportional counter is the diffusion current of neon atoms emerging from the tape. A calculation of the diffusion current of non-radioactive neon atoms at the Mylar-air interface gives a reasonable idea of the losses of activity related to diffusion only. Figure 3 presents the time evolution of the out-of-tape diffusion current. A constant implantation current over a 1.5 s period was assumed to distribute the Ne atoms uniformly in the center of the tape over a depth range of 20  $\mu\text{m}$ . Although the implantation is limited to the first 1.5 s, the diffusion current is seen to reach its maximum at about 0.5 s after the implantation stopped. From the perspective

of a  $^{18}\text{Ne}$  half-life measurement ( $t_{1/2}=1.7\text{ s}$ ), this peaking time makes the bookkeeping of the diffusion losses extremely difficult, as the diffusion losses will superimpose on the radioactive decay. Moreover, the fast drop in the diffusion current during the normal detect-time implies a fast loss of neon atoms: once out in the air, the neon atoms will rapidly pass out of the active detection volume.

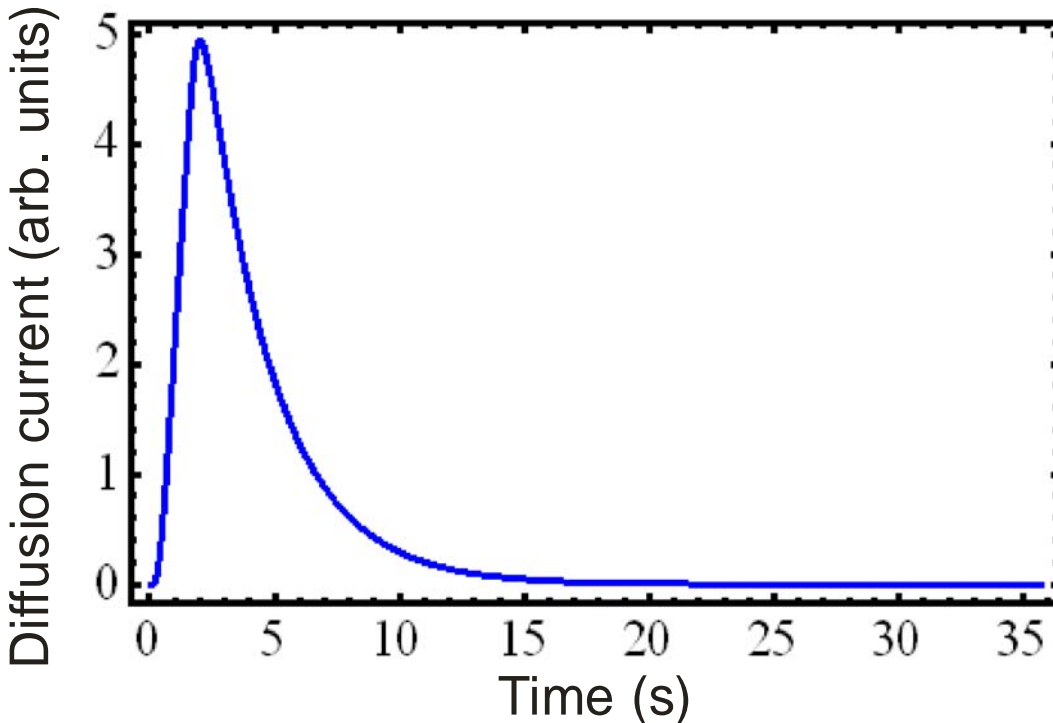


**FIG. 3.** Calculated time evolution of the diffusion current at the Mylar-air interface. The neon atoms are assumed to be uniformly implanted in the central 20  $\mu\text{m}$  of the Mylar tape for a time interval of 1.5 s.

The final step in our model-analysis of the diffusion process was to determine the time evolution of the non-radioactive neon atoms present in the active volume of the detector. In real measurements, after the implantation of the radioactive ions in the tape, the beam is turned off, and then the activity is moved in about 0.18 s to the center of our  $4\pi$  proportional counter where the decays are counted and multiscaled. The equivalent for the transport of the non-radioactive neon atoms requires the continuous removal of the neon atoms that exit the tape during the 0.18-s transport time. Thus we are faced with the full loss of all neon atoms that escaped out of the tape during both the collect and move time intervals. With all these effects considered, we calculate that about 85% of the implanted neon atoms are still present in tape at the beginning of the detection time. The diffusion of these atoms out of the active volume of the detector is presented in Fig.4. The diffusion losses show a decay-like evolution with an equivalent diffusion half life of 1.9 s.

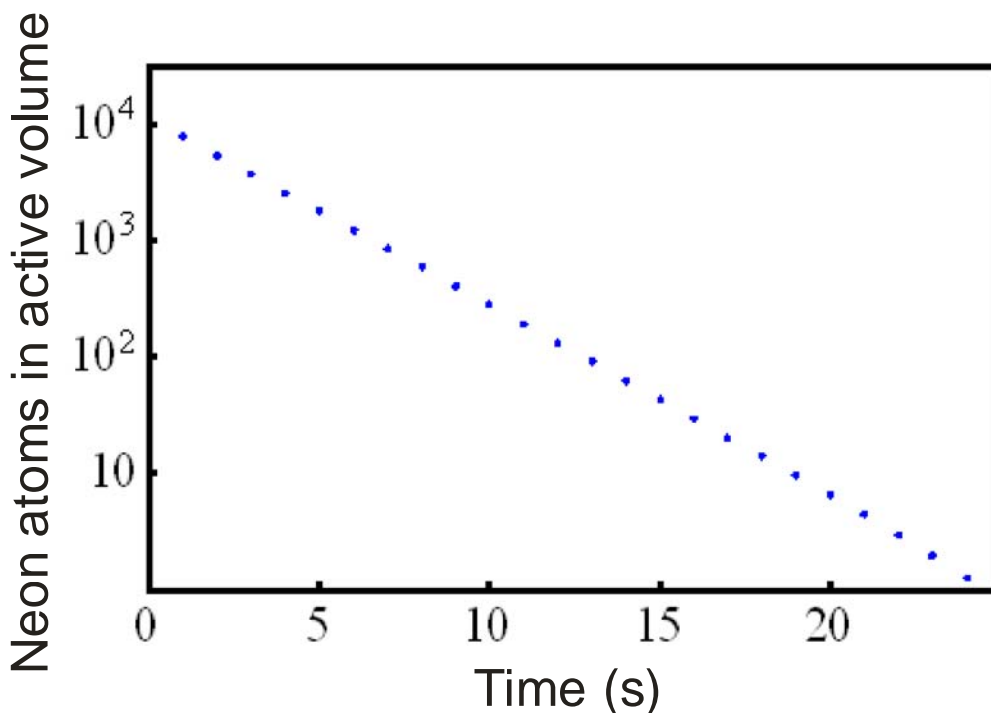


**FIG. 4.** Calculated time evolution of the total number of (stable) neon atoms in the active volume of the detector during the “detection” time. A total of  $10^4$  neon atoms were uniformly implanted in the Mylar tape for 1.5 s, and then the tape surface was wiped for 0.18 s (equivalent to the losses occurring during the transport of the activity). The diffusion induced migration of the neon atoms shows an exponential loss in the total retained neon atoms with an equivalent half life of 1.9 s.

While the trend predicted by these results is consistent with the experimental observations, caution must be exercised in taking the numbers too seriously since the value of the diffusion coefficient for neon in Mylar came from a rather old measurement [3]. In the case of another noble gas, argon, a more recent value for its diffusion coefficient in Mylar [5] differs significantly from the corresponding value in [3]. Moreover, as our Mylar tape is coated with a thin Al layer, it is likely that it will introduce some delay in the neon release. In view of these uncertainties, we conclude that it would be virtually impossible to extract a precise half-life for  $^{18}\text{Ne}$  from a system such as ours that uses Mylar tape to hold the implanted samples.

- [1] V.E. Jacob, J.C. Hardy, J.F. Brinkley, C.A. Gagliardi, V.E. Mayes, N. Nica, M. Sanchez-Vega, G. Tabacaru, L. Trache and R.E. Tribble, *Phys. Rev. C* **74**, 055502 (2006).
- [2] G. Azuelos and J.E. Kitching, *Phys. Rev. C* **12**, 563 (1975).
- [3] R. Asha, R.M. Barrera and D.G. Palmer, *Polymer* **11**, 421 (1970).
- [4] CRC Handbook of Chemistry 89E, p6-192
- [5] *Polymer* **42**, 2413 (2001).

## Digital beta counting for high-precision nuclear beta-decay experiments

L. Chen and J. C. Hardy

In the past year we have made further tests on the digital  $\beta$ -counting system first described in our last progress report [1]. The goal of this project is to pursue a more robust signal processing system for our high-precision superallowed  $\beta$  -decay half-life measurements [2] based on a  $4\pi$  proportional gas counter. Digital signal processing (DSP) allows one to perform very subtle analysis of detector signals long after the experiment is finished, and the method is naturally free from the constraints of on-line processing procedures. One can minimize on-line signal processing so as to maximize the physical information stored for later analysis. Then, in the off-line analysis stage, one can use DSP algorithms to build various data processing chains geared to investigate the effects of different parameter settings – for example, dead time or discriminator level – or to test different analysis ideas.

In high-precision lifetime experiments the genuine  $\beta$  -decay events must be counted with very high efficiency, precision and accuracy. In order to achieve this, the pulse waveforms must first be recorded with a relatively high resolution so that detailed off-line analysis can be performed. The high-speed digitizer we are using, National Instruments PCI-5154 [3], has all the key characteristics required. The digitizer can sample 2 input channels at 1GS/s rate simultaneously (up to 2GS/s if operated in single channel mode) and has a 256 MB on-board memory for each channel. It is an 8-bit digitizer, and the voltage dynamic-range can be configured from 0.1 V to 5 V. The dead-time of the digitizer is less than 1  $\mu$ s, which is dominated by the reference (stop) trigger re-arm time. Since very high efficiency is essential in our measurements, the signal from the gas counter must be amplified with high gain. After extensive tests, we settled on two cascaded fast amplification stages, the first a fast timing preamplifier, ORTEC VT-120A, and the second an SR445A amplifier from Stanford Research Systems, to amplify our gas-counter signal with a combined gain of 1000. Both amplifiers have very short rise times, so the original pulse shape from the detector was well maintained for digitizing. With  $\times 1000$  gain the amplifiers provided a sufficiently strong signal for digital measurement and, based on our plateau analysis of the detector response as a function of applied bias voltage, we believe the  $\beta$  detection efficiency is  $>99.5\%$ .

Figure 1 displays captured waveforms for nine genuine  $\beta$  -decay waveforms in the upper panel and nine “spurious” pulses – spontaneous detector discharges – in the lower panel. Apparently spurious pulses have a quite different shape compared to genuine  $\beta$  -decay pulses. Generally speaking, spurious peaks are quite fast and narrow but with a wide range of amplitudes. Note that most of the narrow spurious pulses are not counted by a conventional counting chain since the amplification stage of that system has a much longer shaping time (several micro-seconds), which has the effect of reducing the amplitude of most spurious pulses to below the discrimination level.

A typical pulse-width distribution is displayed in Fig. 2. The valley in the width distribution between the spurious and  $\beta$  peaks is obvious but unfortunately it is not deep enough to effect a clean separation based on pulse width alone, so additional pulse-shape analysis is required. A software filter, or discriminator, was designed and tested, which combined a composite analysis based on pulse width, rise time, amplitude and total integral. The pulses were filtered in two steps. In the first, a pulse was

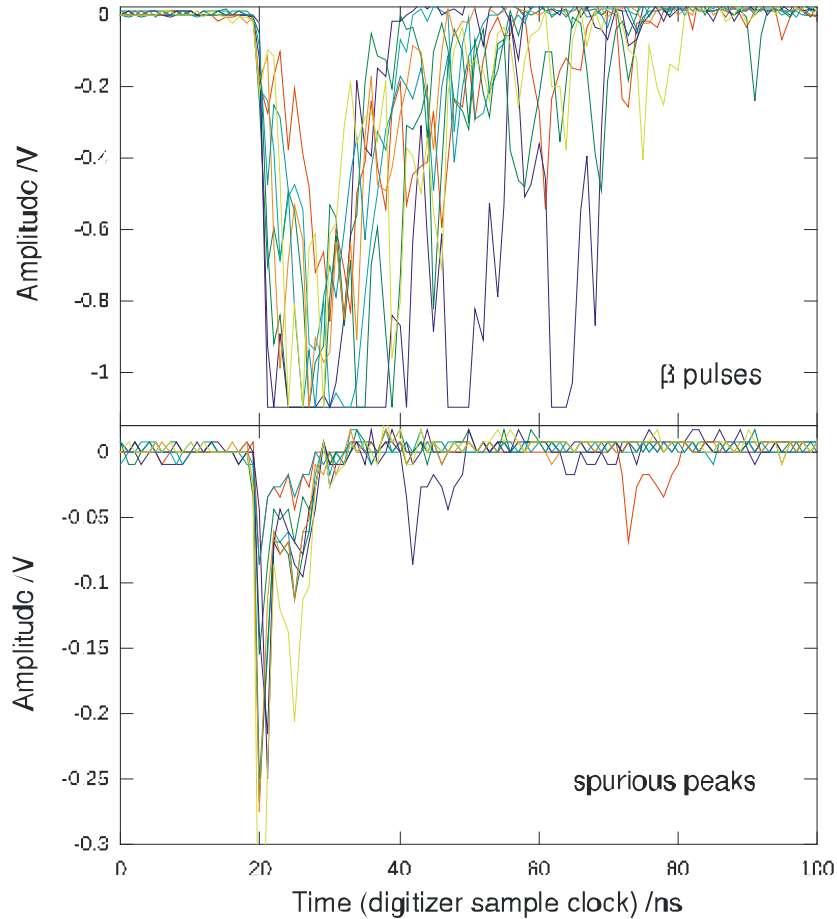


**FIG. 1.** Waveforms captured by the high-speed digitizer. The upper panel shows 9 captured  $\beta$  signals and the lower panel shows 9 “spurious peaks”. The limits of the digitizer dynamic range can be seen on some of the  $\beta$  signals.

qualified as a  $\beta$  event or marked as a spurious or undetermined pulse based on its width: a very small width clearly signifies a spurious event while a very large width indicates a true  $\beta$  event; pulse widths in the region of the valley in Fig. 2 are deemed to require further analysis in a second step involving a detailed pulse-shape analysis. By determining the slope of each pulse’s falling edge, and the pulse integral-to-amplitude ratio, we were able to separate true  $\beta$  events from spurious ones. A plateau we obtained by applying this combined filter is plotted in Fig. 3 and its slope is seen to be below  $\sim 0.5\%$  per 100 V between 2600 V and 2825 V. This plateau is wider and flatter than those obtained with our conventional electronic chain. Thus, in principle the digital system provides a better way to count  $\beta$  particles.

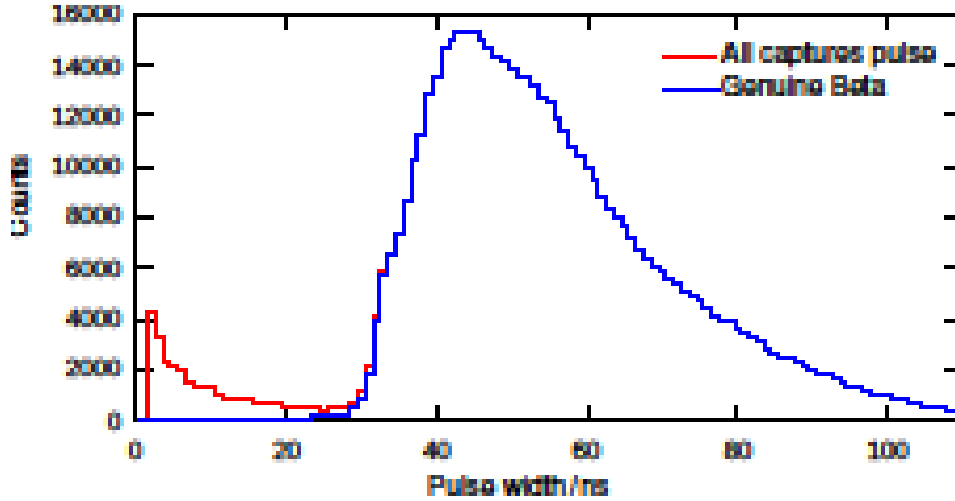


**FIG. 2.** Width distribution of pulses before and after the filter. The data were taken with a detector bias of 2800 V and a 5 kBq  $\beta$  source.

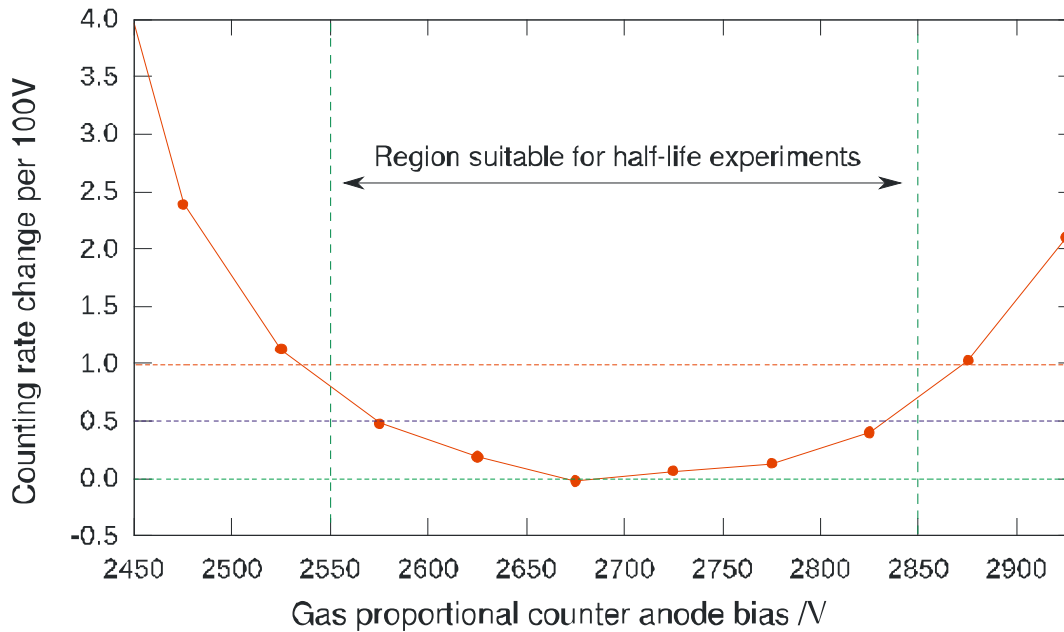


**FIG. 3.** The plateau for our  $4\pi$  proportional gas counter as measured with our new digital-counting system. Data were taken with a 5 kBq  $^{90}\text{Sr}$   $\beta$  source; the measuring time for each point was 400 seconds.

It turns out that the number of spurious pulses increases rather rapidly with the effective detector bias as demonstrated in Fig. 4. We can see that it is the rise of spurious pulses at higher bias that actually causes the end of the plateau. Furthermore, evidently the higher plateau slope obtained with conventional

counting systems is mainly caused by those spurious pulses. More details of the spurious-peak problem in proportional counters can be found in a rather early review paper [4].

The DAQ software as well as all the off-line analysis software were developed on the LabVIEW platform. LabVIEW provided a native control of our digital devices (all made available by National Instruments) and we found that using it for digital data analysis was reasonably efficient since many handy functions for hardware control and data processing are available, ready to use, in LabVIEW.

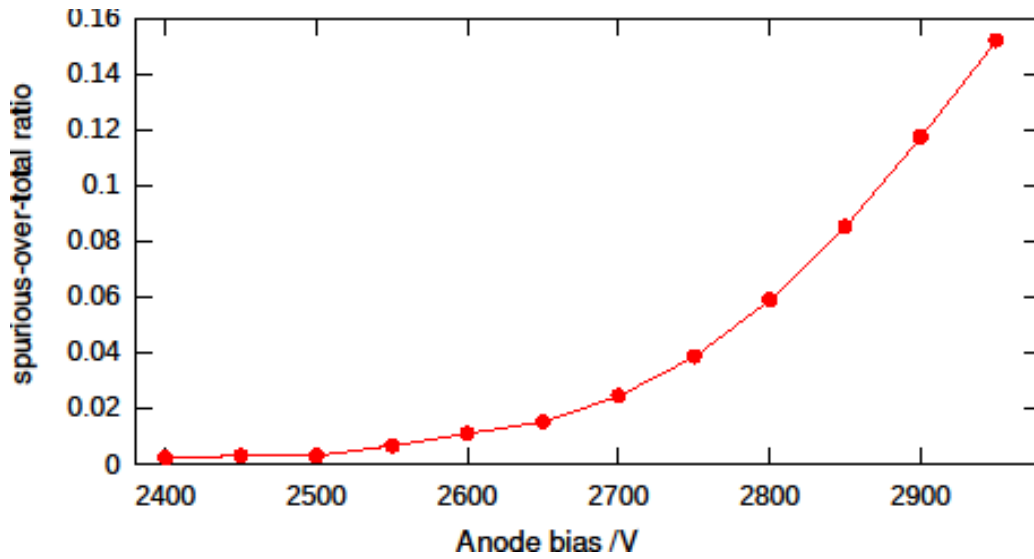


**FIG. 4.** The ratio of the number of spurious pulses to the total number of captured pulses. The data are taken from the  $4\pi$  proportional gas counter with a 5 kBq  $^{90}\text{Sr}$   $\beta$  source.

- [1] L. Chen and J.C. Hardy, *Progress in Research*, Cyclotron Institute, Texas A&M University (2009-2010), p. V-22.
- [2] J.C. Hardy and I.S. Towner, *Phys. Rev. C* **79**, 055502 (2009).
- [3] <http://www.ni.com/digitizers>.
- [4] P.J. Campion, *Nucl. Instrum. Methods, Phys. Res.* **112**, 75 (1973).

## Preparation of an $^{115}\text{In}$ source

J. Goodwin, N. Nica, and J. C. Hardy

We required an  $^{115}\text{In}$  target for neutron activation to produce an  $^{116}\text{In}$  source as part of our program to measure and test Internal Conversion Coefficients [1]. Since enriched  $^{115}\text{In}$  is only available as indium(III)-oxide powder,  $\text{In}_2\text{O}_3$ , we first investigated methods for producing a thin indium target using the oxide powder of natural indium, which is considerably less expensive. We prepared the final target with  $\text{In}_2\text{O}_3$  enriched to 99.83% and supplied to us by Trace Sciences International.

According to the CRC Handbook of Chemistry and Physics [2], indium-oxide is not soluble in water but is soluble in acids. For our purposes we chose nitric acid,  $\text{HNO}_3$ . The procedure we found to be the most successful started with our preparing a glass slide by completely covering it with a piece of 4- $\mu\text{m}$ -thick Mylar. We then took a 12- $\mu\text{m}$ -thick piece of Mylar with adhesive on one side and placed it, adhesive side down, over the thin Mylar, wrapping its ends around the glass slide to attach the combination to the slide. This provided a non-stick surface upon which the target material could be placed, while allowing the finished product to be gently lifted off the glass slide without risk of serious deformation.

Next we weighed out approximately 1 mg of the oxide powder using a Mettler balance and placed the material on the Mylar surface of the prepared slide. A few drops of nitric acid were then injected into the powder with a small disposable syringe. The powder dissolved in the acid and the solution was subsequently dried on a standard laboratory heater/stirrer. The drying process left a fine powder evenly-spaced in a roughly circular configuration. By inspection under a microscope, we found the grains of powder to be  $< 2 \mu\text{m}$  in diameter. Once the powder was completely dry, the Mylar substrate supporting it was gently lifted off the slide, and immediately covered with a matching piece of 12- $\mu\text{m}$ -thick Mylar, adhesive side down. The edges were then trimmed, leaving no adhesive surface still exposed. This process produced a very thin sample of  $^{115}\text{In}_2\text{O}_3$ , 1-2  $\mu\text{m}$  thick) with a covering of Mylar on one side of 16  $\mu\text{m}$ , and on the other, of 12  $\mu\text{m}$ .

The finished samples will be transported at a future date to the Triga Reactor at the Nuclear Science Center, Texas A&M University for irradiation. Our group anticipates that the irradiation will occur in late June or early July, 2011.

[1] N. Nica, J.C. Hardy, V. Horvat, V.E. Jacob, V. Siller, and M.B. Trzhaskovskaya, *Progress in Research*, Cyclotron Institute, Texas A&M University (2010-2011), p. I-32.

[2] *CRC Handbook of Chemistry and Physics*, CRC Publishing (Cleveland, Ohio), D.R. Lide (ed.), 2009.

## Spectra of time differences between consecutive pulses measured with a new TDC-based data-acquisition system

V. Horvat and J. C. Hardy

For accurate high-precision measurements of  $\beta$ -decay half-lives, a new data acquisition system [1] based on a multichannel time-to-digital converter (TDC) has been set up as an alternative to the CAMAC-based system that is currently in use. The new system stores each event (*i.e.*, arrival of a logic pulse) in a raw format by recording the corresponding TDC channel and the time (within 16 ps) since acquisition started. This way a histogram of the time  $\Delta t$  between consecutive events can be constructed and used, for example, to investigate the system's dead time. Furthermore, a longer dead time can be imposed in the analysis and its effect on the measured half-life can be examined.

We have tested the TDC-based data-acquisition system by studying the pulses due to  $\beta$  particles emitted from a radioactive source ( $^{90}\text{Sr}$ - $^{90}\text{Y}$ ) [1]. It was found that the histogram of  $\Delta t$  followed an exponential decay curve (with the decay constant equal to the event rate) as expected, but only for  $\Delta t > 10 \mu\text{s}$ . A smaller-than-expected number of events was observed for  $\Delta t$  between 1  $\mu\text{s}$  and 10  $\mu\text{s}$ . This effect was explained based on the shape and extent of the analog pulses from the fast filter amplifier, which were subsequently converted to logic pulses by the discriminator before being sent to the TDC. In particular, since the negative pulses from the fast filter amplifier typically become slightly positive before returning to the base line, a pulse that arrives between the crossover time of the previous pulse and its return to the base line is piled up and has a reduced chance of crossing the discriminator threshold, *i.e.*, it has an increased chance of not being converted to a logical pulse and counted. In addition, excessive counts were observed in the  $\Delta t$  spectrum for  $\Delta t < 1 \mu\text{s}$ . At the time, this was thought to be due to multiple pulsing. Consequently, to prevent the reduction of the system's throughput due to multiple pulsing, a dead time of 0.5  $\mu\text{s}$  was imposed electronically by means of a gate and delay generator.

Meanwhile, the TDC-based data-acquisition system was used in several  $\beta$ -decay half-life measurements involving secondary ion beams from MARS ( $^{10}\text{C}$ ,  $^{26\text{m}}\text{Al}$ ,  $^{19}\text{Ne}$ , and  $^{18}\text{Ne}$ ). For these measurements the beta decay rate at the beginning of the measuring cycle was intentionally set significantly higher than usual in order to enhance the dead-time related effects. In all the measurements except those with the  $^{10}\text{C}$  beam the TDC-based data acquisition system was used in parallel with the standard CAMAC-based data acquisition system. For  $\beta$  particles, the signal processing was split after the discriminator, so that different gate and delay generators were used by the two systems to set the imposed dominant dead time (IDDT). For the TDC-based system the IDDT was set close to a minimum (about 20 ns), while that for the CAMAC-based system was set to 3  $\mu\text{s}$ . However, after imposing an IDDT of 3  $\mu\text{s}$  to the data collected with the TDC-based system, it was found that the beta-decay spectra obtained with the two systems were virtually identical. This way it was established that the two systems were equivalent.

In addition, many measured  $\Delta t$  spectra were obtained both for the  $\beta$ -particle events and the beam-particle (heavy-ion) events. These spectra provided further insight into timing properties of the generated signals. In the former case, it was confirmed that the counting rate at the beginning of the measuring

cycle determines the “decay constant” of the spectrum for  $\Delta t > 4 \mu\text{s}$  as expected, while for  $\Delta t < 4 \mu\text{s}$  the shape of the spectrum is determined mostly by the shape and extent of the analog pulses from the fast filter amplifier (which in turn depend on the amplifier settings). Due to the small IDDT of 20 ns, the latter conclusion was now established to be true even in the region of  $\Delta t$  below 0.5  $\mu\text{s}$ . An example of the  $\Delta t$  spectrum for  $\Delta t \leq 10 \mu\text{s}$  is shown in Figure 1. It should be noted that this spectrum has its starting point well above the IDDT value.

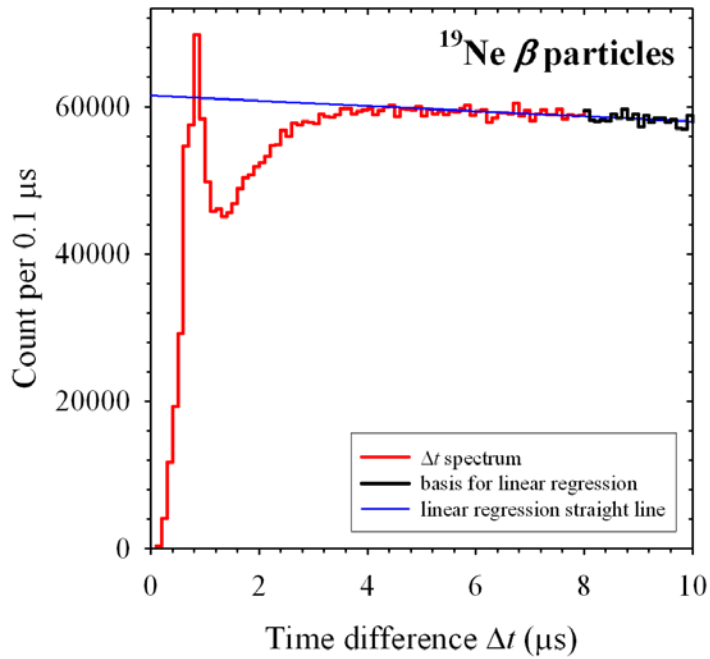


**FIG. 1.** An example of a measured  $\Delta t$  spectrum of  $\beta$ -particle events in the decay of  $^{19}\text{Ne}$ .

Therefore, contrary to the previous assessment that the excessive counts observed in the  $\Delta t$  spectrum of  $\beta$  events at  $\Delta t < 1 \mu\text{s}$  were due to multiple pulsing, it is now established those counts are, in fact, also determined by the shape of the analog pulses from the fast filter amplifier. Namely, a signal from the fast filter amplifier normally crosses the threshold level as it drops to its minimum value and then it crosses the threshold level for the second time as it rises back toward the baseline. If another signal piles up during the time interval between the second crossing of the threshold and the baseline crossover time of the previous signal, it will have an *increased* chance of crossing the discriminator threshold, being converted to a logical pulse and counted.

Consequently, a proper Monte Carlo simulation of the measured spectra must include these effects. For the present situation we proceeded by observing the shape of the measured  $\Delta t$  histogram and finding the critical point at  $\Delta t = \Delta t_c$ , at which it stops deviating from the shape expected based on the actual distribution of counting rates. (For the histogram shown in Figure 1,  $\Delta t_c = 4 \mu\text{s}$ .) Then the entire histogram was normalized so that the value of its maximum channel equaled one. Each channel between 0 and  $\Delta t_c$  was then interpreted as the pulse detection probability  $p$  for the corresponding time  $\Delta t$  elapsed

since the detection of the previous pulse. This is justified by the fact that the “expected shape” over the relatively short time interval between 0 and  $\Delta t_c$  can be regarded as being effectively constant. The value of  $p$  at  $\Delta t_c$  (which was found to be only slightly less than 1) was assumed to apply to all  $\Delta t > \Delta t_c$ .

The obtained  $\Delta t$ -dependence of probability  $p$  was subsequently implemented in the  $\beta$ -decay Monte Carlo simulation program as follows. For each generated event after the very first one, the time  $\Delta t$  “elapsed” since the previous event is calculated and the corresponding value of  $p$  is found. Acceptance of the new event is determined by a random number generator. If the returned random number from the interval (0,1) is less than  $p$ , the new event is accepted. Otherwise, it is ignored. It was found that the pulse detection probability function does not depend significantly on the pulse rate, so that a single histogram of  $p$  can be used for all emulated decay cycles. Examination of this effect as well as the additional effect of the IDDT on the measured half-life is underway.

The measured  $\Delta t$  spectra for the signals originating from the heavy-ion detector reveal arrays of fully resolved peaks separated by the period  $\tau$  of the radio-frequency (RF) power supply for the cyclotron dee electrodes. Figure 2 (a) shows an example of such a spectrum for the beam of  $^{26m}\text{Al}$  at the average particle rate of  $1.7 \times 10^5 \text{ s}^{-1}$  and  $\tau$  equal to 62.3 ns. Although the zeroth peak is absent and the first peak is cut off because of the dead time of the signal-processing electronics, it can be estimated that the probability of two ions occurring in RF cycles separated by  $n\tau$  ranges from 1.2 % for  $n = 2$  to 1.0 % for  $n = 20$ .

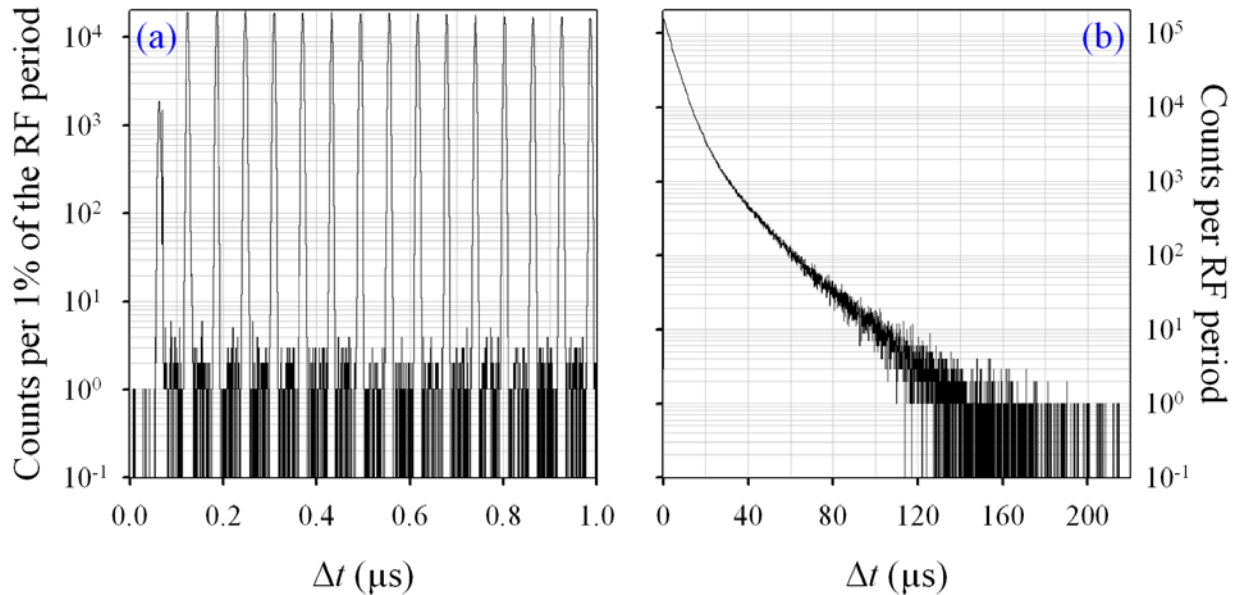


**FIG. 2.** Measured histograms of time differences  $\Delta t$  between consecutive signals from the heavy-ion detector for the secondary beam of  $^{26m}\text{Al}$  from MARS. Both spectra are from the same run and differ only in the range of  $\Delta t$  being covered in the plot.

Figure 2 (b) shows the same spectrum as Figure 2 (a) does, except that the full range of  $\Delta t$  is covered and the bin size equals  $\tau$ . This way the peak structure is not apparent. Normalization of the area of this spectrum to a total number of 1 results in a histogram giving the probability for detecting two ions

within the time interval  $(\Delta t, \Delta t + \tau)$  shown as a function of  $\Delta t$ . The sum of the contents of all channels below a given  $\Delta t$  yields the probability  $P$  for detecting two ions within the time interval  $T < \Delta t$ . Consequently,  $1 - P$  is the probability for detecting two ions within the time interval  $T \geq \Delta t$ . The two probability functions are shown in Figure 3. The results are in qualitative agreement with expectations based on Poisson statistics, considering that the particle rate during the measurement was not exactly constant. The graphs shown in Figure 2 and Figure 3 may be useful in the analysis of an experiment in which time differences are measured (such as those between two events or between an event and the arrival of the beam particle that caused it).

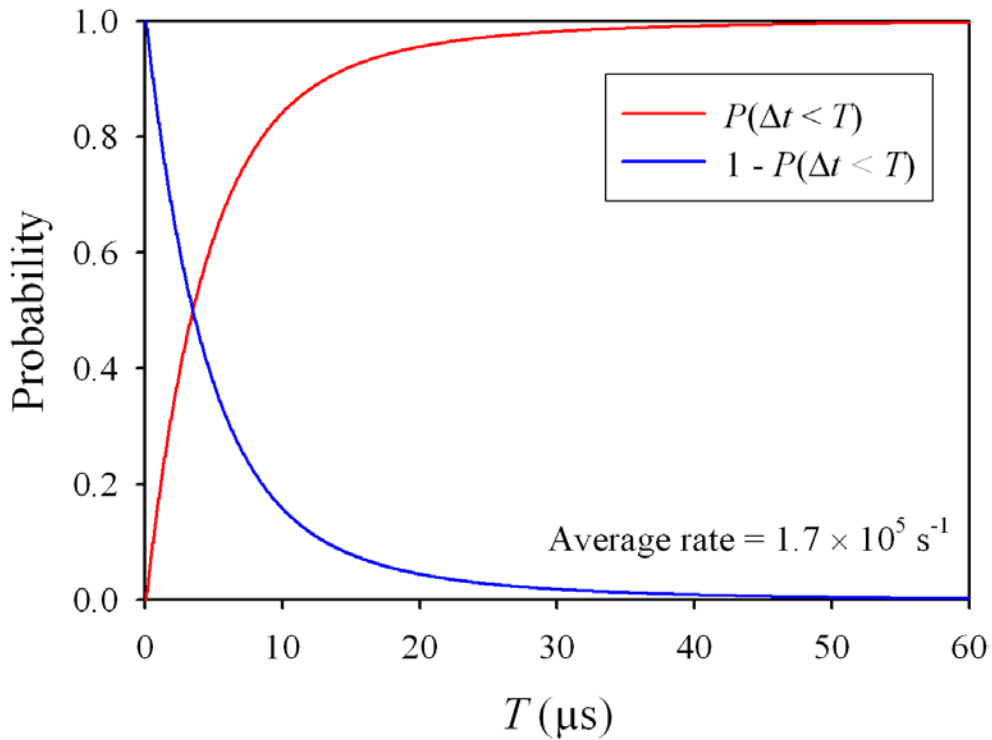


**FIG. 3.** Probability for detecting two ions within time interval  $T < \Delta t$  (shown by the red curve) and  $T \geq \Delta t$  (shown by the blue curve) derived from the histogram shown in Figure 2.

[1] V. Horvat and J.C. Hardy, *Progress in Research*, Cyclotron Institute, Texas A&M University (2009-2010) p. V-24.

## Assembly and test runs of decay detector for ISGMR study

J. Button, R. Polis, C. Canahui, Krishichayan, Y. -W. Lui, and D. H. Youngblood

### 1. $\Delta E$ - $\Delta E$ - E Plastic Scintillator Array Decay Detector

In order to study the Isoscalar Giant Monopole Resonance in unstable nuclei, we have designed and built and are testing a  $\Delta E$ -  $\Delta E$  - E decay detector composed of plastic scintillator arrays. The elements of this detector and its parameters are described in Ref. [1].

Currently, the decay detector is nearly completed. A new set of 12 horizontally aligned and 14 vertically aligned scintillator strips have been prepared for installation. The original design for holding vertical scintillator strips has been found to be unsuitable and is still being re-worked. Testing has been done to eliminate detector elements or identify elements in need of modification (scintillator strips and blocks, photomultiplier tubes, optical fibers, or light windows).

### 2. Calculating Light Output

Two methods for the calculation of relative light output of plastic scintillator when ions of a particular energy pass through or are stopped in the scintillator will be compared for suitability in calibrating light output from the experimental setup. An empirical relationship such as the Birks formula[2], which relates light output to the stopping power directly, is a convenient method because of the widespread availability of stopping power tables for energetic ions passing through matter[3]. Also, the stopping power may be calculated directly by the Bethe-Bloch formula [5]. The Birks formula becomes a hindrance when the experiment involves many ion types, since the parameters  $L_0$  and  $K$  will vary by ion type. For this situation, models with a specific  $Z$  dependence have been proposed. One such model (Energy Deposition by Secondary Electrons) relates light output  $\frac{dL}{dx}$  to the number of energy carriers (electron-hole pairs or excited molecular structures) created due to energy loss of the ion in the scintillating material [6]. Non-linearities in the light response originates when the energy carrier density exceeds the quenching density,  $\rho_q$ . The number of energy carriers,  $\frac{dN_e}{dx}$ , is obtained via radial integration of the energy carrier density  $\rho(r)$ , where  $x$  is the ion path through the scintillating material and  $r$  is a distance perpendicular to  $x$  indicating the path of energy carriers through the material. For plastic scintillators like BC408, the specific detector response,  $\frac{dL}{dx}$ , is related to the number of energy carriers by equation 1.

$$\frac{dL}{dx} = C \frac{dN_e}{dx} \left( 1 - F \frac{dN_e/dx}{A + dN_e/dx} \right) \quad (1)$$

The fit parameters C, F, A and  $\rho_q$  were obtained by fitting to published experimental data where the ion is stopped in the scintillator [4] (Fig. 1). These parameters were then used to obtain the expected light

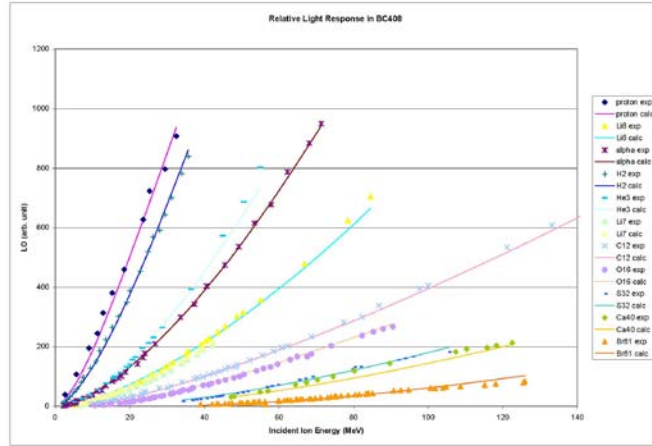


**FIG. 1.** Comparison of EDSE model to experiment [4] for various ions, where the ion is stopped in the material. The fit parameters are  $C = 11.51$ ,  $A = 266.38$ ,  $F = .882$ ,  $\rho_q = 1.83 \cdot 10^{26}$ .

response due to protons or alpha ions that only deposit a small portion of their energy in 1 mm thick strip scintillators (Fig. 2).

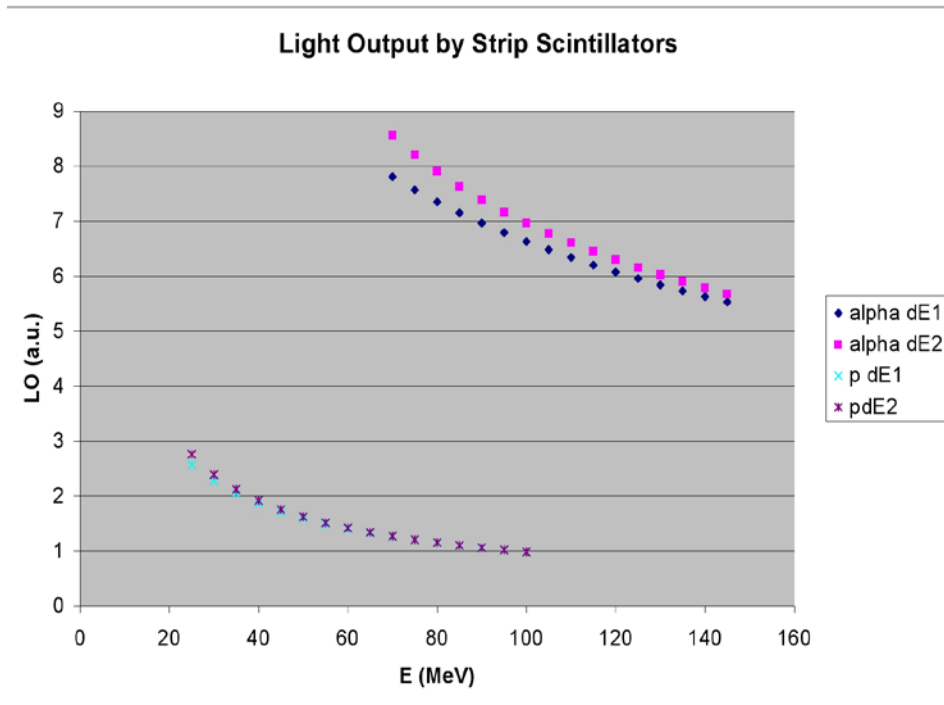


**FIG. 2.** Calculation of light output in  $\Delta E1$  and  $\Delta E2$  for protons and alpha ions.

### 3. $^{90}\text{Sr}$ Beta Source Testing

The light output response by a 1 cm diameter cylindrical BC408 plastic scintillator due to  $^{90}\text{Sr}$  beta electrons was measured. This cylindrical scintillator was then used to compare performance between all 1 cm diameter photomultiplier tubes. A scintillator of this thickness is sufficient for stopping all electrons produced in the decay of  $^{90}\text{Sr} \rightarrow ^{90}\text{Y} + \beta^-$  (Q value of 546 keV). The  $^{90}\text{Y}$  undergoes a subsequent beta decay (Q value of 2.4 MeV). The signal from the photomultiplier tube was passed through a spectrum amplifier, sent to a multichannel analyzer, and recorded by computer.

To calibrate the measured spectrum to the known energy spectrum, one can make a Fermi-Kurie plot (Fig. 3) [8]. When this transformation is applied, the tail part of the energy cross-section is linear with respect to the electron energy (Eq. 2), making it very simple to find the end point of the spectrum ( $\sim 2.4$  MeV). At this energy scale, the relationship between light response by the plastic scintillator and the energy deposited into the scintillator by the beta electron is linear. The response by the photomultiplier tube, the spectrum amplifier, and the multichannel analyzer are each assumed to be linear as well.

$$\sqrt{\frac{dN(p_{e^-})/dE}{p_{e^-}^2 F(Z_D, p_{e^-})}} \propto (E - E_{e^-}) |M_{fi}| \quad (2)$$

$p_{e^-}$  is electron momentum,  $F(Z_D, p_{e^-})$  is the Fermi Function, and  $|M_{fi}|$  is the transition matrix element.

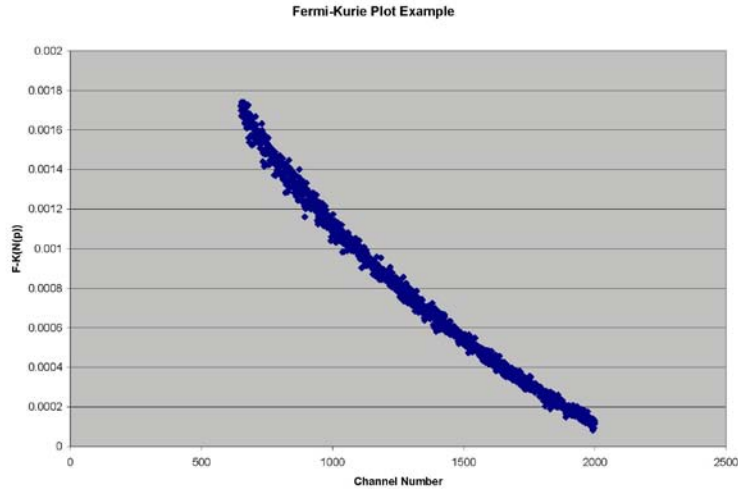


**FIG. 3.** Example of a Fermi-Kurie plot.

The normalized spectrum measured by each photomultiplier tube was graded against the average response from all photomultiplier tubes (Fig. 4). The gain with the same voltage applied differed by as much as 100%. A set of tubes whose gains agreed to 15% were chosen for the detector.

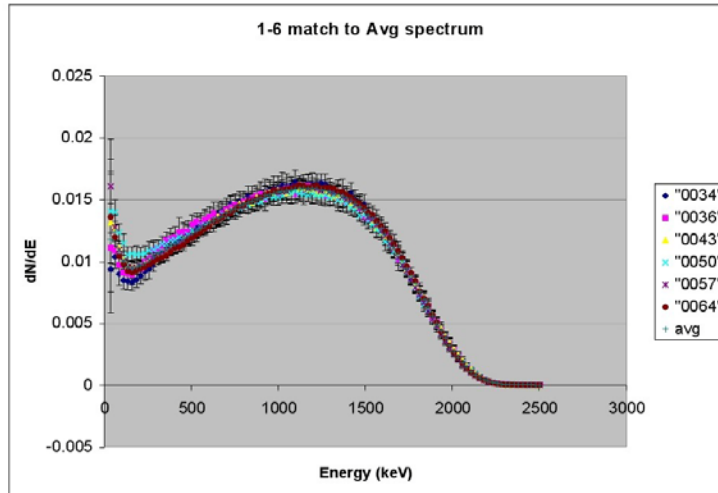


**FIG. 4.** Normalized and calibrated spectra from separate photomultiplier tubes and the average spectrum from all tubes. The observed peaks are from the beta decay of  $^{90}\text{Y}$ .

#### 4. Modifications to Detector Design and Assembly

In order to make and secure the joint between the scintillator and the optic fiber bundle, a thin, plastic sleeve was made to fit over the joint. The sleeve ensures proper alignment between the scintillator and fiber bundle over the course of the optical cement curing time (~24 hours) (Fig. 5)

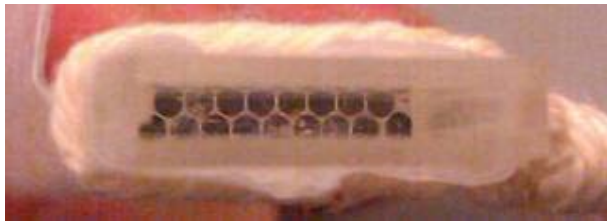


**FIG. 5.** Optic Fiber Bundle enclosed by thin strips of plastic: open cavity is filled with optical cement and thin strip scintillator in order to make a secure and rigid joint.

Scintillator strips are held onto their alignment frame at two points: at the sleeve joint by an aluminum clamp which can be screwed into place on the frame and at the end of the scintillator strip by a

small neodymium magnet (Fig. 6). The strips at  $0^\circ$ , however, are only half the length as all other strips and are only supported at the sandwich joint. In the future, the brass collimator at  $0^\circ$  will be modified so that these strips may also be held in place at their ends.

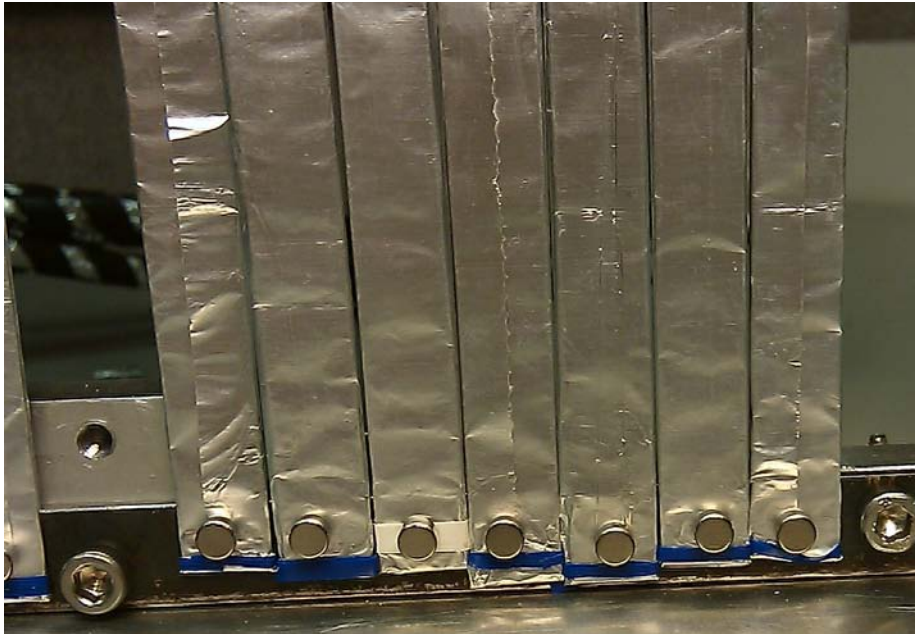


**FIG. 6.** Magnets used to hold vertical scintillator strips

In prior test runs, the optical cement joints between the block scintillators and their odd-shaped light-guides and between the odd-shaped light-guides and cylindrical light-guides were prone to breaking upon installation into a plate which is mounted onto the top of the target chamber lid. A holder supports each block separately by an o-ring which goes around the cylindrical light-guide and an aluminum clamp with a crush gland machined into it which bolts onto the plate (Fig. 7), which has five holes at positions

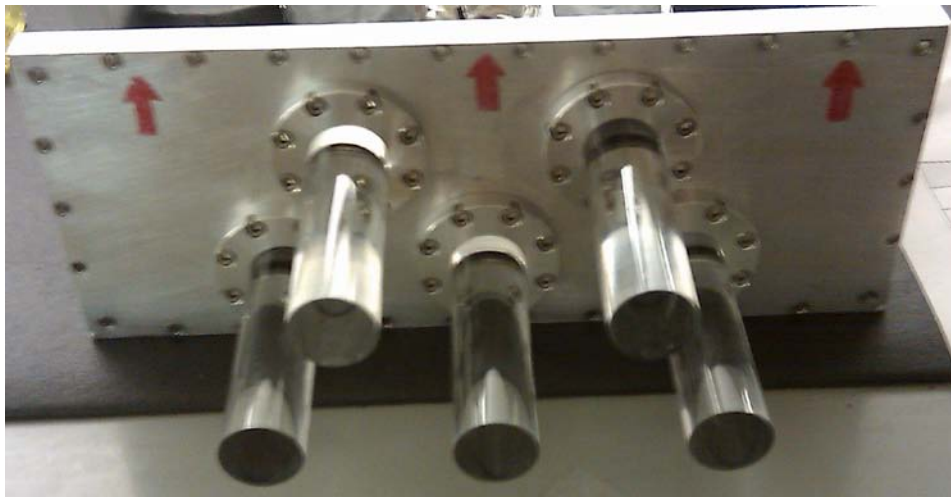


**FIG. 7.** Plate and Holders support each block scintillator and its light guides.

corresponding to the position of the five block scintillators. In order to prevent breaking, great care must be taken in making the optical cement joints. Proper alignment can be achieved by sandwiching the joint between a scintillator and its light guide with four blocks of plywood (Fig. 8). Wax paper is sufficient to prevent cementing the scintillator or light-guide to the plywood. After this joint has been made for each of the blocks, the blocks are then bundled together and held in a box (Fig. 9). The cylindrical light guides are clamped by each holder onto the plate. Dowel pins along the edge of the box are used to align the plate onto the top of the box, ensuring that the cylindrical light-guides are properly aligned with their corresponding odd-shaped light-guides.



**FIG. 8.** Making the joint between a block scintillator and its light-guide.



**FIG. 9.** Box used for aligning cylindrical light-guides to odd-shaped light-guides.

## 5. Test Run and Analysis

For the June 2010 test run, the decay detector consisted of 3 block scintillators, 15 vertical scintillators, and 12 horizontal scintillators. Data were taken using beams of 100 MeV  $\alpha$  particles and 30 MeV protons on  $^{12}\text{C}$  and  $^{58}\text{Ni}$  targets. During this test, much time was dedicated to identifying components that were not working properly. With the exception of one signal from a horizontal strip, all scintillator strip signals were taken without amplification. The horizontal layer of strips was used as a trigger. All triggered events were recorded. Only those events having a coincidence between the horizontal and vertical arrays were analyzed.

Ratios of elastic peak position ( $\text{LO}(\alpha)/\text{LO}(p)$ ) in the individual spectra of various strip

scintillators were calculated and compared to measurement in Table I. Some strips had poor agreement with calculation, and this was determined to be due to poor optical connections between fiber bundle and scintillator. Insufficient gain from the electronics may have also been a significant factor.

**Table I.** Comparison of 100 MeV  $\alpha$  and 30 MeV proton elastic peaks at various angles through 1 mm thick BC408 plastic scintillator. EDSE model is used to arrive at the calculated ratio of alpha to proton peak positions.

	est. angle (deg.)	energy $\alpha$ (MeV)	energy_p (MeV)	LO( $\alpha$ )/LO(p) calc.	LO( $\alpha$ )/LO(p) exp	% diff calc. to exp.	dE $\alpha$ (MeV)	dE_p (MeV)
v9	5.5	99.7	30.0	2.9	2.9	-1.4%	9.0	1.9
v12	21.2	95.5	26.7	2.7	2.6	3.9%	9.4	2.1
v14	30.2	91.2	29.3	2.9	2.4	20.5%	9.7	2.0
h1	37.5	86.8	29.0	3.0	3.9	-23.2%	10.1	2.0
h3	29.9	91.3	29.3	2.9	2.8	5.9%	9.5	2.0
h4	25.9	93.4	29.5	2.9	2.2	33.9%	9.3	2.0
h5	21.2	95.5	29.7	2.9	2.1	37.7%	9.2	2.0
h6	16.2	97.4	29.8	2.9	2.1	35.1%	9.1	1.9
h7	11.0	98.8	29.9	2.9	2.9	-2.1%	9.0	1.9
h9L	0.0	100.0	30.0	2.8	2.6	10.5%	9.0	1.9
h10	5.5	99.7	30.0	2.8	2.8	0.8%	9.1	1.9
h11	11.0	98.8	29.9	2.9	2.0	40.1%	9.2	2.0
h9R	0.0	100.0	30.0	2.8	3.2	-11.3%	9.0	1.9

Another test run was done in December 2010 with 30 MeV protons incident on targets of  $^{12}\text{C}$  and  $^{58}\text{Ni}$ . Analysis on data collected at this time focused on the attenuation of the light response by the thin, strip scintillators for charged ions incident upon a scintillator at different positions relative to the optical connection with the fiber bundle. This was examined in detail using horizontal strip H3 because it was the newest strip installed into the array and had the best light response of all scintillator strips. Spectra obtained from H3 in coincidence with the 5 E blocks were considered only because the E blocks showed better uniformity in terms of response from block to block. Taking into consideration the wrapping used (a layer of aluminum foil) and the position of H3, the energy of elastically scattered protons off of a target of  $^{12}\text{C}$  should range from 28.8 MeV to 29.1 MeV, only a spread of 1%. In Figure 10 however, the spread of the light response along the length of H3 is nearly 53%. The effective length of H3 was taken to be 14.2 cm since that is the width of the E block array and because only events in coincidence with the E block array were considered. The positions of the elastic peak in each of the 5 spectra were measured (Fig. 10). The expected positions of the elastic peak in each spectrum are shown in Figure 11. The measured peak positions were then corrected by the expected change in light response and then plotted against position along strip H3. Even though the expected change is very small, it was assumed that this method would give a more precise estimate of the attenuation length, which was found to be 12.1 +/- 4.5 cm (Fig. 12).

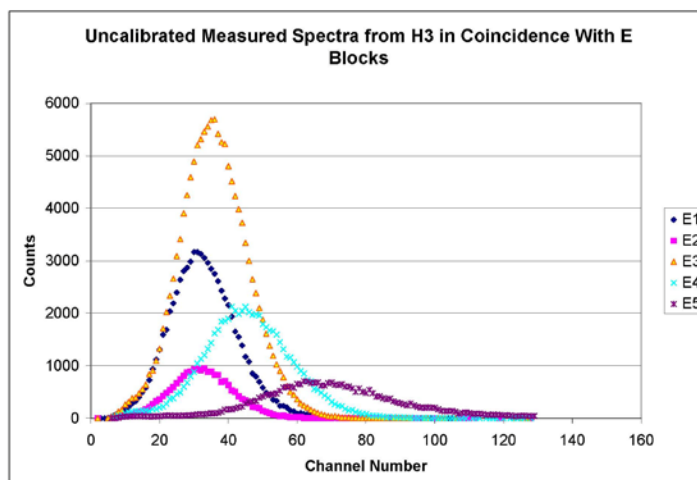


**FIG. 10.** 30MeV proton on  $^{12}\text{C}$ ; raw spectra from scintillator strip H3 in coincidence with the 5 E blocks.

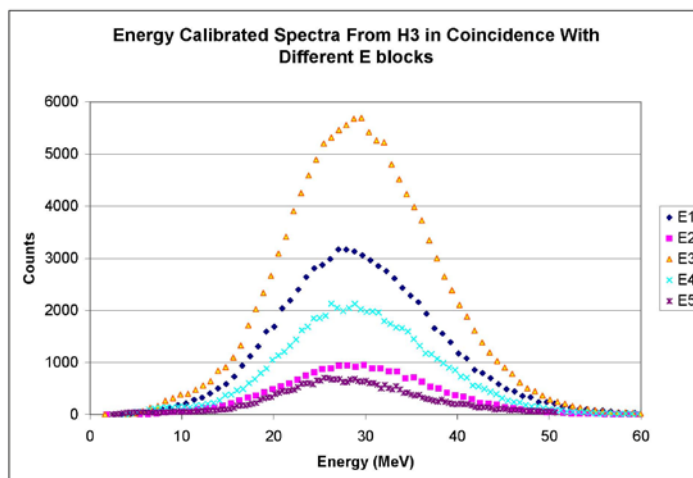


**FIG. 11.** 30MeV proton on  $^{12}\text{C}$ ; calibrated spectra from scintillator strip H3 in coincidence with the 5 E blocks.

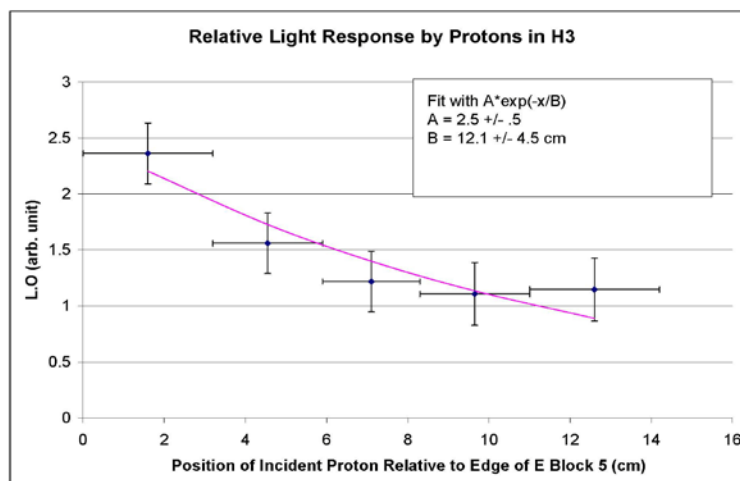


**FIG. 12.** Estimate of the attenuation length (12.1 +/- 4.5 cm) of light response signal in scintillator strip H3. Block E5 is on the side nearest the optical connection for H3, and so the edge of E5 was taken as the 0 cm position. Block E1 ends at 14.2 cm.

## 6. Conclusions

Much time was spent on understanding the light response by thin, strip scintillators. The amount of light attenuation with distance from the optical connection is non-negligible and must be taken into account if the horizontal and vertical strip arrays are to be used to measure the energy loss of incident ions.

Further consideration of the methods for aligning the thin, strip scintillators is also required. These scintillator strips are prone to crazing, which reduces the light transport efficiency of the strips drastically. In order to extend the time in which these scintillators are usable, the mounting frame design must be changed so as to eliminate all bending forces on the strips, which have been observed to be the leading cause of crazing.

- [1] J. Button, R. Polis *et al.*, *Progress in Research*, Cyclotron Institute Texas A&M University (2008-2009), p. V-30.
- [2] J.B. Birks, *Phys. Rev.* **86**, 569 (1952).
- [3] J.F. Ziegler, J.P. Biersack, U. Littmark, *The Stopping and Range of Ions in Solids*, (Pergamon Press, New York, 1999).
- [4] F.D. Becchetti, C.E. Thorn, M.J. Levine, *Nucl. Instrum. Methods* **138**, 93 (1976).
- [5] H. Bethe, *Z. Phys.* **76**, 293 (1932).
- [6] K. Michaelian, *Nucl. Instrum. Methods Phys. Res.* **A356**, 297 (1995).

- [7] International Commission on Radiation Units and Measurements. *ICRU Report 37, Stopping Powers for Electrons and Positrons*. (1984)
- [8] K. Heyde, *Basic Ideas and Concepts in Nuclear Physics: An Introductory Approach*, (Institute of Physics Publishing, Philadelphia, 2004).

**SECTION VI**  
**PUBLICATIONS**

## PAPERS PUBLISHED

April 1, 2010 – March 31, 2011

**Tests of nuclear half-lives as a function of host temperature: refutation of recent claims**, J.C. Hardy, J.R. Goodwin, V.V. Golovko and V.E. Iacob, *Appl. Rad. and Isot.* **68**, 1550 (2010).

**Superaligned nuclear  $\beta$  decay: symmetry breaking, CVC and CKM unitarity**, J.C. Hardy and I.S. Towner, *Nucl. Phys. A* **844**, 138c (2010).

**Precise half-life measurement of the superallowed  $\beta^+$  emitter  $^{26}\text{Si}$** , V.E. Iacob, J.C. Hardy, A. Banu, L. Chen, V.V. Golovko, J. Goodwin, V. Horvat, N. Nica, H.I. Park, L. Trache and R.E. Tribble, *Phys. Rev. C* **82**, 035502 (2010).

**Precise half-life measurement of the superallowed  $\beta^+$  emitter  $^{38}\text{K}^m$** , G.C. Ball, G. Boisvert, P. Bricault, R. Churchman, M. Domsbky, T. Lindner, J.A. Macdonald, E. Vandervoort, S. Bishop, J.M. D'Auria, J.C. Hardy, V.E. Iacob, J.R. Leslie and H.-B. Mak, *Phys. Rev. C* **82**, 045501 (2010).

**Measurement of the half-life of  $^{198}\text{Au}$  in a nonmetal: High precision measurement shows no host-material dependence**, J.R. Goodwin, N. Nica, V.E. Iacob, A. Dibidad and J.C. Hardy, *Phys. Rev. C* **82**, 044320 (2010).

**Comparative tests of isospin-symmetry-breaking corrections to superallowed  $0^+ \rightarrow 0^+$  nuclear  $\beta$  decay**, I.S. Towner and J.C. Hardy, *Phys. Rev. C* **82**, 065501 (2010).

**Astrophysical reaction rates obtained by indirect techniques**, R.E. Tribble, T. Al-Abdullah, A. Alharbi, J. Äystö, A. Banu, V. Burjan, F. Carstoiu, X. Chen, H.L. Clark, T. Davidson, C. Fu, C.A. Gagliardi, J.C. Hardy, V.E. Iacob, J. Jokinen, V. Kroha, Y.-W. Lui, M. McCleskey, A. Mukhamedzhanov, N. Nica, H.I. Park, B. Roeder, A. Saastamoinen, E. Simmons, G. Tabacaru, Y. Tokimoto, L. Trache, P.J. Woods, and Y. Zhai, *The 10<sup>th</sup> International Symposium on Origin of Matter and Evolution of Galaxies: OMEG-2010, AIP Conference Proceedings* **1289**, 239 (2010).

**Experimental study of  $\beta$ -delayed proton decay of  $^{23}\text{Al}$  for nucleosynthesis in novae**, A. Saastamoinen, L. Trache, A. Banu, M.A. Bentley, T. Davinson, J.C. Hardy, V.E. Iacob, M. McCleskey, B.T. Roeder, E. Simmons, G. Tabacaru, R.E. Tribble, P.J. Woods and J. Äystö, *Phys. Rev. C* **83**, 045808 (2011).

**$Q_{\text{EC}}$  values of the superallowed  $\beta$  emitters  $^{10}\text{C}$ ,  $^{34}\text{Ar}$ ,  $^{39}\text{Ca}$  and  $^{46}\text{V}$** , T. Eronen, D. Gorelov, J. Hakala, J.C. Hardy, A. Jokinen, A. Kankainen, I.D. Moore, H. Penttila, M. Reponen, J. Rissanen, A. Saastamoinen and J. Aysto, *Phys. Rev. C* **83**, 055501 (2011).

**Exotic nuclei and nuclear/particle astrophysics (III). From nuclei to stars**, Proceedings of the 23<sup>rd</sup> Carpathian Summer School of Physics, Sinaia, Romania (June 2010). AIP Conference Proceedings, Vol. **1304** edited by L. Trache, S. Stoica and A. Smirnov (Melville, New York, 2010)

**Studies of astrophysically interesting nucleus Al-23**, A. Saastamoinen, L. Trache, A. Banu *et al.*, Nuclear Physics in Astrophysics IV (NPAIV 2009), J. Phys. Conference Series **202**, Pages (2010).

**First measurement of the O-18(p, alpha)N-15 cross section at astrophysical energies**, M. La Cognata, C. Spitaleri, A.M. Mukhamedzhanov *et al.*, Nuclear Physics in Astrophysics IV (NPAIV 2009), J. Phys. Conference Series **202**, Pages (2010).

**Nuclear reactions with rare isotope beams – experiment**, L. Trache, Exotic Nuclei and Nuclear – Particle Astrophysics III: From Nuclei to Stars, AIP Conference Proceedings **1304**, 32 (2010).

**Astrophysically important reaction rates for novae and x-ray bursts from proton breakup at intermediate energies**, A. Banu, L. Trache, F. Carstoiu *et al.*, Exotic Nuclei and Nuclear – Particle Astrophysics III: From Nuclei to Stars, AIP Conference Proceedings **1304**, 339 (2010).

**Use of neutron transfer reactions to indirectly determine neutron capture cross sections on neutron-rich nuclei**, M. McCleskey, A.M. Mukhamedzhanov, R.E. Tribble *et al.*, Exotic Nuclei and Nuclear – Particle Astrophysics III: From Nuclei to Stars, AIP Conference Proceedings **1304**, 387 (2010).

**$\beta$ -decay of Al-23 and nova nucleosynthesis**, A. Saastamoinen, L. Trache, A. Banu *et al.*, Exotic Nuclei and Nuclear – Particle Astrophysics III: From Nuclei to Stars, AIP Conference Proceedings **1304**, 411 (2010).

**Very low energy protons from the beta decay of proton rich nuclei for nuclear astrophysics**, E. Simmons, L. Trache, A. Banu *et al.*, Exotic Nuclei and Nuclear – Particle Astrophysics III: From Nuclei to Stars, AIP Conference Proceedings **1304**, 415 (2010).

**Indirect approach to the H-2(d,p)H-3 reaction study**, R. Sparta, R.G. Pizzone, C. Spitaleri *et al.*, Exotic Nuclei and Nuclear – Particle Astrophysics III: From Nuclei to Stars, AIP Conference Proceedings **1304**, 420 (2010).

**Measurement of the beta-p emission of Mg-20 and the breakout from the hot CNO cycle**, J.P. Wallace, G. Lotay, P.J. Woods *et al.*, Exotic Nuclei and Nuclear – Particle Astrophysics III: From Nuclei to Stars, AIP Conference Proceedings **1304**, 429 (2010).

**The outreach session. Round table: "Science and society. Do (all) countries need science?!"** L. Trache, Exotic Nuclei and Nuclear – Particle Astrophysics III: From Nuclei to Stars, AIP Conference Proceedings **1304**, 481 (2010).

**Indirect methods for nuclear astrophysics with radioactive nuclear beams**, L. Trache, 5<sup>th</sup> European Summer School on Experimental Nuclear Astrophysics, AIP Conference Proceedings 1213, 125 (2010).

**Use of neutron transfer reactions to indirectly determine neutron capture cross sections on neutron-rich nuclei**, M. McCleskey, A.M. Mukhamedzhanov, R.E. Tribble *et al.*, 5<sup>th</sup> European Summer School on Experimental Nuclear Astrophysics, AIP Conference Proceedings 1213, 225 (2010).

**Very low energy protons from the beta decay of proton rich nuclei for nuclear astrophysics**, E. Simmons, L. Trache, A. Banu *et al.*, 5<sup>th</sup> European Summer School on Experimental Nuclear Astrophysics, AIP Conference Proceedings 1213, 239 (2010).

**The H-2(d,p)H-3 reaction at astrophysical energies studied via the Trojan Horse method and pole approximation validity test**, R. Sparta, R.G. Pizzone, C. Spitaleri *et al.*, 5<sup>th</sup> European Summer School on Experimental Nuclear Astrophysics, AIP Conference Proceedings 1213, 242 (2010).

**Astrophysical reaction rates obtained by indirect techniques**, R.E. Tribble, T. Al-Abdullah, A. Alharbi *et al.*, 10<sup>th</sup> International Symposium on Origin of Matter and Evolution of Galaxies, AIP Conference Proceedings 1269, 239 (2010).

**Elastic and inelastic scattering of 240-MeV <sup>6</sup>Li ions from <sup>40</sup>Ca and <sup>48</sup>Ca and tests of a systematic optical potential**, Krishichayan, X. Chen, Y.-W. Lui, J. Button, and D. H. Youngblood, Phys. Rev. C 81, 044612 (2010).

**First observation of <sup>14</sup>F**, V.Z. Goldberg, B.T. Roeder, G.V. Rogachev, G.G. Chubarian, E.D. Johnson, C. Fu, A.A. Alharbi, M.L. Avila, A. Banu, M. McCleskey, J.P. Mitchell, E. Simmons, G. Tabacaru, L. Trache, and R.E. Tribble, Phys.Lett. B 692, 307 (2010).

**Highly excited alpha-cluster states in <sup>32</sup>S studied with the thick target inverse kinematics method**, M. Norrby, T. Lonroth, V.Z. Goldberg, G.V. Rogachev, M.S. Golovkov, K.-M. Kallman, M. Lattuada S.V. Petrov, S. Romano, B.B. Skorodumov, G.P. Tiourin, W.H. Trzaska, A. Tumino, and A.N. Vorontsov, Eur. Phys. J. A 46, 5 (2010).

**The Texas–Edinburgh–Catania silicon array (TECSA): A detector for nuclear astrophysics and nuclear structure studies with rare isotope beams**, B.T. Roeder, M. McCleskey, L. Trache, A.A. Alharbi, A. Banu, S. Cherubini, T. Davinson, V.Z. Goldberg, M. Gulino, R.G. Pizzone, E. Simmons, R. Sparta, A. Spiridon, C. Spitaleri, J.P. Wallace, R.E. Tribble, and P.J. Woods, Nucl. Instrum. Methods Phys. Res. A 634, 71 (2011).

**Use of neutron transfer reactions to indirectly determine neutron capture cross sections on neutron-rich nuclei**, M. McCleskey, A.M. Mukhamedzhanov, R.E. Tribble, E. Simmons, A. Spiridon, A.

Banu, B. Roeder, V. Goldberg, L. Trache, X.F. Chen, and Y.-W. Lui, Fifth European School on Experimental Nuclear Astrophysics, Santa Tecla, Sicily, (Italy), AIP Conference Proceeding, **1213**, 225 (2010).

**Determination of the axial-vector weak coupling constant with ultracold neutrons**, J. Liu, M.P. Mendenhall, A.T. Holley, H.O. Back, T.J. Bowles, L.J. Broussard, R. Carr, S. Clayton, S. Currie, B.W. Filippone, A. Garcia, P. Geltenbort, K.P. Hickerson, J. Hoagland, G.E. Hogan, B. Hona, T.M. Ito, C.-Y. Liu, M. Makela, R.R. Mammei, J.W. Martin, D. Melconian, C.L. Morris, R.W. Pattie, Jr., A. Perez Galvan, M.L. Pitt, B. Plaster, J.C. Ramsey, R. Rios, R. Russell, A. Saunders, S.J. Seestrom, W.E. Sondheim, E. Tatar, R.B. Vogelaar, B. VornDick, C. Wrede, H. Yan, and A.R. Young (UCNA Collaboration), Phys. Rev. Lett. **105**, 181803 (2010).

**Fragment separator ACCULINNA-2**, S.A. Krupko, A.S. Fomichev, V. Chudoba, A.V. Daniel, M.S. Golovkov, V.A. Gorshkov, L.V. Grigorenko, Yu.Ts. Oganessian, S.I. Sidorchuk, R.S. Slepnev, S.V. Stepantsov, O.B. Tarasov, G.M. TerAkopian, R. Wolski, S.N. Ershov, V.K. Lukyanov, B.V. Danilin, A.A. Korshennikov, V.Z. Goldberg, I.G. Mukha, H. Simon, M. Pfitzner, N.K. Timofeyuk, M.V. Zhukov, K. Lawrie, and R.T. Newman, International Symposium on Exotic Nuclei, Sochi, Russia, AIP Conference Proceeding **1224**, 516 (2010).

**$\gamma$ -ray strength function method and its application to  $^{107}\text{Pd}$** , H. Utsunomiya, S. Goriely, H. Akimune, H. Harada, F. Kitatani, S. Goko, H. Toyokawa, K. Yamada, T. Kondo, O. Itoh, M. Kamata, T. Yamagata, Y.-W. Lui, I. Daoutidis, D. P. Arteaga, S. Hilaire, and A. J. Koning, Phys. Rev. C **82**, 064610 (2010).

**Transverse collective flow and mid-rapidity emission of isotopically identified light charged particles**, Z. Kohley, L.W. May, S. Wuenschel, M. Colonna, M. Di Toro, M. Zielinska-Pfabe, K. Hagel, R. Tripathi, A. Bonasera, G.A. Souliotis, D.V. Shetty, S. Galanopoulos, M. Mehlman, W. B. Smith, S.N. Soisson, B.C. Stein, and S.J. Yennello. Phys. Rev. C **83**, 044601 (2011).

**Investigation of transverse collective flow of intermediate mass fragments**, Z. Kohley, L.W. May, S. Wuenschel, A. Bonasera, K. Hagel, R. Tripathi, R. Wada, G.A. Souliotis, D.V. Shetty, S. Galanopoulos, M. Mehlman, W. B. Smith, S.N. Soisson, B.C. Stein, and S.J. Yennello. Phys. Rev. C **82**, 064601 (2010).

**Measuring the temperature of hot nuclear fragments**, S. Wuenschel, A. Bonasera, L.W. May, G.A. Souliotis, R. Tripathi, S. Galanopoulos, Z. Kohley, K. Hagel, D.V. Shetty, K. Huseman, S.N. Soisson, B.C. Stein, and S.J. Yennello. Nucl. Phys. **A843**, 1, (2010).

**Isoscaling, SMM and the symmetry energy: Connecting the dots**, P. Marini, A. Botvina, A. Bonasera, Z. Kohley, L.W. May, R. Tripathi, S. Wuenschel, S.J. Yennello, AIP Conference Proceeding **1304**, 382 (2010).

**Isoscaling studies in the  $^{86}\text{Kr} + ^{112,124}\text{Sn}, ^{197}\text{Au}$  reactions at beam energy of 30 MeV/u**, R. Tripathi, B.C. Stein, Z. Kohley, L.W. May, P. Marini, A. Bonasera, G.A. Souliotis, S. Wuenschel, S. Galanopoulos, D.V. Shetty, K. Huseman, S.N. Soisson, S.J. Yennello. Proceeding of DAE Symp. on Nucl. Phys. **55**, 484 (2010).

**Penning trap mass spectrometry of neutron-rich Fe and Co isotopes around N=40 with LEBIT**, R. Ferrer, M. Block, C. Bachelet, C. M. Campbell, M. Facina, C. M. Folden III, C. Guénaut, S. Schwarz, B. Barquest, G. Bollen, A. A. Kwiatkowski, D. L. Lincoln, A. M. Prinke, R. Ringle, J. Savory, and P. Schury, D. J. Morrissey and G. K. Pang, Phys. Rev. C **81**, 044318 (2010).

**Power law behavior of the isotope yield distributions in the multifragmentation regime of heavy ion reactions**, M. Huang, R. Wada, Z. Chen, T. Keutgen, S. Kowalski, K. Hagel, M. Barbui, A. Bonasera, C. Bottosso, T. Materna, J. B. Natowitz, L. Qin, M. R. D. Rodrigues, P. K. Sahu, K. J. Schmidt, and J. Wang, Phys. Rev. C **82**, 054602 (2010)

**A new stopping power parameterization for 0.1-15 MeV/nucleon heavy and superheavy ions in solids and gases**, M. Barbui, D. Fabris, M. Lunardon, S. Moretto, G. Nebbia, S. Pesente, G. Viesti, K. Hagel, J. B. Natowitz, R. Wada, Nucl. Instrum. Methods Phys. Res. **B268**, 2377 (2010).

**Symmetry energy of dilute warm nuclear matter**, J.B. Natowitz, G. Ropke, S. Typel, D. Blaschke, A. Bonasera, K. Hagel, T. Klahn, S. Kowalski, L. Qin, S. Shlomo, R. Wada, H.H. Wolter, Phys. Rev. Lett. **104**, 202501 (2010).

**Kaon and pion production in central Au+Au collisions at  $\sqrt{s} = 62.4$  GeV**, I. C. Arsene, I. G. Bearden, D. Beavis, S. Bekele, C. Besliu, B. Budick, H. Bøggild, C. Chasman, C. H. Christensen, P. Christiansen, H. H. Dalgaard, R. Debbé, J. J. Gaardhøje, K. Hagel, H. Ito, A. Jipa, E. B. Johnson, C. E. Jørgensen, R. Karabowicz, N. Katrynska, E. J. Kim, T. M. Larsen, J. H. Lee, G. Løvhøiden, Z. Majka, M. J. Murray, J. Natowitz, B. S. Nielsen, C. Nygaard, D. Pal, A. Qviller, F. Rami, C. Ristea, O. Ristea, D. Röhlich, S. J. Sanders, P. Staszé, T. S. Tveter, F. Videbæk, R. Wada, H. Yang, Z. Yin, and I. S. Zgura, Phys. Lett. B **687**, 36 (2010).

**The isospin dependence of the nuclear equation of state near the critical point**, M. Huang, A. Bonasera, Z. Chen, R. Wada, K. Hagel, J.B. Natowitz, P.K.Sahu, L. Qin, T. Keutgen, S. Kowalski, T. Materna, J. Wang, M.Barbui, C. Bottosso, M. R.D.Rodrigues, Phys. Rev. C **81**, 044618 (2010)

**Secondary neutrons as the main source of neutron-rich fission products in the bombardment of a thick U target by 1 GeV protons**, A.E. Barzakh, G. Lhersonneau, L.Kh. Batist, D.V. Fedorov, V.S. Ivanov, K.A. Mezilev, P.L. Molkanov, F.V. Moroz, S.Yu. Orlov, V.N. Panteleev, Yu.M. Volkov, O. Alyakrinskiy, M. Barbui, L. Stroe and L.B. Tecchio, Eur. Phys. J. A **47**, 70 (2011).

**A novel approach to isoscaling: The role of the order parameter  $m = N-f-Z(f)/A(f)$** , M. Huang, Z. Chen, S. Kowalski *et al.*, Nucl. Phys. **A847**, 233 (2010).

**Isobaric yield ratios and the symmetry energy in heavy-ion reactions near the Fermi energy**, M. Huang, Z. Chen, S. Kowalski *et al.*, Phys. Rev. C **81**, 044620 (2010).

**Experimental investigations of clustering in low density nuclear matter**, J.B. Natowitz, K. Hagel, R. Wada *et al.*, Carpathian Summer School of Physics Conference, in Exotic Nuclei and Nuclear – Particle Astrophysics III: From Nuclei to Stars, AIP Conference Proceedings **1304**, 135 (2010).

**Low density nuclear matter in Fermi energy collisions**, L. Qin, K. Hagel, R. Wada *et al.*, International Workshop on Nuclear Dynamics in Heavy-Ion Reactions and the Symmetry Energy (IWND2009), Int. J. Mod. Phys. E **19**, 1513 (2010).

**The isospin dependence of the nuclear phase transition near the critical point**, Z. Chen, R. Wada, A. Bonasera *et al.*, International Workshop on Nuclear Dynamics in Heavy-Ion reactions and the Symmetry Energy (IWND2009), Int. J. Mod. Phys. E **19**, 1570 (2010).

**Isoscaling and the symmetry energy in the multifragmentation regime of heavy-ion collisions**, Z. chen, S. Kowalski, M. Huang *et al.*, Phys. Rev. C **81**, 064613 (2010).

**Isospin dependence of the nuclear equation of state near the critical point**, M. Hunag, Z. Chen, S. Kowalski *et al.*, Phys. Rev. C **81**, 044620 (2010).

**Isospin- and momentum-dependence effective interactions for the baryon octet and the properties of hybrid stars**, J. Xu, L.W. Chen, C.M. Ko, and B.A. Li, Phys. Rev. C **81**, 055803 (2010).

**Transition density and pressure in hot neutron stars**, J. Xu, L.W. Chen, C.M. Ko, and B.A. Li, Phys. Rev. C **81**, 055805 (2010).

**Density slope of the nuclear symmetry energy from the neutron skin thickness of heavy nuclei**, L. W. Chen, C.M. Ko, B.A. Li, and J. Xu, Phys. Rev. C **82**, 024321 (2010).

**Incompressibility of asymmetric nuclear matter**, L.W. Chen, B.J. Cai, C. Shen, C.M. Ko, J. Xu, and B.A. Li, Int. J. Mod. Phys. E **19**, 1675 (2010).

**Transition density and pressure at the inner edge of neutron star crusts**, J. Xu, C.M. Ko, L.W. Chen, B.A. Li, and H.R. Ma, Int. J. Mod. Phys. E **19**, 1705 (2010).

**Medium effects on charged pion ratio in heavy ion collisions**, C.M. Ko, Y. Oh, and J. Xu, Int. J. Mod. Phys. E **19**, 1763 (2010).

**Density matrix expansion for the isospin- and momentum-dependent MDI interaction**, J. Xu and C.M. Ko, Phys. Rev. C **82**, 044311 (2010).

**J/ψ production and elliptic flow in relativistic heavy ion collisions**, T. Song, C.M. Ko, S.H. Lee, and J. Xu, Phys. Rev. C **83**, 014914 (2010).

**Dilepton production in schematic causal viscous hydrodynamics**, T. Song, K.C. Han, and C.M. Ko, Phys. Rev. C **83**, 024904 (2010).

**Effects of triangular flow on di-hadron azimuthal correlations in relativistic heavy ion collisions**, J. Xu and C.M. Ko, Phys. Rev. C **83**, 021903(R) (2010).

**Pb-Pb collisions at  $\sqrt{s_{NN}}=2.76$  TeV in a multiphase transport model**, J. Xu and C.M. Ko, Phys. Rev. C **83**, 034904 (2010).

**Energy release from hadron-quark phase transition in neutron stars and the axial  $w$  mode of gravitational waves**, W. Lin, B.A. Li, J. Xu, C.M. Ko, and D.H. Wen, Phys. Rev. C **83**, 045802 (2010).

**Identifying multiquark hadrons from heavy ion collisions**, S. Cho, T. Furumoto, T. Hyodo, D. Jido, C.M. Ko, S.H. Lee, M. Nielsen, A. Ohnishi, T. Sekihara, S. Yasui, and K. Yazaki, Phys. Rev. Lett. **106**, 212001 (2011).

**Jet conversion and quark coalescence in relativistic heavy-ion collisions**, C.M. Ko, IL Nuovo Cimento, **34**, 13 (2011).

**Charms in relativistic heavy ion collisions**, C.M. Ko, S.H. Lee, W. Liu, Y. Oh, S. Yasui, and B.W. Zhang, Proceedings of XXVI Max Born Symposium on Strong Interactions, Wroclaw, Poland, July 9-11, 2009, edited by D. Blaschke, K. Redlich, L. Turko, and D. Zablocki, Acta Phys. Polo. B, Proc. Suppl., **3**, 601-610 (2010).

**Charmonium production and elliptic flow in relativistic heavy ion collisions**, C.M. Ko, S.H. Lee, T. Song, and J. Xu, Proceedings of International Workshop on Hot and Cold Baryonic Matter, Budapest, Hungary, August 15-20, 2010, EPJ Web of Conferences **13**, 04001: 1-8 (2011).

**Exotics from Heavy Ion Collisions**, A. Ohnishi, S. Cho, T. Furumoto, T. Hyodo, D. Jido, C.M. Ko, S.H. Lee, M. Nielsen, T. Sekihara, S. Yasui, and K. Yazaki, Proceedings of International Conference on Structure of Baryons, Osaka, Japan, December 7-11 (2010).

**Astrophysical  $S$  factor for the  $^{15}\text{N}(p,\gamma)^{16}\text{O}$  reaction**, A.M. Mukhamedzhanov, M. La Cognata, and V. Kroha, Phys. Rev. C **83**, 044604 (2011).

**Solar fusion cross sections. II. The pp chain and CNO cycles**, E.G. Adelberger, A. Garcí'a, R.G. Hamish Robertson, and K.A. Snover, A.B. Balantekin, K. Heeger, and M.J. Ramsey-Musolf, D. Bemmerer and A. Junghans, C.A. Bertulani, J.-W. Chen, H. Costantini and P. Prati, M. Couder, E. Uberseder, and M. Wiescher, R. Cyburt, B. Davids, S. J. Freedman, M. Gai, D. Gazit, L. Gialanella and G. Imbriani, U. Greife, M. Hass, W.C. Haxton, T. Itahashi, K. Kubodera, K. Langanke, D. Leitner, M. Leitner, P. Vetter, and L. Winslow, L.E. Marcucci, T. Motobayashi, A. Mukhamedzhanov R.E. Tribble, Kenneth M. Nollett, F.M. Nunes, T.-S. Park, P.D. Parker, R. Schiavilla, E.C. Simpson, C. Spitaleri, F. Strieder and H.-P. Trautvetter, K. Suemmerer, and S. Typel, *Rev. Mod. Phys.* **83**, 195 (2011).

**Distortion effects on Trojan Horse applications**, R.G. Pizzone, C. Spitaleri, A.M. Mukhamedzhanov, L.D. Blokhintsev, C.A. Bertulani, B.F. Irgaziev, M. La Cognata, L. Lamia and S. Romano, *Few-Body Systems* **50**, 319 (2011).

**Indirect measurement of  $^{17}\text{O}(p,\alpha)^{14}\text{N}$  cross section at ultra-low energies**, M. L. Sergi, C. Spitaleri A. Coc, A. Mukhamedzhanov, V. Burjan, S. Cherubini, V. Crucill'a, M. Gulino, F. Hammache, Z. Hons, B. Irgaziev, G. Kiss, V. Kroha, M. La Cognata, L. Lamia, R.G. Pizzone, S.M.R. Puglia, G.G. Rapisarda, S. Romano, N. de Sereville, E. Somorjai, S. Tudisco and A. Tumino, *J. Phys: Conference Series* **202**, 012021 (2010).

**Study of the  $^6\text{Li}(n, \alpha)^3\text{H}$  reaction via the  $^2\text{H}$  quasi-free break-up**, M. Gulino, C. Spitaleri, S. Cherubini, V. Crucillà, M. La Cognata, L. Lamia, R.G. Pizzone, S. Romano, M.L. Sergi, A. Tumino, Li Chengbo, Z. Elekes, E. Somorjai, V. Burjan, V. Kroha and A Mukhamedzhanov, *J. Phys. G* **37**, 125105 (2010).

**Effect of high-energy resonances on the  $^{18}\text{O}(p, \alpha)^{15}\text{N}$  reaction rate at AGB and post-AGB relevant temperatures**, M. La Cognata, C. Spitaleri and A. M. Mukhamedzhanov, *Astrophys. J.* **723**, 1512 (2010).

**Recent studies on Trojan Horse method**, Silvio Cherubinia, Claudio Spitaleri, Marisa Gulino, Marco La Cognata, Rosario G. Pizzone, Livio Lamia, Giuseppe G. Rapisarda, Stefano Romano, Letizia Sergi, Akram Mukhamedzhanov, Livius Trache, R.E. Tribble, Shigeru Kubono, Hidetoshi Yamaguchi, and Aurora Tumino, *Acta Phys. Polonica B* **42**, 769 (2011).

**Unitary correlation in nuclear reaction theory: Separation of nuclear reactions and spectroscopic factor**, A.M. Mukhamedzhanov and A.S. Kadyrov, *Phys. Rev. C* **82**, 051601(R) (2010).

**Excitation of compound states in the subsystems as indirect tool in nuclear astrophysics**, A.M. Mukhamedzhanov, M. La Cognata, C. Spitaleri, and R. E. Tribble, *Eur. J. Phys. Web of Conferences* **2**, 13001 (2010).

**Asymptotic normalization coefficient and important astrophysical process  $^{15}\text{N}(p, \gamma)^{16}\text{O}$** , A.M. Mukhamedzhanov, A. Banu, P. Bem, V. Burjan, C.A. Gagliardi, V.Z. Goldberg, Z. Hons, V. Kroha, M. La Cognata, S. Piskor, R.G. Pizzone, S. Romano, E. Simeckova, C. Spitaleri, L. Trache and R.E. Tribble, *J. Phys. Conference Series* **202**, 012017 (2010).

**Indirect study of the  $^2\text{H}(d,p)^3\text{H}$  and  $^2\text{H}(d,n)^3\text{He}$  reactions at astrophysical energies via the Trojan Horse method**, A. Tumino, C. Spitaleri, A.M. Mukhamedzhanov, S. Typel, M. Aliotta, V. Burjan, M. Gimenez del Santo, G.G. Kiss, V. Kroha and Z. Hons, *Few-Body Systems* **50**, 323 (2011),

**Improved results on the extraction of  $^{11}\text{B}(p,\alpha)^8\text{Be}$  S(E)-factor via the Trojan Horse method**, L. Lamia, C. Spitaleri, S. Romano, N. Carlin, S. Cherubini, Cheng-Bo Li, V. Crucillà, M.G. Del Santo, M. Gulino, G.G. Kiss, V. Kroha, S. Kubono, M. La Cognata, A.M. Mukhamedzhanov, R.G. Pizzone, S.M.R. Puglia, Qun-Gang Wen, G.G. Rapisarda, M.L. Sergi, Shu-Hua Zhou, E. Somorjai, F. Souza, A. Szanto de Toledo, G. Tabacaru, S. Tudisco, A. Tumino, Y. Wakabayashi, H. Yamaguchi, *Memorie della Società Astronomica Italiana Supplement*, **14**, 39 (2010).

**DWBA momentum distribution and its effect on THM**, M. La Cognata, C. Spitaleri, A. Mukhamedzhanov, V. Goldberg, B. Irgaziev, L. Lamia, R.G. Pizzone, M.L. Sergi and R.E. Tribble, *Nucl. Phys.* **A834**, 658c (2010),

**Damping effects on centroid energies of isoscalar compression modes**, D.C. Fuls, V.M. Kolomietz, S.V. Lukanov, and S. Shlomo, *EPL* **90**, 20006 (2010).

**Symmetry energy of dilute warm nuclear matter**, J.B. Natowitz, G. Ropke, S. Typel, D. Blaschke, A. Bonasera, K. Hagel, T. Klahn, S. Kowalski, L. Qin, S. Shlomo, R. Wada, and H.H. Walter, *Phys. Rev. Lett.* **104**, 202501 (2010).

**Modern energy density functional for properties of nuclei and the nuclear matter equation of state**, S. Shlomo, *Phys. At. Nucl.* **73**, 1390 (2010).

**Freeze-out properties of hot nuclear matter created in heavy-ion collisions**, S. Shlomo, *Nucl. Phys. At. Energy* **4(11)**, 347 (2010).

**Event-by-event jet quenching**, Ricardo Rodriguez, Rainer J. Fries, and Enrique Ramirez, *Phys. Lett. B* **693**, 108 (2010).

**Scaling of elliptic flow, recombination and sequential freeze-out of hadrons in heavy-ion collisions**, Min He, Rainer J. Fries, and Ralf Rapp, *Phys. Rev. C* **82**, 034907 (2010).

**Event-by-event jet quenching and higher fourier moments of hard probes**, Rainer J. Fries and Ricardo Rodriguez, *Nucl. Phys.* **A855**, 424 (2011).

**High energy nuclear collisions: Theory overview**, Rainer J. Fries, *Pramana* **75**, 235 (2010).

**Quark recombination in heavy ion collisions**, Rainer J. Fries, PoS, Workshop on Critical Examination of RHIC Paradigms (CERP2010), Austin, Texas, April 2010.

**The A(1)(1260) as a rho-pi resonance in nuclear matter**, D. Cabrera, D. Jido, R. Rapp, and L. Roca, *Prog. Theor. Phys.* **123** (2010) 719-742.

**Charmonium and bottomonium in heavy-ion collisions**, R. Rapp, D. Blaschke and P. Crochet, *Prog. Part. Nucl. Phys.* **65**, 209 (2010).

**Medium modifications of the rho meson in nuclear photoproduction**, F. Riek, R. Rapp, T.-S. H. Lee, and Y. Oh, *Phys. Rev. C* **82**, 015202 (2010).

**Quarkonia and heavy-quark relaxation times in the quark-gluon Pplasma**, F. Riek and R. Rapp, *Phys. Rev. C* **82**, 035201 (2010).

**Charmonium in medium: from correlators to experiment**, X. Zhao and R. Rapp, *Phys. Rev. C* **82**, 064905 (2010).

**The CBM physics book: compressed baryonic matter in laboratory experiments**, B. Friman, C. Höhne, J. Knoll, S. Leupold, J. Randrup, R. Rapp and P. Senger (editors), *Lect. Notes Phys.* **814**, 1 (2011).

**In-medium vector mesons, dileptons and chiral restoration**, R. Rapp, *AIP Conf. Proc.* **1322**, 55 (2010).

**Axialvector resonance in nuclear matter**, D. Cabrera, D. Jido, R. Rapp and L. Roca, *AIP Conf. Proc.* **1322**, 90 (2010).

**Scaling properties at freeze-out in relativistic heavy-ion collisions**, M.M. Aggarwal *et al.* (STAR Collaboration), *Phys. Rev. C* **83**, 034910 (2011).

**Strange and multi-strange particle production in Au+Au collisions at  $\sqrt{s_{NN}} = 62.4$  GeV**, M.M. Aggarwal *et al.* (STAR Collaboration), *Phys. Rev. C* **83**, 024901 (2011).

**Measurement of the parity-violating longitudinal single-spin asymmetry for the  $W^\pm$  boson production in polarized proton-proton collisions at  $\sqrt{s_{NN}} = 500$  GeV**, M.M. Aggarwal *et al.* (STAR Collaboration), *Phys. Rev. Lett.* **106**, 062002 (2011).

**New experimental constraints for the standard model from muon decay**, R. Bayes, J.F. Bueno, A. Hillairet, Yu.I. Davydov, P. Depommier, W. Faszler, C.A. Gagliardi, A. Gaponenko, D.R. Gill, A. Grossheim, P. Gumplinger, M.D. Hasinoff, R.S. Henderson, J. Hu, D.D. Koetke, R.P. McDonald, G.M. Marshall, E.L. Mathie, R.E. Mischke, K. Olchanski, A. Olin, R. Openshaw, J.-M. Poutissou, R. Poutissou, V. Selivanov, G. Sheffer, B. Shin, T.D.S. Stanislaus, R. Tacik, R.E. Tribble, *Phys. Rev. Lett.* **106**, 041804 (2011).

**Measurement of the bottom contribution to non-photon electron production in p+p collisions at  $\sqrt{s_{NN}} = 200$  GeV**, M.M. Aggarwal *et al.* (STAR Collaboration), *Phys. Rev. Lett.* **105**, 202301 (2010).

**Parton energy loss in heavy-ion collisions via direct-photon and charged-particle azimuthal correlations**, B.I. Abelev *et al.* (STAR Collaboration), *Phys. Rev. C* **82**, 034909 (2010).

**Balance functions from Au+Au, d+Au and p+p collisions at  $\sqrt{s_{NN}} = 200$  GeV**, M.M. Aggarwal *et al.* (STAR Collaboration), *Phys. Rev. C* **82**, 024905 (2010).

**Azimuthal di-hadron correlations in d+Au and Au+Au collisions at  $\sqrt{s_{NN}} = 200$  GeV measured at the STAR detector**, M.M. Aggarwal *et al.* (STAR Collaboration), *Phys. Rev. C* **82**, 024912 (2010).

**Upsilon cross section in p+p collisions at  $\sqrt{s_{NN}} = 200$  GeV**, B.I. Abelev *et al.* (STAR Collaboration), *Phys. Rev. D* **82**, 012004 (2010).

**Higher moments of net-proton multiplicity distributions at RHIC**, M.M. Aggarwal *et al.* (STAR Collaboration), *Phys. Rev. Lett.* **105**, 022302 (2010).

**Three-particle coincidence of the long range pseudorapidity correlation in high energy nucleus-nucleus collisions**, B.I. Abelev *et al.* (STAR Collaboration), *Phys. Rev. Lett.* **105**, 022301 (2010).

**Inclusive  $\pi^0$ ,  $\eta$ , and direct photon production in p+p and d+Au collisions at  $\sqrt{s_{NN}} = 200$  GeV**, B.I. Abelev *et al.* (STAR Collaboration), *Phys. Rev. C* **81**, 064904 (2010).

**Longitudinal scaling property of the charge balance function in Au+Au collisions at 200 GeV**, B.I. Abelev *et al.* (STAR Collaboration), *Phys. Lett. B* **690**, 239 (2010).

**Observation of charge-dependent azimuthal correlations and possible local strong parity violation in heavy ion collisions**, B.I. Abelev *et al.* (STAR Collaboration), *Phys. Rev. C* **81**, 054908 (2010).

**Solar fusion cross sections II: The pp chain and CNO cycles**, E.G. Adelberger, A. Garcia, R.G. Hamish Robertson, K.A. Snover, A.B. Balantekin, K. Heeger, M.J. Ramsey-Musolf, D. Bemmerer, A. Junghans, C.A. Bertulani, J.-W. Chen, H. Costantini, D. Prati, M. Couder, E. Uberseder, M. Wiescher, R. Cyburt, B. Davids, S.J. Freedman, M. Gai, D. Gazit, L. Gialanella, G. Imbriani, U. Griefe, M. Hass, W.C.

Haxton, T. Itahashi, K. Kubodera, K. Langanke, D. Leitner, M. Leitner, P. Vetter, L. Winslow, L.E. Marcucci, T. Motobayashi, A. Mukhamedznahov, R.E. Tribble, K.M. Nollet, F.M. Nunes, T.-S.Park, P.D. Parker, R. Schiavilla, E.C. Simpson, C. Spitaleri, F. Strieder, H.-P. Trautvetter, K. Suemmerer, S. Typel, *Rev. Mod. Phys.* **83**, 195 (2011).

**Identified high  $p_T$  spectra in Cu+Cu collisions at  $\sqrt{s_{NN}} = 200$  GeV**, B.I. Abelev *et al.* (STAR Collaboration), *Phys. Rev. C* **81**, 054907 (2010).

**Charged and strange hadron elliptic flow in Cu+Cu collisions at  $\sqrt{s_{NN}} = 62.4$  and 200 GeV**, B.I. Abelev *et al.* (STAR Collaboration), *Phys. Rev. C* **81**, 044902 (2010).

**Observation of  $\pi^+\pi^-\pi^+\pi^-$  photoproduction in ultra-peripheral heavy ion collisions at  $\sqrt{s_{NN}} = 200$  GeV at the STAR detector**, B.I. Abelev *et al.* (STAR Collaboration), *Phys. Rev. C* **81**, 044901 (2010).

**Identified charged hadron production in p+p collisions at  $\sqrt{s_{NN}} = 62.4$  and 200 GeV**, A. Adare *et al.* (PHENIX Collaboration), *Phys. Rev. C* **83**, 064903 (2011).

**High  $p_T$  non-photonic electron production in p+p collisions at  $\sqrt{s_{NN}} = 200$  GeV**, H. Agakishiev *et al.* (STAR Collaboration), *Phys. Rev. D* **83**, 052006 (2011).

**Studies of di-jet survival and surface emission bias in Au+Au collisions via angular correlations with respect to back-to-back leading hadrons**, H. Agakishiev *et al.* (STAR Collaboration), *Phys. Rev. C* **83**, 061901 (2011).

**Measurement of neutral mesons in p+p collisions at  $\sqrt{s_{NN}} = 200$  GeV and scaling properties of hadron production**, A. Adare *et al.* (PHENIX Collaboration), *Phys. Rev. D* **83**, 052004 (2011).

**Cross section and double helicity asymmetry for  $\eta$  mesons and their comparison to neutral pion production in p+p collisions at  $\sqrt{s_{NN}}=200$  GeV**, A. Adare *et al.* (PHENIX Collaboration), *Phys. Rev. D* **83**, 032001 (2011).

**Nuclear modification factors of phi mesons in d+Au, Cu+Cu and Au+Au collisions at  $\sqrt{s_{NN}}=200$  GeV**, A. Adare *et al.* (PHENIX Collaboration), *Phys. Rev. C* **83**, 024909 (2011).

**High  $p_T$  direct photon and  $\pi^0$  triggered azimuthal jet correlations and measurement of  $k_T$  for isolated direct photons in p+p collisions at  $\sqrt{s_{NN}}=200$  GeV**, A. Adare *et al.* (PHENIX Collaboration), *Phys. Rev. D* **82**, 072001 (2010).

# **SECTION VII**

## **APPENDIX**

## TALKS PRESENTED

April 1, 2010 – March 31, 2011

*Testing CVC and CKM unitarity via superallowed nuclear beta decay*, J.C. Hardy and I.S. Towner, **J.C. Hardy, Invited talk**, LX International Conference on Nuclear Physics “Nucleus 2010,” St Petersburg, Russia (July 2010).

*Are beta-decay half-lives affected by external conditions?* **J.C. Hardy, Invited talk**, 21<sup>st</sup> International Conference on the Application of Accelerators in Research and Industry “CAARI 2010”, Fort Worth, Texas (August 2010).

*$V_{ud}$  from nuclear decays*, I.S. Towner and J.C. Hardy, **I.S. Towner, Invited talk**, 6th International Workshop on the CKM Unitarity Triangle, CKM2010, Warwick, United Kingdom (September 2010).

*Precise Superallowed  $\beta$ -decay Measurements (the cases of  $^{26}\text{Si}$ , and  $^{34}\text{Ar}$ )*, V.E. Iacob, J.C. Hardy, A. Banu, L. Chen, V.V. Golovko, J. Goodwin, V. Horvat, N. Nica, H.I. Park, L. Trache and R.E. Tribble, **V.E. Iacob, Invited talk**, Carpathian Summer School of Physics 2010: exotic nuclei and nuclear/particle astrophysics (III), Sinaia, Romania (June 2010).

*Further test of internal-conversion with a measurement in  $^{197}\text{Pt}$* , **N. Nica**, Third Workshop for Radioactive Decay Data Evaluators at LMRI-CIEMAT, Madrid, Spain (June 2010).

*$\beta$ -decay of  $^{23}\text{Al}$  and nova nucleosynthesis*, **A. Saastamoinen**, L. Trache, A. Banu, M. A. Bentley, T. Davinson, J. C. Hardy, V. E. Iacob, D. G. Jenkins, A. Jokinen, M. McCleskey, B. Roeder, E. Simmons, G. Tabacaru, R. E. Tribble, P. J. Woods, and J. Äystö, Carpathian Summer School of Physics 2010: exotic nuclei and nuclear/particle astrophysics (III), Sinaia, Romania (June 2010).

*Further test of internal-conversion with a measurement in  $^{119}\text{Sn}$* , **N. Nica**, Nuclear Data Week at Santa Fe, Santa Fe, New Mexico, (November 2010).

*Precise half-life measurement of  $^{46}\text{V}$* , **H.I. Park**, J.C. Hardy, V.E. Iacob, L. Chen, J. Goodwin, N. Nica, E. Simmons, L. Trache and R.E. Tribble, APS Meeting, Santa Fe, New Mexico (November 2010).

*Do radioactive half-lives depend on the earth-sun distance?* **J. Goodwin**, J.C. Hardy, V.E. Iacob and V.V. Golovko, APS Meeting, Santa Fe, New Mexico (November 2010).

*Current Topics in Nuclear Astrophysics*, **R.E. Tribble, Invited Plenary Talk**, XLIX International Winter Meeting on Nuclear Physics, Bormio, Italy (January, 2011).

*Development of New Techniques to Determine Neutron-induced Reaction Rates*, **R.E. Tribble, Invited Talk**, 2011 Stewardship Science Academic (SSAA) Symposium, Washington, D.C. (February 2011).

*Astrophysical reaction rates that are important for  $^{18}\text{F}$  and  $^{22}\text{Na}$  in stellar explosions*, **R.E. Tribble, Invited Talk**, Astronomy with Radioactivities VII, Phillip Island, Victoria, Australia (March 2011).

*Perspectives on the 2007 Long Range Plan for U.S. Nuclear Science*, **R.E. Tribble, Invited Presentation**, National Research Council committee to assess the status of the U.S. nuclear physics program (May 2010).

*Low Energy Tests of the Electroweak Standard Model*, **R.E. Tribble**, **Invited Talk**, Symposium on Nucleon Structure and Electroweak Precision Tests: Past and Future, University of Illinois (May 2010).

*Asymptotic Normalization Coefficients: an Indirect Method for Nuclear Astrophysics*, **R.E. Tribble**, **Invited Talk**, Carpathian Summer School, Sinaia, Romani (June 2010).

*Science and Technology to Strengthen National Competitiveness*, **R.E. Tribble**, **Invited Talk**, Carpathian Summer School, Sinaia, Romania (June 2010).

*Connections Between Stellar Evolution and Nuclear Physics*, **R.E. Tribble**, Colloquium, Texas A&M Commerce, Commerce, Texas (September 2010).

*Connections Between Stellar Evolution and Nuclear Physics*, **R.E. Tribble**, Colloquium, Ohio University, Athens, Ohio (October 2010).

*Exploring the Proton Spin with STAR*, **C.A. Gagliardi**, **Colloquium**, Physics Dept., University of Houston, Houston, Texas (March 2011).

*Exploring the Proton Spin with STAR*, **C.A. Gagliardi**, **Colloquium**, Physics Dept., Yale University, New Haven, Connecticut (February 2011).

*Gluon Polarization Measurements with STAR*, **C.A. Gagliardi**, **Invited Talk** (for the STAR Collaboration), 2<sup>nd</sup> Summer Prog. Nucl. Spin Physics, Brookhaven, New York (July 2010).

*Decay Spectroscopy for H-burning Reactions in Novae and XRB*, **L. Trache**, **Invited Talk**, CEA, Service Physique Nucleaire, Saclay, France (June 2010).

*Nuclear Reactions with Rare Isotope Beams – Experiment*, **L. Trache**, **Invited Lecture**, 23<sup>rd</sup> Carpathian Summer School of Physics, Sinaia, Romania (June 2010).

*Decay Spectroscopy for Nuclear Astrophysics. H-burning reactions in Novae and XRB Studied with  $\beta$ - and  $\beta$ -delayed Proton-decay*, **L. Trache**, **Invited Lecture**, the Pan-American Study Institute PASI2010, Joao Pessoa, Brazil (August 2010).

*ANCs from Nuclear Breakup for Nuclear Astrophysics*, **L. Trache**, the SAMURAI International Workshop 2011, RIKEN Nishina Center for Accelerator Based Science, Wako-shi, Japan (March 2011).

*The TECSA Commissioning Run*, **B.T. Roeder**, APS DNP Meeting, Santa Fe, New Mexico (November 2010).

*Simulations for the Samurai-Si Silicon Detectors*, **B.T. Roeder**, the SAMURAI International Workshop 2011, RIKEN Nishina Center for Accelerator Based Science, Wako-shi, Japan (March 2011).

*Mysteries of GMR Strengths in  $A \sim 90$  Region*, **Krishichavan**, D.H. Youngblood, Y.-W. Lui, and J. Button, APS DNP Meeting, Santa Fe, New Mexico (November 2010).

*Precision  $\beta$ -decay Studies Using Neutral Atom Traps*, **D. Melconian**, **Invited Talk**, International Conference on Nuclear Physics, Saint Petersburg, Russia (July 2010).

*The  $\beta^+$  Decay of  $^{37}\text{K}$  as a Multi-faceted Probe of Fundamental Physics*, **D. Melconian**, **Invited Talk**, the 2<sup>nd</sup> International Ulaanbaatar Conference on Nuclear Physics and Applications, Ulaanbaatar, Mongolia (July 2010).

*Experimental Status of  $V_{ud}$  and Near-Term Future Prospects*, **D. Melconian**, **Invited Talk**, 6<sup>th</sup> International Workshop on the CKM Unitarity Triangle, Warwick, United Kingdom (September 2010).

*Correlation Measurements in Nuclear  $\beta$  Decays*, **D. Melconian**, **Invited Talk**, Violations of discrete Symmetries in Atoms and Nuclei, Trento, Italy (November 2010).

*A new Research Program for Medical Radioisotope Production at the Texas A&M University*, **A. A. Alharbi**, 240<sup>th</sup> ACS meeting, Boston, Massachusetts (August 2011).

*Gluon polarization and jet production at STAR*, **Pibero Djawotho**, Seminar, Department of Physics and Astronomy, Stony Brook University, Stony Brook, New York (February 2011).

*$\pi^0$ -Charged Particle Correlations at  $2.5 < \eta < 4.0$  from  $p+p$  Collisions at  $s = 200 \text{ GeV}$* , **J.L. Drachenberg** (for the STAR Collaboration), 2010 APS DNP Meeting, Santa Fe, New Mexico (November 2010).

*New Trigger Logic for the Forward Meson Spectrometer*, **J.C. Martinez** (for the STAR Collaboration), 2010 APS DNP Meeting, Santa Fe, New Mexico (November 2010).

*Gluon Polarization and Jet Production at STAR*, **P. Djawotho** (for the STAR Collaboration), 19<sup>th</sup> International Spin Physics Symposium, Juelich, Germany (September 2010).

*Upsilon Production in STAR*, **P. Djawotho**, **Invited Talk** (for the STAR Collaboration), International Workshop on Heavy Quarkonium, Fermilab, Batavia, Illinois (May 2010).

*Gamma-jet Correlation and Parton Energy Loss in QCD Medium*, **Ahmed Hamed**, The Lake Louise Winter Institute 2010, Alberta, Canada (February 2011).

*Azimuthal Distributions of High- $p_T$   $\gamma$  and  $\pi^0$  with Respect to the Reaction Plane*, **Ahmed Hamed**, Hot Quarks 2010 Workshop, La-Londe-les-Maures, Cote d'Azur, France (June 2010).

*Azimuthal Correlations of Direct  $\gamma$  and  $\pi^0$  with Charged hadrons at STAR*, **Ahmed Hamed**, 2010 RHIC/AGS Annual User's Meeting, Brookhaven National Laboratory, Upton, New York (June 2010).

*Experimental Review of High- $p_T$  Phenomena at Mid-Rapidity at RHIC*, **Ahmed Hamed**, Workshop on Critical Examination of RHIC Paradigms, University of Texas, Austin, Texas (April 2010).

*Upsilon Production and Upsilon-Hadron Correlations*, **Matthew Cervantes**, 2011 Winter Workshop on Nuclear Dynamics, Winter Park, Colorado (February 2011).

*Clustered Low Density Nuclear Matter in Near Fermi Energy Collisions*, **J.B. Natowitz**, **Invited Talk**, 2<sup>nd</sup> Workshop on State of the Art in Nuclear Cluster Physics, MAY 25-28, 2010 University of Libre Brussels, Brussels, Belgium (May 2010).

*Experimental Investigations of Clustering in Low Density Nuclear Matter*, **J.B. Natowitz**, **Invited Talk**, Carpathian Summer School of Physics Conference, Sinaia, Romania (June 2010).

*Clustering in Low Density Nuclear Matter*, **J.B. Natowitz**, **Invited Talk**, 241<sup>st</sup> ACS Meeting, Seaborg Award Symposium, Anaheim, California (March 2011).

*Strangelets – Status Quo*, **Katarzyna Schmidt**, Department of Chemistry, Texas A&M University, College Station, Texas (February 2011).

*Isotopic Effects in Nuclear Reactions and the Symmetry Energy at Sub-saturation Densities*, **S.J. Yennello**, **Invited Talk**, International Workshop on Nuclear Symmetry Energy at Medium Energies (ASY-EOS 2010), Noto, Italy (May 2010).

*Investigation of the Symmetry Energy from the Transverse Collective Flow of Intermediate Mass Fragments*, **S.J. Yennello**, **Invited Talk**, International Nuclear Physics Conference, Vancouver, Canada (July 2010).

*Investigation of the Symmetry Energy from Measurements of Transverse Collective Flow*, **S.J. Yennello**, **Invited Talk**, International Symposium on Nuclear Symmetry Energy (NuSYM10), RIKEN, Wako, Japan (July 2010).

*Investigating the Symmetry Energy of Nuclear Matter with Heavy-ion Reactions*, **S.J. Yennello**, **Invited Talk**, XXXIV Symposium on Nuclear Physics, Cocoyoc, Morelos, Mexico (January 2011).

*Investigating the Symmetry Energy of the Nuclear Equation of State*, **S.J. Yennello**, **Invited Talk**, 241<sup>st</sup> ACS Meeting, Anaheim, California (March 2011).

*How Cutting Edge Science Can Prepare a Diverse Technical Workforce for the Future*, **S.J. Yennello**, **Invited Talk**, 241<sup>st</sup> ACS Meeting, Anaheim, California (March 2011).

*Le Chatelier's Principle Meets the Extra Dimensions of M-theory*, **S.J. Yennello**, **Invited Talk**, 241<sup>st</sup> ACS Meeting, Anaheim, California (March 2011).

*Elucidating the Symmetry Energy of Nuclear Matter with Heavy-ion Reactions*, **S.J. Yennello**, **Invited Talk**, 2010 APS DNP Meeting, Santa Fe, New Mexico (November 2010).

*Student Career Panel*, **S.J. Yennello**, 241<sup>st</sup> ACS Meeting, Anaheim, California (March 2011).

*Fragment Flows and Cluster*, **Z. Kohley**, 2<sup>nd</sup> International Symposium on Nuclear Symmetry Energy, Northampton, Massachusetts (June, 2010).

*Fragment Flows and Midrapidity Emission*, **Z. Kohley**, Gordon Research Conference (June 2010).

*Fragment Flows in the Fermi Energy Regime and Near-Barrier Fusion with Radioactive Ion Beams*, **Z. Kohley**, National Superconducting Cyclotron Laboratory, Michigan State University, East Lansing, Michigan (April 2010).

*Transverse Collective Flow of Light Charged Particles and Intermediate Mass Fragments in the Fermi Energy Regime*, **Z. Kohley**, Oak Ridge National Laboratory, Oak Ridge, Tennessee (May 2010).

*Observation of Critical Behavior from Nuclear Fragment Yield Ratios*, **R. Tripathi**, A. Bonasera, S. Wuenschel, L. W. May, Z. Kohley, G. A. Souliotis, S. Galanopoulos, K. Hagel, D. V. Shetty, K. Huseman, S. N. Soisson, B. C. Stein, and S. J. Yennello, International Nuclear Physics Conference, Vancouver, Canada (July 2010).

*Isoscaling, SMM and the Symmetry Energy: Connecting the Dots*, **Paola Marini**, International Workshop on Nuclear Symmetry Energy at Medium Energies (ASY-EOS 2010), Noto, Italy (May 2010).

*Isoscaling, SMM and the Symmetry Energy: Connecting the Dots*, **Paola Marini**, Exotic Nuclei and Nuclear/Particle Astrophysics (III): From Nuclei to Stars - Carpathian Summer School of Physics, Sinaia, Romania (June 2010).

*Constraining the Symmetry Term in the Nuclear Equation of State at Sub-Saturation Densities and Finite Temperatures*, **Paola Marini**, ACS Meeting, Anaheim, California (March 2011).

*Dissociation of CO Molecular Ions Produced in Collisions with 2.5 MeV/u Xe<sup>34+</sup>*, **V. Horvat**, 41<sup>st</sup> Annual Meeting of the APS Division of Atomic, Molecular and Optical Physics, Houston Texas (May 2010).

*Heavy Element Chemistry at Texas A&M University*, **C.M. Folden III**, 241<sup>st</sup> American Chemical Society National Meeting, Anaheim, California (March 2011).

*New Gas Stopper for Heavy Element Chemistry Research at the Texas A&M Cyclotron Institute*, **M. C. Alfonso**, 241<sup>st</sup> American Chemical Society National Meeting, Anaheim, California (March 2011).

*Future Heavy Element Plans at Texas A&M University*, **C. M. Folden III**, **Invited Talk**, Workshop on Future Directions in Heavy Element Science, Berkeley, California, (December 2010).

*Master's-Level Certificate Program in Nuclear Forensics at Texas A&M University*, **C. M. Folden III**, 240<sup>th</sup> American Chemical Society National Meeting, Boston, Massachusetts (August 2010).

*Development of a Gas Stopping Cell for Heavy Element Chemistry Research at the Texas A&M Cyclotron Institute*, **M. C. Alfonso**, 240<sup>th</sup> American Chemical Society National Meeting, Boston, Massachusetts, (August 2010).

*Strings, Jets and Quark Coalescence in Transport Models*, **C.M. Ko**, **Invited talk**, International Workshop on Critical Examination of RHIC Paradigms, Austin, Texas (April 2010).

*Overview of Relativistic Heavy Ion Collisions*, **C.M. Ko**, **Invited talk**, International Workshop on Exotics in Heavy Ion Collisions, Kyoto, Japan (May 2010).

*Exotic Hadrons from Heavy Ion Collisions*, **C.M. Ko**, **Invited talk**, International Mini-Symposium on Exotics in Heavy Ion Collisions, Kyoto, Japan (May 2010).

*Charmonium Production and Elliptic Flow in Relativistic Heavy Ion Collisions*, **C.M. Ko**, **Invited talk**, International Workshop on Hot and Cold Baryonic Matter, Budapest, Hungary (August 2010).

*Identified Hadrons of Intermediate and High Transverse Momenta in Relativistic Heavy Ion Collisions*, **C.M. Ko**, **Invited talk**, International Workshop on Interplay between Soft and Hard Interactions in Particle Production at Ultra-Relativistic Energies, Catania, Italy (September 2010).

*Triangular Flow in Relativistic Heavy Ion Collisions*, **C.M. Ko**, **Invited talk**, International Workshop on In-Medium Effects in Hadronic and Partonic Systems, Obergurgl, Austria (February 2011).

*Particle production in heavy ion collisions*, **C.M. Ko, Colloquium**, Institute for Theoretical Physics, University of Frankfurt, Frankfurt, Germany (October 2010).

*Probing the high density matter in heavy ion collisions*, **C.M. Ko, Colloquium**, Department of Physics and Astronomy, Texas A&M University at Commerce, Commerce, Texas (March 2011).

*Astrophysical Factors for  $^{15}\text{N}(p,\gamma)^{16}\text{O}$  and  $^4\text{He}(d,\gamma)^6\text{Li}$  - Lessons from Recent Experiments by Notre Dame-LUNA and GSI*, **A.M. Mukhamedzhanov, Invited Talk**, Lawrence Livermore National Laboratory, Livermore, California (February 2011).

*The Combined Method for Transfer Reactions*, **A.M. Mukhamedzhanov, Invited Talk**, ECT\* Workshop on Reactions and Nucleon Properties in Rare Isotopes, Trento, Italy (April 2010).

*Comparison of the Direct and Indirect Techniques for Some CNO Cycle Reactions*, **A.M. Mukhamedzhanov, Invited Talk**, ATOMKI, Debrecen, Hungary (May 2010).

*Interaction of Mini-black Holes with Nucleons*, **A.M. Mukhamedzhanov, Invited Talk**, Surrey University, Guilford, United Kingdom (June 2010).

*Unitary Correlations in Nuclear Reaction Theory: Separation of Nuclear Reactions and Spectroscopic Factors*, **A.M. Mukhamedzhanov, Invited Talk**, ATOMKI, Debrecen, Hungary (September 2010).

*Unitary Correlations in Nuclear Reaction Theory: Separation of Nuclear Reactions and Spectroscopic Factors*, **A.M. Mukhamedzhanov, Invited Talk**, ECT\* Workshop on Limits of existence of Light Nuclei, Trento, Italy (October 2010).

*ANC for  $^7\text{Be} \rightarrow ^3\text{He} + \alpha$  from Elastic Scattering Phase Shift and Astrophysical Factor for  $^3\text{He} + \alpha \rightarrow ^7\text{Be} + \gamma$* , **A.M. Mukhamedzhanov, Invited Talk**, Workshop on  $^3\text{He} + \alpha \rightarrow ^7\text{Be} + \gamma$  astrophysical factor, ATOMKI, Debrecen, Hungary (November 2010).

*Freeze-out Properties of Hot Nuclear Matter Created in Heavy-Ion Collisions*, **S. Shlomo, Invited Talk**, The 3<sup>rd</sup> International Conference on Current Problems in Nuclear Physics and Atomic Energy (NPAE-Kyiv2010), Kiev, Ukraine (June 2010).

*Temperature and Density Dependence of Properties of Nuclear matter Deduced from Heavy-Ion Collisions*, **S. Shlomo, Invited Talk**, Capathian Summer School of Physics 2010 (CSSP10), Sinaia, Romania (June 2010).

*Quark Recombination in Heavy Ion Collisions*, **R.J. Fries, Invited Talk**, Workshop on RHIC Paradigms, Austin, Texas (April 2010).

*Quark Recombination in Heavy Ion Collisions*, **R.J. Fries, Invited Talk**, JET Collaboration Meeting, Berkeley, California (June 2010).

*Jet Chemistry and Contributions to EM Probes*, **R.J. Fries, Invited Talk**, INT Workshop on Quantifying Properties of Hot QCD Matter, Institute for Nuclear Theory, University of Washington, Seattle, Washington (July 2010).

*Event-by-Event Jet Quenching and Fourier Moments*, **R.J. Fries**, **Invited Talk**, 4<sup>th</sup> International Conference on Hard and Electromagnetic Probes of High Energy Nuclear Collisions (Hard Probes 2010), Eilat, Israel (October 2010).

*Quark Recombination and Quark Scaling – Still Puzzling?*, **R.J. Fries**, **Invited Talk**, International Workshop on From Strong Fields to Colorful Matter, Asheville, North Carolina (October 2010).

*Probing Quark Gluon Matter*, **R.J. Fries**, **Invited Talk**, RBRC Review Meeting, Brookhaven National Laboratory, Upton, New York (October 2010).

*Event-by-Event Jet Quenching and Fourier Moments*, **R.J. Fries**, **Invited Talk**, APS Division of Nuclear Physics Meeting (DNP 2010), Santa Fe, New Mexico (November 2010).

*Some Challenges and Opportunities for Hard Probes*, **R.J. Fries**, **Invited Seminar**, McGill University, Montreal, Quebec, Canada (November 2010).

*Behavior of Early Time Gluon Fields in High Energy Nuclear Collisions*, **G. Chen**, APS Division of Nuclear Physics Meeting (DNP 2010), Santa Fe, New Mexico (November 2010).

*Quark Equilibrium Recombination and Elliptic Flow Scaling*, **M. He**, APS Division of Nuclear Physics Meeting (DNP 2010), Santa Fe, New Mexico (November 2010).

*Toward a Complete Description of Heavy-Flavor Transport in Medium*, **M. He**, International Workshop on Heavy Quark Production in Heavy-Ion Collisions, Purdue University, West Lafayette, Indiana, (January 2011).

*Quale Energia per il Futuro?*, **A. Bonasera**, Presentation of the book at International Book Fair, Turin, Italy (May 2010).

*Probing the Nuclear Equation of State*, **A. Bonasera**, Oak Ridge National Laboratory, Oak Ridge, Tennessee (February 2011).

*Signals of Critical Behavior of the Finite Nuclei*, **A. Bonasera**, 241<sup>st</sup> ACS Meeting, Anaheim, California (March 2011).

*Energy for the Future?* **A. Bonasera**, **Invited Talk**, Saturday Morning Physics, Texas A&M University, College Station, Texas (March 2011).

*Update on Potential Models*, **F. Riek**, **Invited Talk**, International Workshop on Heavy Quarkonium 2010 (QWG10), Fermilab, Batavia, Illinois (May 2010).

*Heavy Quark/onium in Medium and in Heavy-Ion Collisions*, **R. Rapp**, **Invited Talk**, EMMI Workshop on Quarkonium and Deconfined Matter in the LHC Era, Martina Franca, Italy (June 2010).

*In-Medium Vector Mesons, Dileptons and Chiral Restoration*, **R. Rapp**, **Invited Plenary Talk**, International Workshop on Chiral Symmetry in Hadrons and Nuclei (Chiral 2010), Valencia, Spain (June 2010).

*Heavy Quark/onium in Hot Nuclear Matter*, **R. Rapp**, **Invited Talk**, International program on Quantifying the Properties of Hot QCD Matter, Seattle, Washington (July 2010).

*Electromagnetic Probes of the Medium - Status of the Field*, **R. Rapp**, **Invited Talk**, International program on Quantifying the Properties of Hot QCD Matter, Seattle, Washington (July 2010).

*Dileptons at RHIC: Theoretical Considerations*, **R. Rapp**, **Invited Talk**, International Workshop on Electromagnetic Probes of Strongly Interacting Matter, ECT\*, Trento, Italy (September 2010).

*Theory of Heavy Flavor in the Quark-Gluon Plasma*, **R. Rapp**, **Invited Plenary Talk**, International Conference on Physics and Astrophysics of QGP (ICPAQGP 2010), Goa, India (December 2010).

*Heavy-Quark Diffusions in QGP*, **M. He**, **Invited Talk**, Int. Workshop on Heavy-Quark Production in Heavy-Ion Collisions, Purdue Univ., West Lafayette, Indiana (January 2011).

*Electromagnetic Spectral Functions and the Quark-Hadron Transition*, **R. Rapp**, **Invited Talk**, STAR Di-Electron Focus Meeting, Lawrence Berkeley National Laboratory, Berkeley, California (March 2011).

*Heavy-Quark Probes of the Quark-Gluon Plasma*, **R. Rapp**, **Invited Seminar**, Physics Division, Argonne National Laboratory, Argonne Illinois (April 2010).

*Charmonium Production in Heavy-Ion Collisions*, **X. Zhao**, **Invited seminar**, Lawrence Berkeley National Laboratory, Berkeley, California (June 2010).

*Charmonium Production in Heavy-Ion Collisions*, **X. Zhao**, **Invited seminar**, Iowa State University, Ames, Iowa (June 2010).

*Spektrale Analysis von QCD Materie*, **R. Rapp**, **Invited colloquium**, Giessen University, Germany (June 2010).

*Rho Mesons in Medium at RHIC and JLab*, **R. Rapp**, **Invited Seminar**, Jefferson Laboratory, Newport News, Virginia (March 2011).

*Quark-Gluon Plasma: Theory and Phenomenology*, **R. Rapp**, **Research Lectures** for condensed matter physicists, Texas A&M University, College Station, Texas (March - May 2010).

## RESEARCH PERSONNEL AND ENGINEERING STAFF

April 1, 2010 - March 31, 2011

### Faculty and Research Group Leaders

Aldo Bonasera, Research Scientist  
Charles M. Folden III, Assist. Prof. of Nuclear Chemistry  
Rainer Fries, Assist. Professor of Physics  
Carl A. Gagliardi, Professor of Physics  
John C. Hardy, Professor of Physics  
Che Ming Ko, Professor of Physics  
Dan Melconian, Assist. Professor of Physics  
Saskia Mioduszewski, Assist. Prof. of Physics  
J. B. Natowitz, Professor of Chemistry, Bright Chair  
Ralf Rapp Associate Professor of Physics  
Shalom Shlomo, Senior Scientist  
Robert E. Tribble, Professor of Physics, Director  
Rand L. Watson, Professor of Chemistry - Retired  
Sherry J. Yennello, Professor of Chemistry  
Dave H. Youngblood, Professor of Physics  
Akram M. Zhanov, Senior Scientist

### Research Staff

Marina Barbui, Assist. Research Scientist – From 12/1/10  
Henry Clark, Accelerator Physicist (50%)  
Grigor Chubaryan, Research Scientist  
John C. Hagel, Research Scientist (50%)  
Vladimir Horvat, Research Scientist (50%)  
Victor Iacob, Associate Research Scientist  
Yiu-Wing Lui, Research Scientist  
Ninel Nica, Assist. Research Scientist  
George Souliotis, Associate Research Scientist  
Livius Trache, Research Scientist  
Ryoichi Wada, Research Scientist

### Visiting Scientists

Nuray Er – From 11/1/10  
Vladilen Goldberg  
Taesoo Song – To 6/30/10  
Ian Towner – From 6/25/10 To 9/16/10

### Accelerator Physics and Radiation Line Staff

Joseph Brinkley, Research Associate  
Henry Clark, Accelerator Physicist (50%)  
Vladimir Horvat, Research Scientist (50%)

Bruce Hyman, Research Associate  
George Kim, Accelerator Physicist  
Don May, Accelerator Physicist  
Gabriel Tabacaru, Accelerator Physicist

### Computer Systems Staff

Robert Burch, Jr., Lead Microcomputer/LAN Administrator  
John C. Hagel, Research Scientist (50%)

### Engineering Staff

Greg Derrig, Senior Mechanical Engineer  
Robert Olsen, Senior Mechanical Engineer

### Postdoctoral Research Associates

Abeer Alharbi – To 7/31/10  
Adriana Banu – To 8/25/10  
Marina Barbui – To 11/30/10  
Lixin Chen  
Pibero Djawotho  
Ahmed Hamed  
Min He  
Krishichayan  
Paola Marini  
Alan McIntosh – From 6/14/10  
Gian Luca Pizzone – From 2/16/11  
Felix Riek – To 6/30/10  
Marcia Rodrigues  
Ricardo Rodriguez – To 8/31/10  
Brian Roeder  
Katarzyna Schmidt – From 4/6/10  
Praveen Shidling  
Taesoo Song – From 7/1/10  
Rahul Tripathi – To 3/1/11  
Jun Xu

## STUDENTS

April 1, 2010 - March 31, 2011

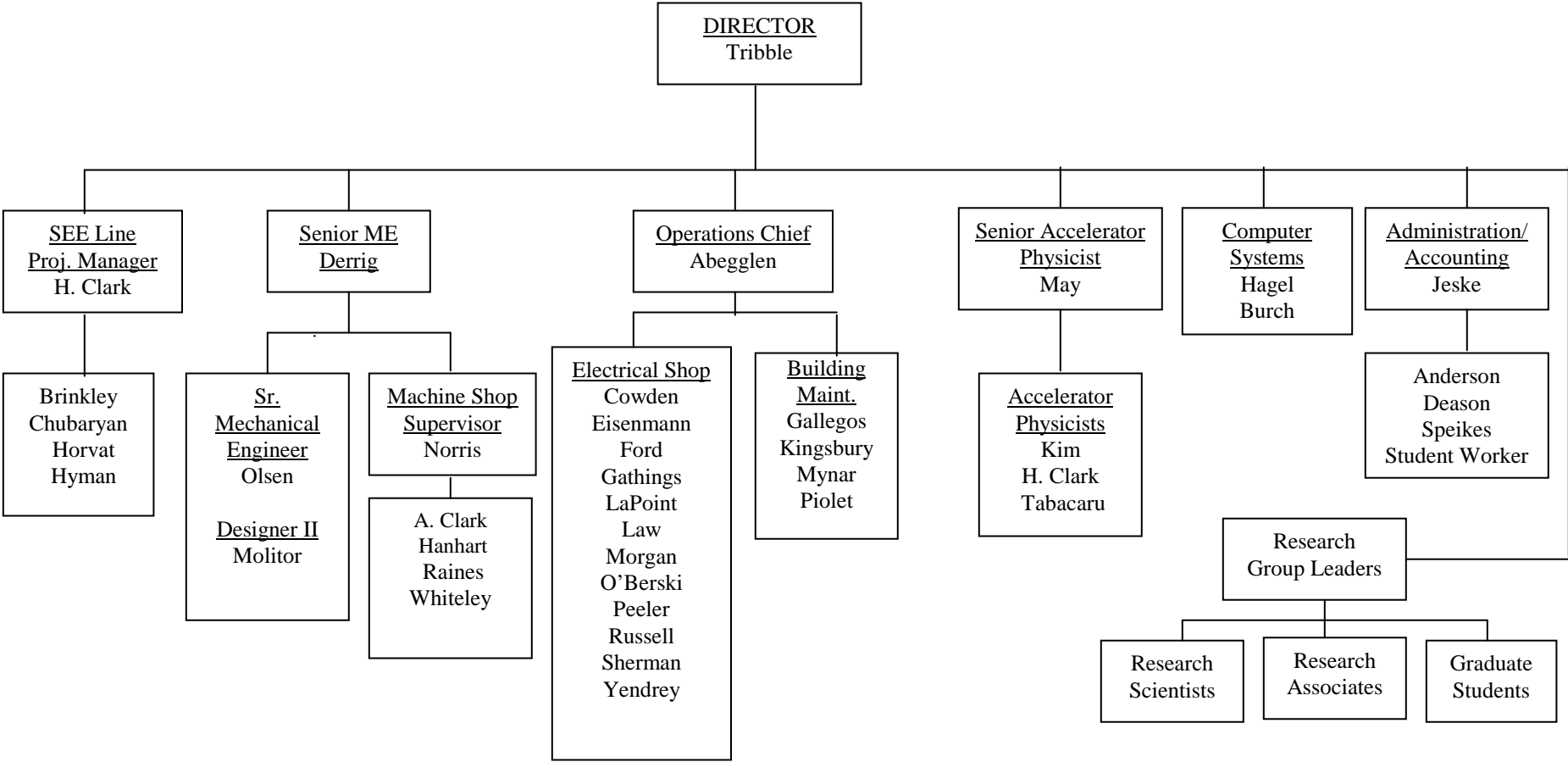
### Graduate Students

Mason Anders – From 5/15/10  
Marisa Alfonso  
Matteo Barbarino – From 1/16/11  
Richard Spence Behling  
Jonathan Button  
Matthew Cervantes  
Roman Chyzh – From 9/1/10  
Guangyao Chen  
Martin Codrington  
James Drachenberg  
Benjamin Fenker – From 1/15/11  
John Goodwin  
Kyong Choi Han  
Lauren Heilborn – From 6/14/10  
Kyle Higgins – From 6/15/10  
Liaoyuan Huo  
Zach Kohley – To 8/31/10  
Feng Li – From 6/1/10  
Larry May  
Demitri Mayarov  
Matthew McCleskey  
Michael Mehlman – From 5/12/10  
Hyo-In Park  
Andrew Raphelt – From 6/1/10  
John Saathoff – To 5/13/10  
Ellen Simmons  
Sarah Soisson – To 12/14/10  
Alexandra Spiridon  
Brian Stein  
Tyler Werke – From 6/22/10  
Xingbo Zhao – To 11/30/10  
Hua Zheng

### Undergraduates and Student Technicians

Giacoma Bonasera  
Todd Hammer – To 8/31/10  
Sarah Loupot – To 8/16/10  
Kyle Molitor – From 6/2/10  
Ashley Noack  
Robert Polis – To 8/16/10  
Amanda Spaw  
Ruslan Vselodovna – From 6/21/10 To 3/21/11

**ORGANIZATIONAL CHART - CYCLOTRON INSTITUTE**



**STUDENTS WHO RECEIVED GRADUATE DEGREES  
FROM THESIS WORK CONDUCTED  
AT  
THE CYCLOTRON INSTITUTE**

**April 1, 2010 – March 31, 2011**

Name	Year	Thesis Title	Advisor	Present Position
Zach Kohley	2010	<i>Transverse Collective Flow and Emission Order of Mid-Rapidity Fragments in Fermi Energy Heavy Ion Collisions</i>	S. J. Yennello	Post Doc., HRIBF, ORNL, Oak Ridge, Tennessee
Xingbo Zhao	2010	<i>Charmonium in Hot Medium</i>	Ralf Rapp	Post Doc., Department of Physics, Iowa State University, Ames, Iowa
Sarah Nicole Soisson	2010	<i>Isospin Dependence of Fragmentation</i>	S. J. Yennello	Senior Member of Technical Staff, Sandia National Lab., Albuquerque, New Mexico

## INSTITUTE COLLOQUIA AND SEMINARS

April 1, 2010-March 31, 2011

### 2010

- |            |  |   |
|------------|--|---|
| May 11     | Dr. J. J. Ressler, Lawrence Livermore National Laboratory, Livermore, California   | <i>Surrogate Reactions for Nuclear Energy Application</i>   |
| May 12     | Professor Lie-Wen Chen, Institute of Nuclear, Particle Astronomy and Cosmology (INPAC) and Department of Physics, Shanghai Jiao Tong University, Shanghai, China | <i>Probing the Nuclear Symmetry Energy with Heavy-Ion Reactions and Neutron Skin Thickness of Heavy Nuclei</i>  |
| May 13     | Professor A. R. Young, Department of Physics, North Carolina State University, Raleigh, North Carolina   | <i>Measurements of Beta-Decay in the Neutron and <math>^{19}\text{Ne}</math> : Some Recent Progress</i>         |
| May 17     | Professor Robert Page, Department of Physics, University of Liverpool, United Kingdom  | <i>Probing Nuclear Structure beyond the Proton Drip Line</i>  |
| May 18     | Dr. Cristian P. Lungu, National Institute for Laser, Plasma and Radiation Physics, Bucharest,  | <i>Study of the Ternary Be-C-W System Formation using Thermionic Vacuum Arc Method</i>                          |
| June 3     | Dr. Paolo Finocchiaro, INFN – Laboratori Nazionali del Sud, Catania, Italy   | <i>Low-Energy Low-Intensity Ion Beam Diagnostics with Detectors</i>   |
| June 15    | Professor M. Norrby, Department of Physics, Abo Akademi University, Turku, Finland   | <i>Alpha Clusters in <math>^{32}\text{S}</math>, <math>^{34}\text{S}</math> and <math>^{40}\text{Ca}</math></i> |
| July 30    | Dr. Martin Petrick, Giessen University, Germany  | <i>Precise Electrostatic Spectrometers for Time-of-Flight Mass Measurements</i>                                 |
| August 24  | Dr. Robert Janssens, Argonne National Laboratory, Argonne, Illinois  | <i>The Hunt for New Shell Structure in Neutron-Rich Nuclei</i>  |
| October 5  | Professor Brian Fields, Department of Astronomy and Physics, University of Illinois, Urbana, Illinois  | <i>Primordial Nucleosynthesis after WMAP: The Lithium Problem and New Physics</i>                               |
| October 12 | Mr. Gregory K. Pang, NSCL, Michigan State University, East Lansing, Michigan   | <i>RF Carpet Development at the NSCL</i>  |

November 8	Dr. Ken-ichiro Yoneda, SAMURAI Team, Riken, Waco, Japan	<i>A New Spectrometer in RIKEN RIBF-SAMURAI</i>
November 9	Professor L. G. Sobotka, Department of Chemistry and Physics, Washington University, St. Louis, Missouri	<i>2p-2p Decay in <math>^8\text{C}</math> and other 2p Decay Cases in Light Nuclei</i>
November 22	Dr. Olena Linnyk, Frankfurt Institute for Advanced Study (FIAS), Frankfurt, Germany	<i>Dilepton Production at SPS and RHIC Energies</i>

## 2011

January 11	Dr. Megan E. Bennett, University of Nevada, Las Vegas, Nevada	<i>Extraction Chromatographic Studies of Rf (Z=104) Homologs using Crown Ether Based Resins</i>
February 15	Dr. Aldo Bonasera, Cyclotron Institute, Texas A&M University, College Station, Texas	<i>Probing the Nuclear Equation of State</i>
February 22	Dr. R. Wada, Cyclotron Institute, Texas A&M University, College Station, Texas	<i>Hot Nuclear Matter Properties and Reaction Dynamics in Intermediate Heavy Ion Reactions</i>
March 8	Dr. Sakir Ayik, Physics Department, Tennessee Tech University, Cookeville, Tennessee	<i>A Stochastic Mean-Field Approach for Nuclear Dynamics</i>
March 15	Professor L. G. Sobotka, Department of Chemistry and Physics, Washington University, St. Louis, Missouri	<i>The Asymmetry Enthalpy-<math>H_{asy}</math></i>
March 23	Dr. Robert Atcher, United States Department of Energy	<i>The US Isotope Production Program</i>
March 30	Professor Michael A. Bentley, Department of Physics, University of York, York, United Kingdom	<i>??Determining the Stellar Origin of the Cosmic <math>\gamma</math>-ray Emitting Nucleus <math>^{26}\text{Al}</math></i>